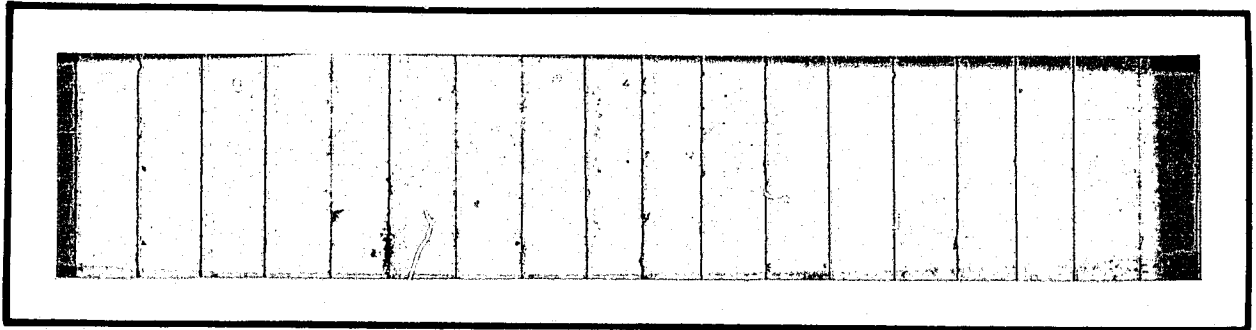


## **General Disclaimer**

### **One or more of the Following Statements may affect this Document**

- This document has been reproduced from the best copy furnished by the organizational source. It is being released in the interest of making available as much information as possible.
- This document may contain data, which exceeds the sheet parameters. It was furnished in this condition by the organizational source and is the best copy available.
- This document may contain tone-on-tone or color graphs, charts and/or pictures, which have been reproduced in black and white.
- This document is paginated as submitted by the original source.
- Portions of this document are not fully legible due to the historical nature of some of the material. However, it is the best reproduction available from the original submission.

CR 151700



# Axiomatix

(NASA-CR-151700) INTEGRATED SOURCE AND  
CHANNEL ENCODED DIGITAL COMMUNICATION SYSTEM  
DESIGN STUDY Final Report (Axiomatix,  
Marina del Rey, Calif.) 362 p HC A02/MF A01

N78-22271

CSCL 17B G3/32

Unclas  
16658



Marina del Rey • California

INTEGRATED SOURCE AND CHANNEL ENCODED  
DIGITAL COMMUNICATION SYSTEM  
DESIGN STUDY

FINAL REPORT

Contract No. NAS 9-15240

Prepared for

NASA Lyndon B. Johnson Space Center  
Houston, Texas 77058

Prepared by

Waddah K. Alem  
Gaylord K. Huth  
Marvin K. Simon

Axiomatix  
13900 Panay Way, Suite 110M  
Marina del Rey, California 90291

Axiomatix Report No. R7803-7  
March 31, 1978

# TABLE OF CONTENTS

	Page
LIST OF TABLES . . . . .	iv
LIST OF FIGURES . . . . .	v
1.0 INTRODUCTION . . . . .	1
2.0 KU-BAND SYSTEM DESIGN EVALUATION . . . . .	3
2.1 Impact of Data Asymmetry on Bit Error Probability of the Ku-Band Return Link . . . . .	3
2.1.1 Asymmetry Models and Definitions . . . . .	4
2.1.2 Error Probability Performance (Perfect Symbol Synchronization) . . . . .	7
2.1.3 Error Probability Performance (Imperfect Symbol Synchronization) . . . . .	8
2.1.4 Error Probability Performance for Asymmetric Manchester Coded Symbols . . . . .	11
2.1.5 The Effect of D.C. Restoration on Error Probability Performance in the Presence of Asymmetry . . . . .	19
2.1.6 The Combined Effects of Bandlimiting and Data Asymmetry on Error Probability Performance . . . . .	24
2.1.7 Performance of a Gated Integrate-and- Dump Filter for Detection of Asymmetric Data . . . . .	33
2.2 Antijam Techniques for Shuttle Communication . . . . .	39
2.2.1 Direct Sequence Pseudonoise Spreading . . . . .	39
2.2.2 Frequency Hopping . . . . .	42
2.2.3 Time Hopping . . . . .	44
3.0 TRACKING TECHNIQUES ANALYSIS . . . . .	47
3.1 Tracking Performance of Unbalanced QPSK Demodulators . . . . .	49
3.1.1 Biphase Costas Loop with Passive Arm Filters . . . . .	49
3.1.2 Biphase Costas Loop with Active Arm Filters . . . . .	54
3.1.3 Biphase Polarity-Type Costas Loop with Passive Arm Filters . . . . .	57
3.2 Performance of the Subcarrier Tracking Loop for the Three-Channel Orbiter Ku-Band Return Link . . . . .	61
3.3 Error Probability Performance of Channels 2 and 3 of the Three-Channel Ku-Band Return Link . . . . .	62



	Page
3.4 Techniques for Improved Tracking of Unbalanced QPSK Modulation . . . . .	70
3.5 Costas Loop Tracking Performance on the Shuttle S-Band Uplink in the Presence of Residual Carrier . . . . .	80
4.0 PAYLOAD COMMUNICATION STUDY . . . . .	90
4.1 Forward Link Bent-Pipe Relay Design . . . . .	90
4.2 Return Link Bent-Pipe Relay Design . . . . .	99
REFERENCES . . . . .	107

#### Appendix

- A. Bit Error Rate Degradation of the Ku-Band Return Link Channel Due to NRZ Data Symbol Asymmetry
- B. Further Considerations on the Effects of Data Asymmetry on Bit Error Rate Performance of the Ku-Band and S-Band Return Link Channels
- C. The Combined Effects of Bandlimiting and NRZ Data Asymmetry on the Bit Error Probability Performance of a Sample Detector
- D. Detection of Asymmetric NRZ Data Using a Gated Integrate-and-Dump Filter
- E. Tracking Performance of Unbalanced QPSK Demodulators; Part I - Biphase Costas Loop with Passive Arm Filters
- F. Tracking Performance of Unbalanced QPSK Demodulators; Part II - Biphase Costas Loop with Active Arm Filters
- G. Tracking Performance of Unbalanced QPSK Demodulators; Part III - Biphase Polarity-Type Costas Loop with Passive Arm Filters
- H. Subcarrier Tracking Analysis for Three-Channel Orbiter Ku-Band Return Link
- I. Error Probability Performance of Unbalanced QPSK Receivers
- J. Practical Design Considerations Associated with Optimum Carrier Reconstruction Techniques for Unbalanced QPSK
- K. On the Equivalence in Performance of a Practical Realization of a MAP Estimation Loop for Balanced QPSK and a Conventional Quadriphase Costas Loop
- L. The Effects of Residual Carrier on Costas Loop Performance as Applied to the Shuttle S-Band Uplink

ORIGINAL PAGE IS  
OF POOR QUALITY

# LIST OF TABLES

	Page
1. Performance Degradation Due to Data Asymmetry with Random Data . . . . .	8
2. No D.C. Restoration . . . . .	32
3. D.C. Restoration by Capacitive Coupling . . . . .	32
4. Antijam Performance of Frequency Hopping . . . . .	45
5. Critical Values of Data Modulation Index on the S-Band Uplink . . . . .	83
6. Tracking Threshold Signal Levels in the PSK Mode . . . . .	85
7. System Parameters for Calculation of $P'/N_0$ . . . . .	86
8. Power-to-Noise Ratio in the Ranging Channel . . . . .	86

# LIST OF FIGURES

	Page
1a. Asymmetric Data Stream Using Asymmetry Model 1 . . . . .	6
1b. Asymmetric Data Stream Using Asymmetry Model 2 . . . . .	6
2. SNR Degradation Due to Data Asymmetry as a Function of Symbol Sync Clock Misalignment . . . . .	10
3. Average Error Probability with Symbol Synchronization Error as a Parameter (3% Asymmetry), NRZ Data . . . . .	12
4. Average Error Probability with Symbol Synchronization Error as a Parameter (6% Asymmetry), NRZ Data . . . . .	13
5a. Asymmetric Manchester Coded Waveform - Asymmetry Model 1 . . . . .	15
5b. Asymmetric Manchester Coded Waveform - Asymmetry Model 2 . . . . .	15
6. SNR Degradation vs. Percent Asymmetry for Manchester and NRZ Coded Data . . . . .	17
7. SNR Degradation vs. Percent Asymmetry for Manchester and NRZ Coded Data . . . . .	18
8. Average Error Probability with Symbol Synchronization Error as a Parameter (3% Asymmetry), Manchester Coded Data . . . . .	20
9. Average Error Probability with Symbol Synchronization Error as a Parameter (6% Asymmetry), Manchester Coded Data . . . . .	21
10. Performance Degradation for Capacitively Coupled Matched Filters; Random Data . . . . .	23
11. Performance Degradation for DC Restoration Based on Symbol Timing . . . . .	25
12. Band Limit and Sample Detector for Binary Data with Asymmetry . . . . .	26
13. Bit Error Probability as a Function of Energy-to- Noise Ratio with Filter Bandwidth - Bit Time Product as a Parameter and Fixed Data Asymmetry; No D.C. Restoration . . . . .	28
14. Energy-to-Noise Ratio as a Function of Data Asymmetry for Fixed Bit Error Probability and Filter Bandwidth - Bit Time Product as a Parameter; No D.C. Restoration . . .	29

	Page
15. Bit Error Probability as a Function of Signal-to-Noise Ratio with Filter Bandwidth - Bit Time Product as a Parameter and Fixed Data Asymmetry; D.C. Restoration by Capacitive Coupling . . . . .	30
16. Energy-to-Noise Ratio as a Function of Data Asymmetry for Fixed Bit Error Probability and Filter Bandwidth - Bit Time Product as a Parameter; D.C. Restoration by Capacitive Coupling . . . . .	31
17. Gated Integrate-and-Dump Filter . . . . .	34
18. Average Error Probability versus Gate Interval at Symbol Edge with Data Asymmetry as a Parameter - No D.C. Restoration . . . . .	36
19. Symbol Energy-to-Noise Ratio versus Data Asymmetry with Gate Interval at Symbol Edge as a Parameter - No D.C. Restoration . . . . .	37
20. Average Error Probability versus Gate Interval at Symbol Edge with Data Asymmetry as a Parameter - D.C. Restoration by Capacitive Coupling . . . . .	38
21. Symbol Energy-to-Noise Ratio versus Data Asymmetry with Gate Interval at Symbol Edge as a Parameter - D.C. Restoration by Capacitive Coupling . . . . .	40
22. Three-Channel Quadrature Multiplex Modulator - Model 1 . . . . .	48
23. Squaring Loss vs. Ratio of Arm Filter Bandwidth to High Data Rate . . . . .	51
24. Tracking Jitter Standard Deviation versus Ratio of Arm Filter Bandwidth to High Data Rate . . . . .	52
25. Tracking Jitter Standard Deviation versus $P_T T_2 / N_0$ . . . . .	53
26. Squaring Loss Improvement Using Integrate-and-Dump Arm Filters as Opposed to Single-Pole Passive Arm Filters . . . . .	55
27. Squaring Loss Improvement Using Integrate-and-Dump Arm Filters as Opposed to Single-Pole Passive Arm Filters . . . . .	56
28. Costas Loop with Hard-Limited In-Phase Channel . . . . .	58
29. Squaring Loss Variations Versus $B_1 / R_2$ with $R_2 / R_1$ and $P_T T_2 / N_0$ as Parameters . . . . .	60

	Page
30. Subcarrier Tracking Jitter versus Ratio of Arm Filter Bandwidth to High Subcarrier Data Rate $R_2$ . . . . .	63
31. Subcarrier Tracking Jitter Versus Ratio of Arm Filter Bandwidth to High Subcarrier Data Rate $R_2$ . . . . .	54
32. Channel 2 Noisy Reference Loss vs. the Ratio of Two-Sided Costas Loop Arm Filter Bandwidth to Channel 2 Data Rate . . . . .	67
33. Channel 3 Noisy Reference Loss vs. the Ratio of Two-Sided Costas Loop Arm Filter Bandwidth to Channel 2 Data Rate . . . . .	68
34. A Practical Realization of the MAP Estimation Loop for QPSK; Passive Arm Filters, Small SNR . . . . .	72
35. A Practical Realization of the MAP Estimation Loop for UQPSK; Passive Arm Filters, Small SNR . . . . .	73
36. A Practical Realization of the MAP Estimation Loop for UQPSK; Passive Arm Filters, Small SNR . . . . .	74
37. Squaring Loss vs. Power Ratio for Unbalanced QPSK; Two-Channel Costas Loop; $n = T_2/T_1 = 1$ . . . . .	75
38. Squaring Loss vs. Power Ratio for Unbalanced QPSK; Two-Channel Costas Loop; $n = T_2/T_1 = 2$ . . . . .	76
39. Squaring Loss Versus Power Ratio for Unbalanced QPSK; Two-Channel Costas Loop; $n = T_2/T_1 = 10$ . . . . .	77
40. A Comparison of the Squaring Loss Performance of One- and Two-Channel Costas Loops . . . . .	79
41. Costas Loop and Ranging Demodulator . . . . .	82
42. Tracking Threshold Power-to-Noise Ratio for PM Mode vs. Ranging Modulation Index with Data Modulation Index as a Parameter . . . . .	88
43. Ranging Channel Power-to-Noise Ratio Versus Ranging Modulation Index with Data Modulation Index as a Parameter . . . . .	89
44. Ku-Band Forward Link Simplified Block Diagram . . . . .	91
45. Costas Loop for Normal and Bent-Pipe Demodulation . . . . .	93
46. Ratio of Subcarrier Bent-Pipe Signal Power to Total Power as a Function of Modulation Indices . . . . .	96

	Page
47. Ratio of Required Power in PM Mode to Power in PSK Mode as a Function of Modulation Indices; $R_d = 5$ dB . . . .	97
48. Ratio of Required Power in PM Mode to Power in PSK Mode as a Function of Modulation Indices; $R_d = 10$ dB . . . .	98
49. Standard Deviation of Tracking Phase Jitter for PM Mode . . . . .	100
50. Return Link Bent-Pipe Link Implementation . . . . .	101
51. Ku-Band Mode 2 FM Transmitter for Return Link Bent-Pipe Mode . . . . .	103
52. Ku-Band Mode 2 FM Receiver for Return Link Bent-Pipe Mode . . . . .	104

## 1.0 INTRODUCTION

This is the final report for the "Integrated Source and Channel Encoded Digital Communication System Design Study" (Contract No. NAS 9-15240). The contract is to evaluate the Ku-band system design, analyze S-band and Ku-band tracking techniques, and study payload communication techniques.

As defined in the Statement of Work, the first task required the evaluation and assessment of the baseline Ku-band system design under development by Hughes Aircraft Corporation (HAC) and study the performance/compatibility problems associated with the SSO/TDRSS RF interface. More specifically, the particular Ku-band carrier, PN despreading, and symbol synchronization strategies, which are selected by HAC for implementation in the Ku-band transponder aboard the Orbiter, are to be assessed and evaluated from a systems performance viewpoint, verifying that system specifications are met. Furthermore, it was required that any critical areas impacting the detailed conceptual and breadboard designs as they develop be identified, discussed and studied and appropriate recommendations made for parameter optimization, as necessary.

During the one-year period covered by the contract, Axiomatix continuously rendered support to HAC in all of the above areas, with the major thrust of its activity directed toward understanding, studying, and proposing potential solutions to the data asymmetry problem prevalent on the Mode 1 high data rate channel of the Ku-band return link. In this link, two selectable modes which provide three channels are available. Channel 1 is used for operational data, whereas Channels 2 and 3 may be assigned a wide variety of digital and analog signals. Additional support was provided by Axiomatix to assess the anti-jam capability of the SSO/TDRSS RF interface. The results of these activities are summarized in Section 2.0, with the detailed analyses, system performance comparisons, and tradeoffs included as Appendices A through D.

As a part of the overall effort to assess the Ku-band system design and to evaluate possible system simplifications/modifications that may be achievable, the second task required a study of the design and implementation of tracking techniques which are suitable for incorporation into the Orbiter Ku-band communication system. Emphasis was

placed on maximizing tracking accuracy and communication system flexibility while minimizing cost, weight, and system complexity of Orbiter and ground system hardware.

Section 3.0 summarizes the results obtained for the performance of several implementations of biphase Costas loops when subjected to the unbalanced QPSK input. The subcarrier tracking loop performance is also summarized in Section 3.0. The detailed analysis of both carrier and subcarrier tracking loops is presented in Appendices E through L.

Section 4.0 describes the payload communication study to assess the design and performance of the forward link and return link bent-pipe relay modes for attached and detached payloads. As part of this study, a design for a forward link bent-pipe is proposed which employs a residual carrier but which is tracked by the existing Costas loop. Detailed analysis of Costas loop tracking for signals with residual carrier is presented in Appendix L. Critical Ku-band system parameters have been identified and optimized such that cost and complexity have been minimized. Finally, Section 4.0 identifies the basic transmission capabilities that can be accommodated by both the forward link and return link bent-pipe relay modes.



## 2.0 KU-BAND SYSTEM DESIGN EVALUATION

As defined in the Statement of Work, this task required Axiomatix to evaluate and assess the baseline Ku-band system design under development by Hughes Aircraft Corporation (HAC) and study the performance/compatibility problems associated with the SSO/TDRSS RF interface. More specifically, the particular Ku-band carrier, PN despread, and symbol synchronization strategies, which are selected by HAC for implementation in the Ku-band transponder aboard the Orbiter, are to be assessed and evaluated from a systems performance viewpoint, verifying that system specifications are met. Furthermore, Axiomatix was required to identify, discuss, and study any critical areas which impact the detailed conceptual and breadboard designs as they develop and to make appropriate recommendations for parameter optimization, as necessary.

During the one-year period covered by this contract, Axiomatix continuously rendered support to HAC in all of the above areas, with the major thrust of its activity directed toward understanding, studying, and proposing potential solutions to the data asymmetry problem prevalent on the Mode 1 high data rate channel of the Ku-band return link. Additional support was provided by Axiomatix to assess the anti-jam capability of the SSO/TDRSS RF interface. The results of these activities are summarized in what follows, with the detailed analyses, system performance comparisons, and tradeoffs included as Appendices A through D.

### 2.1 Impact of Data Asymmetry on Bit Error Probability Performance of the Ku-Band Return Link

In the early months of the Task 1 effort, an area of concern developed over the data asymmetry\* produced by the HAC design of the 50 Mbps (100 Msps) rate 1/2 convolutionally coded data channel of the Ku-band return link through the TDRSS. This data asymmetry was potentially capable of causing several dB degradation to the demodulated data at the TDRSS ground station. Therefore, a suitable asymmetry model had to be developed, the amount of degradation as a function of the amount

---

\*The term "data asymmetry" as used here denotes the condition in which pulses of opposite polarity in the data stream unintentionally have unequal widths.

of asymmetry had to be computed, and the possible solutions to the problem had to be investigated.

The high data rate link from the Shuttle Orbiter through the TDRSS to the ground takes NRZ symbols at 50 Mbps and encodes them with a rate  $1/2$ , constraint length 7, convolutional code. The bit error rate performance of the convolutional decoder depends, among other things, on the symmetry of the modulation. Any asymmetry in the NRZ symbols entering the symbol synchronizer causes a misalignment in the symbol synchronization clock which degrades the integrate-and-dump output and any soft or hard decisions derived from it for input to the decoder. For a specified degree of asymmetry (in terms of a fraction of a symbol interval), the bit error rate degradation is dependent on the transition probability of the data. Clearly, if the data transmitted was either all ones or all minus ones, misalignment of the bit synchronization clock would have no degrading effect on the integrate-and-dump output since, for each symbol, this circuit would integrate up to its maximum value before being dumped. On the other hand, when the data is an alternating sequence, the worst case degradation results, since the transition which occurs at the end of each symbol in combination with the symbol synchronization clock misalignment prevents the integrate-and-dump output from reaching its maximum value.

### 2.1.1 Asymmetry Models and Definitions

To quantitatively determine the degrading effect of NRZ symbol asymmetry on error rate performance, one must develop a suitable asymmetry model which accurately describes the physical source from which the asymmetry originates. During the early definition phase of the study, much confusion reigned over the appropriate model and definition of data asymmetry to be used in meeting the performance specification. After expending considerable effort on resolving the differences among the various models and definitions proposed, it was determined that two possible models were appropriate and, provided that asymmetry was properly defined, either model produced the identical performance degradation due to this asymmetry. In the first model (the one adopted by Axiomatix), the assumption is made that +1 NRZ symbols are elongated by  $\Delta T/2$  (relative to their nominal value of  $T$  sec) when a negative-going data

transition occurs and -1 symbols are shortened by the same amount when a positive-going data transition occurs.\* Otherwise (when no transitions occur), the symbols maintain their nominal T sec width. Thus,  $\Delta T$  represents the relative difference in length between the elongated +1 and shortened -1 symbols. An example demonstrating this model is illustrated in Figure 1a. The second asymmetry model (used in [1,2]) makes the assumption that positive NRZ pulses are shortened whenever adjacent pulses are negative. Thus, a given positive pulse preceded and succeeded by a negative pulse would be reduced in duration at both ends. Stated another way, a positive-going transition occurs early and a negative-going transition occurs late relative to the nominal transition time instants. Letting  $\delta$  represent the fractional (relative to the nominal bit duration T) increase in positive pulse length due to a single adjacent negative pulse, then for a given random data sequence, the shortest pulse would have length  $T(1 - 2\delta)$ , while the longest would have length  $T(1 + 2\delta)$ . Figure 1b illustrates the application of the second asymmetry model to the same bit stream as that used in Figure 1a.

Regardless of which asymmetry model is used, data asymmetry is defined as the difference in length between the shortest and longest pulses in the sequence divided by their sum. For the first model, this definition gives

$$\text{Asymmetry} \triangleq \eta = \frac{T(1 + \frac{\Delta}{2}) - T(1 - \frac{\Delta}{2})}{T(1 + \frac{\Delta}{2}) + T(1 - \frac{\Delta}{2})} = \frac{\Delta}{2}, \quad (1)$$

whereas for the second model, we get

$$\eta = \frac{T(1 + 2\delta) - T(1 - 2\delta)}{T(1 + 2\delta) + T(1 - 2\delta)} = 2\delta. \quad (2)$$

In the absence of noise, the timing instants for the in-phase integrate-and-dump (i.e., the epoch of the symbol synchronization clock) are determined in Appendix A. For the first asymmetry model, these

---

\* Due to symmetry in the data itself, it is immaterial whether the elongated pulse is of positive or negative polarity, and vice versa for the shortened pulse.

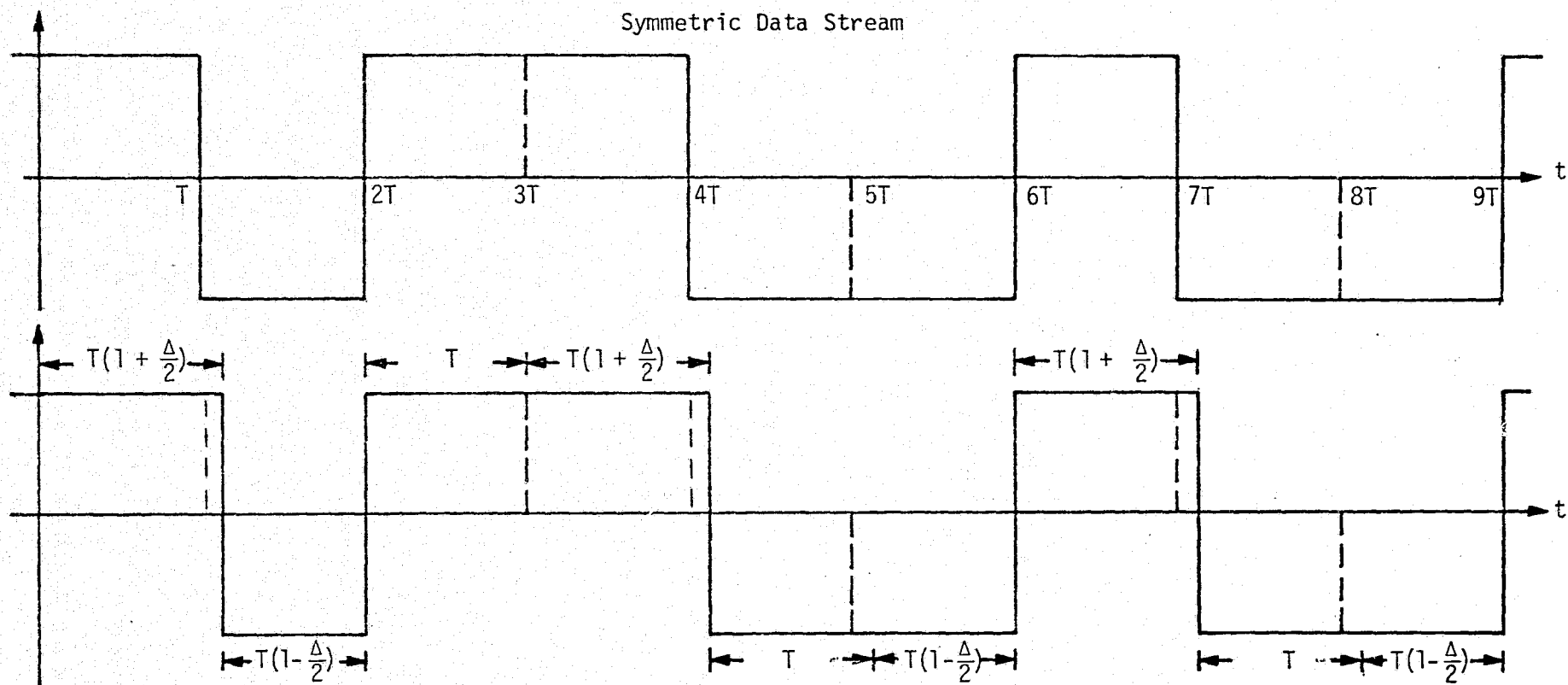


Figure 1a. Asymmetric Data Stream Using Asymmetry Model 1

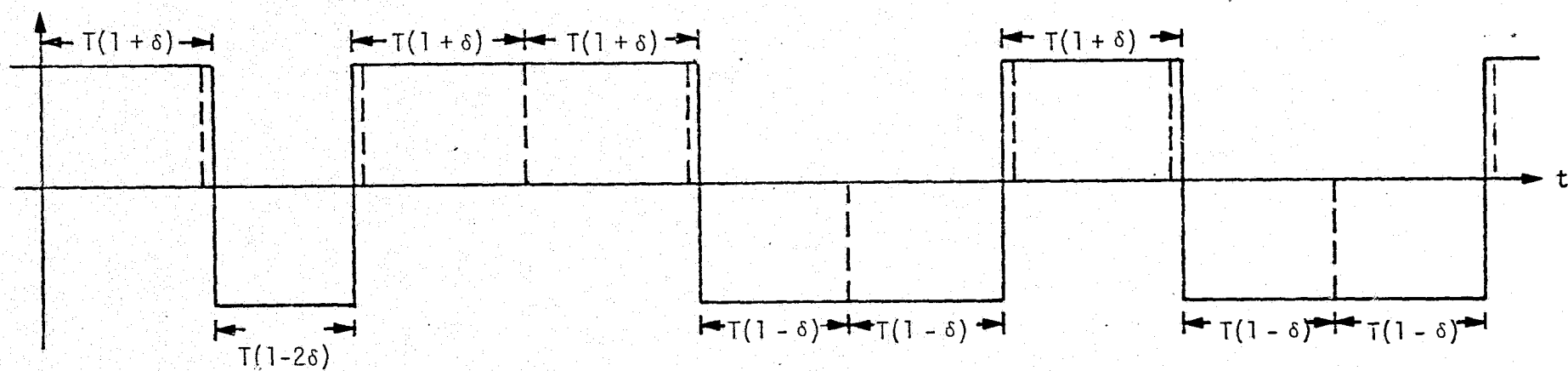


Figure 1b. Asymmetric Data Stream Using Asymmetry Model 2

occur at  $t = T(n + \frac{\Delta}{4})$ ;  $n = 0, \pm 1, \pm 2, \dots$ . For the second model, it can easily be shown that, on the average, the symbol synchronizer will lock up at the nominal transition points of the equivalent symmetric data waveform, i.e.,  $0, \pm T, \pm 2T, \pm 3T, \dots$ .

### 2.1.2 Error Probability Performance (Perfect Symbol Synchronization)

Based on the foregoing definition of asymmetry and the accompanying clock misalignment for the two models, it is straightforward to show that, for random NRZ data, the average symbol error probability associated with hard decisions made on the in-phase integrate-and-dump output of the symbol synchronizer is given by

$$P_E = \frac{5}{16} \operatorname{erfc} \sqrt{E_s/N_0} + \frac{1}{8} \operatorname{erfc} \left[ \sqrt{E_s/N_0} (1 - \eta) \right] + \frac{1}{16} \operatorname{erfc} \left[ \sqrt{E_s/N_0} (1 - 2\eta) \right], \quad (3)$$

where  $E_s$  denotes the symbol energy,  $N_0$  the channel noise spectral density, and

$$\operatorname{erfc} x \triangleq \frac{2}{\sqrt{\pi}} \int_x^{\infty} e^{-t^2} dt. \quad (4)$$

Table 1 contains the symbol energy-to-noise ratio degradations (in dB) for asymmetry values  $\eta \times 100$  of 3%, 7%, 10%, 15%, and 20%, and  $E_s/N_0 = 0, 0.75$ , and 1.5 dB. The values of  $E_s/N_0$  selected correspond to bit energy-to-noise ratios  $E_b/N_0 = 3, 3.75$ , and 4.5 which correspond respectively to decoder bit error probabilities  $P_b = 10^{-3}, 10^{-4}$  and  $10^{-5}$ . The degradations are the additional  $E_s/N_0$  required due to asymmetry to produce the same value of symbol error probability when  $\eta = 0$ , i.e.,  $P_E^0$ , where

$$P_E^0 \triangleq \frac{1}{2} \operatorname{erfc} (\sqrt{E_s/N_0}). \quad (5)$$

It should be noted that the symbol energy-to-noise ratio degradations given in Table 1 assume no channel bandwidth limitation, i.e., ideal rectangular pulse shapes have been assumed for the NRZ data. Any rounding of the pulses caused by channel bandwidth limitation produces an additional symbol energy-to-noise ratio degradation over and above

that due to data asymmetry. However, the bandlimiting degradation and the data asymmetry do not add algebraically but, rather, combine in a way determined by the particular symbol synchronization implementation. More will be said about the combined effects of bandlimiting and NRZ data asymmetry shortly.

Table 1. Performance Degradation Due to Data Asymmetry with Random Data

Asymmetry (%)	$E_s/N_0$ (dB)	$P_b$	Degradation (dB)
3	0	$10^{-3}$	0.135
	0.75	$10^{-4}$	0.135
	1.50	$10^{-5}$	0.135
7	0	$10^{-3}$	0.333
	0.75	$10^{-4}$	0.337
	1.50	$10^{-5}$	0.340
10	0	$10^{-3}$	0.495
	0.75	$10^{-4}$	0.505
	1.50	$10^{-5}$	0.517
15	0	$10^{-3}$	0.799
	0.75	$10^{-4}$	0.824
	1.50	$10^{-5}$	0.854
20	0	$10^{-3}$	1.149
	0.75	$10^{-4}$	1.201
	1.50	$10^{-5}$	1.264

### 2.1.3 Error Probability Performance (Imperfect Symbol Synchronization)

In the previous section, we presented the effect of NRZ data asymmetry on the error probability performance of a convolutionally coded channel, namely, the 50 Mbps channel of the Ku-band return link. Inherent in those results was the assumption that the symbol synchronizer produced a perfect clock which locked up with a misalignment equal to half the asymmetry for asymmetry Model 1 and no misalignment for Model 2. The effect of additional clock misalignment (commonly referred to as symbol sync jitter) which is typical of practical symbol synchronizers, was the next item studied under this task. The results

of this study, which are presented in detail in Appendix B, are now summarized.

For random NRZ data with equiprobable symbols, the average probability of error conditioned on the misalignment ( $\lambda T$ ) of the symbol synchronization clock relative to its nominal position is given by

$$P_E(\lambda) = \frac{5}{16} \operatorname{erfc} \sqrt{E_s/N_0} + \frac{1}{16} \operatorname{erfc} \left[ \sqrt{E_s/N_0} (1 - \eta - 2|\lambda|) \right] \\ + \frac{1}{16} \operatorname{erfc} \left[ \sqrt{E_s/N_0} (1 - \eta + 2|\lambda|) \right] + \frac{1}{16} \operatorname{erfc} \left[ \sqrt{E_s/N_0} (1 - 2\eta) \right]; \\ 0 \leq |\lambda| \leq \frac{\eta}{2}, \quad (6)$$

where either (1) or (2) still applies as the definition of asymmetry. Note that, when  $\lambda = 0$ , (6) reduces to (3). Figure 2 illustrates the SNR degradation at a symbol  $E_s/N_0$  of 1.5 dB (corresponding to a decoded bit error probability of  $10^{-5}$ ) as a function of  $\lambda$  with percent asymmetry  $\eta \times 100$  as a parameter. It is observed that, in the neighborhood of the nominal symbol synchronization lockup point ( $\lambda = 0$ ), the sensitivity of SNR degradation due to asymmetry is extremely small, even for large asymmetry values. This makes the results given in Section 2.1.2 relatively insensitive to the assumption of a hard-locked symbol synchronization, even though this assumption yields the minimum SNR degradation due to asymmetry.

Another approach (not discussed in Appendix B) to assessing SNR degradation due to both asymmetry and symbol synchronization misalignment is to assume a model probability density function  $p(\lambda)$  (p.d.f.) for  $\lambda$  and average the conditional error probability  $P_E(\lambda)$  over this p.d.f. to obtain the average error probability performance [2]. In this regard, we postulate a Tikhonov p.d.f. for  $p(\lambda)$  which is entirely characterized in terms of the variance  $\sigma_\lambda^2$  of the synchronization error. Thus, for NRZ data, we have [3],

$$p(\lambda) = \frac{\exp [\cos 2\pi \lambda / (2\pi \sigma_\lambda)^2]}{I_0 [(1/2\pi \sigma_\lambda)^2]}; \quad |\lambda| \leq \frac{1}{2}. \quad (7)$$

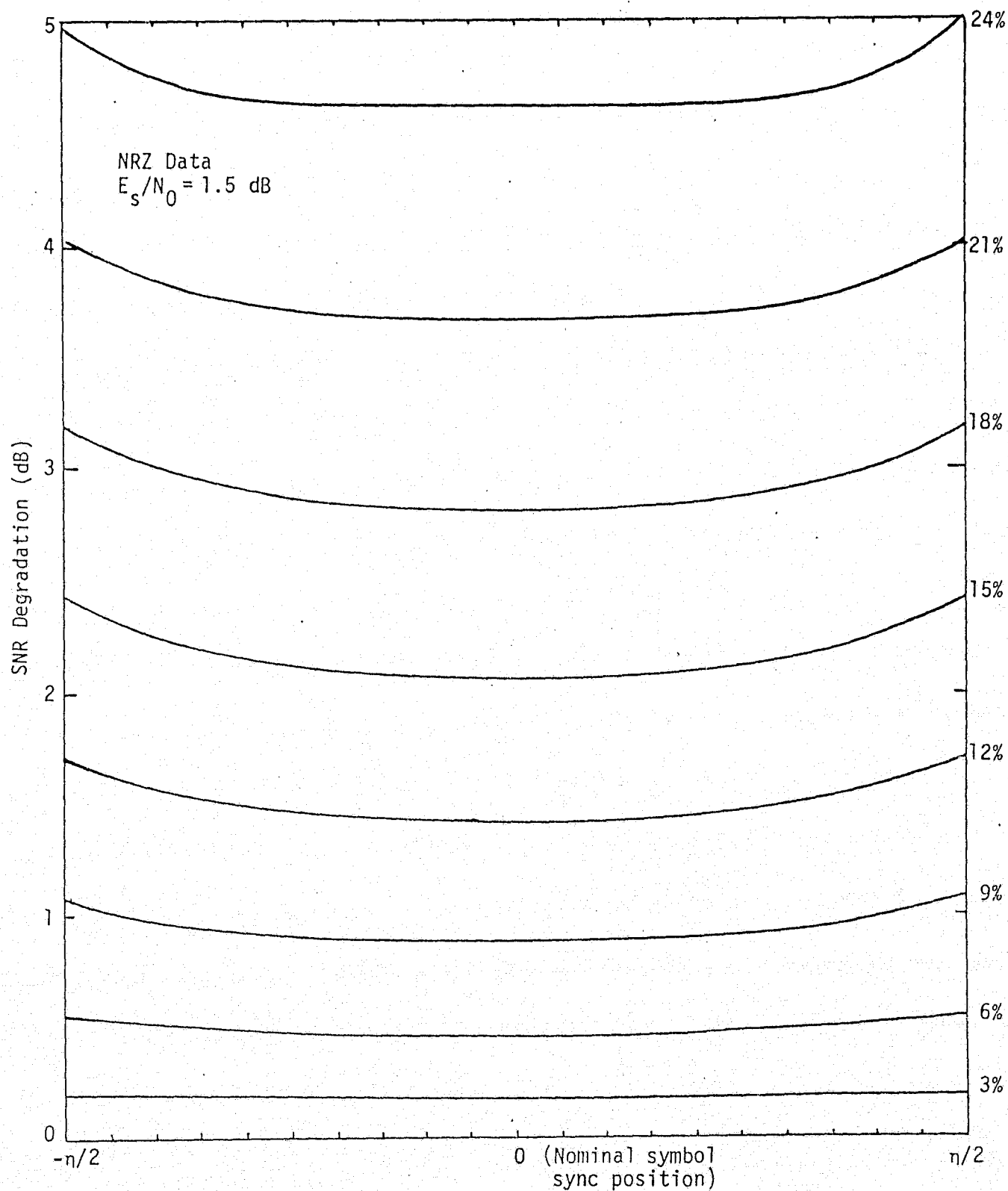


Figure 2. SNR Degradation Due to Data Asymmetry as a Function of Symbol Sync Clock Misalignment



In order to average the conditional error probability over the p.d.f. in (7), we must, in addition to (6), characterize  $P_E(\lambda)$  over the interval  $\eta/2 \leq |\lambda| \leq 1/2$ . Following the procedure given in Appendix B, it is straightforward to show that (also see [2])

$$P_E(\lambda) = \frac{1}{4} \operatorname{erfc} \sqrt{E_s/N_0} + \frac{1}{8} \operatorname{erfc} \left[ \sqrt{E_s/N_0} (1 - \eta - 2|\lambda|) \right] + \frac{1}{8} \operatorname{erfc} \left[ \sqrt{E_s/N_0} (1 - \eta + 2|\lambda|) \right] ; \quad \eta/2 \leq |\lambda| \leq 1/2 . \quad (8)$$

Thus, using (6), (7) and (8), the average error probability can be computed from

$$P_E = \int_{-1/2}^{1/2} P_E(\lambda) p(\lambda) d\lambda . \quad (9)$$

Figures 3 and 4 illustrate  $P_E$  [as computed from (9)] versus  $E_s/N_0$  in dB with  $\sigma_\lambda$  as a parameter for asymmetry values of 3% and 6%, respectively. (These numerical values are taken from [2].) Again at  $E_s/N_0 = 1.5$  dB, the additional degradation due to symbol synchronization jitter is on the order of a few tenths of a dB, even for a timing error (as measured by its standard deviation  $\sigma_\lambda$ ) as large as 7%.

#### 2.1.4 Error Probability Performance for Asymmetric Manchester Coded Symbols

Although Manchester coding cannot be employed on the high rate channel because of bandwidth limitations on the Ku-band return link, such coding is used on the lower rate channels, and thus the effect of asymmetry on the performance of these channels is potentially of interest.

When Manchester coding is employed, then relative to the NRZ sequence, the Manchester coded waveform has 3/2 as many transitions. Thus, since SNR degradation due to asymmetry is directly related to the average transition density of the data sequence, one would intuitively expect that, for the same asymmetry, the Manchester coded case should yield a larger SNR degradation than the corresponding NRZ case. Whether or not and to what extent the above intuitive notion is indeed

ORIGINAL PAGE IS  
OF POOR QUALITY

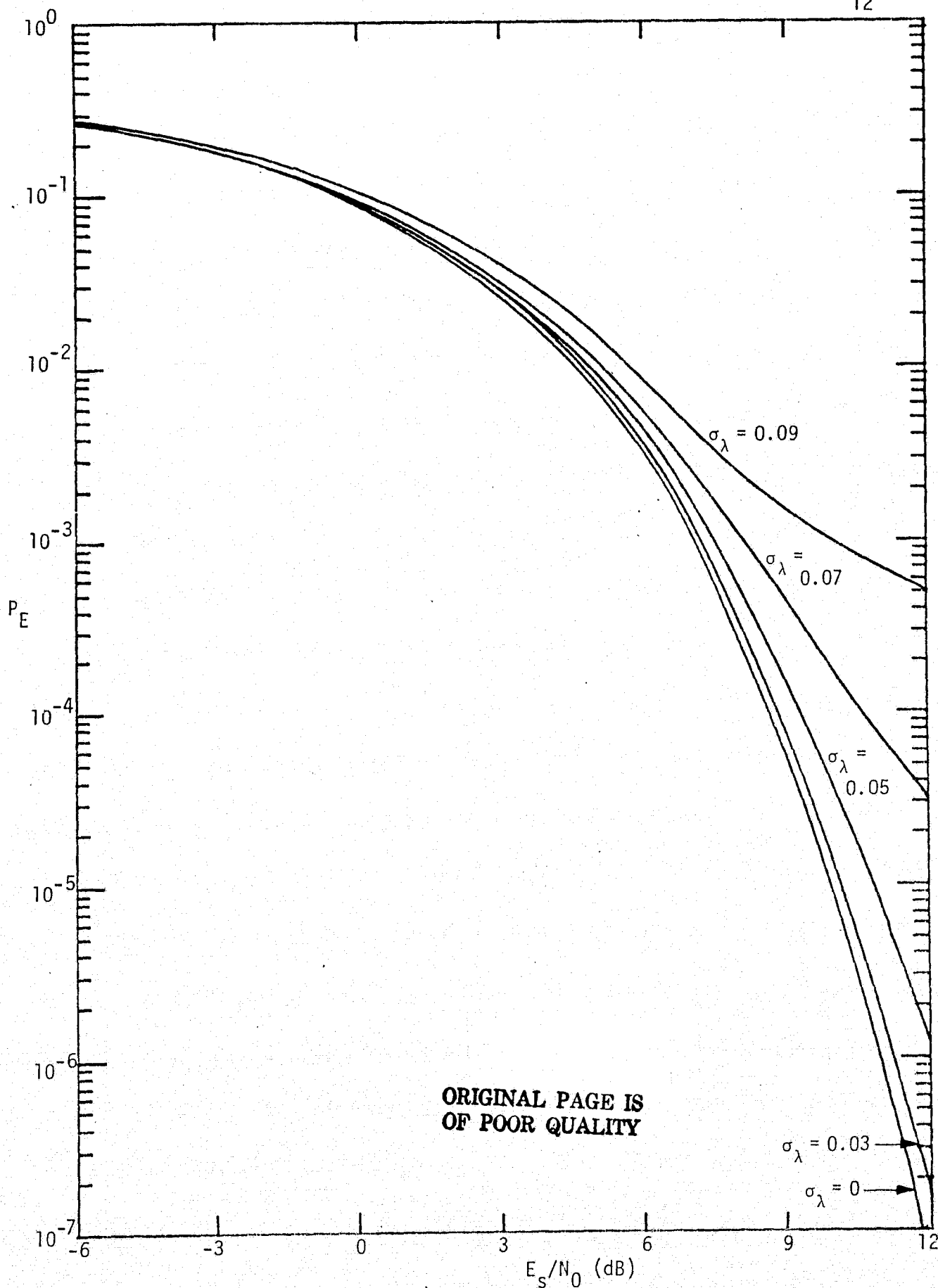


Figure 3. Average Error Probability with Symbol Synchronization Error as a Parameter (3% Asymmetry), NRZ Data

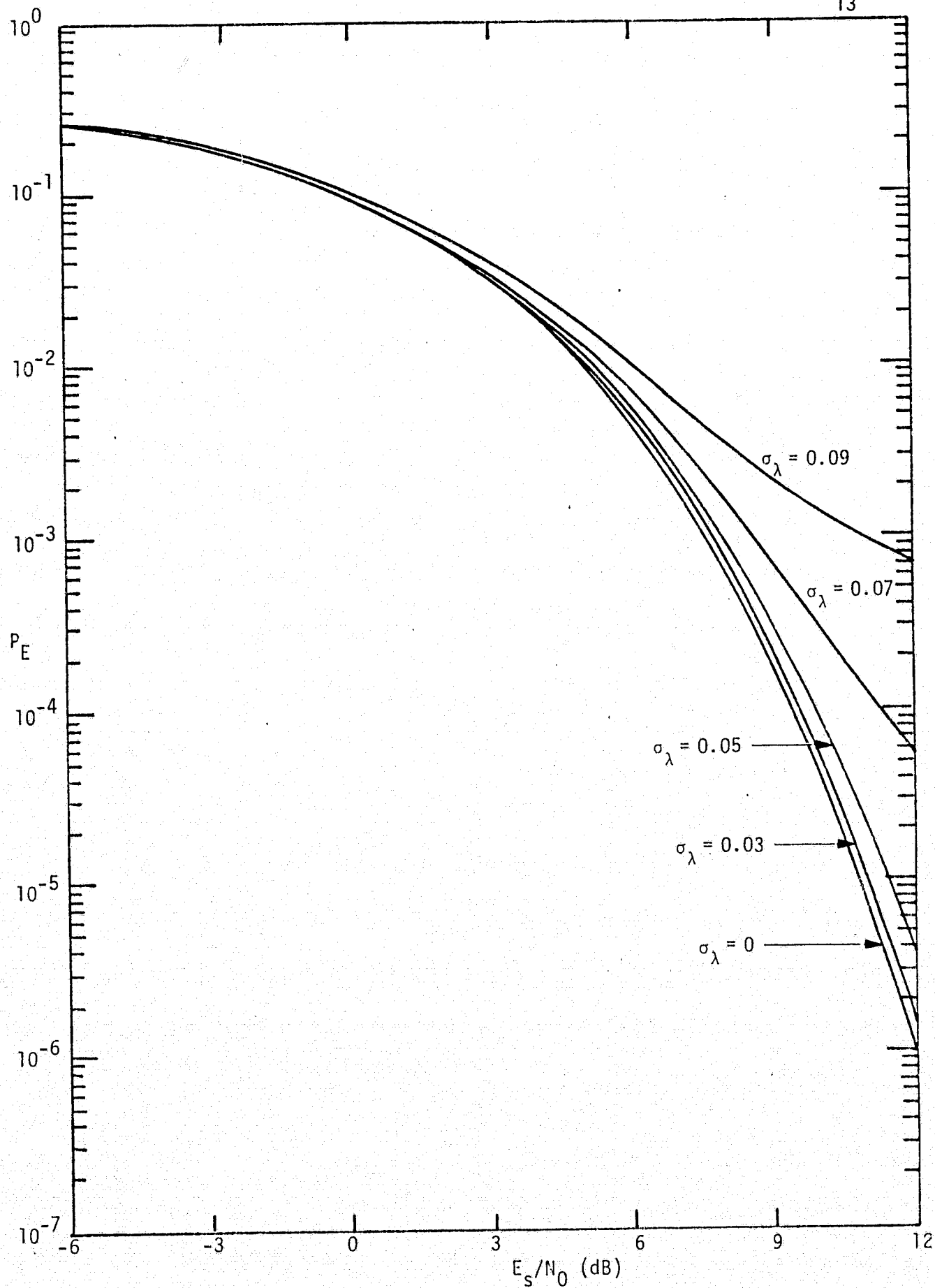


Figure 4. Average Error Probability with Symbol Synchronization Error as a Parameter (6% Asymmetry), NRZ Data

true depends on how one defines percent asymmetry for the Manchester coded case.

To demonstrate this point, consider the NRZ sequence of Figure 1 and the corresponding asymmetric Manchester waveforms which, for the two previous asymmetry models, are illustrated in Figure 5. Here, corresponding to Model 1,  $\Delta/2$  denotes the fractional (relative to the half-symbol time  $T/2$ ) elongation of the positive half pulse in the Manchester coded waveform, and for Model 2,  $\delta$  is accordingly defined relative to the same half-pulse width. Then, defining asymmetry as was done for the NRZ case but now relative to the half-pulse duration gives (for Model 1)

$$\text{Asymmetry} \triangleq \eta = \frac{\frac{T}{2}(1 + \Delta/2) - \frac{T}{2}(1 - \Delta/2)}{\frac{T}{2}(1 + \Delta/2) + \frac{T}{2}(1 - \Delta/2)} = \frac{\Delta}{2} \quad (10)$$

and, for Model 2,

$$\eta = \frac{\frac{T}{2}(1 + 2\delta) - \frac{T}{2}(1 - 2\delta)}{\frac{T}{2}(1 + 2\delta) + \frac{T}{2}(1 - 2\delta)} = 2\delta, \quad (11)$$

which are identical with (1) and (2).<sup>\*</sup> Once again, as in the NRZ case, the in-phase integrate-and-dump output depends, in general, on the polarity of the symbol over which it is integrating and the preceding and succeeding symbols. Thus, evaluating this integrate-and-dump output for the eight possible three-symbol sequences and noting that, for Model 1, the nominal bit synchronization lock-up misalignment is now  $\Delta T/8$ , we get an expression for the average probability of error corresponding to asymmetric Manchester coded random data, namely,

$$P_E = \frac{1}{4} \operatorname{erfc} \left[ \sqrt{E_s/N_0} (1 - \eta) \right] + \frac{1}{4} \operatorname{erfc} \left[ \sqrt{E_s/N_0} (1 - \frac{\eta}{2}) \right]. \quad (12)$$

---

<sup>\*</sup> Note that, while this definition allows for equal percent asymmetry when compared with NRZ, the actual time asymmetry (as measured in seconds) is different for the two cases.

Symmetric NRZ Waveform

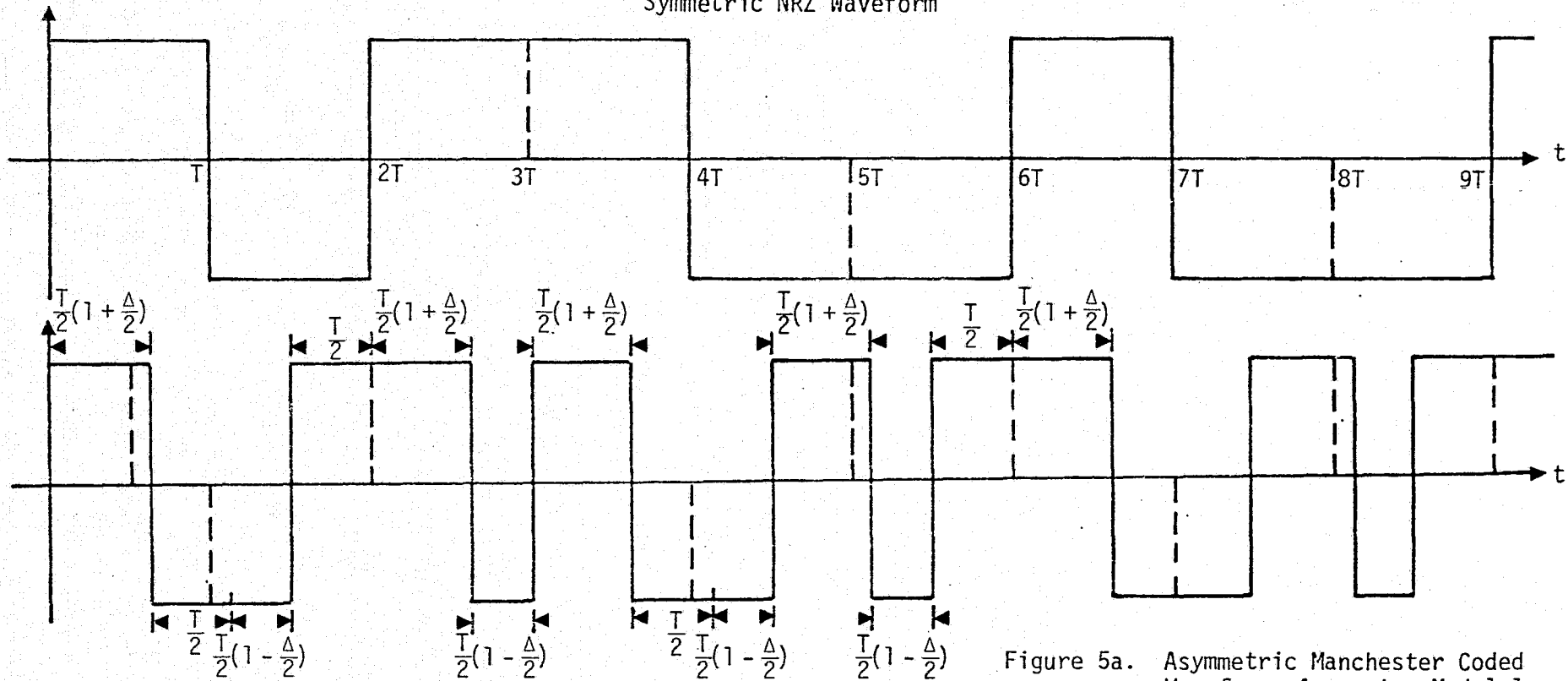


Figure 5a. Asymmetric Manchester Coded Waveform - Asymmetry Model 1

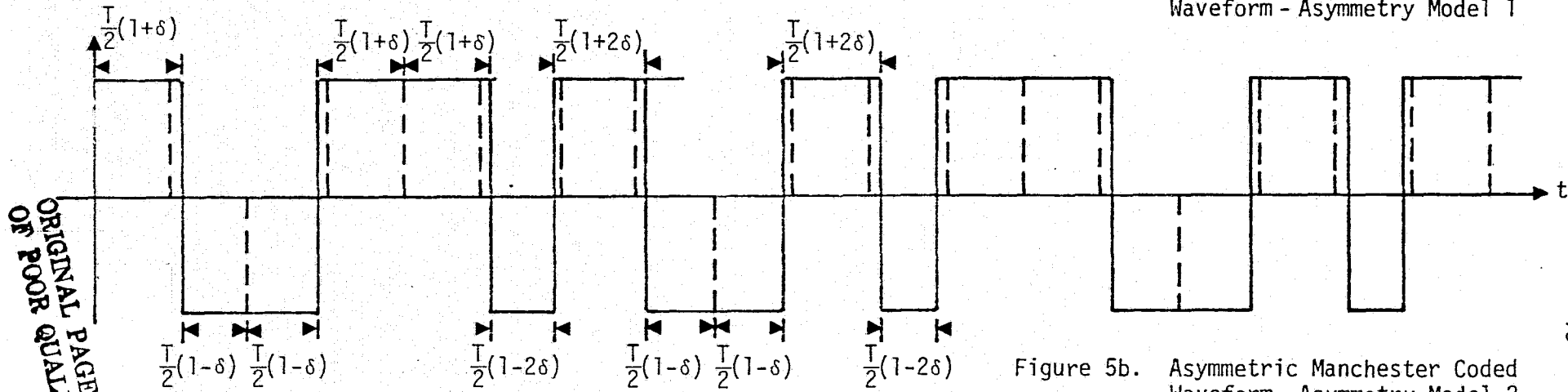


Figure 5b. Asymmetric Manchester Coded Waveform - Asymmetry Model 2

Using (12) and (3), Figure 6 illustrates the SNR degradation in dB versus percent asymmetry for Manchester and, for comparison, NRZ coded data at  $E_s/N_0 = 1.5$  dB. Here note that the Manchester code yields a larger SNR degradation than NRZ for small asymmetry values, while the reverse is true for large percent asymmetries.

If, on the other hand, we define data asymmetry relative to the symbol time  $T$  for both NRZ and Manchester data, then equal percent asymmetry implies equal amounts of asymmetry (in seconds) as measured by the actual time displacements of the waveform transitions. Thus, for Manchester coded data, we have that  $\eta = \Delta/4$  for Model 1 and  $\eta = \delta$  for Model 2. The corresponding expression for error probability is identical to (12) with  $\eta$  replaced by  $2\eta$ . Using this definition, Figure 7 plots SNR degradation in dB versus percent asymmetry for  $E_s/N_0 = 1.5$  dB for Manchester coded data and the corresponding results for NRZ data obtained from (3). Note that now the Manchester coded case always yields a larger SNR degradation for a given percent asymmetry. The conclusion to be reached here is that, in making comparisons between asymmetric NRZ and Manchester coded systems, one must exercise care in selecting a definition which is appropriate to the particular application at hand.

To generalize the results given in (12) to the case of imperfect symbol synchronization, one merely follows the procedure outlined in Appendix B for NRZ data, whereby (6) and (8) are obtained as extensions of (3). In particular, for a timing misalignment of  $\lambda T/2$  (consistent with our first definition of asymmetry relative to the half-pulse width and the fact that the time base for the symbol synchronizer is now  $T/2$ ), the conditional error probability is given by (also see [2])

$$P_E(\lambda) = \begin{cases} \frac{1}{4} \operatorname{erfc} \left[ \sqrt{E_s/N_0} (1 - \eta) \right] + \frac{1}{8} \operatorname{erfc} \left[ \sqrt{E_s/N_0} \left( 1 - \frac{\eta}{2} - |\lambda| \right) \right] \\ \quad + \frac{1}{8} \operatorname{erfc} \left[ \sqrt{E_s/N_0} \left( 1 - \frac{\eta}{2} + |\lambda| \right) \right]; & 0 \leq |\lambda| \leq \frac{\eta}{2} \\ \frac{1}{4} \operatorname{erfc} \left[ \sqrt{E_s/N_0} (1 - 2|\lambda|) \right] + \frac{1}{8} \operatorname{erfc} \left[ \sqrt{E_s/N_0} \left( 1 - \frac{\eta}{2} - |\lambda| \right) \right] \\ \quad + \frac{1}{8} \operatorname{erfc} \left[ \sqrt{E_s/N_0} \left( 1 + \frac{\eta}{2} - |\lambda| \right) \right]; & \frac{\eta}{2} \leq |\lambda| \leq \frac{1}{2} \end{cases} \quad (13)$$

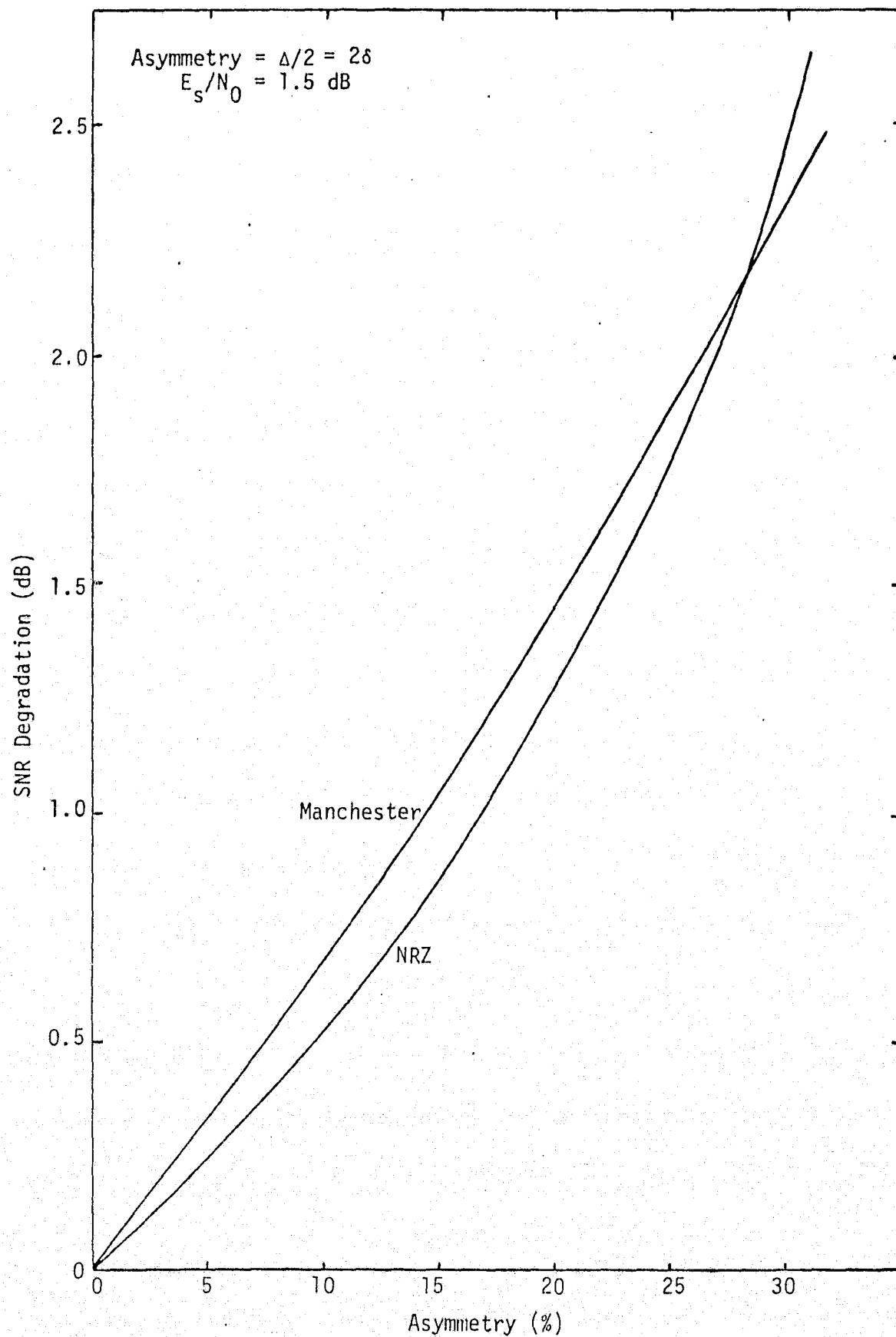


Figure 6. SNR Degradation vs. Percent Asymmetry for Manchester and NRZ Coded Data

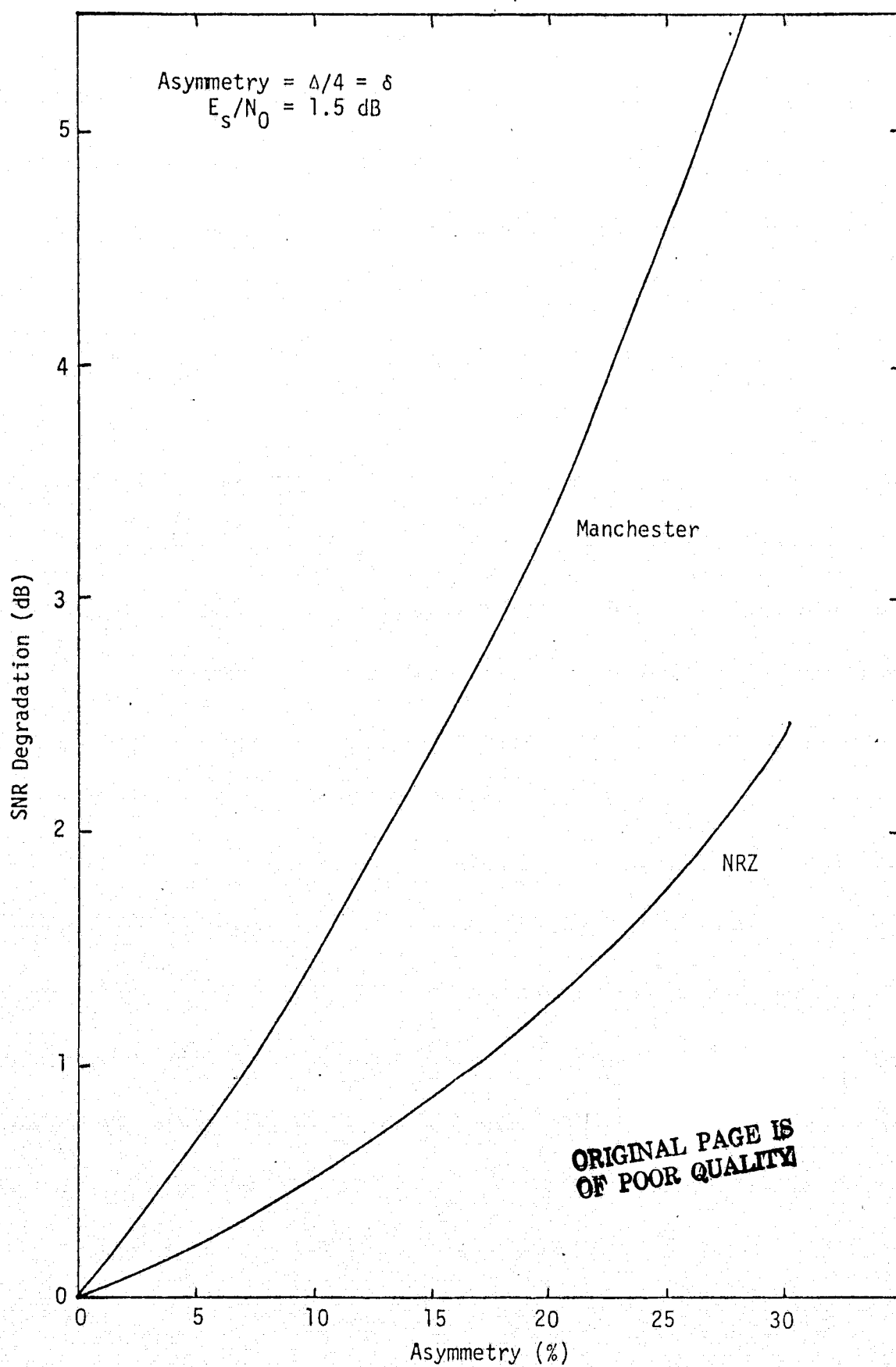


Figure 7. SNR Degradation vs. Percent Asymmetry for Manchester and NRZ Coded Data



Substituting (7) and (12) into (9) results in the average error probability performance for Manchester coded data with asymmetry. The corresponding performance plots analogous to Figures 3 and 4 for NRZ data are given in Figures 8 and 9. Comparing the NRZ and Manchester data results, we observe that, in terms of error probability performance, Manchester data appears to be less sensitive to symbol synchronization error. Of course, it should be pointed out that this conclusion is highly dependent on the time base used as normalization for the asymmetry definition. In fact, if the alternate definition is used, wherein both NRZ and Manchester asymmetries are defined as fractions of the symbol time, then for fixed values of  $\eta$  and  $\sigma_\lambda$ , the error probability performance of Manchester data will always be worse than that for NRZ [2].

#### 2.1.5 The Effect of D.C. Restoration on Error Probability Performance in the Presence of Asymmetry

The investigation of the effects of d.c. restoration\* on communication link performance was prompted by test results [4] conducted in the Electronic Systems Test Laboratory (ESTL) at JSC which indicated significantly less performance degradation than that predicted by the analytic results of the previous sections. In particular, it was found that d.c. restoration tends to reduce the degrading effects of data asymmetry and thus it was necessary to incorporate d.c. restoration into the analytical model in order that the predicted performance better agree with the test results.

The effect of d.c. restoration on data detection is most easily accounted for by artificially shifting the decision threshold (nominally at zero) against which the matched filter output is compared. The amount of this artificial shift in threshold depends upon the specific way in which d.c. restoration comes about.

The simplest method of achieving d.c. restoration is to capacitively couple the input signal to the symbol synchronizer. In this case, the artificial threshold shift equals the d.c. component of the asymmetric

---

\* D.C. restoration refers to the process by which the d.c. value of the asymmetric data waveform is forced to zero.

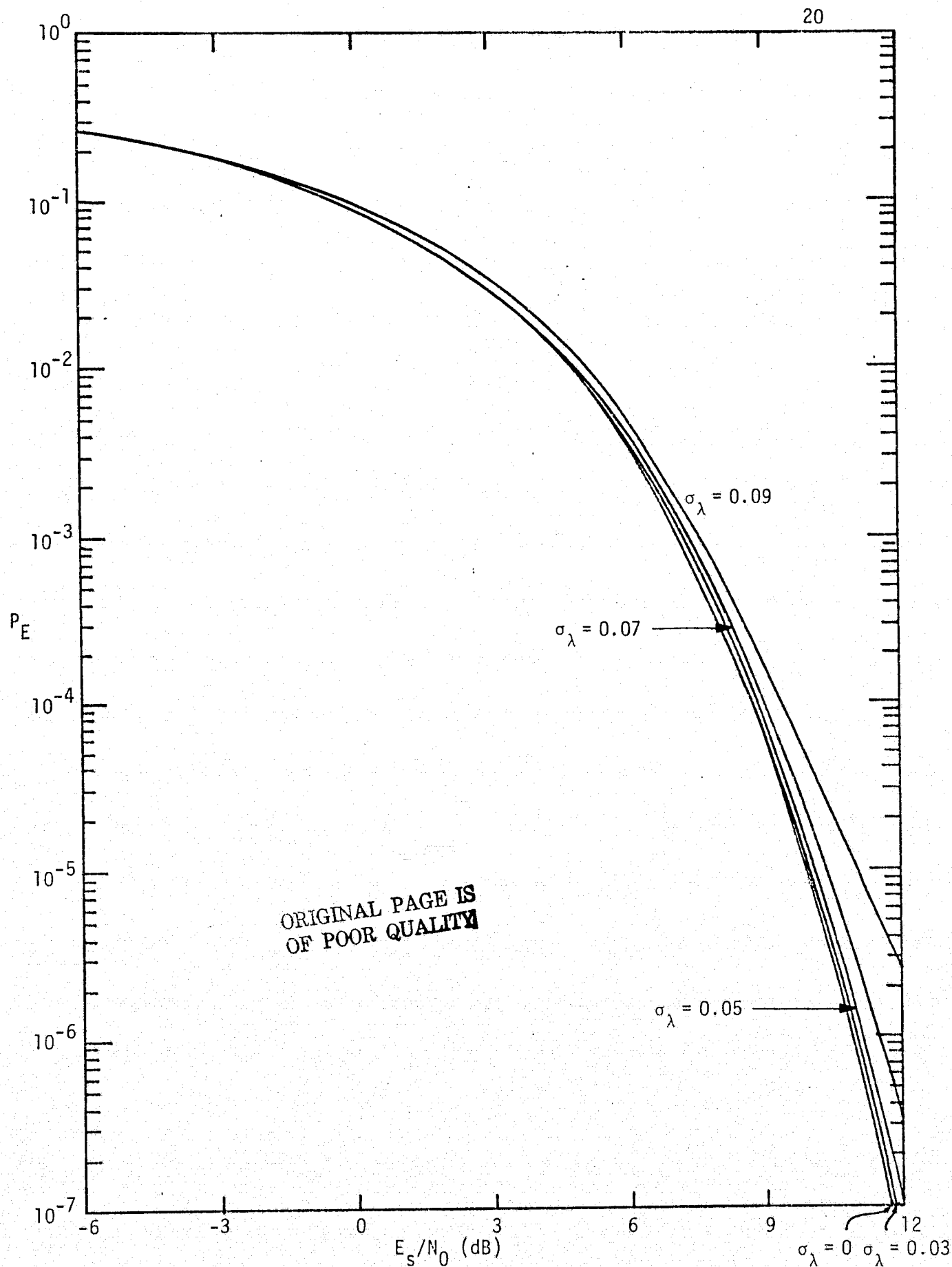


Figure 8. Average Error Probability with Symbol Synchronization Error as a Parameter (3% Asymmetry), Manchester Coded Data

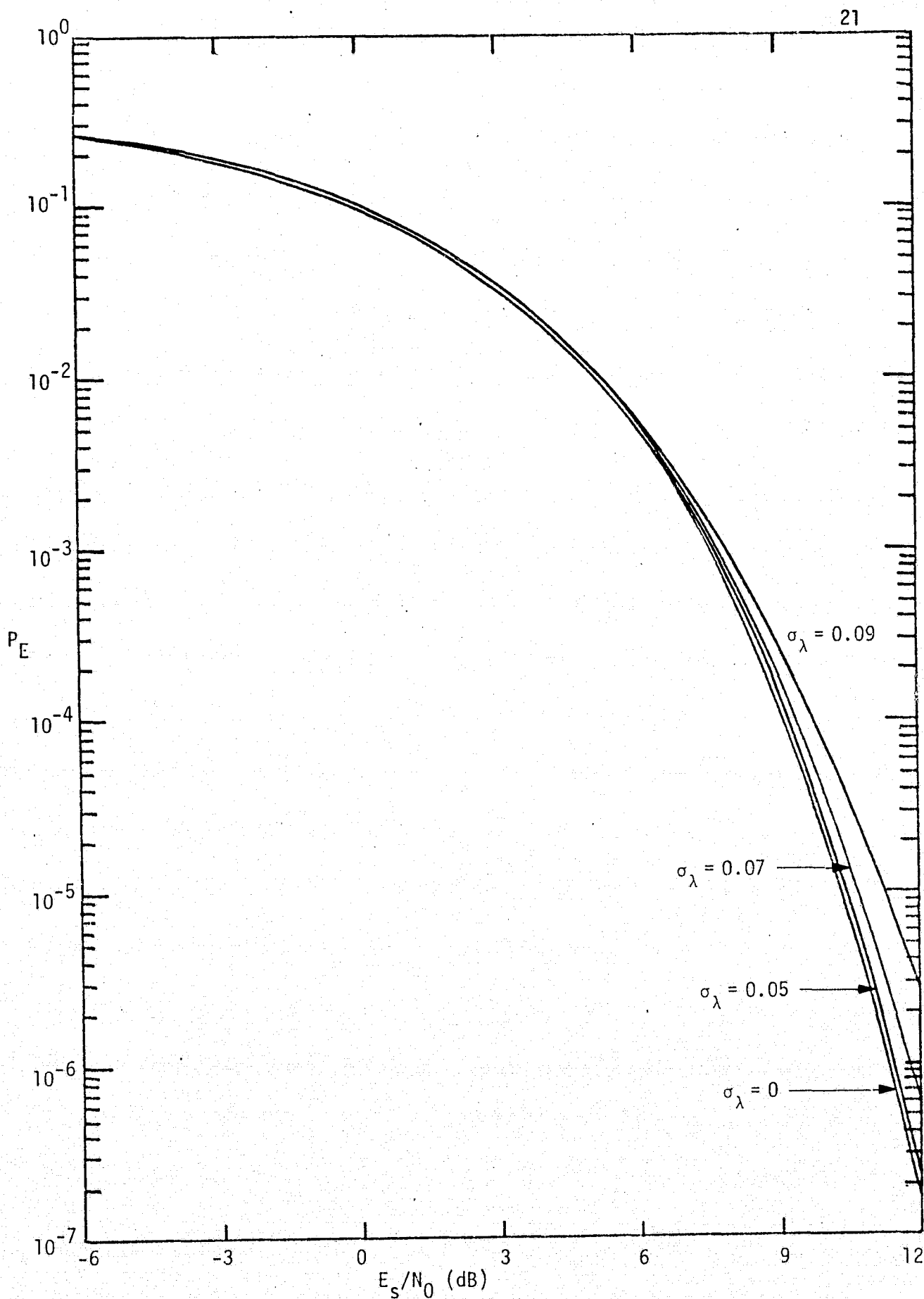


Figure 9. Average Error Probability with Symbol Synchronization Error as a Parameter (6% Asymmetry), Manchester Coded Data

data waveform in front of the capacitor which, for random data with transition density  $D$ , is easily shown to be [4]

$$\Delta_t = \eta D \sqrt{E_s/T}, \quad (14)$$

where  $\sqrt{E_s/T}$  is the data pulse amplitude in Figure 1. Computing the matched filter output for the eight possible three-symbol sequences made up of the present, preceding, and succeeding symbols and shifting these outputs by  $\Delta_t$  gives the result for the error probability performance of asymmetric NRZ data with d.c. restoration by capacitive coupling, namely,

$$P_E = \frac{1}{4} \operatorname{erfc} \left[ \sqrt{E_s/N_0} (1 - \eta D) \right] + \frac{1}{16} \operatorname{erfc} \left[ \sqrt{E_s/N_0} (1 - 2\eta + \eta D) \right] \\ + \frac{1}{8} \operatorname{erfc} \left[ \sqrt{E_s/N_0} (1 - \eta + \eta D) \right] + \frac{1}{16} \operatorname{erfc} \left[ \sqrt{E_s/N_0} (1 + \eta D) \right]. \quad (15)$$

For equiprobable data symbols ( $D = 0.5$ ), (15) simplifies to

$$P_E = \frac{3}{8} \operatorname{erfc} \left[ \sqrt{E_s/N_0} \left(1 - \frac{\eta}{2}\right) \right] + \frac{1}{16} \operatorname{erfc} \left[ \sqrt{E_s/N_0} \left(1 - \frac{3\eta}{2}\right) \right] \\ + \frac{1}{16} \operatorname{erfc} \left[ \sqrt{E_s/N_0} \left(1 + \frac{\eta}{2}\right) \right]. \quad (16)$$

Comparing (16) with (3), we observe that the effect of d.c. restoration is to compensate for the data asymmetry by shifting the effective decision threshold away from the shortened symbols.

For a given value of asymmetry, the value of  $E_s/N_0$  required to obtain  $P_E$  [as computed from (16)] equal to  $10^{-5}$  can be calculated. Comparing this value of  $E_s/N_0$  with that obtained from (5) for the same  $P_E$  gives the SNR degradation for asymmetric NRZ data with d.c. restoration by capacitive coupling. Figure 10 illustrates this SNR degradation versus asymmetry along with the comparable results obtained from (3) corresponding to no d.c. restoration (direct coupling).

Another method of achieving d.c. restoration, which depends specifically on the symbol synchronizer implementation itself, is to require the matched filter output to have zero crossings at the center of each symbol period that starts with a data transition. In this case,

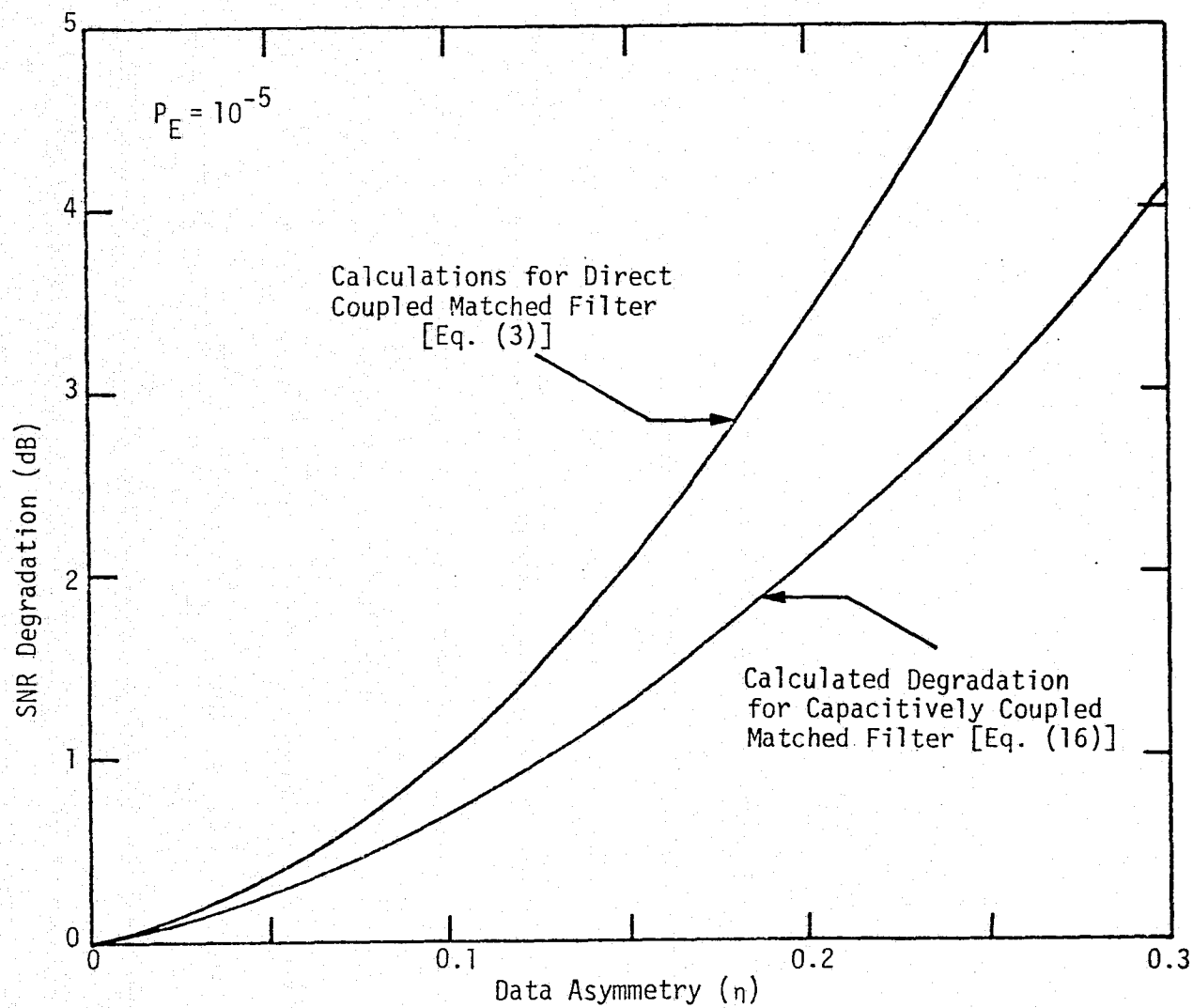


Figure 10. Performance Degradation for Capacitively Coupled Matched Filters;  
Random Data ( $D = 0.5$ )

ORIGINAL PAGE IS  
OF POOR QUALITY

the effective shift in decision threshold relative to its nominal (zero) value is [4]

$$\Delta_t = n \sqrt{E_s/T} . \quad (17)$$

Comparing (17) with (14), we can immediately conclude that the error probability for this method of d.c. restoration is given by (15) with  $D=1$ , i.e.,

$$P_E = \frac{5}{16} \operatorname{erfc} \left[ \sqrt{E_s/N_0} (1 - n) \right] + \frac{1}{8} \operatorname{erfc} \left[ \sqrt{E_s/N_0} \right] + \frac{1}{16} \operatorname{erfc} \left[ \sqrt{E_s/N_0} (1 + n) \right] . \quad (18)$$

Again by determining those values of  $E_s/N_0$  required to obtain  $P_E = 10^{-5}$  for various values of asymmetry, one can compute the SNR degradation for d.c. restoration based on symbol timing. The results of these calculations are illustrated in Figure 11, along with experimental test results taken in the ESTL for the sake of comparison. It is to be noted that the experimental results include the effect of bandlimiting, whereas the theory as predicted by (18) in no way accounts for this effect. Furthermore, the data detector used in the experimental setup is not a true matched filter as is assumed for the analytical model. Surprisingly enough, however, the analytic and experimental results show reasonably good agreement. In the next section, we consider the combined effects of bandlimiting and asymmetry on the performance of a filter-sample type data detector which is a more realistic model of the detector used in the ESTL experimental tests.

#### 2.1.6 The Combined Effects of Bandlimiting and Data Asymmetry on Error Probability Performance

In the previous sections, the degradation of error probability performance due to data asymmetry alone was considered. Since, in reality, a practical receiver operates in the presence of both bandlimiting and data asymmetry, it is important to study the combined effects of these two sources of degradation on its error probability performance. Assuming a filter-sample type detector (see Figure 12)

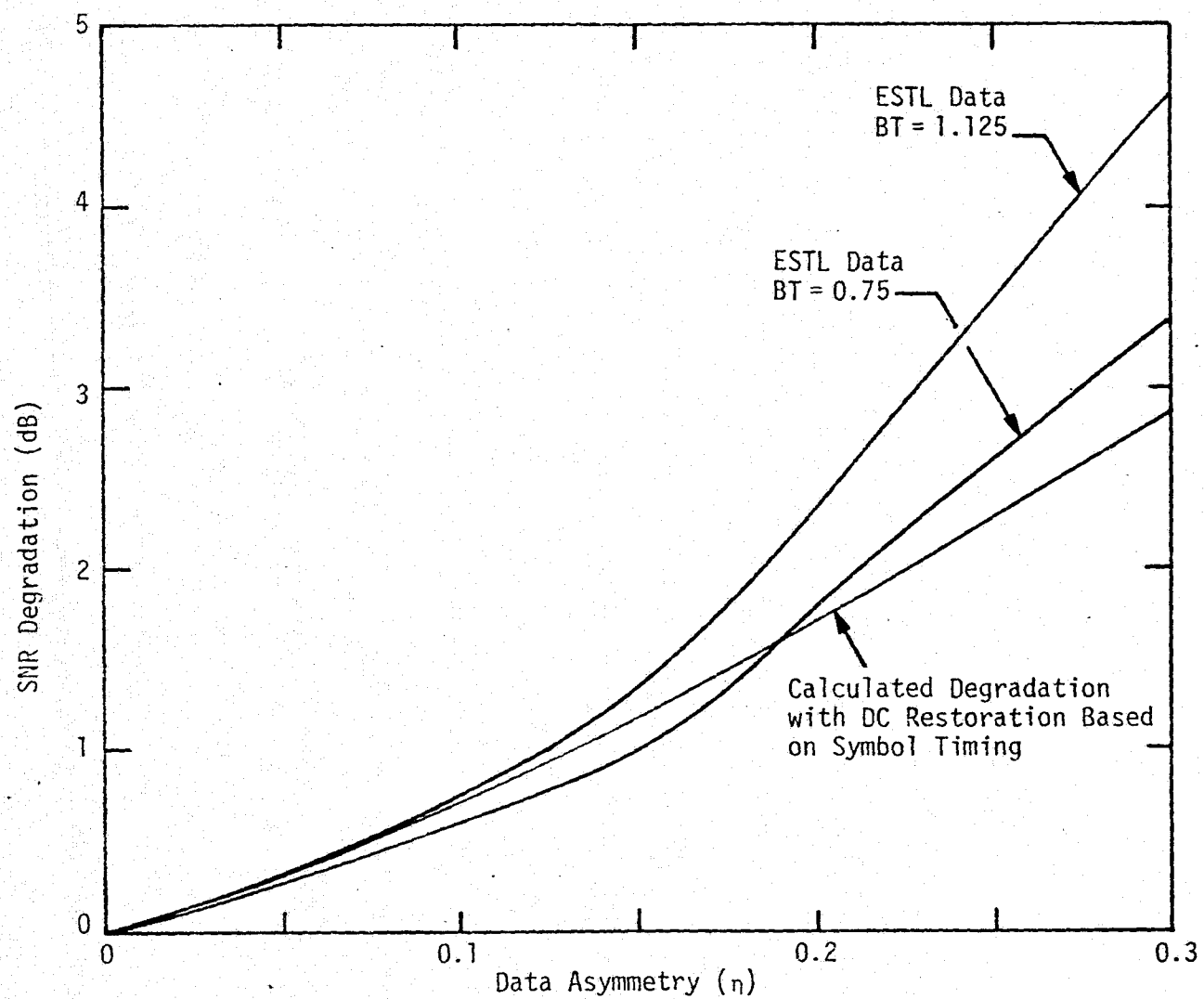


Figure 11. Performance Degradation for DC Restoration Based on Symbol Timing

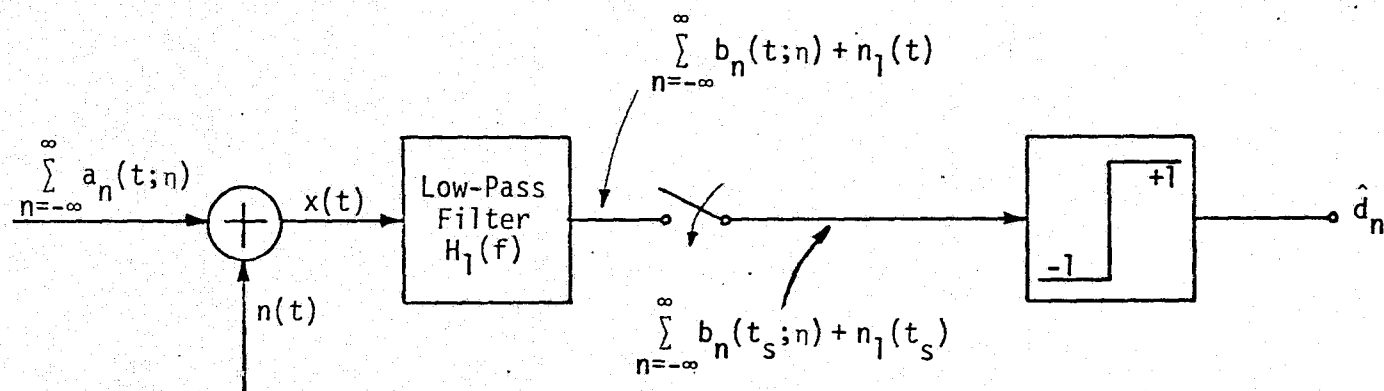


Figure 12. Band Limit and Sample Detector for Binary Data With Asymmetry



and NRZ data, Appendix C investigates in detail the combined degrading effects of intersymbol interference and SNR reduction of the desired signal due to bandlimiting by an ideal low-pass filter and data asymmetry. The results of this analysis, which are first derived assuming no d.c. restoration and later modified to include this effect, are summarized below.

Figure 13 illustrates the bit error probability as a function of energy-to-noise ratio with BT as a parameter and 10% asymmetry while Figure 14 illustrates as a function of asymmetry the required energy-to-noise ratio to achieve a bit error probability of  $10^{-5}$  with BT still the parameter. Both of these figures assume no d.c. restoration. The corresponding results which include d.c. restoration by capacitive coupling are illustrated, respectively, in Figures 15 and 16. It is concluded that, for small values of asymmetry (less than about 10%), the optimum filter bandwidth-bit time product remains equal to 0.9,\* and the corresponding amount of energy-to-noise ratio degradation at a fixed error rate is virtually independent of whether or not d.c. restoration is present. In particular, Tables 2 and 3 summarize typical results for the two cases when  $BT = 0.9$ . The quantity  $\Delta E_s/N_0$  represents the additional  $E_s/N_0$  required at a given value of data asymmetry relative to its value at zero asymmetry.

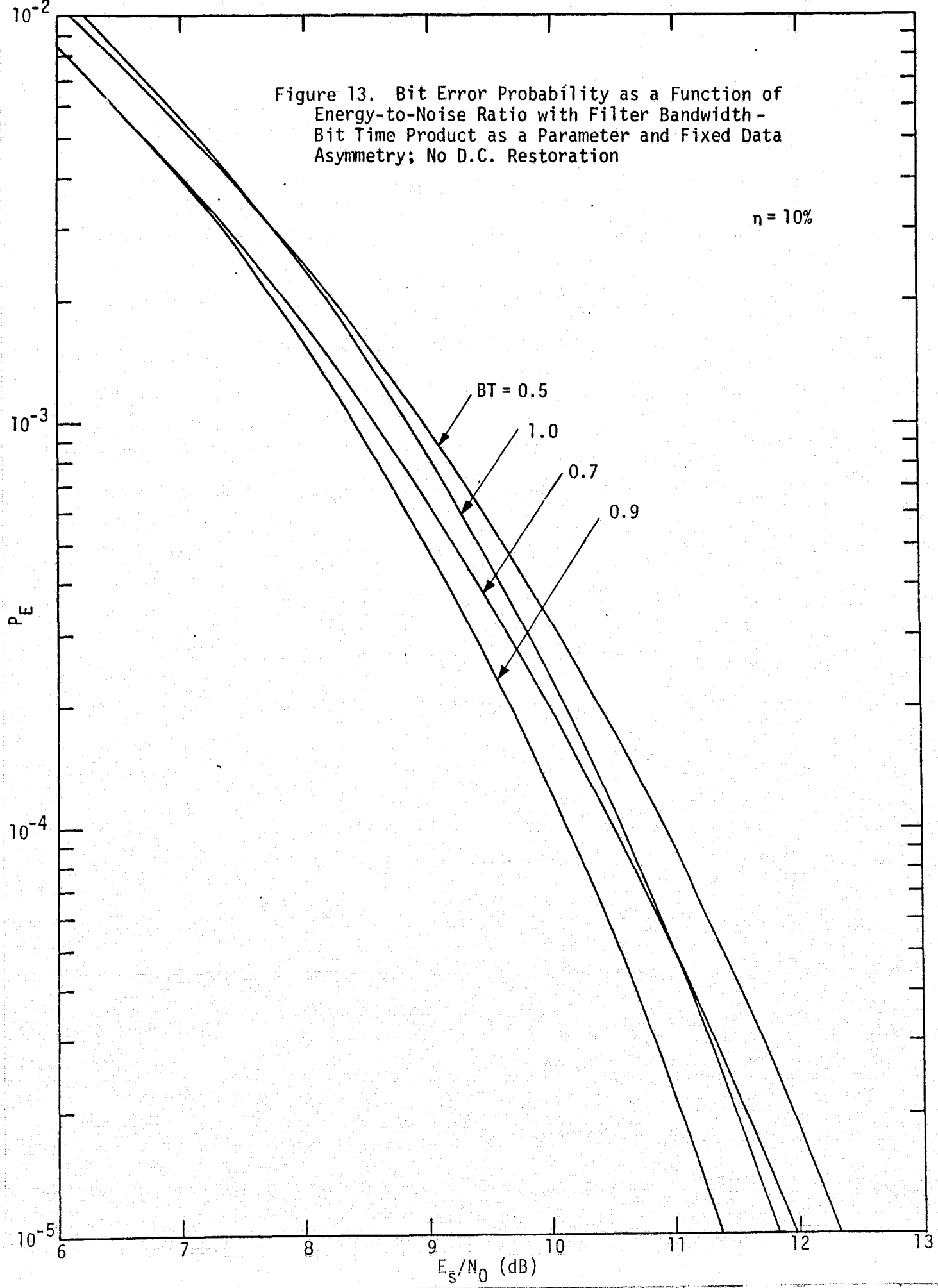
On the other hand, for values of BT other than the optimum, d.c. restoration has a beneficial effect in reducing energy-to-noise ratio degradation due to data asymmetry.

The other conclusion which can be reached by comparing the above numerical results with those in the previous section is that the sample detector is much less sensitive to data asymmetry than the integrate-and-dump detector. This is not surprising when one realizes that the degradation due to data asymmetry for the integrate-and-dump detector comes about because of a reduction in the signal energy as a result of integrating only over a fraction of the total bit interval. By comparison, the reduction in the peak of the filter response at the sampling instant

---

\*A previous study [5] of the degrading effect of ideal low-pass bandlimiting alone on the bit error probability performance of a filter-sample detector revealed that  $BT = 0.9$  was optimum from the standpoint of minimum degradation.

Figure 13. Bit Error Probability as a Function of Energy-to-Noise Ratio with Filter Bandwidth - Bit Time Product as a Parameter and Fixed Data Asymmetry; No D.C. Restoration



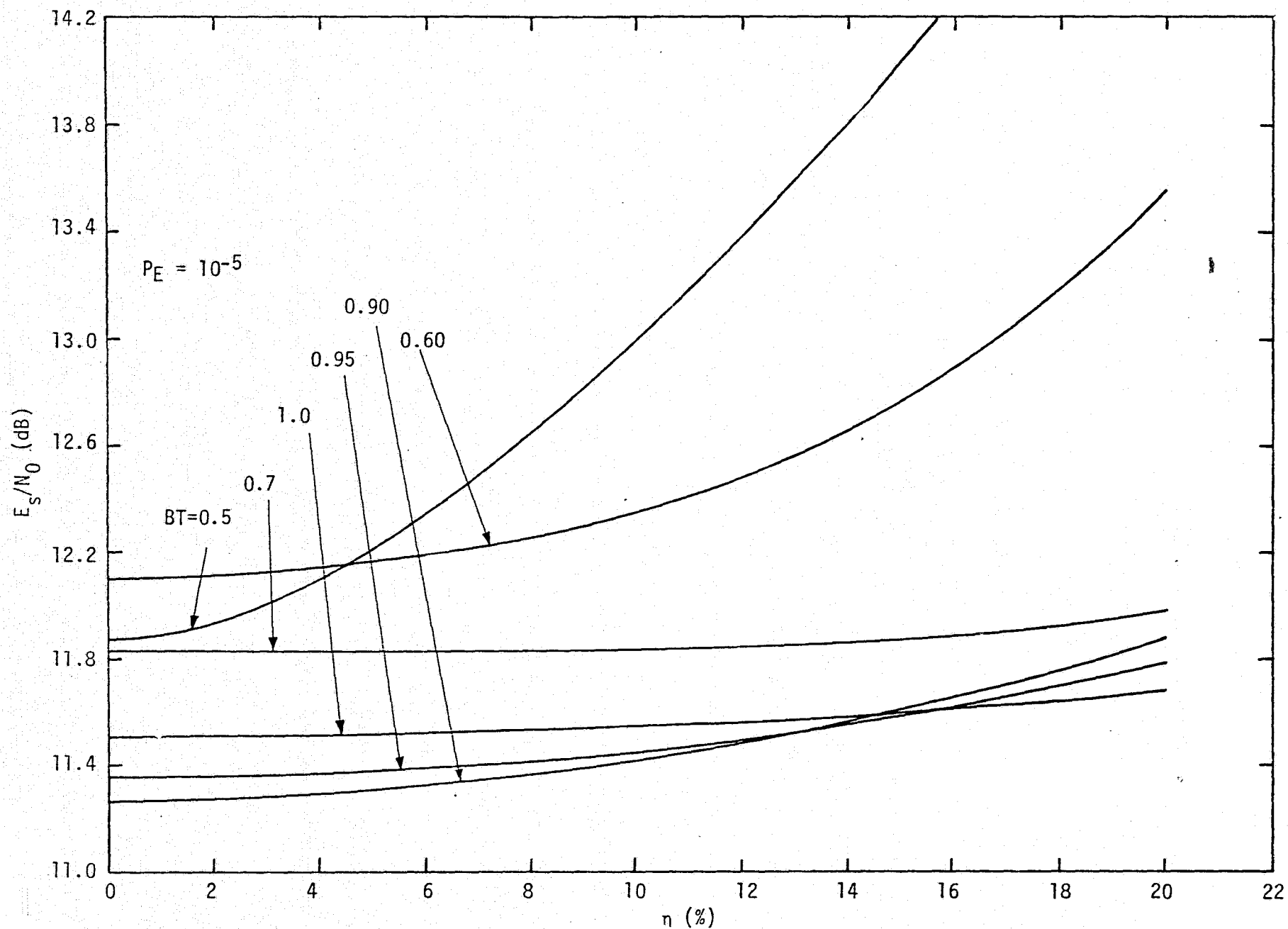
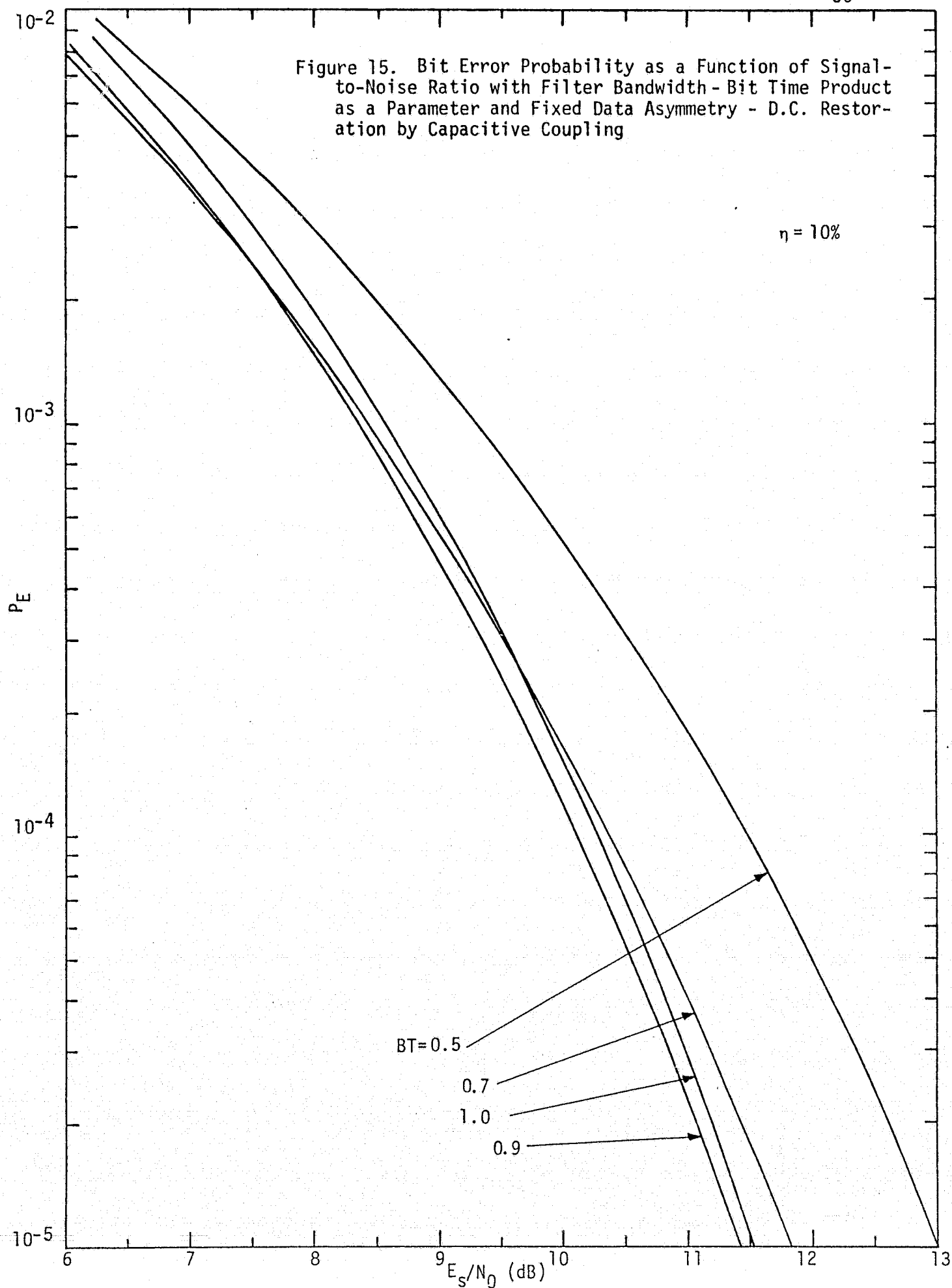


Figure 14. Energy-to-Noise Ratio as a Function of Data Asymmetry for Fixed Bit Error Probability and Filter Bandwidth - Bit Time Product as a Parameter; No D.C. Restoration

Figure 15. Bit Error Probability as a Function of Signal-to-Noise Ratio with Filter Bandwidth - Bit Time Product as a Parameter and Fixed Data Asymmetry - D.C. Restoration by Capacitive Coupling



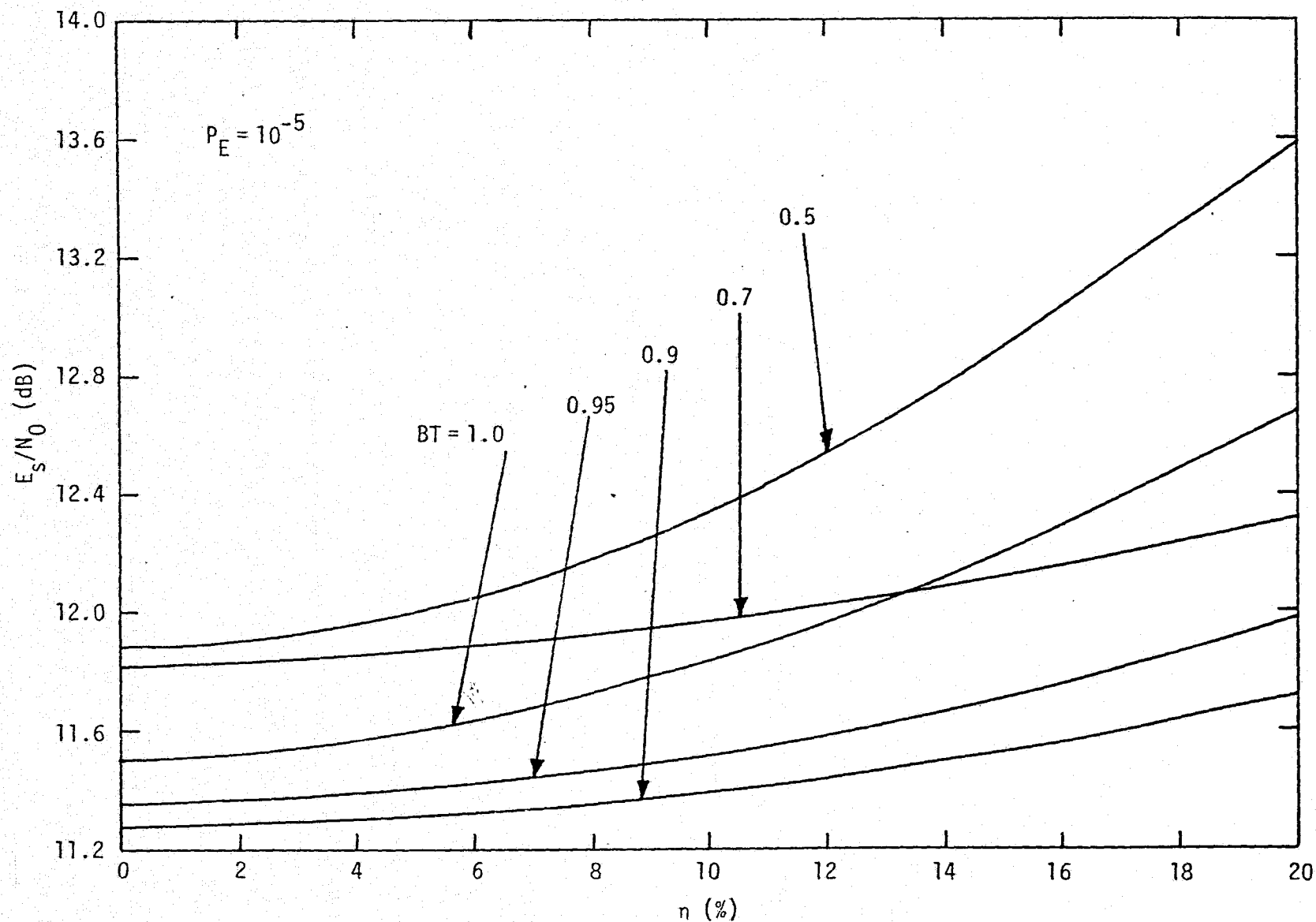


Figure 16. Energy-to-Noise Ratio as a Function of Data Asymmetry for Fixed Bit Error Probability and Filter Bandwidth-Bit Time Product as a Parameter; D.C. Restoration by Capacitive Coupling

Table 2. No D.C. Restoration

$P_E = 10^{-4}$			$P_E = 10^{-5}$		
$\eta$ (%)	$E_S/N_0$ (dB)	$\Delta E_S/N_0$ (dB)	$\eta$ (%)	$E_S/N_0$ (dB)	$\Delta E_S/N_0$ (dB)
0	9.97	0	0	11.28	0
2.5	9.98	0.01	2.5	11.29	0.01
5.0	10.00	0.03	5.0	11.32	0.04
7.5	10.06	0.09	7.5	11.37	0.09
10.0	10.13	0.16	10.0	11.43	0.15
15.0	10.31	0.34	15.0	11.63	0.35

Table 3. D.C. Restoration by Capacitive Coupling

$P_E = 10^{-4}$			$P_E = 10^{-5}$		
$\eta$ (%)	$E_S/N_0$ (dB)	$\Delta E_S/N_0$ (dB)	$\eta$ (%)	$E_S/N_0$ (dB)	$\Delta E_S/N_0$ (dB)
0	9.97	0	0	11.28	0
2.5	9.99	0.02	2.5	11.30	0.02
5.0	10.02	0.05	5.0	11.32	0.04
10.0	10.12	0.15	10.0	11.40	0.12
15.0	10.25	0.28	15.0	11.54	0.26
20.0	10.44	0.47	20.0	11.73	0.45

ORIGINAL PAGE IS  
OF POOR QUALITY

due to data asymmetry should have a considerably lesser effect. In fact, in the absence of bandlimiting, the integrate-and-dump detector would still yield considerable  $E_s/N_0$  degradation due to data asymmetry, whereas the sample detector would show none. Of course, the sample detector without bandlimiting would produce infinite noise power and, thus, on an absolute  $E_s/N_0$  basis would be far worse than the integrate-and-dump.

#### 2.1.7 Performance of a Gated Integrate-and-Dump Filter for Detection of Asymmetric Data

This section deals with still another implementation of a data detector for asymmetric data, namely, the gated integrate-and-dump filter (see Figure 17). The motivation for studying the performance of such a detector stems from several considerations. First, from an implementation point of view, the gated integrate-and-dump has the advantage that operation at high data rates can be accomplished with smaller circuit losses than the ideal integrate-and-dump since the constraint on its switching times at the symbol transition instants can now be considerably relaxed. Second, since the input data stream possesses asymmetry, the ideal integrate-and-dump is no longer the optimum detector, and it is thus possible that an alternate (possibly simpler to implement) detector could yield superior performance.

Appendix D discusses in detail the performance of the gated integrate-and-dump filter as a function of data asymmetry and gating interval and demonstrates the relation between these parameters which optimizes this performance. Only the case of NRZ data is treated; however, as before, the results are obtained for both the case of no d.c. restoration and the case of d.c. restoration by capacitive coupling. These results are summarized as follows.

In the absence of d.c. restoration, the average error probability performance of the gated integrate-and-dump is given by

$$P_E = \begin{cases} \frac{5}{16} \operatorname{erfc} \left[ \sqrt{E_s/N_0} (1 - 2\epsilon) \right] + \frac{1}{8} \operatorname{erfc} \left[ \sqrt{E_s/N_0} \left( \frac{1 - \eta}{\sqrt{1 - 2\epsilon}} \right) \right] \\ \quad + \frac{1}{16} \operatorname{erfc} \left[ \sqrt{E_s/N_0} \left( \frac{1 - 2\eta + 2\epsilon}{\sqrt{1 - 2\epsilon}} \right) \right]; & 0 \leq \epsilon \leq \eta/2 \\ \frac{1}{2} \operatorname{erfc} \left[ \sqrt{E_s/N_0} (1 - 2\epsilon) \right]; & \eta/2 \leq \epsilon \leq 1/2 \end{cases} \quad (19)$$

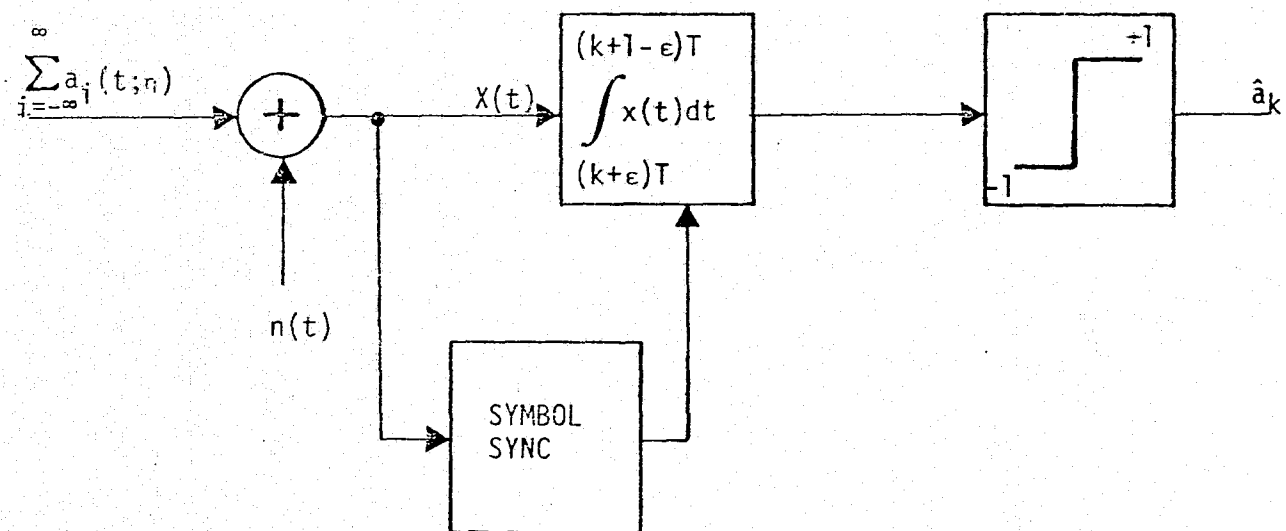


Figure 17. Gated Integrate-and-Dump Filter



Figure 18 is a plot of  $P_E$  versus  $\epsilon$  with  $\eta$  as a parameter and  $E_s/N_0 = 9.6$  dB (corresponding to  $P_E = 10^{-5}$  when  $\epsilon = \eta = 0$ ). We observe from this figure that, for a given value of data asymmetry  $\eta$ ,  $P_E$  is minimized by choosing  $\epsilon = \eta/2$ . Figure 19 is an illustration of the symbol energy-to-noise ratio (in dB) required to achieve an average error rate of  $10^{-5}$  in the presence of data asymmetry. The curve labeled  $\epsilon = 0$  corresponds to the performance of the ideal integrate-and-dump (see also Figure 3 of Appendix A). The remaining curves indicate a constant  $E_s/N_0$  for values of  $\eta \leq 2\epsilon$  in accordance with the second equation of (19) followed by an increase in  $E_s/N_0$  with  $\eta$  as required by the first equation of (19). Note that each of these curves cross the  $\epsilon = 0$  curve at some value of  $\eta$ , say  $\eta_0$ , which means that, for  $\eta > \eta_0$ , the gated integrate-and-dump outperforms the ideal integrate-and-dump in the sense of requiring less  $E_s/N_0$  for a given average probability of error. The dashed curve in Figure 19 represents the performance corresponding to selecting  $\epsilon = \eta/2$  at each value of  $\eta$  and is thus the best achievable with the gated integrate-and-dump.

When d.c. restoration by capacitive coupling is present, then the analogous result to (19) is

$$P_E = \begin{cases} \frac{1}{4} \operatorname{erfc} \left[ \sqrt{E_s/N_0} (1 - 2\epsilon)(1 - \eta D) \right] + \frac{1}{16} \operatorname{erfc} \left[ \sqrt{E_s/N_0} (1 - 2\epsilon)(1 + \eta D) \right] \\ + \frac{1}{16} \operatorname{erfc} \left[ \sqrt{E_s/N_0} \left( \frac{1 - 2\eta + \eta D + 2\epsilon(1 - \eta D)}{\sqrt{1 - 2\epsilon}} \right) \right] \\ + \frac{1}{8} \operatorname{erfc} \left[ \sqrt{E_s/N_0} \left( \frac{1 - \eta + \eta D - 2\epsilon \eta D}{\sqrt{1 - 2\epsilon}} \right) \right]; & 0 \leq \epsilon \leq \eta/2 \\ \\ \frac{1}{4} \operatorname{erfc} \left[ \sqrt{E_s/N_0} (1 - 2\epsilon)(1 - \eta D) \right] + \frac{1}{4} \operatorname{erfc} \left[ \sqrt{E_s/N_0} (1 - 2\epsilon)(1 + \eta D) \right]; & \eta/2 \leq \epsilon \leq 1/2. \end{cases} \quad (20)$$

Figure 20 again illustrates  $P_E$  versus  $\epsilon$  with  $\eta$  as a parameter and  $E_s/N_0 = 9.6$  dB, where  $P_E$  is now computed from (20). We observe from this figure that, for a given value of data asymmetry, there exists a value of  $\epsilon$  which minimizes  $P_E$ ; however, unlike Figure 18, this value

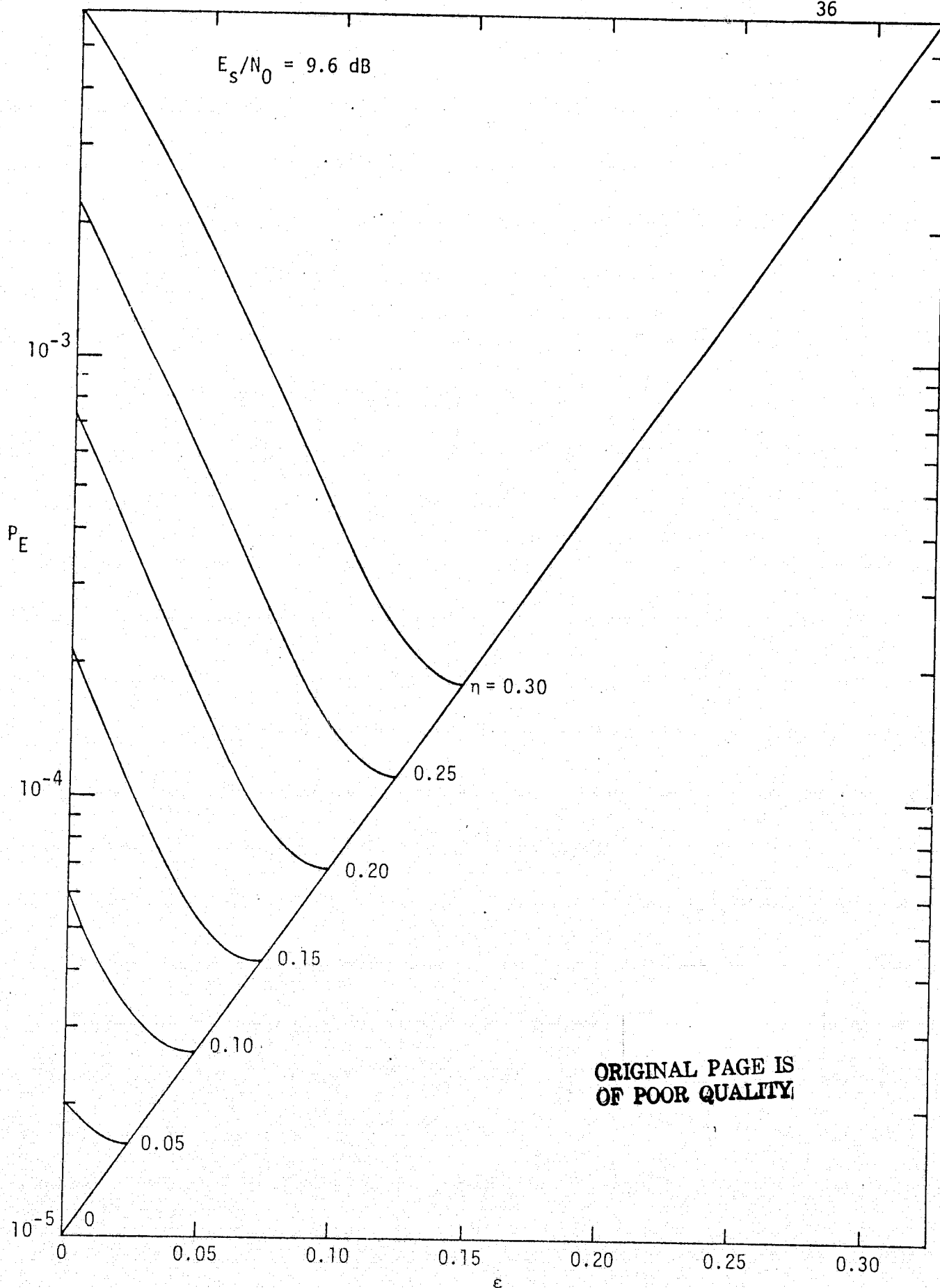


Figure 18. Average Error Probability versus Gate Interval at Symbol Edge with Data Asymmetry as a Parameter - No D.C. Restoration

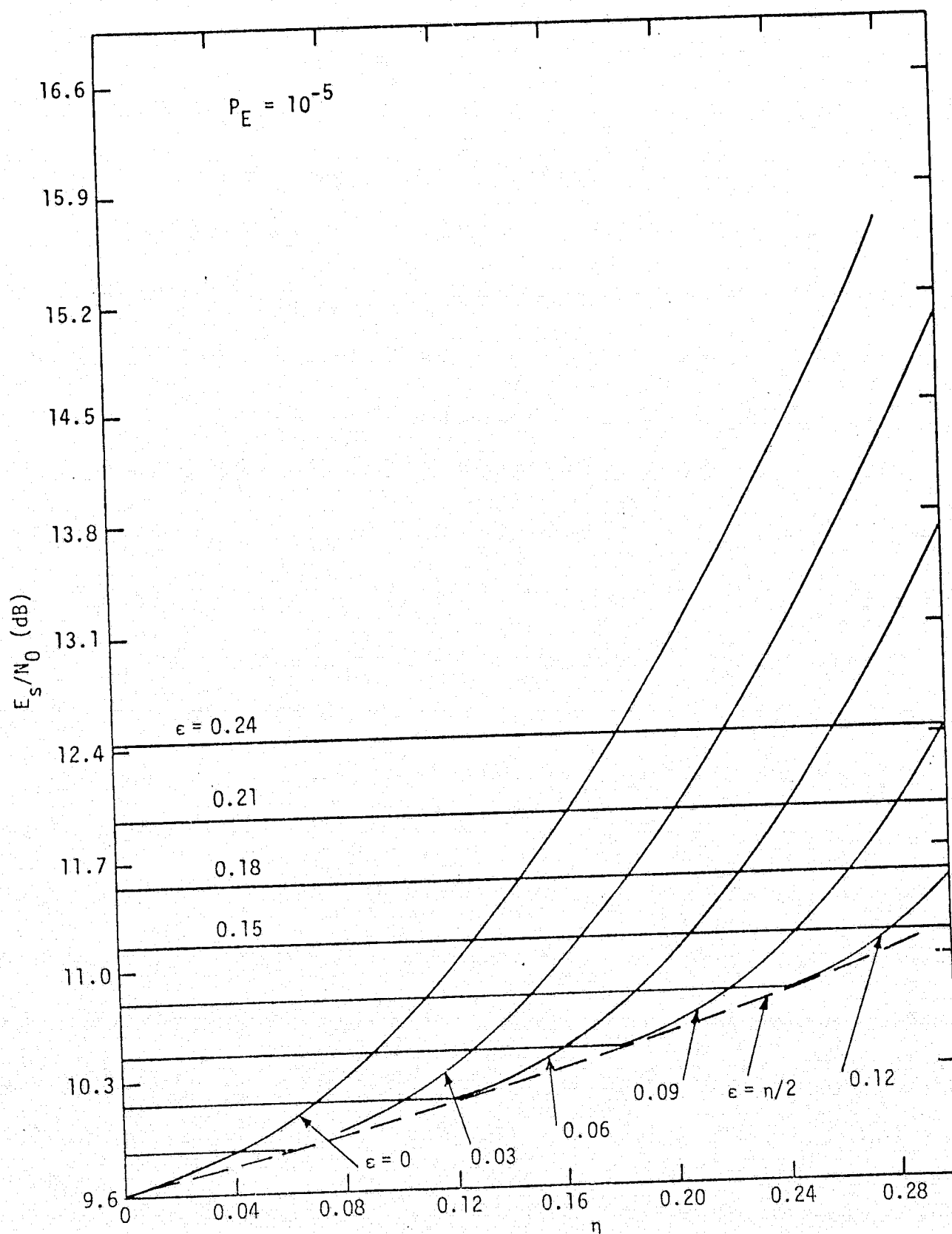


Figure 19. Symbol Energy-to-Noise Ratio versus Data Asymmetry with Gate Interval at Symbol Edge as a Parameter - No D.C. Restoration

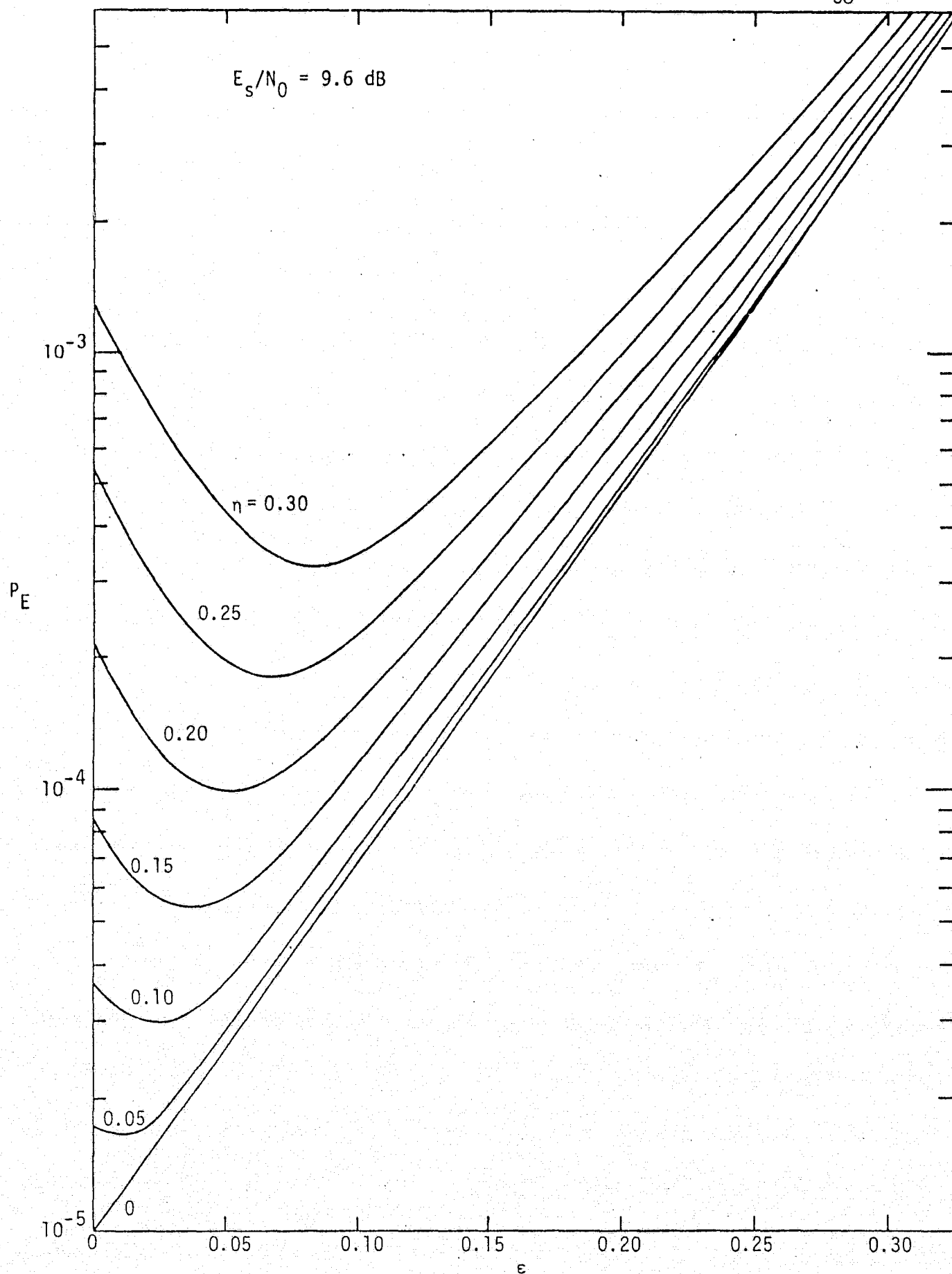


Figure 20. Average Error Probability versus Gate Interval at Symbol Edge with Data Asymmetry as a Parameter - D.C. Restoration by Capacitive Coupling

of  $\epsilon$ , namely,  $\epsilon_{\min}$ , is not equal to  $n/2$ . Figure 21 is the analogous figure to Figure 19 when d.c. restoration is present. Again, the dashed curve corresponds to  $\epsilon = \epsilon_{\min}$  which represents the best achievable performance using the gated integrate-and-dump as a data detector. Comparing Figure 21 with Figure 19, we observe the considerable reduction in SNR degradation due to data asymmetry when d.c. restoration is employed. This improvement is analogous to that achieved when other types of data detectors are used.

In conclusion, the use of a gated integrate-and-dump filter for detection of asymmetric NRZ data can, depending upon the amount of data asymmetry present, produce significant improvement in SNR degradation due to asymmetry relative to that of an ideal integrate-and-dump filter.

## 2.2 Antijam Techniques for Shuttle Communication

There are three basic techniques for antijam communication. These techniques are direct sequence pseudonoise (DSPN), frequency hopping (FH), and time hopping (TH), and any hybrid of these techniques.

### 2.2.1 Direct Sequence Pseudonoise Spreading

The most straightforward way to widen the spectrum of a data signal is to multiply (modulate) it by a wideband signal. Such a spreading signal must have correlation properties that aid in acquisition and tracking. One of the best signals fitting these specifications is the binary pseudonoise (PN) signal. This type of spread spectrum is used on the S-band and Ku-band Shuttle forward links to provide the low flux density over a 4 kHz bandwidth.

The antijam performance of a DSPN system is easily computed. Assume that the additive interfering signal has noise power  $N$  within the PN bandwidth. No matter what its initial bandwidth, when the received signal is demodulated, this interference is spread over the PN bandwidth. Note that the ratio of required energy per bit to single-sided noise spectral density is given by

$$\left(\frac{E_b}{N_0}\right)_{\text{req}} = \frac{ST_b}{NT_c}, \quad (21)$$

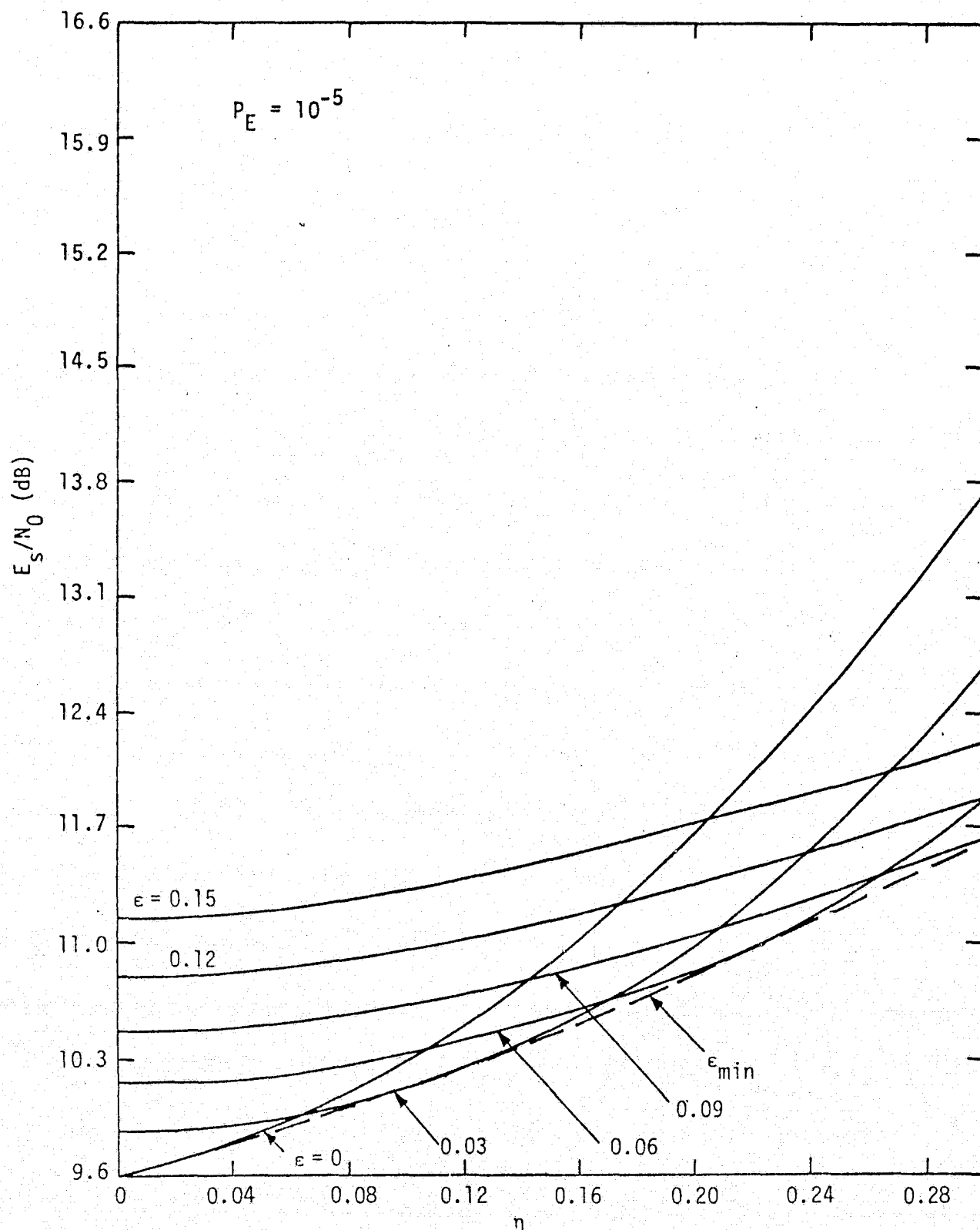


Figure 21. Symbol Energy-to-Noise Ratio versus Data Asymmetry with Gate Interval at Symbol Edge as a Parameter - D.C. Restoration by Capacitive Coupling

where  $S$  is the signal power,  $N$  is the noise power in the PN bandwidth,  $T_b$  is the bit duration, and  $T_c$  is the PN chip duration.

For a tone jammer of the carrier frequency with power  $J$  and white noise power in the PN bandwidth equal to  $N_0/T_c$ , then

$$N = \frac{N_0}{T_c} + J. \quad (22)$$

Therefore,

$$\left(\frac{E_b}{N_0}\right)_{\text{req}} = \frac{S T_b}{\left(\frac{N_0}{T_c} + J\right) T_c} = \frac{S T_b}{N_0 + J T_c} = \frac{1}{\frac{N_0}{S T_b} + \frac{J}{S} \left(\frac{T_c}{T_b}\right)}. \quad (23)$$

Let the available  $E_b/N_0 = S T_b/N_0$  be denoted  $(E_b/N_0)_a$ ; then

$$\frac{J}{S} \left(\frac{T_c}{T_b}\right) = \frac{1}{(E_b/N_0)_{\text{req}}} - \frac{1}{(E_b/N_0)_a}. \quad (24)$$

Define the circuit margin in the presence of white noise only equal to  $M$ ; that is,

$$M = \frac{(E_b/N_0)_a}{(E_b/N_0)_{\text{req}}}. \quad (25)$$

Rewriting (24),

$$\left(\frac{E_b}{N_0}\right) \frac{J}{S} \left(\frac{T_c}{T_b}\right) = M - 1 \quad (26)$$

or

$$\frac{T_c}{T_b} = \frac{(M - 1)}{(E_b/N_0)_a (J/S)}. \quad (27)$$

**ORIGINAL PAGE IS  
OF POOR QUALITY**

Note that  $1/T_b$  is equal to the bit rate  $R_b$  and  $1/T_c$  is equal to the PN chip rate  $R_c$ . Therefore,

$$R_c = R_b \frac{(E_b/N_0)_a (J/S)}{(M - 1)}. \quad (28)$$

As an example of the use of (28), consider the S-band forward link. Let the required  $E_b/N_0$  for a bit error rate of  $10^{-4}$  be

$$\begin{aligned} \left(\frac{E_b}{N_0}\right)_{\text{req}} &= \underbrace{3.5 \text{ dB}}_{\substack{\text{rate } 1/3, K=7 \\ \text{convolutional} \\ \text{coding required} \\ \text{for } P_b = 10^{-4}}} + \underbrace{1.5 \text{ dB}}_{\substack{\text{loss in} \\ \text{bit sync}}} + \underbrace{1.0}_{\substack{\text{loss in PN} \\ \text{despreading}}} + \underbrace{1.0}_{\substack{\text{TDRS} \\ \text{loss}}} \\ &= 7 \text{ dB}. \end{aligned} \quad (29)$$

Let the available  $(E_b/N_0)_a$  for  $R_b = 32$  kbps be

$$\left(\frac{E_b}{N_0}\right)_a = 8 \text{ dB}, \quad (30)$$

and let J/S be 20 dB; then

$$R_c = (32 \text{ kbps}) \frac{(J/S) (E_b/N_0)_a}{(M-1)} = 78 \text{ Mbps}. \quad (31)$$

Note that, since the energy is normalized to the bit rate rather than the coded symbol rate ( $3 \times 32 = 96$  kbps), the bit rate is used in (28). Also note that (28) assumes a PN code length of infinite period but, in actual practice, the PN code rate must be greater than  $T_b/T_c$ . Therefore, in this case, the code length must be 4095 or greater. This example illustrates the disadvantage of using DSPN to achieve antijam communication for moderate data rates and small circuit margins in white noise. The main disadvantage is that extremely high chip rates are required and, as a consequence, the synchronization time becomes unacceptably long.

### 2.2.2 Frequency Hopping

Another method of antijam modulation is frequency hopping (FH). Using this technique, the carrier is hopped over a large number of frequencies (i.e., large bandwidth). The carrier frequency selection process is controlled by a PN sequence which could be nonlinear to



deter determining the selection code by the jammer. Since the frequency hopping rate is of the order of the bit rate and much less than the total hopping bandwidth, the acquisition of a FH system is much easier than a PN system with similar bandwidth.

The antijam performance of a FH system depends on the type of jamming. For example, if the jammer placed equal power at each of the possible carrier frequencies, then the FH processing gain over a non-frequency hopping system is

$$PG_{FH} = \text{number of carrier frequencies} = \frac{B}{R}, \quad (32)$$

where  $B$  is the total available bandwidth and  $R$  is the larger of the frequency hop rate or the bit rate. If, instead of jamming each possible carrier frequency, the jammer could jam 0.2 of the carrier frequencies with enough power to cause an error (probability  $1/2$ ), then the bit error rate would be 10%. Thus, to protect against partial band jamming, an error correcting code must be employed; otherwise, an error would be made every time a carrier frequency from the jammed band was selected.

It is important to note that only noncoherent frequency hopping is being considered, since large hopping bandwidths make it impractical to maintain phase coherence across the total bandwidth. Therefore, each hop has an independent phase but the phase is constant over the hop. Because of the noncoherent frequency hopping, unless a very slow frequency hopping rate is used which would allow frequency following by the jammer, it is impractical to lock up a carrier tracking loop at each frequency hop. Therefore, in the Shuttle application, a modification to the carrier recovery must be made to the demodulator. Probably the simplest modification is to employ differential PSK (DPSK) and derive the carrier phase by comparing the successive bits.

To calculate the antijam performance of a FH system, effective signal-to-noise ratio is defined as

$$\left(\frac{E_b}{N_0}\right)_{\text{eff}} = \left(\frac{B}{R_b}\right) \frac{S}{J}, \quad (33)$$

where  $B$  is the hopping bandwidth,  $R_b$  is the bit rate,  $J$  is the interference power, and  $S$  is the signal power. Note that, in using  $(E_b/N_0)_{\text{eff}}$ , it is assumed that the thermal noise is insignificant to the jammer power (i.e., 10 dB less than  $J$ ). For DPSK modulation with soft decision Viterbi decoding (rate 1/2 or rate 1/3), the required  $(E_b/N_0)_{\text{eff}}$  is shown in Table 4.

For FH-PN/DPSK, the data modulation is first spread with a PN code as in DSPN and then the carrier is hopped. Using (33), the required bandwidth can be determined for the example used in the DSPN case. For rate 1/3 Viterbi decoding,  $(E_b/N_0)_{\text{eff}} = 7.8$  dB at  $P_b = 10^{-5}$ . Thus,

$$\left(\frac{E_b}{N_0}\right)_{\text{eff}} = \left(\frac{B}{R_b}\right) \frac{S}{J} = 7.8 \text{ dB} , \quad (34)$$

with  $R_b = 32$  kbps for the S-band and  $(J/S) = 20$  dB, then

$$B = 19.6 \text{ MHz} . \quad (35)$$

For the Ku-band forward link,  $R_b$  is equal to 216 kbps. With no coding on the Ku-band forward link,  $(E_b/N_0)_{\text{eff}} = 42.6$  dB for  $P_b = 10^{-5}$ . To achieve  $(J/S) = 20$  dB, then

$$B = 393 \text{ GHz} , \quad (36)$$

which is clearly impractical. However, if rate 1/3 Viterbi decoding is used, then  $(E_b/N_0)_{\text{eff}} = 7.8$  dB and  $B = 130$  MHz.

Note again that (33) assumes a reasonably high circuit margin in thermal noise. If this cannot be achieved, then a finer antijam performance analysis can be made. But even if  $B$  was required to be greater than 130 MHz, the synchronization requirements would not be increased over the modest requirements of the FH system in the example because the synchronization time is independent of the hopping bandwidth.

### 2.2.3 Time Hopping

Whereas FH channelizes via different carrier frequencies within a given bandwidth, time hopping (TH) channelizes via time slots within

Table 4. Antijam Performance of Frequency Hopping

Signal Format	Required $(E_b/N_0)_{\text{eff}}$ Worst Case Jamming	
	FH/DPSK (dB)	FH-PN/DPSK (dB)
No Coding $P_b = 10^{-3}$ $P_b = 10^{-5}$	27.0	22.6
	47.0	42.6
R = 1/2 Viterbi Decoding $P_b = 10^{-3}$ $P_b = 10^{-5}$	10.4	6.1
	14.3	10.0
R = 1/3 Viterbi Decoding $P_b = 10^{-3}$ $P_b = 10^{-5}$	9.2	4.9
	12.3	7.8

ORIGINAL PAGE IS  
OF POOR QUALITY

a given time frame. A burst transmission is employed within the slot selected by a PN code or nonlinear sequence. Provided the TH transmitter can operate at a high peak power but with low duty factor, the TH system has the same antijam performance as the FH system. The TH system does not appear practical for the Shuttle system unless the transmitter is converted to a high peak power pulsed operation.

As a conclusion to the antijam techniques for the Shuttle communications, it appears that a frequency hopping system could provide the best antijam performance for the Shuttle S-band and Ku-band forward links with some modification to the demodulator in deriving carrier phase.

### 3.0 TRACKING TECHNIQUES ANALYSIS

As a part of the overall effort to assess the Ku-band system design and to evaluate possible system simplifications/modifications that may be achievable, this task requires Axiomatix to study the design and implementation of tracking techniques which are suitable for incorporation into the Orbiter Ku-band communication system. Emphasis is placed on maximizing tracking accuracy and communications system flexibility while minimizing cost, weight, and system complexity of Orbiter and ground system hardware.

In a host of previous studies [6-13], much consideration has been given to implementation of the three-channel Orbiter modulator, whose purpose is to generate a signal for simultaneous transmission of three channels of information on the Ku-band return link. One of the possible structures for Mode 1 is referred to as the Three-Channel Quadrature Multiplex Modulator [9], wherein the high data rate channel (50 Mbps) is biphase modulated on an in-phase carrier and the two lower rate channels (192 kbps and up to 2 Mbps), after being biphase modulated onto quadrature squarewave subcarriers and summed, are amplitude modulated onto the quadrature carrier (see Figure 22). The receiver for the three-channel quadrature multiplex signal employs biphase Costas loops for carrier and subcarrier recovery. While the performance of the carrier recovery loop has previously been investigated [6, Appendix C], the companion performance analysis for the subcarrier loop has not. Thus, the first part of this task focuses on developing the theory necessary to carry out this analysis. In particular, we begin with a fundamental study of the tracking performance of biphase Costas loops when subjected to an unbalanced QPSK input. The plural usage in the phrase "biphase Costas loops" refers to the fact that we shall study several different Costas loop implementations, each of which has advantages over the others, depending on the application. Following these more general analyses, we shall apply the results specifically to the subcarrier tracking loop of the Ku-band return link.

ORIGINAL PAGE IS  
OF POOR QUALITY

ORIGINAL PAGE IS  
OF POOR QUALITY

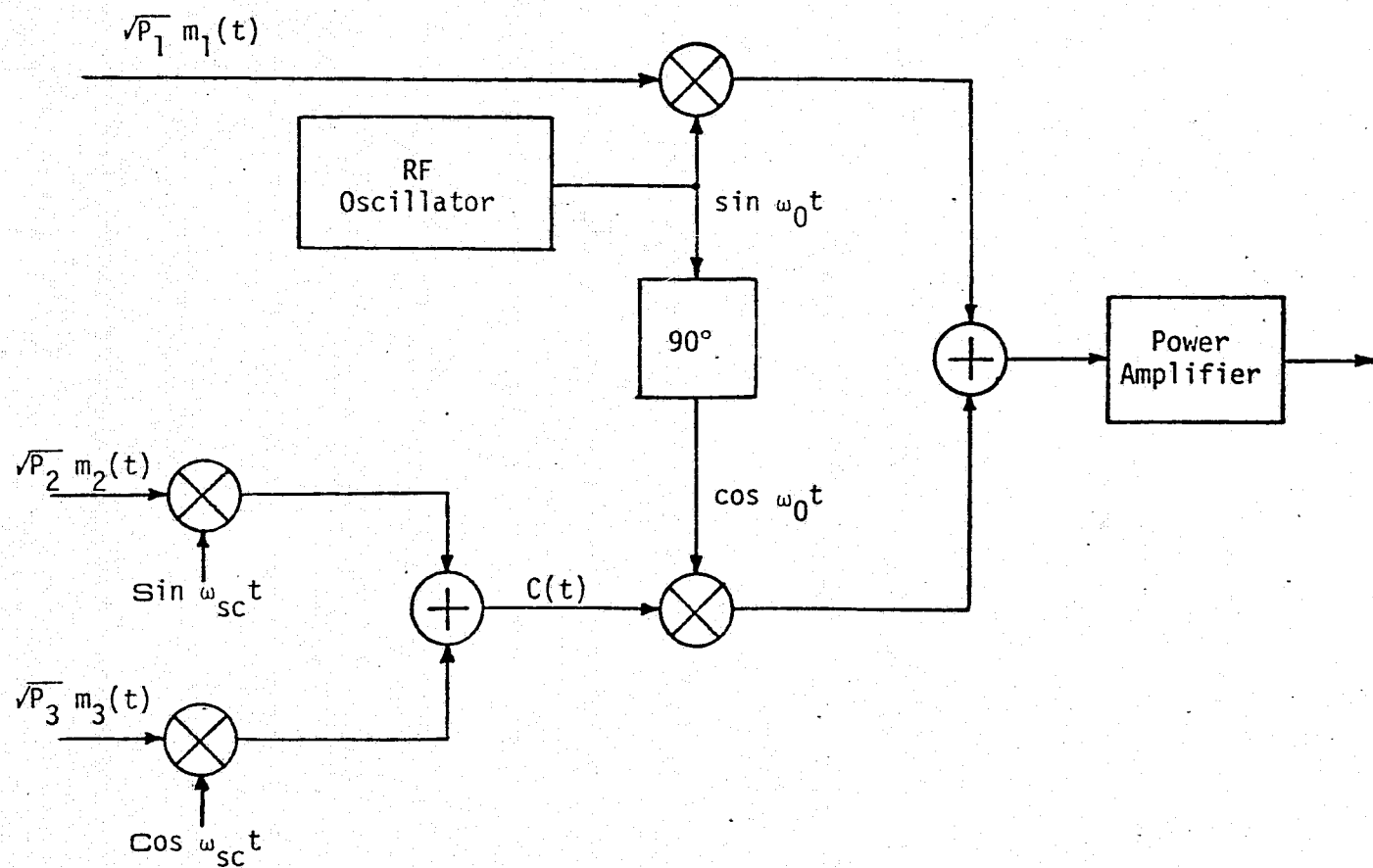


Figure 22. Three-Channel Quadrature Multiplex Modulator - Mode 1

### 3.1 Tracking Performance of Unbalanced QPSK Demodulators

Unbalanced quadriphase-shift-keying (QPSK) used on the Ku-band return link is an attractive means for transmitting two digital data streams which have different average powers. The two data streams are not constrained to have identical data rates nor must they have the same data format; e.g., one might be an NRZ sequence and the other a Manchester code. In fact, it is the difference in data rates which causes the unbalance of power when it is desired to have symbol energies and therefore error rates on the two channels within the same order of magnitude.

#### 3.1.1 Biphase Costas Loop With Passive Arm Filters

Previous results [14,15] have indicated that, when the unbalanced power ratio is large, e.g., approximately 4:1 or greater, a biphase Costas loop is a more efficient demodulator than a fourth-power tracking loop. These results, however, accounted only for the filtering effect produced by the two passive arm filters of the loop on the equivalent additive noise perturbing the loop. When the bandwidth of these filters is selected on the order of the data rate, as is typical of optimum Costas loop design for tracking purposes [16,17], the filtering degradations of the data modulations themselves and the cross-modulation noise produced by their multiplication in the loop often cannot be neglected.

An analysis that incorporates these additional filtering effects into the performance characterization of a biphase Costas loop demodulator of unbalanced QPSK is presented in Appendix E. Many of the results obtained in this appendix are in the form of closed-form expressions which can easily be evaluated numerically for design and performance prediction purposes. The generality of the results enables them to be applied to a wide variety of applications, in particular, the performance of the subcarrier tracking loop for the three-channel Orbiter Ku-band return link, which will be discussed later on. For the moment, we shall briefly summarize the results given in Appendix E.

It is common practice to characterize the tracking performance of a Costas loop by the variance of the loop phase error  $2\varphi$ , often referred to as the tracking phase jitter. In the linear region of operation, an expression for this quantity is given by

$$\sigma_{2\varphi}^2 = \frac{4}{\rho S_L}, \quad (37)$$

where  $\rho \triangleq P_T/N_0 B_L$  is the total power ( $P_T$ ) to noise spectral density ( $N_0$ ) ratio in the loop bandwidth ( $B_L$ ) and  $S_L$  is the so-called squaring loss, which represents the additional degradation in equivalent loop signal-to-noise ratio relative to a linear loop, i.e., one in which there exists no noise  $\times$  noise or signal  $\times$  noise error signal components. Thus, from (37), we see that characterization of the loop squaring loss in terms of system parameters is sufficient for predicting the loop's tracking performance.

As a numerical illustration of this characterization, consider the case where the low rate modulation  $m_1(t)$  is Manchester coded data, the high rate modulation  $m_2(t)$  is NRZ data, and the arm filters are single-pole Butterworth (RC) filters. Then Figure 23 illustrates (for fixed fractional channel powers  $\eta_1$  and  $\eta_2$  corresponding to a 4:1 power ratio on the two channels) the behavior of  $S_L$  as a function of the ratio of two-sided arm filter noise bandwidth  $B_1$  to the higher of the two data rates  $R_2 = 1/T_2$ , with the ratio of data rates  $R_2/R_1$  and  $P_T T_2/N_0$  as parameters. Assuming  $P_T/N_0$  to be fixed, then the variation of squaring loss with  $P_T T_2/N_0$  directly reflects the effect of changing the high data rate  $R_2$ . Furthermore, at low values of  $B_1/R_2$ , we observe from Figure 23 that additional interesting peaks and valleys of the squaring loss characteristic occur. These extrema represent tradeoffs between S $\times$ S distortion and cross-modulation noise or S $\times$ N power, depending on which of the latter dominates the total noise.

The corresponding numerical evaluation of the tracking jitter, for a fixed ratio of arm filter noise bandwidth to the loop noise bandwidth ( $B_1/B_L$ ) is shown in Figure 24. The minimum values of  $\sigma_\varphi$  for some ratios of  $R_2/R_1$  represent best design points when the combined effect of N $\times$ N distortion and cross-modulation noise or S $\times$ N power is minimal. Assuming  $P_T/N_0$  to be fixed, the variation of  $\sigma_\varphi$  with  $P_T T_2/N_0$  is shown in Figure 25. As is intuitively true, the tracking jitter performance improves with the increase of  $P_T T_2/N_0$ .



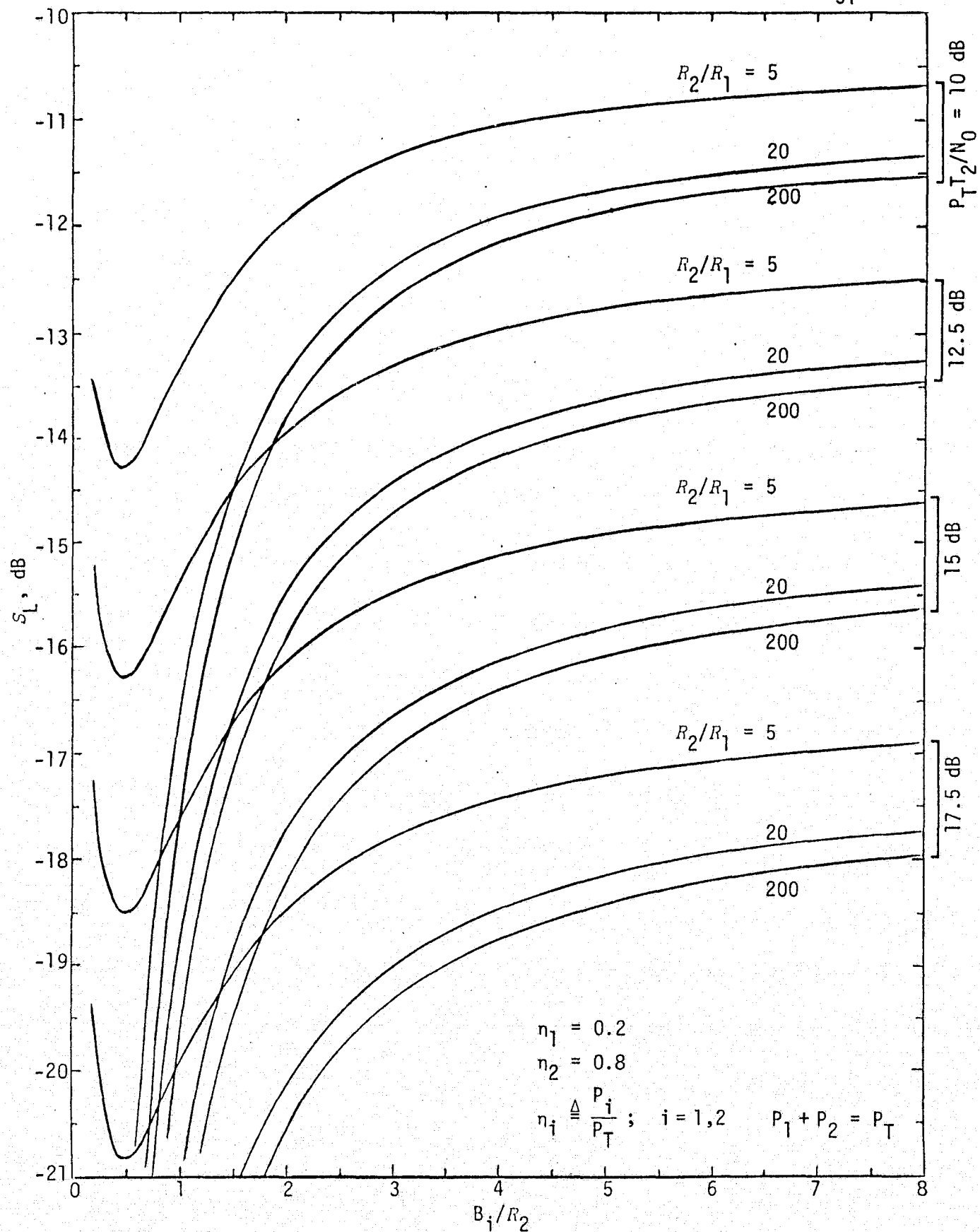


Figure 23. Squaring Loss vs. Ratio of Arm Filter Bandwidth to High Data Rate;  $P_T T_2/N_0$  and  $R_2/R_1$  are parameters;  $m_1(t)$  is Manchester code,  $m_2(t)$  is NRZ;  $R_2 \geq 2R_1$

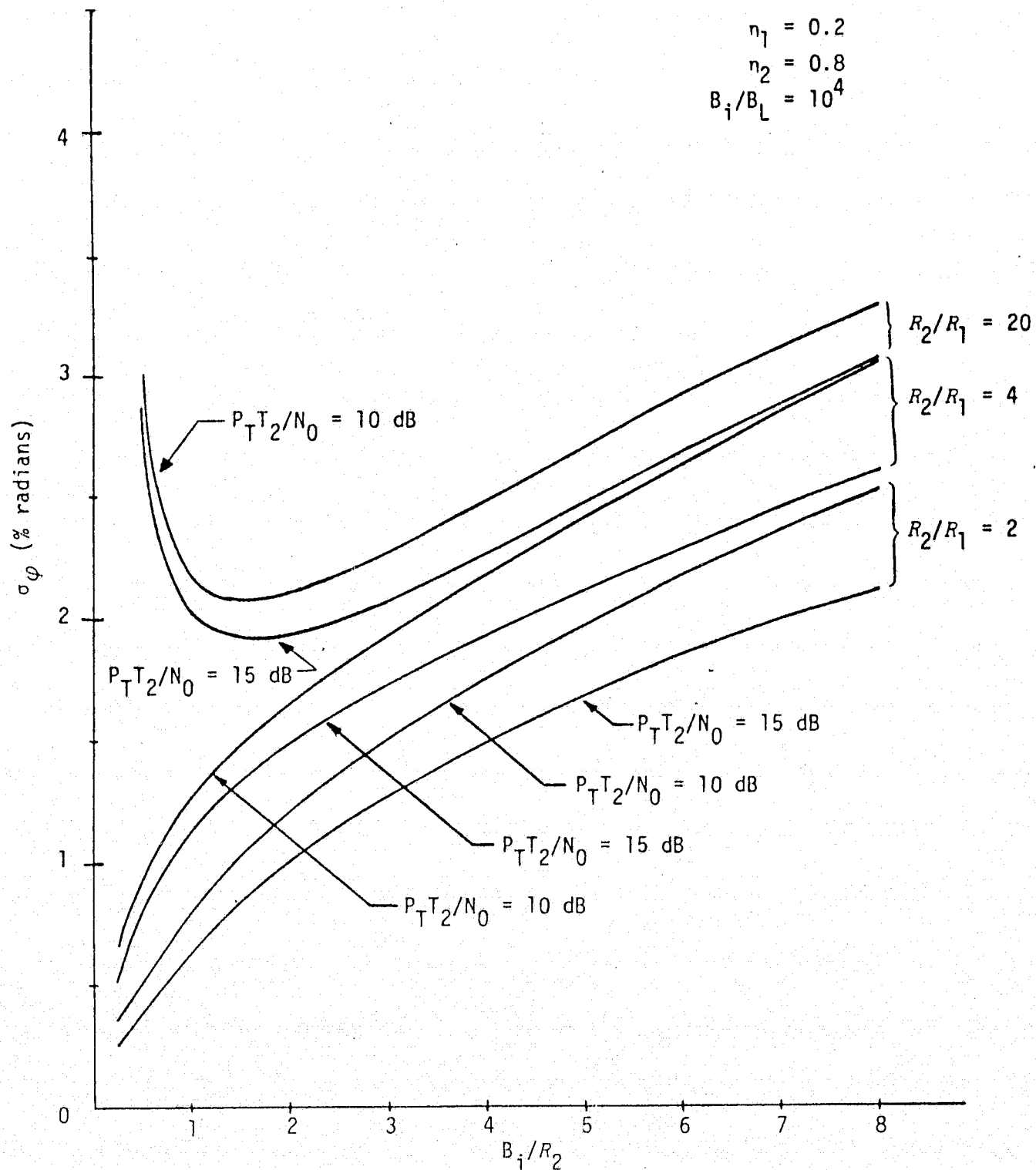


Figure 24. Tracking Jitter Standard Deviation versus Ratio of Arm Filter Bandwidth to High Data Rate;  $P_T T_2/N_0$  and  $R_2/R_1$  are parameters;  $m_1(t)$  is Manchester code,  $m_2(t)$  is NRZ;  $R_2 \geq R_1$ .

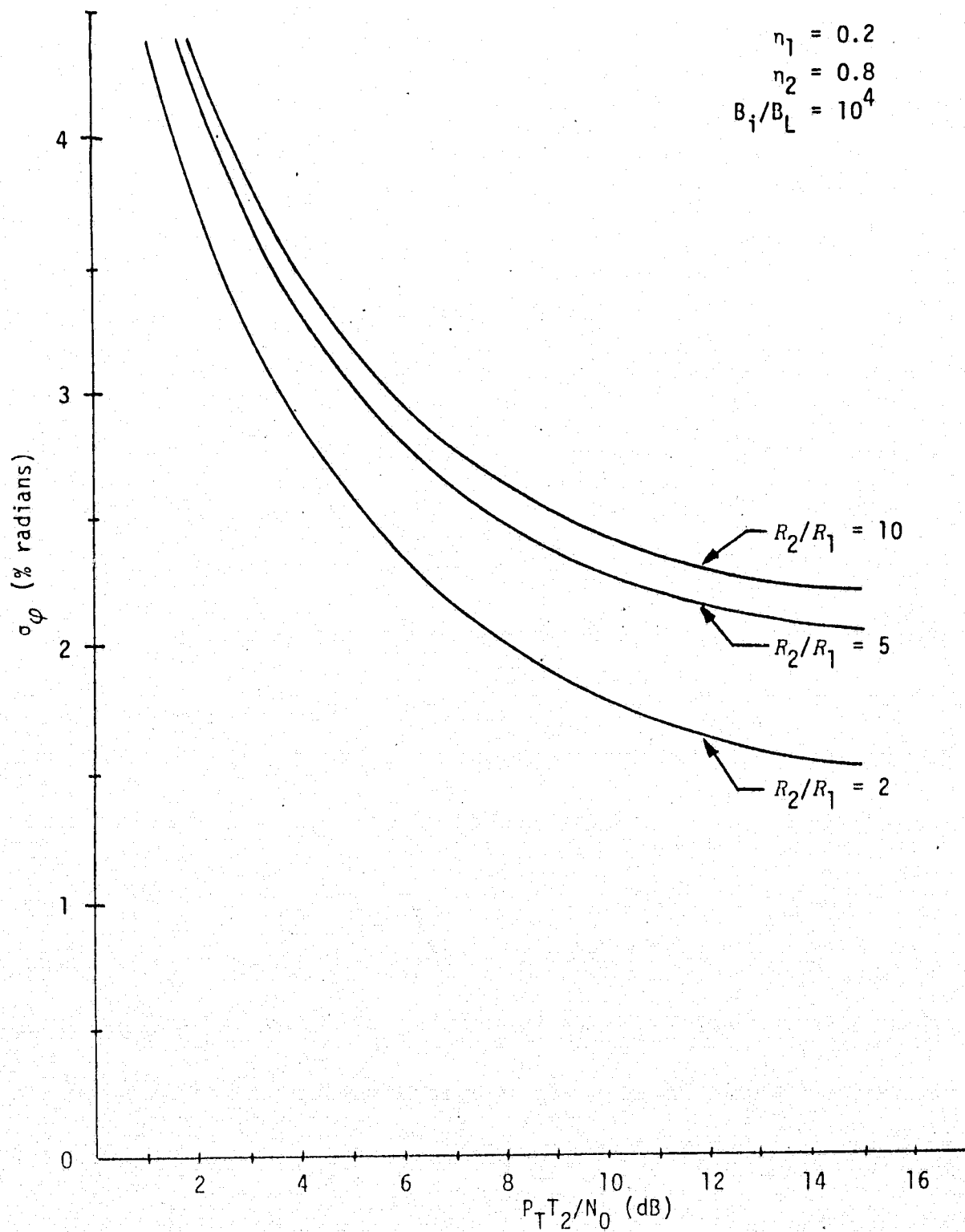


Figure 25. Tracking Jitter Standard Deviation versus  $P_T T_2 / N_0$ ;  $B_i/R_2 = 4$ ;  $R_2/R_1$  is a parameter;  $m_1(t)$  is Manchester code,  $m_2(t)$  is NRZ;  $R_2 \geq R_1$ .

### 3.1.2 Biphase Costas Loop With Active Arm Filters

In a previous Costas loop study for biphase modulation [16], it was demonstrated that considerable improvement in tracking performance could be obtained by employing active arm filters of the integrate-and-dump type as opposed to passive arm filters. An investigation of whether a similar performance improvement can be obtained for an unbalanced QPSK modulation is presented in detail in Appendix F. The highlights of this investigation are summarized as follows.

In Section 3.1.1, we observed that, for given values of the data rate ratio  $R_2/R_1$ , power ratio  $P_1/P_2$ , and total signal-to-noise ratio in the high data rate bandwidth  $P_T T_2/N_0$ , an optimum arm filter bandwidth or, equivalently,  $B_i/R_2$ , exists in the sense of maximizing  $S_L$  (i.e., minimizing the squaring loss). Using that value of  $B_i/R_2$ , namely,  $(B_i/R_2)_{\text{opt}}$ , and defining the corresponding value of  $S_L$  by  $S_{L_{\text{opt}}}$ , then the minimum improvement in tracking performance (or, equivalently, in squaring loss performance) obtained by employing active integrate-and-dump arm filters as opposed to active arm filters is given by  $I \triangleq S_L/S_{L_{\text{opt}}}$ , where  $S_L$  is used here to denote the squaring loss of the Costas loop with integrate-and-dump arm filters.

Closed-form expressions for  $S_L$  are derived in Appendix F for all combinations of NRZ and Manchester data formats for the two channels and both synchronized and unsynchronized symbol clocks. As an example, assuming single-pole (RC) arm filters as the basis of comparison for the Costas loop with passive arm filters and assuming unsynchronized symbol clocks for the Costas loop with integrate-and-dump filters, Figures 26 and 27 illustrate  $I$  (in dB) versus the channel power ratio  $P_1/P_2$  with the data rate ratio  $R_2/R_1$  as a parameter and values of total power-to-noise ratio  $P_T T_2/N_0$  typical of coded and uncoded systems. We observe from these figures that the improvement in squaring loss performance of using integrate-and-dump filters as opposed to single-pole arm filters is an increasing function of  $P_1/P_2$  and depends heavily on the choice of data formats for  $m_1(t)$  and  $m_2(t)$ .

Similarly, using many numerical illustrations, it is shown in Appendix F that, for a fixed ratio of data rates and total power-to-noise ratio in the higher data bandwidth, the squaring loss itself

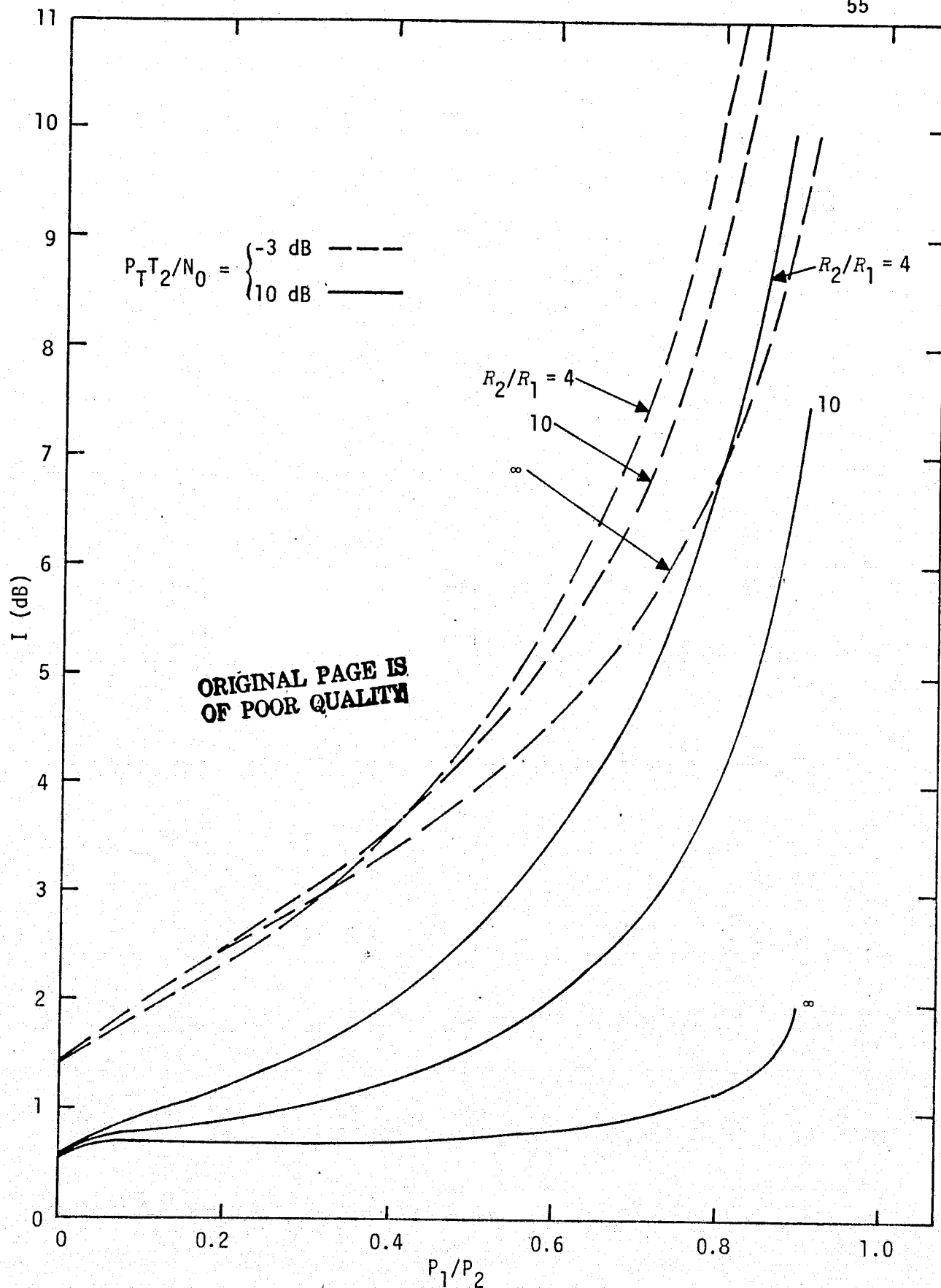


Figure 26. Squaring Loss Improvement (in dB) Using Integrate-and-Dump Arm Filters as Opposed to Single-Pole Passive Arm Filters;  $m_1(t)$  is Manchester,  $m_2(t)$  is NRZ

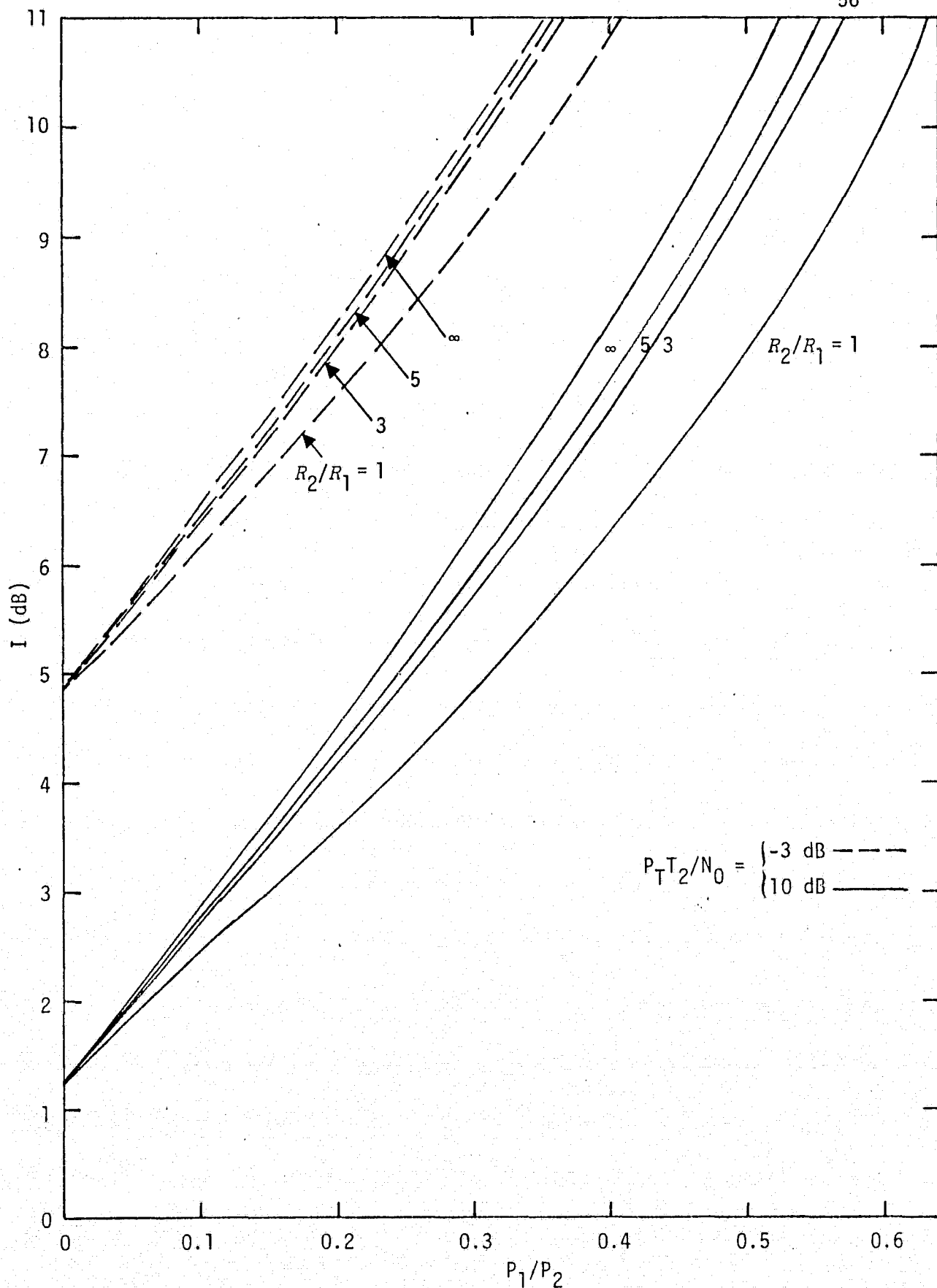


Figure 27. Squaring Loss Improvement (in dB) Using Integrate-and-Dump Arm Filters as Opposed to Single-Pole Passive Arm Filters;  $m_1(t)$  is NRZ,  $m_2(t)$  is Manchester

increases as the ratio of powers in the two channels increases, and the rate at which this loss increases (tracking performance deteriorates) also depends heavily upon the data formats in each channel. Thus, it is concluded that, when the ratio of data rates is on the same order of magnitude as the inverse of the power ratio, i.e., approximately equal signal energies in the two channels, the biphase Costas loop can be used as an efficient demodulator of QPSK. On the other hand, if the energy in the two channels is very unbalanced, e.g., one channel is coded and one is uncoded, then it is still possible to efficiently use a biphase Costas loop for demodulation of unbalanced QPSK, provided that the higher data rate channel is Manchester coded. It is understood that the foregoing conclusions are quite general and are not intended to rule out specific design situations in which sufficient total power-to-noise ratio is available to tolerate large squaring losses. In an individual situation, one must resort to the specific numerical results given in the illustrations to determine the suitability of employing a biphase Costas loop for demodulation of unbalanced QPSK.

### 3.1.3 Biphase Polarity-Type Costas Loop With Passive Arm Filters

In Sections 3.1.1 and 3.1.2, we addressed the problem of tracking an unbalanced QPSK signal with a conventional biphase Costas loop with analog input phase detectors and an analog third multiplier (the one that forms the loop error signal). Because of dc offsets associated with analog multipliers, it is common practice to hard-limit the in-phase\* channel arm filter output and replace the analog third multiplier with a chopper-type device (switched multiplier) which typically exhibits much less offset (see Figure 28). While it is also possible to replace the input in-phase and quadrature analog phase detectors with switched multipliers, the impact of doing so on the resulting tracking performance is minimal since the arm filters will pass only the first harmonic of these phase detector outputs. Thus, aside from the  $8/\pi^2$  power loss associated with the first harmonic of a square wave, the

---

\*For unbalanced quadriphase, we shall arbitrarily refer to the in-phase channel as that corresponding to the point of data extraction for the higher power signal.

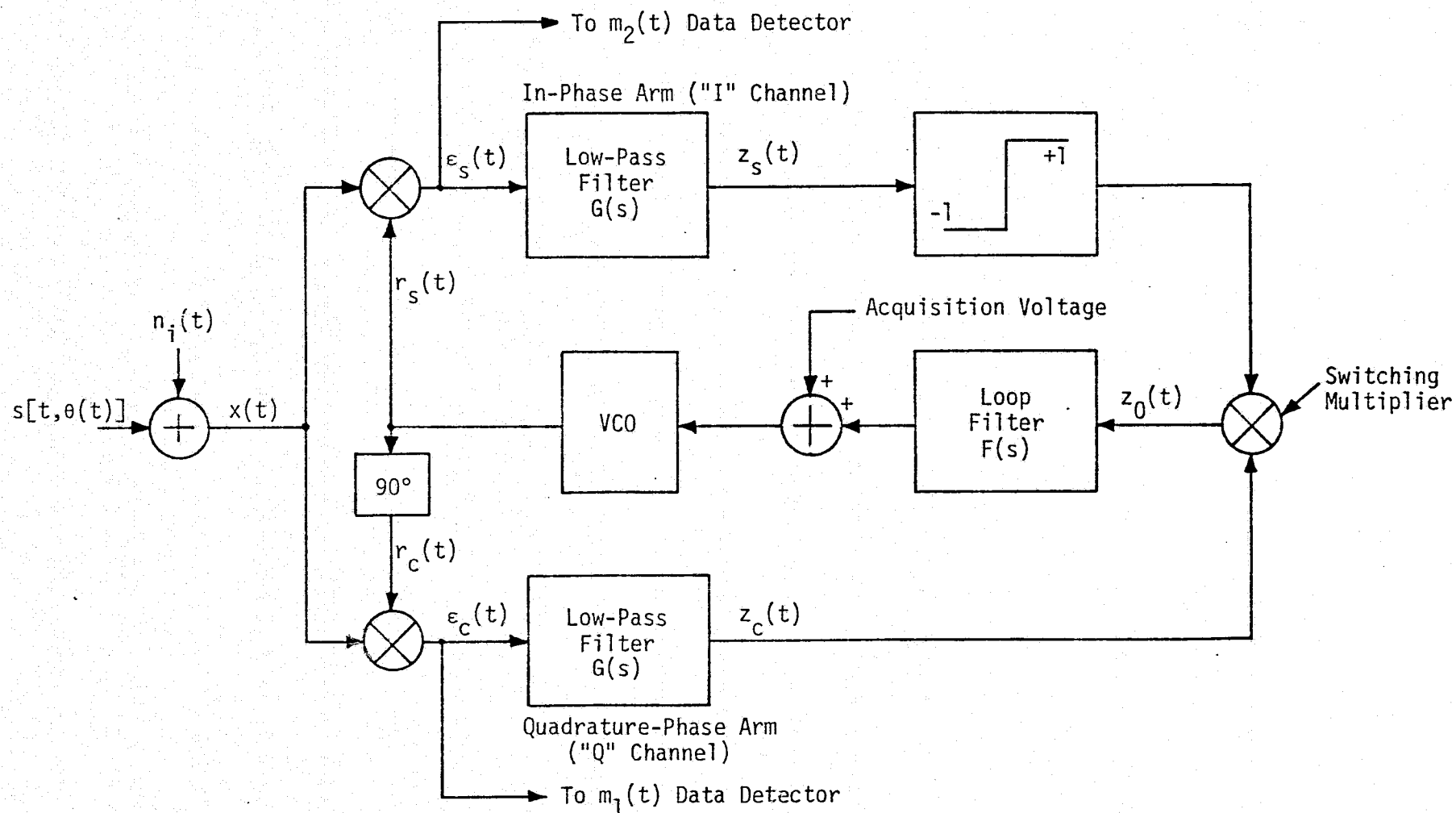


Figure 28. Costas Loop with Hard-Limited In-Phase Channel



performance of the loop would be identical to that given in Section 3.1.1 for an analog third multiplier or that to be presented here for a switched third multiplier. For ease of terminology, we shall refer to a conventional biphase Costas loop with a switched third multiplier as a "biphase polarity-type Costas loop" or, even simpler, a "polarity-type Costas loop."

Generally speaking, introduction of a limiter (hard or soft) into a system results in signal suppression, the amount of which is a function of the signal-to-noise ratio at the limiter input. This signal suppression, in turn, reduces the total loop gain and, as a consequence, the loop bandwidth. Another potential problem with the limiter under strong signal conditions is that it may increase the tendency of the loop to false lock.

Appendix G discusses in detail the tracking behavior of the polarity-type Costas loop with unbalanced QPSK input and compares its performance with that of the conventional Costas loop discussed in Section 3.1.1 and Appendix E. In particular, for the case of single-pole Butterworth (RC) arm filters and a particular combination of NRZ and Manchester coded data on the two channels, the squaring loss (tracking jitter penalty relative to a linear loop) is evaluated and illustrated as a function of the ratio of arm filter bandwidth to higher data rate and total signal power-to-noise ratio in this higher data rate bandwidth. Also numerically illustrated is the corresponding mean-squared tracking jitter performance as a function of these same receiver parameters. A summary of these results is given as follows. Figure 29 illustrates the variations of  $S_L$  versus  $B_1/R_2$  with  $P_{T2}/N_0$  as a parameter. Superimposed on these curves (in dashed lines) are the corresponding results obtained from Figure 23 for the biphase Costas loop with passive arm filters. We observe from these numerical results that, for high signal-to-noise ratios, the hard-limited loop actually outperforms the conventional loop and, depending on the data rate ratio, the improvement (in terms of squaring loss) might be as high as 2.8 dB. Also, for a given signal-to-noise ratio and a given arm filter bandwidth to high data rate ratio, the squaring loss does not change significantly with data rates when the ratio of the data

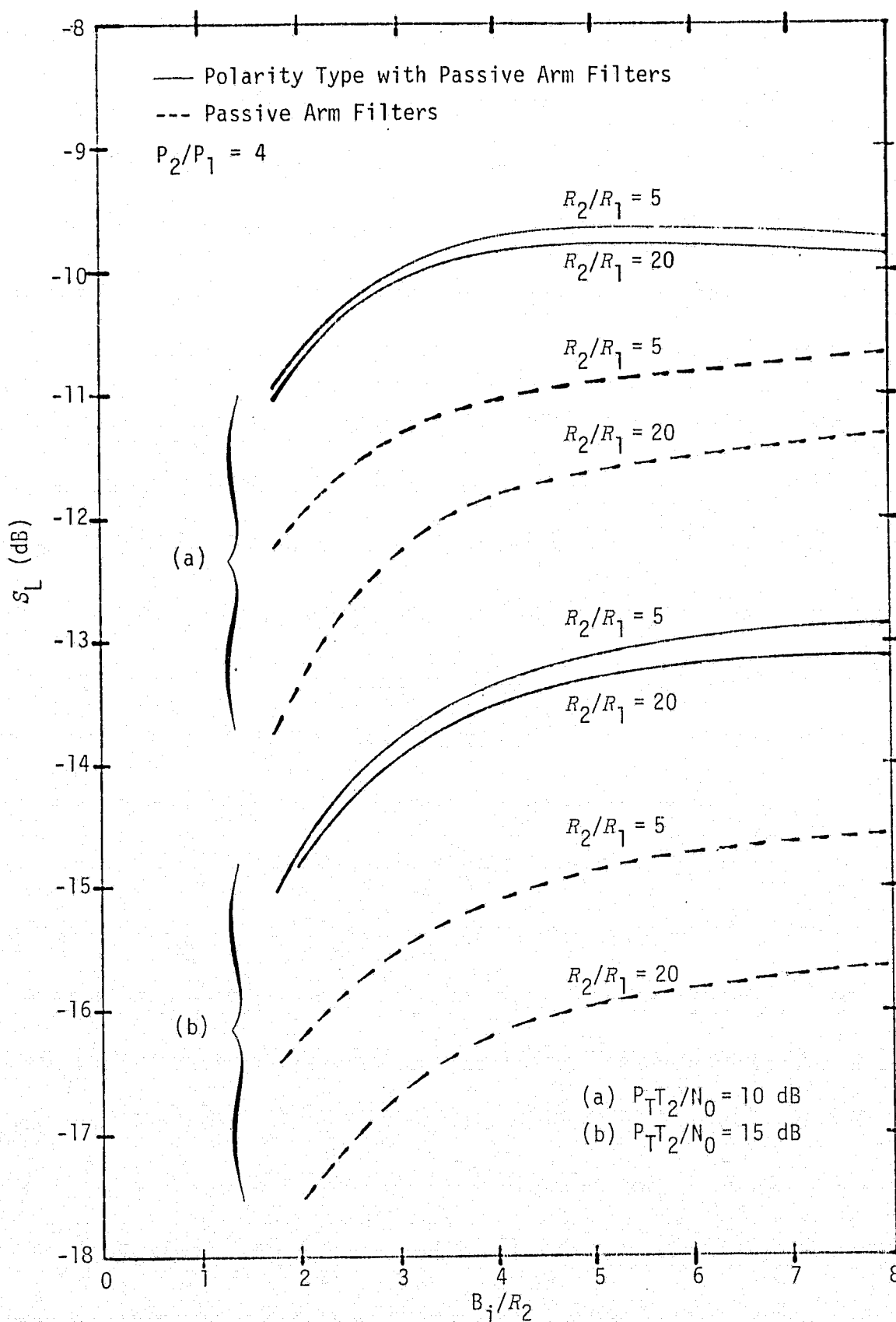


Figure 29. Squaring Loss Variations Versus  $B_i/R_2$  with  $R_2/R_1$  and  $P_T T_2/N_0$  as Parameters;  $m_1(t)$  is Manchester code,  $m_2(t)$  is NRZ.

ORIGINAL PAGE IS  
OF POOR QUALITY

rates is high. This is particularly true for small values of arm filter bandwidth to high data rate ratio. A comparison with the dotted curves of Figure 29 reveals that the same is not true for the conventional Costas loop with passive arm filters. However, the fact that the polarity-type Costas loop produces an improvement in tracking performance at high signal-to-noise ratios over the biphase Costas loop with passive arm filters is not surprising in view of similar results recently demonstrated for biphase modulation [18].

### 3.2 Performance of the Subcarrier Tracking Loop for the Three-Channel Orbiter Ku-Band Return Link

Having examined the many ways in which a biphase Costas loop can track an unbalanced QPSK signal, we are now in a better position to analyze the tracking performance of the subcarrier loop for the three-channel Orbiter Ku-band return link. The primary difference between the subcarrier loop tracking behavior and that of the loops discussed in Section 3.1 is the fact that the in-phase and quadrature data modulations which are input to the subcarrier loop are biphase modulated onto quadrature square-wave subcarriers as opposed to sine-wave subcarriers. A secondary difference is the fact that, since the output of the quadrature phase detector of the carrier tracking loop serves as the input to the subcarrier loop, the performance of the latter depends on the carrier tracking loop phase error. An analysis which takes both of these differences into account is given in Appendix H. For simplicity of numerical evaluation, it was found convenient to assume perfect carrier tracking. The additional degradation due to the phase tracking jitter of the carrier loop itself can be easily assessed from the results of a previous report [6, Appendix C] wherein the performance of a Costas loop for recovering the carrier from the three-channel quadrature multiplex signal was studied.

Some specific results from Appendix H are summarized below. In addition to perfect carrier tracking which was already mentioned, the following assumptions were made. The subcarrier frequency is 8.5 MHz, the high rate modulation  $m_1(t)$  in Mode 1 is a rate 1/2, constraint length 7, convolutional code (NRZ format) with data rate  $R_1 = 50$  Mbps, and the arm filters in the subcarrier loop are one-pole Butterworth (RC).

Under these assumptions, Figures 30 and 31 illustrate the subcarrier tracking jitter behavior for a fixed ratio of arm filter noise bandwidth to loop noise bandwidth ( $B_i/B_L$ ). In particular, Figure 30 illustrates the case where  $m_2(t)$  is NRZ data at 500 kbps and  $m_3(t)$  is Manchester coded data at 192 kbps, while Figure 31 corresponds to the same parameter values as Figure 30 with the exception that  $m_2(t)$  is now also Manchester coded. In both figures, the rms tracking jitter,  $\sigma_\phi$  (in % radians), is plotted versus the ratio of two-sided arm filter noise bandwidth ( $B_i$ ) to the higher data rate ( $R_2$ ) with total power-to-noise ratio in the higher data rate bandwidth ( $P_T T_2/N_0$ ) as a parameter. It is observed that the changes in the subcarrier tracking jitter as a function of  $B_i/R_2$  are more obvious when  $m_2(t)$  and  $m_3(t)$  are both Manchester codes than when  $m_2(t)$  is NRZ and  $m_3(t)$  is Manchester.

Upon establishing a subcarrier reference signal, the two lower rate modulations,  $m_2(t)$  and  $m_3(t)$ , can then be demodulated. The error probability performance associated with these two data demodulations is the subject of discussion in the next section.

### 3.3 Error Probability Performance of Channels 2 and 3 of the Three-Channel Ku-Band Return Link

Evaluation of error probability performance of BPSK, QPSK, and offset (staggered) QPSK receivers has been extensively covered in the literature [19-24]. While the techniques used there are certainly applicable to demodulation of unbalanced QPSK as on the two lower rate channels of the three-channel signal, the complexity of the evaluation when the ratio of data rates in the two channels is large prompts one to look for a simpler calculation procedure. Indeed, such an approach is possible when the noisy reference loss\* is small or, equivalently, the effective signal-to-noise ratio in the tracking loop bandwidth is large, i.e., the loop operates in its so-called linear region. Making such an assumption for purposes of error probability performance evaluation is quite reasonable when one realizes that this very same assumption

---

\*"Noisy reference loss" is defined here as the equivalent increase in signal power required to produce the same error probability as obtainable in a perfectly synchronized system.

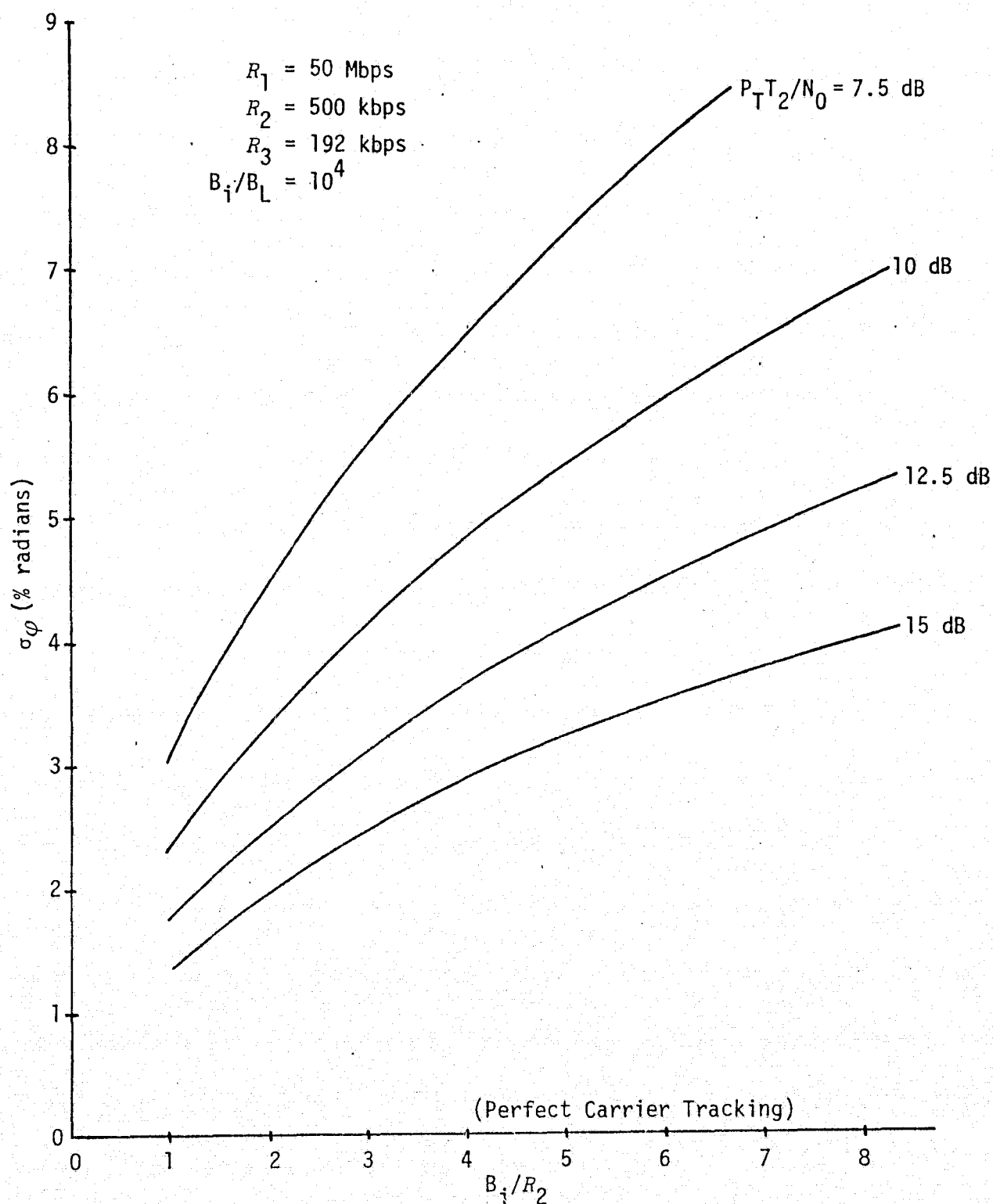


Figure 30. Subcarrier Tracking Jitter versus Ratio of Arm Filter Bandwidth to High Subcarrier Data Rate  $R_2$ ;  $P_T T_2/N_0$  is a parameter;  $m_1(t)$  and  $m_2(t)$  are NRZ,  $m_3(t)$  is Manchester;  $R_1 > R_2 > R_3$ .

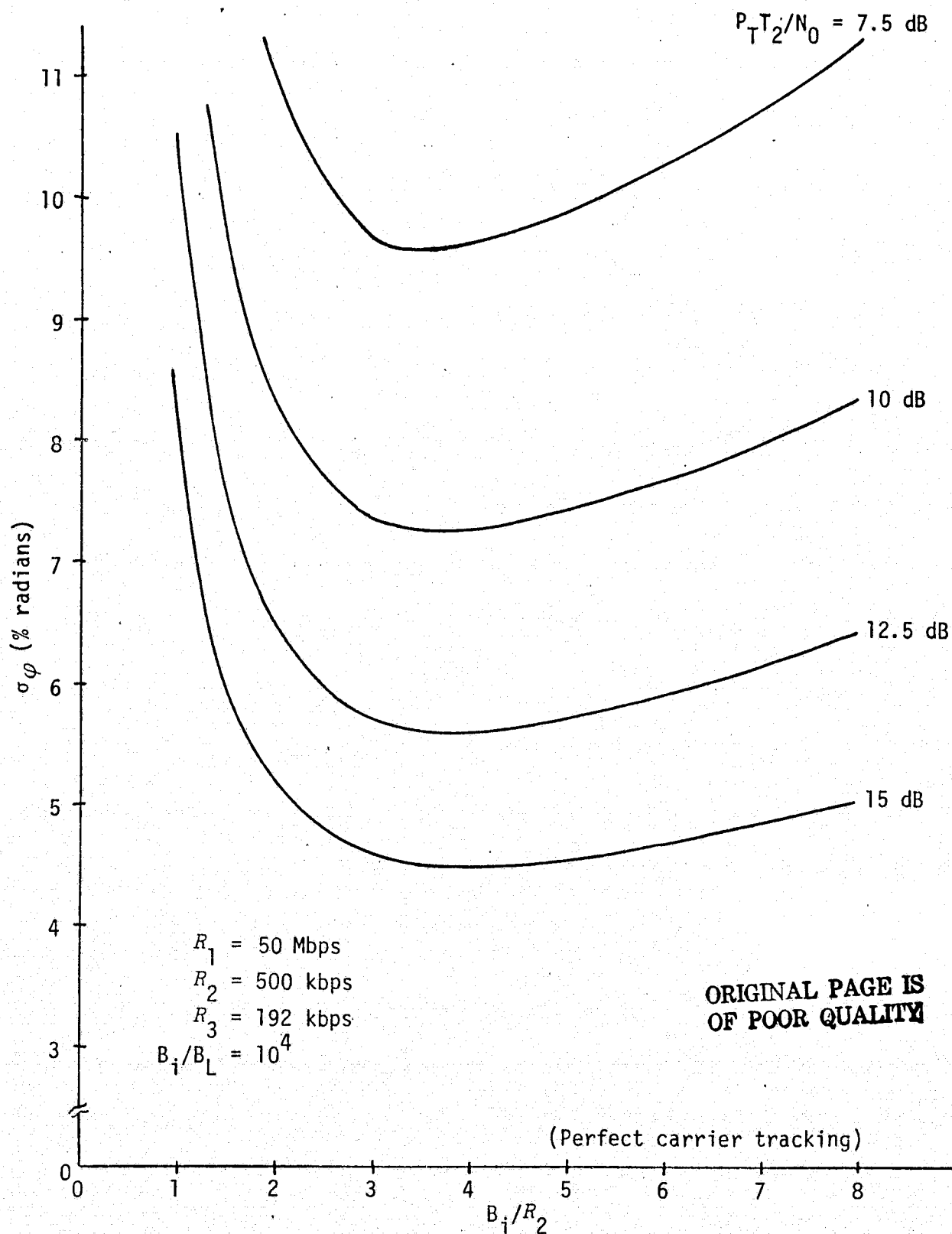


Figure 31. Subcarrier Tracking Jitter Versus Ratio of Arm Filter Bandwidth to High Subcarrier Data Rate  $R_2$ ;  $P_T T_2 / N_0$  is a parameter;  $m_1(t)$  is NRZ,  $m_2(t)$  and  $m_3(t)$  are Manchester codes;  $R_1 > R_2 > R_3$

has already been implied in assessing the tracking performance of the subcarrier loop. The approach taken is to expand the error probability conditioned on the subcarrier loop phase error  $\phi$  in a power (Maclaurin) series in  $\phi$  and then, keeping only the first few terms of this series, average this conditional error probability over the probability density function (p.d.f.) of  $\phi$ . By doing this, we obtain the additional error probability due to a noisy subcarrier reference as an additive term directly proportional to the mean-squared phase jitter  $\sigma_\phi^2$  directly associated with the receiver's subcarrier tracking loop. In this regard, the results derived in Appendix F play an important role in assessing this error probability performance. Finally, similar arguments can be advanced to give closed-form results for the noisy reference loss itself.

Appendix I contains a detailed discussion of the general problem of assessing the error probability performance of unbalanced QPSK receivers under the above-mentioned assumptions. The key results from this discussion are summarized as follows. In terms of the total signal-to-noise ratio  $R_{T2}$  ( $R_{T2} = P_T T_2 / N_0$ ) in the higher data rate bandwidth and the transmitted modulation indices  $\eta_2$  and  $\eta_3$  defined by

$$R_{T2} = \frac{(P_2 + P_3)T_2}{N_0}; \quad \eta_i = \frac{P_i}{P_2 + P_3}; \quad i = 2, 3, \quad (38)$$

the error probability performance of Channels 2 and 3 become

$$P_{E2} = \frac{1}{2} \operatorname{erfc} \sqrt{R_{T2} \eta_2} + \frac{1}{2} \sqrt{\frac{R_{T2} \eta_2}{\pi}} \exp(-R_{T2} \eta_2) \left[ 1 + 2R_{T2} \eta_3 \bar{m}_{32}^2 \right] \sigma_\phi^2$$

$$P_{E3} = \frac{1}{2} \operatorname{erfc} \sqrt{R_{T2} \gamma_T \eta_3} + \frac{1}{2} \sqrt{\frac{R_{T2} \gamma_T \eta_3}{\pi}} \exp(-R_{T2} \gamma_T \eta_3) \left[ 1 + 2R_{T2} \eta_2 \bar{m}_{32}^2 \right] \sigma_\phi^2, \quad (39)$$

where  $\gamma_T \triangleq R_2/R_3$  is the ratio of data rates and the normalized mean-squared crosstalk  $\bar{m}_{32}^2$  is tabulated in Table 2 of Appendix F for various combinations of data formats in the two channels. The corresponding expressions for the noisy reference loss (in dB) itself are

$$\begin{aligned}
 L_2 &= \frac{10 \log_{10} \left\{ 1 + R_2 \left[ 1 + 2R_3 \left( \frac{\bar{m}_{32}^2}{\gamma_T} \right) \right] \sigma_\phi^2 \right\}}{R_2} \\
 L_3 &= \frac{10 \log_{10} \left\{ 1 + R_3 \left[ 1 + 2R_2 \bar{m}_{32}^2 \right] \sigma_\phi^2 \right\}}{R_3} .
 \end{aligned} \tag{40}$$

In applying the results of (39) and (40) to Channels 2 and 3 to the three-channel SSO Ku-band return link signal, we again assume that  $m_2(t)$  is NRZ data with a maximum rate  $R_2 = 2$  Mbps and  $m_3(t)$  is a Manchester coded data stream at  $R_3 = 192$  kbps. We further assume that the power allocation is chosen so that, for the given data rate ratio  $\gamma_T = R_2/R_3 = 10.42$ , the signal-to-noise ratios  $R_2, R_3$  in the two channels are made equal, i.e., both channels operate at the same error rate. Thus,  $R_2 = R_3$  implies  $P_2 T_2 = P_3 T_3$  and the modulation indices  $\eta_2, \eta_3$  become

$$\begin{aligned}
 \eta_2 &\triangleq \frac{P_2}{P_2 + P_3} = \frac{\gamma_T}{\gamma_T + 1} = 0.9124 \\
 \eta_3 &\triangleq \frac{P_3}{P_2 + P_3} = \frac{1}{\gamma_T + 1} = 0.0876 .
 \end{aligned} \tag{41}$$

Further, it is typical to design the Costas loop bandwidth on the order of  $R_2/100$  (or less) since most of the power is in the high rate channel which controls the performance of the tracking loop. Thus, assuming  $B_L/R_2 = 0.01$ ,\* Figures 32 and 33 illustrate  $L_2$  and  $L_3$  of (40) versus  $B_L/R_2$  for error probabilities of  $10^{-4}$ ,  $10^{-5}$ , and  $10^{-6}$ , corresponding respectively to  $R_2 = R_3 = 8.4, 9.6$ , and  $10.5$  dB. Several conclusions may be drawn from these figures. First, the noisy reference loss on Channel 2 is considerably smaller than that of Channel 3. The principal

---

\* Smaller values of  $B_L/R_2$  as would be typical in practical receiver design would yield insignificant losses in  $L_2$  and  $L_3$ .



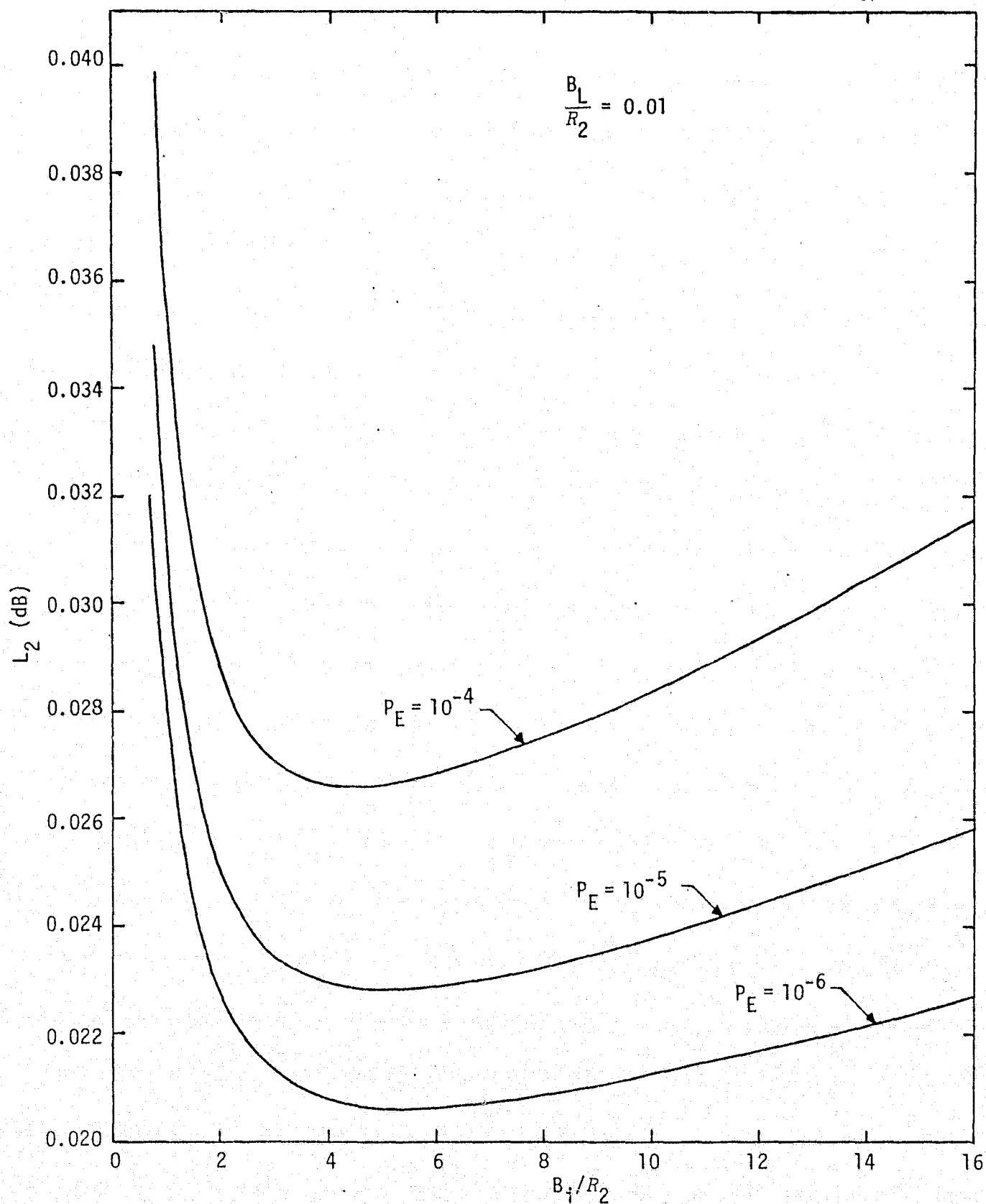


Figure 32. Channel 2 Noisy Reference Loss (in dB) vs. the Ratio of Two-Sided Costas Loop Arm Filter Bandwidth to Channel 2 Data Rate;  $m_3(t)$  is 192 kbps Manchester coded data,  $m_2(t)$  is 2 Mbps NRZ data.

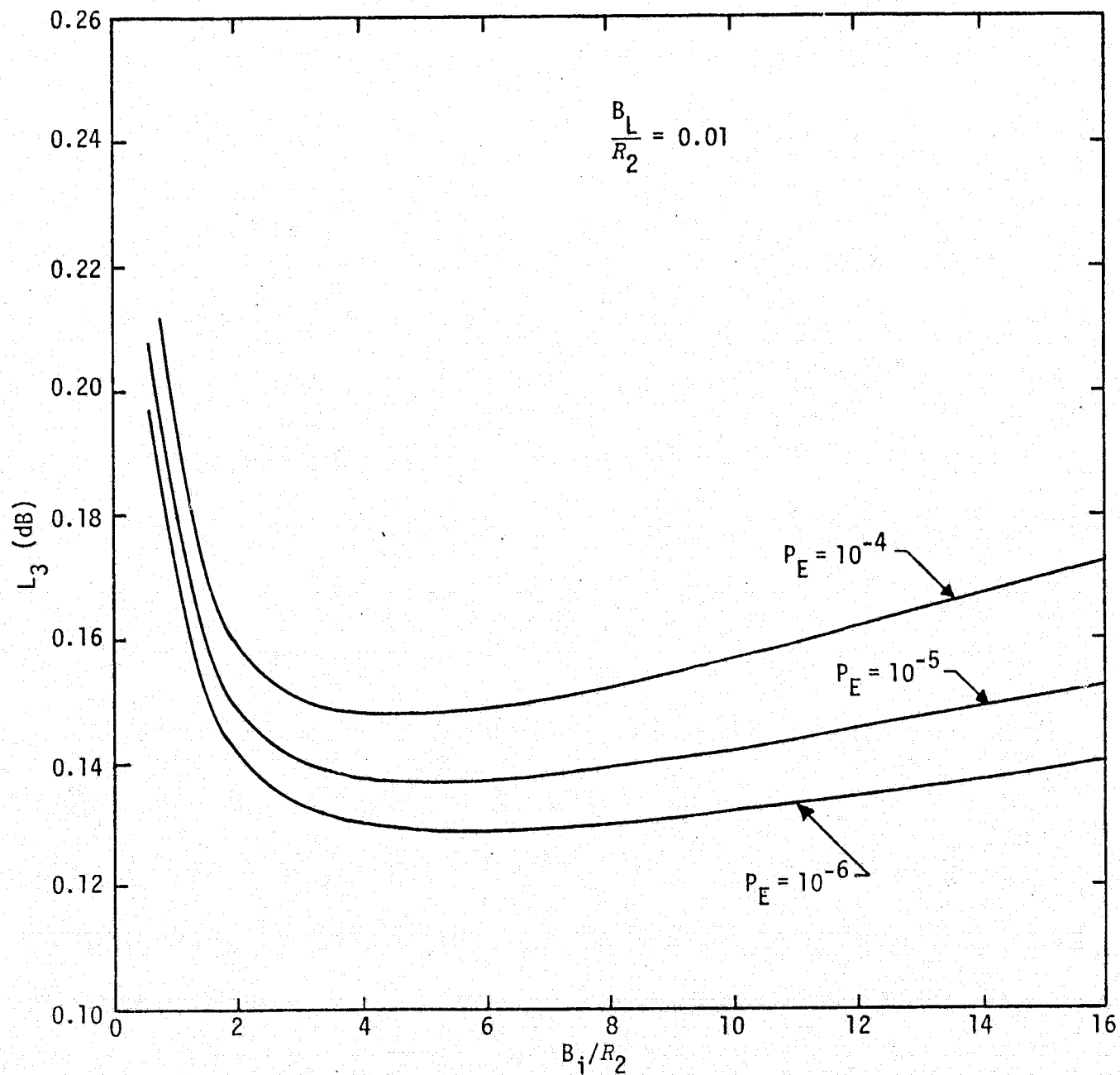


Figure 33. Channel 3 Noisy Reference Loss (in dB) vs. the Ratio of Two-Sided Costas Loop Arm Filter Bandwidth to Channel 2 Data Rate;  $m_3(t)$  is 192 kbps Manchester coded data,  $m_2(t)$  is 2 Mbps NRZ data.

reason for this can be easily explained in terms of the result in (40), where it is observed that the effective cross-modulation loss on Channel 2,  $\tilde{m}_{32}^2$ , is divided by  $\gamma_T$ , which in this case has a value equal to 10.42. Secondly, for either channel, the noisy reference loss decreases with increasing error probability. This is intuitively satisfying when one realizes that the slope of the error probability versus signal-to-noise ratio curve becomes steeper as  $P_E$  becomes smaller and thus, for a given  $\sigma_\phi$ , the parallel ideal and noisy synchronization error probability curves become closer together. Finally, we observe that there exists an optimum arm filter bandwidth (for fixed  $R_2$ ) in the sense of minimizing  $L_i$ ,  $i=2,3$ . Since only  $\sigma_\phi^2$  depends upon this bandwidth, it is clear that this bandwidth choice is identical to that which minimizes  $\sigma_\phi^2$  or, equivalently, the loop squaring loss. Note that, if  $B_L/R_2$  is decreased, then the noisy reference loss will also decrease, since the equivalent loop signal-to-noise ratio  $\rho$  increases.

In summary then, it is concluded that the crosstalk degradation due to noisy subcarrier demodulation references is quite small (on the order of tenths of a dB or less, depending on the particular channel and the ratio of loop bandwidth to data rate in that channel). When the higher data rate channel is 1 Mbps Manchester coded data, then since both channels are now Manchester coded, the crosstalk loss would be even smaller.

While the results of Appendix I have been directed principally toward the demodulation of unbalanced QPSK by a conventional (single-channel) Costas loop, the expressions for average error probability [see (39)] and noisy reference loss [see (40)] apply in a much broader sense. In particular, the two-channel type Costas loops discussed in [25,26] have a mean-squared phase jitter given by (37) where, however,  $S_L$  is a much more complex function of the various system parameters such as data rates and channel power ratios. Nevertheless, once  $S_L$  (and thus  $\sigma_\phi^2$ ) is determined, (39) and (40) apply directly toward evaluation of the noisy synchronization reference effects of these loops on error probability performance. Further discussion of the performance of two-channel Costas loops along these and other lines is presented in the next section. Finally, other possible applications of the results derived in Appendix I pertain to demodulation of

unbalanced QPSK using a biphase Costas loop with switching type multipliers. Once again, (39) and (40) apply, provided that an expression for the squaring loss can be found (see, for example, Appendix G).

### 3.4 Techniques for Improved Tracking of Unbalanced QPSK Modulation

As part of the ongoing effort to investigate tracking techniques for improving communications efficiency on board the SSO, Axiomatix undertook to reexamine previous work [25,26] on the problems of carrier synchronization of an unbalanced QPSK (UQPSK) signal format, starting with the well-known maximum a posteriori (MAP) estimation technique as motivation for deriving closed loop tracking configurations. Such carrier reconstruction implementations are suggested upon examining the gradient of the likelihood function whose solution is the MAP estimator of carrier phase.

In general, the closed loop implementation which results from application of MAP estimation theory to the problem of carrier phase estimation (herein referred to as the MAP estimation loop) is impractical, primarily because of the difficulty of implementing the hyperbolic tangent nonlinearity suggested by using the gradient of the likelihood function as an error control signal in the loop. To arrive at practical realizations, one ordinarily approximates this nonlinearity with simpler, more easily implementable functions. In the past, authors have employed the approximations

$$\tanh x = \operatorname{sgn} x ; \quad x \text{ large} \quad (42)$$

$$\text{and} \quad \tanh x = x ; \quad x \text{ small} . \quad (43)$$

Since the input to the nonlinearity is a monotonic function of signal-to-noise ratio (SNR), then the approximations of (42) and (43) correspond, respectively, to conditions of high and low SNR.

In Appendix J, we reexamine some of these approximations and the optimum structures which result. Using a slightly more sophisticated approximation of the nonlinearity, new and interesting structures are presented, first for QPSK as an example and then for UQPSK, which overcome some of the deficiencies posed by MAP receiver structures for these

same modulations suggested by authors in the past. The equivalence of the new QPSK structure (Figure 34) with the well-known quadriphase Costas loop is discussed in Appendix K. Furthermore, it is demonstrated that the new UQPSK structure (Figure 35) allows carrier reconstruction at all ratios of data rates and powers in the two channels, even in the limit of balanced QPSK.

In addition to arriving at new structures for optimum tracking of balanced and unbalanced QPSK, the practicality of the two-channel type carrier reconstruction loop for UQPSK is discussed in detail in Appendix J, paying particular attention to its sensitivity to variations in channel gains. Rather than go into the details of the performance of the loop in Figure 35, we instead investigated in Appendix J the sensitivity to gain variations of the simpler loop (Figure 36) found in [25,26] and used these results qualitatively as being indicative of two-channel Costas-type configurations. Actually, to make life even simpler, we performed our sensitivity analysis on the equivalent loop to Figure 36, where active (integrate-and-dump) arm filters were used in place of the passive arm filters and, furthermore, the channel gains  $2\sqrt{P_1}/N_0$  and  $2\sqrt{P_2}/N_0$  were replaced by arbitrary channel gains  $\sqrt{K_1}$  and  $\sqrt{K_2}$ .

It is shown there that, whereas the channel gains  $\sqrt{K_1}$  and  $\sqrt{K_2}$  were "optimally" chosen in [25,26] from MAP estimation considerations, a different selection of these gains based upon directly optimizing the loop's tracking performance can yield as much as a 10 dB improvement in this performance. The significance of this statement is not so much the fact that the tracking performance can be enhanced by a better choice of gains, particularly since these gains are now theoretically signal-to-noise ratio dependent, but rather the high degree of sensitivity of the performance of the MAP estimation-type loop to variations in the channel gains themselves.

To provide quantitative verification of these points, Figures 37 through 39 illustrate the squaring loss  $S_L$ , corresponding to the two possible selections of channel gains, versus the power ratio  $\lambda_p$  with the data rate ratio  $\lambda_t = n$  ( $n$  integer) fixed and the total power-to-noise ratio in the high data rate bandwidth  $\epsilon_1 = P_T T_1 / N_0 = -3$  dB and 10 dB. The values of  $n$  selected for these plots range from balanced ( $n=1$ ) to

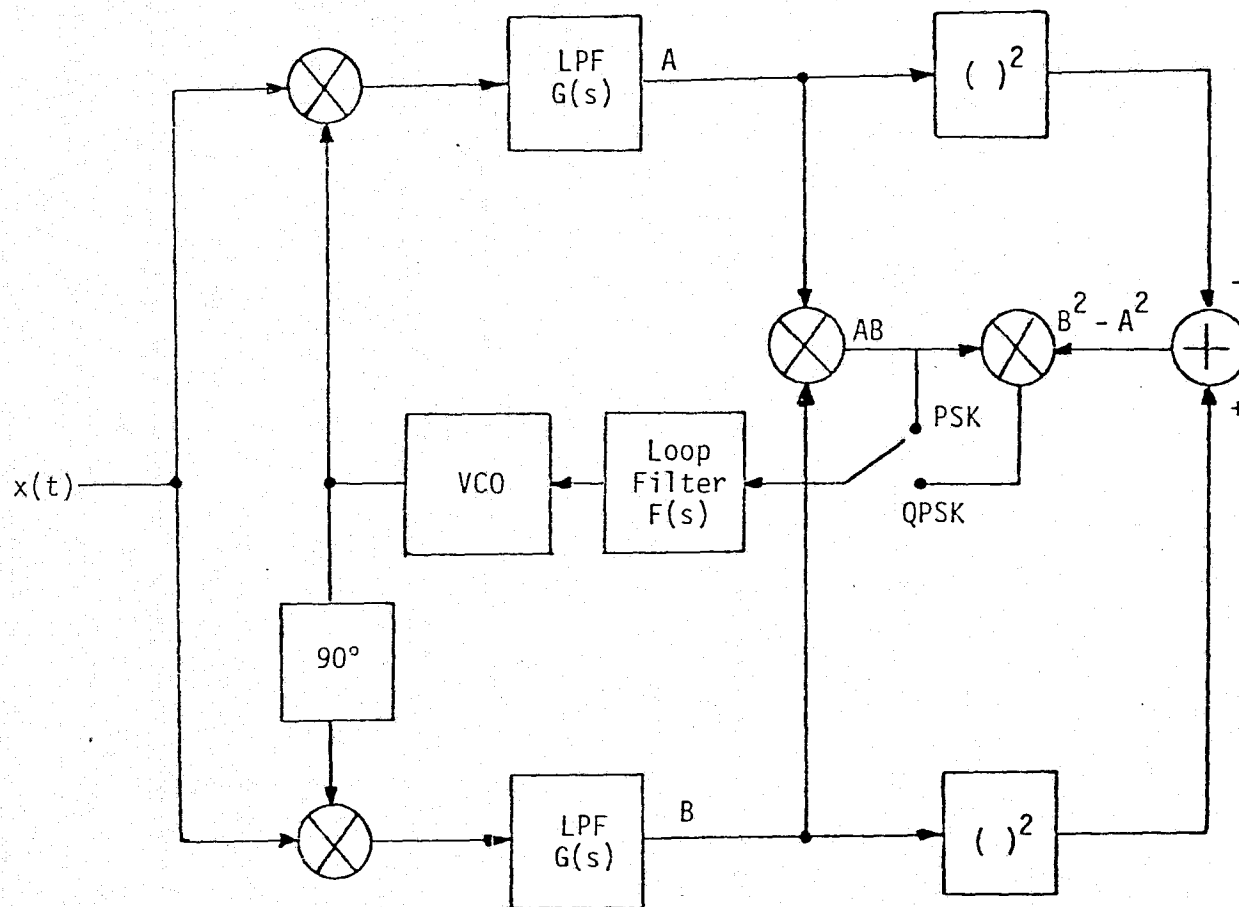


Figure 34. A Practical Realization of the MAP Estimation Loop for QPSK; Passive Arm Filters, Small SNR

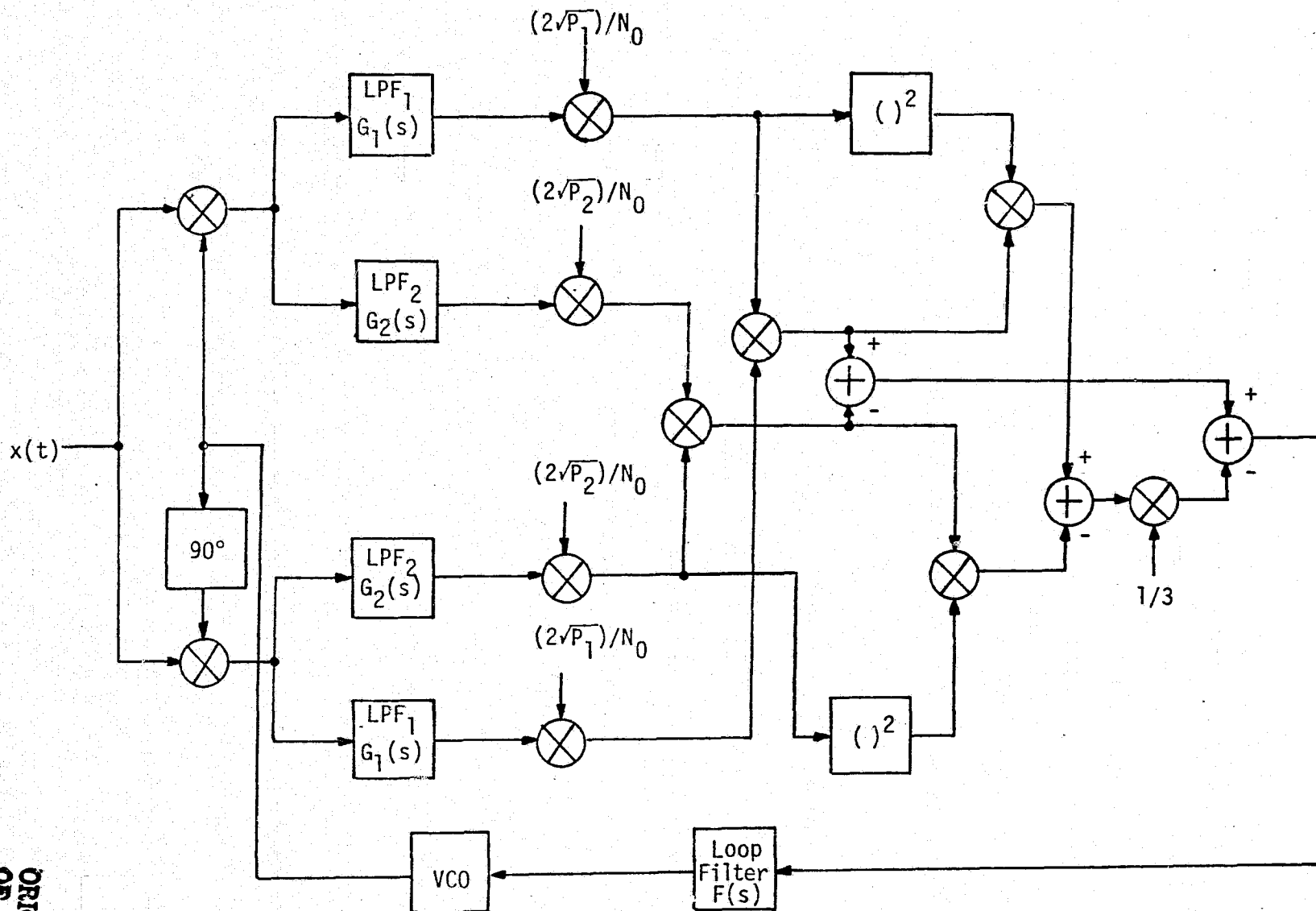


Figure 35. A Practical Realization of the MAP Estimation Loop for UQPSK; Passive Arm Filters, Small SNR;  $\tanh x = x - x^3/3$

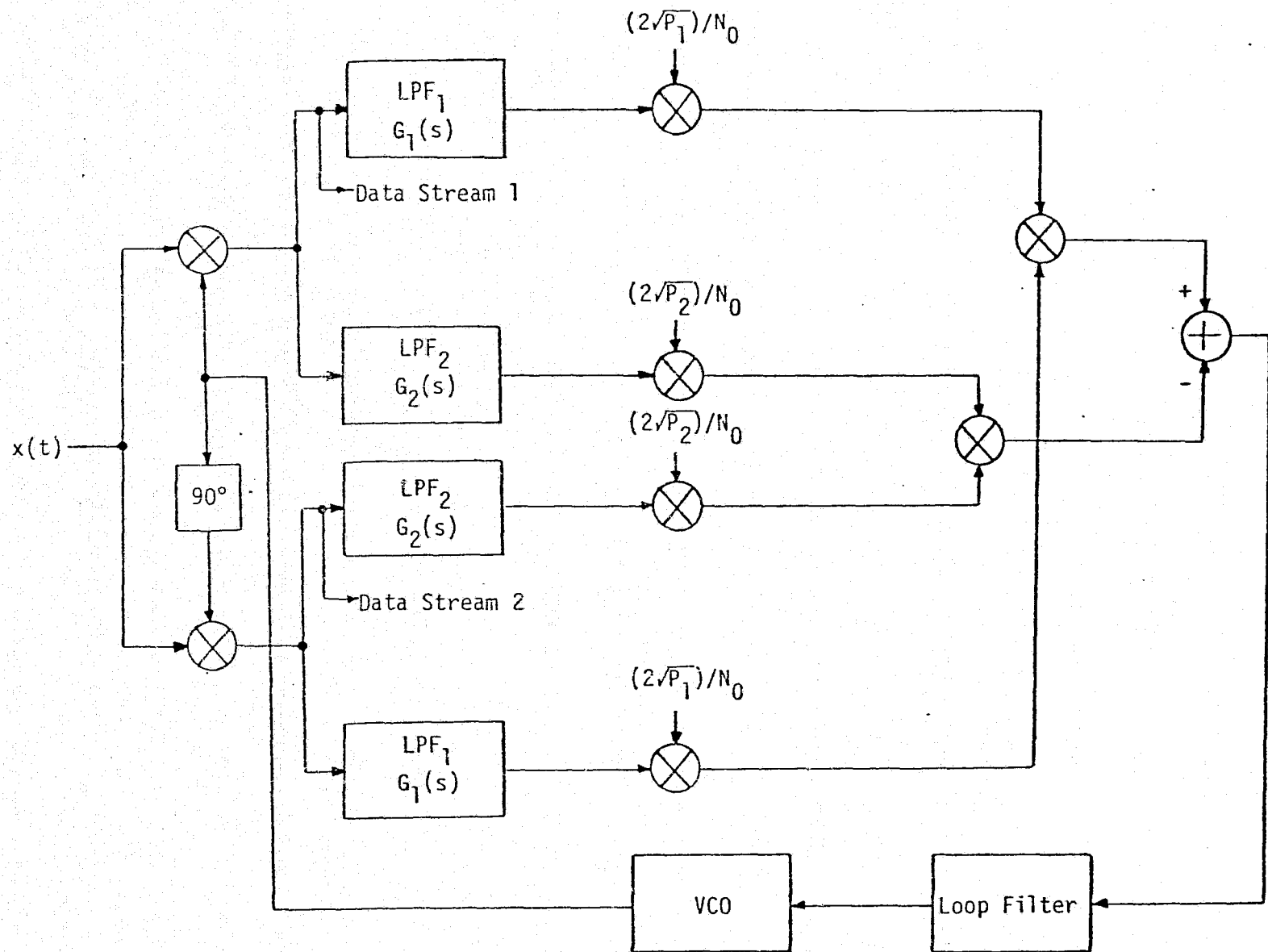


Figure 36. A Practical Realization of the MAP Estimation Loop for UQPSK; Passive Arm Filters, Small SNR;  $\tanh x \approx x$



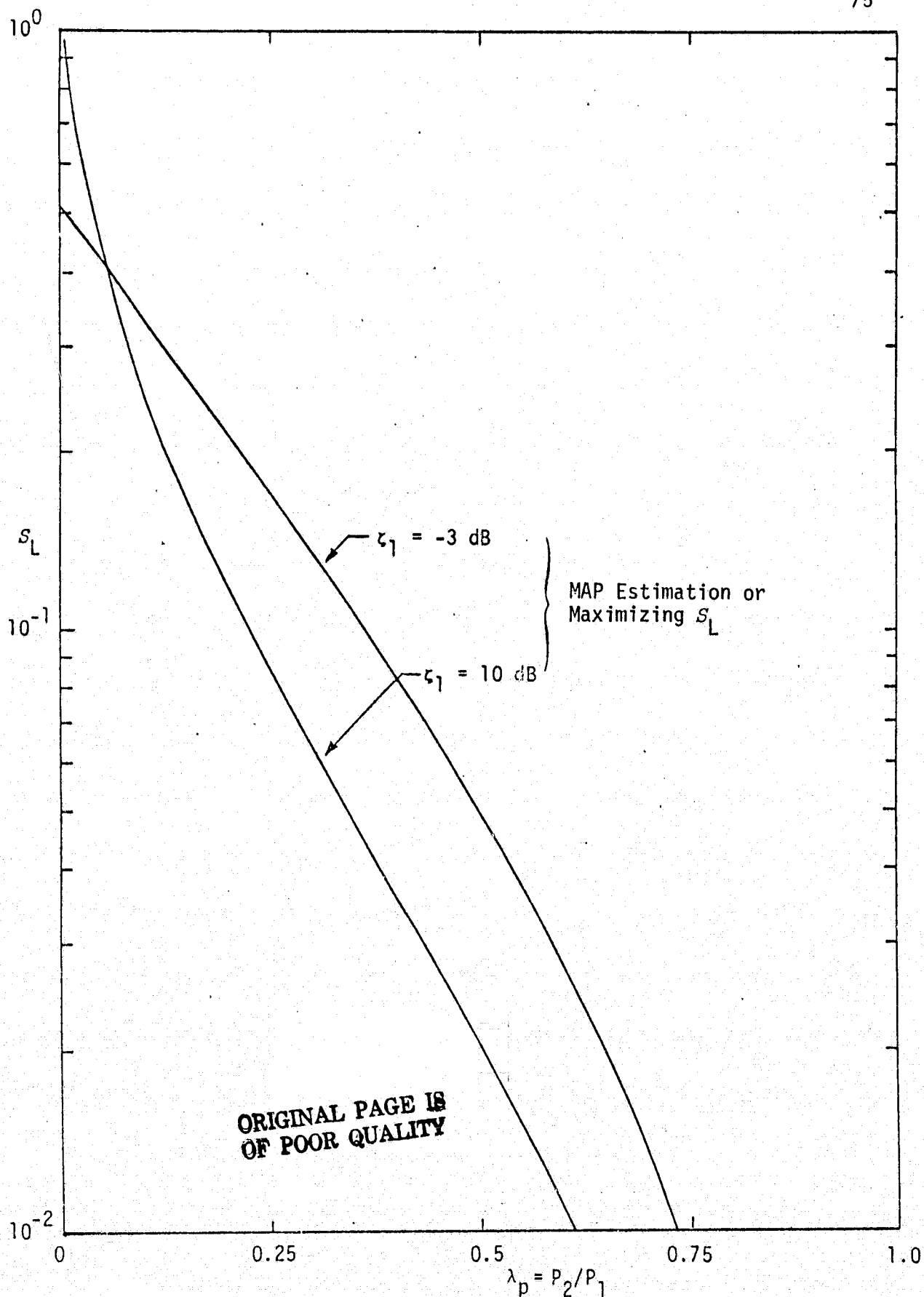


Figure 37. Squaring Loss vs. Power Ratio for Unbalanced QPSK; Two-Channel Costas Loop;  $n = T_2/T_1 = 1$

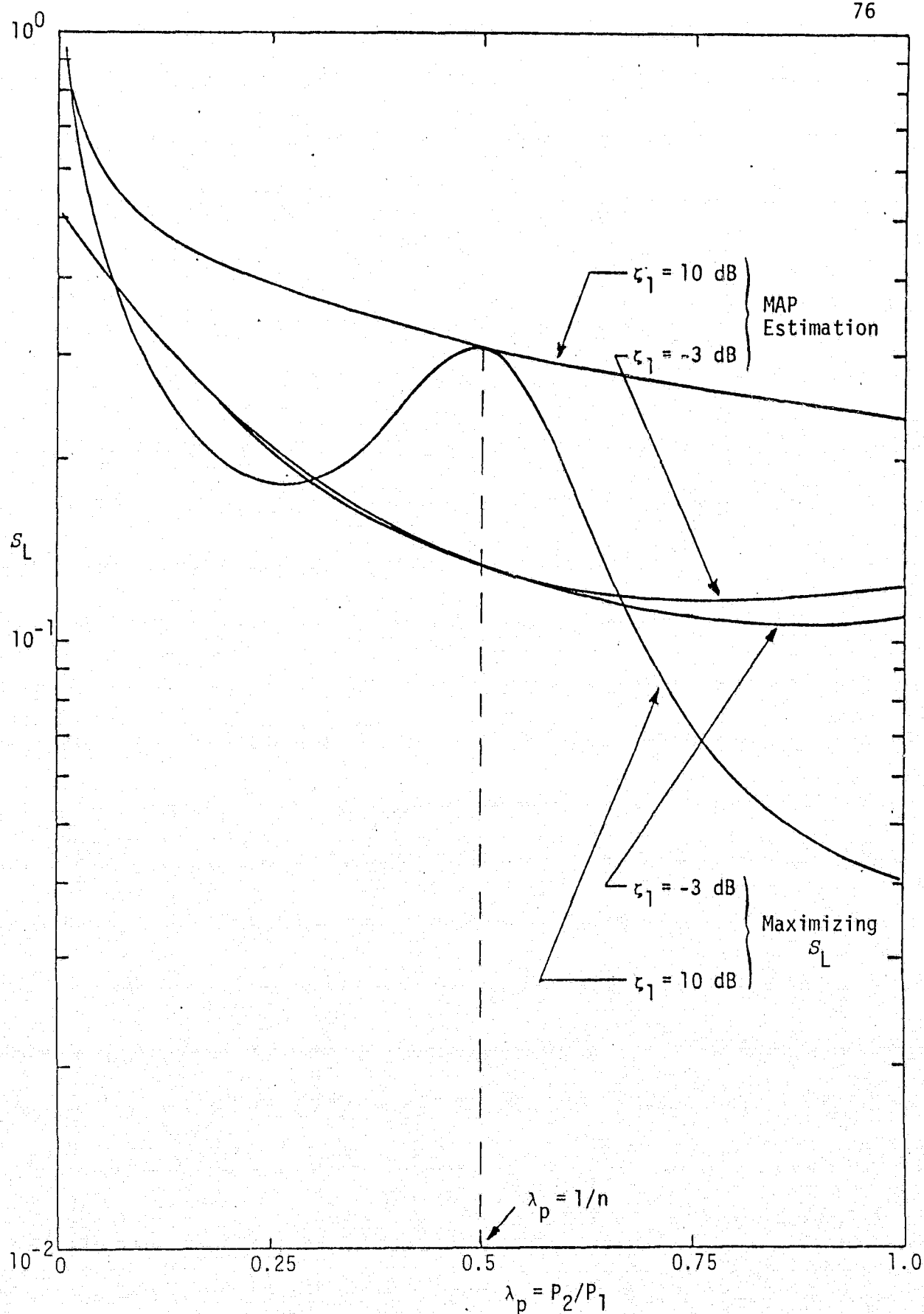


Figure 38. Squaring Loss vs. Power Ratio for Unbalanced QPSK; Two-Channel Costas Loop;  $n = T_2/T_1 = 2$

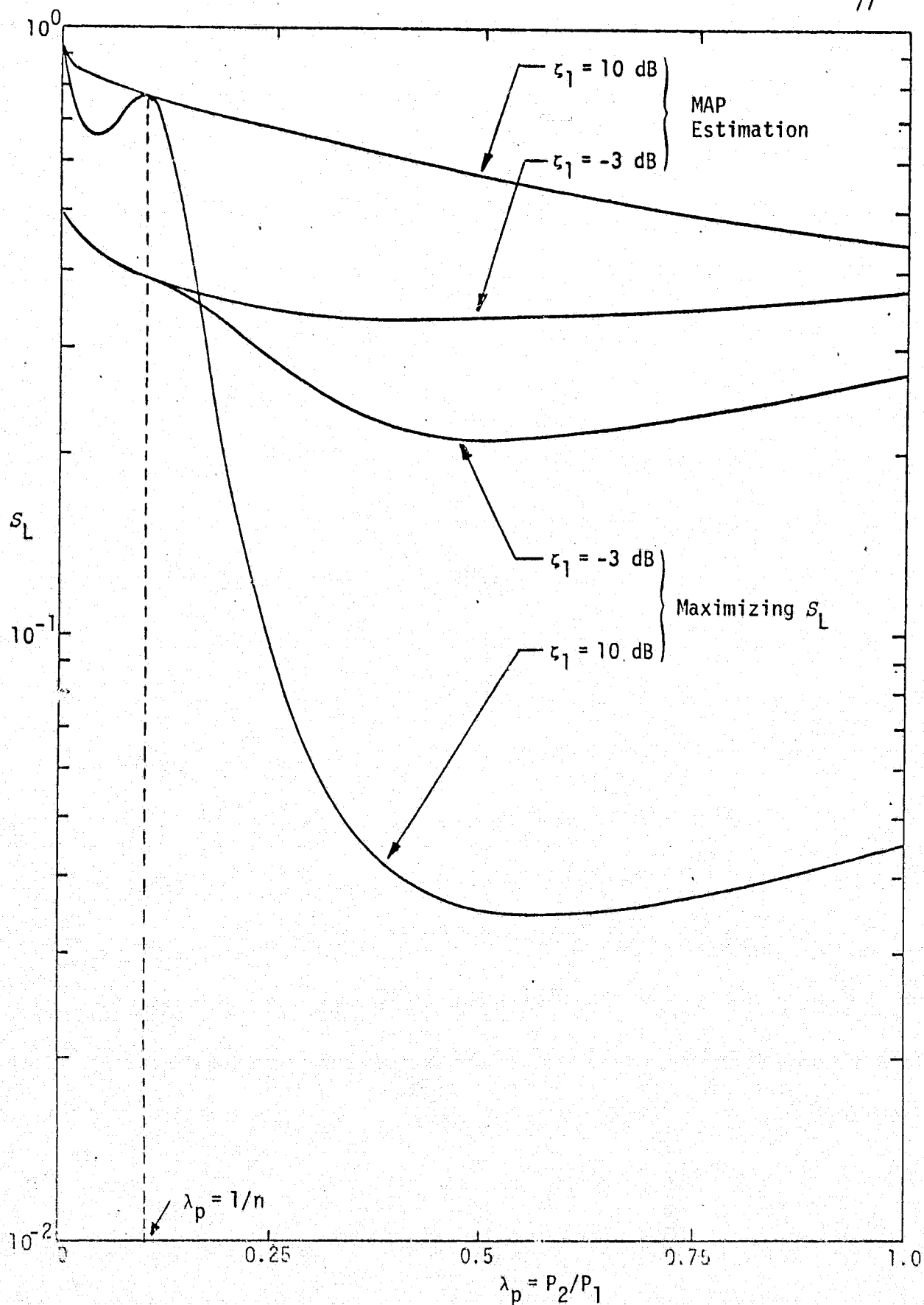


Figure 39. Squaring Loss Versus Power Ratio for Unbalanced QPSK; Two-Channel Costas Loop;  $n = T_2/T_1 = 10$

highly unbalanced ( $n=10$ ) data rates. Several points are worthy of note from the results in these figures. First, from Figure 37, we observe that, for the balanced data rate case ( $n=1$ ,  $\lambda_p$  arbitrary), both channel gain selections produce the identical squaring loss. Another case where the two channel gain selections produce the same result is that for which the channels have equal energy, i.e.,  $\lambda_p = 1/n$ . Since, from [25,26], the "optimum" value of  $K_2/K_1$  as motivated by MAP estimation theory is

$$\frac{K_2}{K_1} = \frac{\lambda_p}{n}, \quad (44)$$

which is independent of signal-to-noise ratio, then for the equal energy case, we have  $K_2/K_1 = \lambda_p^2$ .

Second, the difference between the true optimum squaring loss and the value given by selecting the channel gains as in [25,26] increases with increasing  $n$ . Also, for fixed  $n$ , these differences are much more significant at higher values of total power-to-noise ratio  $\zeta_1$  in the high data rate bandwidth than at the lower values. As an example, for  $n=10$  and  $\zeta_1 = 10$  dB, we see from Figure 39 that, for equal powers ( $\lambda_p = 1$ ), the optimum squaring loss is 10 dB smaller than that predicted by MAP estimation channel gain selection. The same comparison at  $\zeta_1 = -3$  dB only shows a 1.4 dB improvement.

Third, the true optimum (minimum) squaring loss decreases with increasing  $\zeta_1$ , regardless of the values of  $n$  and  $\lambda$ , except for the case of small  $\lambda_p$  and  $n=1$ .

Finally, it can be shown that Figure 37 is representative of the one-channel Costas loop performance for all  $n$  and  $\lambda_p$ ; hence, these curves represent lower bounds on the squaring loss performance for the two-channel configuration. That is, for fixed  $\zeta_1$  and  $\lambda_p$ , the two-channel Costas loop will exhibit a smaller squaring loss for any data rate ratio  $n$  than the value indicated in Figure 37. This performance comparison between one- and two-channel Costas loops is made in Figure 40 where the ratio  $S_L = S_{L|2\text{-channel}}/S_{L|1\text{-channel}}$  (in dB) is plotted versus  $\lambda_p$  with  $\zeta_1$  (in dB) as a parameter and  $\lambda_p = 1/n$ . Clearly, for  $\lambda_p$  approaching unity, the improvement becomes infinite; however, we

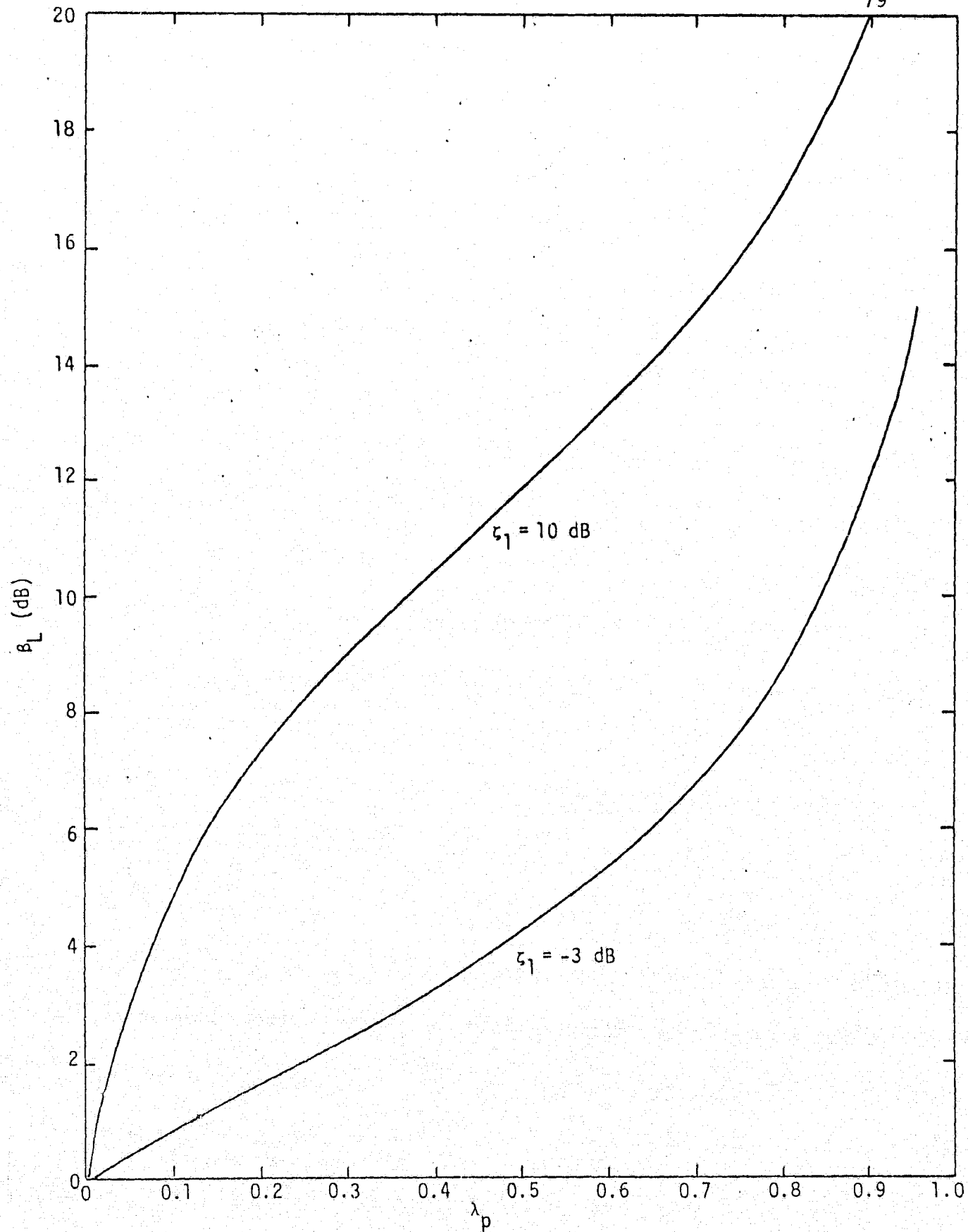


Figure 40. A Comparison of the Squaring Loss Performance of One- and Two-Channel Costas Loops;  $\lambda_p = 1/n$

recall that, in this limiting case, neither the one-channel nor the two-channel loop is capable of tracking at all, i.e.,  $S_L$  goes to zero for both.

In conclusion, we point out that the MAP estimation theory provides good intuition for implementing closed loop tracking configurations for UQPSK modulation; however, care must be exercised in selecting the ratio of gains between the two channels of the resulting configuration. In this regard, two options are available, namely, (1) that gain ratio which is motivated by MAP estimation theory and is independent of signal-to-noise ratio and (2) that ratio which minimizes the loop squaring loss and is dependent on signal-to-noise ratio. The difference in squaring loss between these two choices of gain ratios can be as much as 10 dB for certain values of data rate ratio and power ratio. When the signal energies in the channels are chosen equal, then both gain ratios also become equal and yield identical squaring loss performance. Even in this case, the two-channel Costas loop of [25,26] is capable of tracking balanced quadriphase. By an extension of the power series approximation used for the hyperbolic tangent nonlinearity which arises from the MAP estimation approach, we have been able to demonstrate a carrier reconstruction loop for UQPSK (Figure 35) which should yield better performance than the above-mentioned two-channel loop as the modulation becomes more balanced; in particular, it acts like a quadriphase Costas loop in the limiting case of balanced QPSK. A detailed analysis of the tracking performance of this loop will be considered in the future.

### 3.5 Costas Loop Tracking Performance on the Shuttle S-Band Uplink in the Presence of Residual Carrier

We conclude the tracking techniques analysis task with an investigation of the effects of residual carrier on the Costas loop tracking performance of the Shuttle S-band uplink.

Traditionally, a Costas loop is intended for use in receivers which must reconstruct a carrier reference from an input signal whose carrier component is totally suppressed, e.g., a biphase modulated carrier. On the Shuttle S-band uplink, however, during the time when both data and a ranging subcarrier are linearly modulated on the same

carrier, the data modulation index is not  $\pi/2$ . Thus, in this instance, the Costas loop is called upon to accurately track a signal whose carrier component is not completely suppressed.

A simple block diagram which, for the sake of analysis, characterizes this situation is illustrated in Figure 41. Included in this illustration are the means by which the data and the ranging subcarrier are extracted using the in-phase demodulation reference generated by the loop.

Several key questions arise relative to the performance of the Costas loop under these unorthodox conditions:

1. Is the loop capable of successfully tracking the input independently of the value of the data modulation index?
2. Is it possible to extract the ranging subcarrier as shown if the data modulation is removed?
3. What is the additional threshold power-to-noise ratio required to operate the loop in the PM (ranging and data) mode as compared to the PSK (data only) mode?
4. What tradeoffs exist between power in the ranging channel and loop threshold performance as a function of the data and ranging modulation indices?

The answers to these and other questions related to the performance of Costas loops in the presence of residual carrier are given in Appendix L, where a theory is established for such performance as a function of the parameters which characterize the system tracking behavior. The key results from Appendix L are summarized below.

First, it is demonstrated that, in the residual carrier mode of operation, there exists a critical data modulation index below which the loop will not operate, regardless of the value of signal-to-noise ratio. An expression for this critical modulation index is given as follows. Consider the Costas demodulator illustrated in Figure 41 whose input signal is of the form

$$s(t, \theta) = \sqrt{2P} \sin [\omega_0 t + \beta_d d(t) + \beta_s \sin (\omega_{sc} t + \theta_r(t)) + \theta], \quad (45)$$

where  $P$  is the total received power,  $\omega_0$  is the carrier radian frequency and  $\theta$  the corresponding input phase to be estimated,  $\beta_d$  is the data

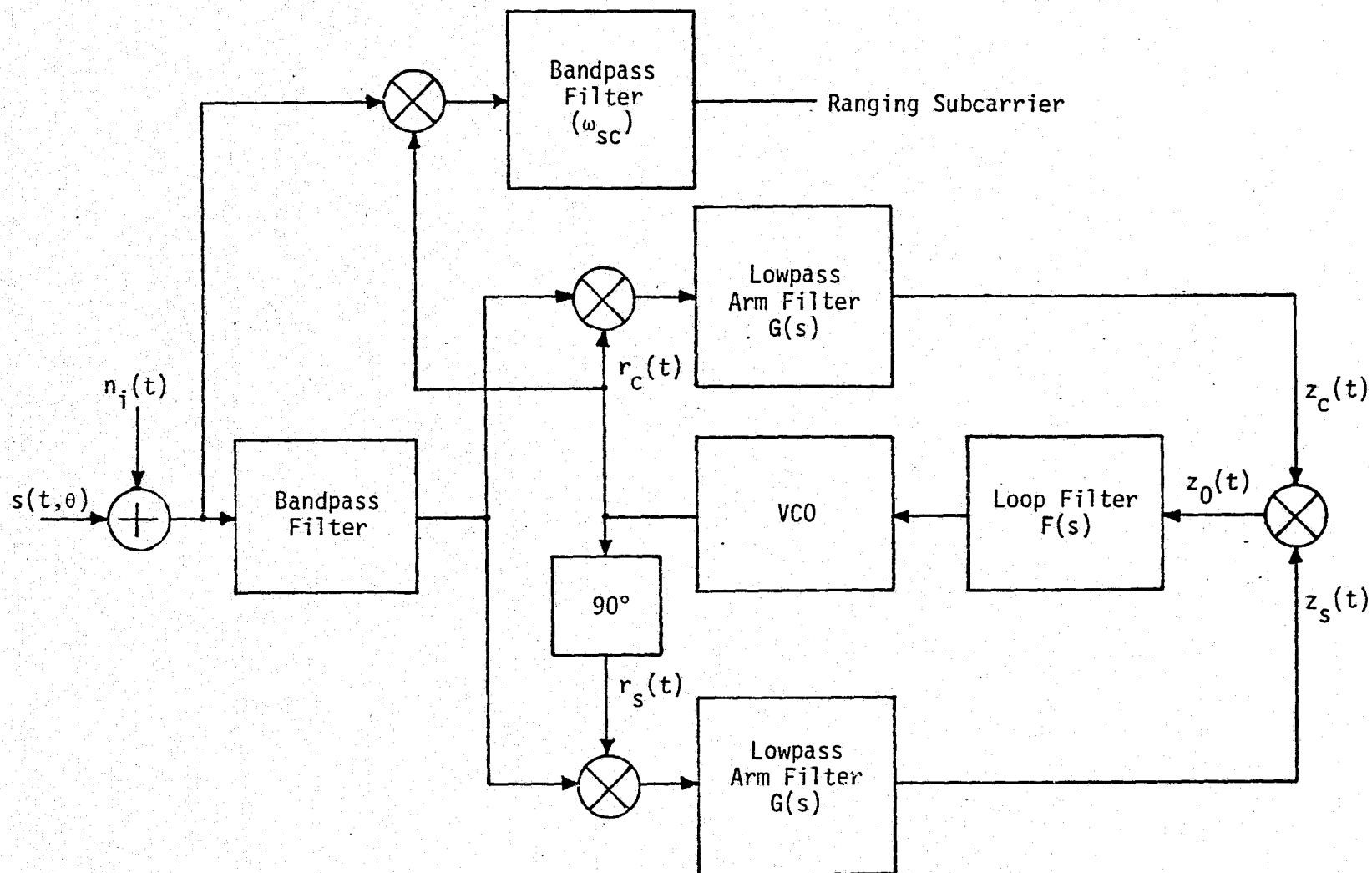


Figure 41. Costas Loop and Ranging Demodulator



modulation index with  $d(t)$  the data waveform, and  $\beta_s$  is the ranging subcarrier modulation index with  $\omega_{sc}$  the radian subcarrier frequency and  $\theta_r(t)$  the tone ranging modulation. Then, if

$$D_m \triangleq \langle \hat{d}^2(t) \rangle = \int_{-\infty}^{\infty} S_m(f) |G(j 2\pi f)|^2 df \quad (46)$$

represents the power in the data modulation at the arm filter output with  $S_m(f)$  denoting the power spectral density of the unfiltered data  $d(t)$ , when

$$\cot^2 \beta_d = D_m, \quad (47)$$

the loop S-curve vanishes and the loop will not lock at any loop signal-to-noise ratio. For values of  $\beta_d$  less than the critical value satisfying (47), the loop locks at  $\varphi = \pm(2n+1)\pi/2$ ,  $n=0,1,2,\dots$ . For values of  $\beta_d$  greater than this critical value, the loop locks at  $\varphi = \pm n\pi$ ,  $n=0,1,2,\dots$ .

Table 5 tabulates the critical values of data modulation index for the various data symbol rates  $R_s$  of interest on the S-band uplink, wherein the data is Manchester coded and the Costas loop arm filters are assumed to be single-pole Butterworth (RC) with 3 dB cutoff frequency  $f_c$  and two-sided noise bandwidth  $B_i = \pi f_c$ .

Table 5. Critical Values of Data Modulation Index on the S-Band Uplink

$R_s$	$f_c$	$B_i/R_s$	$D_m$	$(\beta_d)_{crit}$
32 kbps (Low Data Rate Uncoded)	134 kHz	13.155	0.886	0.8157 rad
96 ksps (Low Data Rate Coded)	134 kHz	4.385	0.6636	0.8872 rad
72 kbps (High Data Rate Uncoded)	308 kHz	13.44	0.8884	0.815 rad
216 ksps (High Data Rate Coded)	308 kHz	4.48	0.670	0.8848 rad

Second, the performance of the ranging channel is characterized both when data modulation is on and when it is off. For either case, the signal power in the ranging channel is given by

$$P_r = 2P \cos^2 \beta_d J_1^2(\beta_s) \overline{\cos^2 \varphi} \quad (48)$$

where, for large  $\rho S_L$ ,

$$\overline{\cos^2 \varphi} \approx 1 - \frac{1}{\rho S_L} \quad (49)$$

Then, when the data modulation is on, we note from (45) that, as the value of  $\beta_d$  is increased beyond its critical value as determined from (47), the carrier becomes more suppressed and thus the Costas loop tends to track better. However, as  $\beta_d$  is increased,  $\cos \beta_d$  decreases and thus [from (48)] the power in the ranging channel  $P_r$  tends to decrease because of this. Since the power in the ranging channel is proportional to both  $\cos^2 \beta_d$  and the accuracy of Costas loop tracking (through the factor  $\overline{\cos^2 \varphi}$ ), a tradeoff exists with regard to the selection of the data modulation index.

When the data modulation is removed, i.e.,  $\beta_d = 0$ , then as previously mentioned, the loop will now lock up around  $\varphi = \pi/2$  (as opposed to  $\varphi = 0$ ). This is equivalent to saying that the in-phase and quadrature demodulation reference signals switch roles. Thus, since the ranging subcarrier component in the input signal  $s(t, \theta)$  is now demodulated by the quadrature carrier reference signal, then from (48), we have that (for large loop signal-to-noise ratio)  $P_r \approx 0$ . The conclusion to be reached then is that, in order to extract range information as in Figure 41, the data modulation cannot be turned off at the transmitter.

The third key result concerns the comparison of threshold tracking performance in the PM versus the PSK mode. Tracking threshold is typically specified as the minimum input signal level for which the mean time to loss of lock is greater than or equal to 10 seconds. This condition is uniquely specified by the loop signal-to-noise ratio or, equivalently,  $\sigma_{2\varphi}$ . Thus, two modes of operation, e.g., PM and PSK,

will have identical tracking thresholds if the total power-to-noise ratio  $P/N_0$  is adjusted in one relative to the other to produce the same  $\sigma_{2\varphi}$  in both.

The baseline design of the S-band network transponder under development by TRW calls for  $\beta_s = 1.0$  rad and  $\beta_d = 1.1$  rad. Performance tests on the engineering model, as reported in the network transponder CDR package [27], reveal the following tracking threshold signal levels in the PSK mode (through TDRS):

Table 6. Tracking Threshold Signal Levels in the PSK Mode

Data Rate	Temperature	Signal Level
Low Data Rate (32 kbps uncoded or 96 ksps coded)	70°F	-104.2 dBm
	120°F	-102.4 dBm
	-20°F	-104.2 dBm
High Data Rate (72 kbps uncoded or 216 ksps coded)	70°F	-103.7 dBm
	120°F	-101.4 dBm
	-20°F	(SSP will not hold lock -100 dBm)

The input noise power spectral density is -151 dBm/Hz. Thus, the maximum measured  $P/N_0$  is 48.6 for the low rate and 49.6 for the high rate modes. Assuming these threshold values of  $P/N_0$  for PSK operation through the TDRS, Table 7 tabulates the values of various system parameters leading up to the calculation of  $P'/N_0$  (total power-to-noise ratio in the PM mode). Also indicated in the table is the dB increase in power-to-noise ratio required to go from the PSK to the PM mode through the TDRS.

Table 8 illustrates the power-to-noise ratio  $P_r/N_0$  in the ranging channel [as computed from (48)] for the same parameters as in Table 7 and operation in the PM mode.

Finally, tracking threshold performance is examined as a function of data and ranging modulation indices. This threshold, when operating in the PM mode, can be reduced (relative to that in the PSK mode) by reducing the ranging modulation index  $\beta_s$  and/or increasing the data modulation index  $\beta_d$  (i.e., suppressing the carrier more).

Table 7. System Parameters for Calculation of  $P'/N_0$ 

$$P/N_0 = 48.6 \text{ dB}, \beta_s = 1.0 \text{ rad}, \beta_d = 1.1 \text{ rad}$$

Data Rate	$K_D D_m$	$PT/N_0$ (dB)	$\rho_i$ (dB)	$P'/N_0$ (dB)	$\Delta P/N_0$ (dB)
32 kbps	0.829	3.549	-4.642	54.23	5.63
96 ksps	0.5078	-1.223	-4.642	55.01	6.41
72 kbps	0.8326	0.0267	-8.257	53.83	5.23
216 ksps	0.5166	-4.745	-8.257	54.50	5.90

Table 8. Power-to-Noise Ratio in the Ranging Channel

$$P/N_0 = 48.6 \text{ dB}, \beta_s = 1.0 \text{ rad}, \beta_d = 1.1 \text{ rad},$$

$$B_L = 200 \text{ Hz}$$

Data Rate	$P_r/N_0$ (dB)
32 kbps	43.21
96 ksps	43.97
72 kbps	42.78
216 ksps	43.41

Unfortunately, however, both of these changes also reduce the power-to-noise ratio in the ranging channel. To see these effects quantitatively, Figure 42 illustrates the tracking threshold power-to-noise ratio for PM operation as a function of ranging modulation index for fixed data modulation index, and Figure 43 illustrates the ranging channel power-to-noise ratio as a function of these same parameters. The value of  $P/N_0$  for PSK operation is again chosen equal to 48.6 dB and the results are given for both uncoded and coded low data rates. We observe from Figure 42 that, as  $\beta_d$  approaches  $\pi/2$  (fully suppressed carrier), the tracking threshold becomes virtually insensitive to data rate. A similar phenomenon is observed in Figure 43 for the ranging channel power-to-noise ratio. Using the information in these curves, along with the ranging channel bandwidth and the required signal-to-noise ratio in this bandwidth turned around to ground, one can select values of  $\beta_s$  and  $\beta_d$  to meet the additional requirements on increase in tracking threshold for PM versus PSK operation.

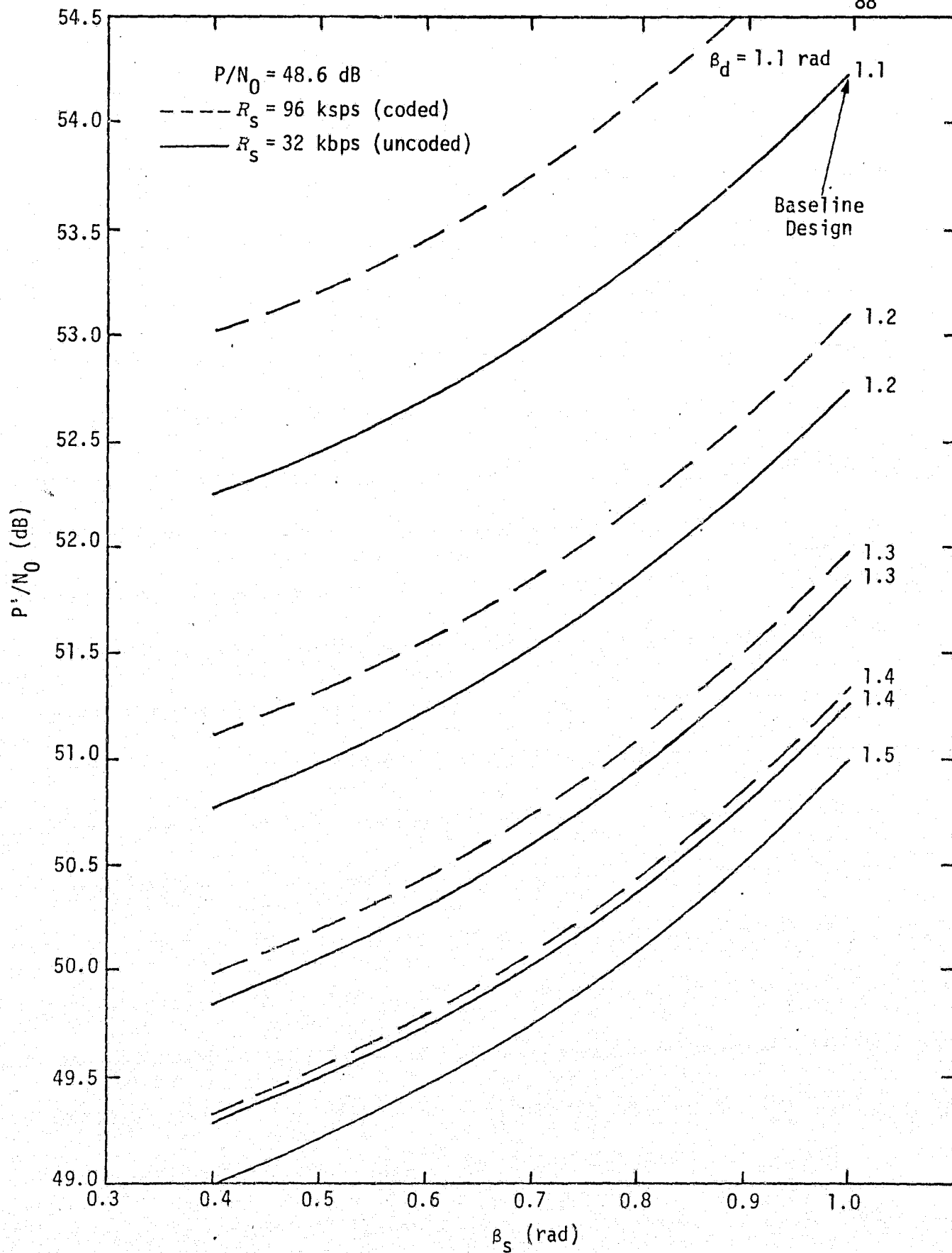


Figure 42. Tracking Threshold Power-to-Noise Ratio for PM Mode vs. Ranging Modulation Index with Data Modulation Index as a Parameter

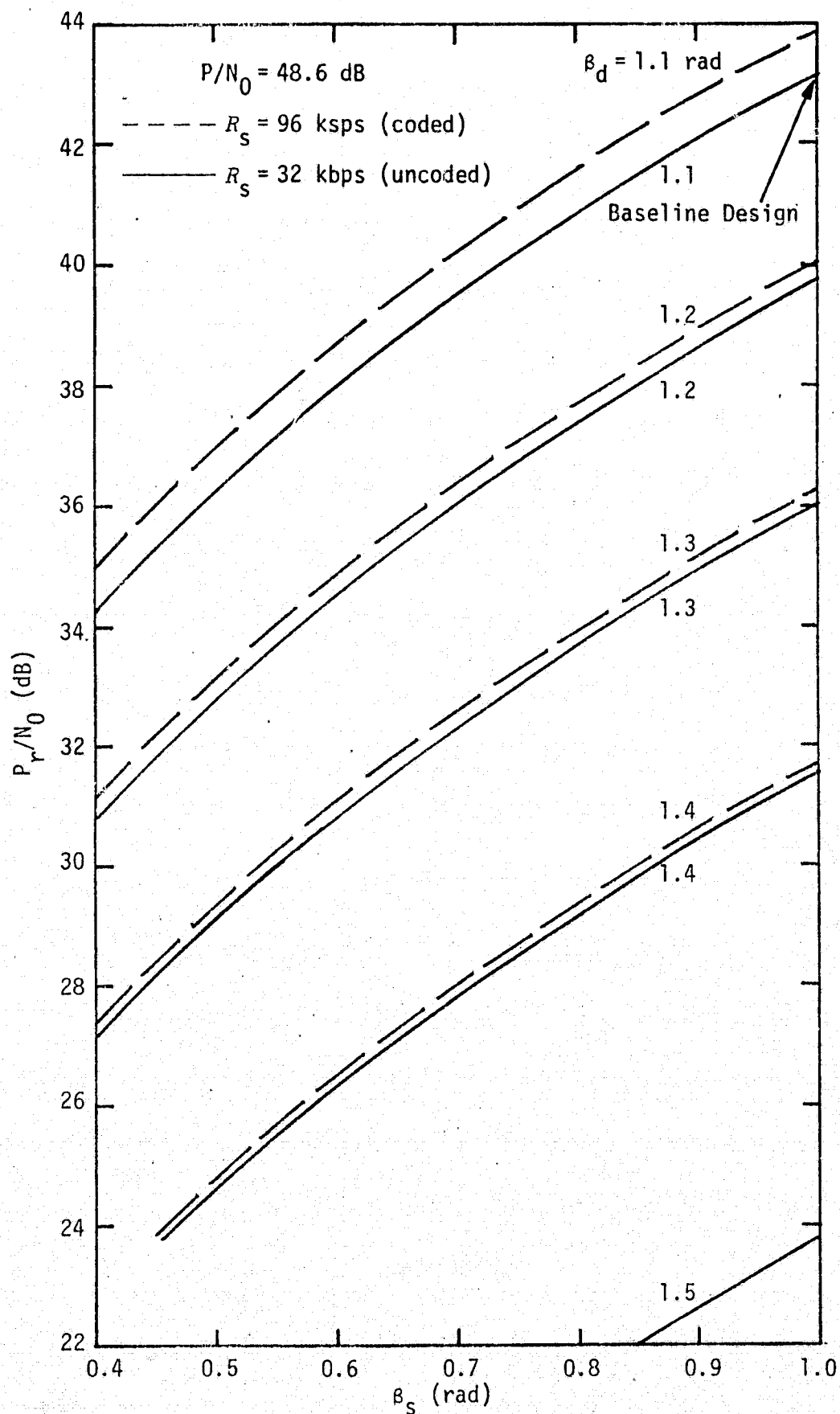


Figure 43. Ranging Channel Power-to-Noise Ratio Versus Ranging Modulation Index with Data Modulation Index as a Parameter

C-2

#### 4.0 PAYLOAD COMMUNICATIONS STUDY

The Ku-band system currently provides a return link wideband and narrowband bent-pipe. This study assessed the design and performance of the return link bent-pipe relay mode for attached and detached payloads. As part of this study, a design for a forward link bent-pipe is also proposed, and its performance is evaluated for attached and detached payloads. Critical Ku-band system parameters have been identified and optimized such that cost and complexity have been minimized, and the basic data transmission capabilities that can be accommodated for payloads have been identified for both forward link and return link bent-pipe relay modes.

##### 4.1 Forward Link Bent-Pipe Relay Design

The present Ku-band system design does not include provision for a forward link bent-pipe relay mode. This section proposes a possible modification to the Hughes Aircraft Company (HAC) Ku-band forward link design to accommodate forward link bent-pipe signals to attached or detached payloads. A simplified block diagram of the HAC forward link design is shown in Figure 44. The RF receiver is in the Deployed Electronic Assembly (DEA). The input to the Electronic Assembly 1 (EA-1) is at 647 MHz IF. The EA-1 provides IF amplification, automatic gain control (AGC), and automatic level control (ALC) for the remaining demodulation circuits in EA-1. The PN spread spectrum modulation is removed by the PN tracking loop while the Costas loop tracks the carrier to complete the demodulation of the data. The output of the EA-1 is buffered with an AGC. The input to the Signal Processor Assembly (SPA) is either switched to the Network Signal Processor (NSP) directly or bit and frame synchronized in the SPA. In the second mode, the demultiplexed 72 kbps operational data is sent to the NSP while the demultiplexed 128 kbps data is sent to the payload processor. In order to implement a forward link bent-pipe mode, an additional output is needed from the Costas loop and an additional switch is needed in the SPA. The switch in the SPA allows either normal data, bent-pipe data modulated on the carrier, or bent-pipe data modulated on a subcarrier to be output to the payload.

ORIGINAL PAGE IS  
OF POOR QUALITY



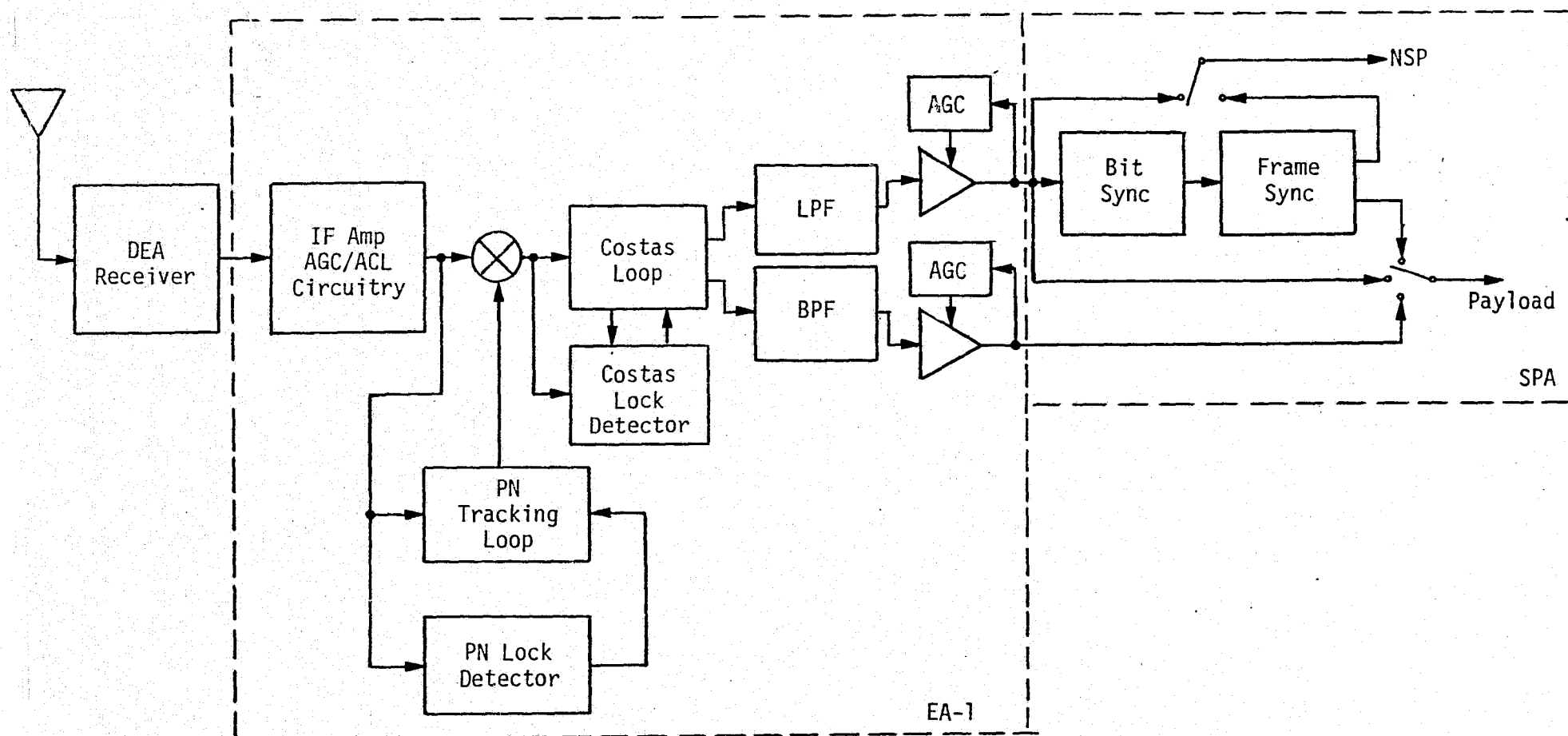


Figure 44. Ku-Band Forward Link Simplified Block Diagram

The outputs of the Costas loop for normal data and the bent-pipe data are presented in Figure 45. In the normal data demodulation, the Costas loop has been designed to reconstruct a carrier reference from the input signal whose signal component is totally suppressed (e.g., a biphase modulated carrier). For the bent-pipe mode, the Costas loop must accurately track a signal whose carrier component is not completely suppressed. As is the case for a Costas loop with a ranging waveform modulated on the subcarrier of the received signal, several key questions arise relative to the performance of the Costas loop when bent-pipe data is present. These questions are repeated here for convenience.

1. Is the loop capable of successfully tracking the input independent of the value of the data modulation index?
2. Is it possible to extract the bent-pipe data modulated on a subcarrier if the normal data modulation is removed?
3. What is the additional threshold signal-to-noise ratio required to operate the loop in the PM (i.e., residual carrier) mode as compared to the PSK mode?
4. What tradeoffs exist between the power in the bent-pipe channel and loop threshold performance as a function of the normal data and the bent-pipe data modulation indices?

Appendix L presents the detailed analysis to answer these questions for the general case of Costas loop tracking in the presence of a residual carrier. To determine the performance of the Costas loop with the bent-pipe data, consider the input signal of the form

$$s(t, \theta) = \sqrt{2P} \sin [\omega_0 t + \beta_d d(t) + \beta_s \sin (\omega_{sc} t + \theta_{bp}(t)) + \theta], \quad (50)$$

where  $P$  is the total received power,  $\omega_0$  is the carrier radian frequency and  $\theta$  is the corresponding input phase to be estimated,  $\beta_d$  is the data modulation index with  $d(t)$  either the normal data waveform or the bent-pipe data waveform when modulated on the carrier, and  $\beta_s$  is the bent-pipe subcarrier modulation index with  $\omega_{sc}$  the radian subcarrier frequency and  $\theta_{bp}(t)$  the bent-pipe data waveform. Using the results presented in Section 3.5 and Appendix L, the performance of the sub-carrier bent-pipe channel is characterized both when  $\beta_d$  is equal to zero



(i.e., data modulating the carrier directly is not present) and when  $\beta_d$  is nonzero (i.e., data modulating the carrier directly is present) by the bent-pipe signal power  $P_{bp}$  to the total power  $P$ .

$$\frac{P_{bp}}{P} = 2 \cos^2 (\beta_d) J_1^2 (\beta_s) \left[ 1 - \frac{1}{\rho S_L} \right], \quad (51)$$

where  $\rho$  is the signal-to-noise ratio in the loop bandwidth  $B_L$  given by

$$\rho = \frac{P}{N_0 B_L} \quad (52)$$

and where  $S_L$  is the squaring loss in the Costas loop. The squaring loss  $S_L$  is derived in Appendix L to be

$$S_L = \frac{J_0^4 (\beta_s) [D_m \sin^2 (\beta_d) - \cos^2 (\beta_d)]^2}{J_0^2 (\beta_s) [\cos^2 (\beta_d) + D_m K_D \sin^2 (\beta_d)] + \frac{B_i/R_s}{4 R_d} + R_d J_0^4 (\beta_s) \frac{\sin^2 (2\beta_d)}{2}} \quad (53)$$

for NRZ data. The data distortion factor  $D_m$  for NRZ data with RC filters as the lowpass arm filters in the Costas loop is given by

$$D_m = 1 - \frac{1}{2B_i/R_s} \left[ 1 - \exp \left( -\frac{2B_i}{R_s} \right) \right]. \quad (54)$$

The factor  $D_m K_D$  in (53) is found in Appendix L to be

$$D_m K_D = 1 - \frac{3 - (3 + 2B_i/R_s) \exp (-2B_i/R_s)}{4B_i/R_s}. \quad (55)$$

The term  $B_i/R_s$  is the ratio of the two-sided noise bandwidth of the lowpass arm filters in the Costas loop to the data rate. The signal energy per bit-to-single-sided noise spectral density,  $R_d$ , is given by

$$R_d = \frac{P}{N_0 R_s}. \quad (56)$$

ORIGINAL PAGE IS  
OF POOR QUALITY

Figure 46 presents the ratio of subcarrier bent-pipe signal power  $P_{bp}$  to total power  $P$  as a function of modulation indices. The curves of Figure 46 are computed from (51). It may be observed that the curves for  $R_d = 5$  dB and  $R_d = 10$  dB coincide, and hence the bent-pipe data demodulation performance is insensitive to  $R_d$ .

Another key performance parameter is the additional power required to operate the Costas loop in the PM mode. Let  $P'$  denote the signal power in the PM mode to achieve the same performance as PSK data with power  $P$ . Then the ratio of  $P'/P$  is the factor by which the signal power must be increased in order not to degrade the normal data bit error probability. Appendix L shows that

$$\frac{P'}{P} = -\frac{B}{2A} + \sqrt{\left(\frac{B}{2A}\right)^2 - \frac{C}{A}}, \quad (57)$$

where

$$\begin{aligned} A &= J_0^4(\beta_s) [D_m \sin^2(\beta_s) - \cos^2(\beta_d)] \\ B &= -J_0^2(\beta_s) [\cos^2(\beta_d) + D_m K_D \sin^2(\beta_d)] \left[ \frac{D_m^2}{D_m K_D + \frac{(B_i/R_s)}{4R_d}} \right] \\ C &= -\frac{(B_i/R_s)}{4R_d} \left[ \frac{D_m^2}{D_m K_D + \frac{(B_i/R_s)}{4R_d}} \right]. \end{aligned} \quad (58)$$

Figures 47 and 48 present the ratio  $P'/P$  as a function of modulation indices for  $R_d = 5$  dB and  $R_d = 10$  dB, respectively. From these figures, it may be seen that, as  $\beta_d$  increases (i.e., approaches PSK), the ratio  $P'/P$  approaches 1. Also, as  $R_d$  is increased, there is only a small increase in the ratio  $P'/P$  for large  $\beta_d$  but, for  $\beta_d = 1.1$ , increasing  $R_d$  from 5 dB to 10 dB increases the required  $P'/P$  by 0.4 dB.

The tracking performance of the Costas loop in the PM mode is also an important design parameter. The tracking phase jitter which degrades the power in the data and subcarrier bent-pipe channels has variance

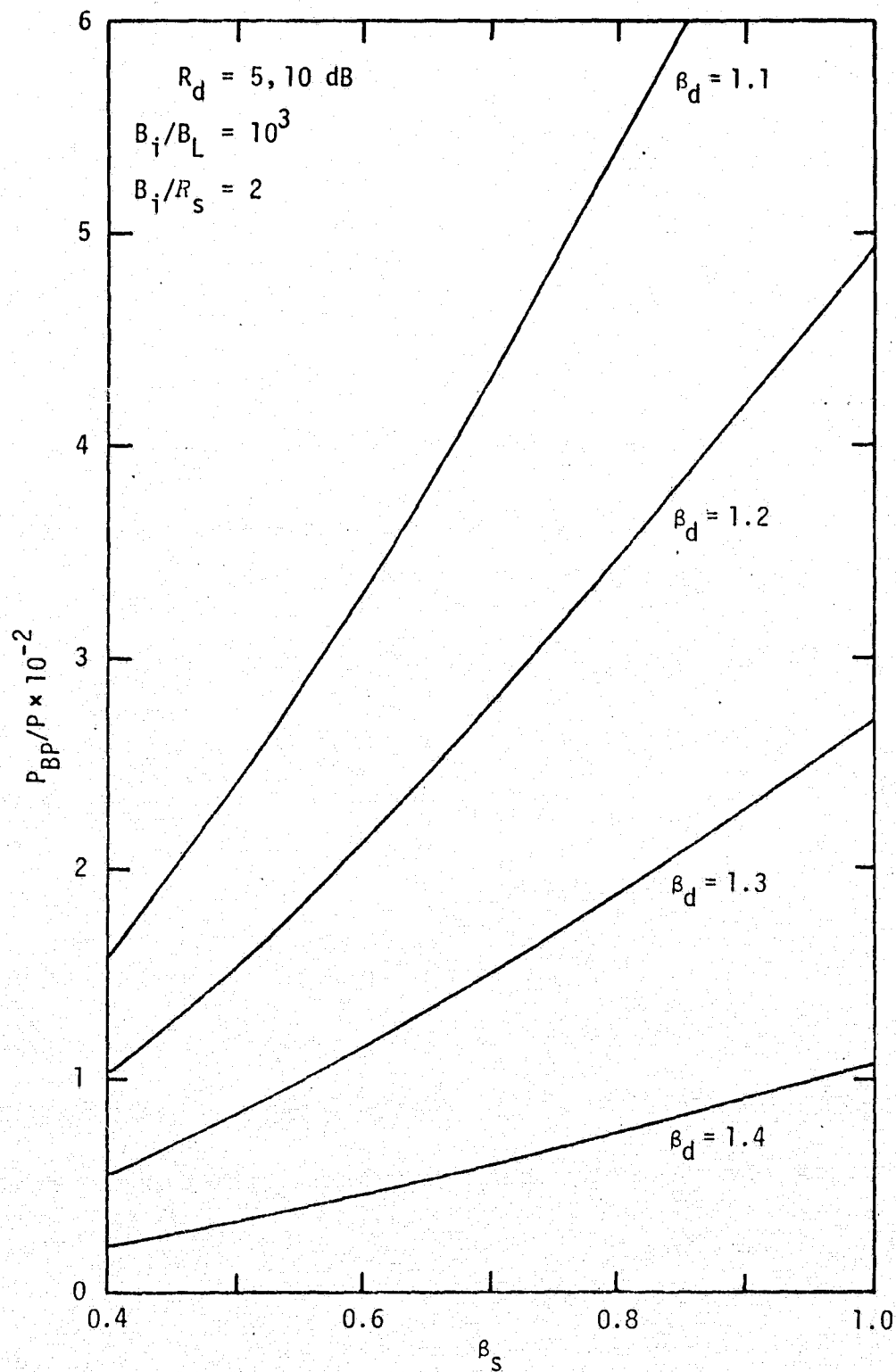


Figure 46. Ratio of Subcarrier Bent-Pipe Signal Power to Total Power as a Function of Modulation Indices

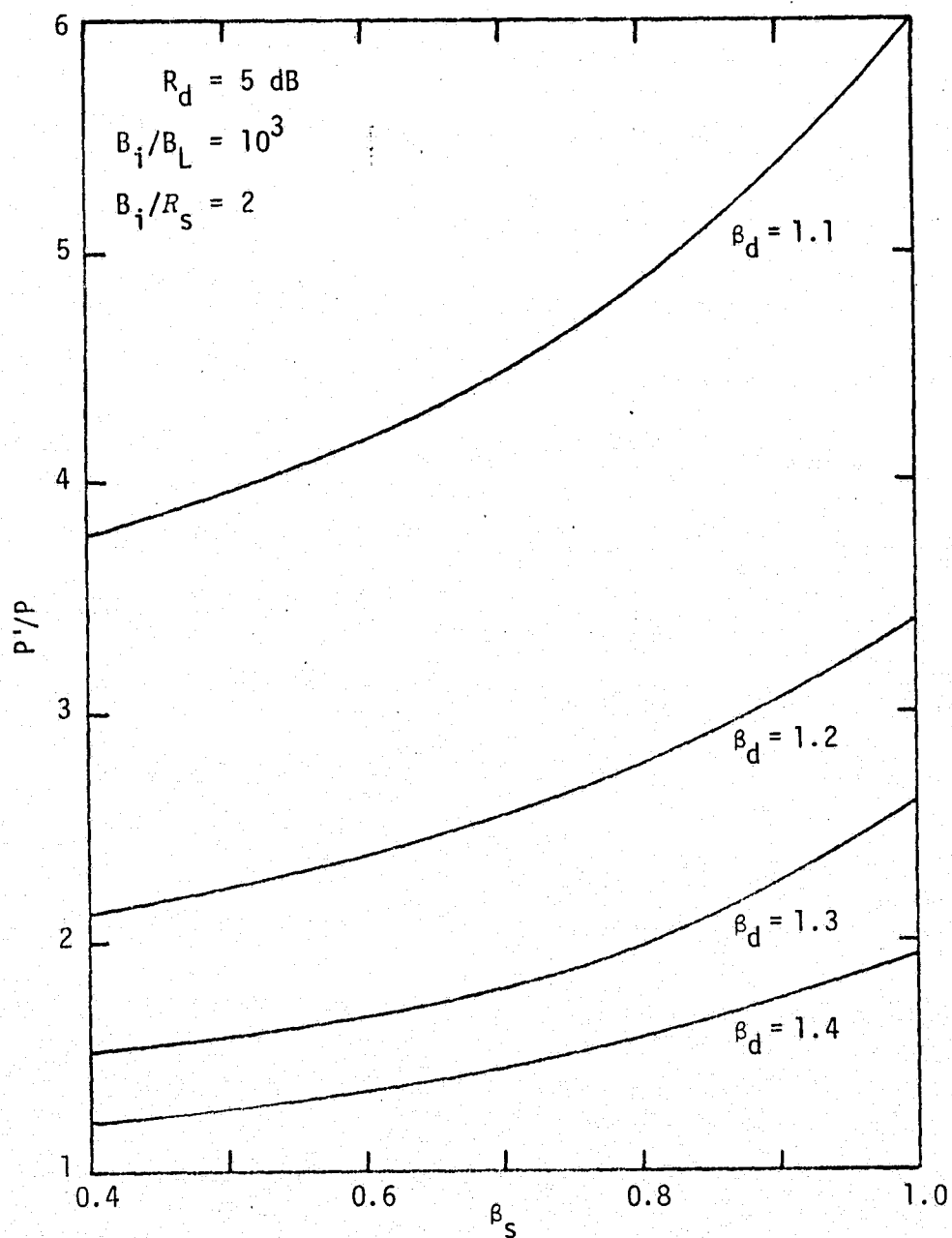


Figure 47. Ratio of Required Power in PM Mode to Power in PSK Mode as a Function of Modulation Indices;  $R_d = 5 \text{ dB}$

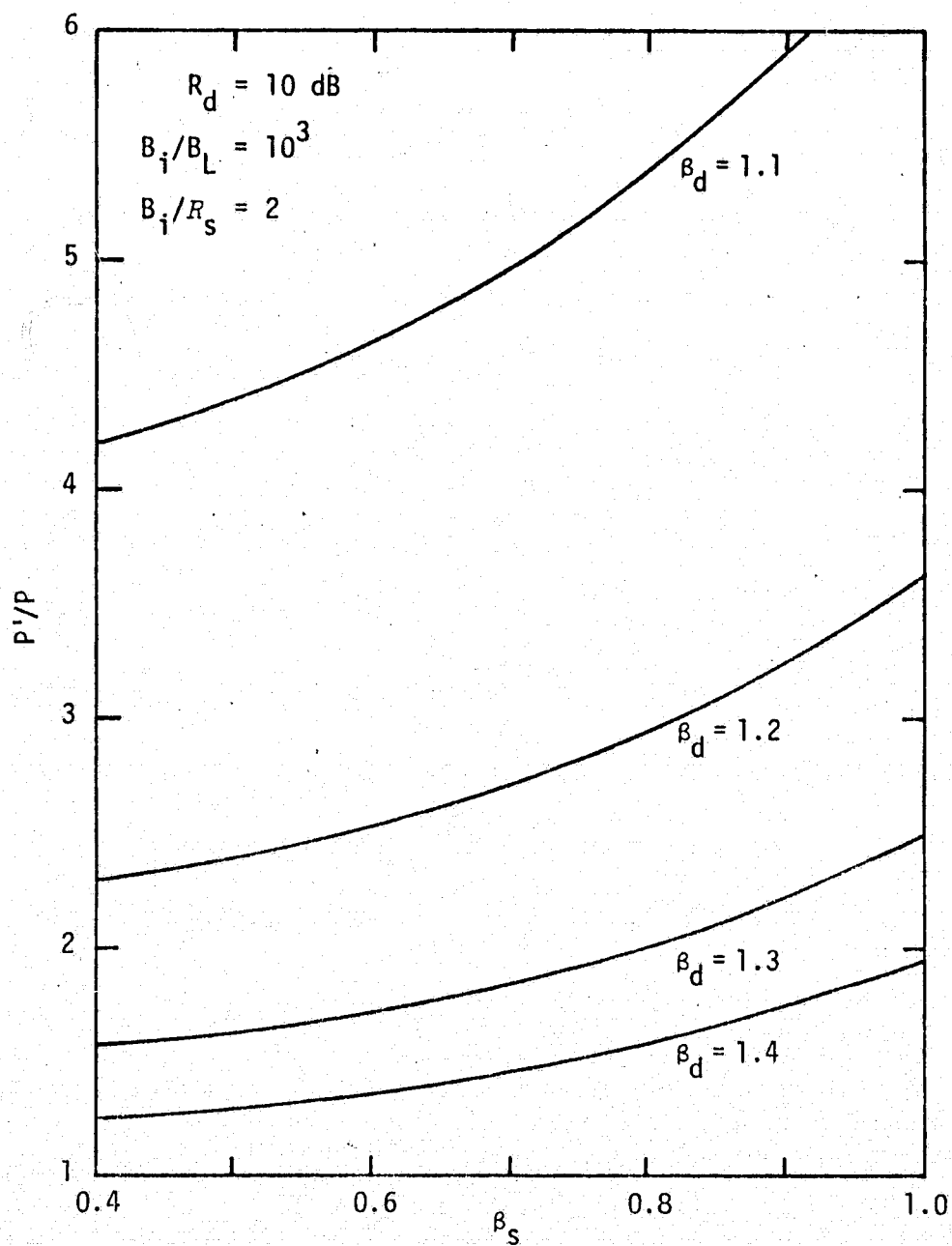


Figure 48. Ratio of Required Power in PM Mode to Power in PSK Mode as a Function of Modulation Indices;  $R_d = 10$  dB



$$\sigma_{\phi}^2 = \frac{1}{\rho S_L}, \quad (59)$$

where  $\rho$  and  $S_L$  are given by (52) and (53), respectively. For  $\beta_S = 1.0$  and  $\beta_d = 1.1$ , the standard deviation  $\sigma_{\phi}$  of the tracking phase jitter in percent radians is presented in Figure 49 as a function of  $R_d$  and the ratio of Costas loop arm filter to normal data rate. Note that increasing the ratio of  $B_i/R_S$  greater than 2 drastically degrades the tracking performance. The optimum value of  $B_i/R_S$  for the PSK mode is 1.4 and this seems to be a good value for the PM mode as well. Therefore, the Costas loop need not be modified for bent-pipe operation but the additional output from the quadrature arm is required in EA-1 if bent-pipe data is to be modulated on a subcarrier. Also, as Figures 46 through 48 have shown, there will be some degradation to the normal data in the PM mode, depending on the modulation indices.

#### 4.2 Return Link Bent-Pipe Relay Design

The return link bent-pipe mode for payloads allows transmission of data that is not in the standard NASA format. Thus, multiple formats and multiple modulators/demodulators can be used by the payloads. The design goal for the bent-pipe mode is to minimize the signal processing in the Orbiter for data that does not meet the standard NASA format. Therefore, no Orbiter control of command or telemetry for the bent-pipe data is proposed. Rather, the Orbiter will act as a relay which will either merely make a frequency translation at IF or perform RF demodulation and remodulation on a new carrier.

The block diagram for the return link bent-pipe is shown in Figure 50. Channel 1 is primarily an analog commercial TV channel with a bandwidth of 4.2 MHz. Alternately, however, Channel 1 may consist of one of the other data channels shown, namely, 4.5 MHz of analog data or up to 4 MHz of NRZ digital data.

The remaining channels are to be modulated onto an 8.5 MHz square-wave unbalanced QPSK subcarrier. The power split is 4:1. The 20% input is designated as Channel 3 and consists of a 192 kbps Bi- $\phi$ -L data channel from the network signal processor. The 80% input, Channel 2, is generally from the payload system and consists of up to 2 Mbps of

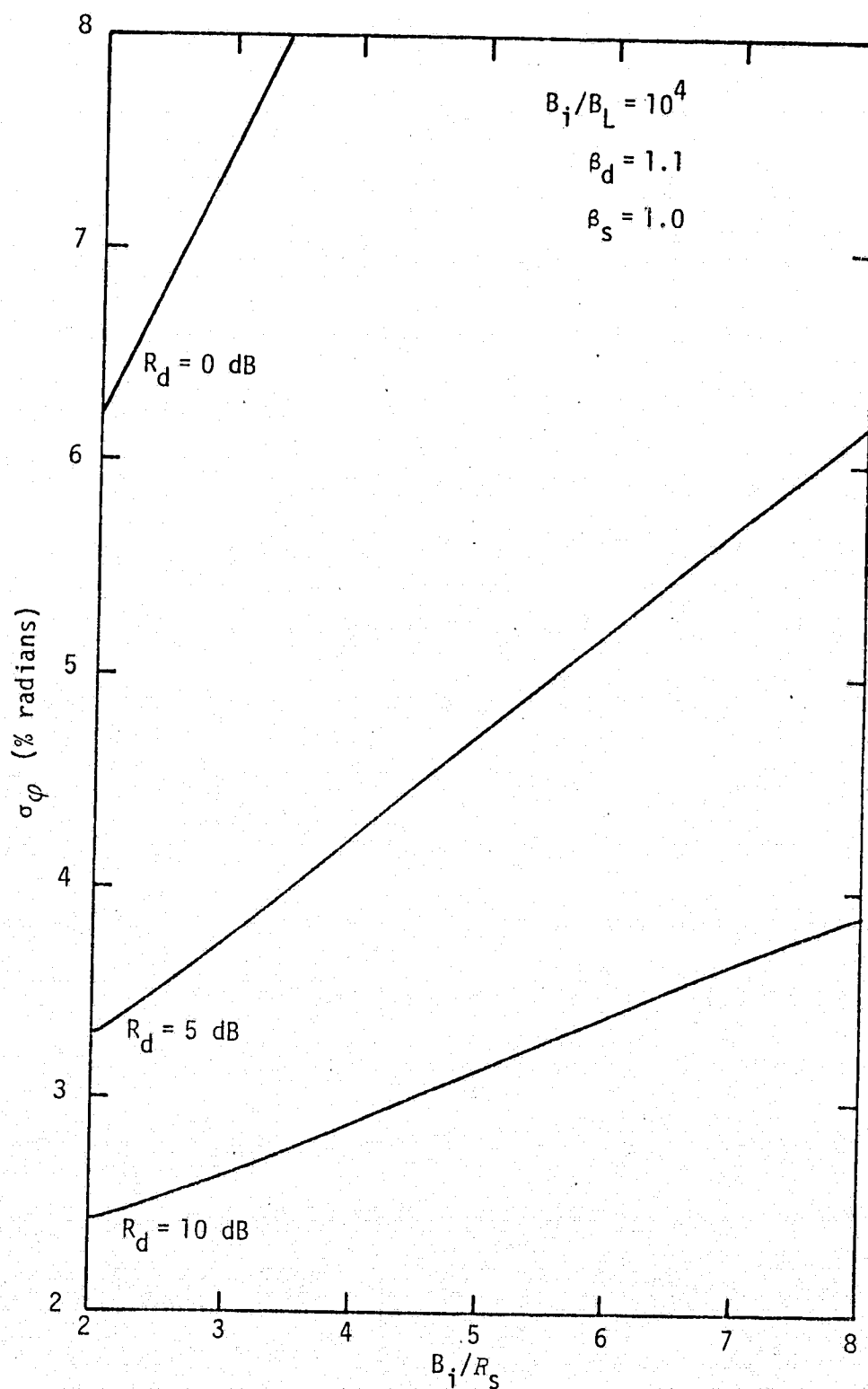


Figure 49. Standard Deviation of Tracking Phase Jitter for PM Mode

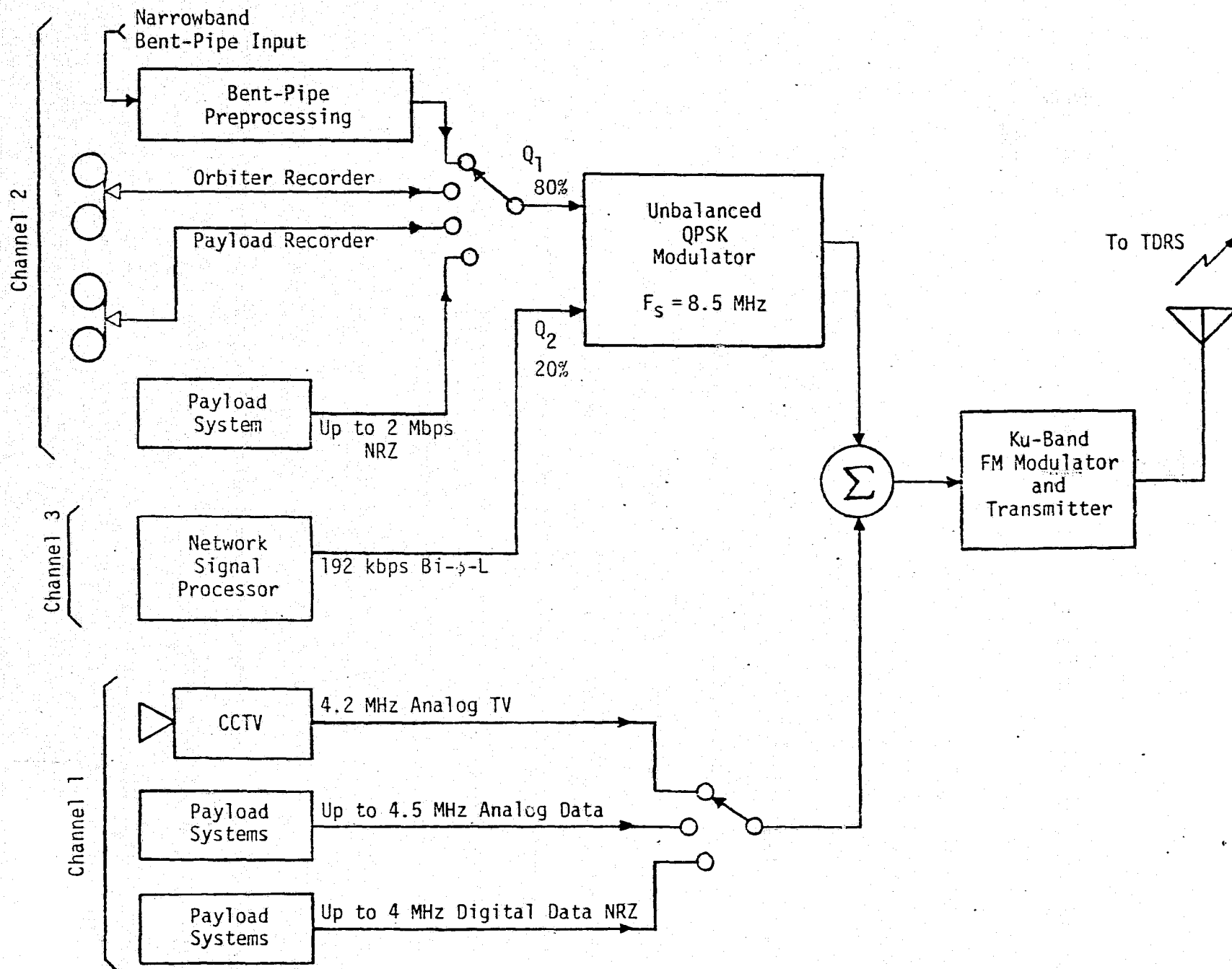


Figure 50. Return Link Bent-Pipe Link Implementation

data in the NRZ format. As shown in Figure 50, Channel 2 may also consist of information from recorder playbacks.

Among the various candidate signal formats that are expected to be transmitted via nonstandard bent-pipe is a 16 kbps Bi- $\phi$ -L data stream on a 1.024 MHz subcarrier. A block diagram of the transmitter is shown in Figure 51. Figure 52 shows a block diagram for a possible implementation of the ground receiver. At the receiver, the post-detection filter for the 8.5 MHz subcarrier has a bandwidth of 7.6 MHz. The LPF for the analog TV channel is 4.2 MHz. The 16 kbps data signal on the 1.024 MHz subcarrier was also tested in Channel 1 as shown in Figure 52. The bandwidth of the prefilter for the 1.024 MHz subcarrier is set at 160 kHz.

The FM deviations are set at the transmitter by adjusting the gains  $G_1$ ,  $G_2$  and  $G_3$ , each individually with the other signal inputs removed, as follows:

<u>Gain</u>	<u>Channel</u>	<u><math>\pm \Delta F</math></u>
$G_1$	8.5 MHz subcarrier	6 MHz
$G_2$	TV - Channel 1	11 MHz
$G_3$	16 kbps on 1.024 MHz sub-carrier in Channel 1	5 MHz

The total range of the instantaneous frequency deviation is  $2\Delta F$  in each of the above cases.

In the wideband bent-pipe mode, the bent-pipe payload data is transmitted in Channel 1. The concern in this mode is that, for low signal bandwidths (or low data rates), the S/N in the 4.5 MHz bandwidth at the transmitter will be so small that the FM discriminator on the ground will be below threshold. However, the S/N in the 4.5 MHz bandwidth at the transmitter will not affect the performance of the bent-pipe mode, but rather the S/N in the signal bandwidth is the parameter that determines the performance. This occurs because the noise at the transmitter is treated as signal by the FM discriminator so FM threshold will not occur unless the total received signal power (i.e., signal plus noise from the transmitter) is too small compared to the noise power at the receiver. Thus, the FM discriminator restores

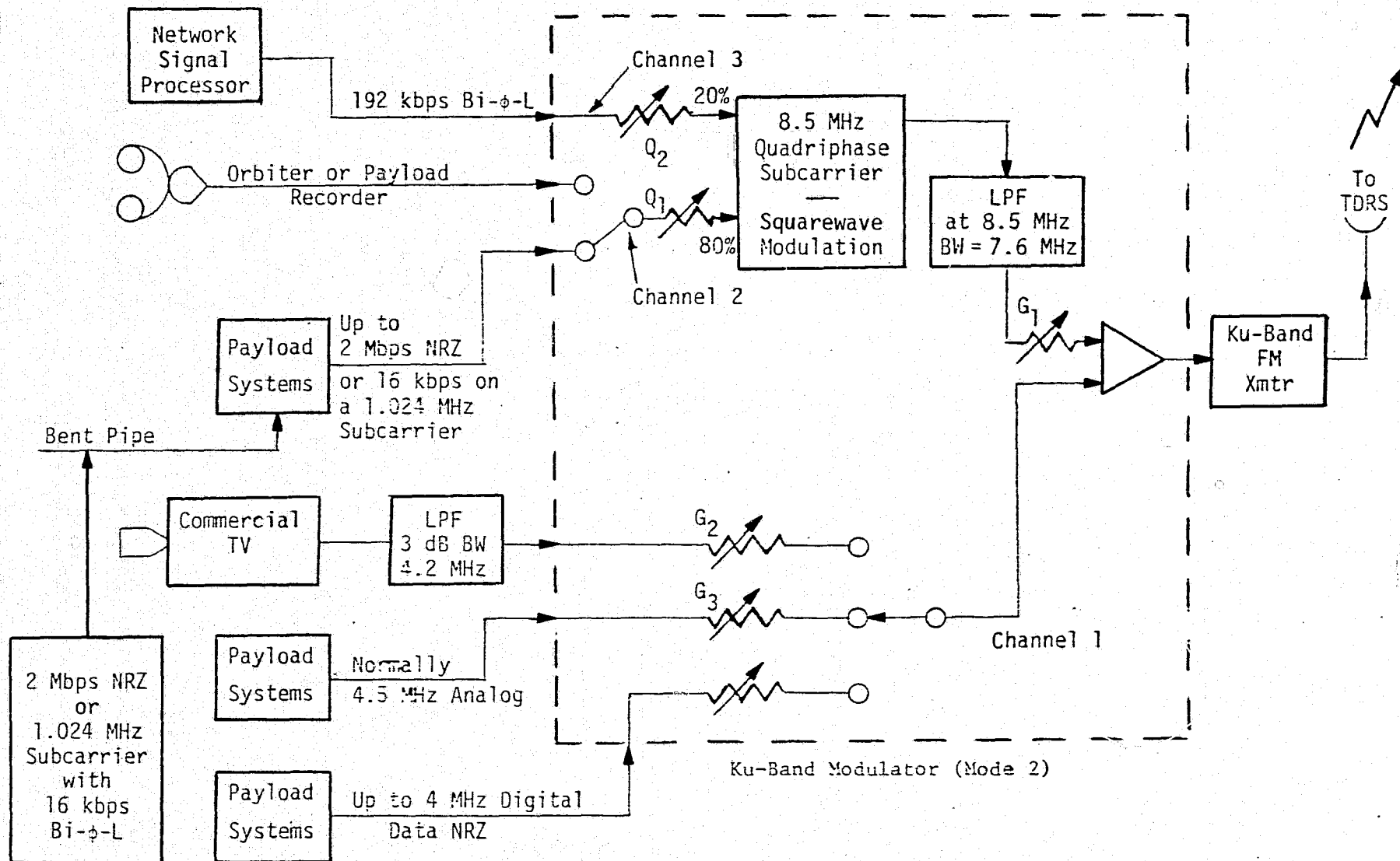


Figure 51. Ku-Band Mode 2 FM Transmitter for Return Link Bent-Pipe Mode

ORIGINAL PAGE IS  
OF POOR QUALITY

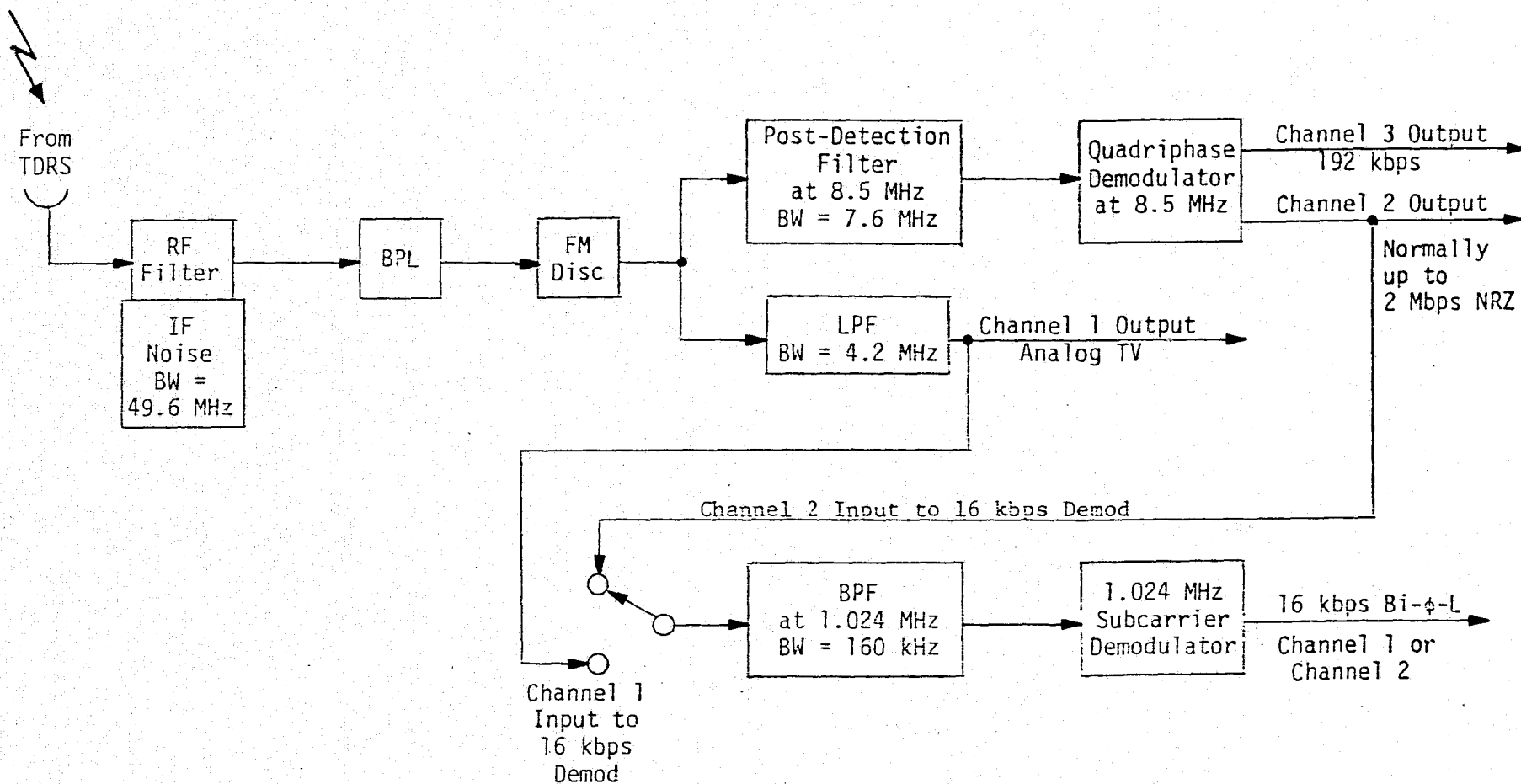


Figure 52. Ku-Band Mode 2 FM Receiver for Return Link Bent-Pipe Mode

the signal-plus-noise waveform that was present at the transmitter. Following the FM discriminator, the post-detection signal demodulator must contain a filter matched to the transmitted signal if the signal is to be optimally demodulated. If the post-detection filter is matched to a signal with a 4.5 MHz bandwidth, then demodulating a 16 kbps signal will not be optimum, and required S/N in the 4.5 MHz bandwidth will have to be increased drastically. Therefore, the performance of the wideband bent-pipe mode is a function of the ground post-detection demodulation filter being matched to the transmitted signal and not due to the FM threshold.

In the narrowband bent-pipe mode, the bent-pipe payload data is transmitted in Channel 2. The main concern in this mode is the S/N in the 4.5 MHz bandwidth of the Payload Interrogator (PI) will be so small that the ground subcarrier tracking loop presented in Section 3.2 will lose lock and the operational data will also be lost. If the S/N in the PI 4.5 MHz bandwidth is small, then the effective data rate in Channel 2 will be 4.5 Mbps. Since the ground subcarrier tracking loop is designed for a maximum of 2 Mbps in Channel 2, the signal distortion due to lowpass filtering of 4.5 Mbps will increase, and the squaring loss of the Costas loop will increase also. Therefore, the ground subcarrier tracking loop performance will degrade and lose lock at a much higher received S/N in the 2 MHz bandwidth. In order to establish the required S/N in the PI 4.5 MHz bandwidth for the narrowband bent-pipe mode, a test of the HAC digital implementation of the subcarrier UQPSK modulator should be made for the narrowband bent-pipe signals at low S/N. Depending on the effective bandwidth of the HAC subcarrier modulator, the PI 4.5 MHz bandwidth may have little significance.

A proposed way of combating low S/N in PI bandwidth is to devise a squelch circuit that would not send a signal to the Ku-band system from the PI unless the S/N in the PI bandwidth was greater than 7 dB. The design of the squelch circuit is a problem because, without knowledge of the signal structure, which is unlikely in the bent-pipe mode, it is difficult to determine the signal waveform from noise. It should be noted that, instead of a squelch, the ground operations could always

command the Ku-band system out of the narrowband bent-pipe mode if the ground subcarrier tracking loop loses lock and the operational data is not being demodulated.

To solve the low S/N problem in the narrowband bent-pipe mode, a test should be made with the HAC digital subcarrier UQPSK modulator, and an analysis of low S/N signals in Channel 2 should be developed to compare against the test results.



## REFERENCES

1. W. C. Lindsey and W. R. Braun. "Signal-to-Noise Ratio Degradations Due to Data Asymmetry for Uncoded and Coded BPSK Communication Channels," LinCom Technical Memorandum to B. H. Batson (NASA/JSC), July 8, 1977.
2. R. S. Orr. "The Impact of Data Asymmetry on Bit Error Performance," Stanford Telecommunications, Inc., Technical Report (prepared under Subcontract No. 7023 to Operations Research, Inc., in support of Prime Contract No. NAS 5-23841 to NASA/GSFC), July 21, 1977.
3. W. C. Lindsey and M. K. Simon. Telecommunication Systems Engineering, Englewood Cliffs, N.J.: Prentice-Hall, Inc., 1973, Ch. 9.
4. J. W. Seyl. "Communications Performance Degradation Due to Bit Asymmetry," NASA/JSC Technical Memorandum EE7-8/77-194, August 22, 1977.
5. N. M. Shehadeh and K. Tu. "The Effects of Band-Limiting of a PCM/NRZ Signal on the Bit-Error Probability Using a Sample Detector," Proceedings of the IEEE, September 1970, pp. 1400-1401.
6. G. K. Huth et al. "Integrated Source and Channel Encoded Digital Communication System Design Study - Final Report," Axiomatix Report No. R7607-3 (under Contract NAS 9-13467), July 31, 1976.
7. S. Udalov. "Feasibility Study of an Interplex Modulation System for the Orbiter's Ku-Band Link," Axiomatix Report No. R7410-5 (under Contract NAS 9-13467), October 7, 1974.
8. S. Udalov. "Multiplexing Modulation Format for the Orbiter's Ku-Band Return Link," Axiomatix Report No. R7502-1 (under Contract NAS 9-13467), February 13, 1975.
9. D. Cartier et al. "Shuttle Communications Design Study - Final Report," Magnavox Report DRL No. T-975, March 31, 1975.
10. K. Tu. "Performance Analysis of the Proposed Three Channel Quadrature Modulation System," Lockheed Electronics Co., Inc., February 1976.
11. W. C. Lindsey. "Power Division Analysis of a Three Channel Unbalanced QPSK Signal Out of a Bandpass Limiter," LinCom Corp. Report TR No. 04-7604-8, April 1976.
12. M. K. Simon. "An Analysis of the Power Division Structure of a Bandpass Hardlimited Three-Channel Signal with Sinusoidal Subcarriers," Appendix G of Axiomatix Report No. R7703-2 (under Contract No. NAS 9-14614), March 31, 1977.

13. M. K. Simon. "Power Allocation Properties and Costas Loop Sub-carrier Tracking Performance Associated with a Digital Phase Shift Implementation of the Three-Channel Orbiter Ku-Band Modulator," Axiomatix Report No. R7709-4 (under Contract No. NAS 9-14614), September 29, 1977.
14. C. L. Weber. "Candidate Receivers for Unbalanced QPSK," 1976 ITC Proceedings, Vol. XII, pp. 455-464.
15. B. K. Levitt, J. R. Lesh, and J. C. Springett. "Shuttle/TDRSS Ku-Band Telemetry Study," Final Report 900-742, Jet Propulsion Laboratory, Pasadena, California, April 5, 1976.
16. M. K. Simon and W. C. Lindsey. "Optimum Performance of Suppressed Carrier Receivers with Costas Loop Tracking," IEEE Transactions on Communications, Vol. COM-25, February 1977, pp. 215-226.
17. W. C. Lindsey and M. K. Simon. "Optimum Design and Performance of Costas Receivers Containing Soft Bandpass Limiters," IEEE Transactions on Communications, special issue on Spread Spectrum Communications, Vol. COM-25, No. 8, August 1977, pp. 822-831.
18. M. K. Simon. "Tracking Performance of Costas Loops with Hard-Limiting In-Phase Channel," to appear in the April 1978 issue of the IEEE Transactions on Communications.
19. W. C. Lindsey. "Phase-Shift-Keyed Signal Detection with Noisy Reference Signals," IEEE Transactions on Aerospace Electronic Systems, Vol. AES-2, July 1966, pp. 393-401.
20. W. C. Lindsey and M. K. Simon. "The Effect of Loop Stress on the Performance of Phase-Coherent Communication Systems," IEEE Transactions on Communication Technology, Vol. COM-18, No. 5, October 1970, pp. 569-588.
21. R. J. Sherman. "Quadri-Phase Shift Keyed Signal Detection with Noisy Reference Signals," EASCON'69 Convention Record, pp. 46-52.
22. W. C. Lindsey and M. K. Simon. "Carrier Synchronization and Detection of Polyphase Signals," IEEE Transactions on Communications, Vol. COM-20, No. 3, June 1972, pp. 441-454.
23. S. A. Rhodes. "Performance of Offset-QPSK Communications with Partially-Coherent Detection," National Telecommunications Conference Record, November 1973, pp. 32A-1 - 32A-6.
24. M. K. Simon and J. G. Smith. "Offset Quadrature Communications with Decision-Feedback Carrier Synchronization," IEEE Transactions on Communications, Vol. COM-22, No. 10, October 1974, pp. 1576-1584.

25. W. R. Braun and W. C. Lindsey. "Carrier Synchronization Techniques for Unbalanced QPSK Signals - Parts I & II," submitted for publication in the IEEE Transactions on Communications. Part I also presented at the 1977 International Conference on Communications, Chicago. Part II presented at the 1977 National Telecommunications Conference, Los Angeles.
26. W. C. Lindsey and W. R. Braun. "TDRSS Communication Analysis and Modeling Study, Phase I Report," LinCom Corp. Report TR-09-7614-2, Pasadena, California, October 15, 1976.
27. "Shuttle Communications and Tracking Equipment by TRW for Rockwell International/NASA: Monthly Review, Network Transponder CDR," TRW Systems Group, Redondo Beach, California, November 15-18, 1977.

APPENDIX A

BIT ERROR RATE DEGRADATION OF THE KU-BAND RETURN LINK CHANNEL  
DUE TO NRZ DATA SYMBOL ASYMMETRY

ORIGINAL PAGE IS  
OF POOR QUALITY

## APPENDIX A

### BIT ERROR RATE DEGRADATION OF THE KU-BAND RETURN LINK CHANNEL DUE TO NRZ DATA SYMBOL ASYMMETRY

by

Marvin K. Simon

The high data rate link from the Shuttle Orbiter through the TDRSS to the ground takes NRZ symbols at 50 Mbps and encodes them with a rate 1/2, constraint length 7, convolutional code. The bit error rate performance of the convolutional decoder depends, among other things, on the symmetry of the modulation. Any asymmetry in the NRZ symbols entering the symbol synchronizer causes a misalignment in the symbol synchronization clock which degrades the integrate-and-dump output and any soft or hard decisions derived from it for input to the decoder. For a specified degree of asymmetry (in terms of a fraction of a symbol interval), the bit error rate degradation is dependent on the transition probability of the data. Clearly, if the data transmitted was either all ones or all minus ones, then misalignment of the bit synchronization clock would have no degrading effect on the integrate-and-dump output since, for each symbol, this circuit would integrate up to its maximum value before being dumped. On the other hand, when the data is an alternating sequence, then the worst case degradation results, since the transition which occurs at the end of each symbol in combination with the symbol synchronization clock misalignment prevents the integrate-and-dump output from reaching its maximum value.

To quantitatively determine the degrading effect of NRZ symbol asymmetry on error rate performance, consider first the alternating NRZ sequence illustrated in Figure 1a, where the +1 symbols are elongated by  $\Delta T/2$  (relative to their nominal value of  $T$  sec) and the -1 symbols are shortened by the same amount. Thus,  $\Delta T$  represents the relative difference in length between the +1 and -1 symbols. The data asymmetry is defined as the ratio of the difference in length between the +1 and -1 symbols to the sum of their lengths, i.e.,

$$\text{Asymmetry} \triangleq \frac{T(1 + \frac{\Delta}{2}) - T(1 - \frac{\Delta}{2})}{T(1 + \frac{\Delta}{2}) + T(1 - \frac{\Delta}{2})} = \frac{\Delta}{2} . \quad (1)$$

In the absence of noise, the timing instants for the in-phase integrate-and-dump (i.e., the epoch of the symbol synchronization clock) are determined as follows. The mid-phase integrate-and-dump in the symbol

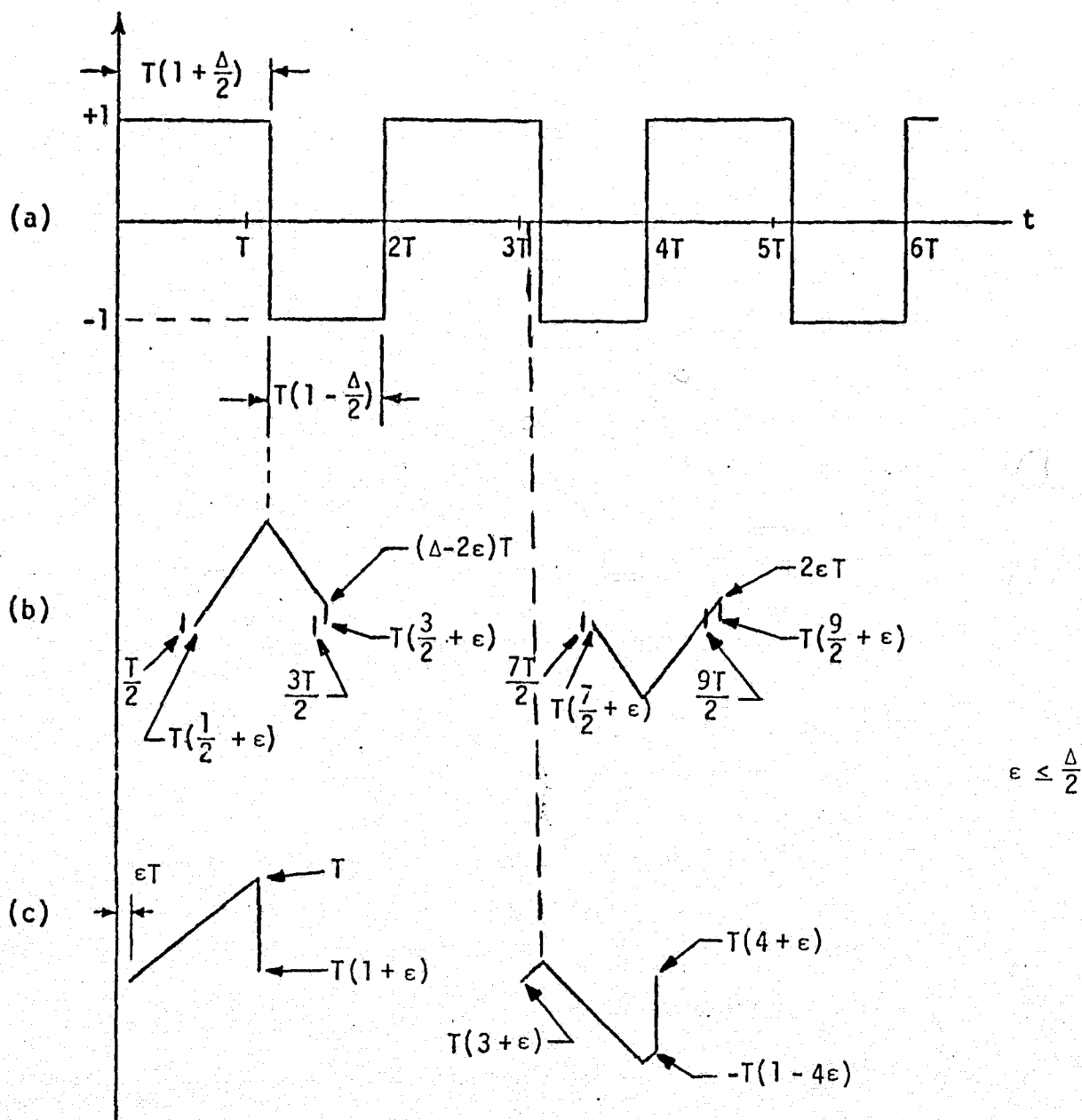


Figure 1. Symbol Synchronization Waveforms: (a) Input Alternating Data Sequence; (b) Mid-Phase Integrate-and-Dump Output; (c) In-Phase Integrate-and-Dump Output

synchronizer integrates across the transitions in the data symbol stream and determines the magnitude of the symbol synchronization error signal. In the steady state, this error signal must have zero value, on the average. Letting  $\epsilon T$  denote the misalignment of the symbol synchronization clock, then from Figure 1b we see that, when integrating across a negative data transition, the output of the mid-phase integrate-and-dump is given by

$$V_- = \left(\frac{1}{2} + \frac{\Delta}{2} - \epsilon\right)T - \left(\frac{1}{2} - \frac{\Delta}{2} + \epsilon\right)T = (\Delta - 2\epsilon)T. \quad (2)$$

When integrating across a positive data transition, the same output is given by

$$V_+ = -\left(\frac{1}{2} - \epsilon\right)T + \left(\frac{1}{2} + \epsilon\right)T = 2\epsilon T. \quad (3)$$

Figure 1c illustrates the in-phase integrate-and-dump output for the two types of data transition (negative and positive). For the negative data transition, we notice that the in-phase integrate-and-dump output reaches its maximum value and thus no degradation results. For the positive data transition, this same output is degraded by the factor  $(1 - 4\epsilon)$ . Thus, since the symbol synchronization clock misalignment  $\epsilon$  is determined by equating the average of the product of the mid-phase integrate-and-dump output and the sign of the difference of two adjacent in-phase integrate-and-dump outputs (or, equivalently, the sign of the data transition) to zero, i.e.,  $V_+ - V_- = 0$ . Thus, from (2) and (3),

$$2\epsilon T - (\Delta - 2\epsilon)T = 0, \quad (4)$$

or

$$\epsilon = \frac{\Delta}{4}. \quad (5)$$

Assuming then a clock misalignment as in (5) and letting  $E_s$  denote the symbol energy and  $N_0$  the channel noise spectral density, then the average symbol error probability associated with hard decisions made on the in-phase integrate-and-dump outputs is given by

$$P_E^A = \frac{1}{4} \operatorname{erfc}(\sqrt{E_s/N_0}) + \frac{1}{4} \operatorname{erfc}[\sqrt{E_s/N_0}(1 - \Delta)], \quad (6)$$

where

$$\operatorname{erfc} x \triangleq \frac{2}{\sqrt{\pi}} \int_x^\infty e^{-t^2} dt, \quad (7)$$

and the "A" superscript on  $P_E$  refers to the result for an alternating data symbol sequence.

When the input data is random with equiprobable symbols, then the in-phase integrate-and-dump output depends, in general, on the polarity of the symbol over which it is integrating and that of the preceding and succeeding symbols. Thus, one must compute the in-phase integrate-and-dump output for each of the eight possible three-symbol sequences (see Figure 2) and their corresponding conditional error probabilities. Then averaging these conditional error probabilities over the equal probabilities of the eight equally-likely three-symbol sequences gives the average error probability  $P_E^R$ , i.e.,

$$P_E^R = \frac{1}{8} \left\{ 5 \left[ \frac{1}{2} \operatorname{erfc} \sqrt{E_s/N_0} \right] + 2 \left[ \frac{1}{2} \operatorname{erfc} \left( \sqrt{E_s/N_0} \left( 1 - \frac{\Delta}{2} \right) \right) \right] + \frac{1}{2} \operatorname{erfc} \left( \sqrt{E_s/N_0} (1 - \Delta) \right) \right\} \\ = \frac{5}{16} \operatorname{erfc} \sqrt{E_s/N_0} + \frac{1}{8} \operatorname{erfc} \left[ \sqrt{E_s/N_0} \left( 1 - \frac{\Delta}{2} \right) \right] + \frac{1}{16} \operatorname{erfc} \left[ \sqrt{E_s/N_0} (1 - \Delta) \right] \quad (8)$$

where the "R" superscript on  $P_E$  refers to the result for a random data symbol sequence.

Tables 1 and 2 contain the symbol energy-to-noise ratio degradations (in dB) for asymmetry values [see (1)] of 3, 7, 10, 15 and 20% ( $\Delta = 0.06, 0.14, 0.20, 0.30$ , and  $0.40$ ) and  $E_s/N_0 = 0, 0.75$ , and  $1.5$  dB. The values of  $E_s/N_0$  selected correspond to bit energy-to-noise ratios  $E_b/N_0 = 3, 3.75$ , and  $4.5$  which, respectively, correspond to decoder bit error probabilities  $P_b = 10^{-3}, 10^{-4}$ , and  $10^{-5}$ . The degradations are obtained from (6) and (8) by computing the additional  $E_s/N_0$  required due to asymmetry to produce the same value of symbol error probability when  $\Delta = 0$ , i.e.,  $P_E^0$ , where

$$P_E^0 \triangleq \frac{1}{2} \operatorname{erfc} (\sqrt{E_s/N_0}). \quad (9)$$

It should be noted that the symbol energy-to-noise ratio degradations given in these tables assume no channel bandwidth limitation, i.e., ideal rectangular pulse shapes have been assumed for the NRZ data. Any rounding of the pulses caused by channel bandwidth limitation produces an additional symbol energy-to-noise ratio degradation over and above that due to data asymmetry. However, the bandlimiting degradation and the data asymmetry do not add algebraically but rather combine in a way determined by the particular symbol synchronization implementation.



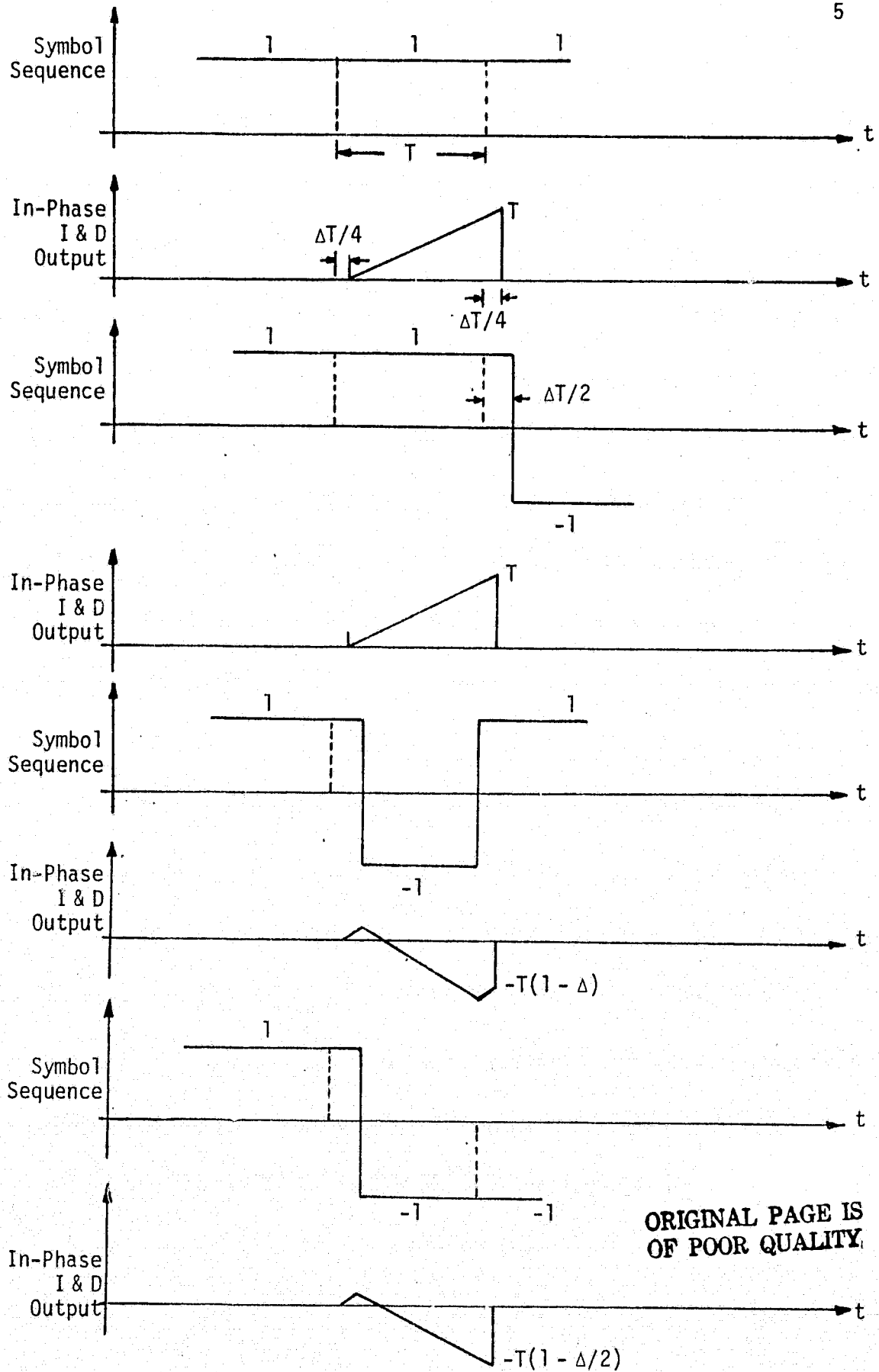


Figure 2. In-Phase Integrate-and-Dump Behavior for Eight Possible Three-Symbol Sequences

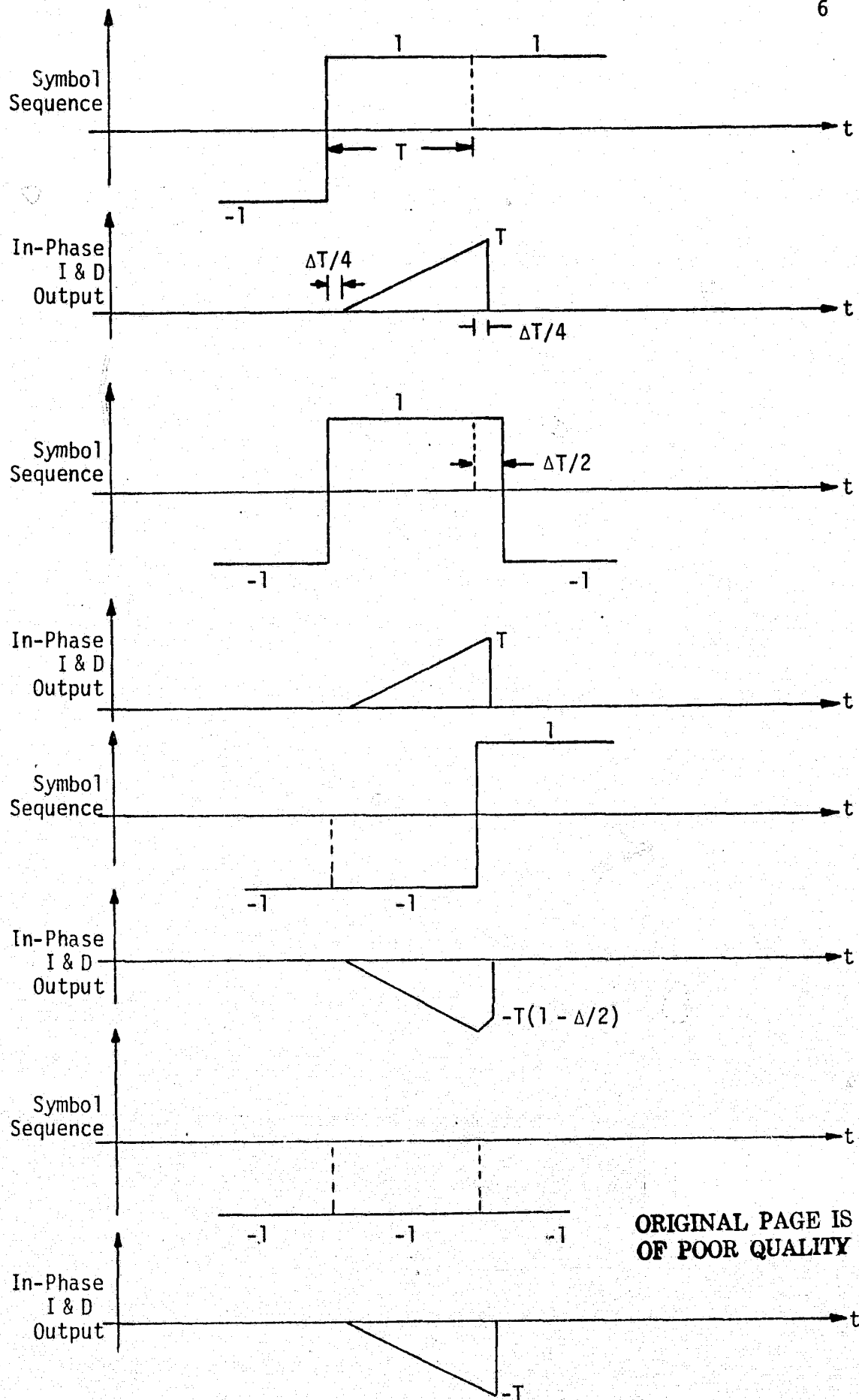


Figure 2 (continued)

Table 1. Alternating Data

Asymmetry (%)	$E_s/N_0$ (dB)	$P_b$	Degradation (dB)
3	0	$10^{-3}$	0.275
	0.75	$10^{-4}$	0.275
	1.50	$10^{-5}$	0.275
7	0	$10^{-3}$	0.68
	0.75	$10^{-4}$	0.69
	1.50	$10^{-5}$	0.70
10	0	$10^{-3}$	1.025
	0.75	$10^{-4}$	1.045
	1.50	$10^{-5}$	1.070
15	0	$10^{-3}$	1.693
	0.75	$10^{-4}$	1.748
	1.50	$10^{-5}$	1.811
20	0	$10^{-3}$	2.530
	0.75	$10^{-4}$	2.645
	1.50	$10^{-5}$	2.778

Table 2. Random Data

Asymmetry (%)	$E_s/N_0$ (dB)	$P_b$	Degradation (dB)
3	0	$10^{-3}$	0.135
	0.75	$10^{-4}$	0.135
	1.50	$10^{-5}$	0.135
7	0	$10^{-3}$	0.333
	0.75	$10^{-4}$	0.337
	1.50	$10^{-5}$	0.340
10	0	$10^{-3}$	0.495
	0.75	$10^{-4}$	0.505
	1.50	$10^{-5}$	0.517
15	0	$10^{-3}$	0.799
	0.75	$10^{-4}$	0.824
	1.50	$10^{-5}$	0.854
20	0	$10^{-3}$	1.149
	0.75	$10^{-4}$	1.201
	1.50	$10^{-5}$	1.264

For uncoded NRZ data, we find from (9) that, for  $P_E^0 = 10^{-5}$ , we require  $E_s/N_0 = 9.6$  dB. The corresponding additional  $E_s/N_0$  (SNR degradation) due to asymmetry required to produce a  $10^{-5}$  error probability is illustrated in Figure 3 as a function of percent asymmetry. In this figure, we have let  $T_+$  denote  $T(1 + \Delta/2)$  and  $T_-$  denote  $T(1 - \Delta/2)$  in accordance with the definition of asymmetry given in (1). Also illustrated in this figure is the SNR degradation due to asymmetry where the asymmetry is in accordance with Goddard's definition given by

$$\text{Asymmetry} = \frac{T_+ - T_-}{2T_-} = \frac{T(1 + \frac{\Delta}{2}) - T(1 - \frac{\Delta}{2})}{2T(1 - \frac{\Delta}{2})} = \frac{\Delta}{2(1 - \frac{\Delta}{2})}, \quad (10)$$

or equivalently,

$$\Delta = \frac{2(\text{Asymmetry})}{1 + \text{Asymmetry}}. \quad (11)$$

Thus, for a given asymmetry,  $\Delta$  as computed from (11) is substituted in (8) from which the necessary  $E_s/N_0$  to yield  $P_E^0 = 10^{-5}$  is computed. Comparing this  $E_s/N_0$  with 9.6 dB yields the SNR degradation plotted in Figure 3.

In conclusion, we note that an analysis of the data symmetry problem is also presented in [1,2] using, however, a slightly different model for the way in which the asymmetry comes about. The assumption made there is that positive NRZ pulses are shortened whenever adjacent pulses are negative. Thus, a given positive pulse preceded and succeeded by a negative pulse would be reduced in duration at both ends. Letting  $\delta$  represent the fractional (relative to the nominal bit duration  $T$ ) increase in positive pulse length to a single adjacent negative pulse, then for a given random data sequence, the longest pulse would have length  $1 + 2\delta$ , while the shortest would have length  $1 - 2\delta$ . If, as before, asymmetry is defined as the difference in length between the shortest and longest pulses in the sequence divided by their sum, then using the model in [1,2], we get

$$\text{Asymmetry} = \frac{T(1 + 2\delta) - T(1 - 2\delta)}{T(1 + 2\delta) + T(1 - 2\delta)} = 2\delta. \quad (12)$$

Also, using this same model, it can easily be shown that, on the average, the symbol synchronizer will lock up at the nominal transition points of the equivalent symmetric data waveform, i.e.,  $0, T, 2T, 3T, \dots$

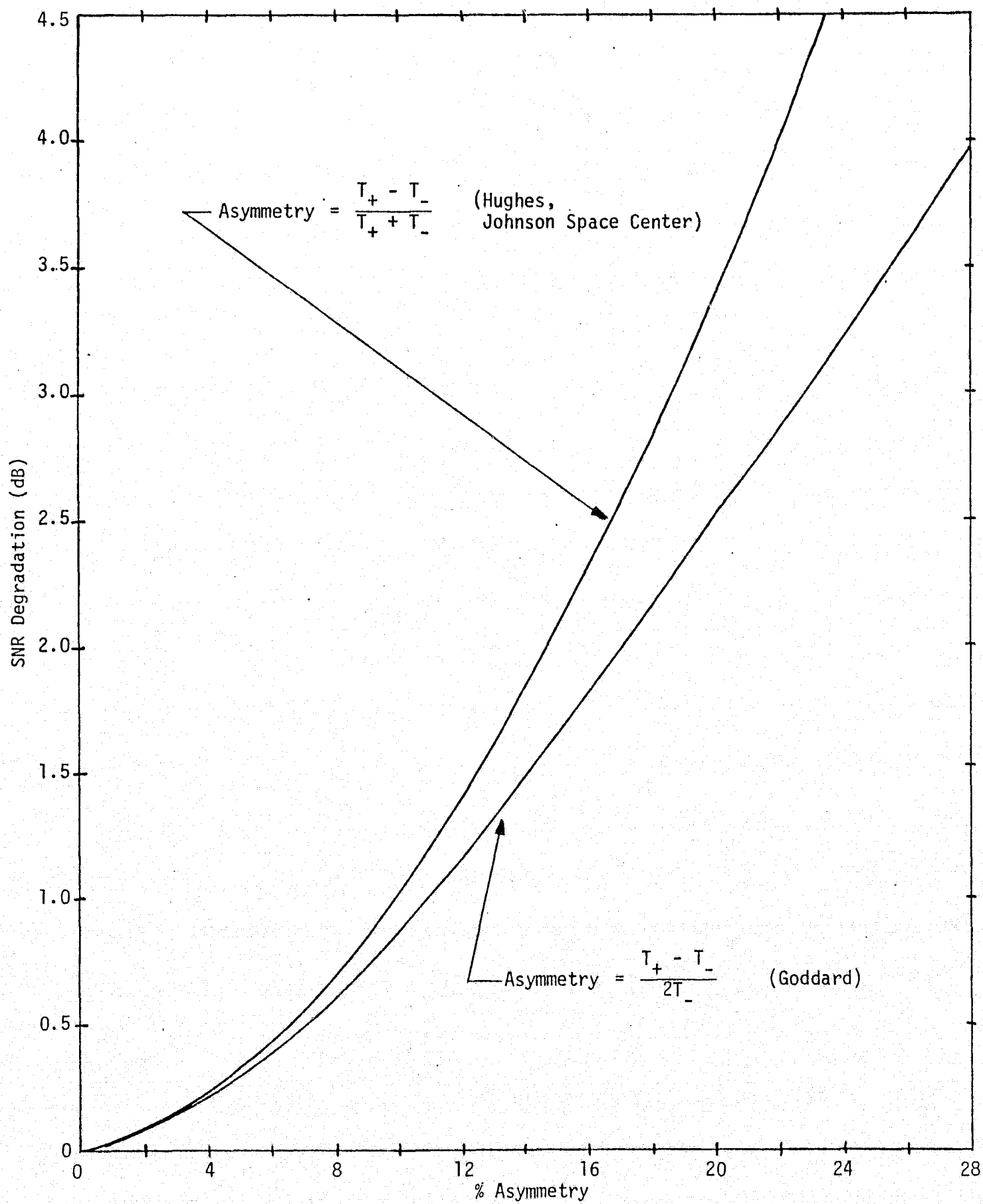


Figure 3. Uncoded NRZ Bit Synchronization Asymmetry Performance Degradation

Finally, using the definition of (12) and the above statement regarding the relative timing of the symbol synchronization clock and the data, the result given in [1,2] for average error probability due to data asymmetry is identical to our Equation (8). Thus, properly applied, either symbol synchronization asymmetry model will yield the same results.

#### REFERENCE

1. Lindsey, W. C., and Braun, W. R. "TDRSS Communication Analysis and Modeling Study, Phase I Report," TR-09-7614-2, LinCom Corp., Pasadena, California, October 15, 1976.
2. Orr, R. S. "The Impact of Data Asymmetry on Bit Error Performance," Stanford Telecommunications, Inc., Palo Alto, California, July 21, 1977.

APPENDIX B

FURTHER CONSIDERATIONS ON THE EFFECTS OF DATA ASYMMETRY ON  
BIT ERROR RATE PERFORMANCE OF THE KU-BAND AND  
S-BAND RETURN LINK CHANNELS

## APPENDIX B

### FURTHER CONSIDERATIONS ON THE EFFECTS OF DATA ASYMMETRY ON BIT ERROR RATE PERFORMANCE OF THE KU-BAND AND S-BAND RETURN LINK CHANNELS

by

Marvin K. Simon

In Appendix A and [1], we investigated the bit error rate degradation of the Ku-band return link channel due to NRZ data symbol asymmetry. Inherent in these results was the assumption that the symbol synchronizer was of such a type (e.g., data transition tracking loop [2]) as to produce a symbol sync clock which, on the average (e.g., no noise), locks up with a misalignment equal to half the asymmetry. While this assumption is believed to be typical of a wide variety of symbol synchronizers which employ an integrate-and-dump filter as a data detector, one might nevertheless ask the question: How sensitive is this SNR degradation due to asymmetry to perturbations of the symbol sync clock misalignment about its above-assumed value? Having this information would also tend to make the results somewhat independent of symbol sync configuration. In this appendix, we derive an expression for symbol error probability in the presence of data asymmetry and conditioned on an arbitrary clock misalignment whose value is allowed to range over the data asymmetry interval. SNR degradation for the coded NRZ case is then given as a function of this clock misalignment with percent data asymmetry as a parameter.

Despite the fact that the high rate Ku-band return link is coded NRZ data, it is also desirable to have theoretical results for SNR degradation due to asymmetry corresponding to coded Manchester data. This would allow comparison with measurements previously made by TRW on the S-band return link. Thus, the second part of this report has as its end result a plot of SNR degradation in dB versus percent asymmetry for coded Manchester data at a bit error rate of  $10^{-5}$  (symbol SNR equal to 1.5 dB). Also plotted on the curve for purposes of comparison will be the corresponding results (taken from Table 2 of [1]) for NRZ data.

#### Probability of NRZ Symbol Error in the Presence of Data Asymmetry and Arbitrary Clock Misalignment

For random NRZ data with equiprobable symbols, the in-phase integrate-and-dump output depends, in general, on the polarity of the symbol over which it is integrating and that of the preceding and



succeeding symbols. Letting  $\epsilon T$  denote (as in [1]) the misalignment of the symbol sync clock, then the in-phase integrate-and-dump output for each of the eight possible three-symbol sequences is tabulated below.

<u>Symbol Sequence</u>	<u>In-Phase Integrate-and-Dump Output</u>
1 1 1	T
1 1 -1	T
1 -1 1	$-T(1 - \Delta)$
1 -1 -1	$-T(1 - \Delta + 2\epsilon)$
-1 1 1	T
-1 1 -1	T
-1 -1 1	$-T(1 - 2\epsilon)$
-1 -1 -1	-T

Thus, since each of these three-symbol sequences are equally likely, the average probability of error conditioned on  $\epsilon$  is given by

$$\begin{aligned}
 P_E^R(\epsilon) = & \frac{5}{16} \operatorname{erfc} \sqrt{E_s/N_0} + \frac{1}{16} \operatorname{erfc} [\sqrt{E_s/N_0} (1-2\epsilon)] \\
 & + \frac{1}{16} \operatorname{erfc} [\sqrt{E_s/N_0} (1 - \Delta + 2\epsilon)] + \frac{1}{16} \operatorname{erfc} [\sqrt{E_s/N_0} (1 - \Delta)]
 \end{aligned}
 \tag{1}$$

where the "R" superscript on  $P_E$  refers to the result for a random data sequence. First note that, for  $\epsilon = \Delta/4$ , (1) reduces to (8) of [1]. Secondly,  $P_E^R(\epsilon)$  is a symmetric function of  $\epsilon$  around the point  $\Delta/4$ , i.e., equal positive and negative variations of  $\epsilon$  around the nominal position  $\Delta/4$  produce equal SNR degradations above that previously given in [1]. Figure 1 illustrates the SNR degradation at a symbol  $E_s/N_0$  of 1.5 dB (corresponding to a decoded bit error probability of  $10^{-5}$ ) as a function of  $\epsilon$  for  $0 \leq \epsilon \leq \Delta/2$  and percent asymmetry  $\Delta/2 \times 100$  as a parameter. We observe that, in the neighborhood of the nominal symbol sync lockup point,  $\epsilon = \Delta/4$ , the sensitivity of SNR degradation due to asymmetry is extremely small, even for large asymmetry values on the order of 25%. Thus, we conclude that the results given in [1] are relatively insensitive to the assumption of a hard-locked symbol sync at the midasymmetry point, even though this assumption yields the minimum SNR degradation due to asymmetry.

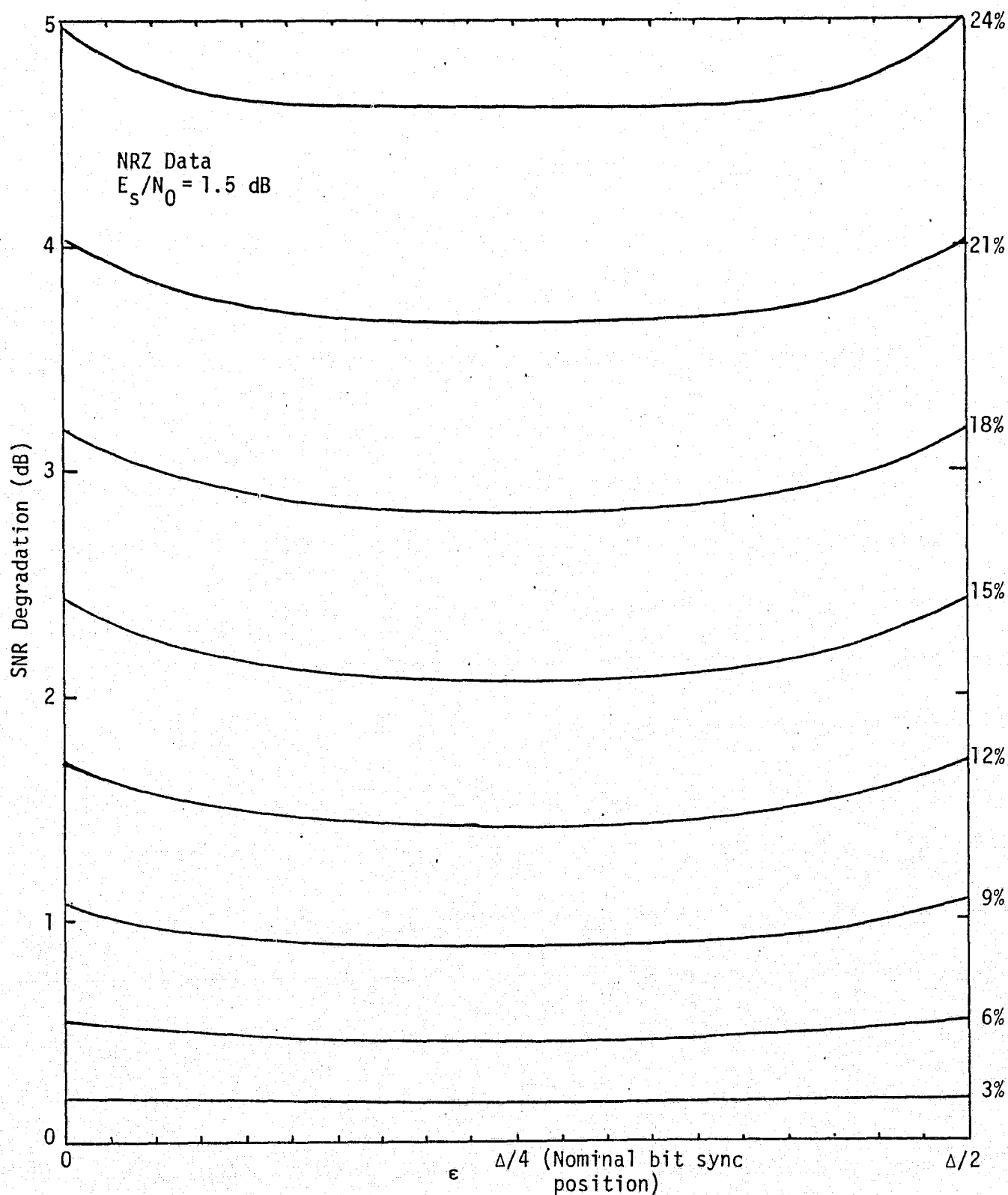


Figure 1. SNR Degradation Due to Data Asymmetry as a Function of Symbol Sync Clock Misalignment

### Probability of Manchester Symbol Error in the Presence of Data Asymmetry

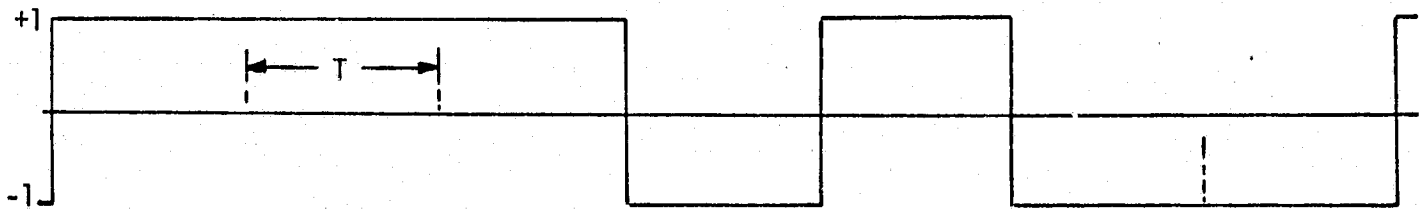
When Manchester coding is employed, then relative to the NRZ sequence, the Manchester coded waveform has  $3/2$  as many transitions. Thus, since SNR degradation due to asymmetry is directly related to the average transition density of the data sequence, one would intuitively expect that, for a fixed amount of asymmetry (in seconds), the Manchester coded case should yield a larger SNR degradation than the corresponding NRZ case. Indeed, this is true, as we shall soon demonstrate. On the other hand, depending on how one defines percent asymmetry for the Manchester coded case (two possibilities are suggested), a plot of SNR degradation versus percent asymmetry might result in a different conclusion than the above. This shall also be demonstrated by numerical example.

Consider an NRZ sequence and the corresponding Manchester waveform with asymmetry illustrated in Figure 2. Here  $\Delta/2$  denotes the fractional (relative to the half symbol time  $T/2$ ) elongation of the positive half pulse in the Manchester coded waveform. Once again, as in the NRZ case, the in-phase integrate-and-dump output depends, in general, on the polarity of the symbol over which it is integrating and the preceding and succeeding symbols. For the eight possible three-symbol sequences, the in-phase integrate-and-dump output is tabulated below, assuming a nominal bit sync lock-up misalignment of  $\Delta T/8$ .

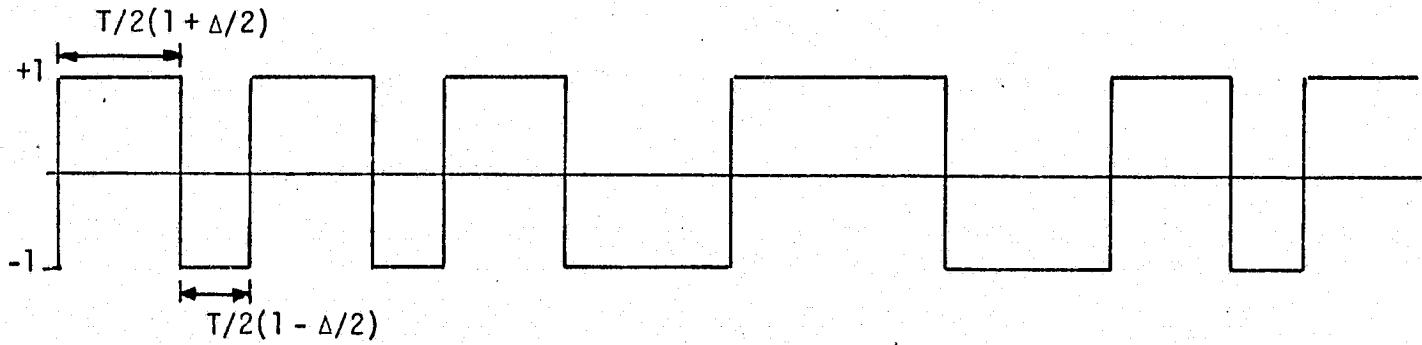
<u>Symbol Sequence</u>	<u>In-Phase Integrate-and-Dump Output</u>
1 1 1	$T(1 - \Delta/2)$
1 1 -1	$T(1 - \Delta/4)$
-1 1 -1	$T(1 - \Delta/4)$
-1 1 1	$T(1 - \Delta/2)$
-1 -1 -1	$-T(1 - \Delta/2)$
-1 -1 1	$-T(1 - \Delta/2)$
1 -1 -1	$-T(1 - \Delta/4)$
1 -1 1	$-T(1 - \Delta/4)$

Thus, the average probability of error for random Manchester coded data is

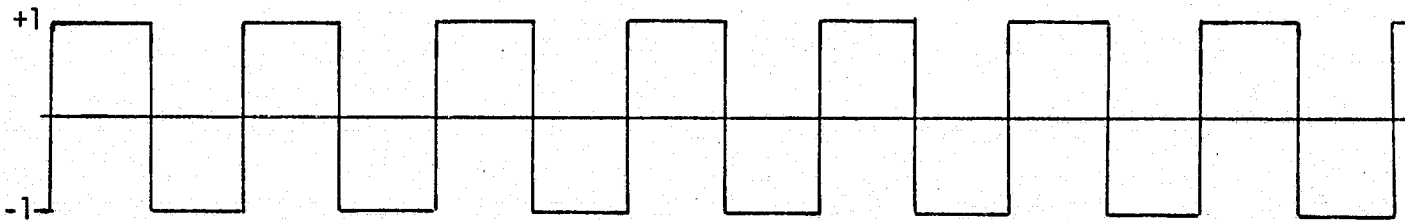
(a) NRZ Sequence



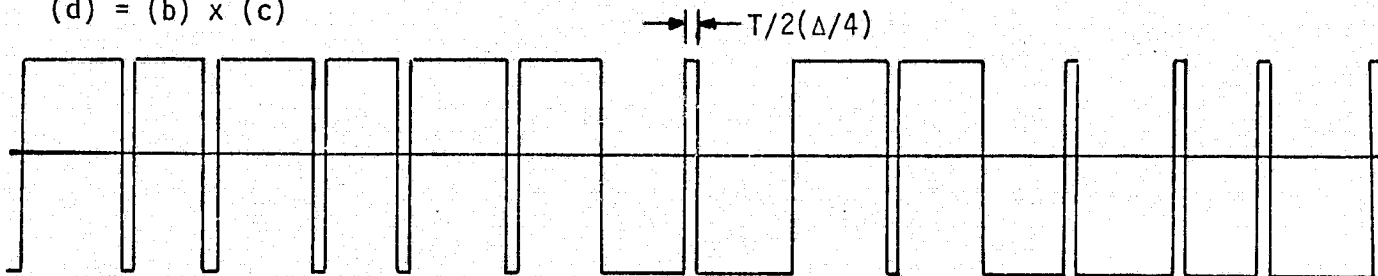
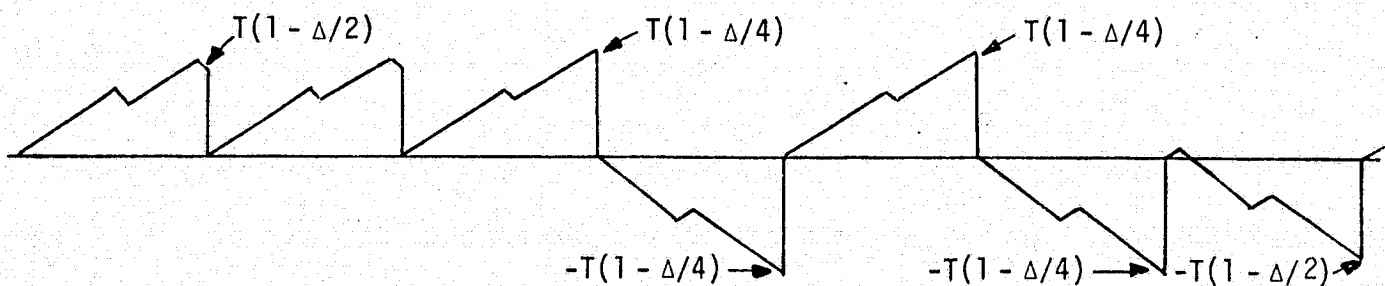
(b) Manchester Sequence with Data Asymmetry



(c) Symbol Sync Clock



(d) = (b) x (c)

(e) =  $\int_0^T (d) dt$  = In-Phase Integrate-and-Dump Output

ORIGINAL PAGE IS  
OF POOR QUALITY

Figure 2. Data Asymmetry Effects for Manchester Coded Data

$$P_E^R = \frac{1}{4} \operatorname{erfc} [\sqrt{E_s/N_0} (1 - \Delta/2)] + \frac{1}{4} \operatorname{erfc} [\sqrt{E_s/N_0} (1 - \Delta/4)] . \quad (2)$$

If we define percent asymmetry relative to the inverse of the data rate (i.e.,  $T$ ), then a given amount of asymmetry (in seconds) produces the same percent asymmetry for either NRZ or Manchester coded data. Thus, from Figure 2, we have, for Manchester coded data, that

$$\text{Asymmetry} = \Delta/4 . \quad (3)$$

Using this definition, Figure 3 plots SNR degradation in dB versus percent asymmetry for Manchester coded data and  $E_s/N_0 = 1.5$ . For comparison, the corresponding results for NRZ obtained in [1] are also illustrated. Note that the Manchester coded case always yields a larger SNR degradation for a given percent asymmetry. This conclusion is in accordance with our previous observations relative to the increased average transition density of Manchester coded data relative to NRZ.

If asymmetry is defined as was done for NRZ but now is relative to the half-pulse duration, then

$$\text{Asymmetry} = \frac{(T/2)^+ - (T/2)^-}{(T/2)^+ + (T/2)^-} = \frac{\frac{T}{2}(1 + \Delta/2) - \frac{T}{2}(1 - \Delta/2)}{\frac{T}{2}(1 + \Delta/2) + \frac{T}{2}(1 - \Delta/2)} = \frac{\Delta}{2} . \quad (4)$$

Note that, for this definition, a given percent asymmetry (i.e.,  $\Delta/2 \times 100$ ) results in twice as much asymmetry (in seconds) for Manchester than it does for NRZ. Nevertheless, using this definition, Figure 4 illustrates SNR degradation in dB versus percent asymmetry for Manchester coded data at  $E_s/N_0 = 1.5$  dB. The NRZ curve is again included for comparison and is identical with that given in Figure 3. Here note that, for small asymmetry values, the Manchester code yields a larger SNR degradation than NRZ while, for large percent asymmetries, the reverse is true. Thus, in drawing conclusions relative to the performance of Manchester versus NRZ coded data in the presence of data asymmetry, one must exercise care in applying their definitions of data asymmetry.

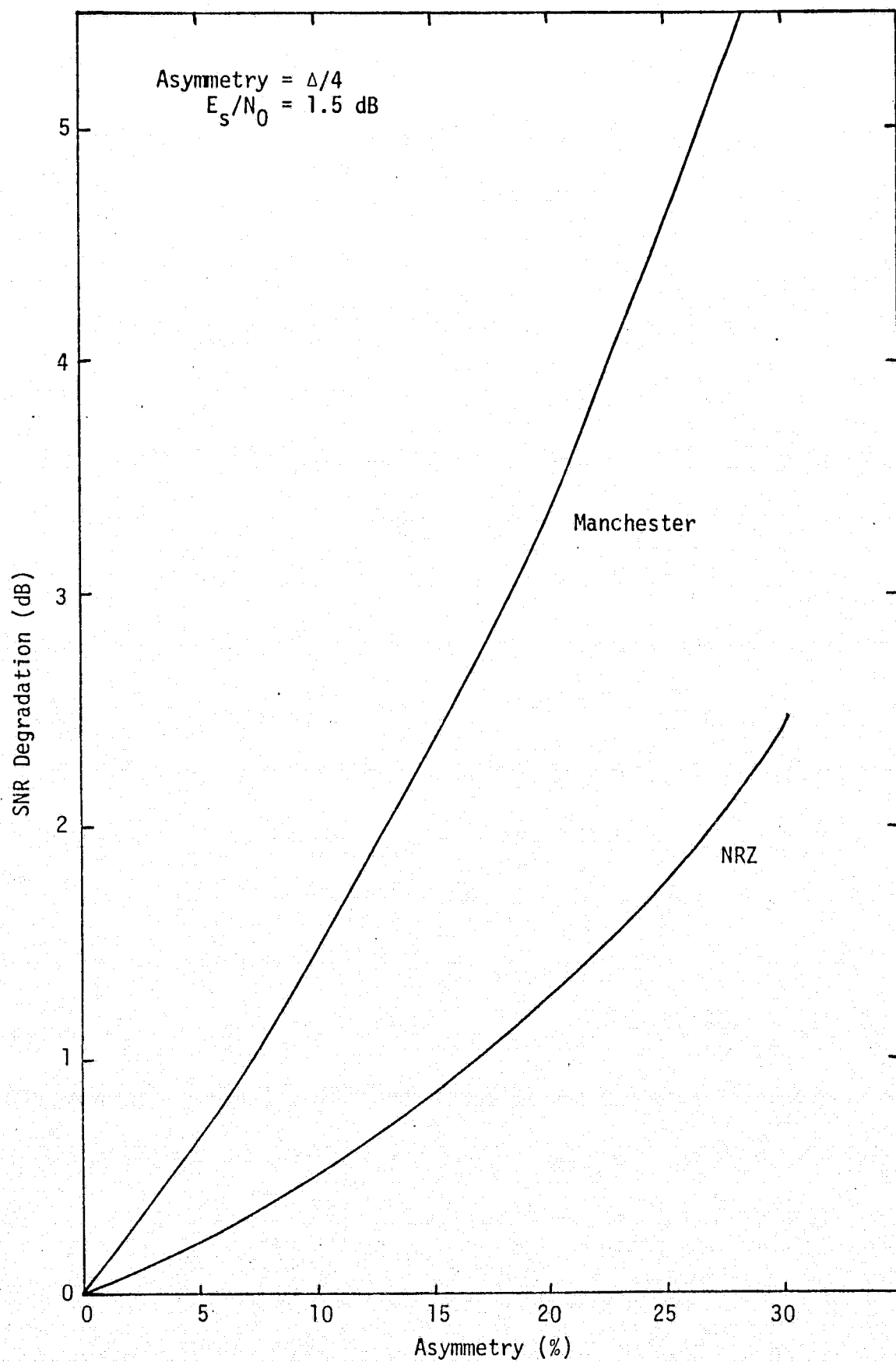


Figure 3. SNR Degradation vs. Percent Asymmetry for Manchester and NRZ Coded Data

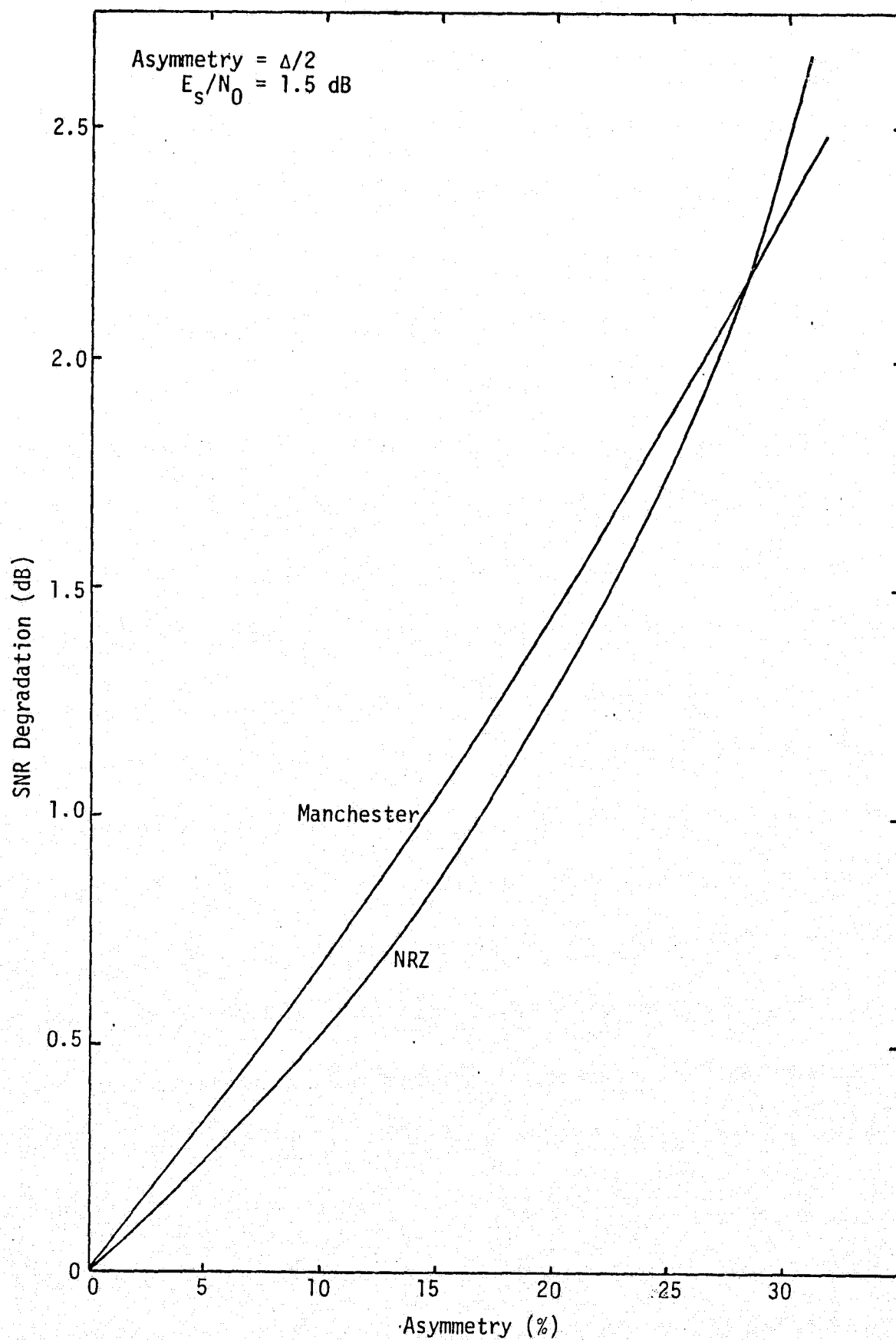


Figure 4. SNR Degradation vs. Percent Asymmetry for Manchester and NRZ Coded Data

## REFERENCES

1. M. K. Simon. "Bit Error Rate Degradation of the Ku-Band Return Link Channel Due to NRZ Data Symbol Asymmetry," Axiomatix Report No. R7707-2, July 8, 1977.
2. M. K. Simon and W. C. Lindsey. Telecommunication Systems Engineering. Prentice-Hall, Inc., Englewood Cliffs, N.J., 1973, Chapter 9.

ORIGINAL PAGE IS  
OF POOR QUALITY



APPENDIX C

THE COMBINED EFFECTS OF BANDLIMITING AND NRZ DATA ASYMMETRY  
ON THE BIT ERROR PROBABILITY PERFORMANCE  
OF A SAMPLE DETECTOR

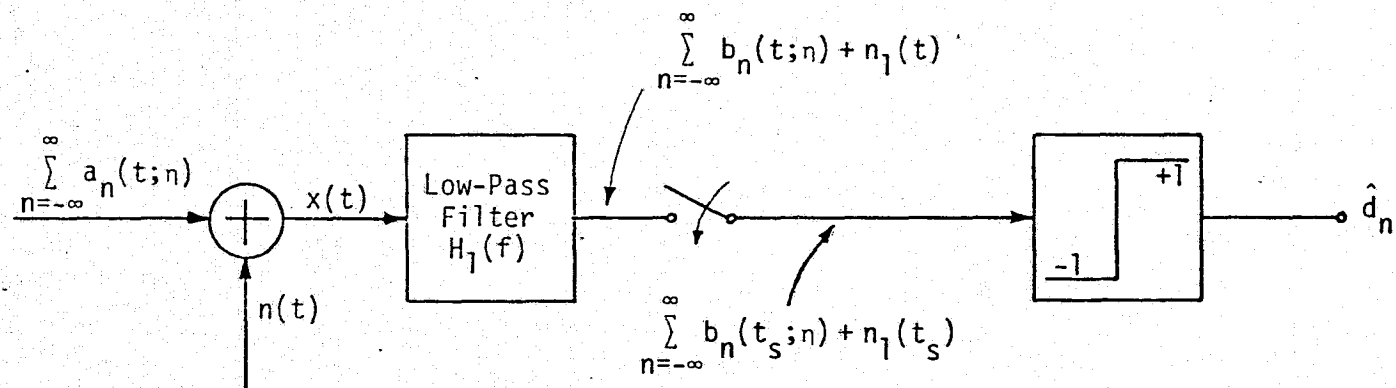


Figure 1. Band Limit and Sample Detector for Binary Data With Asymmetry

$$\sum_{n=-\infty}^{\infty} a_n(t;0) = \sum_{n=-\infty}^{\infty} d_n p(t - nT), \quad (1)$$

where  $d_n$  is the polarity ( $\pm 1$ ) of the  $n$ th data bit, and  $p(t)$  is the pulse shape which, for NRZ data, is defined by

$$p(t) = \begin{cases} A; & 0 \leq t \leq T \\ 0; & \text{otherwise,} \end{cases} \quad (2)$$

with  $A$  denoting its amplitude and  $T$  its nominal bit period. In the presence of data asymmetry, this same data stream is described by

$$a_n(t;n) = \begin{cases} A; & nT \leq t \leq (n+1)T \quad \text{if } d_n = d_{n+1} = 1 \\ A; & nT \leq t \leq (n+1+n)T \quad \text{if } d_n = -d_{n+1} = 1 \\ -A; & (n+n)T \leq t \leq (n+1+n)T \quad \text{if } d_n = d_{n+1} = -1 \\ -A; & (n+n)T \leq t \leq (n+1)T \quad \text{if } d_n = -d_{n+1} = -1 \end{cases} \quad (3)$$

Since the ideal low-pass filter in Figure 1 has transfer function

$$H_1(f) = \begin{cases} 1; & -B \leq f \leq B \\ 0; & \text{elsewhere} \end{cases} \quad (4)$$

then the transfer function  $B_n(f;n)$  of the response of this filter to the  $n$ th data bit  $a_n(t;n)$  is

$$B_n(f;n) \triangleq \mathcal{F}\{a_n(t;n)\} = \begin{cases} d_n A T_n \left( \frac{\sin \pi f T_n}{\pi f T_n} \right) e^{-j\pi f (T_n + 2nT)}; & -B \leq f \leq B \\ 0; & \text{elsewhere} \end{cases} \quad (5)$$

where

$$T_n = \begin{cases} T; & \text{if } d_n = d_{n+1} \\ T(1+d_n); & \text{if } d_n = -d_{n+1} \end{cases} \quad (6)$$

the corresponding time response  $b_n(t;n)$  is given by

$$\begin{aligned} b_n(t;n) &= \int_{-B}^B B_n(f;n) e^{j2\pi f t} df \\ &= \frac{2 d_n A}{\pi} \int_0^{\pi B T_n} \left( \frac{\sin x}{x} \right) \cos \left[ x \left( 1 - \frac{2t}{T_n} + \frac{2T \left[ n + \frac{n}{2}(1 - d_n) \right]}{T_n} \right) \right] dx. \end{aligned} \quad (7)$$

ORIGINAL PAGE IS  
OF POOR QUALITY

The total response of the filter to the doubly infinite pulse train can be expressed as

$$\begin{aligned}
 y(t;n) &= \sum_{n=-\infty}^{\infty} b_n(t;n) = \frac{2d_0 A}{\pi} \int_0^{\pi B T_0} \left( \frac{\sin x}{x} \right) \cos \left[ x \left( 1 - \frac{2t}{T_0} + \frac{2T \left[ \frac{n}{2} (1 - d_0) \right]}{T_0} \right) \right] dx \\
 &= \sum_{\substack{n=-\infty \\ n \neq 0}}^{\infty} \frac{2d_n A}{\pi} \int_0^{\pi B T_n} \left( \frac{\sin x}{x} \right) \cos \left[ x \left( 1 - \frac{2t}{T_n} + \frac{2T \left[ n + \frac{n}{2} (1 - d_n) \right]}{T_n} \right) \right] dx. \quad (8)
 \end{aligned}$$

The first term in (8) is the desired signal which, for  $BT_0 \leq 1$ , peaks at a value of  $t$  such that the argument of the cosine function equals zero. Thus, for  $d_0 = 1$ , this peak occurs at [see (6)]

$$t = \begin{cases} \frac{T}{2}; & \text{if } d_0 = d_1 \\ \frac{T}{2}(1+n); & \text{if } d_0 = -d_1 \end{cases} \quad (9)$$

For  $d_0 = -1$ , the peak occurs at

$$t = \begin{cases} \frac{T}{2}(1+2n); & \text{if } d_0 = d_1 \\ \frac{T}{2}(1+n); & \text{if } d_0 = -d_1 \end{cases} \quad (10)$$

Since, for random data,  $d_0$  and  $d_1$  are each equally likely to take on values  $+1$  and  $-1$ , then, on the average, the peak of the desired signal occurs at  $t = \frac{T}{2}(1+n) \triangleq t_s$ , where  $t_s$  denotes the desired sampling time.

The second term in (8) is the intersymbol interference due to bandlimiting the input signal. Thus, when sampled at  $t = t_s$ , the total response becomes

$$\begin{aligned}
 y(t_s;n) &= \frac{2d_0 A}{\pi} \int_0^{\pi B T} \left( \frac{\sin x}{x} \right) \cos \left[ x \frac{n}{2} (d_0 + d_1) \right] dx \\
 &+ \sum_{\substack{n=-\infty \\ n \neq 0}}^{\infty} \frac{2d_n A}{\pi} \int_0^{\pi B T \xi_n} \left( \frac{\sin x}{x} \right) \cos \left[ x \left( 1 - \frac{(1+n d_n)}{\xi_n} + \frac{2n}{\xi_n} \right) \right] dx, \quad (11)
 \end{aligned}$$

where

$$\xi_n \triangleq 1 + \frac{n}{2} (d_n - d_{n+1}). \quad (12)$$

Alternately, after some trigonometric simplification,

$$y(t_s; n) = \frac{2d_0 A}{\pi} \left\{ \frac{1}{2} \text{Si} [\pi BT (1 + nd_0)] + \frac{1}{2} \text{Si} [\pi BT (1 - nd_1)] \right\} \\ + \sum_{\substack{n=-\infty \\ n \neq 0}}^{\infty} \frac{2d_n A}{\pi} \left\{ \frac{1}{2} \text{Si} [\pi BT (2n+1 - nd_{n+1})] + \frac{1}{2} \text{Si} [\pi BT (2n-1 - nd_n)] \right\} \quad (13)$$

where

$$\text{Si}(y) \triangleq \int_0^y \frac{\sin x}{x} dx. \quad (14)$$

The total filter response sampled at  $t_s$  is then hardlimited to determine the estimate  $\hat{d}_0$  of the zeroth bit polarity  $d_0$ . The probability of error  $P_E$  in making this decision is given by

$$P_E = \frac{1}{2} \overline{\text{Prob} \left\{ y(t_s; n) + n_1(t_s) < 0 \mid d_0 = 1 \right\}} \\ + \frac{1}{2} \overline{\text{Prob} \left\{ y(t_s; n) + n_1(t_s) > 0 \mid d_0 = -1 \right\}}, \quad (15)$$

where  $n_1(t)$  is the low-pass filtered noise process which is zero mean Gaussian with variance  $\sigma^2 = N_0 B$ , and the overbar denotes statistical averaging over the joint distribution of the doubly infinite data sequence  $\{d_n\}$ ;  $n \neq 0$ . As an approximation to (15), we shall assume that the contribution to the total intersymbol interference caused by bits further away than  $N$  bit intervals from the bit being detected ( $d_0$ ) is negligible. Stated another way, we shall consider only the intersymbol interference effects of the  $N$  preceding and  $N$  subsequent bits on the bit under detection, where the value of  $N$  typically depends on the product  $BT$ . For  $BT \leq 1$ , a value of  $N = 5$  is sufficient.

Making the above simplification in (15) produces the result

$$P_E = \frac{1}{2} \left\{ \frac{1}{2^{2N+1}} \sum_{i=1}^{2N+1} \frac{1}{2} \text{erfc} \left[ \sqrt{\frac{E}{N_0}} D_{1i}(BT, n) \right] \right\} \\ + \frac{1}{2} \left\{ \frac{1}{2^{2N+1}} \sum_{i=1}^{2N+1} \frac{1}{2} \text{erfc} \left[ \sqrt{\frac{E}{N_0}} D_{-1i}(BT, n) \right] \right\} \quad (16)$$

where  $E \triangleq A^2 T$  is the energy per bit,

$$\operatorname{erfc} x \triangleq \frac{2}{\sqrt{\pi}} \int_x^{\infty} e^{-y^2} dy, \quad (17)$$

and\*

$$\begin{aligned} D_{1i}(BT, n) &\triangleq \frac{1}{\sqrt{2BT}} \left[ \left. \frac{b_0^{(i)}(t_s; n)}{A} \right|_{d_0=1} + \sum_{\substack{n=-N \\ n \neq 0}}^N \left. \frac{b_n^{(i)}(t_s; n)}{A} \right|_{d_0=1} \right] \\ D_{-1i}(BT, n) &\triangleq \frac{1}{\sqrt{2BT}} \left[ \left. \frac{b_0^{(i)}(t_s; n)}{A} \right|_{d_0=-1} + \sum_{\substack{n=-N \\ n \neq 0}}^N \left. \frac{b_n^{(i)}(t_s; n)}{A} \right|_{d_0=-1} \right]. \end{aligned} \quad (18)$$

From (13), we find that

$$\begin{aligned} \left. \frac{b_0^{(i)}(t_s; n)}{A} \right|_{d_0=1} &= \frac{1}{\pi} \left\{ S_i [\pi BT (1+n)] + S_i [\pi BT (1-d_1^{(i)} n)] \right\} \\ \left. \frac{b_n^{(i)}(t_s; n)}{A} \right|_{d_0=1} &= \frac{d_n^{(i)}}{\pi} \left\{ S_i [\pi BT (2n+1-d_{n+1}^{(i)} n)] - S_i [\pi BT (2n-1-d_n^{(i)} n)] \right\}; \\ &\quad n \neq 0, -1 \\ \left. \frac{b_{-1}^{(i)}(t_s; n)}{A} \right|_{d_0=1} &= -\frac{d_{-1}^{(i)}}{\pi} \left\{ S_i [\pi BT (1+n)] - S_i [\pi BT (3+d_{-1}^{(i)} n)] \right\} \end{aligned} \quad (19)$$

and

$$\begin{aligned} \left. \frac{b_0^{(i)}(t_s; n)}{A} \right|_{d_0=-1} &= \frac{1}{\pi} \left\{ S_i [\pi BT (1-n)] + S_i [\pi BT (1-d_1^{(i)} n)] \right\} \\ \left. \frac{b_n^{(i)}(t_s; n)}{A} \right|_{d_0=-1} &= -\frac{d_n^{(i)}}{\pi} \left\{ S_i [\pi BT (2n+1-d_{n+1}^{(i)} n)] - S_i [\pi BT (2n-1-d_n^{(i)} n)] \right\}; \\ &\quad n = 0, -1 \end{aligned} \quad (20a)$$

\*The superscript  $i$  on  $b_0(t_s; n)$  and  $b_n(t_s; n)$  refers to the evaluation of these quantities for the  $i$ th data sequence  $\{d_n^{(i)}\} \triangleq (d_{-N}^{(i)}, d_{-N+1}^{(i)}, \dots, d_{-1}^{(i)}, d_1^{(i)}, d_2^{(i)}, \dots, d_{N+1}^{(i)})$ ;  $i = 1, 2, \dots, 2N+1$ .

$$\frac{b_{-1}^{(i)}(t_s; n)}{A} \Big|_{d_0=1} = \frac{d_{-1}}{\pi} \left\{ \text{Si} [\pi BT (1 - n)] - \text{Si} [\pi BT (3 + d_{-1}^{(i)} n)] \right\} \quad (20c)$$

Substituting (19) and (20) in (18) and simplifying yields the final result

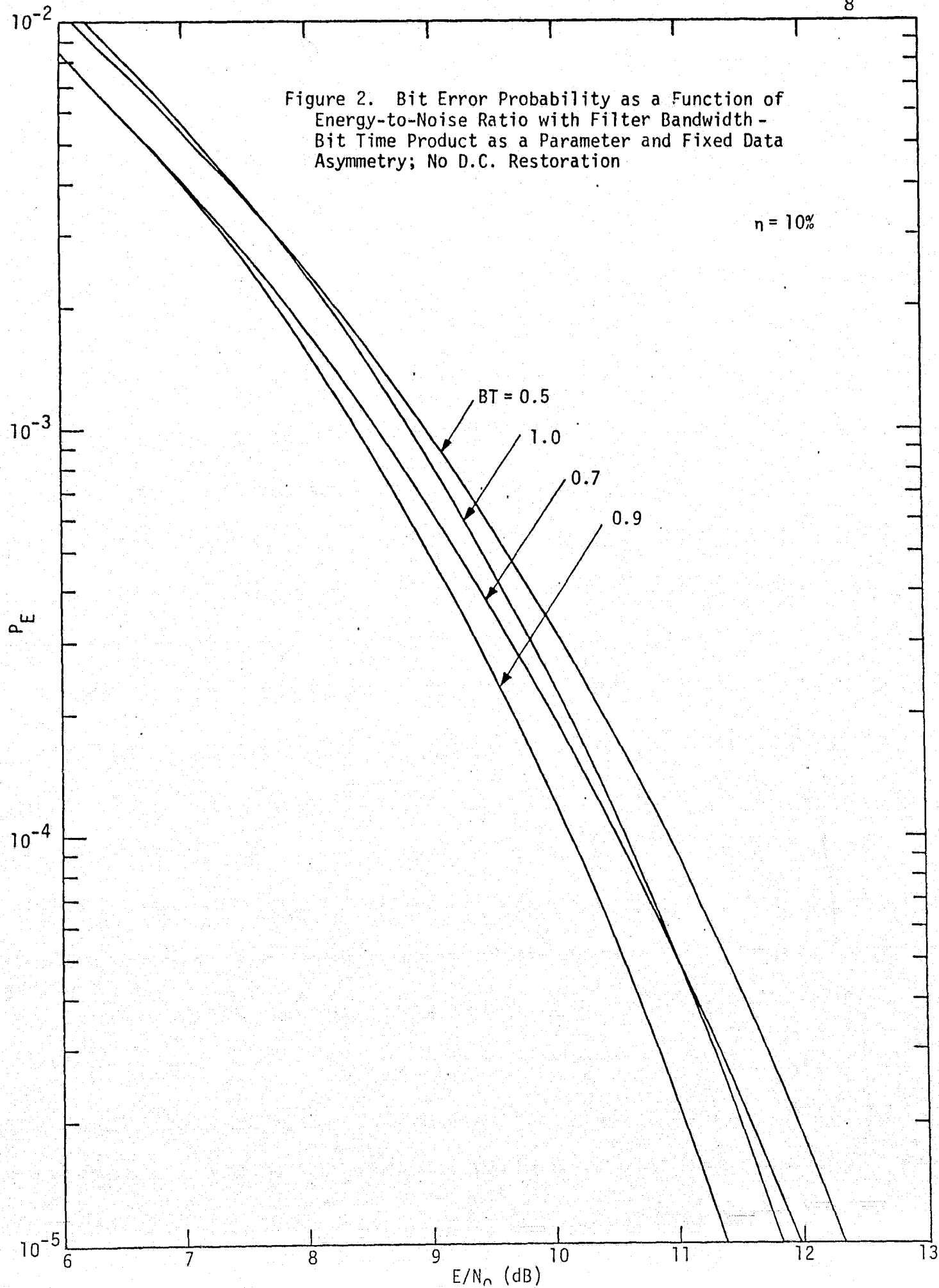
$$\begin{aligned} D_{1i}(BT, n) &= \frac{1}{\sqrt{2BT}} \left\{ \sum_{n=-N}^{N-1} \left[ (d_n^{(i)} - d_{n+1}^{(i)}) S(2n+1 - n d_{n+1}^{(i)}) \right] \Big|_{d_0^{(i)}=1} \right. \\ &\quad \left. + d_{-N}^{(i)} S(2N+1 + n d_{-N}^{(i)}) + d_N^{(i)} S(2N+1 - n d_{N+1}^{(i)}) \right\} \\ D_{-1i}(BT, n) &= - \frac{1}{\sqrt{2BT}} \left\{ \sum_{n=-N}^{N-1} \left[ (d_n^{(i)} - d_{n+1}^{(i)}) S(2n+1 - n d_{n+1}^{(i)}) \right] \Big|_{d_0^{(i)}=-1} \right. \\ &\quad \left. + d_{-N}^{(i)} S(2N+1 + n d_{-N}^{(i)}) + d_N^{(i)} S(2N+1 - n d_{N+1}^{(i)}) \right\} \quad (21) \end{aligned}$$

where

$$S(x) \triangleq \frac{1}{\pi} \text{Si}(\pi BT x) \quad (22)$$

Combining (16) and (21), one obtains the average error probability performance of the sample detector in the presence of ideal low-pass bandlimiting and data asymmetry. This performance is illustrated in Figure 2, with  $BT$  a parameter and fixed data asymmetry, namely  $n=0.1$  (10%). In this and the remaining numerical illustrations, the number  $N$  of preceding and succeeding bits whose intersymbol interference is taken into account has been set equal to 4. Comparing Figure 2 with the same figure in [2], where data asymmetry was absent, we observe a similar behavior as a function of  $BT$ , namely, the average bit error probability in the presence of 10% data asymmetry is again minimum for  $BT=0.9$ . To what extent this is true at other values of data asymmetry is demonstrated in Figures 3 and 4 when, for fixed error probabilities of  $10^{-4}$  and  $10^{-5}$ , respectively, the energy-to-noise ratio required to achieve this error rate is plotted as a function of percent data asymmetry with  $BT$  again as a parameter. Relative to the  $E/N_0$  values at  $n=0$ , the curves of Figures 3 and 4 illustrate the combined degradation due to intersymbol interference (bandwidth limiting) and data asymmetry.

Figure 2. Bit Error Probability as a Function of Energy-to-Noise Ratio with Filter Bandwidth - Bit Time Product as a Parameter and Fixed Data Asymmetry; No D.C. Restoration





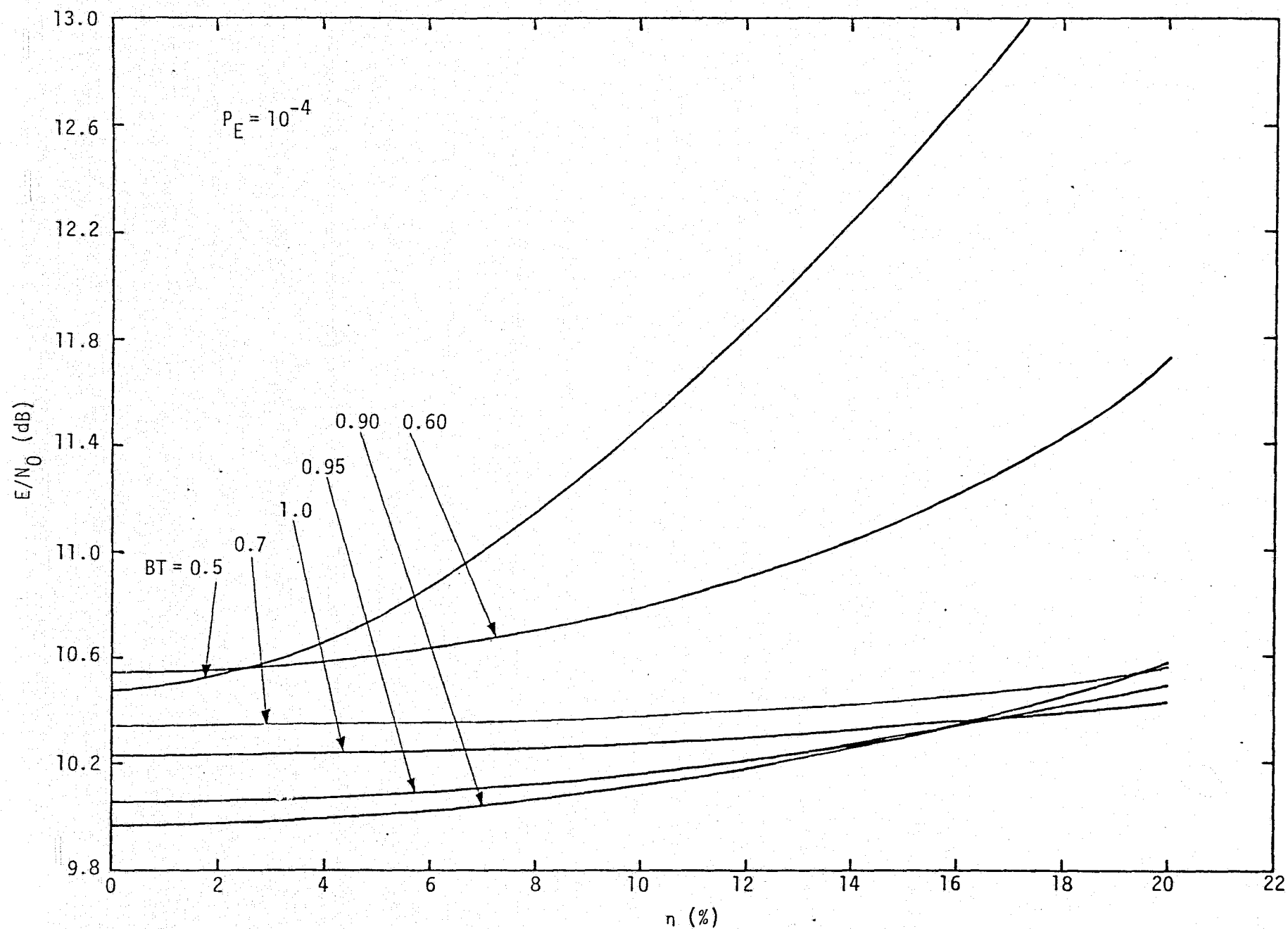


Figure 3. Energy-to-Noise Ratio as a Function of Data Asymmetry for Fixed Bit Error Probability and Filter Bandwidth - Bit Time Product as a Parameter; No D.C. Restoration

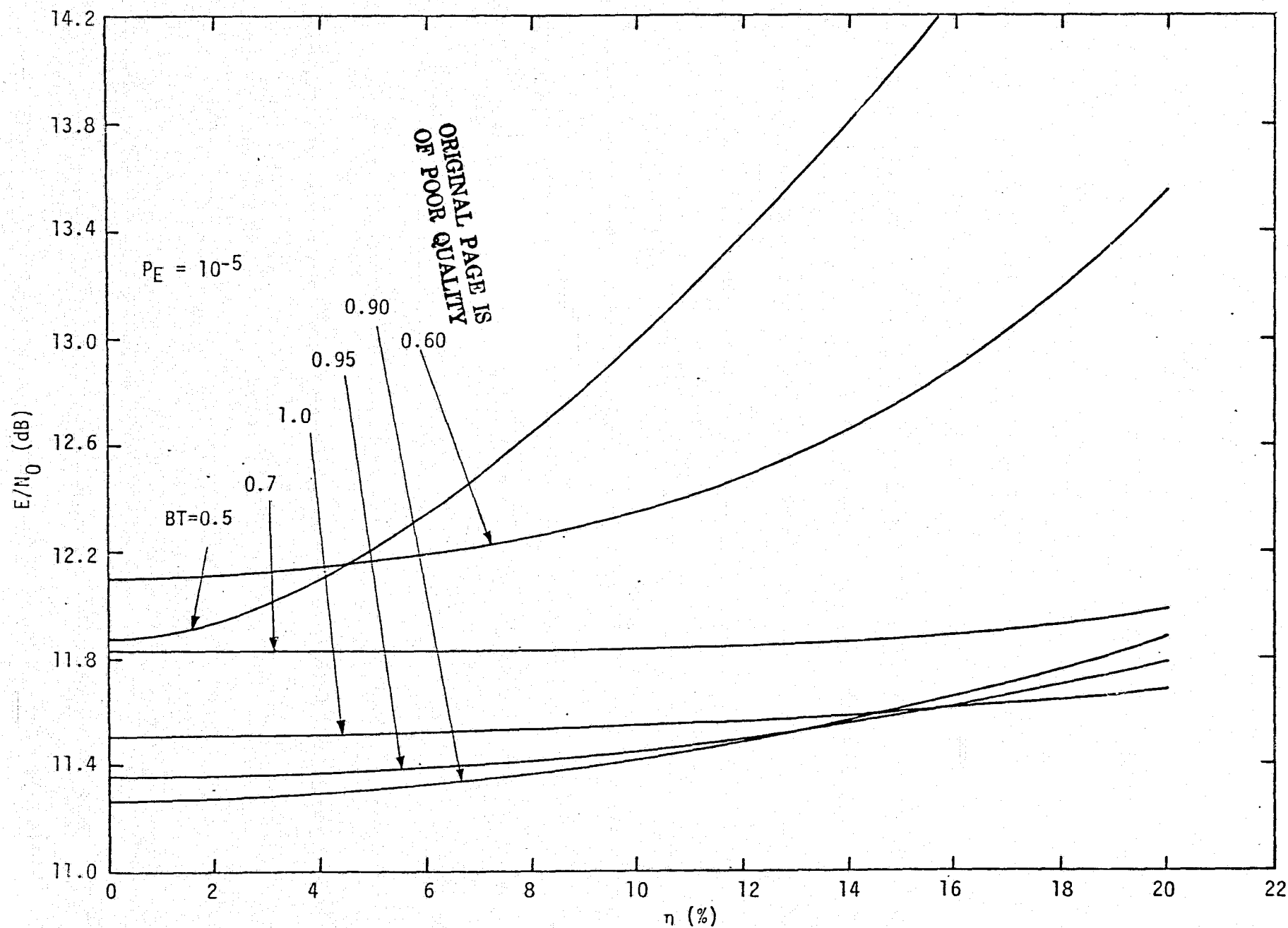


Figure 4. Energy-to-Noise Ratio as a Function of Data Asymmetry for Fixed Bit Error Probability and Filter Bandwidth - Bit Time Product as a Parameter; No D.C. Restoration

### 3.0 PERFORMANCE OF A BAND LIMIT AND SAMPLE DETECTOR IN THE PRESENCE OF NRZ DATA ASYMMETRY - D.C. RESTORATION BY CAPACITIVE COUPLING

In [7], it was shown that, when the input signal is coupled through a capacitor, and hence the actual d.c. component in the signal vanishes, the degradation due to data asymmetry is reduced. The reason for this is that the d.c. restoration has the effect of producing an artificial shift in the decision threshold away from the shortened symbols (the culprits in the degradation due to data asymmetry). We will show here that, for the sample detector with bandlimiting, a similar reduction in data asymmetry degradation occurs when the input signal is capacitively coupled.

Following the approach taken in [7], let  $D$  denote the transition density of the input NRZ data stream, e.g., for random data,  $D = 0.5$ . Then the average value of this data stream is  $nDA$ . Alternately, the positive (longer) signal level is now  $A(1 - nD)$  and the negative (shorter) signal level is now  $-A(1 + nD)$ . These levels replace  $A$  and  $-A$ , respectively in (3). The impact of this on, for example, the time response  $b_n(t; n)$  of (7) is that  $A$  is replaced by  $A(1 - d_n n D)$ . Thus,

$$b_n(t; n) = \frac{2 d_n (1 - d_n n D) A}{\pi} \times \int_0^{\pi B T n} \left( \frac{\sin x}{x} \right) \cos \left[ x \left( 1 - \frac{2t}{T n} + \frac{2T \left[ n + \frac{n}{2} (1 - d_n) \right]}{T n} \right) \right] dx \quad (23)$$

and, since the argument of the cosine function is unchanged by the capacitive coupling, the proper sampling time is still  $t_s = \frac{T}{2}(1 + n)$ . Using (23) rather than (7), one should have little difficulty in directly seeing how to modify  $D_{1i}(BT, n)$  and  $D_{-1i}(BT, n)$  of (21) for use in the error probability expression of (16). Specifically, we now have that

$$\begin{aligned}
D_{1i}(BT, n) &= \frac{1}{\sqrt{2BT}} \\
&\times \left\{ \sum_{n=-N}^{N-1} \left\{ \left[ d_n^{(i)} (1 - n D d_n^{(i)}) - d_{n+1}^{(i)} (1 - n D d_{n+1}^{(i)}) \right] S(2N+1 - n d_{n+1}^{(i)}) \right\} \right\} \Big|_{d_0^{(i)}=1} \\
&\quad + d_{-N}^{(i)} (1 - n D d_{-N}^{(i)}) S(2N+1 + n d_{-N}^{(i)}) + d_N^{(i)} (1 - n D d_N^{(i)}) S(2N+1 - n d_{N+1}^{(i)}) \Big\} \\
D_{-1i}(BT, n) &= - \frac{1}{\sqrt{2BT}} \\
&\times \left\{ \sum_{n=-N}^{N-1} \left\{ \left[ d_n^{(i)} (1 - n D d_n^{(i)}) - d_{n+1}^{(i)} (1 - n D d_{n+1}^{(i)}) \right] S(2n+1 - n d_{n+1}^{(i)}) \right\} \right\} \Big|_{d_0^{(i)}=-1} \\
&\quad + d_{-N}^{(i)} (1 - n D d_{-N}^{(i)}) S(2N+1 + n d_{-N}^{(i)}) + d_N^{(i)} (1 - n D d_N^{(i)}) S(2N+1 - n d_{N+1}^{(i)}) \Big\}
\end{aligned} \tag{24}$$

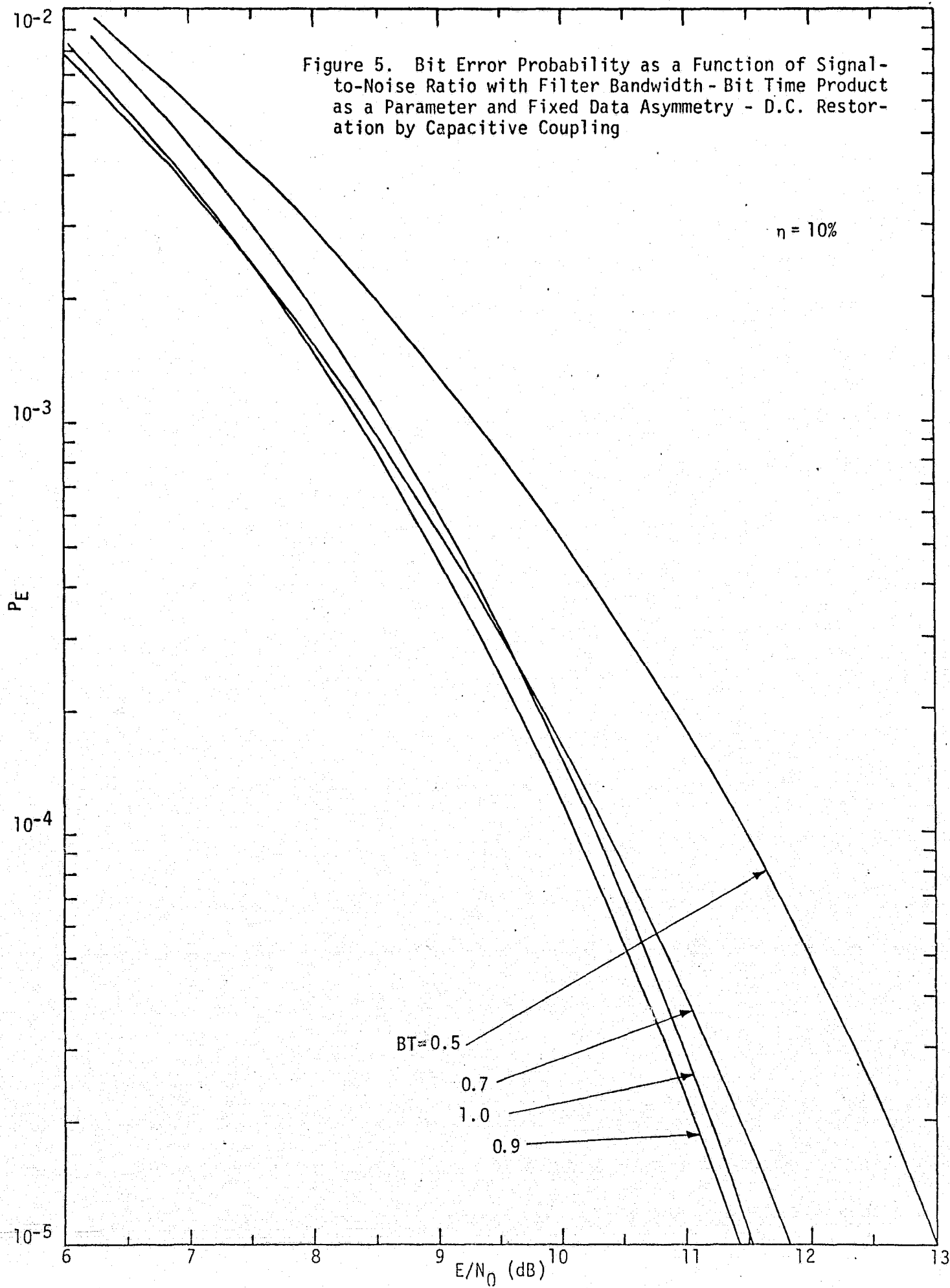
with  $S(x)$  still defined in (22)

Analogous to Figure 2, the error probability performance of the filter-sample detector with data asymmetry and d.c. restoration by capacitive coupling is illustrated in Figure 5 with BT once again a parameter,  $n=0.1$ , and transition density  $D=0.5$ . Comparing Figure 5 with Figure 2, we observe that, for a fixed error probability, and data asymmetry, the required  $E/N_0$  at the optimum  $BT=0.9$  is virtually independent of whether d.c. restoration is present or not. On the other hand, for other values of BT, e.g., 0.5, the required  $E/N_0$  can be much smaller when d.c. restoration is employed. Finally, Figures 6 and 7 demonstrate the corresponding results to Figures 3 and 4 for the d.c. restoration case. Here, the value  $BT=0.9$  appears to be optimum for all data asymmetries in the sense of minimum required  $E/N_0$  at a fixed  $P_E$ .

#### 4.0 CONCLUSIONS

The combined degrading effects of intersymbol interference due to bandlimiting and data asymmetry have been assessed for a filter-sample

Figure 5. Bit Error Probability as a Function of Signal-to-Noise Ratio with Filter Bandwidth - Bit Time Product as a Parameter and Fixed Data Asymmetry - D.C. Restoration by Capacitive Coupling



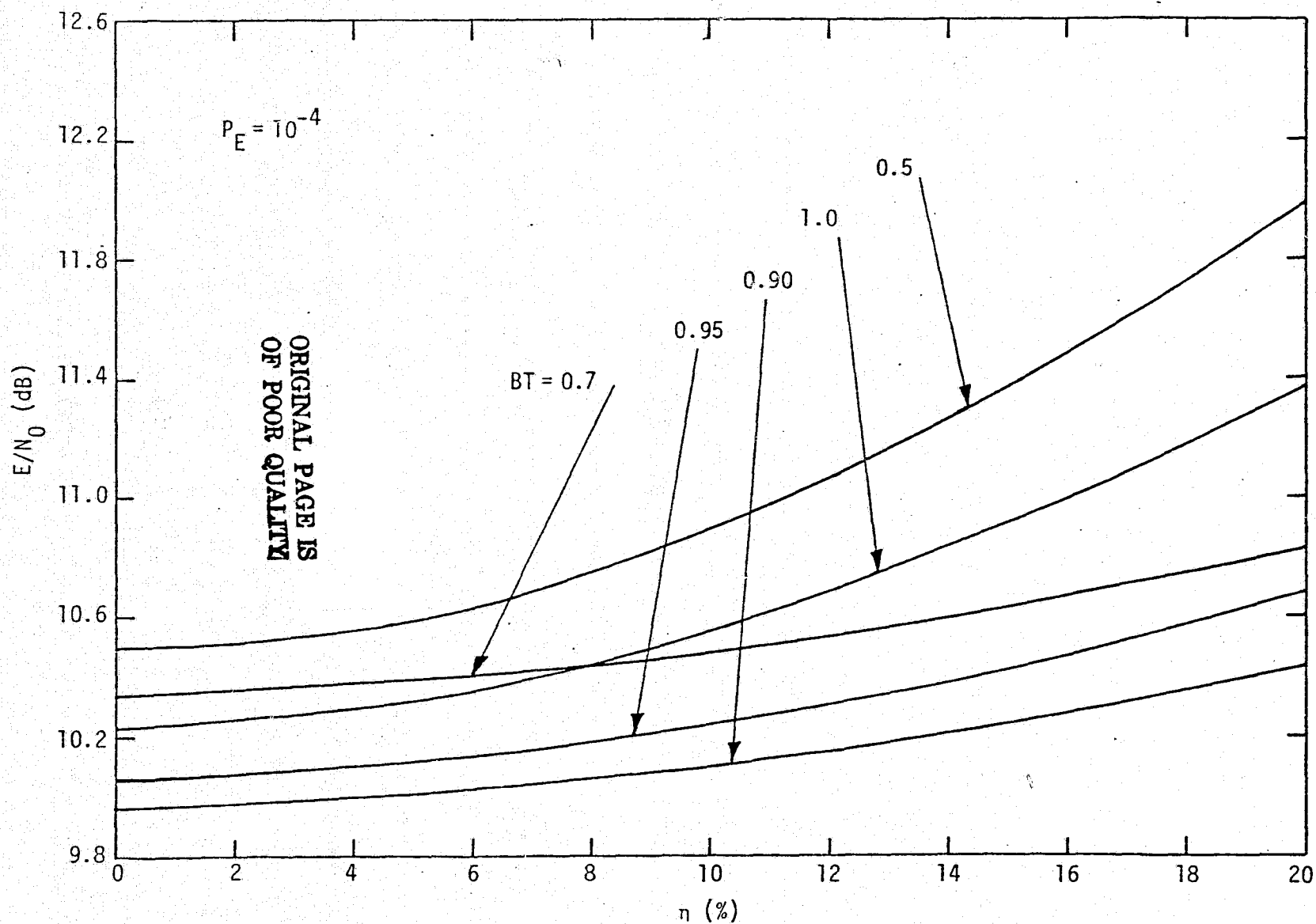


Figure 6. Energy-to-Noise Ratio as a Function of Data Asymmetry for Fixed Bit Error Probability and Filter Bandwidth - Bit Time Product as a Parameter; D.C. Restoration by Capacitive Coupling

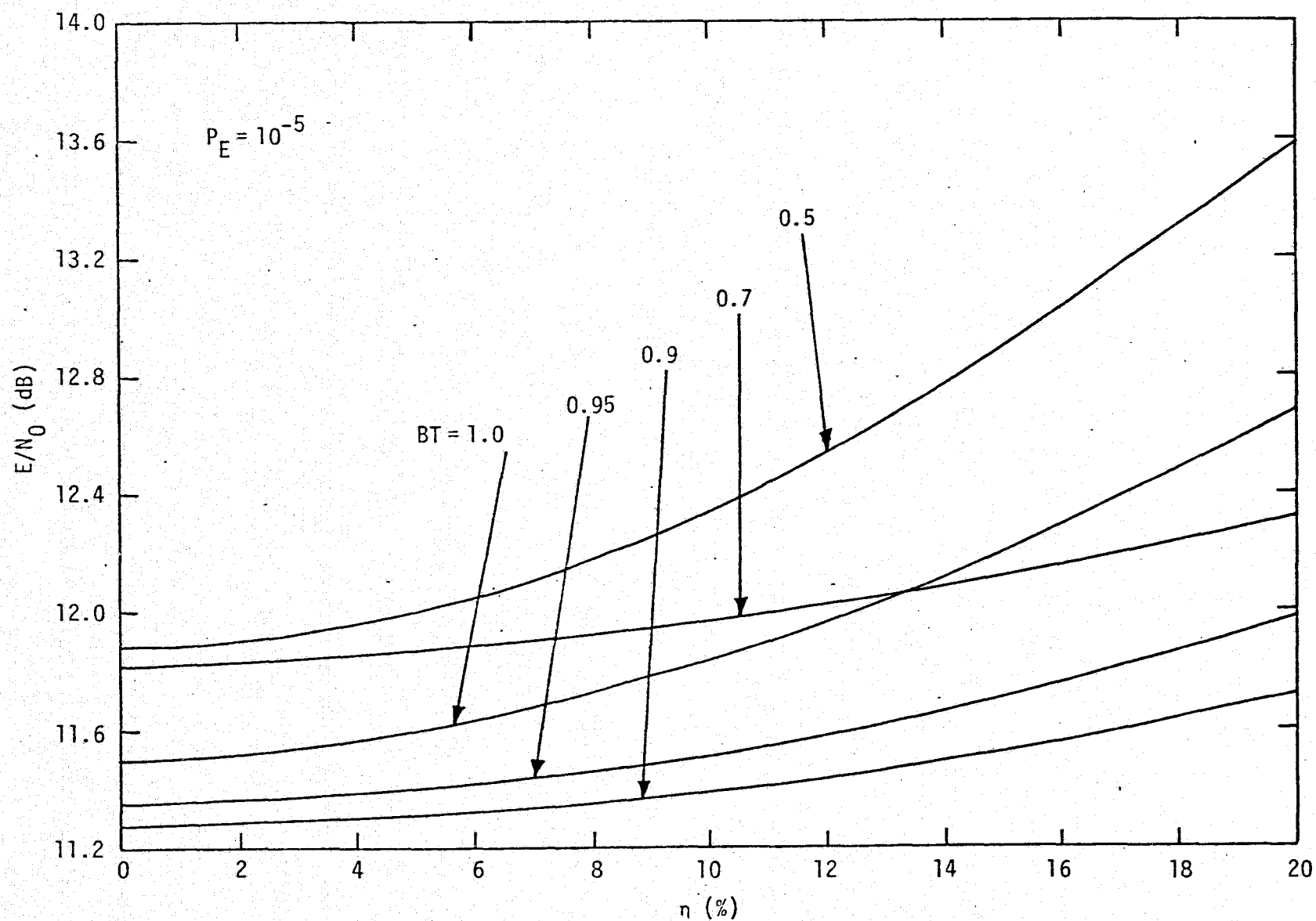


Figure 7. Energy-to-Noise Ratio as a Function of Data Asymmetry for Fixed Bit Error Probability and Filter Bandwidth - Bit Time Product as a Parameter; D.C. Restoration by Capacitive Coupling

type detector. For small values of asymmetry (less than about 10%), the optimum filter bandwidth-bit time product remains equal to 0.9 and the corresponding amount of energy-to-noise ratio degradation at a fixed error rate is virtually independent of whether or not d.c. restoration is present. In particular, Tables 1 and 2 summarize typical results for the two cases when  $BT = 0.9$ . The quantity  $\Delta E/N_0$  represents the additional  $E/N_0$  required at a given value of data asymmetry relative to its value at  $\eta = 0$ .

On the other hand, for values of  $BT$  other than the optimum, d.c. restoration has a beneficial effect in reducing energy-to-noise ratio degradation due to data asymmetry.

The other conclusion which can be reached by comparing the numerical results of this appendix with those in [8] is that the sample detector is much less sensitive to data asymmetry than the integrate-and-dump detector. This is not surprising when one realizes that the degradation due to data asymmetry for the integrate-and-dump detector comes about because of a reduction in the signal energy as a result of integrating only over a fraction of the total bit interval. By comparison, the reduction in the peak of the filter response at the sampling instant due to data asymmetry should have a considerably lesser effect. In fact, in the absence of bandlimiting, the integrate-and-dump detector would still yield considerable  $E/N_0$  degradation (see [3-7]) due to data asymmetry, whereas the sample detector would show none. Of course, the sample detector without bandlimiting would produce infinite noise power and thus, on an absolute  $E/N_0$  basis, would be far worse than the integrate-and-dump.



Table 1. No. D.C. Restoration

$P_E = 10^{-4}$			$P_E = 10^{-5}$		
$\eta$ (%)	$E/N_0$ (dB)	$\Delta E/N_0$ (dB)	$\eta$ (%)	$E/N_0$ (dB)	$\Delta E/N_0$ (dB)
0	9.97	0	0	11.28	0
2.5	9.98	0.01	2.5	11.29	0.01
5.0	10.00	0.03	5.0	11.32	0.04
7.5	10.06	0.09	7.5	11.37	0.09
10.0	10.13	0.16	10.0	11.43	0.15
15.0	10.31	0.34	15.0	11.63	0.35

Table 2. D.C. Restoration by Capacitive Coupling

$P_E = 10^{-4}$			$P_E = 10^{-5}$		
$\eta$ (%)	$E/N_0$ (dB)	$\Delta E/N_0$ (dB)	$\eta$ (%)	$E/N_0$ (dB)	$\Delta E/N_0$ (dB)
0	9.97	0	0	11.28	0
2.5	9.99	0.02	2.5	11.30	0.02
5.0	10.02	0.05	5.0	11.32	0.04
10.0	10.12	0.15	10.0	11.40	0.12
15.0	10.25	0.28	15.0	11.54	0.26
20.0	10.44	0.47	20.0	11.73	0.45

## REFERENCES

1. H. F. Martinides and G. L. Reijns. "Influence of Bandwidth Restriction on the Signal-to-Noise Performance of a PCM/NRZ Signal," IEEE Transactions on Aerospace and Electronic Systems, Vol. AES-4, No. 1, January 1968, pp. 35-40.
2. N. M. Shehadeh and K. Tu. "The Effects of Band-Limiting of a PCM/NRZ Signal on the Bit-Error Probability Using a Sample Detector," Proceedings of the IEEE, September 1970, pp. 1400-1401.
3. M. K. Simon. "Bit Error Rate Degradation of the Ku-Band Return Link Channel Due to NRZ Data Symbol Asymmetry," Axiomatix Report No. R7707-2, July 8, 1977.
4. M. K. Simon. "Further Considerations on the Effects of Data Asymmetry on Bit Error Rate Performance of the Ku-Band and S-Band Return Link Channels," Axiomatix Report No. R7708-2, August 3, 1977.
5. W. C. Lindsey and W. R. Braun. "Signal-to-Noise Ratio Degradations Due to Data Asymmetry for Uncoded and Coded BPSK Communication Channels," LinCom Technical Memorandum to B. H. Batson (NASA/JSC), July 8, 1977.
6. R. S. Orr. "The Impact of Data Asymmetry on Bit Error Performance," Stanford Telecommunications, Inc., Technical Report (prepared under Subcontract No. 7023 to Operations Research, Inc., in support of Prime Contract No. NAS 5-23841 to NASA/Goddard), July 21, 1977.
7. R. S. Orr. "The Impact of Data Asymmetry on the Bit Error Performance of Convolutionally Encoded Data," Stanford Telecommunications, Inc., Technical Report (prepared under Subcontract No. 7023 to Operations Research, Inc., in support of Prime Contract No. NAS 5-23841 to NASA/Goddard), July 26, 1977.
8. J. W. Seyl. "Communications Performance Degradation Due to Bit Asymmetry," NASA/JSC Technical Memorandum EE7-8/77-194, August 22, 1977.

APPENDIX D

DETECTION OF ASYMMETRIC NRZ DATA USING A  
GATED INTEGRATE-AND-DUMP FILTER

## APPENDIX D

### DETECTION OF ASYMMETRIC NRZ DATA USING A GATED INTEGRATE-AND-DUMP FILTER

by

Marvin K. Simon

#### 1.0 INTRODUCTION

It is well known that the optimum detector (in the sense of minimum error probability) of symmetric NRZ data is an integrate-and-dump filter whose integration time extends over the entire data symbol interval. When the input data stream possesses asymmetry, then the ideal integrate-and-dump filter is no longer the optimum detector; thus, it is possible that an alternate (possibly simpler to implement) detector could yield superior performance. In Appendix C (see also [1]), the performance of a filter-sampler type data detector when the input was asymmetric NRZ data was investigated. It was shown there that, by optimizing the ratio of filter bandwidth to data rate, one could, for sufficient data asymmetry, outperform the ideal integrate-and-dump filter. An alternate approach is to use a gated integrate-and-dump filter (Figure 1) where the gating interval can be selected to minimize the error probability for a given amount of data asymmetry. Such a selection results in the best achievable error probability performance using a gated integrate-and-dump at each value of asymmetry. Alternately, the gating interval may be fixed at a value which represents a compromise between the additional SNR degradation (over that of the ideal integrate-and-dump) which can be tolerated when no asymmetry exists and the SNR improvement obtained at the maximum value of data asymmetry expected. In either case, the selection of a gated integrate-and-dump filter has the additional implementation advantage of operation at high speed with smaller circuit losses since the constraint on its switching times at the symbol transition instants can now be considerably relaxed.

The purpose of this appendix is to present the performance of the gated integrate-and-dump filter as a function of data asymmetry and gating interval and demonstrate the relation between these two parameters which optimizes this performance. As in previous studies, the results will be given for both the case of no d.c. restoration and the case of d.c. restoration by capacitive coupling. The numerical results

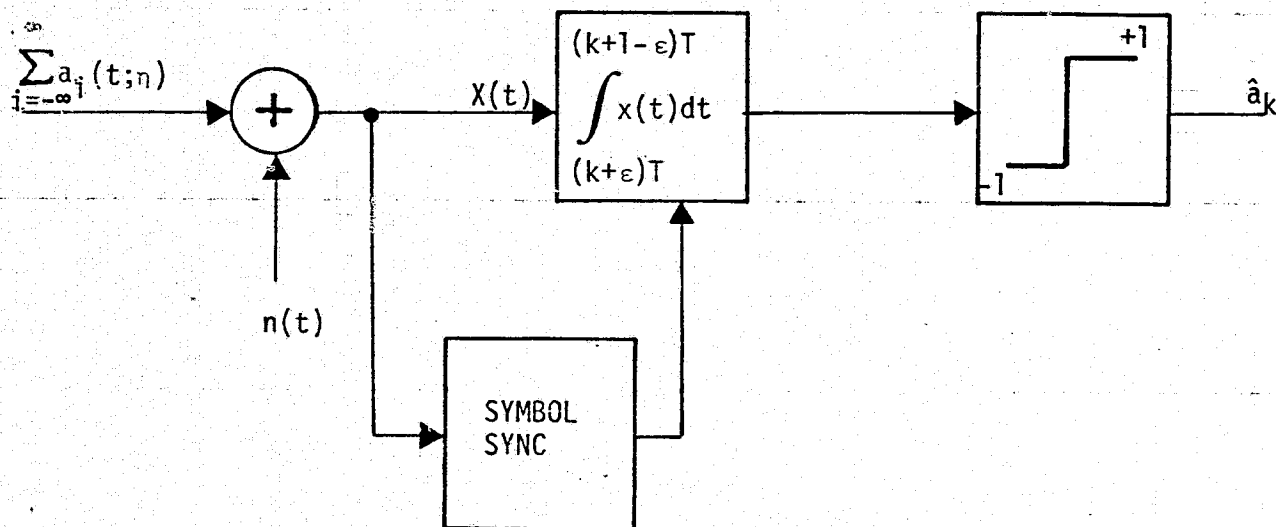


FIGURE 1. GATED INTEGRATE-AND DUMP FILTER

ORIGINAL PAGE IS  
OF POOR QUALITY

presented permit the above-mentioned tradeoff between additional SNR degradation at no asymmetry and SNR improvement at maximum asymmetry to be made.

## 2.0 PERFORMANCE OF GATED INTEGRATE-AND-DUMP DETECTOR IN THE PRESENCE OF NRZ DATA ASYMMETRY - NO D.C. RESTORATION

When the input data is random with equiprobable symbols, then the gated integrate-and-dump (GI&D) depends, in general, on the polarity of the symbol over which it is integrating and that of the preceding and succeeding symbols. Thus, one must compute these outputs for each of the eight possible three-symbol sequences (analogous to the approach taken in [2] for the ideal integrate-and-dump) and their corresponding conditional error probabilities. Then averaging these conditional error probabilities over the equal probabilities of the eight three-symbol sequences gives the average error probability performance of the GI&D detector.

When asymmetry is present, the GI&D outputs can be grouped into four distinct categories. Arbitrarily assuming that the +1 symbols are elongated by  $\eta T$  (relative to their nominal value of  $T$  sec) and the -1 symbols are shortened by the same amount, then for all four three-symbol sequences whose middle symbol is +1, the mean GI&D output  $\bar{x}$  is

$$\bar{x} = \sqrt{E_s T} (1 - 2\epsilon), \quad (1)$$

where  $E_s$  is the symbol energy,  $\epsilon$  is the fractional (relative to  $T$ ) gate interval at each end of the symbol, and  $\eta$  is the fractional data asymmetry. Similarly, for the three-symbol sequence in which all symbols are -1, the GI&D output is

$$\bar{x} = -\sqrt{E_s T} (1 - 2\epsilon). \quad (2)$$

The remaining three possible sequences are split up as follows. For the sequence whose middle symbol is -1 and both adjacent symbols are +1, we get

$$\bar{x} = \begin{cases} -\sqrt{E_s T} (1 - 2\eta + 2\epsilon) ; & 0 \leq \epsilon \leq \frac{\eta}{2} \\ -\sqrt{E_s T} (1 - 2\epsilon) ; & \frac{\eta}{2} \leq \epsilon \leq \frac{1}{2} \end{cases} \quad (3)$$

while for the two sequences whose middle symbol is -1 and only one adjacent symbol is +1, we get

$$\bar{x} = \begin{cases} -\sqrt{E_s T} (1 - \eta) ; & 0 \leq \epsilon \leq \frac{\eta}{2} \\ -\sqrt{E_s T} (1 - 2\epsilon) ; & \frac{\eta}{2} \leq \epsilon \leq \frac{1}{2} \end{cases} \quad (4)$$

For all eight possible three-symbol sequences, the standard deviation  $\sigma_x$  of the GI&D output is easily determined to be

$$\sigma_x = \sqrt{\frac{N_0 T}{2} (1 - 2\epsilon)} . \quad (5)$$

Finally, then, the average error probability  $P_E$  is given by

$$P_E = \frac{1}{2} \operatorname{erfc} \left( \frac{|\bar{x}|}{\sqrt{2} \sigma_x} \right) \quad (6)$$

where

$$\operatorname{erfc} x = \frac{2}{\sqrt{\pi}} \int_x^\infty \exp(-t^2) dt \quad (7)$$

and the overbar denotes statistical averaging over the eight equiprobable three-symbol data sequences. Substituting equations (1) through (5) into (6) and the fact that each three-symbol sequence occurs with probability 1/8 gives the final result:

$$P_E = \begin{cases} \frac{5}{16} \operatorname{erfc} \left[ \sqrt{\frac{E_s}{N_0}} (1 - 2\epsilon) \right] + \frac{1}{8} \operatorname{erfc} \left[ \sqrt{\frac{E_s}{N_0}} \left( \frac{1 - \eta}{\sqrt{1 - 2\epsilon}} \right) \right] \\ + \frac{1}{16} \operatorname{erfc} \left[ \sqrt{\frac{E_s}{N_0}} \left( \frac{1 - 2\eta + 2\epsilon}{\sqrt{1 - 2\epsilon}} \right) \right] ; & 0 \leq \epsilon \leq \frac{\eta}{2} \\ \\ \frac{1}{2} \operatorname{erfc} \left[ \sqrt{\frac{E_s}{N_0}} (1 - 2\epsilon) \right] ; & \frac{\eta}{2} \leq \epsilon \leq \frac{1}{2} \end{cases} \quad (8)$$

Figure 2 is a plot of  $P_E$  versus  $\epsilon$  with  $\eta$  as a parameter and  $E_s/N_0 = 9.6$  dB (corresponding to  $P_E = 10^{-5}$  when  $\epsilon = \eta = 0$ ). We observe from this figure that, for a given value of data asymmetry  $\eta$ ,  $P_E$  is minimized by choosing  $\epsilon = \eta/2$ . Figure 3 is an illustration of the symbol energy-to-noise ratio (in dB) required to achieve an average error rate of  $10^{-5}$  in the presence of data asymmetry. The curve labeled  $\epsilon = 0$  corresponds to the performance of the ideal I&D (also see Figure 3 of [2]). The remaining curves indicate a constant  $E_s/N_0$  for values of  $\eta \leq 2\epsilon$  in accordance with the second equation of (8) followed by an increase in  $E_s/N_0$  with  $\eta$  as required by the first equation of (8). Note that each of these curves cross the  $\epsilon = 0$  curve at some value of  $\eta$ , say  $\eta_0$ , which means that, for  $\eta > \eta_0$ , the GI&D outperforms the ideal I&D in the sense of requiring less  $E_s/N_0$  for a given average probability of error. The dashed curve in Figure 3 represents the performance corresponding to selecting  $\epsilon = \eta/2$  at each value of  $\eta$  and is thus the best achievable with the GI&D.

### 3.0 PERFORMANCE OF GATED INTEGRATE-AND-DUMP DETECTOR IN THE PRESENCE OF NRZ DATA ASYMMETRY - D.C. RESTORATION BY CAPACITIVE COUPLING

When the GI&D is capacitively coupled, then d.c. restoration of the input data stream takes place. For NRZ data of transition density  $D$  (e.g.,  $D = 0.5$  for random data), the average value of the data stream is  $\eta D \sqrt{E_s/T}$ . Thus, after d.c. restoration, the positive (elongated) symbol now has a level  $\sqrt{E_s/T} (1 - \eta D)$  and the negative (shortened) symbol has the level  $-\sqrt{E_s/T} (1 + \eta D)$ . The impact of this unbalance in positive and negative symbol levels on the output of GI&D for the eight possible three-symbol sequences is summarized below.

$$\bar{x} = \sqrt{E_s/T} (1 - 2\epsilon)(1 - \eta D); \quad \text{all four three-symbol sequences whose middle symbol is +1} \quad (9)$$

$$\bar{x} = -\sqrt{E_s/T} (1 - 2\epsilon)(1 + \eta D); \quad \text{sequence in which all three symbols are -1} \quad (10)$$

$$\bar{x} = \begin{cases} -\sqrt{E_s/T} [1 - 2\eta + \eta D + 2\epsilon (1 - \eta D)]; & 0 \leq \epsilon \leq \frac{\eta}{2} \\ -\sqrt{E_s/T} (1 - 2\epsilon)(1 + \eta D); & \frac{\eta}{2} \leq \epsilon \leq \frac{1}{2} \end{cases}$$

sequence in which middle symbol is -1 and both adjacent symbols are +1 (11)



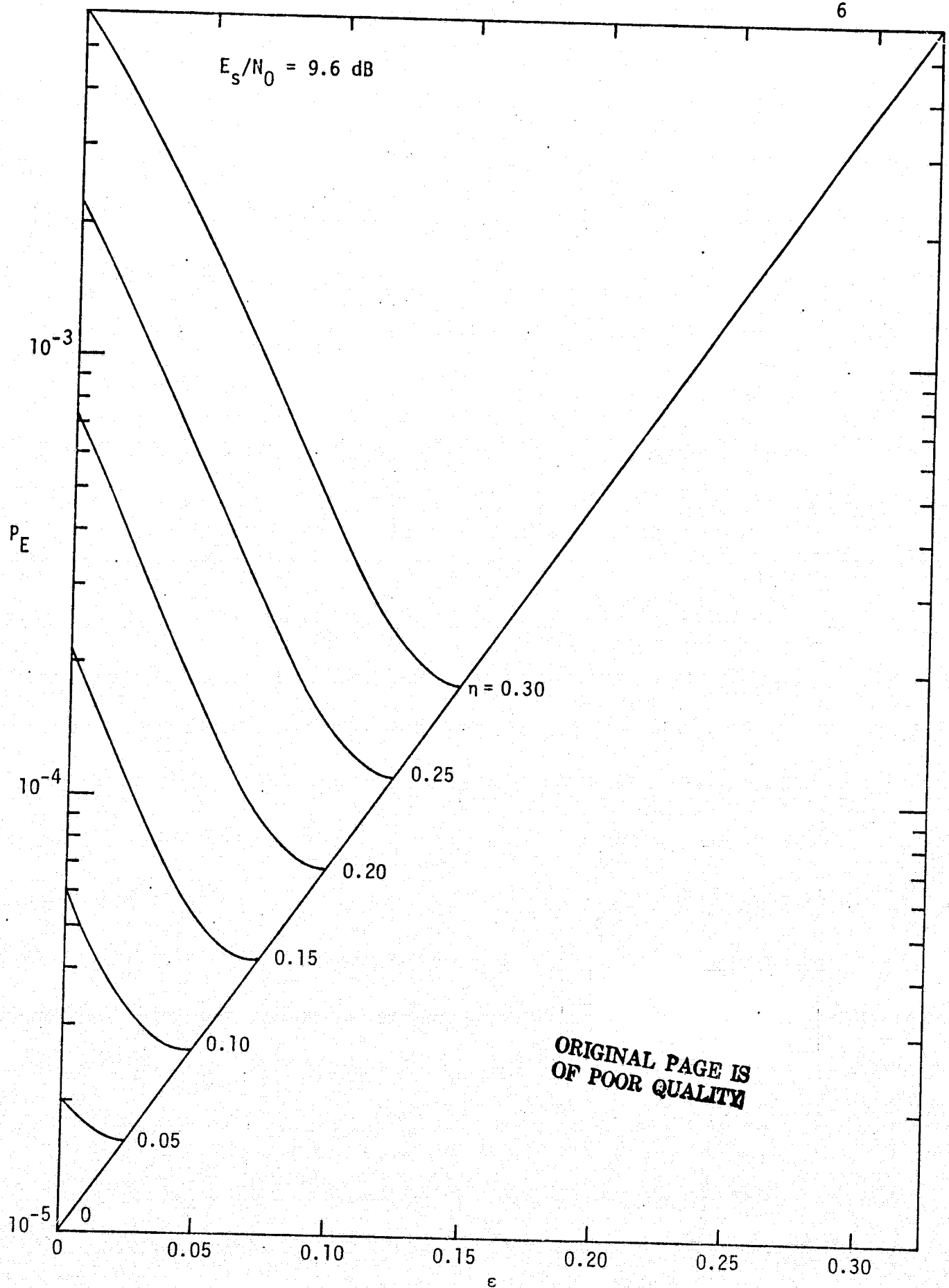


Figure 2. Average Error Probability versus Gate Interval at Symbol Edge with Data Asymmetry as a Parameter - No D.C. Restoration

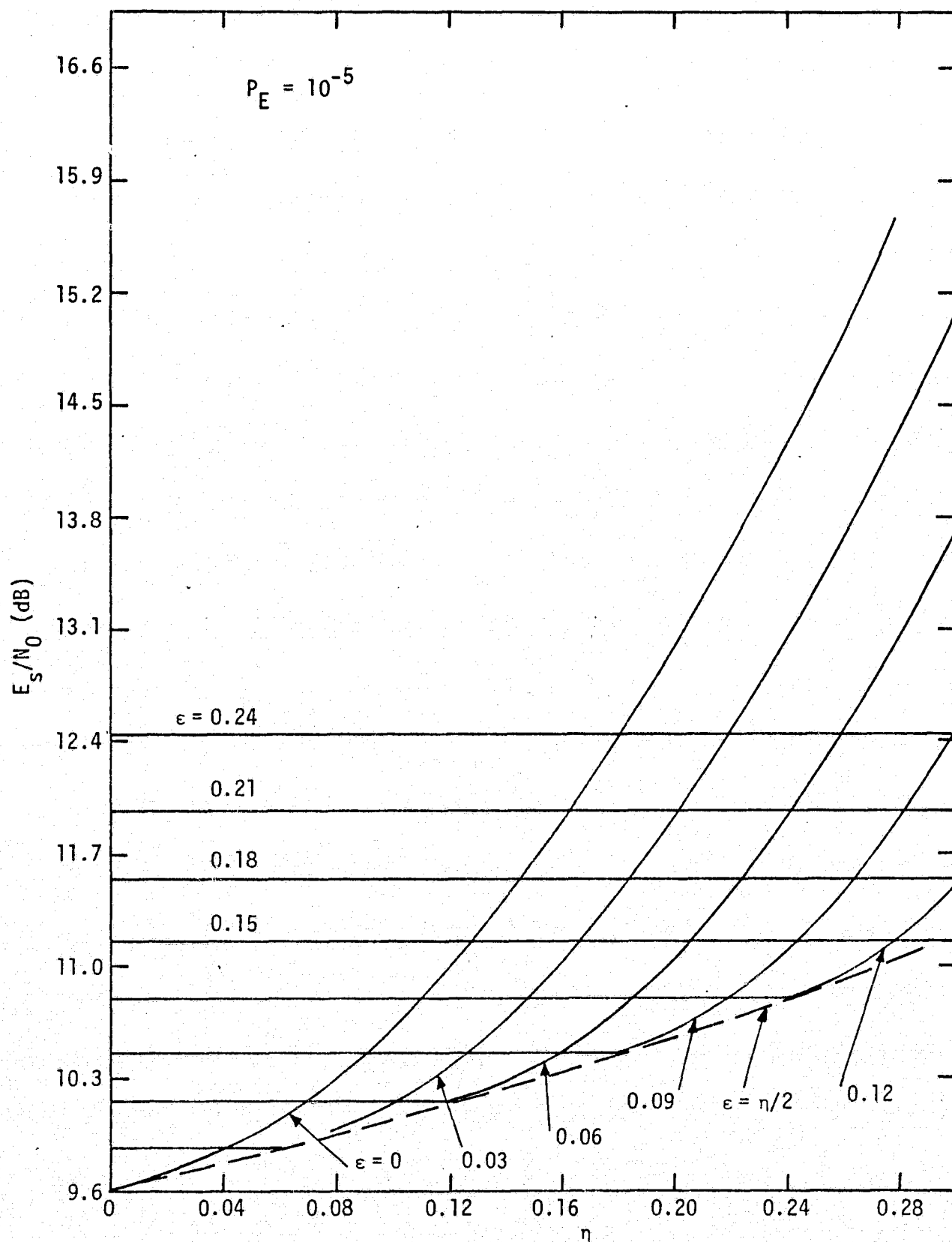


Figure 3. Symbol Energy-to-Noise Ratio versus Data Asymmetry with Gate Interval at Symbol Edge as a Parameter - No D.C. Restoration

$$\bar{x} = \begin{cases} -\sqrt{E_s T} [1 - \eta + \eta D - 2\epsilon \eta D]; & 0 \leq \epsilon \leq \frac{\eta}{2} \\ -\sqrt{E_s T} (1 - 2\epsilon)(1 + \eta D); & \frac{\eta}{2} \leq \epsilon \leq \frac{1}{2} \end{cases}$$

two sequences in which middle symbol is -1 and one adjacent symbol is +1

(12)

Since the standard deviation of the GI&D output is unaffected by the d.c. restoration, (5) still applies and thus the average probability of error is given by

$$P_E = \begin{cases} \frac{1}{4} \operatorname{erfc} \left[ \sqrt{\frac{E_s}{N_0}} (1 - 2\epsilon) (1 - \eta D) \right] + \frac{1}{16} \operatorname{erfc} \left[ \sqrt{\frac{E_s}{N_0}} (1 - 2\epsilon) (1 + \eta D) \right] \\ + \frac{1}{16} \operatorname{erfc} \left[ \sqrt{\frac{E_s}{N_0}} \left( \frac{1 - 2\eta + \eta D + 2\epsilon(1 - \eta D)}{\sqrt{1 - 2\epsilon}} \right) \right] \\ + \frac{1}{8} \operatorname{erfc} \left[ \sqrt{\frac{E_s}{N_0}} \left( \frac{1 - \eta + \eta D - 2\epsilon \eta D}{\sqrt{1 - 2\epsilon}} \right) \right]; & 0 \leq \epsilon \leq \frac{\eta}{2} \\ \frac{1}{4} \operatorname{erfc} \left[ \sqrt{\frac{E_s}{N_0}} (1 - 2\epsilon) (1 - \eta D) \right] + \frac{1}{4} \operatorname{erfc} \left[ \sqrt{\frac{E_s}{N_0}} (1 - 2\epsilon) (1 + \eta D) \right]; & \frac{\eta}{2} \leq \epsilon \leq \frac{1}{2} \end{cases} \quad (13)$$

Figure 4 again illustrates  $P_E$  versus  $\epsilon$  with  $\eta$  as a parameter and  $E_s/N_0 = 9.6$  dB, where  $P_E$  is now computed from (13). We observe from this figure that, for a given value of data asymmetry, there exists a value of  $\epsilon$  which minimizes  $P_E$ ; however, unlike Figure 2, this value of  $\epsilon$ , namely  $\epsilon_{\min}$ , is not equal to  $\eta/2$ . Figure 5 is the analogous figure to Figure 3 when d.c. restoration is present. Again, the dashed curve corresponds to  $\epsilon = \epsilon_{\min}$  which represents the best achievable performance using the GI&D as a data detector. Comparing Figure 5 with Figure 3, we observe the considerable reduction in SNR degradation due to data asymmetry when d.c. restoration is employed. This improvement is analogous to that achieved when other types of data detectors are used [2].

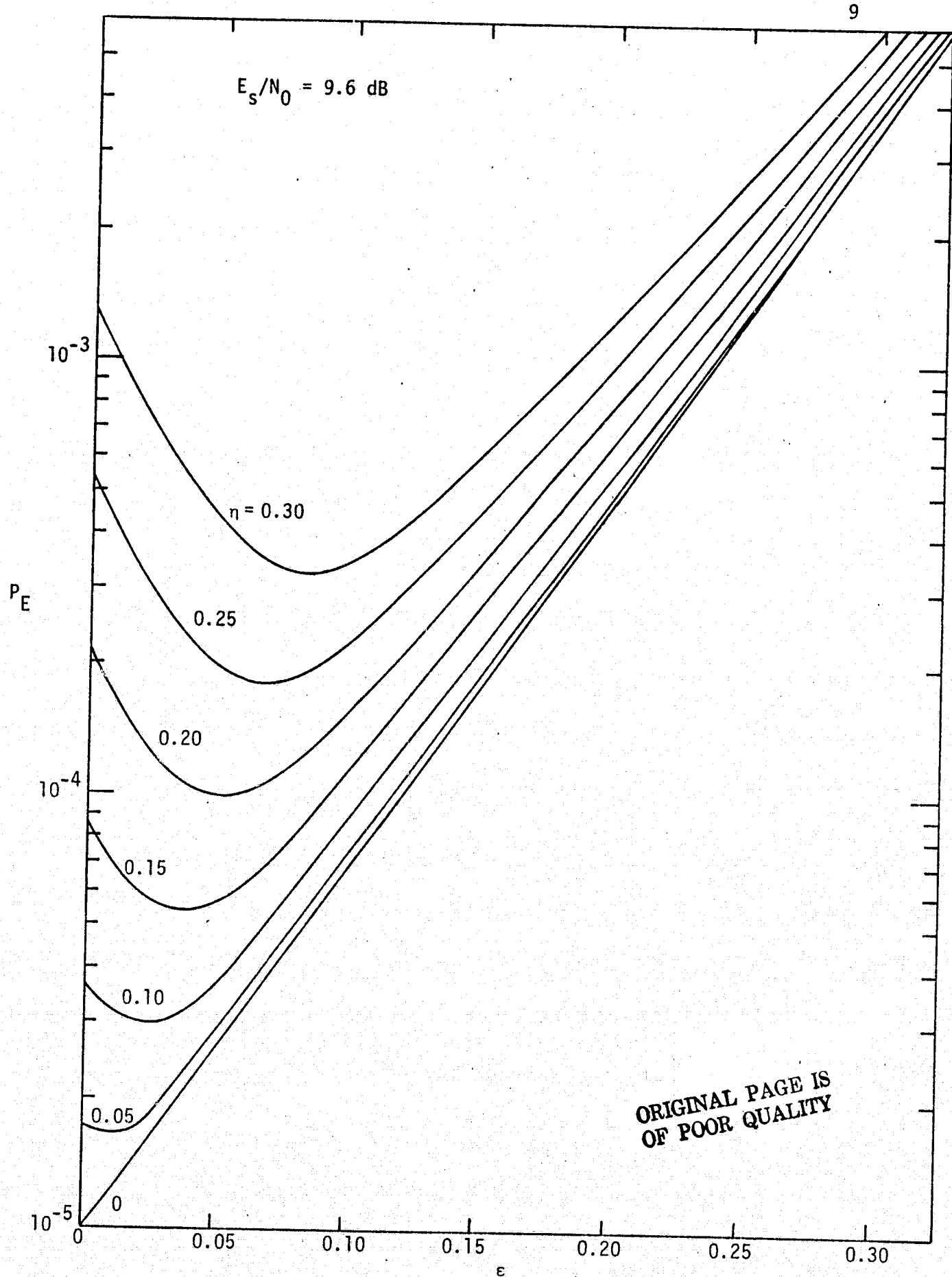


Figure 4. Average Error Probability versus Gate Interval at Symbol Edge with Data Asymmetry as a Parameter - D.C. Restoration by Capacitive Coupling

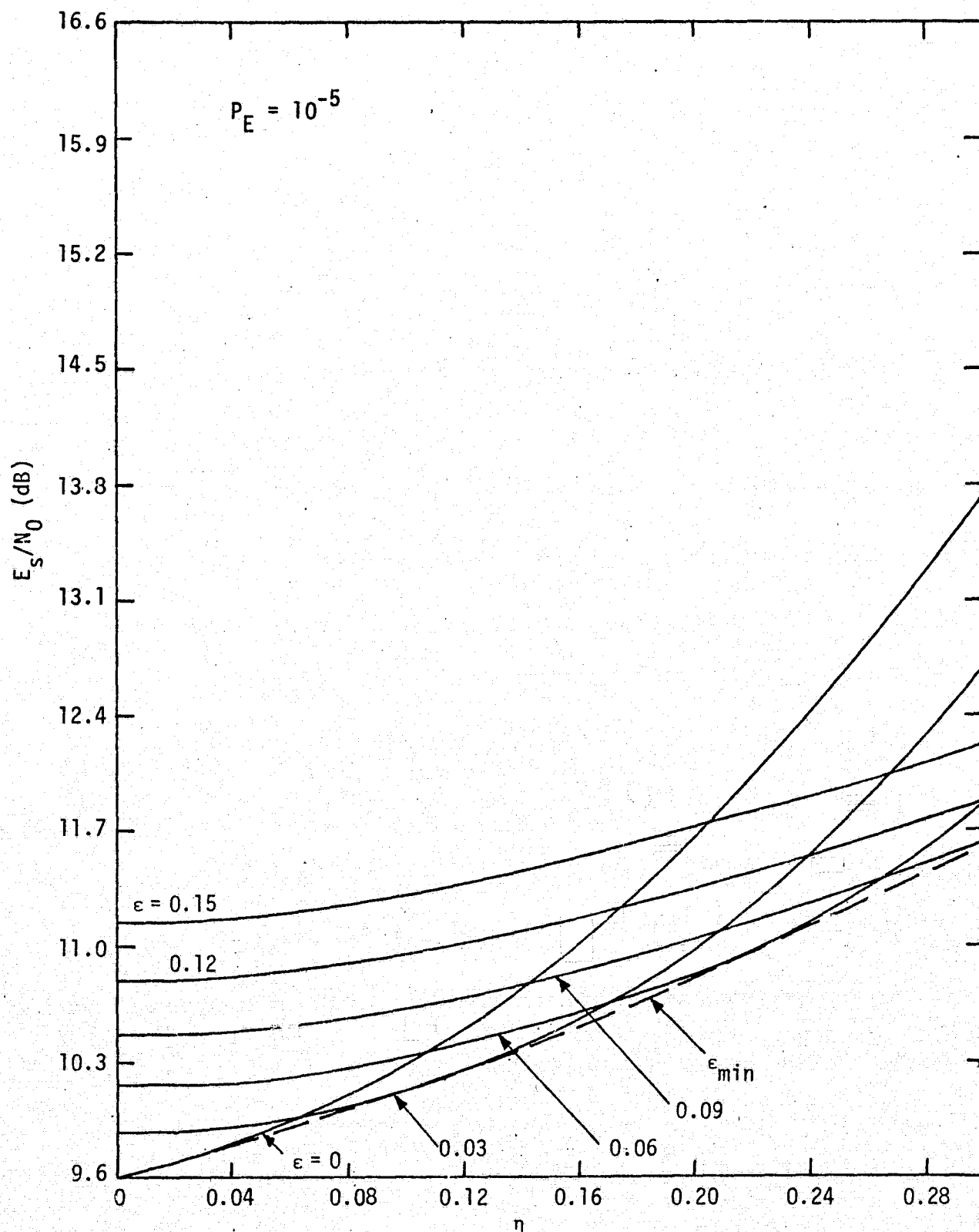


Figure 5. Symbol Energy-to-Noise Ratio versus Data Asymmetry with Gate Interval at Symbol Edge as a Parameter - D.C. Restoration by Capacitive Coupling

#### 4.0 CONCLUSIONS

The use of a gated integrate-and-dump filter for detection of asymmetric NRZ data can, depending upon the amount of data asymmetry present, produce significant improvement in SNR degradation due to asymmetry relative to that of an ideal integrate-and-dump filter. Such a filter has the further implementation advantage of allowing finite switching times at the symbol transition time instants. Since, for no data asymmetry, the performance of the gated integrate-and-dump is inferior to that of the ideal integrate-and-dump (matched filter), a tradeoff exists between the two filter types depending upon the amount of asymmetry present in the data. Whether or not d.c. restoration is present, there exists a value of gate interval for a given value of asymmetry which minimizes the average error probability performance of the receiver and thus represents the best achievable performance using a gated integrate-and-dump. The particular value of gate interval which achieves this minimum does, however, depend upon whether d.c. restoration is used or not.

## REFERENCES

1. M. K. Simon. "The Combined Effects of Bandlimiting and NRZ Data Asymmetry on the Bit Error Probability Performance of a Sample Detector," Axiomatix Report No. R7711-6, November 21, 1977.
2. M. K. Simon. "Bit Error Rate Degradation of the Ku-Band Return Link Channel Due to NRZ Data Symbol Asymmetry," Axiomatix Report No. R7707-2, July 8, 1977.

## APPENDIX E

### TRACKING PERFORMANCE OF UNBALANCED QPSK DEMODULATORS PART I - BIPHASE COSTAS LOOP WITH PASSIVE ARM FILTERS



## APPENDIX E

### TRACKING PERFORMANCE OF UNBALANCED QPSK DEMODULATORS PART I - BIPHASE COSTAS LOOP WITH PASSIVE ARM FILTERS

by

Marvin K. Simon  
Waddah K. Alem

#### INTRODUCTION

Unbalanced quadriphase-shift-keying (QPSK) is an attractive means for transmitting two digital data streams which have different average powers. The two data streams are not constrained to have identical data rates nor must they have the same data format; e.g., one might be an NRZ sequence and the other a Manchester code. In fact, it is the difference in data rates which causes the unbalance of power when it is desired to have symbol energies and therefore error rates on the two channels within the same order of magnitude.

Previous results [1,2] have indicated that when the unbalanced power ratio is large, e.g., approximately 4:1 or greater, a biphase Costas loop is a more efficient demodulator than a fourth-power tracking loop. These results, however, accounted only for the filtering effect produced by the loop's two arm filters on the equivalent additive noise perturbing the loop. When the bandwidth of these filters is selected on the order of the data rate, as is typical of optimum Costas loop design [3,4], the filtering degradations of the data modulations themselves and the cross-modulation noise produced by their multiplication in the loop often cannot be neglected.

The purpose of this report is to incorporate these additional filtering effects into the analysis of a biphase Costas loop demodulator of unbalanced QPSK. Many of the results obtained herein are in the form of closed-form expressions which can easily be evaluated numerically for design and performance prediction purposes. The generality of the results enables them to be applied to a wide variety of applications such as the performance of a subcarrier tracking loop for the three-channel Space Shuttle Orbiter (SSO) Ku-band return link [5].

#### SYSTEM MODEL AND LOOP EQUATION OF OPERATION

Consider the Costas loop illustrated in Figure 1 when input  $x(t)$  is an unbalanced QPSK signal plus noise, i.e.,

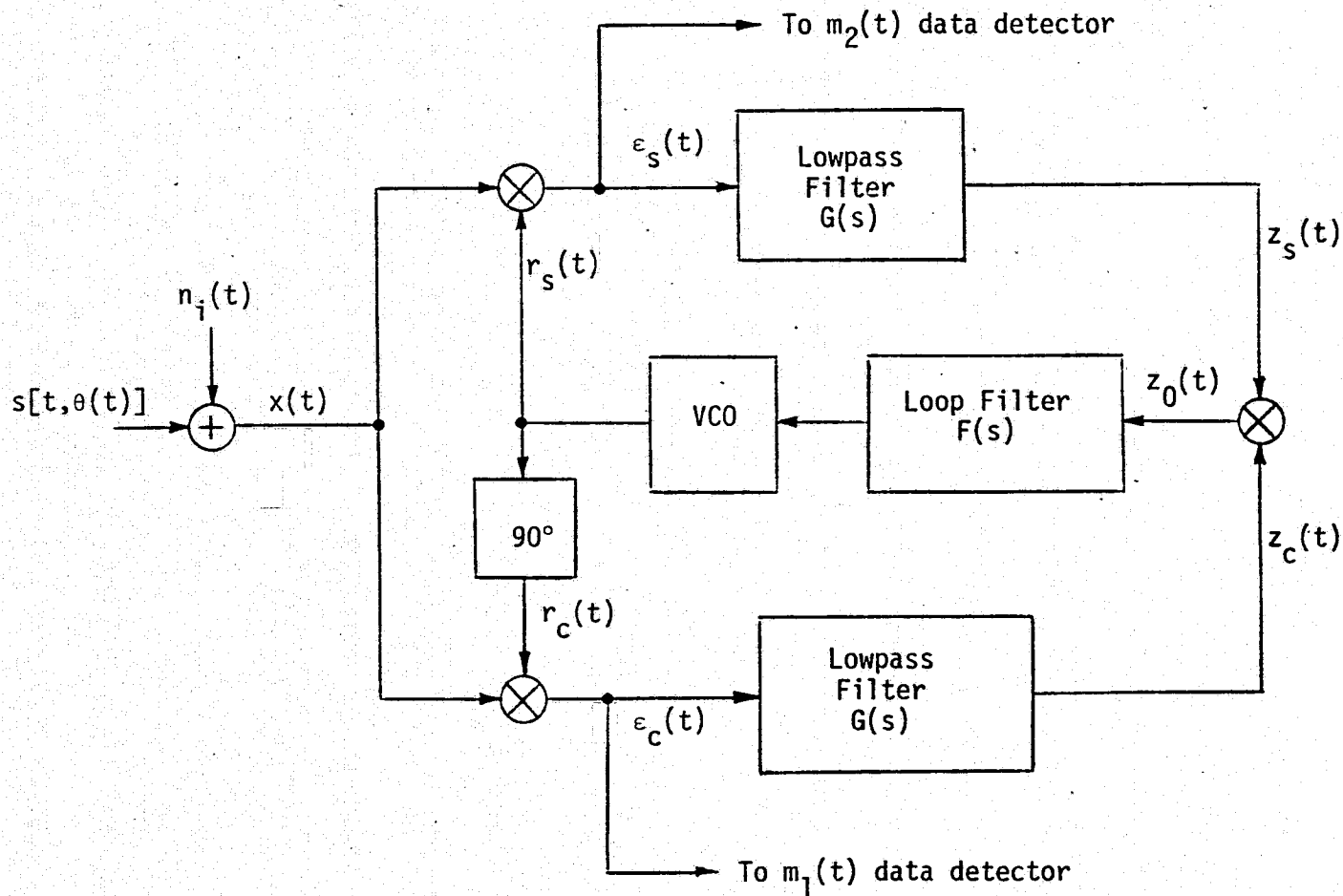


Figure 1. Costas Loop for Carrier Tracking of Unbalanced Quadriphase

$$x(t) = \sqrt{2P_1} m_1(t) \cos \phi(t) + \sqrt{2P_2} m_2(t) \sin \phi(t) + n_i(t), \quad (1)$$

where  $\phi(t) \triangleq \omega_0 t + \theta(t)$  with  $\omega_0$  the radian carrier frequency and  $\theta(t) = \theta_0 + \Omega_0 t$  the input phase to be estimated,  $m_1(t)$  and  $m_2(t)$  are independent data modulations, and  $n_i(t)$  is the additive channel noise which can be expressed in the form of a narrowband process about the actual frequency of the observed data, i.e.,

$$n_i(t) = \sqrt{2} \{N_c(t) \cos \phi(t) - N_s(t) \sin \phi(t)\}. \quad (2)$$

In (2),  $N_c(t)$  and  $N_s(t)$  are approximately statistically independent, stationary, white Gaussian noise processes with single-sided noise spectral density  $N_0$  w/Hz, and single-sided bandwidth  $B_H < \omega_0/2\pi$ .

The input signal  $x(t)$  is demodulated by the quadrature reference signals

$$\begin{aligned} r_s(t) &= \sqrt{2} K_1 \sin \hat{\phi}(t) \\ r_c(t) &= \sqrt{2} K_1 \cos \hat{\phi}(t) \end{aligned} \quad (3)$$

to produce the corresponding phase detector outputs (ignoring second harmonic terms):

$$\begin{aligned} \varepsilon_s(t) &\triangleq K_m x(t) r_s(t) = K_1 K_m \left[ \sqrt{P_2} m_2(t) - N_s(t) \right] \cos \phi(t) \\ &\quad - K_1 K_m \left[ \sqrt{P_1} m_1(t) + N_c(t) \right] \sin \phi(t) \\ \varepsilon_c(t) &\triangleq K_m x(t) r_c(t) = K_1 K_m \left[ \sqrt{P_2} m_2(t) - N_s(t) \right] \sin \phi(t) \\ &\quad + K_1 K_m \left[ \sqrt{P_1} m_1(t) + N_c(t) \right] \cos \phi(t) \end{aligned} \quad (4)$$

where  $\varphi(t) \triangleq \phi(t) - \hat{\phi}(t)$  is the loop phase error. After lowpass filtering  $\varepsilon_s(t)$  and  $\varepsilon_c(t)$  with arm filters  $G(s)$ , these signals become, respectively,

$$\begin{aligned} z_s(t) &\triangleq G(p) \varepsilon_s(t) = K_1 K_m \left[ \sqrt{P_2} \hat{m}_2(t) - \hat{N}_s(t) \right] \cos \varphi(t) \\ &\quad - K_1 K_m \left[ \sqrt{P_1} \hat{m}_1(t) + \hat{N}_c(t) \right] \sin \varphi(t) \end{aligned} \quad (5a)$$

$$z_c(t) \triangleq G(p) \varepsilon_c(t) = K_1 K_m \left[ \sqrt{P_2} \hat{m}_2(t) - \hat{N}_s(t) \right] \sin \varphi(t) + K_1 K_m \left[ \sqrt{P_1} \hat{m}_1(t) + \hat{N}_c(t) \right] \cos \varphi(t) \quad (5b)$$

where the "hats" denote filtering of the corresponding signals; e.g.,  $\hat{m}_1(t) \triangleq G(p) m_1(t)$ . Thus, the output of the third multiplier is the dynamic error signal

$$\begin{aligned} z_0(t) &\triangleq z_c(t) z_s(t) \\ &= \frac{K_1^2 K_m^2}{2} \left\{ \left[ P_2 \hat{m}_2^2(t) - P_1 \hat{m}_1^2(t) \right] \sin 2\varphi(t) \right. \\ &\quad + 2 \sqrt{P_1 P_2} \hat{m}_1(t) \hat{m}_2(t) \cos 2\varphi(t) \\ &\quad + \left[ \hat{N}_s^2(t) - \hat{N}_c^2(t) - 2\sqrt{P_2} \hat{m}_2(t) \hat{N}_s(t) \right. \\ &\quad \left. - 2\sqrt{P_1} \hat{m}_1(t) \hat{N}_c(t) \right] \sin 2\varphi(t) \\ &\quad + \left[ 2\sqrt{P_2} \hat{m}_2(t) \hat{N}_c(t) - 2\sqrt{P_1} \hat{m}_1(t) \hat{N}_s(t) \right. \\ &\quad \left. - 2 \hat{N}_c(t) \hat{N}_s(t) \right] \cos 2\varphi(t) \left. \right\}. \end{aligned} \quad (6)$$

The instantaneous frequency of the VCO output is related to  $z_0(t)$  by

$$\frac{d\hat{\phi}(t)}{dt} = K_V [F(p) z_0(t)] + \omega_0 \quad (7)$$

and hence the stochastic equation of loop operation becomes

$$\begin{aligned} \frac{2d\varphi(t)}{dt} &= 2\Omega_0 - KF(p) \left\{ \left[ P_2 \hat{m}_2^2(t) - P_1 \hat{m}_1^2(t) \right] \sin 2\varphi(t) \right. \\ &\quad + 2\sqrt{P_1 P_2} \hat{m}_1(t) \hat{m}_2(t) \cos 2\varphi(t) \\ &\quad \left. + v_2[t, 2\varphi(t)] \right\} \end{aligned} \quad (8)$$

where

$$\begin{aligned}
v_2[t, 2\varphi(t)] \triangleq & \left[ \hat{N}_s^2(t) - \hat{N}_c^2(t) - 2\sqrt{P_2} \hat{m}_2(t) \hat{N}_s(t) \right. \\
& \left. - 2\sqrt{P_1} \hat{m}_1(t) \hat{N}_c(t) \right] \sin 2\varphi(t) \\
& + \left[ 2\sqrt{P_2} \hat{m}_2(t) \hat{N}_c(t) - 2\sqrt{P_1} \hat{m}_1(t) \hat{N}_s(t) \right. \\
& \left. - 2 \hat{N}_c(t) \hat{N}_s(t) \right] \cos 2\varphi(t) \quad (9)
\end{aligned}$$

and  $K \triangleq K_1^2 K_m^2 K_V$ . As has been previously done [3,4] in problems of this type, we shall now decompose each of the signal terms in (8) into its mean value plus the variation about this mean, e.g.,

$$\hat{m}_1^2(t) \sin 2\varphi(t) = \overline{\hat{m}_1^2(t)} \sin 2\varphi(t) + \left[ \hat{m}_1^2(t) - \overline{\hat{m}_1^2(t)} \right] \sin 2\varphi(t) \quad (10)$$

where the overbar denotes statistical expectation and  $\langle \rangle$  denotes time averaging.\* It is easily shown that

$$\overline{\hat{m}_k^2(t)} \triangleq D_k = \int_{-\infty}^{\infty} S_{m_k}(f) |G(j2\pi f)|^2 df; \quad k=1,2 \quad (11)$$

and since  $m_1(t)$  and  $m_2(t)$  are independent,

$$\overline{\hat{m}_1(t) \hat{m}_2(t)} = 0. \quad (12)$$

In (11),  $S_{m_k}(f)$  denotes the power spectral density of  $m_k(t)$ ;  $k=1,2$ ; and  $|G(j2\pi f)|^2$  is the magnitude squared of the arm filter transfer function. Rewriting (8) using the above decompositions gives

$$\frac{2d\varphi(t)}{dt} = 2\Omega_0 - KF(p) \left\{ [P_2 D_2 - P_1 D_1] \sin 2\varphi(t) + n_e(t, 2\varphi) \right\} \quad (13)$$

where the total equivalent additive noise  $n_e(t, 2\varphi)$  is given by

$$\begin{aligned}
n_e(t, 2\varphi) \triangleq & v_2(t, 2\varphi) - P_1 n_1(t) \sin 2\varphi(t) + P_2 n_2(t) \sin 2\varphi(t) \\
& + 2\sqrt{P_1 P_2} n_{12}(t) \cos 2\varphi(t) \quad (14)
\end{aligned}$$

---

\*The additional time averaging is necessary since  $\hat{m}_1^2(t)$  and  $\hat{m}_2^2(t)$  are cyclostationary processes. Alternately, one may include a random phase in these two processes and statistically average them over the uniform distribution of this phase [6].

with the self-noise  $n_k(t)$ ;  $k=1,2$ ; and the cross-modulation noise  $n_{12}(t)$  defined by

$$\begin{aligned} n_k(t) &\triangleq \hat{m}_k^2(t) - \overline{\langle \hat{m}_k^2(t) \rangle} ; k=1,2 \\ n_{12}(t) &\triangleq \hat{m}_1(t) \hat{m}_2(t) . \end{aligned} \quad (15)$$

#### STATISTICAL CHARACTERIZATION OF THE EQUIVALENT ADDITIVE NOISE

The self-noise and cross-modulation noise processes all have zero mean and a continuous power spectral density component. Since the bandwidth of these processes is very wide with respect to the loop bandwidth, it is sufficient to find for each one only the power spectral density at the origin which, when multiplied by the loop bandwidth, gives the contribution to the total noise power of that modulation component. From (14), the autocorrelation of  $n_e(t, 2\varphi)$  is easily shown to be

$$\begin{aligned} R_e(\tau, 2\varphi) &\triangleq \overline{\langle n_e(t, 2\varphi) n_e(t+\tau, 2\varphi) \rangle} \\ &= P_1^2 \sin^2 2\varphi R_{n_1}(\tau) + P_2^2 \sin^2 2\varphi R_{n_2}(\tau) \\ &\quad + 4 P_1 P_2 \cos^2 2\varphi R_{n_{12}}(\tau) \\ &\quad + 4 \{ [P_1 R_{\hat{m}_1}(\tau) + P_2 R_{\hat{m}_2}(\tau)] R_{\hat{N}}(\tau) + R_{\hat{N}}^2(\tau) \} \end{aligned} \quad (16)$$

where

$$\begin{aligned} R_{\hat{m}_k}(\tau) &\triangleq \overline{\langle \hat{m}_k(t) \hat{m}_k(t+\tau) \rangle} = \int_{-\infty}^{\infty} S_{m_k}(f) |G(j2\pi f)|^2 e^{j2\pi f \tau} df ; k=1,2 \\ R_{n_k}(\tau) &\triangleq \overline{\langle n_k(t) n_k(t+\tau) \rangle} ; k=1,2 \\ R_{n_{12}}(\tau) &\triangleq \overline{\langle n_{12}(t) n_{12}(t+\tau) \rangle} = R_{\hat{m}_1}(\tau) R_{\hat{m}_2}(\tau) \\ R_{\hat{N}}(\tau) &\triangleq \overline{\langle \hat{N}_c(t) \hat{N}_c(t+\tau) \rangle} = \overline{\langle \hat{N}_s(t) \hat{N}_s(t+\tau) \rangle} \\ &= \frac{N_0}{2} \int_{-\infty}^{\infty} |G(j2\pi f)|^2 e^{j2\pi f \tau} df . \end{aligned} \quad (17)$$

The equivalent noise power spectral density at the origin is then

$$N_e(2\varphi) = 2 \int_{-\infty}^{\infty} R_e(\tau, 2\varphi) d\tau. \quad (18)$$

Substituting (16) together with (17) into (18) and using Parseval's Theorem yields

$$\begin{aligned} N_e(2\varphi) = & P_1^2 \sin^2 2\varphi S_{n_1}(0) + P_2^2 \sin^2 2\varphi S_{n_2}(0) \\ & + 8 P_1 P_2 \cos^2 2\varphi \int_{-\infty}^{\infty} S_{m_1}(f) S_{m_2}(f) |G(j2\pi f)|^4 df \\ & + 4 \left\{ P_1 N_0 \int_{-\infty}^{\infty} S_{m_1}(f) |G(j2\pi f)|^4 df + P_2 N_0 \int_{-\infty}^{\infty} S_{m_2}(f) |G(j2\pi f)|^4 df \right. \\ & \left. + \frac{N_0^2}{2} \int_{-\infty}^{\infty} |G(j2\pi f)|^4 df \right\}, \end{aligned} \quad (19)$$

where [3]

$$S_{n_k}(0) \triangleq 2 \int_{-\infty}^{\infty} R_{n_k}(\tau) d\tau = 4 T_k \sum_{n=1}^{\infty} R_{\hat{m}_k}^2(n T_k); \quad k = 1, 2$$

with  $R_k = 1/T_k$  the data rate of the digital modulation  $m_k(t)$ ;  $k = 1, 2$ . In [3], it was shown that, for cases of practical interest, the effect of the self-noise power on loop tracking performance was negligible. Thus, for all practical purposes, we may concern ourselves only with  $N_e(2\varphi)$  evaluated at  $\varphi = 0$ , i.e.,

$$N_e \triangleq N_e(2\varphi) \Big|_{\varphi=0} = 8 P_1 P_2 D_{12} + 4 \left\{ P_1 N_0 D_1 K_{D_1} + P_2 N_0 D_2 K_{D_2} + \frac{N_0^2 B_i}{2} K_L \right\} \quad (20)$$

where  $D_k$ ;  $k = 1, 2$ ; is defined in (11),

$$\begin{aligned} D_{12} & \triangleq \int_{-\infty}^{\infty} S_{m_1}(f) S_{m_2}(f) |G(j2\pi f)|^4 df \\ K_{D_k} & \triangleq \frac{\int_{-\infty}^{\infty} S_{m_k}(f) |G(j2\pi f)|^4 df}{\int_{-\infty}^{\infty} S_{m_k}(f) |G(j2\pi f)|^2 df}; \quad k = 1, 2 \\ K_L & \triangleq \frac{\int_{-\infty}^{\infty} |G(j2\pi f)|^4 df}{\int_{-\infty}^{\infty} |G(j2\pi f)|^2 df} \end{aligned} \quad (21)$$

and

$$B_i \triangleq \int_{-\infty}^{\infty} |G(j2\pi f)|^2 df \quad (22)$$

is the two-sided arm filter lowpass bandwidth.

#### EFFECTIVE LOOP SIGNAL-TO-NOISE RATIO AND PHASE JITTER

From the loop equation of operation given in (13), we can see that the effective loop signal-to-noise ratio is given by

$$\rho_e = \frac{(P_2 D_2 - P_1 D_1)^2}{N_e B_L} \quad (23)$$

where  $B_L$  is the single-sided loop bandwidth. Substituting (20) into (23) and simplifying results in

$$\rho_e = \frac{\rho}{4} S_L \quad (24)$$

where  $\rho \triangleq P_T / N_0 B_L$  with the total power  $P_T = P_1 + P_2$ , and  $S_L$  is the loop "squaring loss" which is given by

$$S_L = \frac{\frac{(P_2 D_2 - P_1 D_1)^2}{P_T}}{P_1 D_1 K_{D1} + P_2 D_2 K_{D2} + \frac{N_0 B_i}{2} K_L + \frac{2 P_1 P_2 D_{12}}{N_0}} \quad (25)$$

Defining the modulation indices,

$$\eta_k \triangleq \frac{P_i}{P_T}; \quad k=1,2 \quad (26)$$

then (25) simplifies to

$$S_L = \frac{(\eta_2 D_2 - \eta_1 D_1)^2}{\eta_1 D_1 K_{D1} + \eta_2 D_2 K_{D2} + \left(\frac{N_0 B_i}{2 P_T}\right) K_L + 2 \eta_1 \eta_2 \left(\frac{P_T}{N_0}\right) D_{12}} \quad (27)$$

Ordinarily, to optimize tracking performance, i.e., maximize  $\rho_e$ , the arm filter bandwidth is selected relative to the higher of the two data rates. Thus, arbitrarily assuming that  $R_2 > R_1$ , we rewrite (27) in the final form



$$S_L = \frac{(\eta_2 D_2 - \eta_1 D_1)^2}{\eta_1 D_1 K_{D_1} + \eta_2 D_2 K_{D_2} + \frac{B_i/R_2}{2R_{T2}} K_L + 2\eta_1 \eta_2 R_{T2} \left( \frac{D_{12}}{T_2} \right)} \quad (28)$$

where  $R_{T2} \triangleq P_{T2}/N_0$ .

What remains is to characterize the tracking phase jitter performance. In the linear region of operation, the variance of the loop phase error  $2\varphi$  is given by

$$\sigma_{2\varphi}^2 = \frac{1}{\rho_e} = \frac{4}{\rho S_L} \quad (29)$$

Since the demodulation reference signals of (3) are at  $\omega_0$  rather than  $2\omega_0$ , then the tracking jitter on the output data streams is

$$\sigma_{\varphi}^2 = \frac{1}{4} \sigma_{2\varphi}^2 = \frac{1}{\rho S_L} \quad (30)$$

We conclude then that characterization of the loop squaring loss in terms of the system parameters is sufficient for predicting the loop's tracking performance.

#### SQUARING LOSS EVALUATION FOR PRACTICAL FILTERS AND DATA MODULATION SPECTRA

To graphically illustrate the theory previously developed, it would be convenient to obtain closed-form expressions for the parameters defined in equations (11), (21), and (22) for practical filters and data modulation formats. Indeed, such is possible for certain special cases of interest as we shall now illustrate. Let us consider a simple RC filter with 3 dB cutoff frequency  $f_c$  for the Costas loop arm filters. Then,

$$|G(j2\pi f)|^2 = \frac{1}{1 + (f/f_c)^2} \quad (31)$$

Substituting (31) into (22) and carrying out the integration gives the relationship between two-sided noise bandwidth and cutoff frequency, namely,

$$B_i = \pi f_c \quad (32)$$

Also, from (21), substituting the square of (31) into the numerator of the expression for  $K_L$  and recognizing that the denominator is merely equivalent to  $B_i$  of (32) gives, upon integration,

$$K_L = \frac{1}{2} \quad (33)$$

Evaluation of  $D_k$ ,  $K_{D_k}$ ;  $k=1,2$ , and  $D_{12}$  requires that we further specify the forms of the two data modulations. For NRZ data with power spectral density

$$S_{m_k}(f) = T_k \frac{\sin^2 \pi f T_k}{(\pi f T_k)^2}, \quad (34)$$

it has been previously shown [3] that

$$\begin{aligned} D_k &= 1 - \frac{1}{2B_i/R_k} [1 - \exp(-2B_i/R_k)] ; \quad k=1,2 \\ K_{D_k} &= \frac{1 - \frac{3 - (3 + 2B_i/R_k) \exp(-2B_i/R_k)}{4B_i/R_k}}{1 - \frac{1}{2B_i/R_k} [1 - \exp(-2B_i/R_k)]} ; \quad k=1,2 \end{aligned} \quad (35)$$

For Manchester codes, the power spectral density is

$$S_{m_k}(f) = T_k \frac{\sin^4 (\pi f T_k/2)}{(\pi f T_k/2)^2} ; \quad k=1,2 \quad (36)$$

Recognizing the trigonometric identity

$$\sin^4 x = \sin^2 x - \frac{1}{4} \sin^2 2x, \quad (37)$$

then (36) can be rewritten as

$$S_{m_k}(f) = 2 \left( \frac{T_k}{2} \right) \frac{\sin^2 (\pi f T_k/2)}{(\pi f T_k/2)^2} - T_k \frac{\sin^2 \pi f T_k}{(\pi f T_k)^2} ; \quad k=1,2 \quad (38)$$

which spectrally looks like the difference of two NRZ spectra of different data rates. In view of this, it is obvious from (21) that, for Manchester codes,

ORIGINAL PAGE IS  
OF POOR QUALITY

$$D_k^{\text{MANCH}} = 2 D_k^{\text{NRZ}} \Big|_{R_k=2R_k} - D_k^{\text{NRZ}} ; \quad k=1,2$$

$$K_{D_k}^{\text{MANCH}} = \frac{1}{D_k^{\text{MANCH}}} \left\{ 2 D_k^{\text{NRZ}} K_{D_k}^{\text{NRZ}} \Big|_{R_k=2R_k} - D_k^{\text{NRZ}} K_{D_k}^{\text{NRZ}} \right\};$$

$$k=1,2 . \quad (39)$$

Substituting (35) into (39) and simplifying yields the following results for Manchester codes:

$$D_k = 1 - \frac{1}{2B_i/R_k} [3 - 4 \exp(-B_i/R_k) + \exp(-2B_i/R_k)] ; \quad k=1,2$$

$$K_{D_k} = \frac{1 - \frac{9 - 4(3+B_i/R_k) \exp(-B_i/R_k) + (3+2B_i/R_k) \exp(-2B_i/R_k)}{4B_i/R_k}}{1 - \frac{3 - 4 \exp(-B_i/R_k) + \exp(-2B_i/R_k)}{2B_i/R_k}} ;$$

$$k=1,2 . \quad (40)$$

All that remains is to derive expressions for the cross-modulation coefficient  $D_{12}$  corresponding to the various combinations of modulation formats and relative data rates. Starting out with the simplest case (at least algebraically), we shall assume that  $m_1(t)$  and  $m_2(t)$  are both NRZ data streams with respective bit rates  $R_1$ ,  $R_2$ , and  $R_2 > R_1$ . Then, from (21), (31), and (34), we have that

$$D_{12} = \frac{1}{\pi^4 T_1 T_2} \int_{-\infty}^{\infty} \frac{\sin^2 \pi f T_1 \sin^2 \pi f T_2}{f^4} \left[ \frac{1}{1 + (f/f_c)^2} \right]^2 df . \quad (41)$$

Using a partial fraction expansion followed by considerable integral evaluations and manipulations, we arrive at the final answer, namely,

ORIGINAL PAGE IS  
OF POOR QUALITY

$$\begin{aligned}
D_{12} = & T_2 \left(1 - \frac{T_2}{3T_1}\right) - T_2 \left(\frac{T_2}{T_1}\right) \frac{1}{(B_i/R_2)^2} \\
& + \frac{1}{8} T_2 \left(\frac{T_2}{T_1}\right) \frac{1}{(B_i/R_2)^3} \left\{ 5 - (5 + 2B_i/R_2) \exp(-2B_i/R_2) \right. \\
& \quad - (5 + 2B_i/R_1) \exp(-2B_i/R_1) \\
& \quad + \frac{1}{2} \left[ 5 + 2\left(\frac{T_1}{T_2} - 1\right) B_i/R_2 \right] \exp \left[ -2\left(\frac{T_1}{T_2} - 1\right) B_i/R_2 \right] \\
& \quad \left. + \frac{1}{2} \left[ 5 + 2\left(\frac{T_1}{T_2} + 1\right) B_i/R_2 \right] \exp \left[ -2\left(\frac{T_1}{T_2} + 1\right) B_i/R_2 \right] \right\} \\
& \quad R_2 > R_1 \quad (42)
\end{aligned}$$

$m_1(t)$  is NRZ,  $m_2(t)$  is NRZ.

If  $m_1(t)$  is now a Manchester code while  $m_2(t)$  is still NRZ, then using (36) in addition to (21), (31), and (34) gives

$$D_{12} = \frac{4}{\pi^4 T_1 T_2} \int_{-\infty}^{\infty} \frac{\sin^4 \pi f T_1/2 \sin^2 \pi f T_2}{f^4} \left[ \frac{1}{1 + (f/f_c)^2} \right]^2 df. \quad (43)$$

Once again using the trigonometric identity of (37),  $D_{12}$  of (43) simplifies to

$$\begin{aligned}
D_{12} = & \frac{2}{\pi^4 (T_1/2) T_2} \int_{-\infty}^{\infty} \frac{\sin^2 \pi f T_1/2 \sin^2 \pi f T_2}{f^4} \left[ \frac{1}{1 + (f/f_c)^2} \right]^2 df \\
& - \frac{1}{\pi^4 T_1 T_2} \int_{-\infty}^{\infty} \frac{\sin^2 \pi f T_1 \sin^2 \pi f T_2}{f^4} \left[ \frac{1}{1 + (f/f_c)^2} \right]^2 df. \quad (44)
\end{aligned}$$

Comparing (44) with (41), we immediately arrive at the following results:

$$\begin{aligned}
D_{12}^{\text{MANCH NRZ}} &= 2 D_{12}^{\text{NRZ NRZ}} \Big|_{R_1=2R_1} - D_{12}^{\text{NRZ NRZ}}; \quad R_2 \geq 2R_1 \\
D_{12}^{\text{MANCH NRZ}} &= 2 D_{12}^{\text{NRZ NRZ}} \Big|_{\substack{R_2=2R_1 \\ R_1=R_2}} - D_{12}^{\text{NRZ NRZ}}; \quad R_1 \leq R_2 \leq 2R_1. \quad (45)
\end{aligned}$$

Letting  $m_1(t)$  now be NRZ and  $m_2(t)$  a Manchester code, we get the remaining result:

$$D_{12}^{\text{NRZ MANCH}} = 2 D_{12}^{\text{NRZ NRZ}} \Big|_{R_2=2R_2} - D_{12}^{\text{NRZ NRZ}} ; R_2 \geq R_1 . \quad (46)$$

Finally, when both  $m_1(t)$  and  $m_2(t)$  are Manchester codes, we have

$$D_{12} = \frac{16}{\pi^4 T_1 T_2} \int_{-\infty}^{\infty} \frac{\sin^4 \pi f T_1/2 \sin^4 \pi f T_2/2}{f^4} \left[ \frac{1}{1 + (f/f_c)^2} \right]^2 df . \quad (47)$$

To simplify (47) in terms of previously given results, we require the trigonometric identity:

$$\begin{aligned} \sin^4 ax \sin^4 bx &= \sin^2 ax \sin^2 bx - \frac{1}{4} \sin^2 2ax \sin^2 bx \\ &\quad - \frac{1}{4} \sin^2 ax \sin^2 2bx + \frac{1}{16} \sin^2 2ax \sin^2 2bx . \end{aligned} \quad (48)$$

Making use of (48) in (47), we see, for example, that

$$\begin{aligned} D_{12}^{\text{MANCH MANCH}} &= 4 D_{12}^{\text{NRZ NRZ}} \Big|_{\substack{R_1=2R_1 \\ R_2=2R_2}} - 2 D_{12}^{\text{NRZ NRZ}} \Big|_{R_1=2R_1} \\ &\quad - 2 D_{12}^{\text{NRZ NRZ}} \Big|_{R_2=2R_2} + D_{12}^{\text{NRZ NRZ}} ; R_2 \geq 2R_1 . \\ D_{12}^{\text{MANCH MANCH}} &= 4 D_{12}^{\text{NRZ NRZ}} \Big|_{\substack{R_1=2R_1 \\ R_2=2R_2}} - 2 D_{12}^{\text{NRZ NRZ}} \Big|_{R_2=2R_2} - 2 D_{12}^{\text{NRZ NRZ}} \Big|_{\substack{R_2=2R_1 \\ R_1=R_2}} \\ &\quad + D_{12}^{\text{NRZ NRZ}} ; 2R_1 \geq R_2 \geq R_1 \end{aligned} \quad (49)$$

Expressions for  $D_{12}$ , corresponding to (45), (46), and (49), in terms of system parameters can be obtained by substituting (42) into these equations and simplifying. For example, corresponding to the first of the two cases in (45), we get

$$\begin{aligned}
D_{12} = & T_2 (1 - T_2/T_1) - 3T_2 (T_2/T_1) \frac{1}{(B_i/R_2)^2} \\
& + \frac{1}{8} T_2 (T_2/T_1) \frac{1}{(B_i/R_2)^3} \left\{ 15 - 3(5 + 2B_i/R_2) \exp(-2B_i/R_2) \right. \\
& \quad - 4(5 + B_i/R_1) \exp(-B_i/R_1) \\
& \quad + (5 + 2B_i/R_1) \exp(-2B_i/R_1) \\
& \quad + 2 \left[ 5 + 2 \left( \frac{T_1}{2T_2} - 1 \right) B_i/R_2 \right] \exp \left[ -2 \left( \frac{T_1}{2T_2} - 1 \right) B_i/R_2 \right] \\
& \quad - \frac{1}{2} \left[ 5 + 2 \left( \frac{T_1}{T_2} - 1 \right) B_i/R_2 \right] \exp \left[ -2 \left( \frac{T_1}{T_2} - 1 \right) B_i/R_2 \right] \\
& \quad + 2 \left[ 5 + 2 \left( \frac{T_1}{2T_2} + 1 \right) B_i/R_2 \right] \exp \left[ -2 \left( \frac{T_1}{2T_2} + 1 \right) B_i/R_2 \right] \\
& \quad \left. - \frac{1}{2} \left[ 5 + 2 \left( \frac{T_1}{T_2} + 1 \right) B_i/R_2 \right] \exp \left[ -2 \left( \frac{T_1}{T_2} + 1 \right) B_i/R_2 \right] \right\}
\end{aligned}$$

$$R_2 \geq 2R_1 ; \quad (50)$$

whereas for the second case in (45),

$$\begin{aligned}
D_{12} = & T_2 \left[ \frac{T_1}{T_2} - \frac{1}{6} \left( \frac{T_1}{T_2} \right)^2 - 1 + \frac{1}{3} \left( \frac{T_2}{T_1} \right) \right] - 2T_2 \left( 1 - \frac{T_2}{2T_1} \right) \frac{1}{(B_i/R_2)^2} \\
& + \frac{1}{8} T_2 \left( \frac{T_2}{T_1} \right) \frac{1}{(B_i/R_2)^3} \left\{ 15 - 3(5 + 2B_i/R_2) \exp(-2B_i/R_2) \right. \\
& \quad - 4(5 + B_i/R_1) \exp(-B_i/R_1) \\
& \quad + (5 + 2B_i/R_1) \exp(-2B_i/R_1) \\
& \quad + 2 \left[ 5 + 2 \left( 1 - \frac{T_1}{2T_2} \right) B_i/R_2 \right] \exp \left[ -2 \left( 1 - \frac{T_1}{2T_2} \right) B_i/R_2 \right] \\
& \quad - \frac{1}{2} \left[ 5 + 2 \left( \frac{T_1}{T_2} - 1 \right) B_i/R_2 \right] \exp \left[ -2 \left( \frac{T_1}{T_2} - 1 \right) B_i/R_2 \right] \\
& \quad + 2 \left[ 5 + 2 \left( 1 + \frac{T_1}{2T_2} \right) B_i/R_2 \right] \exp \left[ -2 \left( 1 + \frac{T_1}{2T_2} \right) B_i/R_2 \right] \\
& \quad \left. - \frac{1}{2} \left[ 5 + 2 \left( \frac{T_1}{T_2} + 1 \right) B_i/R_2 \right] \exp \left[ -2 \left( \frac{T_1}{T_2} + 1 \right) B_i/R_2 \right] \right\}
\end{aligned}$$

$$R_1 \leq R_2 \leq 2R_1 . \quad (51)$$

Finally, when  $m_1(t)$  is NRZ,  $m_2(t)$  is Manchester, and  $R_2 \geq R_1$ , then corresponding to (46) we have

$$\begin{aligned}
 D_{12} = & \frac{1}{6} T_2 (T_2/T_1) - T_2 (T_2/T_1) \frac{1}{(B_i/R_2)^2} \\
 & + \frac{1}{8} T_2 (T_2/T_1) \frac{1}{(B_i/R_2)^3} \left\{ 15 - 3(5 + 2B_i/R_1) \exp(-2B_i/R_1) \right. \\
 & \quad - 4(5 + B_i/R_2) \exp(-B_i/R_2) \\
 & \quad + (5 + 2B_i/R_2) \exp(-2B_i/R_2) \\
 & \quad + 2 \left[ 5 + 2 \left( 1 - \frac{T_2}{2T_1} \right) B_i/R_1 \right] \exp \left[ -2 \left( 1 - \frac{T_2}{2T_1} \right) B_i/R_1 \right] \\
 & \quad - \frac{1}{2} \left[ 5 + 2 \left( 1 - \frac{T_2}{T_1} \right) B_i/R_1 \right] \exp \left[ -2 \left( 1 - \frac{T_2}{T_1} \right) B_i/R_1 \right] \\
 & \quad + 2 \left[ 5 + 2 \left( 1 + \frac{T_2}{2T_1} \right) B_i/R_1 \right] \exp \left[ -2 \left( 1 + \frac{T_2}{2T_1} \right) B_i/R_1 \right] \\
 & \quad \left. - \frac{1}{2} \left[ 5 + 2 \left( 1 + \frac{T_2}{T_1} \right) B_i/R_1 \right] \exp \left[ -2 \left( 1 + \frac{T_2}{T_1} \right) B_i/R_1 \right] \right\}
 \end{aligned}$$

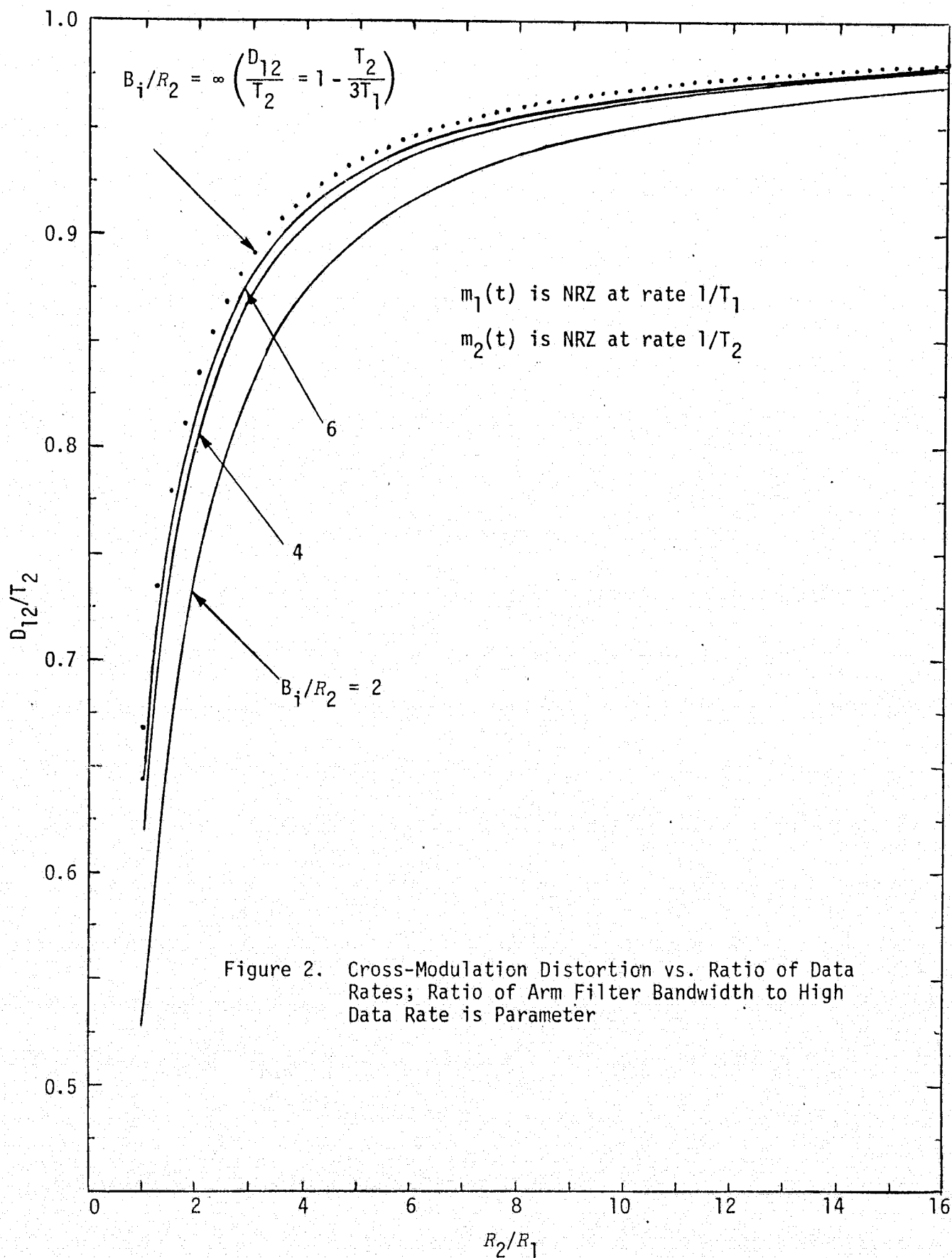
ORIGINAL PAGE IS  
OF POOR QUALITY

$$R_2 \geq R_1 \quad (52)$$

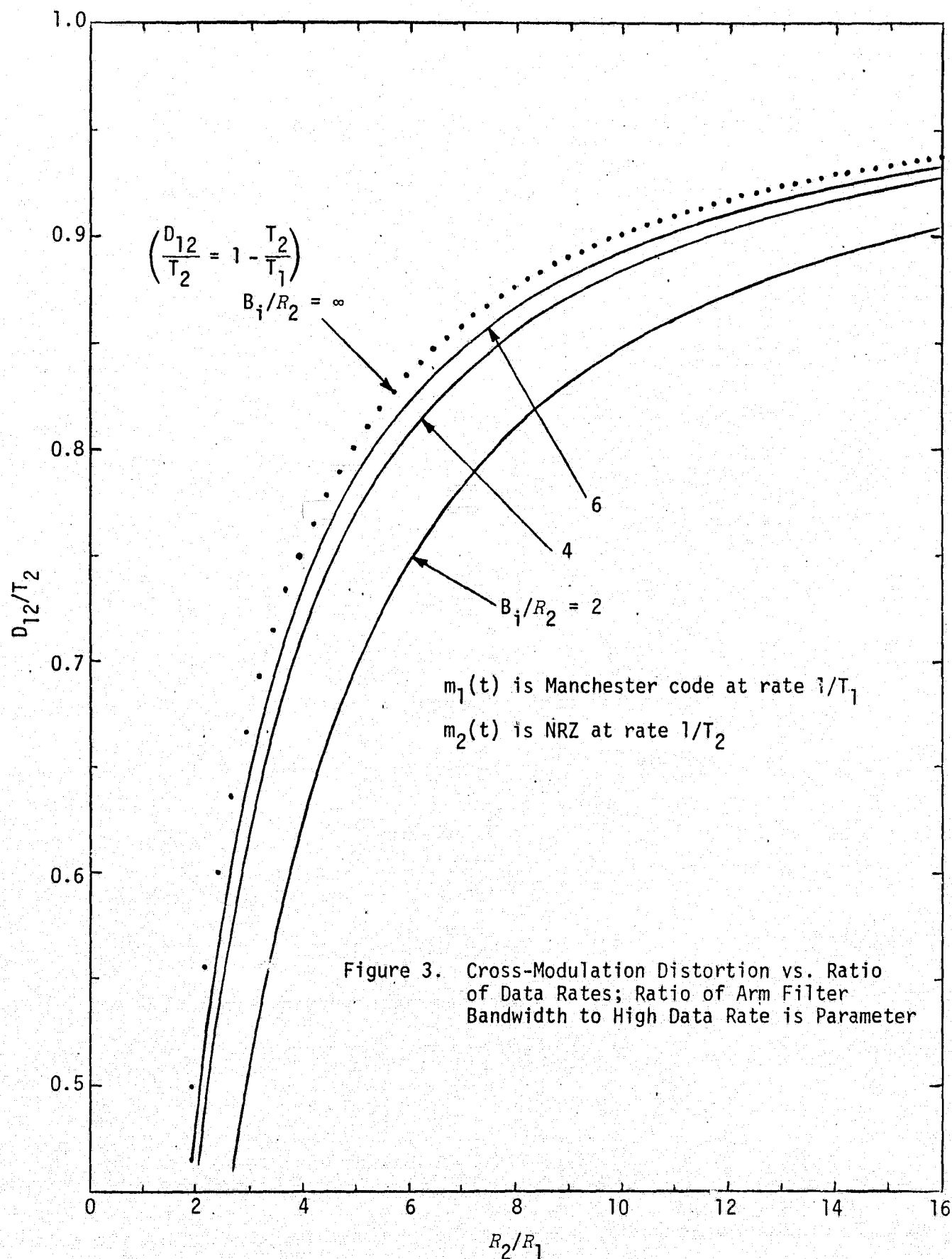
Obtaining a detailed closed-form expression corresponding to (49), i.e., the case of  $m_1(t)$  and  $m_2(t)$  both Manchester coded streams, is left as an exercise for the reader.

#### NUMERICAL RESULTS

Illustrated in Figures 2 and 3 is the behavior of the normalized cross-modulation distortion  $D_{12}/T_2$  as a function of the ratio of the two data rates with the ratio of two-sided arm filter noise bandwidth to high data rate as a parameter. In Figure 2, the results are for the case where both  $m_1(t)$  and  $m_2(t)$  are NRZ data streams and are thus obtained from (42). The results in Figure 3 are obtained from (50) and correspond to the case where  $m_1(t)$  is NRZ and  $m_2(t)$  is a Manchester code, and  $R_2 \geq 2R_1$ . Also illustrated as dotted curves are the limiting curves which ignore the bandlimiting effects of the arm filters. These curves which are obtained







from (42) and (50) by letting  $B_1/R_2 \rightarrow \infty$  correspond to the results given previously [1,2].

We now turn to numerical evaluation of the loop squaring loss (28) which, for a fixed loop bandwidth and ratio of total power-to-noise spectral density, is a direct measure of mean square tracking jitter. Figures 4 through 6 illustrate (for fixed  $\eta_1$  and  $\eta_2$ ) the behavior of  $S_L$  as a function of the ratio of two-sided arm filter noise bandwidth to the higher of the two data rates  $R_2$  with the ratio of data rates  $R_2/R_1$  and  $P_T T_2/N_0$  as parameters. Assuming  $P_T/N_0$  to be fixed, then the variation of squaring loss with  $P_T T_2/N_0$  directly reflects the effect of changing the high data rate  $R_2$ . Furthermore, at low values of  $B_1/R_2$ , we observe from Figures 5 and 6 that additional interesting peaks and valleys of the squaring loss characteristic occur. These extrema represent tradeoffs between  $S_x S$  distortion and cross-modulation noise or  $S_x N$  power, depending on which of the latter dominates the total noise.

The numerical evaluation of the tracking jitter, for a fixed ratio of arm filter noise bandwidth to loop noise bandwidth ( $B_1/B_L$ ) [(30)], is shown in Figures 7 through 14. Figures 7 through 10 illustrate the behavior of  $\sigma_\phi$ , for fixed  $\eta_1, \eta_2$ , as a function of the ratio of the arm filter bandwidth to the higher data rate  $R_2$  for all possible signal format combinations with  $R_2/R_1$  and  $P_T T_2/N_0$  as parameters. The minimum values of  $\sigma_\phi$  for some ratios of  $R_2/R_1$  represent best design points when the combined effect of  $N_x N$  distortion and cross-modulation noise or  $S_x N$  power is minimal. Assuming  $P_T/N_0$  to be fixed, the variation of  $\sigma_\phi$  with  $P_T T_2/N_0$  is shown in Figures 11 and 12 for the case when  $m_1(t)$  and  $m_2(t)$  are NRZ and the case when  $m_1(t)$  is Manchester code and  $m_2(t)$  is NRZ, respectively. As is intuitively true, the tracking jitter performance improves with the increase of  $P_T T_2/N_0$ . Furthermore, for a fixed value of  $B_1/R_2$ , the variations of  $\sigma_\phi$  with  $P_2/P_T = \eta_2$  are shown in Figures 13 and 14 for the two previous cases. The figures show that, as the powers of the two data rates become equal ( $\eta_2 = 1/2$ ), the loop is not able to operate.

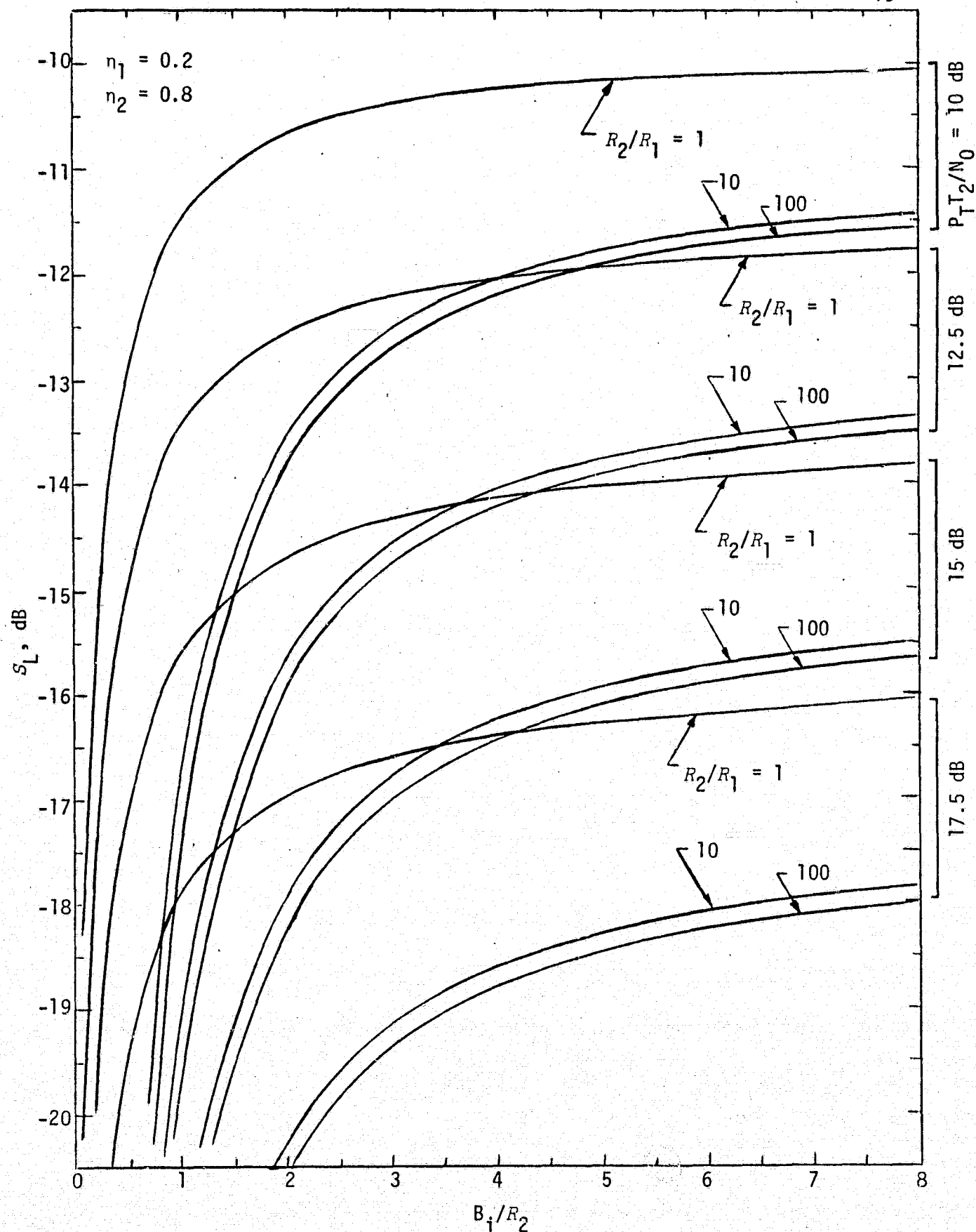


Figure 4. Squaring Loss vs. Ratio of Arm Filter Bandwidth to High Data Rate;  $P_T T_2 / N_0$  and  $R_2 / R_1$  are parameters;  $m_1(t)$  is NRZ,  $m_2(t)$  is NRZ;  $R_2 \geq R_1$

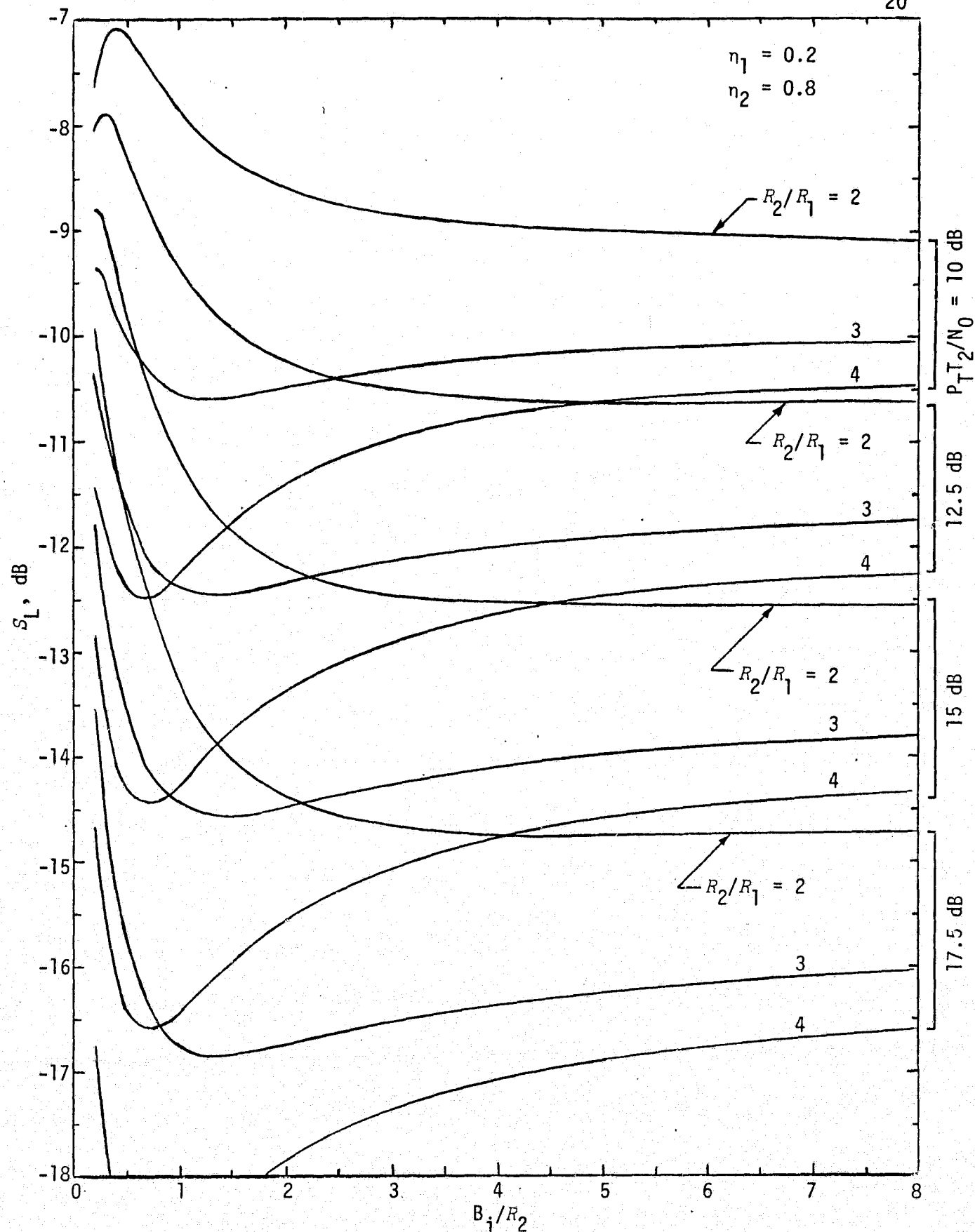


Figure 5a. Squaring Loss vs. Ratio of Arm Filter Bandwidth to High Data Rate;  $P_{T2}/N_0$  and  $R_2/R_1$  are parameters;  $m_1(t)$  is Manchester code,  $m_2(t)$  is NRZ;  $R_2 \geq 2R_1$

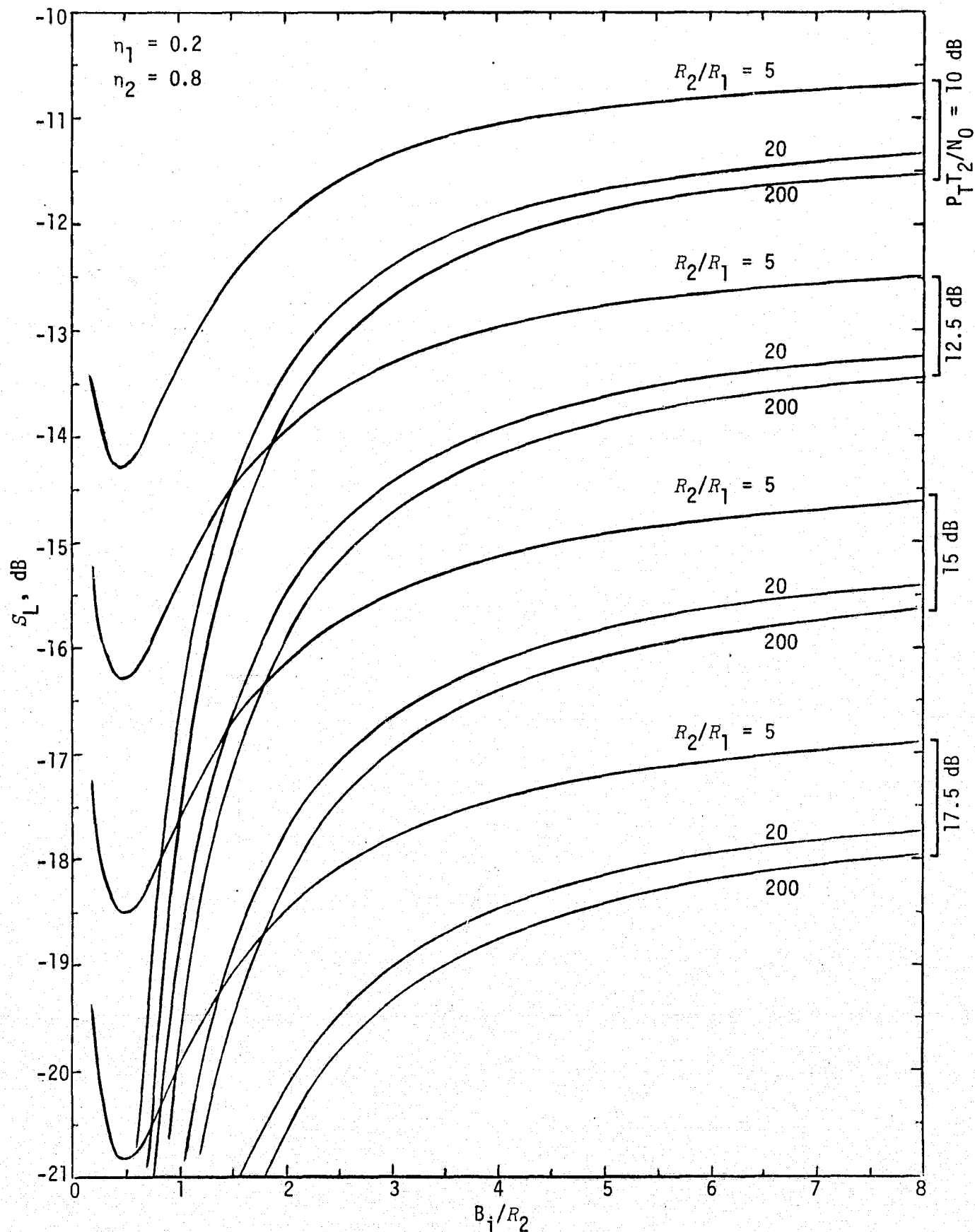


Figure 5b. Squaring Loss vs. Ratio of Arm Filter Bandwidth to High Data Rate;  $P_T T_2 / N_0$  and  $R_2 / R_1$  are parameters;  $m_1(t)$  is Manchester code,  $m_2(t)$  is NRZ;  $R_2 \geq 2R_1$

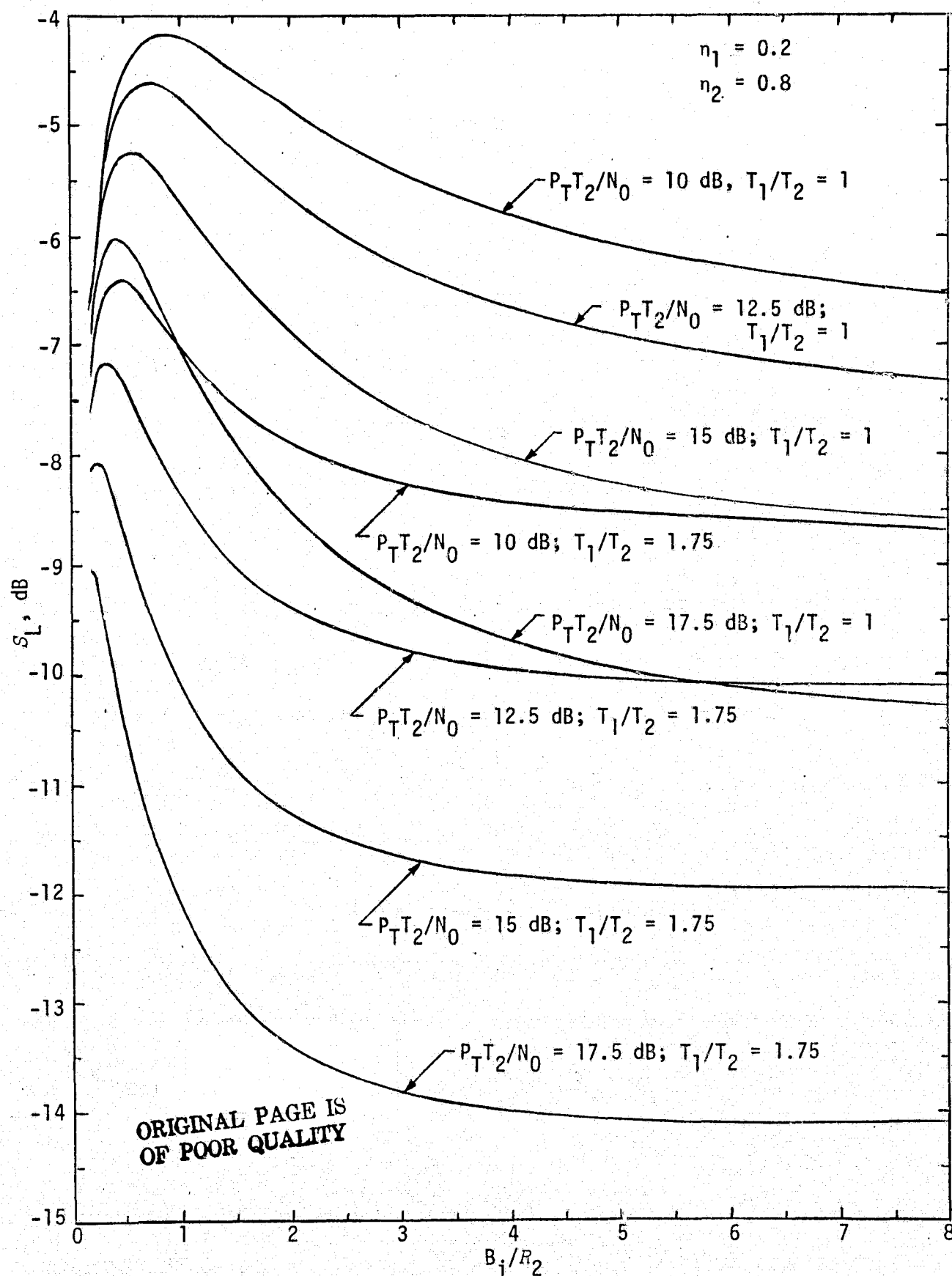


Figure 6. Squaring Loss vs. Ratio of Arm Filter Bandwidth to High Data Rate;  $P_T T_2/N_0$  and  $R_2/R_1$  are parameters;  $m_1(t)$  is Manchester code,  $m_2(t)$  is NRZ;  $R_1 \leq R_2 \leq 2R_1$

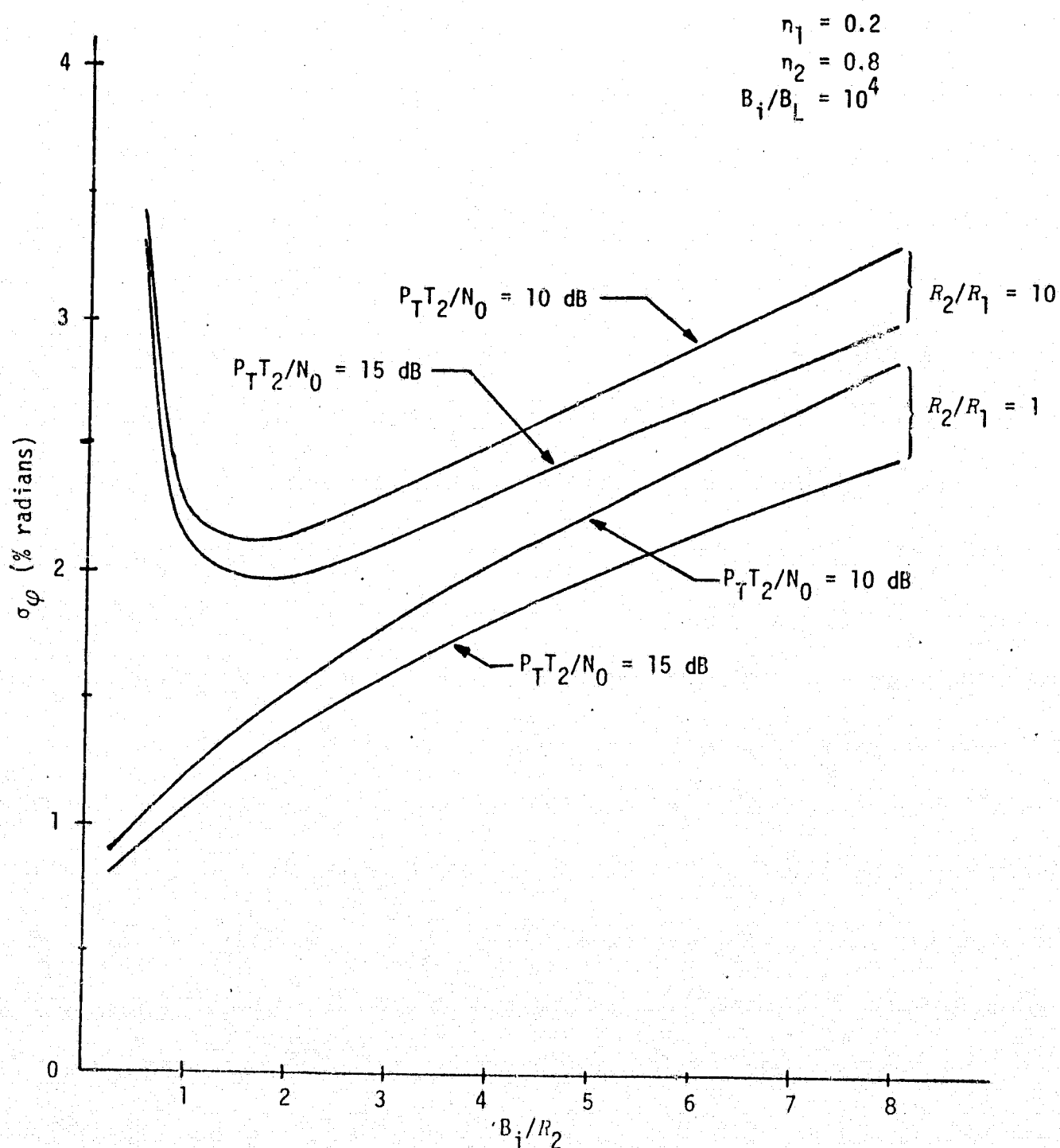


Figure 7. Tracking Jitter Standard Deviation versus the Ratio of Arm Filter Bandwidth to High Data Rate;  $P_T T_2/N_0$  and  $R_2/R_1$  are parameters;  $m_1(t)$  is NRZ,  $m_2(t)$  is NRZ;  $R_2 \geq R_1$ .

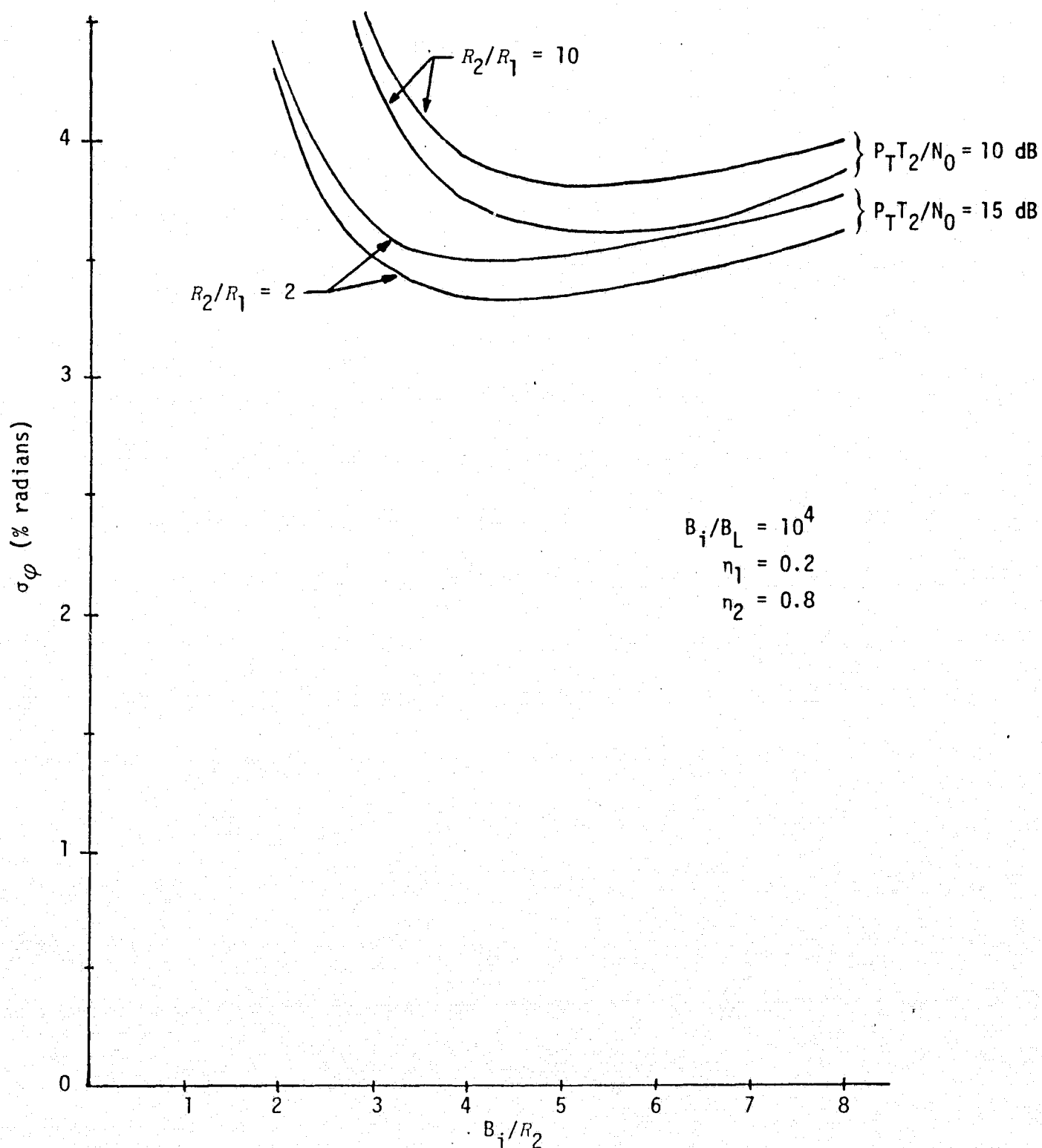


Figure 8. Tracking Jitter Standard Deviation versus Ratio of Arm Filter Bandwidth to High Data Rate;  $P_T T_2/N_0$  and  $R_2/R_1$  are parameters;  $m_1(t)$  is Manchester code,  $m_2(t)$  is Manchester code;  $R_2 \geq R_1$ .

C-3



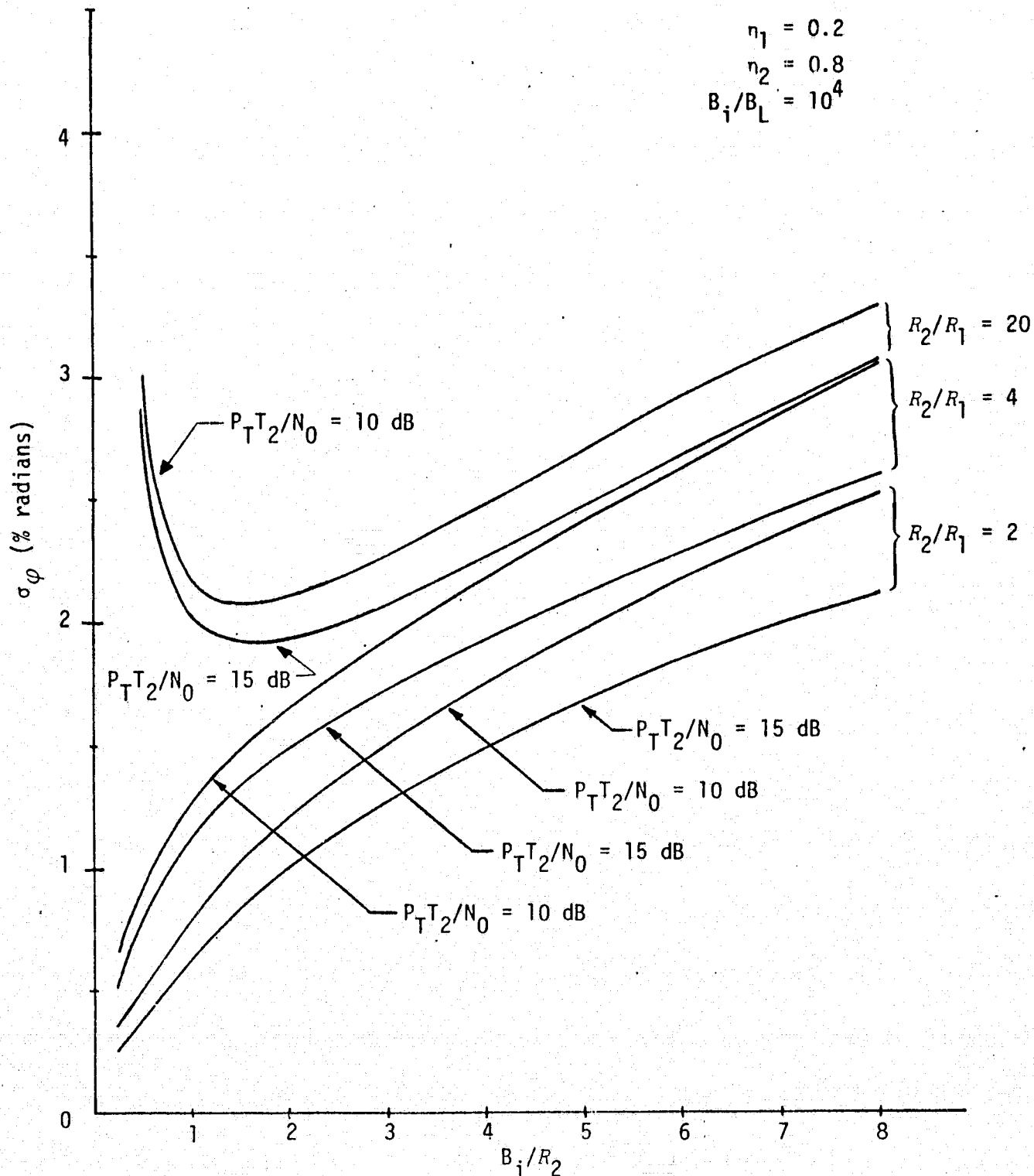


Figure 9. Tracking Jitter Standard Deviation versus Ratio of Arm Filter Bandwidth to High Data Rate;  $P_T T_2 / N_0$  and  $R_2 / R_1$  are parameters;  $m_1(t)$  is Manchester code,  $m_2(t)$  is NRZ;  $R_2 \geq R_1$ .

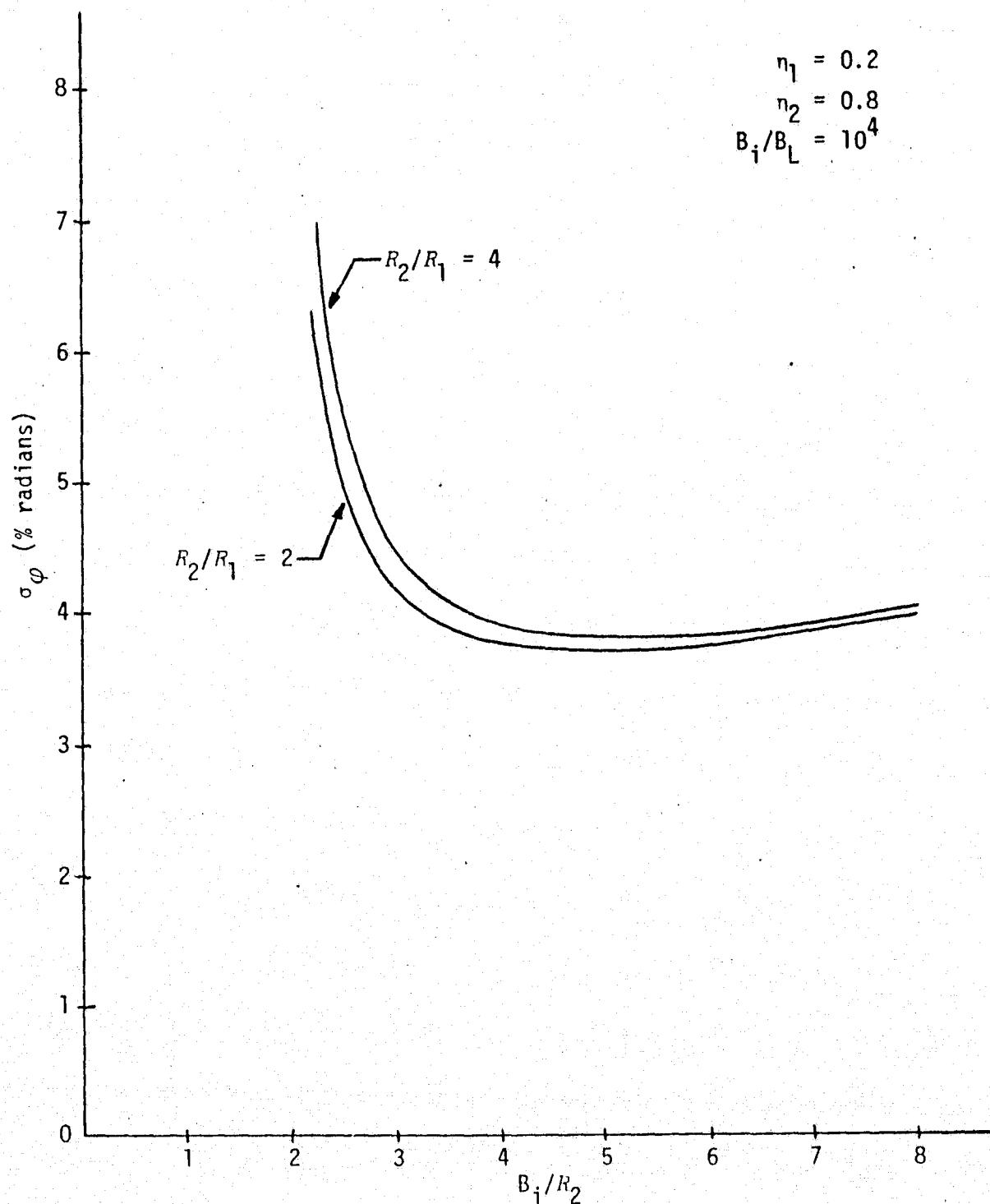


Figure 10. Tracking Jitter Standard Deviation versus Ratio of Arm Filter Bandwidth to High Data Rate;  $P_{T2}/N_0 = 10$  dB,  $R_2/R_1$  is a parameter;  $m_1(t)$  is NRZ,  $m_2(t)$  is Manchester code;  $R_2 \geq R_1$ .

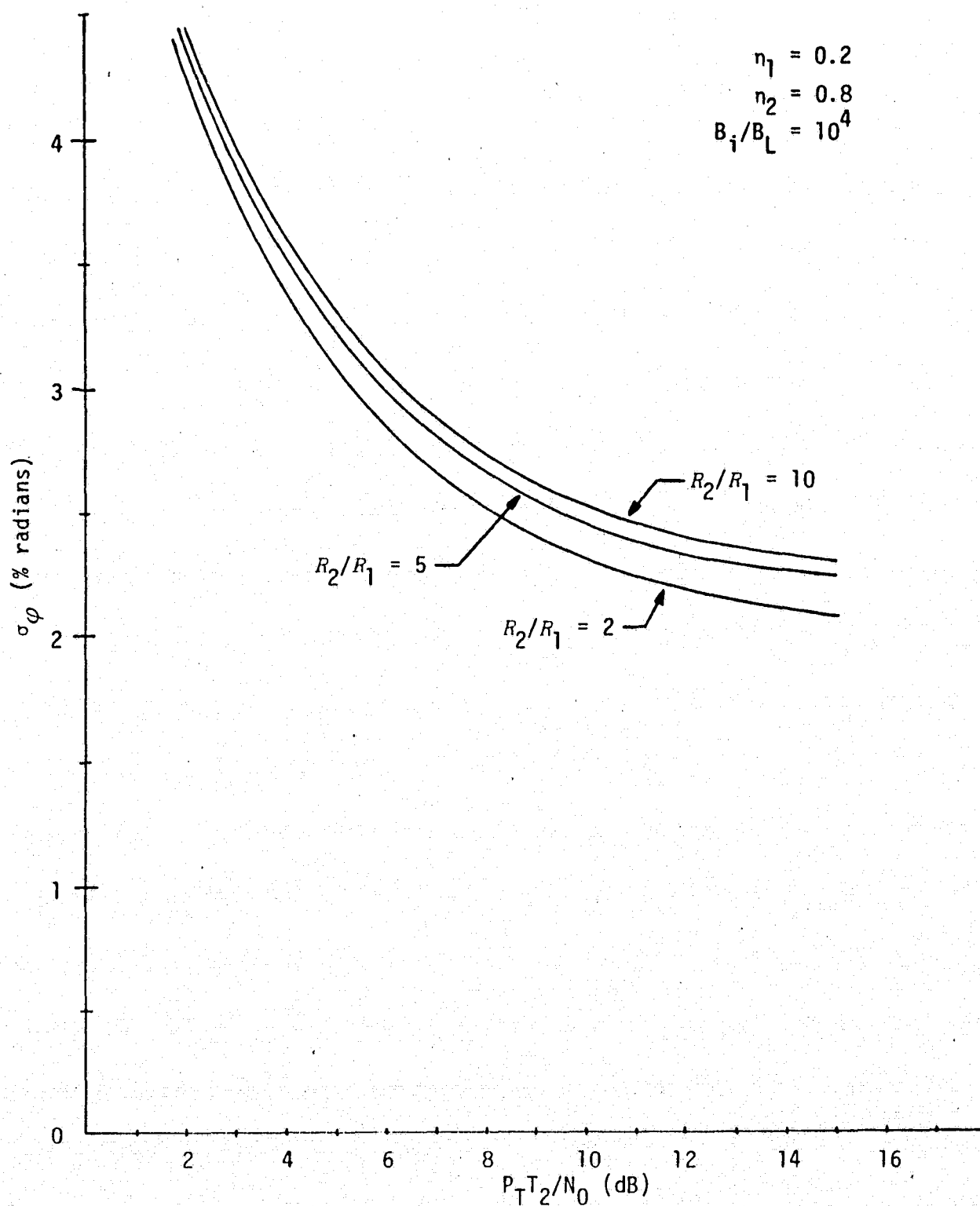


Figure 11. Tracking Jitter Standard Deviation versus  $P_T T_2 / N_0$ ;  $B_i/R_2 = 4$ ;  $R_2/R_1$  is a parameter;  $m_1(t)$  is NRZ,  $m_2(t)$  is NRZ;  $R_2 \geq R_1$ .

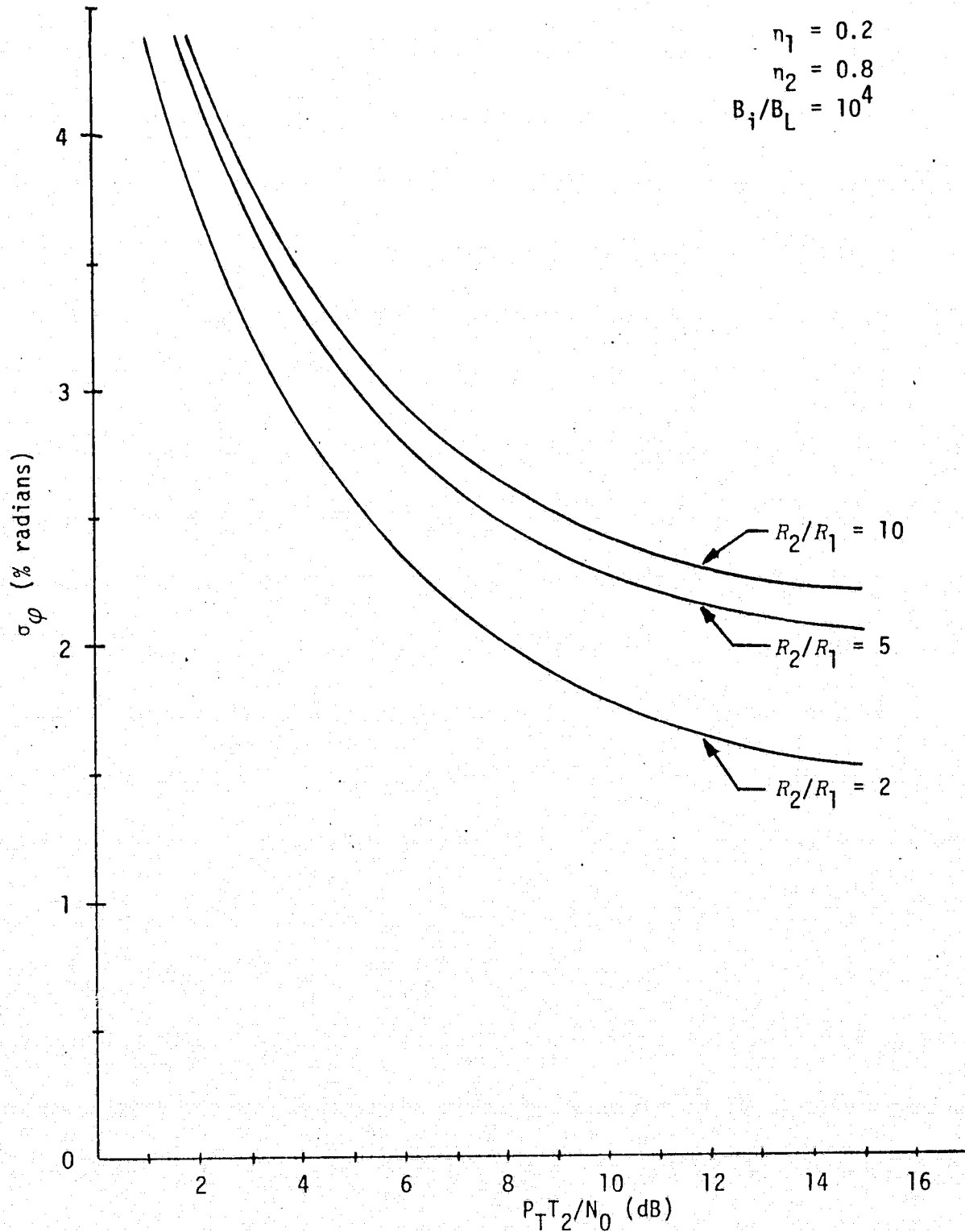


Figure 12. Tracking Jitter Standard Deviation versus  $P_T T_2 / N_0$ ;  $B_i/R_2 = 4$ ;  $R_2/R_1$  is a parameter;  $m_1(t)$  is Manchester code,  $m_2(t)$  is NRZ;  $R_2 \geq R_1$ .

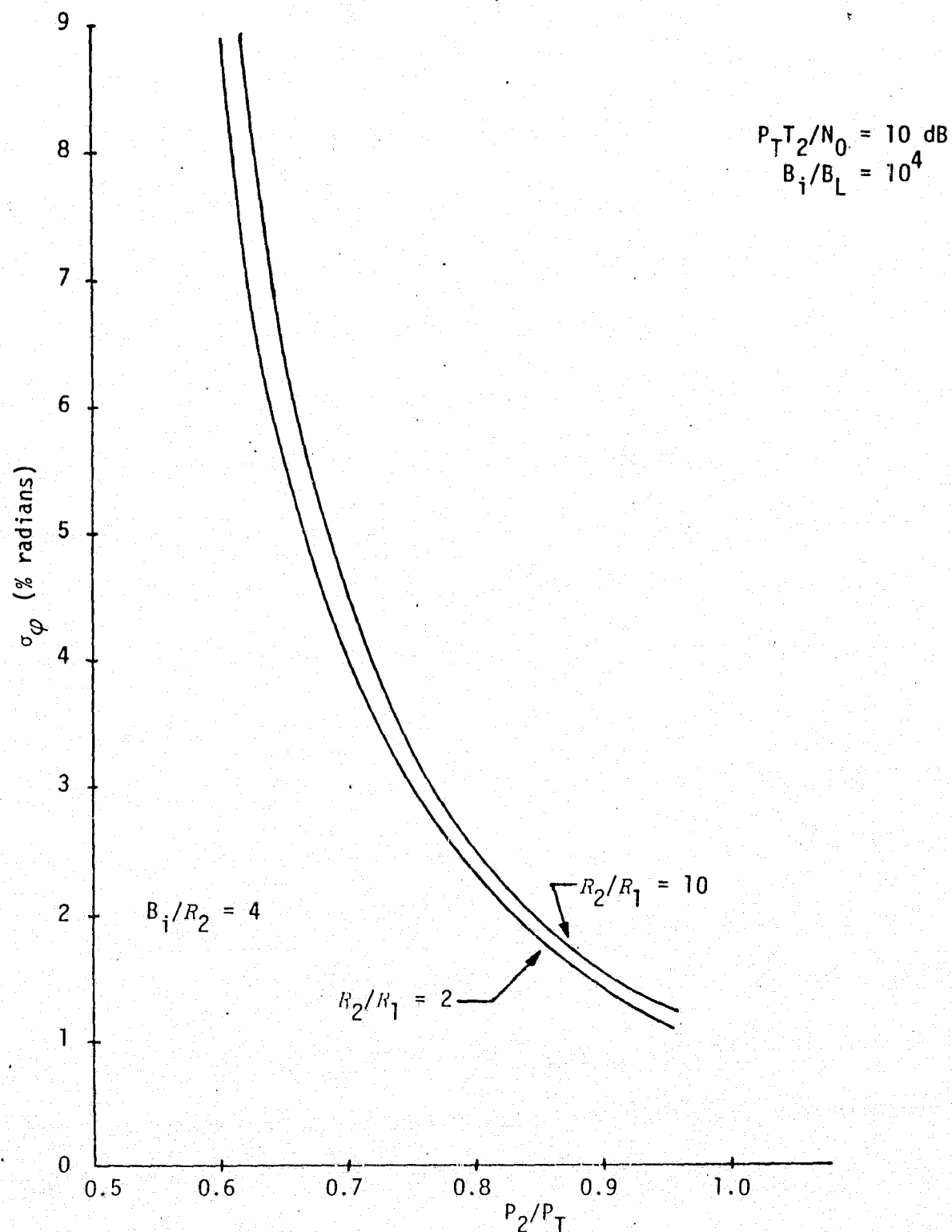


Figure 13. Tracking Jitter Standard Deviation versus  $P_2 / P_T$ ;  $R_2 / R_1$  is a parameter;  $m_1(t)$  is NRZ,  $m_2(t)$  is NRZ;  $R_2 \geq R_1$ .

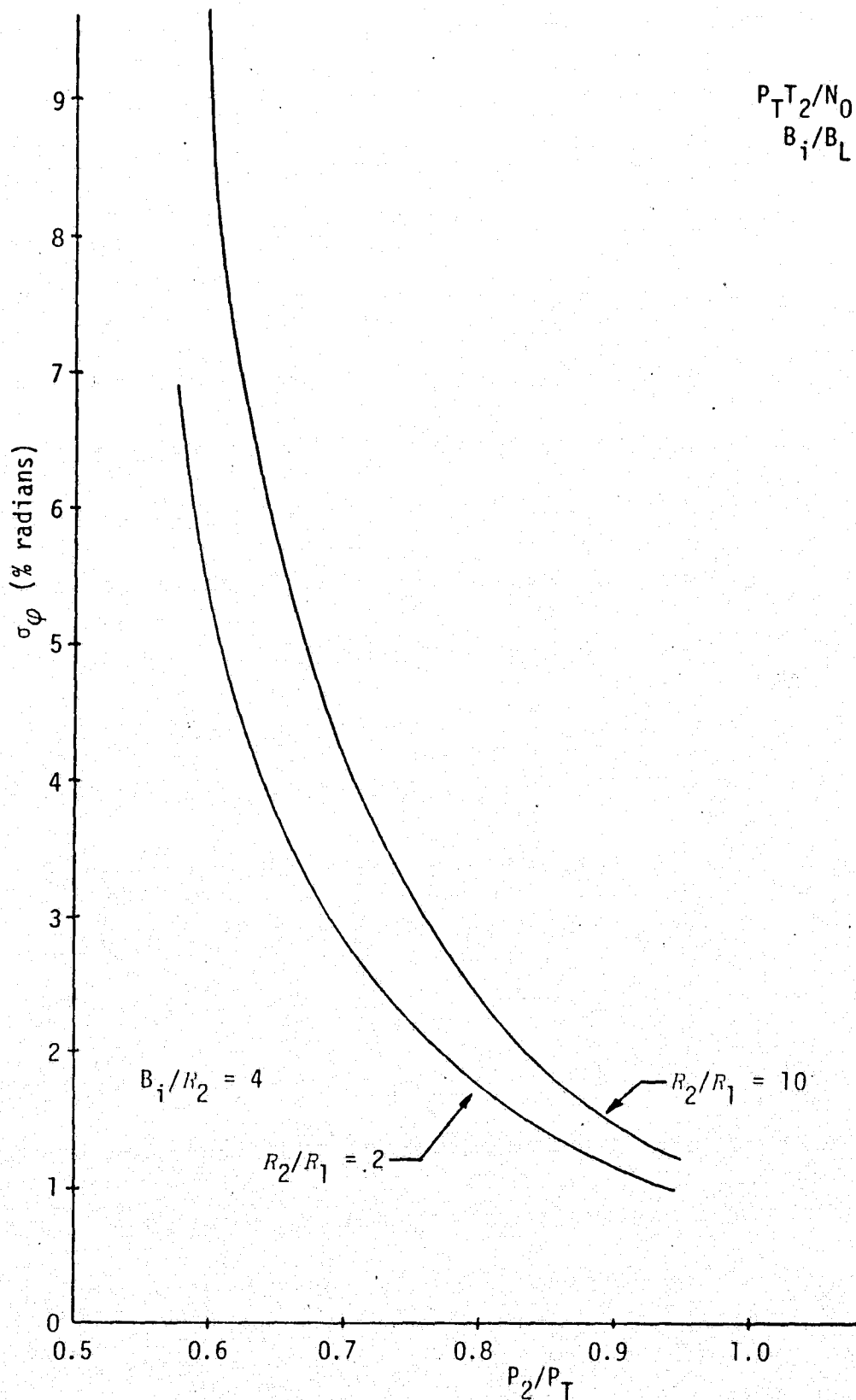


Figure 14. Tracking Jitter Standard Deviation versus  $P_2/P_T$ ;  $R_2/R_1$  is a parameter;  $m_1(t)$  is Manchester code,  $m_2(t)$  is NRZ;  $R_2 \geq R_1$ .

## REFERENCES

1. C. L. Weber. "Candidate Receivers for Unbalanced QPSK," 1976 ITC Proceedings, Vol. XII, pp. 455-464.
2. B. K. Levitt, J. R. Lesh, and J. C. Springett. "Shuttle/TDRSS Ku-Band Telemetry Study," Final Report 900-742, Jet Propulsion Laboratory, Pasadena, California, April 5, 1976.
3. M. K. Simon and W. C. Lindsey. "Optimum Performance of Suppressed Carrier Receivers with Costas Loop Tracking," IEEE Transactions on Communications, Vol. COM-25, No. 2, February 1977, pp. 215-226.
4. W. C. Lindsey and M. K. Simon. "Optimum Design and Performance of Costas Receivers Containing Soft Bandpass Limiters," IEEE Transactions on Communications, special issue on Spread Spectrum Communications, Vol. COM-25, No. 8, August 1977, pp. 822-831.
5. M. K. Simon and W. K. Alem. "Subcarrier Tracking Analysis for Three-Channel Orbiter Ku-Band Return Link," Axiomatix Report No. R7707-4, July 28, 1977.
6. L. Franks. Signal Theory. Englewood Cliffs, N.J.: Prentice-Hall, Inc., 1969.

## APPENDIX F

### TRACKING PERFORMANCE OF UNBALANCED QPSK DEMODULATORS PART II - BIPHASE COSTAS LOOP WITH ACTIVE ARM FILTERS



## APPENDIX F

### TRACKING PERFORMANCE OF UNBALANCED QPSK DEMODULATORS PART II - BIPHASE COSTAS LOOP WITH ACTIVE ARM FILTERS

by

Marvin K. Simon

#### INTRODUCTION

In Part I, we investigated the performance of a biphase Costas loop with passive arm filters insofar as its ability to track an unbalanced QPSK type modulation. In a previous Costas loop study for biphase modulation [1], it was demonstrated that considerable improvement in tracking performance could be obtained by employing active arm filters of the integrate-and-dump type as opposed to passive arm filters. The purpose of this part, then, is to investigate whether a similar performance improvement can be obtained for an unbalanced QPSK modulation.

Before going into the details of such an investigation, we point out that the use of active arm filters in a Costas loop carries with it the assumption that symbol synchronization of the two data streams is known. This assumption, namely, that symbol synchronization be available before carrier synchronization, appears to involve one of those unstable situations in which carrier acquisition cannot be achieved without first having symbol synchronization, and vice versa. If, however, the range of frequencies over which the carrier loop must be acquired is kept small (on the order of the data rate or less) by doppler correction, then the presence of the beat note, which causes the symbol synchronization input to be amplitude modulated by the cosine of the carrier loop phase error, does not destroy the information carried in the symbol transitions from which the synchronization clock is extracted. Hence, for a maximum frequency uncertainty less than the data symbol rate, the symbol synchronizer can be designed to acquire rapidly as the carrier VCO is swept through the region around the zero beat frequency. Thus, a coarse estimate of symbol synchronization is obtained before we have actually acquired the carrier loop or the lock detector has decided to kill the sweep.

## SYSTEM MODEL AND LOOP EQUATION OF OPERATION

To avoid the duplication of effort, we shall, in this section, draw heavily upon the notation, definitions, and results given in Part I. Consider the Costas loop with integrate-and-dump arm filters illustrated in Figure 1, where again the input  $x(t)$  is an unbalanced QPSK signal plus bandlimited Gaussian noise of constant spectral density. Then, by analogy with (5) of Part I, the arm filter outputs are now given by

$$\begin{aligned} z_s(t) &= K_1 K_m T_2 [\sqrt{P_2} \tilde{m}_2(t) - \tilde{N}_s(t)] \cos \varphi(t) \\ &\quad - K_1 K_m T_2 [\sqrt{P_1} \tilde{m}_1(t) + \tilde{N}_c(t)] \sin \varphi(t) \\ z_c(t) &= K_1 K_m T_2 [\sqrt{P_2} \tilde{m}_2(t) - \tilde{N}_s(t)] \sin \varphi(t) \\ &\quad + K_1 K_m T_2 [\sqrt{P_1} \tilde{m}_1(t) + \tilde{N}_c(t)] \cos \varphi(t); \\ &\quad (k-1)T_2 \leq t \leq kT_2, \end{aligned} \quad (1)$$

where\*

$$\begin{aligned} \tilde{m}_i(t) &\triangleq \frac{1}{T_2} \int_{(k-1)T_2}^{kT_2} m_i(t) p_2[t - (k-1)T_2] dt; \quad i=1,2 \\ \tilde{N}_s(t) &\triangleq \frac{1}{T_2} \int_{(k-1)T_2}^{kT_2} N_s(t) p_2[t - (k-1)T_2] dt \\ \tilde{N}_c(t) &\triangleq \frac{1}{T_2} \int_{(k-1)T_2}^{kT_2} N_c(t) p_2[t - (k-1)T_2] dt; \\ &\quad (k-1)T_2 \leq t \leq kT_2, \end{aligned} \quad (2)$$

and  $p_i(t)$ ,  $i=1,2$ , is the basic unit power symbol pulse in the  $i$ th data stream defined to be nonzero only on the interval  $(0, T_i)$ .

Forming the product of  $z_c(t)$  and  $z_s(t)$ , gives the dynamic error signal,

---

\* We assume here, as in Part I, that  $R_2 \geq R_1$  ( $T_2 \leq T_1$ ) and that the integrate-and-dump arm filters are identically designed to accommodate the higher data rate signal.

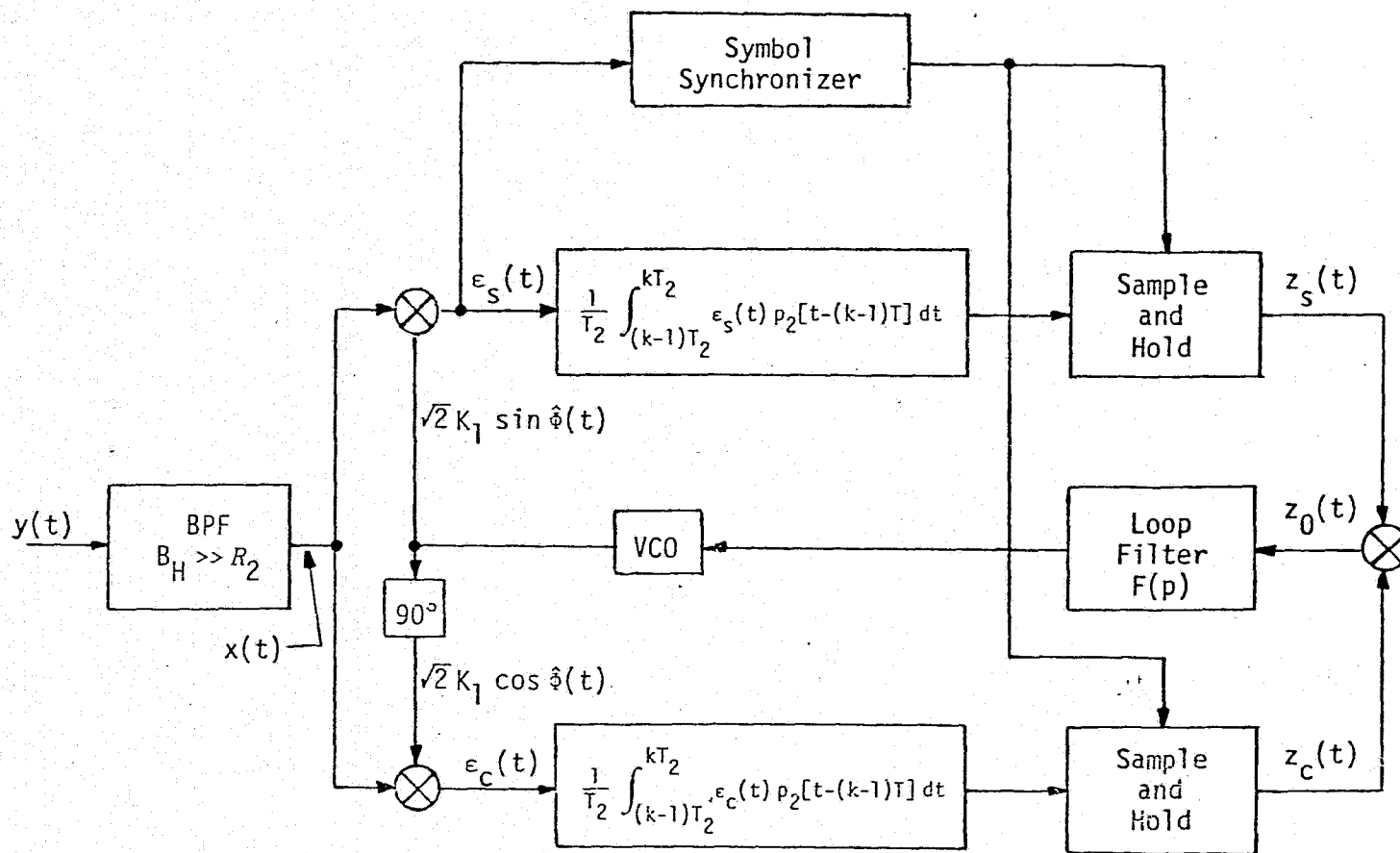


Figure 1. Costas Loop With Active Arm Filters

ORIGINAL PAGE IS  
OF POOR QUALITY

$$z_0(t) = z_c(t) z_s(t) = \frac{K_1^2 K_m^2 T_2^2}{2} \left\{ \left[ P_2 \overline{\tilde{m}_2^2(t)} - P_1 \overline{\tilde{m}_1^2(t)} \right] \sin 2\varphi(t) + 2 \sqrt{P_1 P_2} \overline{\tilde{m}_1(t) \tilde{m}_2(t)} \cos 2\varphi(t) + N_e[t, 2\varphi(t)] \right\} \quad (3)$$

where the total equivalent noise  $N_e[t, 2\varphi(t)]$  is defined by

$$\begin{aligned} N_e[t, 2\varphi(t)] = & [\tilde{N}_s^2(t) - \tilde{N}_c^2(t) - 2\sqrt{P_2} \tilde{m}_2(t) \tilde{N}_s(t) - 2\sqrt{P_1} \tilde{m}_1(t) \tilde{N}_c(t)] \sin 2\varphi(t) \\ & + [2\sqrt{P_2} \tilde{m}_2(t) \tilde{N}_c(t) - 2\sqrt{P_1} \tilde{m}_1(t) \tilde{N}_s(t) - 2\tilde{N}_c(t) \tilde{N}_s(t)] \cos 2\varphi(t) \\ & + \left\{ P_2 [\tilde{m}_2^2(t) - \overline{\tilde{m}_2^2(t)}] - P_1 [\tilde{m}_1^2(t) - \overline{\tilde{m}_1^2(t)}] \right\} \sin 2\varphi(t) \\ & + 2\sqrt{P_1 P_2} [\tilde{m}_1(t) \tilde{m}_2(t) - \overline{\tilde{m}_1(t) \tilde{m}_2(t)}] \cos 2\varphi(t). \quad (4) \end{aligned}$$

In (3) and (4), the overbar denotes statistical expectation and  $\langle \rangle$  denotes time average. Since the VCO phase estimate  $\hat{\theta}(t)$  is related to  $z_0(t)$  via

$$\hat{\theta}(t) = \frac{K_V F(p)}{p} z_0(t), \quad (5)$$

then the stochastic equation of loop operation becomes\*

$$\begin{aligned} 2p\varphi = & -KF(p) \left\{ T_2^2 \left[ P_2 \overline{\tilde{m}_2^2(t)} - P_1 \overline{\tilde{m}_1^2(t)} \right] \sin 2\varphi + 2T_2^2 \sqrt{P_1 P_2} \overline{\tilde{m}_1(t) \tilde{m}_2(t)} \cos 2\varphi + T_2^2 N_e(t, 2\varphi) \right\} \quad (6) \end{aligned}$$

where  $K \triangleq K_V K_1^2 K_m^2$ .

Since the digital modulations can be expressed in the form

$$m_i(t) = \sum_{n=-\infty}^{\infty} a_{ni} p_i(t - nT_i); \quad i=1,2 \quad (7)$$

---

\*For simplicity of notation, we drop the dependence of  $\varphi$  on the time variable  $t$ .

where  $a_{ni}$  is the polarity ( $\pm 1$ ) of the  $n$ th data symbol in the  $i$ th data stream, then assuming that the  $a_{n1}$ 's and  $a_{n2}$ 's are independent, we have from (2) and (7) that

$$\langle \tilde{m}_1(t) \tilde{m}_2(t) \rangle = 0. \quad (8)$$

Furthermore, the third term in (4) represents the self noise of the filtered modulations, which has been shown previously [1] to have a negligible effect on loop performance. Thus, ignoring these self-noise terms and using (8) in (4) and (6) gives the simplified results

$$2p\varphi = -KF(p) \left\{ T_2^2 \left[ P_2 \langle \tilde{m}_2^2(t) \rangle - P_1 \langle \tilde{m}_1^2(t) \rangle \right] \sin 2\varphi + T_2^2 N_e(t, 2\varphi) \right\} \quad (9)$$

where

$$\begin{aligned} N_e(t, 2\varphi) = & [\tilde{N}_s^2(t) - \tilde{N}_c^2(t) - 2\sqrt{P_2} \tilde{m}_2(t) \tilde{N}_s(t) - 2\sqrt{P_1} \tilde{m}_1(t) \tilde{N}_c(t)] \sin 2\varphi \\ & + [2\sqrt{P_2} \tilde{m}_2(t) \tilde{N}_c(t) - 2\sqrt{P_1} \tilde{m}_1(t) \tilde{N}_s(t) - 2\tilde{N}_c(t) \tilde{N}_s(t)] \cos 2\varphi \\ & + 2\sqrt{P_1 P_2} \tilde{m}_1(t) \tilde{m}_2(t) \cos 2\varphi. \end{aligned} \quad (10)$$

Note that the first two terms of the total equivalent noise in (10) represent the traditional signal  $\times$  noise and noise  $\times$  noise terms characteristic of the error signal in Costas loops. The third term of (10) corresponds to the cross-modulation noise of the two data symbol streams.

Linearizing the loop, we have that

$$2\varphi = H_{2\varphi}(p) \left[ \frac{N_e(t)}{P_2 \langle \tilde{m}_2^2(t) \rangle - P_1 \langle \tilde{m}_1^2(t) \rangle} \right] \quad (11)$$

where  $H_{2\varphi}(s)$  is the closed loop transfer function defined by

$$H_{2\varphi}(s) = \frac{[P_2 \langle \tilde{m}_2^2(t) \rangle - P_1 \langle \tilde{m}_1^2(t) \rangle] T_2^2 KF(s)}{s + [P_2 \langle \tilde{m}_2^2(t) \rangle - P_1 \langle \tilde{m}_1^2(t) \rangle] T_2^2 KF(s)} \quad (12)$$

Assuming that the loop noise bandwidth  $B_L$  is much narrower than the noise bandwidth of  $N_e(t)$ , the variance of  $2\varphi$  can be approximated by

$$\sigma_{2\varphi}^2 = \frac{N_e' B_L}{\left[ P_2 \langle \tilde{m}_2^2(t) \rangle - P_1 \langle \tilde{m}_1^2(t) \rangle \right]^2} \quad (13)$$

where

$$2B_L = \frac{1}{2\pi j} \int_{-j\infty}^{j\infty} H_{2\varphi}(s) H_{2\varphi}(-s) ds \quad (14)$$

and

$$N_e' \triangleq 2 \int_{-\infty}^{\infty} \langle R_{N_e}(t, t+\tau) \rangle d\tau \quad (15)$$

with  $R_{N_e}(t, t+\tau)$  denoting the autocorrelation function of  $N_e(t)$ , i.e.,

$$R_{N_e}(t, t+\tau) \triangleq \overline{N_e(t) N_e(t+\tau)}. \quad (16)$$

#### TRACKING PERFORMANCE - THE CASE OF SYNCHRONIZED SYMBOL CLOCKS

We assume first that the two data clocks are synchronous in that they both have a positive-going pulse starting at  $t=0$  and their pulse repetition frequencies are integrally related, i.e.,

$$\gamma_T \triangleq \frac{T_1}{T_2} = n, \quad (17)$$

where  $n \geq 1$  is an integer. Since from (2),  $\tilde{m}_2(t)$  is the output of a matched filter matched to the basic pulse shape of  $m_2(t)$ , then regardless of the data formats of  $m_1(t)$  and  $m_2(t)$ , we have from (7) that

$$\overline{\langle \tilde{m}_2^2(t) \rangle} = 1. \quad (18)$$

On the other hand, evaluation of  $\overline{\langle \tilde{m}_1^2(t) \rangle}$  depends quite heavily on the data formats of  $m_1(t)$  and  $m_2(t)$ . For example, if  $m_1(t)$  is NRZ data and  $m_2(t)$  is Manchester coded data, then

$$\begin{aligned} p_1(t) &= \begin{cases} 1; & 0 \leq t \leq T_1 \\ 0; & \text{otherwise} \end{cases} \\ p_2(t) &= \begin{cases} 1; & 0 \leq t \leq T_2/2 \\ -1; & T_2/2 \leq t \leq T_2 \end{cases} \end{aligned} \quad (19)$$

and

$$\langle \tilde{m}_1^2(t) \rangle = 0. \quad (20)$$

If both  $m_1(t)$  and  $m_2(t)$  are NRZ data, then

$$\langle \tilde{m}_1^2(t) \rangle = 1. \quad (21)$$

These results, together with those for the remaining combinations of formats for  $m_1(t)$  and  $m_2(t)$ , are given in Table 1 below.

Table 1. Evaluation of  $\langle \tilde{m}_1^2(t) \rangle$ ;  $T_1/T_2 = n$

	$m_2(t)$	
	Manchester	NRZ
$m_1(t)$	0 ; $n \geq 2$ 1 ; $n = 1$	1 ; $n$ even $\frac{n-1}{n}$ ; $n$ odd
	NRZ	0 1

Since we have assumed a linear system in writing (13), then insofar as computing the equivalent noise spectral density  $N_e'$ , we may set  $\sin^2 2\varphi = 0$  and  $\cos^2 2\varphi = 1$  in (10). Doing so, we get the simplified result

$$\begin{aligned} N_e(t,0) &= 2\sqrt{P_2} \tilde{m}_2(t) \tilde{N}_c(t) - 2\sqrt{P_1} \tilde{m}_1(t) \tilde{N}_s(t) \\ &\quad - 2\tilde{N}_c(t) \tilde{N}_s(t) + 2\sqrt{P_1 P_2} \tilde{m}_1(t) \tilde{m}_2(t). \end{aligned} \quad (22)$$

Taking the autocorrelation function of the nonstationary process  $N_e(t,0)$  and averaging the resulting expression over  $t$  yields

$$\begin{aligned} \langle R_{N_e}(t,t+\tau) \rangle &= 4 \left[ P_2 \langle \tilde{R}_{\tilde{m}_2 \tilde{N}_c}(t,t+\tau) \rangle + P_1 \langle \tilde{R}_{\tilde{m}_1 \tilde{N}_s}(t,t+\tau) \rangle \right. \\ &\quad \left. + \langle \tilde{R}_{\tilde{N}_c \tilde{N}_s}(t,t+\tau) \rangle + P_1 P_2 \langle \tilde{R}_{\tilde{m}_1 \tilde{m}_2}(t,t+\tau) \rangle \right], \end{aligned} \quad (23)$$

where

$$\begin{aligned}
 \langle \tilde{R}_{\tilde{m}_2 \tilde{N}_c}(t, t+\tau) \rangle &\triangleq \langle \tilde{m}_2(t) \tilde{N}_c(t) \tilde{m}_2(t+\tau) \tilde{N}_c(t+\tau) \rangle \\
 \langle \tilde{R}_{\tilde{m}_1 \tilde{N}_s}(t, t+\tau) \rangle &\triangleq \langle \tilde{m}_1(t) \tilde{N}_s(t) \tilde{m}_1(t+\tau) \tilde{N}_s(t+\tau) \rangle \\
 \langle \tilde{R}_{\tilde{N}_c \tilde{N}_s}(t, t+\tau) \rangle &\triangleq \langle \tilde{N}_c(t) \tilde{N}_s(t) \tilde{N}_c(t+\tau) \tilde{N}_s(t+\tau) \rangle \\
 \langle \tilde{R}_{\tilde{m}_1 \tilde{m}_2}(t, t+\tau) \rangle &\triangleq \langle \tilde{m}_1(t) \tilde{m}_2(t) \tilde{m}_1(t+\tau) \tilde{m}_2(t+\tau) \rangle
 \end{aligned} \quad (24)$$

Since, from the definitions in (2), the noise processes  $\tilde{N}_c(t), \tilde{N}_s(t)$  and the signal processes  $\tilde{m}_1(t), \tilde{m}_2(t)$  are piecewise constant over a  $T_2$ -second interval, then

$$\begin{aligned}
 \langle \tilde{R}_{\tilde{m}_2 \tilde{N}_c}(t, t+\tau) \rangle &= \begin{cases} \sigma_{\tilde{m}_2}^2 \sigma_{\tilde{N}_c}^2 (1 - \frac{|\tau|}{T_2}); & |\tau| \leq T_2 \\ 0; & |\tau| > T_2 \end{cases} \\
 \langle \tilde{R}_{\tilde{m}_1 \tilde{N}_s}(t, t+\tau) \rangle &= \begin{cases} \sigma_{\tilde{m}_1}^2 \sigma_{\tilde{N}_s}^2 (1 - \frac{|\tau|}{T_2}); & |\tau| \leq T_2 \\ 0; & |\tau| > T_2 \end{cases} \\
 \langle \tilde{R}_{\tilde{N}_c \tilde{N}_s}(t, t+\tau) \rangle &= \begin{cases} \sigma_{\tilde{N}_c}^4 (1 - \frac{|\tau|}{T_2}); & |\tau| \leq T_2 \\ 0; & |\tau| > T_2 \end{cases} \\
 \langle \tilde{R}_{\tilde{m}_1 \tilde{m}_2}(t, t+\tau) \rangle &= \begin{cases} \sigma_{\tilde{m}_1}^2 \sigma_{\tilde{m}_2}^2 (1 - \frac{|\tau|}{T_2}); & |\tau| \leq T_2 \\ 0; & |\tau| > T_2 \end{cases}
 \end{aligned} \quad (25)$$

where

$$\sigma_{\tilde{N}}^2 = \langle \tilde{N}_c^2(t) \rangle = \langle \tilde{N}_s^2(t) \rangle = \frac{N_0}{2T_2}$$

$$\sigma_{\tilde{m}_2}^2 = \langle \tilde{m}_2^2(t) \rangle = 1 \quad (26a)$$

and

$$\sigma_{\tilde{m}_1}^2 = \langle \tilde{m}_1^2(t) \rangle$$

ORIGINAL PAGE IS  
OF POOR QUALITY

(26b)



is evaluated from Table 1. Substituting (25) and (26) into (23) yields

$$\langle R_{N_c}(t, t+\tau) \rangle = \begin{cases} 4 \left\{ \left[ P_2 + P_1 \sigma_{\tilde{m}_1}^2 \right] \frac{N_0}{2T_2} + \left( \frac{N_0}{2T_2} \right)^2 + P_1 P_2 \sigma_{\tilde{m}_1}^2 \right\} \left( 1 - \frac{|\tau|}{T_2} \right); & |\tau| \leq T_2 \\ 0; & |\tau| > T_2 \end{cases} \quad (27)$$

Finally, integrating (27) over  $\tau$  between  $-\infty$  and  $+\infty$  [see (15)] gives the equivalent noise spectral density

$$N_e' = 4 N_0 \left[ P_2 + P_1 \sigma_{\tilde{m}_1}^2 + \frac{N_0}{2T_2} + \frac{2 P_1 P_2 T_2}{N_0} \sigma_{\tilde{m}_1}^2 \right] \quad (28)$$

whereupon, from (13), the variance of the  $2\phi$  process becomes

$$\sigma_{2\phi}^2 = \frac{4 N_0 B_L}{(P_1 + P_2)} \left[ \frac{(P_1 + P_2)}{(P_2 - P_1 \sigma_{\tilde{m}_1}^2)^2} \right] \left[ P_2 + P_1 \sigma_{\tilde{m}_1}^2 + \frac{N_0}{2T_2} + \frac{2 P_1 P_2 T_2}{N_0} \sigma_{\tilde{m}_1}^2 \right] \quad (29)$$

Alternately,

$$\sigma_{2\phi}^2 = \frac{4}{\rho S_L}; \quad \rho \triangleq \frac{P_1 + P_2}{N_0 B_L} = \frac{P_T}{N_0 B_L}, \quad (30)$$

where  $S_L$  is the "squaring loss" defined by

$$S_L = \frac{(P_2 - P_1 \sigma_{\tilde{m}_1}^2)^2}{(P_1 + P_2) \left[ P_2 + P_1 \sigma_{\tilde{m}_1}^2 + \frac{N_0}{2T_2} + \frac{2 P_1 P_2 T_2}{N_0} \sigma_{\tilde{m}_1}^2 \right]} \quad (31)$$

In terms of the power ratio  $\gamma_P \triangleq P_1/P_2$ , (31) can be put into the final desired form

$$S_L = \frac{(1 - \gamma_P \sigma_{\tilde{m}_1}^2)^2}{(1 + \gamma_P) \left[ 1 + \gamma_P \sigma_{\tilde{m}_1}^2 + \frac{1 + \gamma_P}{2 R_{T2}} + \frac{2 \gamma_P R_{T2} \sigma_{\tilde{m}_1}^2}{1 + \gamma_P} \right]} \quad (32)$$

where, as in Part I,  $R_{T2} \triangleq (P_1 + P_2)T_2/N_0$  is the total power-to-noise ratio in the high data rate bandwidth. Note that, except for the dependence of  $\sigma_{\tilde{m}_1}^2$  on the data rate ratio  $R_2/R_1$  (see Table 1), the squaring

loss of (32) is, unlike the results in Part I for passive arm filters, independent of this ratio.

Figure 2 illustrates  $S_L$  versus  $\gamma_p$  with  $R_{T2}$  fixed at values typical of coded and uncoded systems, and  $\sigma_{\tilde{m}_1}^2$  as determined from Table 1 corresponding to the specific data formats of  $m_1(t)$  and  $m_2(t)$ . Note that, while the bi-phase Costas loop is unable to track a conventional balanced QPSK signal since, regardless of the value of  $R_{T2}$ ,  $S_L = 0$  when  $n = \gamma_p = 1$  and  $m_1(t)$  and  $m_2(t)$  are of the same format, it is indeed able to track a balanced QPSK-type signal in which  $m_1(t)$  and  $m_2(t)$  have identical data rates and powers but are not the same format. For example, if  $m_1(t)$  is NRZ and  $m_2(t)$  is Manchester coded, or vice versa, then when  $n = 1$ ,  $\sigma_{\tilde{m}_1}^2 = 0$ , and furthermore, when  $\gamma_p = 1$ , we have from (32) that

$$S_L = \frac{1}{2 \left[ 1 + \frac{1}{R_{T2}} \right]}. \quad (33)$$

#### TRACKING PERFORMANCE -- THE CASE OF UNSYNCHRONIZED SYMBOL CLOCKS

More often than not, the two data clocks will be unsynchronized since, typically, the two data streams are generated from totally independent sources. In this situation, there is, in general, no relation between the epochs of the synchronization pulses corresponding to the two data clocks and, furthermore, the ratio of the two data rates need not be an integer. Nevertheless, still assuming that the active arm filters are matched to the pulse shape  $p_2(t)$ , then  $\langle \tilde{m}_2^2(t) \rangle$  is again given by (18). Computation of  $\langle \tilde{m}_1^2(t) \rangle$  for the unsynchronized clock case is a bit more tedious than was the case for synchronized clocks. The nature of the mathematical model required is very much like that used in computing the cross-modulation distortion  $D_{12}$  in Part I. In fact, the results for  $\langle \tilde{m}_1^2(t) \rangle$  corresponding to the various data format combinations for  $m_1(t)$  and  $m_2(t)$  can be obtained directly by taking the limit of  $D_{12}/T_2$  as  $B_1/R_2$  approaches infinity [see equations (42), (50), (51), (52), for example]. These results are summarized in Table 2.

Thus, to compute the loop squaring loss for the unsynchronized clocks case, we use (32) with  $\sigma_{\tilde{m}_1}^2$  now determined from Table 2. Note that, in the limit as  $\gamma_T \rightarrow \infty$ , Table 1 and Table 2 are equivalent; i.e., for a sufficiently large ratio of data rates in the two channels, the loop

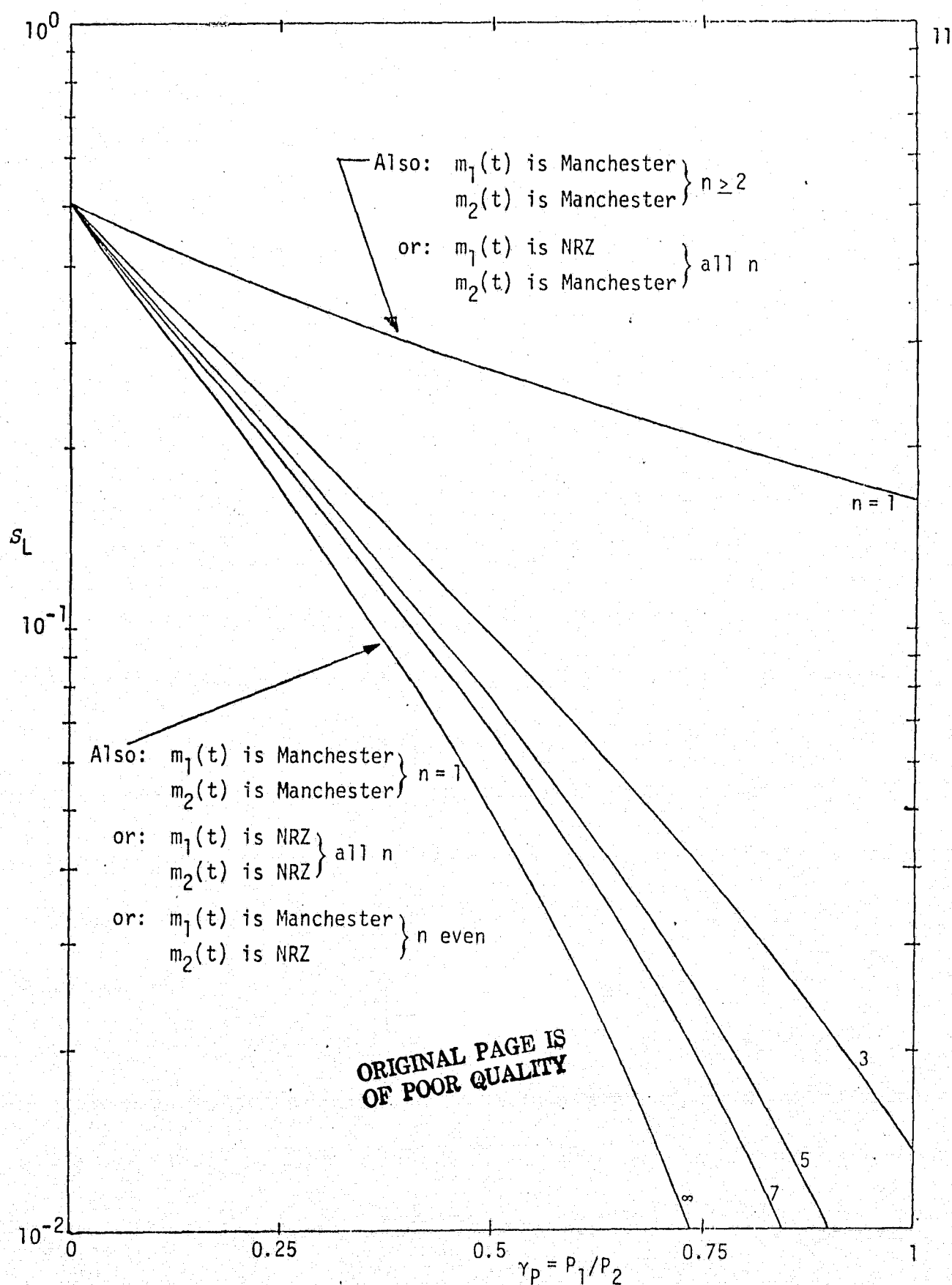


Figure 2a. Squaring Loss versus Ratio of Powers in the Two Data Channels With  $\gamma_T \triangleq T_1/T_2 = n$  as a Parameter;  $R_{T2} = -3$  dB;  $m_1(t)$  is Manchester,  $m_2(t)$  is NRZ;  $n$  odd; Synchronized Data Clocks

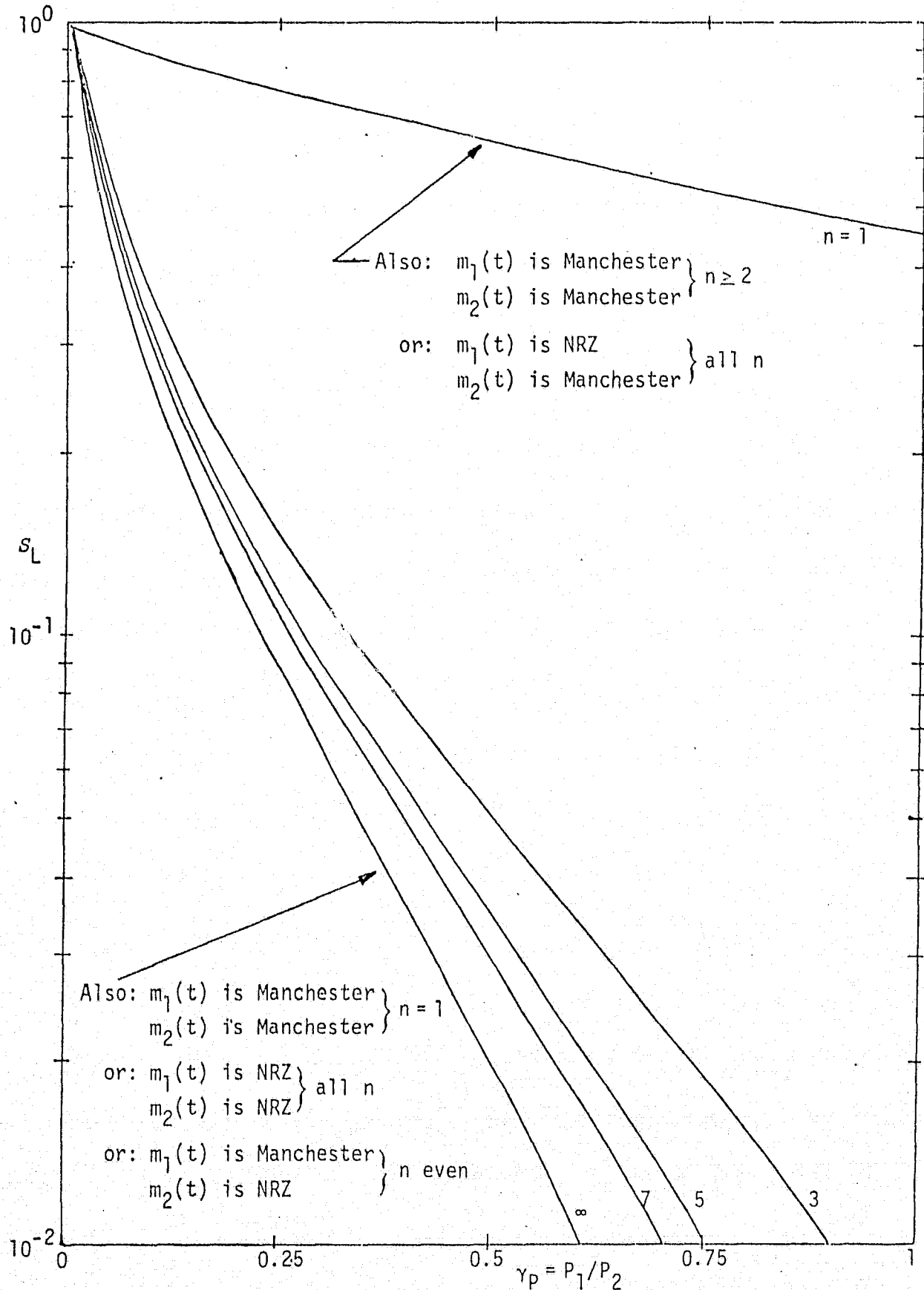


Figure 2b. Squaring Loss versus Ratio of Powers in the Two Data Channels With  $\gamma_T \triangleq T_1/T_2 = n$  as a Parameter;  $R_{T2} = 10$  dB;  $m_1(t)$  is Manchester,  $m_2(t)$  is NRZ;  $n$  odd; Synchronized Data Clocks

tracking performance is approximately the same for synchronized and unsynchronized clocks, as one would intuitively expect. Figures 3 through 6 illustrate  $S_L$  versus  $\gamma_P = P_1/P_2$ , with  $R_{T2} = P_T T_2/N_0$  fixed at the same values as in Figure 2. The curves are distinguished from one another by the formats of the modulations  $m_1(t)$  and  $m_2(t)$ . Note that, when the higher data rate modulation  $m_2(t)$  is Manchester coded, the squaring loss is significantly improved relative to when this same modulation is NRZ. Again, the reason for this stems from the fact that the active arm filters are matched to the pulse shape of  $m_2(t)$  which, for a Manchester code, results in much smaller values of  $\sigma_{\tilde{m}_1}^2$  (see Table 2) than for an NRZ pulse shape. It is important to note that, here again, as for the synchronized clock case, the bi-phase Costas loop is quite capable of tracking a balanced QPSK signal ( $\gamma_T = \gamma_P = 1$ ) when  $m_2(t)$  is Manchester coded.

Table 2. Evaluation of  $\langle \tilde{m}_1^2(t) \rangle$ ;  $T_1/T_2 \triangleq \gamma_T \geq 1$

		$m_2(t)$	
		Manchester	NRZ
$m_1(t)$	Manchester	$\frac{1}{6} [\gamma_T^2 - \frac{5}{\gamma_T} + 12 - 6\gamma_T];$ $R_1 \leq R_2 \leq 2R_1$	$\gamma_T - \frac{1}{6} \gamma_T^2 - 1 + \frac{1}{3\gamma_T};$ $R_1 \leq R_2 \leq 2R_1$
		$\frac{1}{2\gamma_T}; R_2 \geq 2R_1$	$1 - \frac{1}{\gamma_T}; R_2 \geq 2R_1$
	NRZ	$\frac{1}{6\gamma_T}$	$1 - \frac{1}{3\gamma_T}$

#### COMPARISON OF SQUARING LOSS PERFORMANCE - ACTIVE VERSUS PASSIVE ARM FILTERS

We are now in a position to answer the question raised in the first paragraph of the introduction, namely, is there a tracking performance improvement obtained by employing active integrate-and-dump arm filters as opposed to passive arm filters and, if so, how much. To begin this investigation, we borrow a result from Part I, namely, (28), which characterizes the loop squaring loss for passive arm filters. In terms of the

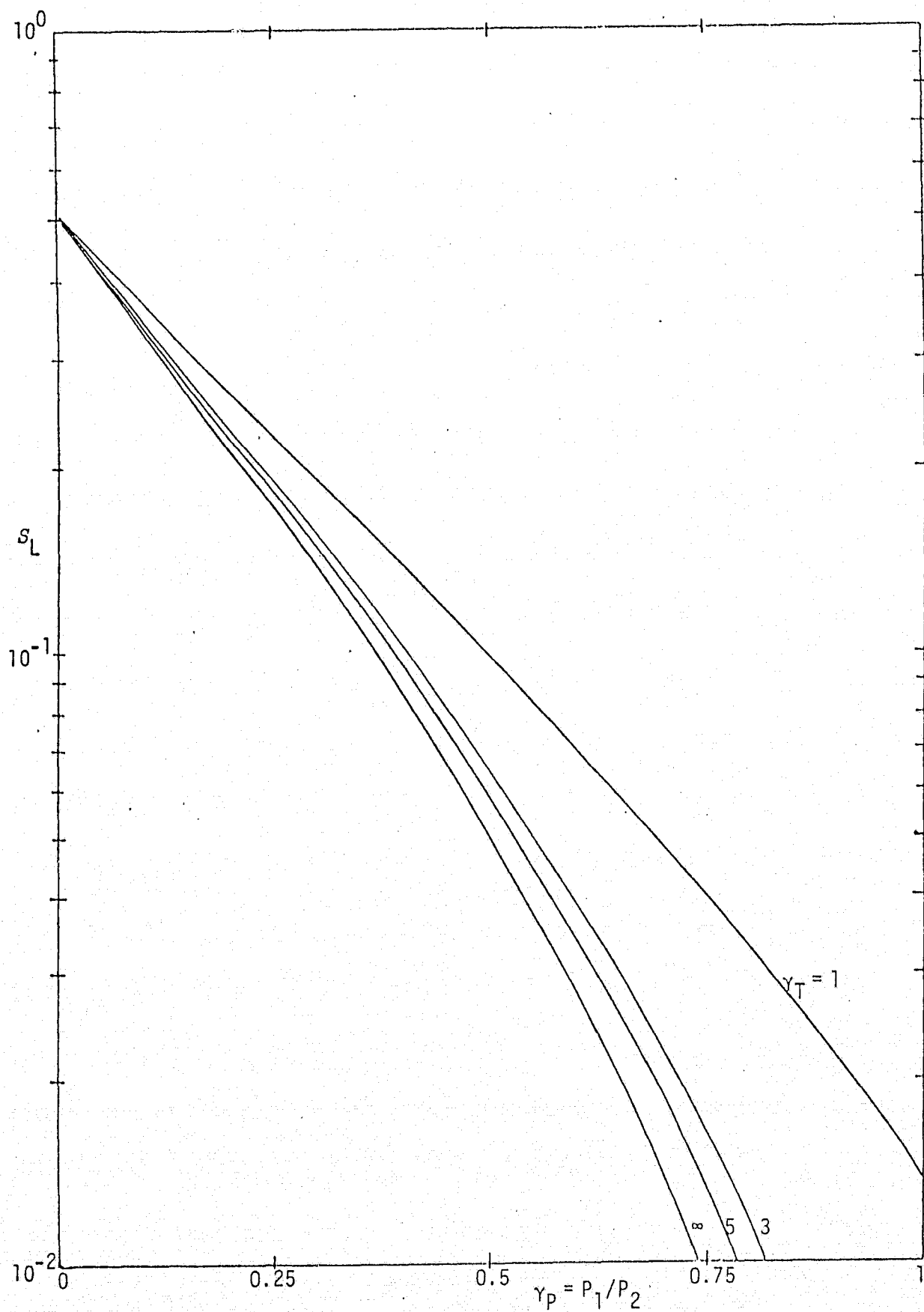


Figure 3a. Squaring Loss versus Ratio of Powers in the Two Data Channels With  $\gamma_T \triangleq T_1/T_2$  as a Parameter;  $R_{T2} = -3$  dB;  $m_1(t)$  is NRZ,  $m_2(t)$  is NRZ; Unsynchronized Data Clocks

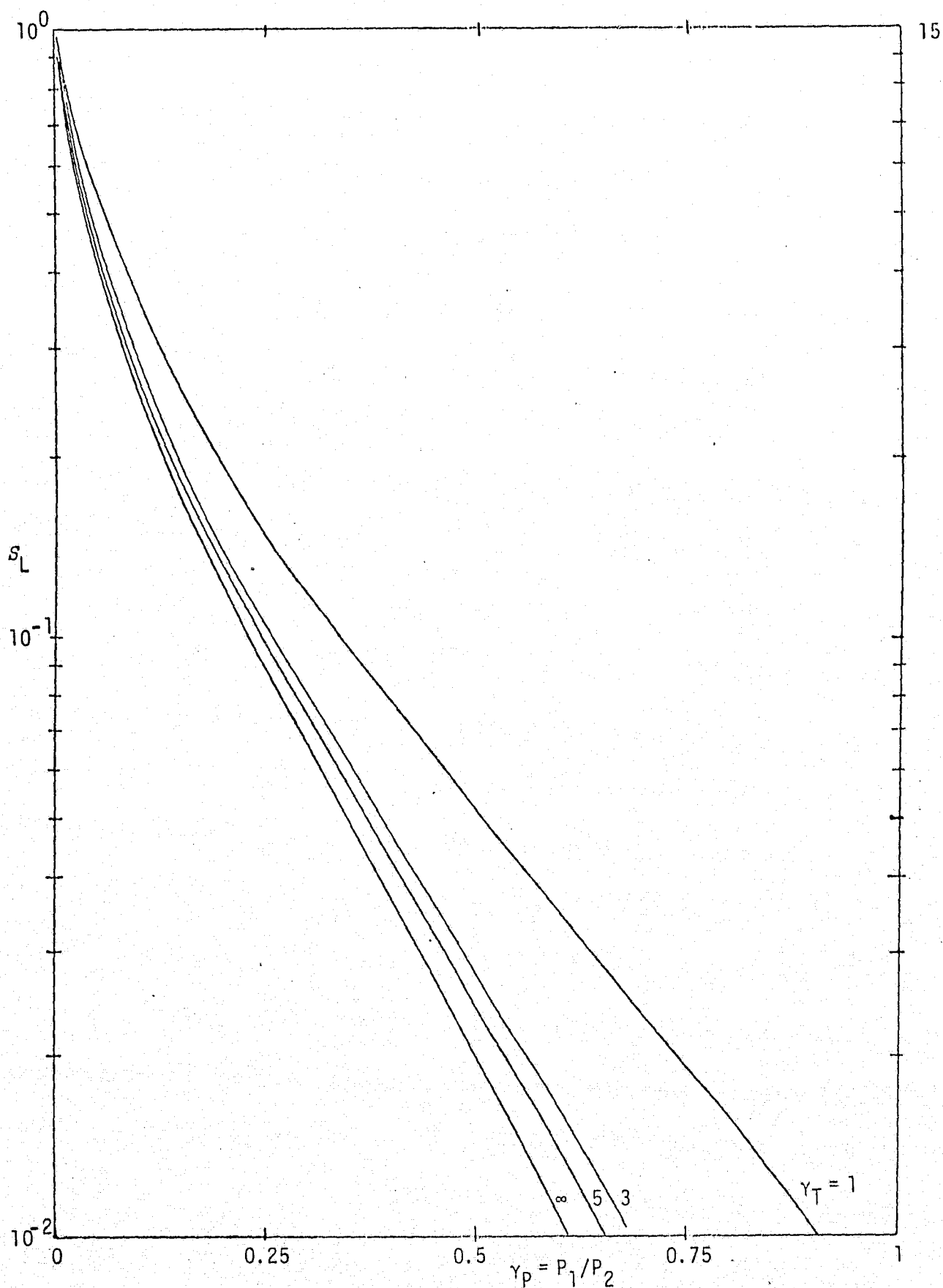


Figure 3b. Squaring Loss versus Ratio of Powers in the Two Data Channels With  $\gamma_T \triangleq T_1/T_2$  as a Parameter;  $R_{T2} = 10$  dB;  $m_1(t)$  is NRZ,  $m_2(t)$  is NRZ; Unsynchronized Data Clocks

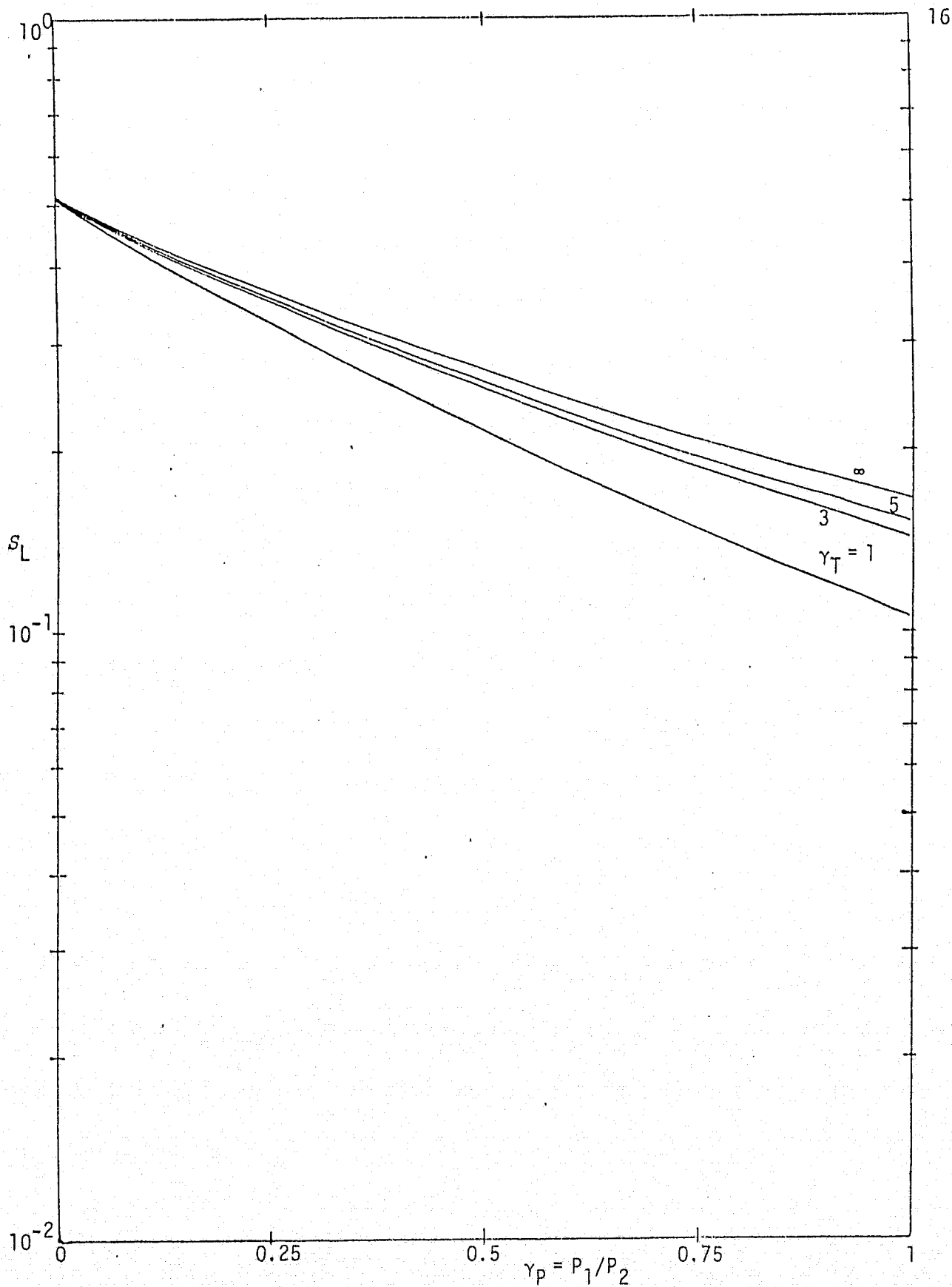


Figure 4a. Squaring Loss versus Ratio of Powers in the Two Data Channels With  $\gamma_T \triangleq T_1/T_2$  as a Parameter;  $R_{T2} = -3$  dB;  $m_1(t)$  is NRZ,  $m_2(t)$  is Manchester; Unsynchronized Data Clocks



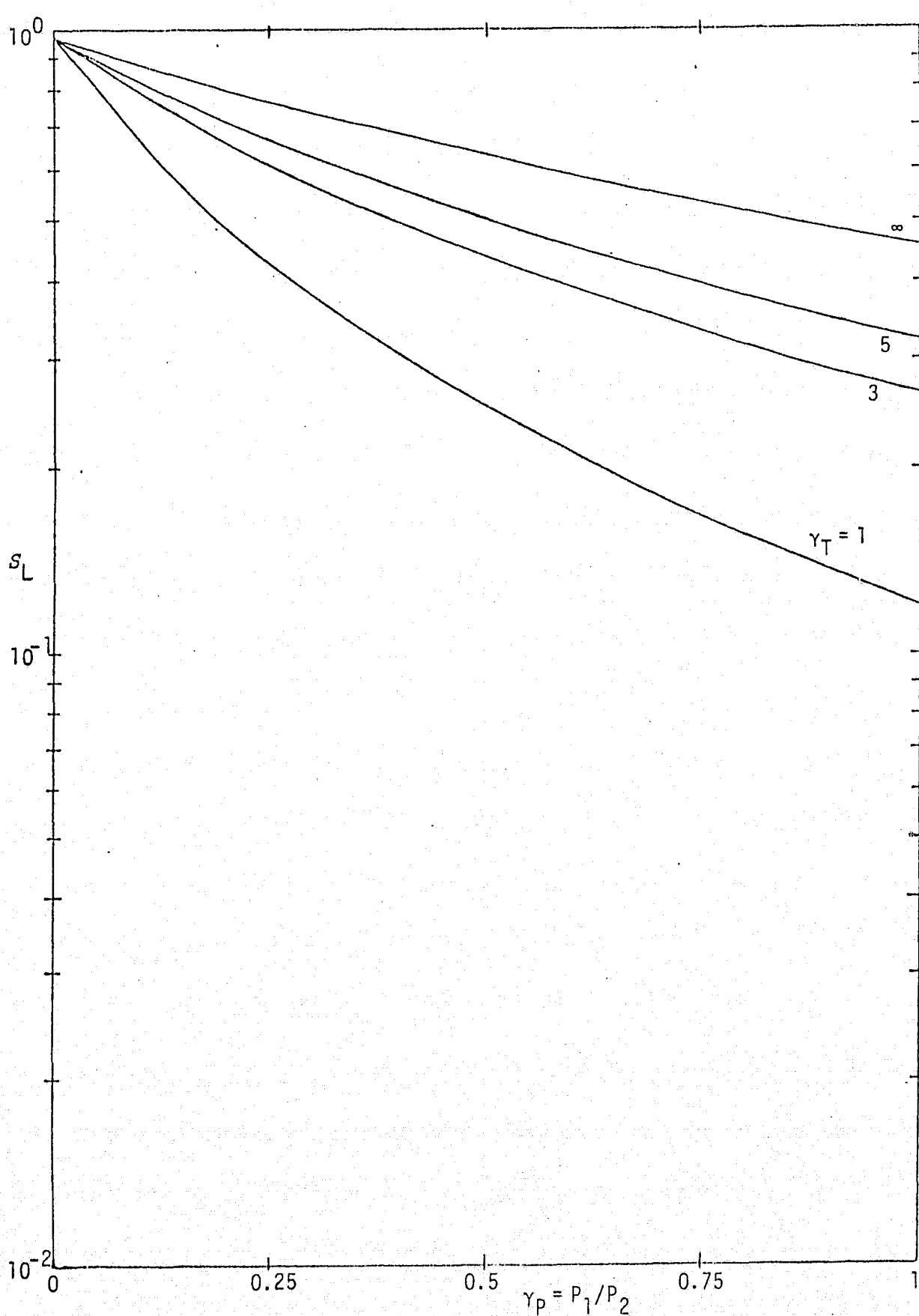


Figure 4b. Squaring Loss versus Ratio of Powers in the Two Data Channels With  $\gamma_T \triangleq T_1/T_2$  as a Parameter;  $R_{T2} = 10$  dB;  $m_1(t)$  is NRZ,  $m_2(t)$  is Manchester; Unsynchronized Data Clocks

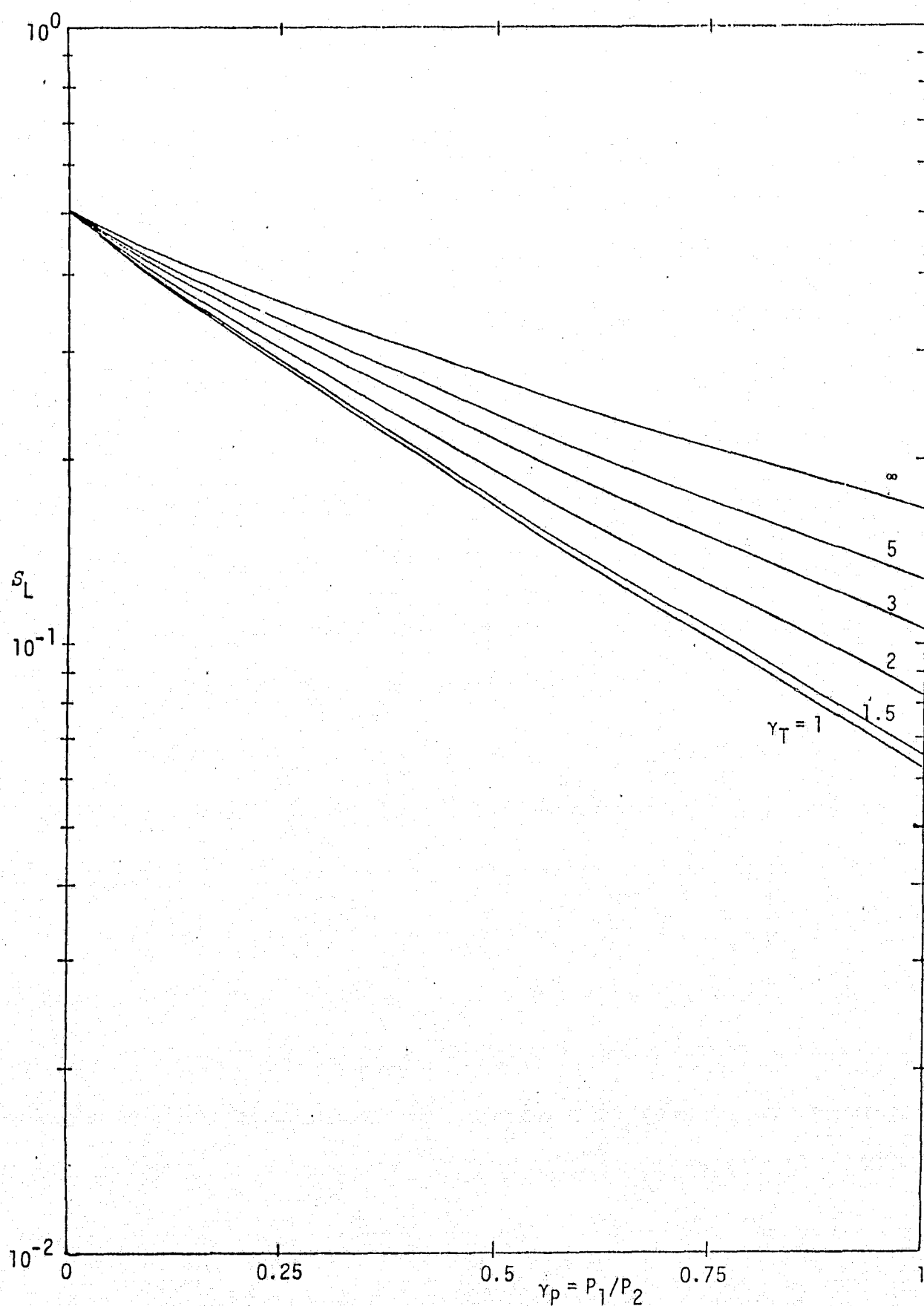
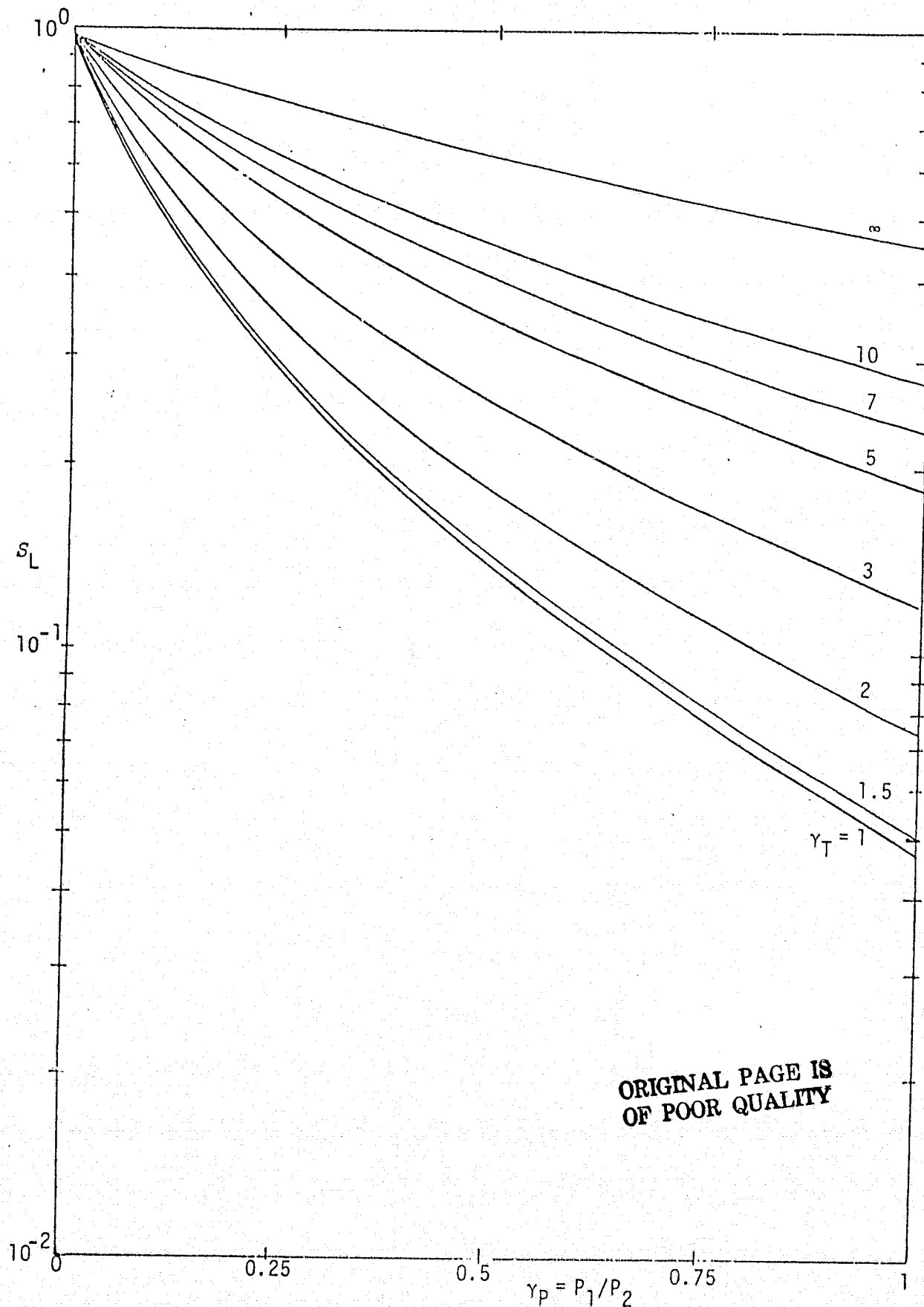


Figure 5a. Squaring Loss versus Ratio of Powers in the Two Data Channels With  $\gamma_T \triangleq T_1/T_2$  as a Parameter;  $R_{T2} = -3$  dB;  $m_1(t)$  is Manchester,  $m_2(t)$  is Manchester; Unsynchronized Data Clocks



ORIGINAL PAGE IS  
OF POOR QUALITY

Figure 5b. Squaring Loss versus Ratio of Powers in the Two Data Channels With  $\gamma_T \triangleq T_1/T_2$  as a Parameter;  $R_{T2} = 10$  dB;  $m_1(t)$  is Manchester,  $m_2(t)$  is Manchester; Unsynchronized Data Clocks

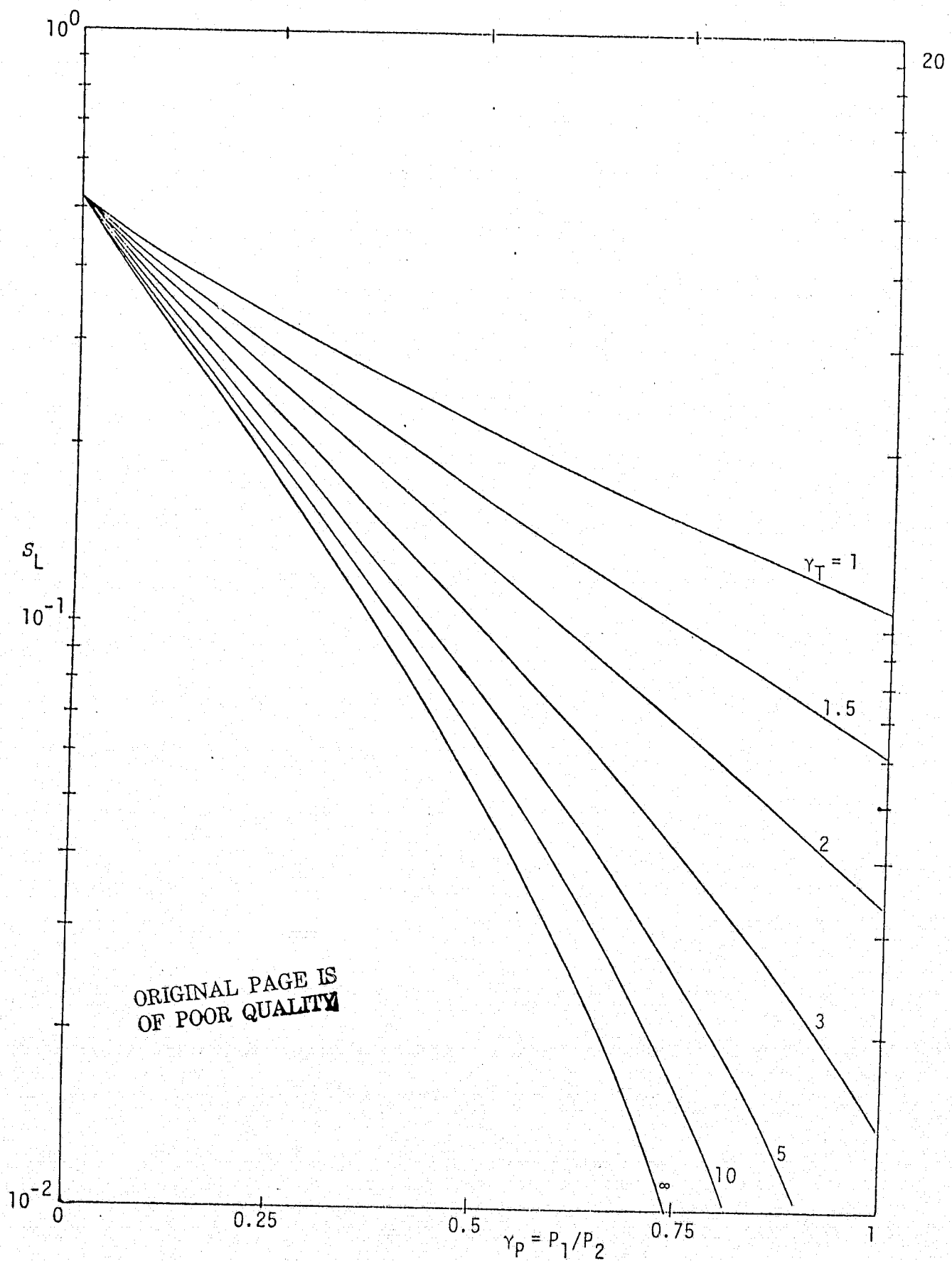


Figure 6a. Squaring Loss versus Ratio of Powers in the Two Data Channels With  $\gamma_T \triangleq T_1/T_2$  as a Parameter;  $R_{T2} = -3$  dB;  $m_1(t)$  is Manchester,  $m_2(t)$  is NRZ; Unsynchronized Data Clocks

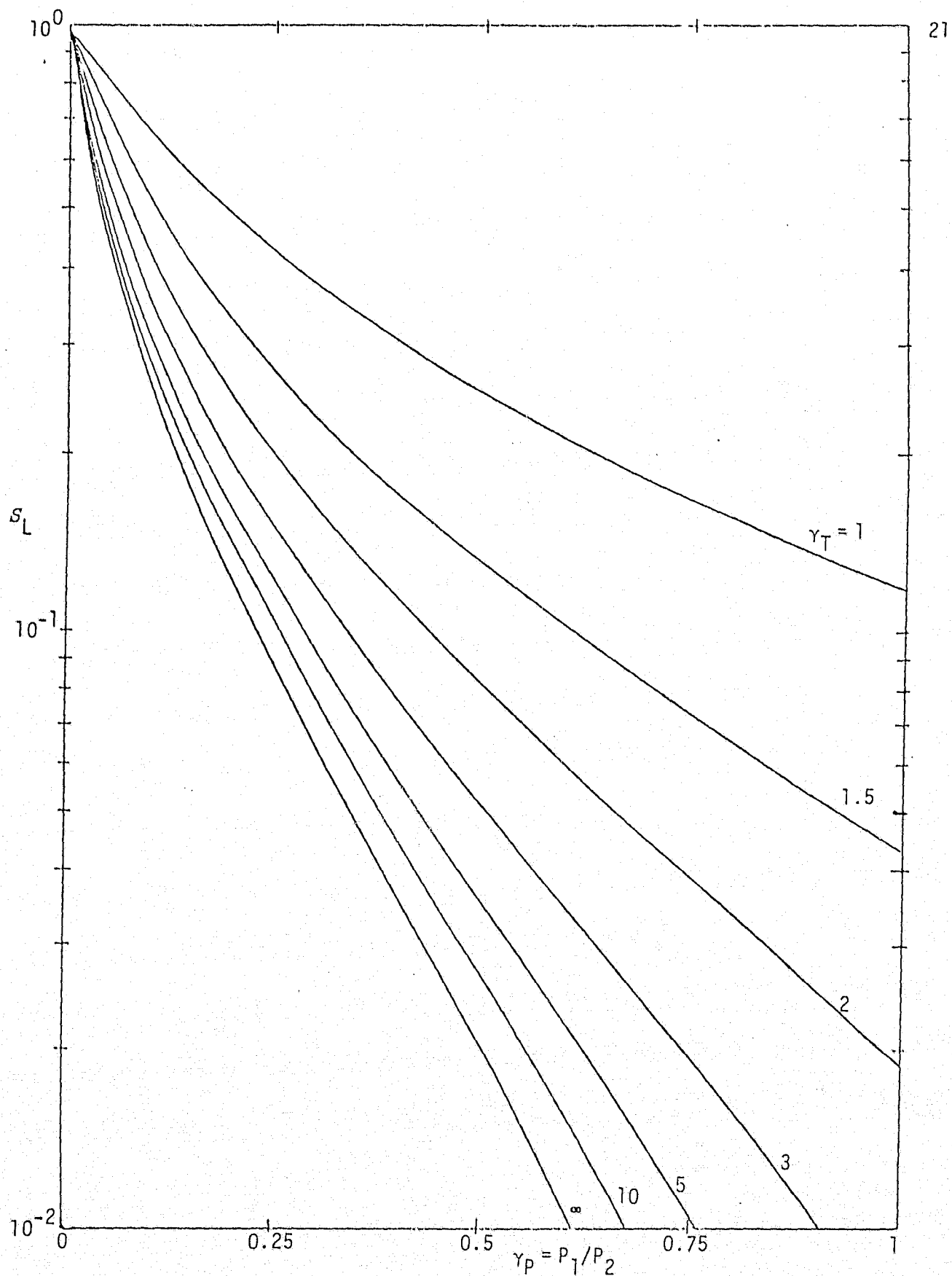


Figure 6b. Squaring Loss versus Ratio of Powers in the Two Data Channels With  $\gamma_T \triangleq T_1/T_2$  as a Parameter;  $R_{T2} = 10$  dB;  $m_1(t)$  is Manchester,  $m_2(t)$  is NRZ; Unsynchronized Data Clocks

notation developed here in Part II, (28) can be rewritten as

$$S_L = \frac{(D_2 - \gamma_P D_1)^2}{(1 + \gamma_P) \left[ D_2 K_{D_2} + \gamma_P D_1 K_{D_1} + K_L \left( \frac{1 + \gamma_P}{2R_{T2}} \right) \left( \frac{B_i}{R_2} \right) + \left( \frac{2\gamma_P R_{T2}}{1 + \gamma_P} \right) \left( \frac{D_{12}}{T_2} \right) \right]}, \quad (34)$$

where  $D_1$ ,  $D_2$ ,  $K_{D_1}$ ,  $K_{D_2}$ , and  $D_{12}$  are all defined in Part I. Note the similarity in form of (34) and (32), corresponding to the squaring loss for integrate-and-dump arm filters.

Since  $D_1$ ,  $D_2$ ,  $K_{D_1}$ ,  $K_{D_2}$ , and  $D_{12}/T_2$  of (34) are only functions of  $B_i/R_2$  and  $\gamma_T$ , then analogous to the biphasic case [1], for given values of  $\gamma_T$ ,  $\gamma_P$ , and  $R_{T2}$ , an optimum value of  $B_i/R_2$  exists in the sense of maximizing  $S_L$  of (34) (i.e., minimizing the squaring loss). Using that value of  $B_i/R_2$ , namely,  $(B_i/R_2)_{\text{opt}}$ , and defining the corresponding value of  $S_L$  by  $S_{L\text{opt}}$ , then the minimum improvement in tracking performance (or, equivalently, in squaring loss performance) is given by the ratio of (32) to (34):

$$I \triangleq \frac{S_L}{S_{L\text{opt}}} = \frac{(1 - \gamma_P \sigma_{\tilde{m}_1}^2)^2 \left[ D_2 K_{D_2} + \gamma_P D_1 K_{D_1} + K_L \left( \frac{1 + \gamma_P}{2R_{T2}} \right) \left( \frac{B_i}{R_2} \right)_{\text{opt}} + \left( \frac{2\gamma_P R_{T2}}{1 + \gamma_P} \right) \left( \frac{D_{12}}{T_2} \right) \right]}{(D_2 - \gamma_P D_1)^2 \left[ 1 + \gamma_P \sigma_{\tilde{m}_1}^2 + \frac{1 + \gamma_P}{2R_{T2}} + \frac{2\gamma_P R_{T2} \sigma_{\tilde{m}_1}^2}{1 + \gamma_P} \right]} \quad (35)$$

Assuming single-pole (RC) arm filters as the basis of comparison, wherein  $K_L = 1/2$  [1], and unsynchronized symbol clocks (i.e.,  $\sigma_{\tilde{m}_1}^2$ , determined from Table 2), Figures 7 through 9 illustrate  $I$  in dB versus the channel power ratio  $\gamma_P$  with the data rate ratio  $\gamma_T$  as a parameter and values of total power-to-noise ratio  $R_{T2}$  typical of coded and uncoded systems. We observe from these figures that the improvement in squaring loss performance of using integrate-and-dump arm filters as opposed to single-pole arm filters is an increasing function of  $\gamma_P$  and depends heavily on the choice of data formats for  $m_1(t)$  and  $m_2(t)$ . Also note that, in the limit, as  $\gamma_T$  approaches infinity,  $D_1 = K_{D_1} = D_{12}/T_2 = 1$  and  $\sigma_{\tilde{m}_1}^2 = 1$  or 0, depending on the data formats of  $m_1(t)$  and  $m_2(t)$ . Thus,  $I$  of (35) simplifies considerably for this special case.

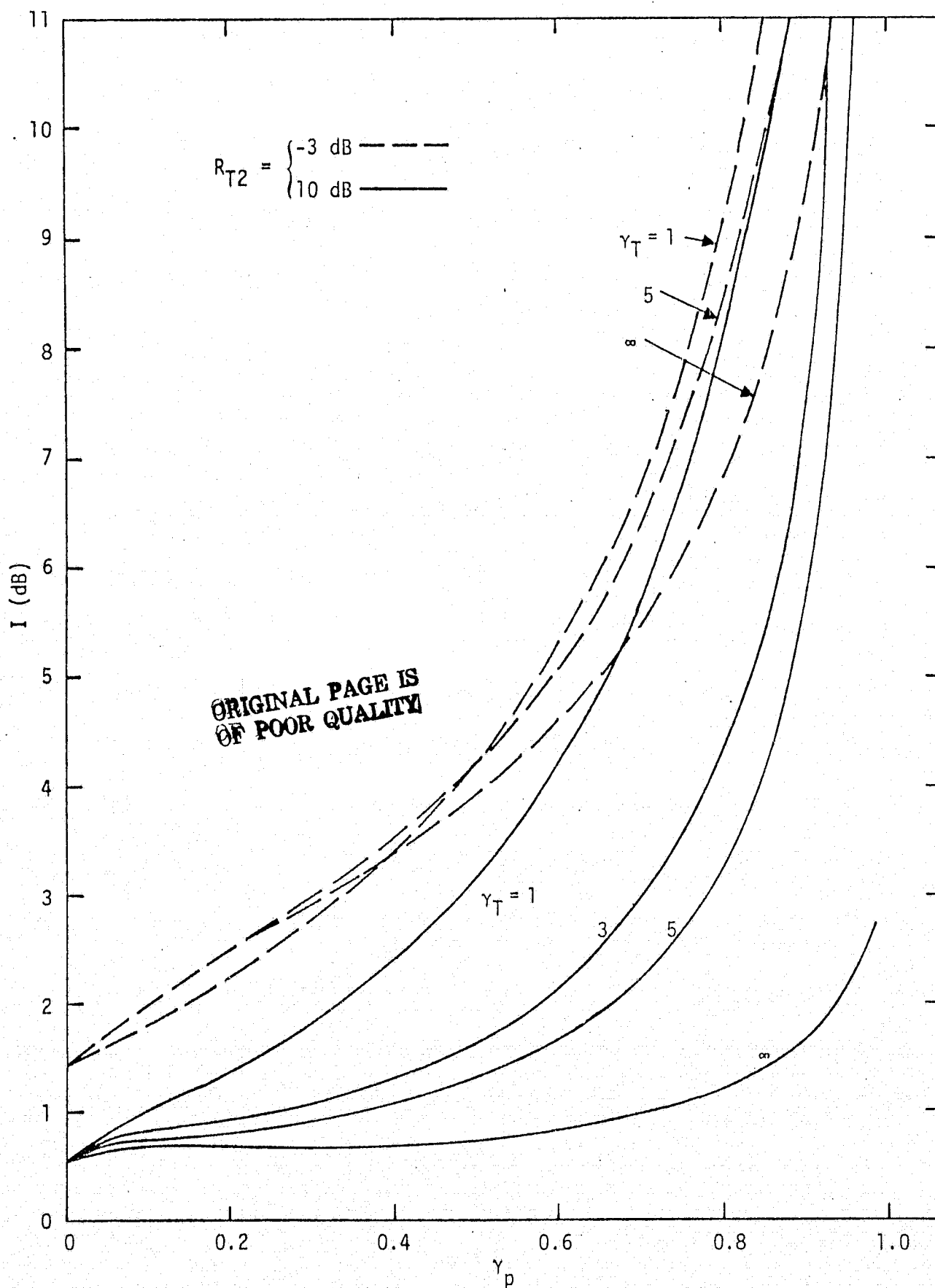


Figure 7. Squaring Loss Improvement (in dB) Using Integrate-and-Dump Arm Filters as Opposed to Single-Pole Passive Arm Filters;  $m_1(t)$  and  $m_2(t)$  are NRZ

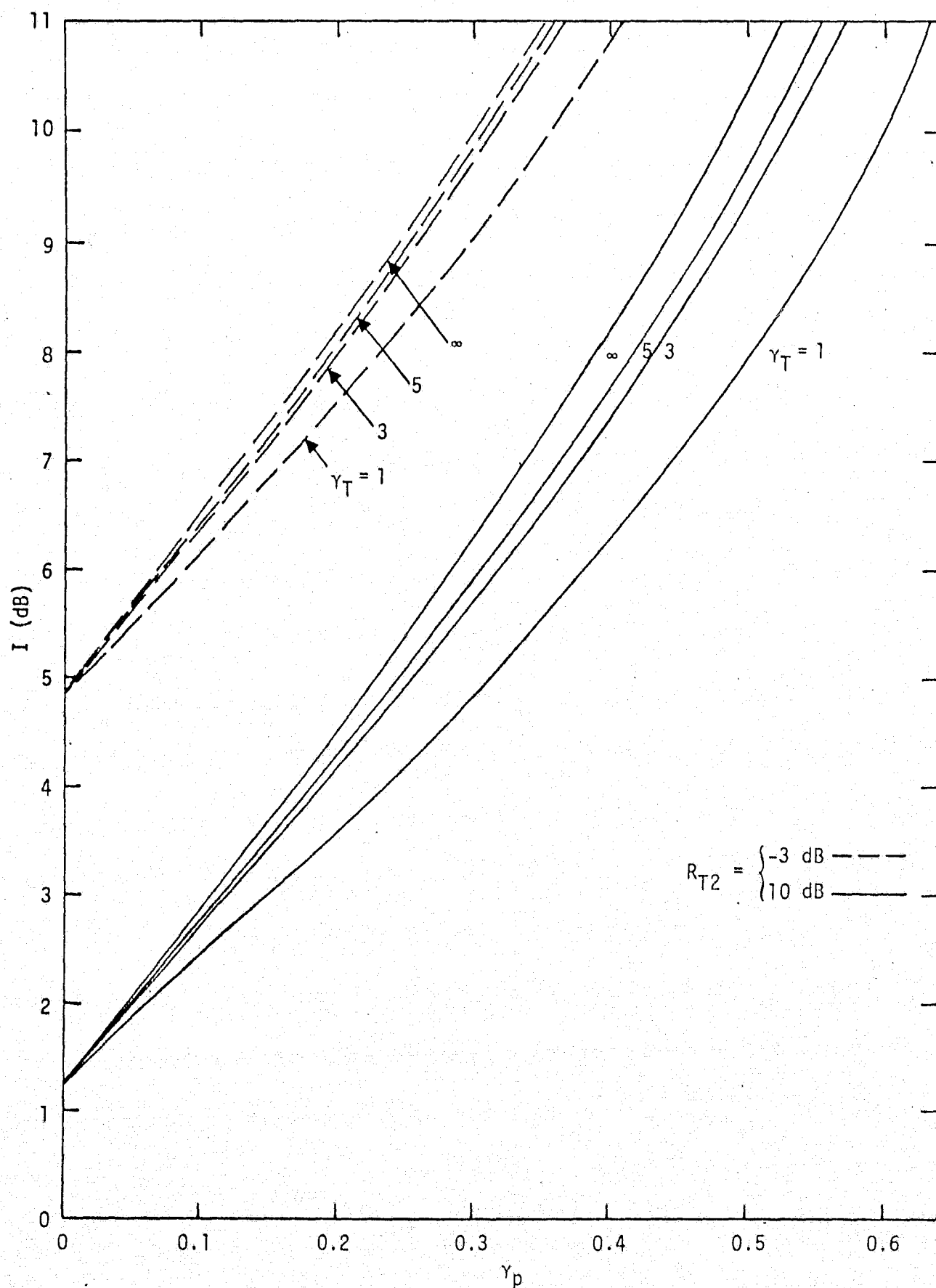


Figure 8. Squaring Loss Improvement (in dB) Using Integrate-and-Dump Arm Filters as Opposed to Single-Pole Passive Arm Filters;  $m_1(t)$  is, NRZ,  $M_2(t)$  is Manchester



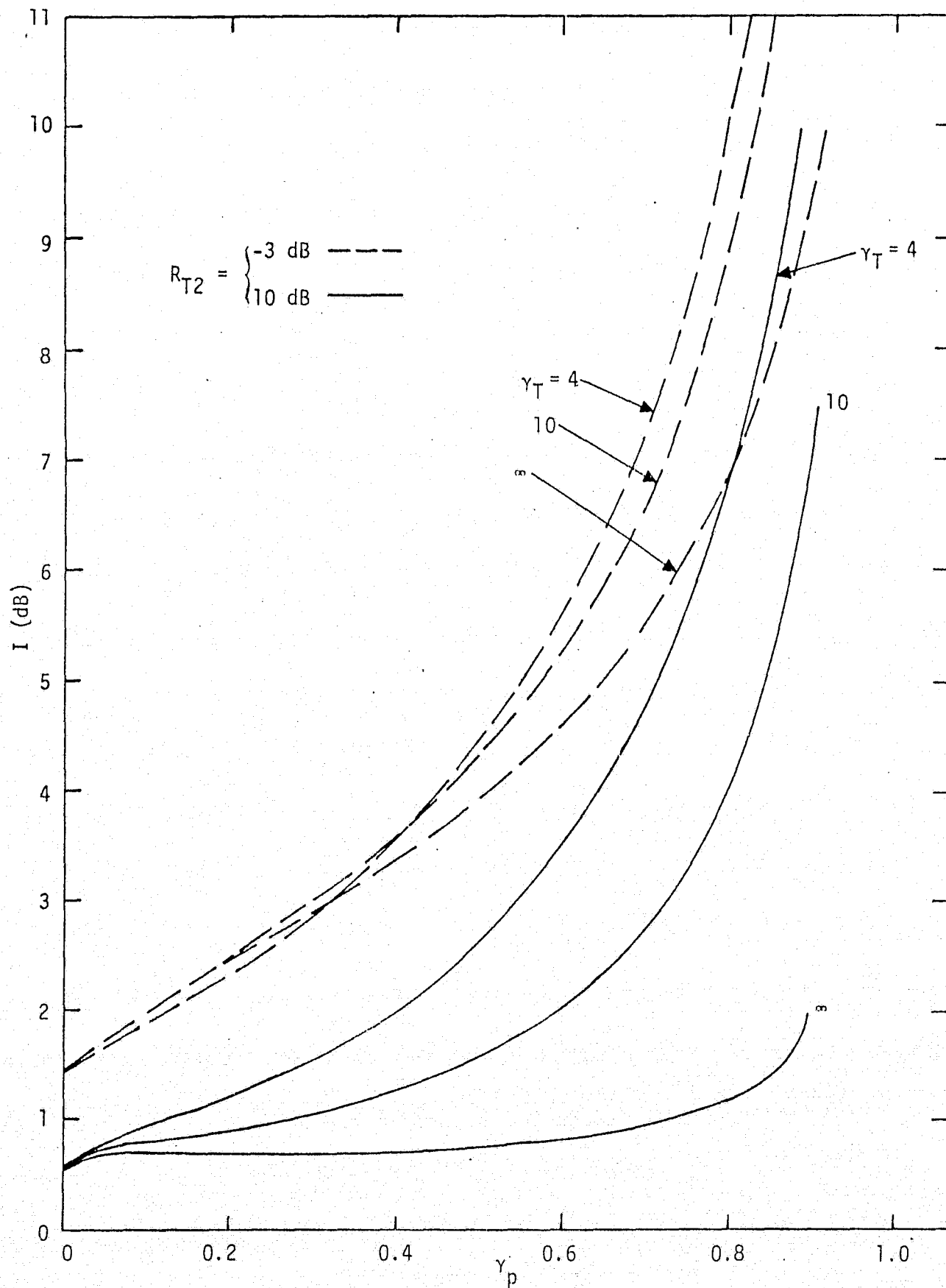


Figure 9. Squaring Loss Improvement (in dB) Using Integrate-and-Dump Arm Filters as Opposed to Single-Pole Passive Arm Filters;  $m_1(t)$  is Manchester,  $m_2(t)$  is NRZ)

## CONCLUSIONS

We have evaluated the performance of a biphase Costas loop with active arm filters when tracking an unbalanced QPSK signal. The cases of synchronized and unsynchronized clocks have been treated and results are given for all possible combinations of NRZ and Manchester formats for the two information channels. It has been shown that, while for a fixed ratio of data rates and total power-to-noise ratio in the higher data bandwidth the squaring loss does indeed increase as the ratio of powers in the two channels increases, the rate at which this loss increases (tracking performance deteriorates) depends heavily upon the data formats in each channel. Thus, it is concluded that, when the ratio of data rates is on the same order of magnitude as the inverse of the power ratio, i.e., approximately equal signal energies in the two channels, the biphase Costas loop can be used as an efficient demodulator of QPSK. On the other hand, if the energy in the two channels is very unbalanced, e.g., one channel is coded and one is uncoded, then it is still possible to efficiently use a biphase Costas loop for demodulation of unbalanced QPSK provided that the higher data rate channel is Manchester coded. It is understood that the foregoing conclusions are quite general and are not intended to rule out specific design situations in which sufficient total power-to-noise ratio is available to tolerate large squaring losses. In an individual situation, one must resort to the specific numerical results given in the illustrations to determine the suitability of employing a biphase Costas loop for demodulation of unbalanced QPSK.

As a final note, the results derived in this part will play an important role in assessing the error probability performance of unbalanced QPSK receivers where the data detector is, in fact, an integrate-and-dump filter. The results of such an investigation are the subject of a future paper by the author.

## REFERENCE

1. Simon, M. K., and Lindsey, W. C. "Optimum Performance of Suppressed Carrier Receivers with Costas Loop Tracking," IEEE Transactions on Communications, Vol. COM-25, No. 2, February 1977, pp. 215-227.

APPENDIX G

TRACKING PERFORMANCE OF UNBALANCED QPSK DEMODULATORS

PART III - BIPHASE POLARITY-TYPE COSTAS LOOP  
WITH PASSIVE ARM FILTERS

## APPENDIX G

### TRACKING PERFORMANCE OF UNBALANCED QPSK DEMODULATORS PART III - BIPHASE POLARITY-TYPE COSTAS LOOP WITH PASSIVE ARM FILTERS

by

Marvin K. Simon  
Waddah K. Alem

#### 1.0 INTRODUCTION

In Parts I and II of this study, we addressed the problem of tracking an unbalanced QPSK signal with a conventional biphase Costas loop with analog input phase detectors, and an analog third multiplier (the one that forms the loop error signal). Because of dc offsets associated with analog multipliers, it is common practice to hard-limit the in-phase\* channel arm filter output and replace the analog third multiplier with a chopper-type device (switched multiplier) which typically exhibits much less offset. While it is also possible to replace the input in-phase and quadrature analog phase detectors with switched multipliers, the impact of doing so on the resulting tracking performance is minimal since the arm filters will pass only the first harmonic of these phase detector outputs. Thus, aside from the  $8/\pi^2$  power loss associated with the first harmonic of a square wave, the performance of the loop would be identical to that given in Part I for an analog third multiplier or that to be presented here in Part III for a switched third multiplier. For ease of terminology, we shall refer to a conventional biphase Costas loop with a switched third multiplier as a "biphase polarity-type Costas loop" or, even simpler, a "polarity-type Costas loop."

Generally speaking, introduction of a limiter (hard or soft) into a system results in signal suppression, the amount of which is a function of the signal-to-noise ratio at the limiter input. This signal suppression, in turn, reduces the total loop gain and, as a consequence, the loop bandwidth. Another potential problem with the limiter under strong signal conditions is that it may increase the tendency of the loop to false lock. This tendency was demonstrated

---

\* For unbalanced quadriphase, we shall refer to the in-phase channel as that corresponding to the point of data extraction for the higher power signal.

in [1,2] for a polarity-type Costas loop with a biphase data input.

The purpose of this appendix is to address the tracking behavior of the polarity-type Costas loop with unbalanced QPSK input and compare its performance with that of the conventional Costas loop discussed in Part I of this same study. In particular, for the case of single-pole Butterworth (RC) arm filters and a particular combination of NRZ and Manchester coded data on the two channels, the squaring loss (tracking jitter penalty relative to a linear loop) is evaluated and illustrated as a function of the ratio of arm filter bandwidth to higher data rate and total signal power-to-noise ratio in this higher data rate bandwidth. Also numerically illustrated is the corresponding mean-squared tracking jitter performance as a function of these same receiver parameters.

## 2.0 SYSTEM MODEL

Consider the Costas loop with hard-limited in-phase channel illustrated in Figure 1. The input  $x(t)$  is, as in Parts I and II, an unbalanced QPSK signal plus noise, i.e.,

$$x(t) = \sqrt{2P_1} m_1(t) \cos \phi(t) + \sqrt{2P_2} m_2(t) \sin \phi(t) + n_i(t), \quad (1)$$

where  $\phi(t)$ ,  $m_1(t)$ ,  $m_2(t)$  and  $n_i(t)$  have been previously defined. To avoid unnecessary duplication, we shall not rederive the expressions for the in-phase and quadrature arm filter outputs,  $z_s(t)$  and  $z_c(t)$ , but rather refer the reader directly to the results in equation (5) of Part I. Thus, hard-limiting  $z_s(t)$  and multiplying by  $z_c(t)$  produces an error signal  $z_0(t)$  at the switching multiplier output (assuming this multiplier has unit gain) which is given by

$$\begin{aligned} z_0(t) &\triangleq z_c(t) \operatorname{sgn} [z_s(t)] \\ &= K_1 K_m \sqrt{P_2} \hat{m}_2(t) \tilde{m}(t) \sin \varphi(t) + K_1 K_m \sqrt{P_1} \hat{m}_1(t) \tilde{m}(t) \cos \varphi(t) \\ &\quad + K_1 K_m \tilde{m}(t) [\hat{N}_c(t) \cos \varphi(t) - \hat{N}_s(t) \sin \varphi(t)], \end{aligned} \quad (2)$$

where

$$\begin{aligned} \tilde{m}(t) &\triangleq \operatorname{sgn} \left\{ \sqrt{P_2} \hat{m}_2(t) \cos \varphi(t) - \sqrt{P_1} \hat{m}_1(t) \sin \varphi(t) \right. \\ &\quad \left. - [\hat{N}_s(t) \cos \varphi(t) + \hat{N}_c(t) \sin \varphi(t)] \right\} \end{aligned} \quad (3)$$

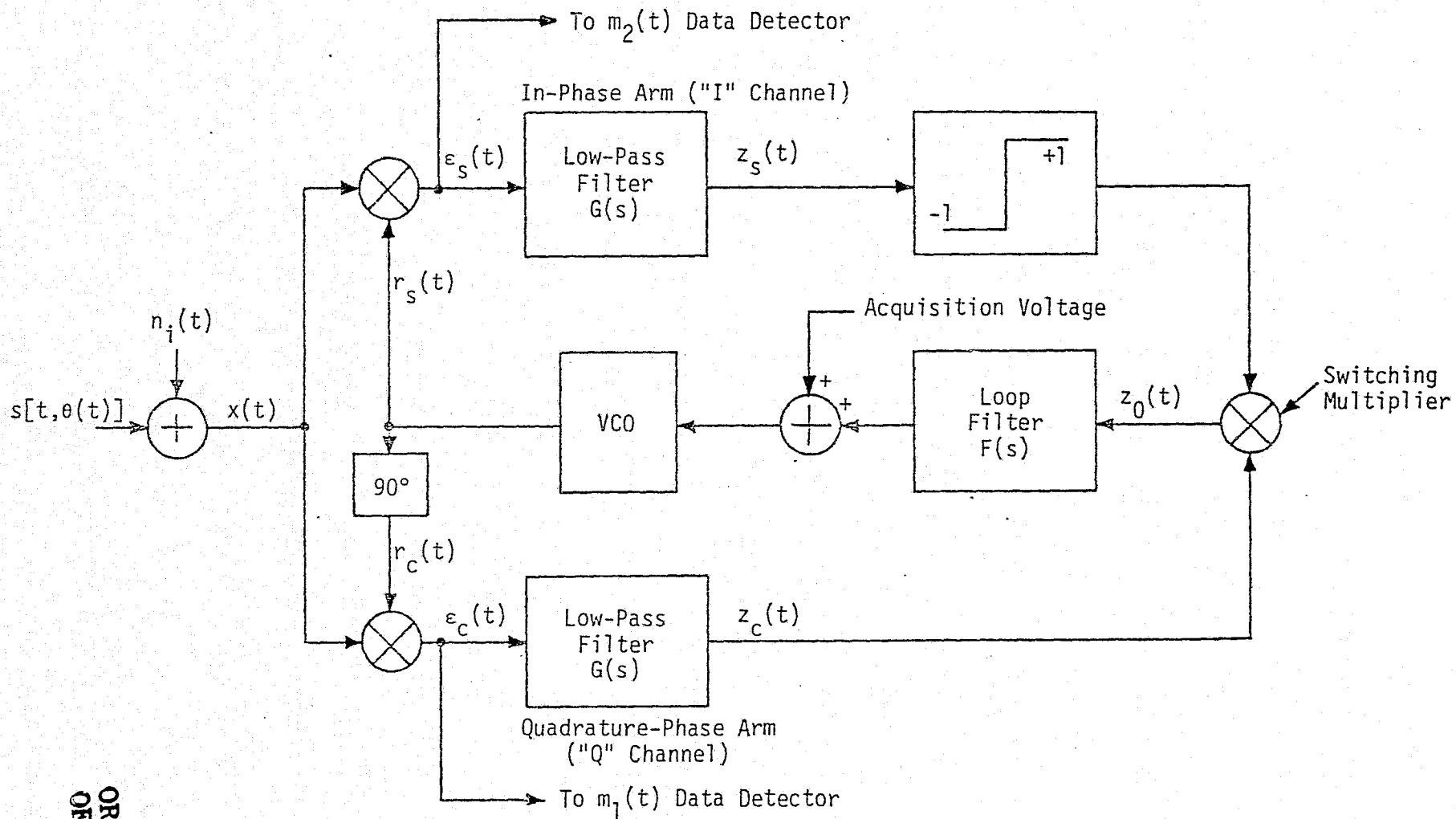


Figure 1. Costas Loop with Hard-Limited In-Phase Channel

ORIGINAL PAGE IS  
OF POOR QUALITY

and  $\text{sgn}(x) \triangleq x/|x|$  denotes the "signum" function of the argument  $x$ . The instantaneous frequency of the VCO output is related to  $z_0(t)$  by

$$\frac{d\hat{\phi}(t)}{dt} = K_V [F(p) z_0(t)] + \omega_0 \quad (4)$$

and hence the stochastic differential equation of operation for the loop in Figure 1 becomes

$$2 \frac{d\varphi(t)}{dt} = 2\Omega_0 - KF(p) \left\{ 2\sqrt{P_2} \hat{m}_2(t) \tilde{m}(t) \sin \varphi(t) + 2\sqrt{P_1} \hat{m}_1(t) \tilde{m}(t) \cos \varphi(t) + 2\tilde{m}(t) \hat{N}[t, \varphi(t)] \right\} \quad (5)$$

where  $K \triangleq K_1 K_m K_V$ , and

$$\hat{N}[t, \varphi(t)] \triangleq \hat{N}_c(t) \cos \varphi(t) - \hat{N}_s(t) \sin \varphi(t). \quad (6)$$

Consider first decomposing  $\hat{m}_2(t) \tilde{m}(t) \sin \varphi(t)$  into

$$\begin{aligned} \hat{m}_2(t) \tilde{m}(t) \sin \varphi(t) &= \overline{\hat{m}_2(t) \tilde{m}(t) \sin \varphi(t)} \\ &+ \left[ \hat{m}_2(t) \tilde{m}(t) \sin \varphi(t) - \overline{\hat{m}_2(t) \tilde{m}(t) \sin \varphi(t)} \right] \end{aligned} \quad (7)$$

where the overbar denotes statistical expectation with respect to both the noise and data modulation processes, and  $\langle \rangle$  denotes time average. Similarly,

$$\begin{aligned} \hat{m}_1(t) \tilde{m}(t) \cos \varphi(t) &= \overline{\hat{m}_1(t) \tilde{m}(t) \cos \varphi(t)} \\ &+ \left[ \hat{m}_1(t) \tilde{m}(t) \cos \varphi(t) - \overline{\hat{m}_1(t) \tilde{m}(t) \cos \varphi(t)} \right] \end{aligned} \quad (8)$$

The first terms of (7) and (8) represent the normalized dc components of the error signal at the switching multiplier output. Since these dc voltages are, in general, a function of the loop phase error (specifically, in this case, a function of twice the loop phase error), it is traditional to refer to their weighted sum as the loop S-curve or tracking characteristic. With this in mind, we can write\*

---

\*For convenience, we drop in our notation herein the dependence of  $\varphi$  on time. Also, the loop bandwidth is assumed to be much less than the data rate and thus  $\varphi(t)$  is essentially constant over a symbol time.

$$\begin{aligned}
2 \sqrt{P_2} \langle \hat{m}_2(t) \tilde{m}(t) \sin \varphi(t) \rangle + 2 \sqrt{P_1} \langle \hat{m}_1(t) \tilde{m}(t) \cos \varphi(t) \rangle &= \\
2 \sqrt{P_2} \langle \hat{m}_2(t) \tilde{m}(t) \rangle \sin \varphi + 2 \sqrt{P_1} \langle \hat{m}_1(t) \tilde{m}(t) \rangle \cos \varphi &\triangleq \sqrt{P_2} f(2\varphi) \\
&= \sqrt{P_2} \tilde{\alpha} f_1(2\varphi), \quad (9)
\end{aligned}$$

where  $f_1(x)$  is a nonlinearity which is periodic in  $x$  with period  $2\pi$  and has unit slope at the origin, i.e.,  $x=0$ . Thus,  $\tilde{\alpha}$  defined by

$$\begin{aligned}
\tilde{\alpha} &\triangleq \left. \frac{df(2\varphi)}{d(2\varphi)} \right|_{\varphi=0} = \frac{1}{2} \left. \frac{df(2\varphi)}{d\varphi} \right|_{\varphi=0} \\
&= \underbrace{\langle \hat{m}_2(t) \tilde{m}(t) \rangle}_{\tilde{\alpha}_2} \Big|_{\varphi=0} + \sqrt{\frac{P_1}{P_2}} \underbrace{\frac{d}{d\varphi} [\langle \hat{m}_1(t) \tilde{m}(t) \rangle]}_{\tilde{\alpha}_1} \Big|_{\varphi=0} \quad (10)
\end{aligned}$$

is the signal amplitude suppression factor which results due to the combined distortion effects on the input modulations  $m_1(t)$  and  $m_2(t)$  of the hard limiter and finite arm filter bandwidth. In the next section, we evaluate this suppression factor for modulation data formats and an arm filter type of current interest in practice.

The second terms in (7) and (8) are zero mean processes which represent the self noises of the filtered, hard-limited data modulations at the switching multiplier output. Thus, defining these self noises by

$$\begin{aligned}
n_{\Delta 1}[t, 2\varphi] &\triangleq 2 \sqrt{P_1} [\hat{m}_1(t) \tilde{m}(t) - \langle \hat{m}_1(t) \tilde{m}(t) \rangle] \cos \varphi \\
n_{\Delta 2}[t, 2\varphi] &\triangleq 2 \sqrt{P_2} [\hat{m}_2(t) \tilde{m}(t) - \langle \hat{m}_2(t) \tilde{m}(t) \rangle] \sin \varphi \quad (11)
\end{aligned}$$

and substituting (11) together with (9) into (5) gives the resulting equation of loop operation

$$2 \frac{d\varphi}{dt} = 2\Omega_0 - K'F(p) \left\{ \sqrt{P_2} \tilde{\alpha} f_1(2\varphi) + 2\tilde{m}(t) \hat{N}(t, \varphi) + n_{\Delta 2}(t, 2\varphi) + n_{\Delta 1}(t, 2\varphi) \right\}. \quad (12)$$

Finally, since for good tracking performance the loop operates in the region of small variations of  $\varphi$  (i.e., its linear region), then since  $n_{\Delta 2}(t, 2\varphi)$  is proportional to  $\sin \varphi$ , its self-noise power in



the narrow loop bandwidth will be vanishingly small when compared with that of the dominant noise component  $\tilde{m}(t)\hat{N}(t, \varphi)$ . Thus, as has been done in similar analyses [3,4], we shall ignore the effect of this self-noise term. Under this assumption (12) reduces to

$$2 \frac{d\varphi}{dt} = 2\Omega_0 - KF(p) \left\{ \sqrt{P_2} \tilde{a} f_1(2\varphi) + \hat{N}_e(t, 2\varphi) \right\} \quad (13)$$

where

$$\hat{N}_e(t, 2\varphi) \triangleq 2\tilde{m}(t)\hat{N}(t, \varphi) + n_{\Delta 1}(t, 2\varphi) \quad (14)$$

is the equivalent additive noise perturbing the loop.

### 3.0 CALCULATION OF THE SIGNAL AMPLITUDE SUPPRESSION FACTOR

The input digital modulations  $m_i(t)$ ;  $i=1,2$ ; may be represented as

$$\begin{aligned} m_2(t) &= \sum_{n=-\infty}^{\infty} a_{n2} p_2(t - nT_2) \\ m_1(t) &= \sum_{n=-\infty}^{\infty} a_{n1} p_1(t - nT_1 - \epsilon) \end{aligned} \quad (15)$$

where  $a_{ni} = \pm 1$  is the polarity ( $\pm 1$ ) of the  $n$ th data symbol in the  $i$ th data stream,  $T_i = 1/R_i$  is the symbol time and  $p_i(t)$  is the symbol pulse shape of the  $i$ th data stream (e.g., for NRZ coding)

$$p_i(t) = \begin{cases} 1; & 0 \leq t \leq T_i \\ 0; & \text{otherwise} \end{cases} \quad (16)$$

and  $\epsilon$  is the random epoch between the two data streams which accounts for the fact that, in general, the two modulations are asynchronous.

After passing through the Costas loop arm filter, these same modulations become

$$\hat{m}_i(t) = \sum_{n=-\infty}^{\infty} a_{ni} \hat{p}_i(t - nT_i); \quad i=1,2 \quad (17)$$

where

$$\hat{p}_i(t) = \int_0^T p_i(\tau) g(t - \tau) d\tau \quad (18)$$

ORIGINAL PAGE IS  
OF POOR QUALITY

with  $g(t)$  the impulse response of the arm filter  $G(s)$ . Thus, from (10)

$$\tilde{\alpha}_2 \triangleq \left. \overline{\langle \hat{m}_2(t) \tilde{m}(t) \rangle} \right|_{\varphi=0} = \frac{1}{T_2} \int_0^{T_2} \overline{\hat{m}_2(t) \tilde{m}(t)} dt \Big|_{\varphi=0} \quad (19)$$

which, from (3) and (17), becomes

$$\tilde{\alpha}_2 = \frac{1}{T_2} \int_0^{T_2} \overline{\left[ \sum_{n=-\infty}^{\infty} a_{n2} \hat{p}_2(t - nT_2) \right] \operatorname{sgn} \left\{ \sqrt{P_2} \sum_{n=-\infty}^{\infty} a_{n2} \hat{p}_2(t - nT_2) - \hat{N}_s(t) \right\}} dt. \quad (20)$$

The statistical average over the filtered Gaussian noise process  $\hat{N}_s(t)$  in (20) can be performed quite easily with the result

$$\operatorname{sgn} \left\{ \sqrt{P_2} \sum_{n=-\infty}^{\infty} a_{n2} \hat{p}_2(t - nT_2) - \hat{N}_s(t) \right\} = \operatorname{erf} \left[ \sqrt{\frac{\rho_2}{2}} \sum_{n=-\infty}^{\infty} a_{n2} \hat{p}_2(t - nT_2) \right] \quad (21)$$

where  $\rho_2 = 2P_2/N_0B_i$  is the high power channel signal-to-noise ratio in the arm filter bandwidth,

$$\operatorname{erf} x \triangleq \frac{2}{\sqrt{\pi}} \int_0^x \exp(-t^2) dt, \quad (22)$$

and  $B_i$  denotes the two-sided noise bandwidth of the low-pass arm filter  $G(s)$ , i.e.,

$$B_i \triangleq \int_{-\infty}^{\infty} |G(j2\pi f)|^2 df. \quad (23)$$

Substituting (21) into (20), we get the somewhat simplified result

$$\tilde{\alpha}_2 = \frac{1}{T_2} \int_0^{T_2} \overline{\left[ \sum_{n=-\infty}^{\infty} a_{n2} \hat{p}_2(t - nT_2) \right] \operatorname{erf} \left[ \sqrt{\frac{\rho_2}{2}} \sum_{n=-\infty}^{\infty} a_{n2} \hat{p}_2(t - nT_2) \right]} dt. \quad (24)$$

In general, evaluation of  $\tilde{\alpha}_2$  as given by (24) is a difficult, if not impossible, task due to the presence of the error function non-linearity which impedes performing the statistical average over the doubly infinite data sequence. Fortunately, however, the problem can be somewhat simplified by noting that, in practical system design, the 3 dB cutoff frequency of the arm filter is chosen on the order of the

data rate or greater to assure good tracking performance. This implies that the tails of  $\hat{p}_2(t)$  beyond a single symbol interval decay rapidly, and thus it is sufficient to consider only the contribution of the data bits  $a_0$  and  $a_{-1}$  insofar as computing the argument of the error function in the interval  $0 \leq t \leq T_2$ .<sup>\*</sup> Assuming then that the data bits are random and take on values  $\pm 1$  with equal a priori probability, we obtain the result

$$\tilde{\alpha}_2 = \frac{1}{2T_2} \int_0^{T_2} \hat{p}_{2+}(t) \operatorname{erf} \left[ \sqrt{\frac{\rho_2}{2}} \hat{p}_{2+}(t) \right] dt + \frac{1}{2T_2} \int_0^{T_2} \hat{p}_{2-}(t) \operatorname{erf} \left[ \sqrt{\frac{\rho_2}{2}} \hat{p}_{2-}(t) \right] dt \quad (25)$$

where

$$\hat{p}_{2\pm}(t) \triangleq \hat{p}_2(t) \pm \hat{p}_2(t+T_2); \quad 0 \leq t \leq T_2. \quad (26)$$

Computation of  $\tilde{\alpha}_1$  defined in (10) is slightly more complicated since the time origin of both data streams is involved and thus an additional average over the random epoch  $\epsilon$  between them is required. Averaging first over the filtered Gaussian noise process  $\tilde{N}[t, \varphi(t)] \triangleq \hat{N}_s(t) \cos \varphi(t) + \hat{N}_c(t) \sin \varphi(t)$  with variance  $\sigma_{\tilde{N}}^2 = N_0 B_i / 2$  gives

$$\begin{aligned} \tilde{\alpha}_1 &= \frac{d}{d\varphi} \left\langle \hat{m}_1(t) \operatorname{erf} \left[ \frac{\sqrt{\rho_2} \hat{m}_2(t) \cos \varphi - \sqrt{\rho_1} \hat{m}_1(t) \sin \varphi}{\sqrt{2} \sigma_{\tilde{N}}} \right] \right\rangle \Big|_{\varphi=0} \\ &= -\sqrt{\frac{2\rho_1}{\pi}} \left\langle \hat{m}_1^2(t) \exp \left\{ -\frac{\rho_2}{2} \hat{m}_2^2(t) \right\} \right\rangle \end{aligned} \quad (27)$$

where

$$\rho_1 \triangleq \frac{P_1}{\sigma_{\tilde{N}}^2} = \frac{2P_1}{N_0 B_i}. \quad (28)$$

Again, because of the independence of the two data streams and the asynchronism of their timing, (27) can be simplified to

<sup>\*</sup> Extension of this approach to take into account intersymbol interference from more than one previous pulse interval follows in a straightforward manner.

$$\tilde{\alpha}_1 = -\sqrt{\frac{2\rho_1}{\pi}} \langle \hat{m}_1^2(t) \rangle \left\langle \exp \left\{ -\frac{\rho_2}{2} \hat{m}_2^2(t) \right\} \right\rangle. \quad (29)$$

The first factor in (29) is easily evaluated as [1]

$$\langle \hat{m}_1^2(t) \rangle \triangleq D_{m_1} = \int_{-\infty}^{\infty} S_{m_1}(f) |G(j 2\pi f)|^2 df, \quad (30)$$

where  $S_{m_1}(f)$  is the power spectral density of the modulation  $m_1(t)$ . The second factor in (29) can be simplified by once again using the approximation of considering only intersymbol interference from the previous pulse as was done in reducing (24) to (26). Thus,

$$\begin{aligned} \tilde{\alpha}_1 = & -\sqrt{\frac{2\rho_1}{\pi}} D_{m_1} \frac{1}{2T_2} \int_0^{T_2} \exp \left[ -\frac{\rho_2}{2} \hat{p}_{2+}^2(t) \right] dt \\ & -\sqrt{\frac{2\rho_1}{\pi}} D_{m_1} \frac{1}{2T_2} \int_0^{T_2} \exp \left[ -\frac{\rho_2}{2} \hat{p}_{2-}^2(t) \right] dt. \end{aligned} \quad (31)$$

Finally, letting

$$\gamma_P \triangleq \frac{P_1}{P_2} \quad (32)$$

denote the ratio of powers in the two data channels, then from (10), (26), (31) and (32), the signal amplitude suppression factor  $\tilde{\alpha}$  is given by

$$\begin{aligned} \tilde{\alpha} = & \frac{1}{2T_2} \int_0^{T_2} \hat{p}_{2+}(t) \operatorname{erf} \left[ \sqrt{\frac{\rho_2}{2}} \hat{p}_{2+}(t) \right] dt + \frac{1}{2T_2} \int_0^{T_2} \hat{p}_{2-}(t) \operatorname{erf} \left[ \sqrt{\frac{\rho_2}{2}} \hat{p}_{2-}(t) \right] dt \\ & - \gamma_P \sqrt{\frac{2\rho_2}{\pi}} D_{m_1} \frac{1}{2T_2} \int_0^{T_2} \exp \left[ -\frac{\rho_2}{2} \hat{p}_{2+}^2(t) \right] dt \\ & - \gamma_P \sqrt{\frac{2\rho_2}{\pi}} D_{m_1} \frac{1}{2T_2} \int_0^{T_2} \exp \left[ -\frac{\rho_2}{2} \hat{p}_{2-}^2(t) \right] dt. \end{aligned} \quad (33)$$

Note from (33) that the effect of the quadrature data channel (Channel 1) on the signal amplitude suppression factor is to reduce its value relative to that [the first two terms of (33)] when the input is a biphase

modulation [4].

As an illustration of the application of the result in (33) to a particular case of practical interest, we consider a Costas loop with single-pole (RC) Butterworth arm filters and input modulations specified as follows. The high data rate modulation  $m_2(t)$  is characterized by NRZ data with pulse shape  $p_2(t)$  specified in (27), while the low data rate channel has a Manchester coded modulation  $m_1(t)$ .

As is well known, an RC filter has a transfer function

$$G(j\omega) = \frac{1}{1 + j \frac{\omega}{\omega_c}} \quad (34)$$

where  $\omega_c = 2\pi f_c$  is the radian 3 dB cutoff frequency. Taking the inverse Fourier transform of (34) and substituting this result, together with (16), into (18) results in

$$\hat{p}_2(t) = [1 - \exp(-\omega_c t)] u(t) - [1 - \exp(-\omega_c (t - T_2))] u(t - T_2) \quad (35)$$

where  $u(t)$  is the unit step function. Thus, from (26), (33), and (35), we obtain

$$\begin{aligned} \tilde{\alpha} = & \frac{1}{2} \int_0^1 \left\{ 1 - 2 \exp[-2(B_i/R_2)x] \right\} \operatorname{erf} \left\{ \sqrt{\frac{\rho_2}{2}} \left\{ 1 - 2 \exp[-2(B_i/R_2)x] \right\} \right\} dx \\ & + \frac{1}{2} \operatorname{erf} \sqrt{\frac{\rho_2}{2}} - \gamma_P \sqrt{\frac{2\rho_2}{\pi}} D_{m_1} \frac{1}{2} \int_0^1 \exp \left\{ -\frac{\rho_2}{2} \left\{ 1 - 2 \exp[-2(B_i/R_2)x] \right\}^2 \right\} dx \\ & - \gamma_P \sqrt{\frac{2\rho_2}{\pi}} D_{m_1} \frac{1}{2} \exp \left( -\frac{\rho_2}{2} \right), \end{aligned} \quad (36)$$

where we have made the substitution  $x = t/T_2$  and taken note of the fact that, for an RC filter, the two-sided noise bandwidth  $B_i$  and 3 dB radian cutoff frequency  $\omega_c$  are related by  $\omega_c = 2B_i$ . Also, the mean-squared value for a Manchester coded modulation after arm filtering is given by [5]

$$D_{m_1} = 1 - \frac{1}{2B_i/R_1} [3 - 4 \exp(-B_i/R_1) + \exp(-2B_i/R_1)] \quad (37)$$

Before illustrating the variation of  $\tilde{\alpha}$  with  $B_i/R_2$ , we must characterize the signal-to-noise ratio  $\rho_2$  in terms of the system parameters. From the definition of  $\rho_2$ , we have that

$$\rho_2 = \frac{2P_2}{N_0 B_i} = \frac{2}{\pi} \left( \frac{P_2 T_2}{N_0} \right) \frac{1}{f_c T_2} = \frac{2}{\pi} R_2 \left( \frac{1}{f_c T_2} \right), \quad (38)$$

or in terms of the ratio of arm filter noise bandwidth to data rate,

$$\rho_2 = \frac{2R_2}{B_i/R_2}. \quad (39)$$

Since, in a given system design, the data detection signal-to-noise ratio  $R_2 \triangleq P_2 T_2 / N_0$  is typically fixed by the requirement on bit error probability performance in the high data rate channel, we shall parameterize  $R_2$  and plot the signal power suppression factor  $\tilde{\alpha}^2$  as a function of  $B_i/R_2$ . Figure 2 illustrates such a plot. The curves are drawn for  $B_i/R_2 \geq 1.5$  or, equivalently,  $\tau_c/T \leq 1/3$ , where  $\tau_c \triangleq 1/\omega_c$  is the arm filter time constant.

For large  $B_i/R_2$ , an appropriate asymptotic expression for  $\tilde{\alpha}^2$  can be obtained from (36) and is given by

$$\tilde{\alpha}^2 = \operatorname{erf}^2 \sqrt{\frac{R_2}{B_i/R_2}} - \gamma_P \sqrt{\frac{4R_2}{\pi B_i/R_2}} \exp \left( -\frac{R_2}{B_i/R_2} \right). \quad (40)$$

Also, in the limit as  $R_2 \rightarrow \infty$ , we obtain the asymptotic expression

$$\tilde{\alpha}^2 = 1 - \frac{1}{2B_i/R_2} [\ln 2 - \exp(-2B_i/R_2)], \quad (41)$$

which is identical to the result obtained for a biphas modulation input [4].

#### 4.0 CALCULATION OF THE EQUIVALENT NOISE SPECTRAL DENSITY $N_e$

In practical applications, the bandwidth of the Costas loop is ordinarily designed to be narrow with respect to the equivalent noise bandwidth of  $\hat{N}_e(t, 2\varphi)$  defined in (14). Thus, we can further approximate  $\hat{N}_e(t, 2\varphi)$  as a delta correlated process with equivalent single-sided noise spectral density

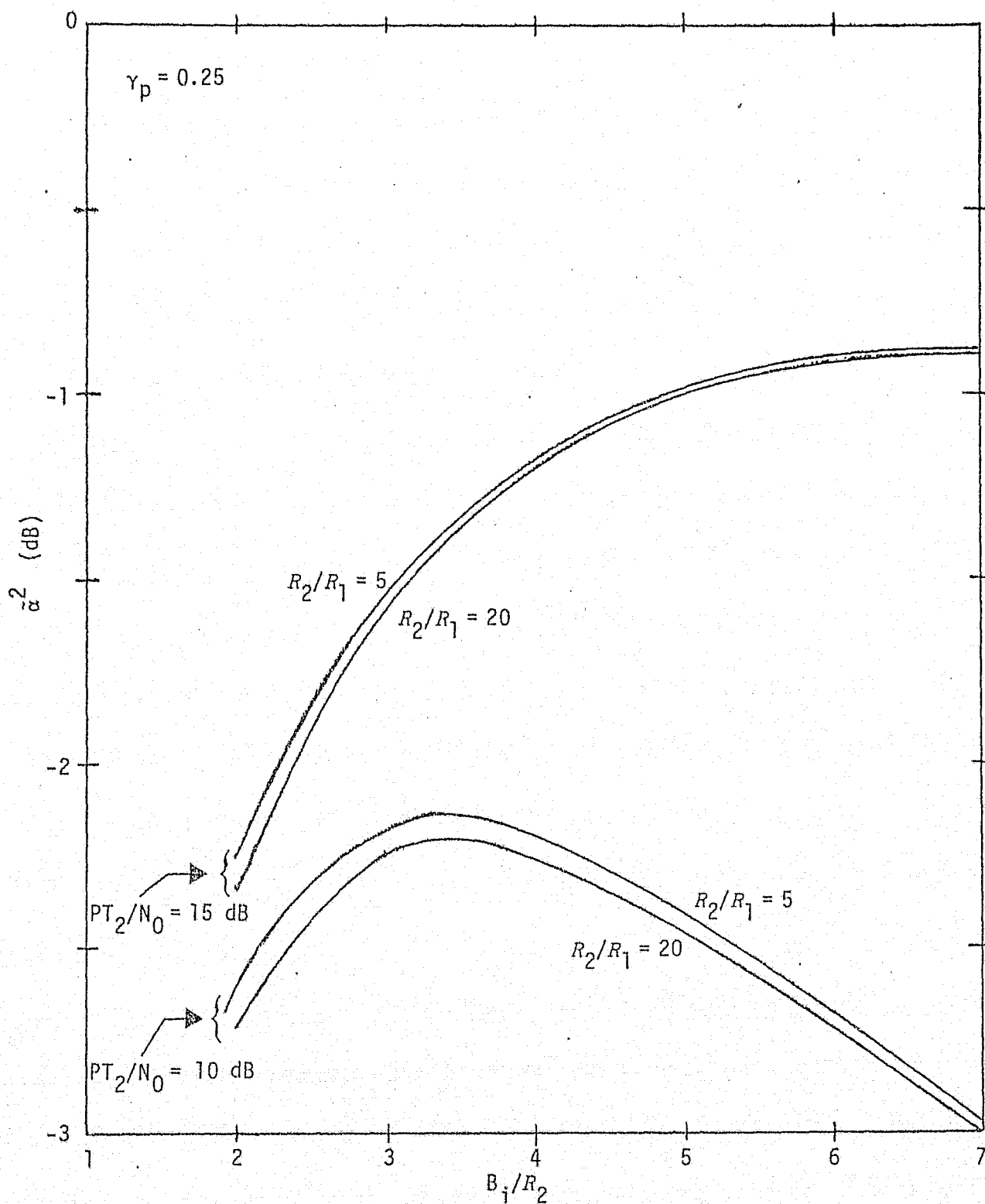


Figure 2. Signal Power Suppression Factor Versus the Ratio of the Two-Sided Arm Bandwidth to the High Data Rate With the Ratio Data Rates and  $PT_2/N_0$  as Parameters

$$N_e \triangleq 2 \int_{-\infty}^{\infty} R_{\hat{N}_e}(\tau) d\tau \quad (42)$$

where

$$R_{\hat{N}_e}(\tau) \triangleq \overline{\langle \hat{N}_e(t, 2\varphi) \hat{N}_e(t+\tau, 2\varphi) \rangle} \quad (43)$$

Since, as previously mentioned, for good tracking performance, the loop will operate in the neighborhood of  $\varphi = 0$ , we shall evaluate (43) and hence (42) only at the point  $\varphi = 0$ . For a conventional Costas loop without the hard limiter in the in-phase arm, the equivalent noise spectral density is indeed independent of  $\varphi$  [3]. Proceeding then under the foregoing assumption, we have from (3), (6), (11), (14) and (43) that\*

$$\begin{aligned} R_{\hat{N}_e}(\tau) &= 4 \overline{\langle \hat{N}_c(t) \hat{N}_c(t+\tau) \operatorname{sgn} \left\{ \sqrt{P_2} \hat{m}_2(t) - \hat{N}_s(t) \right\} \operatorname{sgn} \left\{ \sqrt{P_2} \hat{m}_2(t+\tau) - \hat{N}_s(t+\tau) \right\} \rangle} \\ &\quad + 4 P_1 \overline{\langle \hat{m}_1(t) \hat{m}_1(t+\tau) \operatorname{sgn} \left\{ \sqrt{P_2} \hat{m}_2(t) - \hat{N}_s(t) \right\} \operatorname{sgn} \left\{ \sqrt{P_2} \hat{m}_2(t+\tau) - \hat{N}_s(t+\tau) \right\} \rangle} \\ &= 4 [R_{\hat{N}_c}(\tau) + P_1 R_{\hat{m}_1}(\tau)] \overline{\langle \operatorname{sgn} \left\{ \sqrt{P_2} \hat{m}_2(t) - \hat{N}_s(t) \right\} \operatorname{sgn} \left\{ \sqrt{P_2} \hat{m}_2(t+\tau) - \hat{N}_s(t+\tau) \right\} \rangle} \end{aligned} \quad (44)$$

where

$$R_{\hat{N}_c}(\tau) = \overline{\langle \hat{N}_c(t) \hat{N}_c(t+\tau) \rangle} = \frac{N_0}{2} \int_{-\infty}^{\infty} |G(j 2\pi f)|^2 e^{j 2\pi f \tau} df \quad (45)$$

and

$$R_{\hat{m}_1}(\tau) \triangleq \overline{\langle \hat{m}_1(t) \hat{m}_1(t+\tau) \rangle} = \int_{-\infty}^{\infty} S_{m_1}(f) |G(j 2\pi f)|^2 e^{j 2\pi f \tau} df \quad (46)$$

For the RC filter of (34), it is simple to show that

$$R_{\hat{N}_c}(\tau) = \frac{N_0 B_i}{2} e^{-2B_i |\tau|} \quad (47)$$

Furthermore, for Manchester coded data on Channel 1 with power spectrum

---

\* Note that, because of the independence of  $m_1(t)$  and  $m_2(t)$ , the term  $\overline{\langle \hat{m}_1(t) \hat{m}_1(t) \rangle} \Big|_{\varphi=0} = \overline{\langle \hat{m}_1(t) \operatorname{sgn} [\sqrt{P_2} \hat{m}_2(t) - \hat{N}_s(t)] \rangle}$  in  $n_{\Delta 1}[t, 2\varphi]$  evaluates to zero.



$$S_{m_1}(f) = T_1 \frac{\sin^4\left(\frac{\pi f T_1}{2}\right)}{\left(\frac{\pi f T_1}{2}\right)^2}, \quad (48)$$

we have that

$$R_{\hat{m}_1}(\tau) = \begin{cases} 1 - 3 \frac{|\tau|}{T_1} + \frac{[4e^{-B_i/R_1} - e^{-2B_i/R_1}] \cosh 2B_i \tau - 3e^{-2B_i|\tau|}}{2B_i/R_1}; & 0 \leq |\tau| \leq \frac{T_1}{2} \\ -\left(1 - \frac{|\tau|}{T_1}\right) + \frac{e^{-2B_i|\tau|} [4 \cosh B_i/R_1 - 3] - e^{-2B_i/R_1} \cosh 2B_i \tau}{2B_i/R_1}; & \frac{T_1}{2} \leq |\tau| \leq T_1 \\ \frac{e^{-2B_i|\tau|} [4 \cosh B_i/R_1 - \cosh 2B_i/R_1 - 3]}{2B_i/R_1}; & T_1 \leq |\tau| \leq \infty \end{cases} \quad (49)$$

Thus, what remains is to compute the correlation function of the hard limiter output as required in (44).

The general problem of computing the correlation function at the output of a zero memory nonlinearity (e.g., a hard limiter) when the input is signal plus Gaussian noise can be attacked by a variety of techniques, among which are the transform approach [6], Price's Theorem [7] and the series expansion method [8]. Letting

$$y(t) \triangleq \text{sgn} \{ \sqrt{P_2} \hat{m}_2(t) - \hat{N}_s(t) \}, \quad (50)$$

then to compute the equivalent noise spectral density defined in (42), we must calculate

$$N_e = 8 \int_{-\infty}^{\infty} [R_{\hat{N}}(\tau) + P_1 R_{\hat{m}_1}(\tau)] R_y(\tau) d\tau. \quad (51)$$

As was true for the signal suppression factor and even more so here, evaluation of  $R_y(\tau)$  when  $m_2(t)$  is specified by (15) is difficult if not impossible. Even when one is willing to make the simplifying assumption of requiring that the statistical average on the data be taken only over two data symbols, additional simplifying assumptions are necessary if one is to obtain meaningful numerical results for the equivalent noise spectral density.

ORIGINAL PAGE IS  
OF POOR QUALITY

It is convenient to start with the power series approach of [8] to evaluate  $R_y(\tau)$ , namely,

$$R_y(\tau) = \frac{\left\langle \operatorname{erf} \left[ \sqrt{\frac{\rho_2}{2}} \hat{m}_2(t) \right] \operatorname{erf} \left[ \sqrt{\frac{\rho_2}{2}} \hat{m}_2(t+\tau) \right] \right\rangle}{+ \frac{2}{\pi} \left\langle \exp \left\{ -\frac{\rho_2}{2} [\hat{m}_2^2(t) + \hat{m}_2^2(t+\tau)] \right\} \sum_{k=1}^{\infty} \frac{\rho_{\hat{N}}^k(\tau)}{k!} H_{k-1}(\sqrt{\rho_2} \hat{m}_2(t)) H_{k-1}(\sqrt{\rho_2} \hat{m}_2(t+\tau)) \right\rangle} \quad (52)$$

where  $H_k(x)$  is the  $k$ th degree Hermite polynomial defined by

$$H_k(x) = (-1)^k e^{x^2/2} \frac{d^k}{dx^k} e^{-x^2/2} \quad (53)$$

and

$$\rho_{\hat{N}}(\tau) \triangleq \frac{R_{\hat{N}}(\tau)}{R_{\hat{N}}(0)} = e^{-2B_i|\tau|} \quad (54)$$

The case of interest here is where the data on Channel 2 is uncoded, in which case, the signal-to-noise ratio  $R_2$  would be large to achieve a small error probability on this channel. Thus, since  $\rho_2$  is directly proportional to  $R_2$  for a fixed ratio of arm filter bandwidth to data rate  $R_2$ , then for large  $\rho_2$ , the first term ( $k=1$ ) in the series expansion of (52) will dominate. Thus, keeping only this term and again assuming that the statistical average on the data sequence is computed only over two symbol intervals, we obtain

$$\begin{aligned}
N_e = & 4N_0 B_i \int_{-2T_2}^{2T_2} e^{-2B_i |\tau|} \left[ \frac{1}{T_2} \int_0^{T_2} \overline{\text{erf} \left[ \sqrt{\frac{\rho_2}{2}} \hat{m}_2(t) \right] \text{erf} \left[ \sqrt{\frac{\rho_2}{2}} \hat{m}_2(t+\tau) \right]} dt \right] d\tau \\
& + 4N_0 B_i \left( \frac{2}{\pi} \right) \int_{-2T_2}^{2T_2} e^{-4B_i |\tau|} \left[ \frac{1}{T_2} \int_0^{T_2} \overline{\exp \left\{ -\frac{\rho_2}{2} [\hat{m}_2^2(t) + \hat{m}_2^2(t+\tau)] \right\}} dt \right] d\tau \\
& + 4N_0 B_i \rho_1 \int_{-2T_2}^{2T_2} R_{\hat{m}_1}(\tau) \left[ \frac{1}{T_2} \int_0^{T_2} \overline{\text{erf} \left[ \sqrt{\frac{\rho_2}{2}} \hat{m}_2(t) \right] \text{erf} \left[ \sqrt{\frac{\rho_2}{2}} \hat{m}_2(t+\tau) \right]} dt \right] d\tau \\
& + 4N_0 B_i \left( \frac{2}{\pi} \right) \rho_1 \int_{-2T_2}^{2T_2} R_{\hat{m}_1}(\tau) e^{-2B_i |\tau|} \left[ \frac{1}{T_2} \int_0^{T_2} \overline{\exp \left\{ -\frac{\rho_2}{2} [\hat{m}_2^2(t) + \hat{m}_2^2(t+\tau)] \right\}} dt \right] d\tau
\end{aligned} \tag{55}$$

where  $\hat{m}_2(t)$  and  $\hat{m}_2(t+\tau)$ ;  $0 \leq t \leq T_2$ ,  $0 \leq |\tau| \leq 2T_2$ ; are computed from (17) and (35) and  $R_{\hat{m}_1}(\tau)$  is given by (49). Carrying out the statistical average, we obtain after much manipulation

$$N_e = 4N_0 \beta_N \tag{56}$$

where, analogous to Equation (57) of [4],  $\beta_N$  is defined by

$$\begin{aligned}
\beta_N = & 2B_i/R_2 \int_0^1 e^{-(2B_i/R_2)y} \left[ f_1(y) + e^{-2B_i/R_2} f_3(y) \right] dy \\
& + (2B_i/R_2) \frac{2}{\pi} \int_0^1 e^{-(4B_i/R_2)y} \left[ f_2(y) + e^{-4B_i/R_2} f_4(y) \right] dy \\
& + (2B_i/R_2) \rho_1 \int_0^1 \left[ R_{\hat{m}_1} \left( \frac{y}{R_2} \right) f_1(y) + R_{\hat{m}_1} \left( \frac{y+1}{R_2} \right) f_3(y) \right] dy \\
& + (2B_i/R_2) \frac{2\rho_1}{\pi} \int_0^1 e^{-(2B_i/R_2)y} \left[ R_{\hat{m}_1} \left( \frac{y}{R_2} \right) f_2(y) + e^{-2B_i/R_2} R_{\hat{m}_1} \left( \frac{y+1}{R_2} \right) f_4(y) \right] dy
\end{aligned} \tag{57}$$

with

$$\begin{aligned}
f_1(y) &= \left(\frac{2-y}{4}\right) \operatorname{erf}^2 \sqrt{\frac{\rho_2}{2}} - \int_0^y g_1(x) dx + \int_{1-y}^1 g_1(x) dx \\
&\quad + \frac{1}{2} \int_0^{1-y} g_1(x) g_1(x+y) dx - \frac{1}{4} \int_0^y g_1(x) g_1(x+1-y) dx \\
f_2(y) &= \left(\frac{2-y}{4}\right) \exp^2 (-\rho_2/2) + \int_0^y g_2(x) dx + \int_{1-y}^1 g_2(x) dx \\
&\quad + \frac{1}{2} \int_0^{1-y} g_2(x) g_2(x+y) dx + \frac{1}{4} \int_0^y g_2(x) g_2(x+1-y) dx \\
f_3(y) &= \left(\frac{1-y}{4}\right) \operatorname{erf}^2 \sqrt{\frac{\rho_2}{2}} + \int_0^y g_1(x) dx - \int_{1-y}^1 g_1(x) dx \\
&\quad - \frac{1}{4} \int_0^y g_1(x) g_1(x+y) dx \\
f_4(y) &= \frac{1}{4} \exp^2 (-\rho_2/2) + \frac{1}{2} \int_0^1 g_2(x) dx + \frac{1}{4} \int_0^y g_2(x) g_2(x+1-y) dx \\
&\quad + \frac{1}{4} \int_0^{1-y} g_2(x) g_2(x+y) dx
\end{aligned} \tag{58}$$

and

$$\begin{aligned}
g_1(x) &= \operatorname{erf} \left[ \sqrt{\frac{\rho_2}{2}} \left( 1 - 2e^{-(2B_i/R_2)x} \right) \right] \\
g_2(x) &= \exp \left\{ -\frac{\rho_2}{2} \left[ 1 - 2e^{-(2B_i/R_2)x} \right]^2 \right\}.
\end{aligned} \tag{59}$$

## 5.0 CALCULATION OF SQUARING LOSS AND TRACKING JITTER

We have already observed in previous analyses of this type [3-5] that the performance of Costas loops in either their linear or nonlinear tracking regions is characterized by the behavior of a parameter referred to as squaring loss. This loss represents the additional degradation in equivalent loop signal-to-noise ratio relative to a linear loop, i.e., one in which there exists no noise $\times$ noise or signal $\times$ noise error signal components. More specifically, if in (9) the normalized S-curve  $f_1(2\varphi)$

is replaced by  $2\varphi$ , its linear approximation, then one obtains the linear equation of loop operation from which the effective loop signal-to noise ratio  $\rho'$  insofar as computing the behavior of the  $2\varphi$  process is

$$\rho' = \frac{(\sqrt{P_2} \tilde{\alpha})^2}{N_e B_L}, \quad (60)$$

where  $B_L$  is the single-sided loop noise bandwidth and  $N_e B_L$  represents the noise power of the equivalent noise process  $\hat{N}_e(t, 2\varphi)$  in this bandwidth.

Using (56), we can express (60) in the form

$$\rho' = \frac{1}{4} \left( \frac{P_1 + P_2}{N_0 B_L} \right) \left( \frac{P_2}{P_1 + P_2} \right) \left( \frac{\tilde{\alpha}^2}{\beta_N} \right) = \frac{\rho}{4} S_L \quad (61)$$

and, in addition, for  $\Omega_0 = 0$ , the tracking jitter is given by

$$\sigma_{2\varphi}^2 = \frac{1}{\rho'}, \quad (62)$$

where

$$\rho \triangleq \frac{P_1 + P_2}{N_0 B_L} = \frac{P_T}{N_0 B_L} \quad (63)$$

and

$$S_L \triangleq \left( \frac{1}{1 + \gamma_P} \right) \frac{\tilde{\alpha}^2}{\beta_N} \quad (64)$$

is the so-called squaring loss with  $\tilde{\alpha}$  given by (33),  $\beta_N$  given by (57), and  $\gamma_P$  defined in (32).

Since the modulation reference signals are at  $\omega_0$  rather than  $2\omega_0$ , then the tracking jitter on the output data is

$$\sigma_\varphi^2 = \frac{1}{4} \sigma_{2\varphi}^2 = \frac{1}{\rho S_L}.$$

Using (38) along with the definitions of  $\tilde{\alpha}$ ,  $\beta_N$  and  $S_L$ , Figure 3 illustrates the variations of  $S_L$  versus  $B_i/R_2$  with  $P_T T_2/N_0$  as a parameter. Superimposed on these curves (in dashed lines) are the corresponding results obtained from [5] for the biphase Costas loop with passive arm filters. Figure 4 shows the phase jitter  $\sigma_\varphi$  as a function of  $B_i/R_2$  for the hard-limited loop with  $P_T T_2/N_0$  and  $R_2/R_1$  as parameters. The

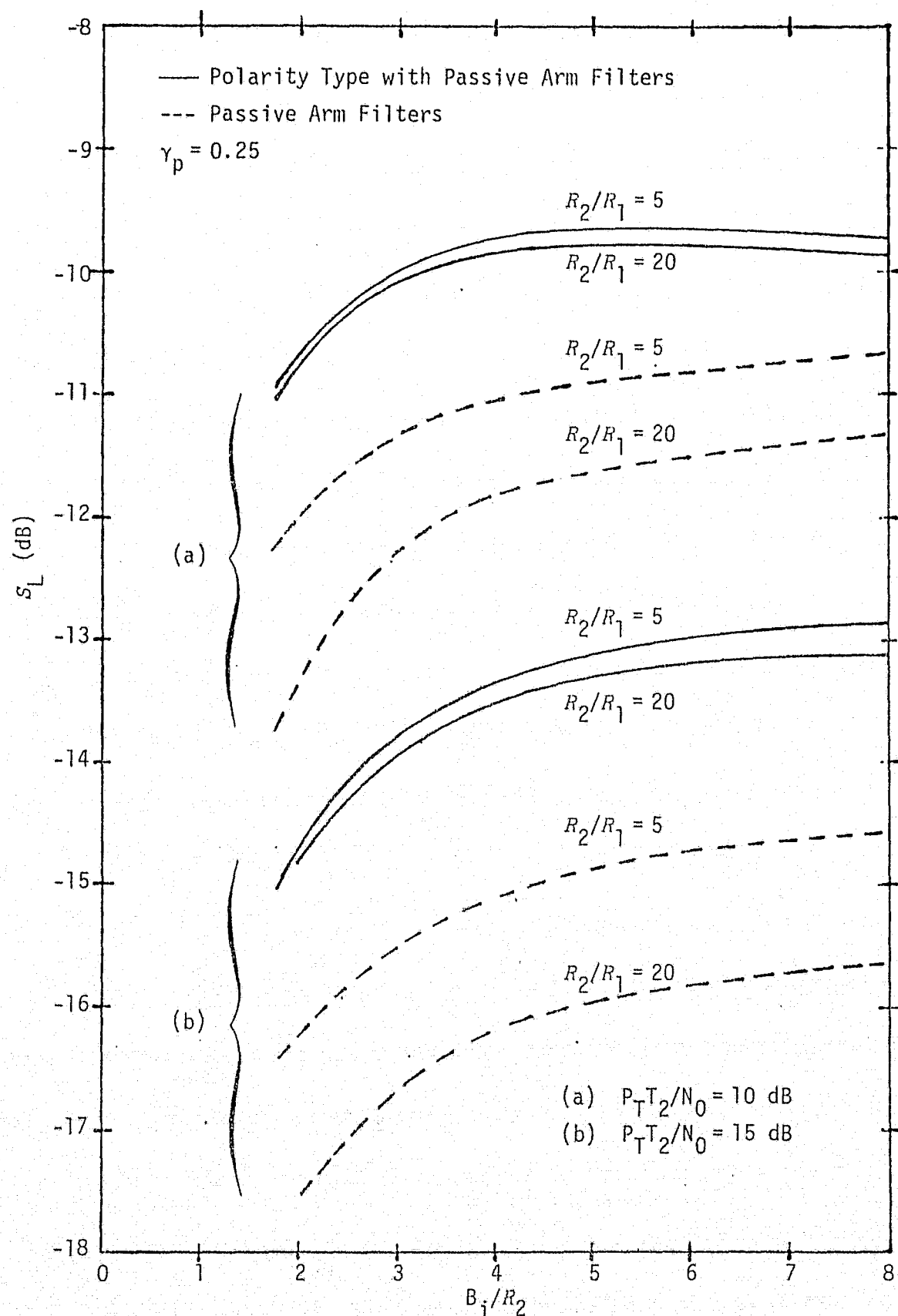


Figure 3. Squaring Loss Variations Versus  $B_i/R_2$  with  $R_2/R_1$  and  $P_T T_2/N_0$  as Parameters;  $m_1(t)$  is Manchester code,  $m_2(t)$  is NRZ.

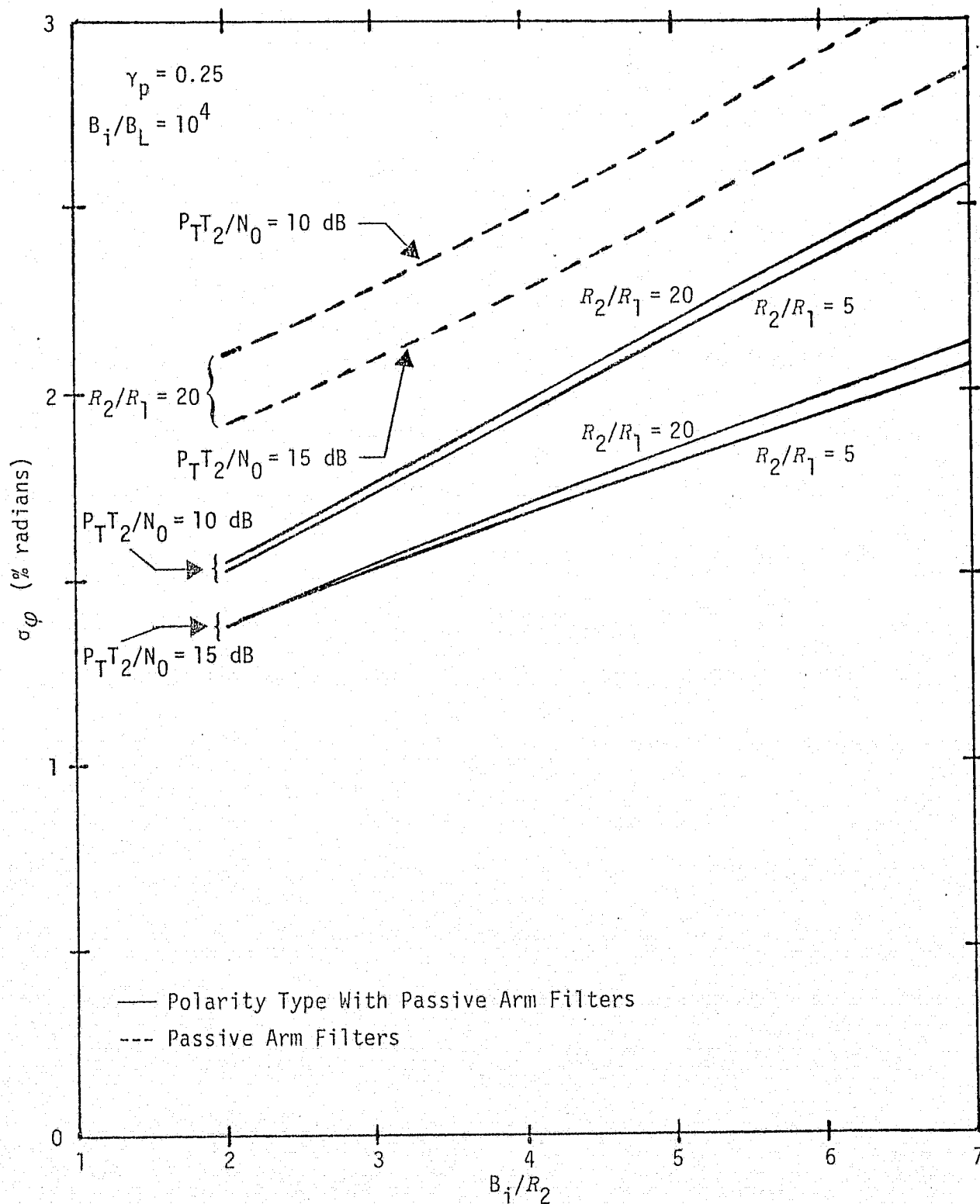


Figure 4. Phase Jitter Versus  $B_1 / R_2$  With  $P_T T_2 / N_0$  and  $R_2 / R_1$  as Parameters

phase jitter of the conventional loop [5] for  $R_2/R_1 = 20$  is also included for comparison. The computations for the phase jitter are based on a typical ratio of  $B_i/B_L = 10^4$ . We observe from these results that, for high signal-to-noise ratios, the hard-limited loop actually outperforms the conventional loop.

## 6.0 CONCLUSION

The squaring loss of biphase polarity-type Costas loops (with a switched third multiplier) has been analyzed in this report. An improvement in the tracking performance of these loops at high signal-to-noise ratios over the biphase Costas loop with passive arm filters has been demonstrated. The numerical evaluation shows that the improvement (in terms of the squaring loss) might be as high as 2.8 dB. It has also been shown for a given signal-to-noise ratio and a given arm filter bandwidth to high data rate ratio that the squaring loss does not change significantly with data rates when the ratio of the data rates is high. This is particularly true for small values of arm filter bandwidth to high data rate ratio.



## REFERENCES

1. M. K. Simon. "False-Lock Performance of Costas Loop with Hard-Limited In-Phase Channel," IEEE Transactions on Communications, Vol. COM-26, No. 1, January 1978, pp. 23-34.
2. M. K. Simon. "On the False Lock Behavior of Polarity-Type Costas Loops with Manchester Coded Input," presented at the 1977 National Telecommunications Conference, Los Angeles, December 5-7, 1977.
3. M. K. Simon and W. C. Lindsey. "Optimum Performance of Suppressed Carrier Receivers and Costas Loop Tracking," IEEE Transactions on Communications, Vol. COM-25, No. 2, February 1977, pp. 215-227.
4. M. K. Simon. "Tracking Performance of Costas Loops with Hard-Limited In-Phase Channel," to appear in the April 1978 issue of the IEEE Transactions on Communications.
5. M. K. Simon and W. K. Alem. "Tracking Performance of Unbalanced QPSK Demodulators: Part I - Biphase Costas Loop with Passive Arm Filters," Axiomatix Report No. R7707-5, July 29, 1977. Also accepted for publication in the IEEE Transactions on Communications.
6. W. B. Davenport, Jr., and W. L. Root. An Introduction to the Theory of Random Signals and Noise. New York: McGraw-Hill Book Co., Inc., 1958.
7. R. Price. "A Useful Theorem for Nonlinear Devices Having Gaussian Inputs," IRE Transactions on Information Theory, June 1958, pp. 69-72.
8. R. W. Kelly and P. R. Hariharan. "Ideal Limiting of Periodic Signals in Random Noise," IEEE Transactions on Aerospace and Electronic Systems, Vol. AES-7, No. 4, July 1971, pp. 644-651.

APPENDIX H

SUBCARRIER TRACKING ANALYSIS FOR THREE-CHANNEL ORBITER  
KU-BAND RETURN LINK

## APPENDIX H

### SUBCARRIER TRACKING ANALYSIS FOR THREE-CHANNEL ORBITER KU-BAND RETURN LINK

by

Marvin K. Simon  
Waddah K. Alem

#### INTRODUCTION

In a previous report (Ref. 1, Appendix C), we studied the performance of a Costas loop for recovering the carrier from the three-channel quadrature multiplex signal transmitted on the Orbiter Ku-band return link. We observed there that the output of the quadrature phase detector of this loop serves as the input to the subcarrier tracking loop (see Figure C-2 of Ref. 1, Appendix C). Upon establishing a subcarrier reference signal, the two lower rate modulations,  $m_2(t)$  and  $m_3(t)$ , can then be demodulated. This appendix presents the tracking performance of a Costas loop used for subcarrier recovery (Figure 1).

#### SYSTEM MODEL AND LOOP EQUATION OF OPERATION

Based upon the above comments, the input signal is of the form (see equation (C-15) of Ref. 1, Appendix C):

$$\begin{aligned} x(t) = & \left[ \sqrt{2P_2} s_2(t) + \sqrt{2P_3} s_3(t) + N_c(t) \right] \cos \varphi_c(t) \\ & + \left[ \sqrt{2P_1} s_1(t) - \underbrace{\sqrt{2P_d} s_1(t) s_2(t) s_3(t)}_{s_d(t)} - N_s(t) \right] \sin \varphi_c(t) \end{aligned} \quad (1)$$

where  $\varphi_c(t)$  = carrier tracking loop phase error

$s_1(t) = m_1(t)$  = high rate modulation

$s_2(t) = m_2(t) \sin \omega_{sc} t$  = low rate modulation #1 on square-wave subcarrier

$s_3(t) = m_3(t) \cos \omega_{sc} t$  = low rate modulation #2 on quadrature square-wave subcarrier. (2)

The square-wave subcarrier frequency  $f_{sc} \triangleq \omega_{sc}/2\pi$  is nominally 8.5 MHz, while the modulation  $m_3(t)$  is operation data at a rate  $R_3 = 192$  kbps and the modulation  $m_2(t)$  has a rate  $R_2$  up to 2 Mbps. Thus, assuming that the input bandpass filter  $H(s)$  has amplitude and phase characteristics which

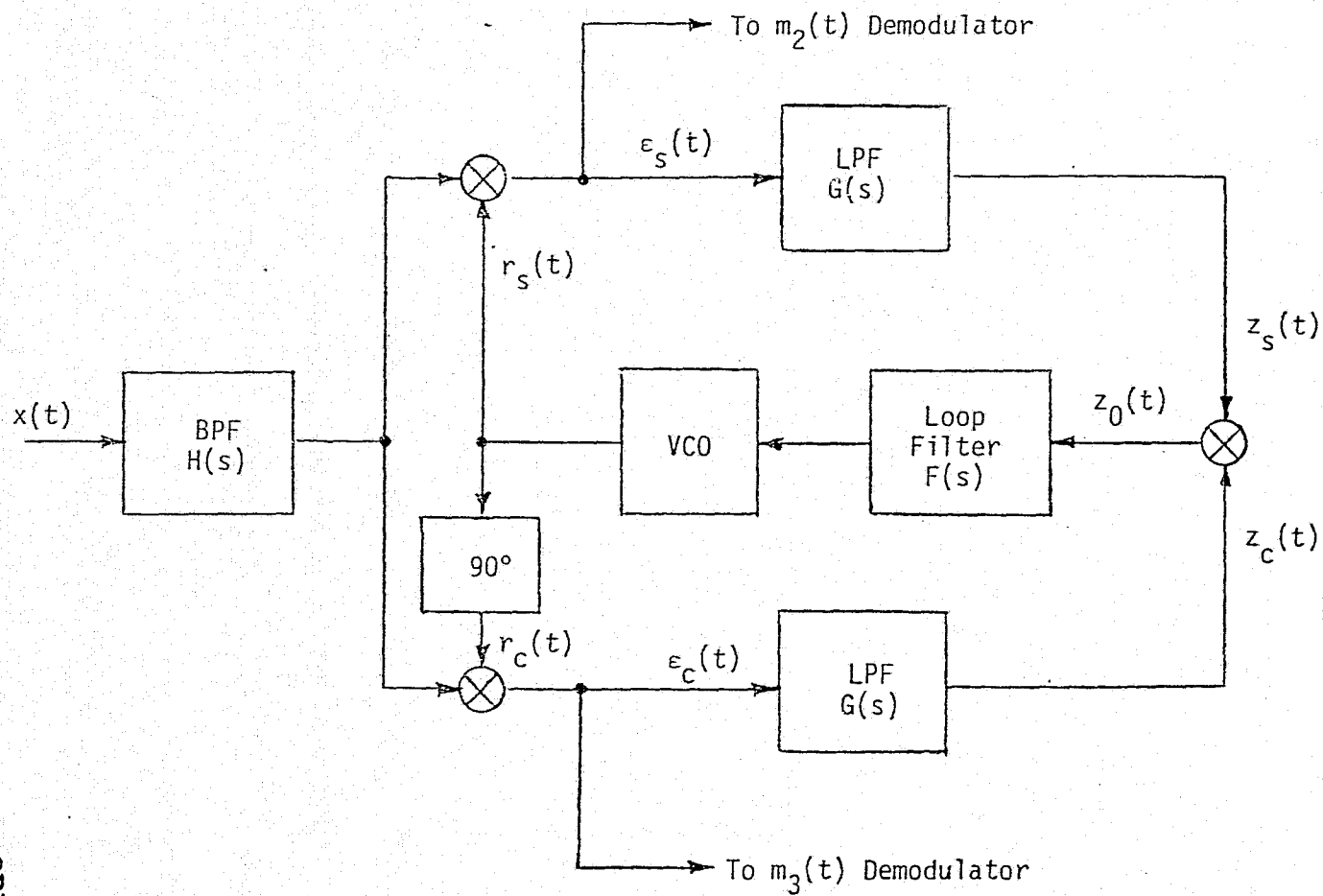


Figure 1. Costas Loop for Subcarrier Tracking

are symmetric around its center frequency  $f_{sc}$ , and a bandwidth which is relatively wide with respect to the two data rates, e.g., on the order of the subcarrier frequency, then letting

$$\begin{aligned} r_s(t) &= \sqrt{2} K_1 \cos [\omega_{sc} t - \varphi_{sc}(t)] \\ r_c(t) &= \sqrt{2} K_1 \sin [\omega_{sc} t - \varphi_{sc}(t)] \end{aligned} \quad (3)$$

and ignoring second harmonics, we get for the quadrature phase detector output:\*

$$\begin{aligned} \varepsilon_c(t) &= K_1 K_m \cos \varphi_c \left[ \frac{4}{\pi} \sqrt{\tilde{p}_2} \hat{m}_2(t) \sin \varphi_{sc} + \frac{4}{\pi} \sqrt{\tilde{p}_3} \hat{m}_3(t) \cos \varphi_{sc} \right. \\ &\quad \left. + \sqrt{2} \hat{N}_c(t) \cos (\omega_{sc} t - \varphi_{sc}) \right] \\ &\quad + K_1 K_m \sin \varphi_c \left[ \sqrt{\tilde{p}_1} \hat{m}_{1c}(t; \omega_{sc}, -\varphi_{sc}) - \sqrt{\tilde{p}_d} \hat{m}_{dc}(t; \omega_{sc}, -\varphi_{sc}) \right. \\ &\quad \left. - \sqrt{2} \hat{N}_s(t) \cos (\omega_{sc} t - \varphi_{sc}) \right]. \end{aligned} \quad (4)$$

In (4),  $K_m$  is the phase detector (multiplier) gain,  $\varphi_{sc}$  is the subcarrier phase error, and the remaining quantities are defined (in operator form) by

$$\begin{aligned} \hat{m}_2(t) &\triangleq H_\ell(p) m_2(t) \\ \hat{m}_3(t) &\triangleq H_\ell(p) m_3(t) \\ \hat{m}_{1c}(t; \omega_{sc}, -\varphi_{sc}) &\triangleq H_\ell(p) [m_1(t) \cos (\omega_{sc} t - \varphi_{sc})] \\ \hat{m}_{dc}(t; \omega_{sc}, -\varphi_{sc}) &\triangleq H_\ell(p) [s_d(t) \cos (\omega_{sc} t - \varphi_{sc})] \end{aligned} \quad (5)$$

and

$$\begin{aligned} \hat{N}_s(t) &\triangleq H(p) N_s(t) \\ \hat{N}_c(t) &\triangleq H(p) N_c(t) \end{aligned} \quad (6)$$

where  $H_\ell(j\omega)$  is the lowpass equivalent of  $H(j\omega)$  and is defined by

$$H_\ell(j\omega) = \frac{1}{2} \left[ H[j(\omega + \omega_{sc})] + H[j(\omega - \omega_{sc})] \right]. \quad (7)$$

---

\* For convenience of notation, we omit the dependence of  $\varphi_c$  and  $\varphi_{sc}$  on  $t$ .

Expanding the filtered noise processes  $\hat{N}_c(t)$  and  $\hat{N}_s(t)$  as

$$\begin{aligned}\hat{N}_c(t) &= \sqrt{2} [\hat{N}_{cc}(t) \cos \omega_{sc} t - \hat{N}_{cs}(t) \sin \omega_{sc} t] \\ \hat{N}_s(t) &= \sqrt{2} [\hat{N}_{sc}(t) \cos \omega_{sc} t - \hat{N}_{ss}(t) \sin \omega_{sc} t],\end{aligned}\quad (8)$$

where  $\hat{N}_{cc}(t)$ ,  $\hat{N}_{cs}(t)$ ,  $\hat{N}_{sc}(t)$ , and  $\hat{N}_{ss}(t)$  are approximately statistically independent, stationary, lowpass Gaussian noise processes with power spectral densities

$$S_{\hat{N}}(\omega) = \frac{N_0}{2} |H_\ell(j\omega)|^2, \quad (9)$$

then substituting (8) into (4) yields

$$\begin{aligned}\epsilon_c(t) &= K_1 K_m \cos \varphi_c \left[ \frac{4}{\pi} \sqrt{\tilde{P}_2} \hat{m}_2(t) \sin \varphi_{sc} + \frac{4}{\pi} \sqrt{\tilde{P}_3} \hat{m}_3(t) \cos \varphi_{sc} \right. \\ &\quad \left. + \hat{N}_{cc}(t) \cos \varphi_{sc} - \hat{N}_{cs}(t) \sin \varphi_{sc} \right] \\ &\quad + K_1 K_m \sin \varphi_c \left[ \sqrt{\tilde{P}_1} \hat{m}_{1c}(t; \omega_{sc}, -\varphi_{sc}) - \sqrt{\tilde{P}_d} \hat{m}_{dc}(t; \omega_{sc}, -\varphi_{sc}) \right. \\ &\quad \left. - \hat{N}_{sc}(t) \cos \varphi_{sc} + \hat{N}_{ss}(t) \sin \varphi_{sc} \right].\end{aligned}\quad (10)$$

Similarly, the output of the in-phase multiplier can be shown to be

$$\begin{aligned}\epsilon_s(t) &= K_1 K_m \cos \varphi_c \left[ \frac{4}{\pi} \sqrt{\tilde{P}_2} \hat{m}_2(t) \cos \varphi_{sc} - \frac{4}{\pi} \sqrt{\tilde{P}_3} \hat{m}_3(t) \sin \varphi_{sc} \right. \\ &\quad \left. - \hat{N}_{cc}(t) \sin \varphi_{sc} - \hat{N}_{cs}(t) \cos \varphi_{sc} \right] \\ &\quad + K_1 K_m \sin \varphi_c \left[ \sqrt{\tilde{P}_1} \hat{m}_{1s}(t; \omega_{sc}, -\varphi_{sc}) - \sqrt{\tilde{P}_d} \hat{m}_{ds}(t; \omega_{sc}, -\varphi_{sc}) \right. \\ &\quad \left. + \hat{N}_{sc}(t) \sin \varphi_{sc} + \hat{N}_{ss}(t) \cos \varphi_{sc} \right],\end{aligned}\quad (11)$$

where (in operational form)

$$\begin{aligned}\hat{m}_{1s}(t; \omega_{sc}, -\varphi_{sc}) &\triangleq H_\ell(p) [m_1(t) \sin(\omega_{sc} t - \varphi_{sc})] \\ \hat{m}_{ds}(t; \omega_{sc}, -\varphi_{sc}) &\triangleq H_\ell(p) [s_d(t) \sin(\omega_{sc} t - \varphi_{sc})].\end{aligned}\quad (12)$$

After lowpass filtering with in-phase and quadrature arm filters  $G(s)$ , the phase detector output signals  $z_c(t)$  and  $z_s(t)$  are given by (10) and (11), respectively, where the "hats" now denote filtering by the cascade  $G_0(s) \triangleq H_\ell(s) G(s)$ . Multiplying these two low pass filter outputs

(assuming, for simplicity, that this multiplier has unit gain) gives the dynamic error signal:

$$\begin{aligned}
 z_0(t) &\triangleq z_c(t) z_s(t) \\
 &= \frac{K_1^2 K_m^2}{2} \left\{ \frac{16}{\pi^2} \cos^2 \varphi_c [\bar{p}_2 \hat{m}_2^2(t) - \bar{p}_3 \hat{m}_3^2(t)] \sin 2\varphi_{sc} \right. \\
 &\quad + \frac{32}{\pi^2} \cos^2 \varphi_c \sqrt{\bar{p}_2 \bar{p}_3} \hat{m}_2(t) \hat{m}_3(t) \cos 2\varphi_{sc} \\
 &\quad + 2 \sin^2 \varphi_c \bar{p}_1 \hat{m}_{1s}(t; \omega_{sc}, -\varphi_{sc}) \hat{m}_{1c}(t; \omega_{sc}, -\varphi_{sc}) \\
 &\quad + 2 \sin^2 \varphi_c \bar{p}_d \hat{m}_{ds}(t; \omega_{sc}, -\varphi_{sc}) \hat{m}_{dc}(t; \omega_{sc}, -\varphi_{sc}) \\
 &\quad - 2 \sin^2 \varphi_c \sqrt{\bar{p}_1 \bar{p}_d} \hat{m}_{1c}(t; \omega_{sc}, -\varphi_{sc}) \hat{m}_{ds}(t; \omega_{sc}, -\varphi_{sc}) \\
 &\quad - 2 \sin^2 \varphi_c \sqrt{\bar{p}_1 \bar{p}_d} \hat{m}_{1s}(t; \omega_{sc}, -\varphi_{sc}) \hat{m}_{dc}(t; \omega_{sc}, -\varphi_{sc}) \\
 &\quad + \frac{4}{\pi} \sin 2\varphi_c \left[ \sqrt{\bar{p}_2} \hat{m}_2(t) \sin \varphi_{sc} + \sqrt{\bar{p}_3} \hat{m}_3(t) \sin \varphi_{sc} \right] \\
 &\quad \cdot \left[ \sqrt{\bar{p}_1} \hat{m}_{1s}(t; \omega_{sc}, -\varphi_{sc}) - \sqrt{\bar{p}_d} \hat{m}_{ds}(t; \omega_{sc}, -\varphi_{sc}) \right] \\
 &\quad + \frac{4}{\pi} \sin 2\varphi_c \left[ \sqrt{\bar{p}_2} \hat{m}_2(t) \cos \varphi_{sc} - \sqrt{\bar{p}_3} \hat{m}_3(t) \cos \varphi_{sc} \right] \\
 &\quad \cdot \left[ \sqrt{\bar{p}_1} \hat{m}_{1c}(t; \omega_{sc}, -\varphi_{sc}) - \sqrt{\bar{p}_d} \hat{m}_{dc}(t; \omega_{sc}, -\varphi_{sc}) \right] \\
 &\quad \left. + v_2(t; \varphi_c, 2\varphi_{sc}) \right\} \tag{13}
 \end{aligned}$$

where

$$v_2(t; \varphi_c, 2\varphi_{sc}) = A_s \sin 2\varphi_{sc} + A_c \cos 2\varphi_{sc} \tag{14}$$

with

$$\begin{aligned}
 A_s \triangleq & \cos^2 \varphi_c [\hat{N}_{cs}^2(t) - \hat{N}_{cc}^2(t)] \sin 2\varphi_{sc} \\
 & + \sin^2 \varphi_c [\hat{N}_{ss}^2(t) - \hat{N}_{sc}^2(t)] \sin 2\varphi_{sc} \\
 & + 2 \sin \varphi_c \cos \varphi_c [\hat{N}_{cc}(t) \hat{N}_{sc}(t) - \hat{N}_{cs}(t) \hat{N}_{ss}(t)] \\
 & - \frac{8}{\pi} \cos^2 \varphi_c \left[ \sqrt{\tilde{p}_2} \hat{N}_{cs}(t) \hat{m}_2(t) + \sqrt{\tilde{p}_3} \hat{N}_{cc}(t) \hat{m}_3(t) \right] \\
 & + \frac{8}{\pi} \sin \varphi_c \cos \varphi_c \left[ \sqrt{\tilde{p}_2} \hat{N}_{ss}(t) \hat{m}_2(t) + \sqrt{\tilde{p}_3} \hat{N}_{sc}(t) \hat{m}_3(t) \right] \\
 & + 2 \sin^2 \varphi_c \left\{ \left[ \sqrt{\tilde{p}_1} \hat{m}_{1c}(t; \omega_{sc}) - \sqrt{\tilde{p}_d} \hat{m}_{dc}(t; \omega_{sc}) \right] \hat{N}_{sc}(t) \right. \\
 & \quad \left. + \left[ \sqrt{\tilde{p}_1} \hat{m}_{1s}(t; \omega_{sc}) - \sqrt{\tilde{p}_d} \hat{m}_{ds}(t; \omega_{sc}) \right] \hat{N}_{ss}(t) \right\} \\
 & - 2 \sin \varphi_c \cos \varphi_c \left\{ \left[ \sqrt{\tilde{p}_1} \hat{m}_{1c}(t; \omega_{sc}) - \sqrt{\tilde{p}_d} \hat{m}_{dc}(t; \omega_{sc}) \right] \hat{N}_{cc}(t) \right. \\
 & \quad \left. + \left[ \sqrt{\tilde{p}_1} \hat{m}_{1s}(t; \omega_{sc}) - \sqrt{\tilde{p}_d} \hat{m}_{ds}(t; \omega_{sc}) \right] \hat{N}_{cs}(t) \right\}
 \end{aligned} \tag{15}$$

and

$$\begin{aligned}
 A_c \triangleq & -2 \sin^2 \varphi_c \hat{N}_{sc}(t) \hat{N}_{ss}(t) - 2 \cos^2 \varphi_c \hat{N}_{cs}(t) \hat{N}_{cc}(t) \\
 & + 2 \sin \varphi_c \cos \varphi_c [\hat{N}_{cs}(t) \hat{N}_{sc}(t) + \hat{N}_{cc}(t) \hat{N}_{ss}(t)] \\
 & + \frac{8}{\pi} \cos^2 \varphi_c \left[ \sqrt{\tilde{p}_2} \hat{N}_{cc}(t) \hat{m}_2(t) - \sqrt{\tilde{p}_3} \hat{N}_{cs}(t) \hat{m}_3(t) \right] \\
 & - \frac{8}{\pi} \sin \varphi_c \cos \varphi_c \left[ \sqrt{\tilde{p}_2} \hat{N}_{sc}(t) \hat{m}_2(t) - \sqrt{\tilde{p}_3} \hat{N}_{ss}(t) \hat{m}_3(t) \right] \\
 & + 2 \sin^2 \varphi_c \left\{ \left[ \sqrt{\tilde{p}_1} \hat{m}_{1c}(t; \omega_{sc}) - \sqrt{\tilde{p}_d} \hat{m}_{dc}(t; \omega_{sc}) \right] \hat{N}_{ss}(t) \right. \\
 & \quad \left. - \left[ \sqrt{\tilde{p}_1} \hat{m}_{1s}(t; \omega_{sc}) - \sqrt{\tilde{p}_d} \hat{m}_{ds}(t; \omega_{sc}) \right] \hat{N}_{sc}(t) \right\} \\
 & - 2 \sin \varphi_c \cos \varphi_c \left\{ \left[ \sqrt{\tilde{p}_1} \hat{m}_{1c}(t; \omega_{sc}) - \sqrt{\tilde{p}_d} \hat{m}_{dc}(t; \omega_{sc}) \right] \hat{N}_{cs}(t) \right. \\
 & \quad \left. - \left[ \sqrt{\tilde{p}_1} \hat{m}_{1s}(t; \omega_{sc}) - \sqrt{\tilde{p}_d} \hat{m}_{ds}(t; \omega_{sc}) \right] \hat{N}_{cc}(t) \right\}
 \end{aligned} \tag{16}$$



and

$$\begin{aligned}
 \hat{m}_{1c}(t; \omega_{sc}) &\triangleq \hat{m}_{1c}(t; \omega_{sc}, 0) = G_0(p) [m_1(t) \cos \omega_{sc} t] \\
 \hat{m}_{1s}(t; \omega_{sc}) &\triangleq \hat{m}_{1s}(t; \omega_{sc}, 0) = G_0(p) [m_1(t) \sin \omega_{sc} t] \\
 \hat{m}_{dc}(t; \omega_{sc}) &\triangleq \hat{m}_{dc}(t; \omega_{sc}, 0) = G_0(p) [s_d(t) \cos \omega_{sc} t] \\
 \hat{m}_{ds}(t; \omega_{sc}) &\triangleq \hat{m}_{ds}(t; \omega_{sc}, 0) = G_0(p) [s_d(t) \sin \omega_{sc} t]. \quad (17)
 \end{aligned}$$

Each of the signal terms in (13) can be broken up into its mean value and a self-modulation component around the mean, e.g.,

$$\begin{aligned}
 \tilde{p}_2 \hat{m}_2^2(t) - \tilde{p}_3 \hat{m}_3^2(t) &= \langle [\tilde{p}_2 \hat{m}_2^2(t) - \tilde{p}_3 \hat{m}_3^2(t)] \rangle \\
 &\quad + \tilde{p}_2 [\hat{m}_2^2(t) - \langle \hat{m}_2^2(t) \rangle] - \tilde{p}_3 [\hat{m}_3^2(t) - \langle \hat{m}_3^2(t) \rangle] \quad (18)
 \end{aligned}$$

As before in analyses of this type (Ref. 1, Appendix C; Ref. 2), we shall neglect the effects of the self-modulation noise components. Furthermore, for the cross-modulation noise components, we may set  $\varphi_c = \varphi_{sc} = 0$ , which eliminates all but that due to the  $\hat{m}_2(t) \hat{m}_3(t)$  product. Finally, by analogy with (21) and (33) of Ref. 1, Appendix J,

$$\begin{aligned}
 \langle \hat{m}_{1s}(t; \omega_{sc}, -\varphi_{sc}) \hat{m}_{1c}(t; \omega_{sc}, -\varphi_{sc}) \rangle &= \\
 \lim_{T_0 \rightarrow \infty} \frac{1}{4jT_1} e^{-j\varphi_{sc}} \sum_{k=-\infty}^{\infty} \int_{-\infty}^{\infty} G_0 \left[ j \left( \omega + \omega_{sc} + \frac{2\pi k}{T_1} \right) \right] P \left[ j \left( \omega + \frac{2\pi k}{T_1} \right) \right] \\
 \times G_0 \left[ j(-\omega + \omega_{sc}) \right] P(-j\omega) \frac{\sin \left[ \left( \frac{2\pi k}{T_1} + 2\omega_{sc} \right) \left( \frac{T_0}{2} \right) \right]}{\left( \frac{2\pi k}{T_1} + 2\omega_{sc} \right) \left( \frac{T_0}{2} \right)} \frac{d\omega}{2\pi} \\
 - e^{j\varphi_{sc}} \sum_{k=-\infty}^{\infty} \int_{-\infty}^{\infty} G_0 \left[ j \left( \omega - \omega_{sc} + \frac{2\pi k}{T_1} \right) \right] P \left[ j \left( \omega + \frac{2\pi k}{T_1} \right) \right] \\
 \times G_0 \left[ j(-\omega - \omega_{sc}) \right] P(-j\omega) \frac{\sin \left[ \left( \frac{2\pi k}{T_1} - 2\omega_{sc} \right) \left( \frac{T_0}{2} \right) \right]}{\left( \frac{2\pi k}{T_1} - 2\omega_{sc} \right) \left( \frac{T_0}{2} \right)} \frac{d\omega}{2\pi} \quad (19)
 \end{aligned}$$

where  $R_1 \triangleq 1/T_1$  is the data symbol rate of  $m_1(t)$ . Since  $(2\pi k)/T_1 \gg \omega_{sc}$  for any  $k \neq 0$ , and for  $k = 0$ ,

$$\lim_{T_0 \rightarrow \infty} \frac{\sin \omega_{sc} T_0}{\omega_{sc} T_0} = 0, \quad (20)$$

then

$$\langle \hat{m}_{1s}(t; \omega_{sc}, -\varphi_{sc}) \hat{m}_{1c}(t; \omega_{sc}, -\varphi_{sc}) \rangle = 0. \quad (21)$$

Similarly,

$$\begin{aligned} \langle \hat{m}_{ds}(t; \omega_{sc}, -\varphi_{sc}) \hat{m}_{dc}(t; \omega_{sc}, -\varphi_{sc}) \rangle &= 0 \\ \langle \hat{m}_{1c}(t; \omega_{sc}, -\varphi_{sc}) \hat{m}_{ds}(t; \omega_{sc}, -\varphi_{sc}) \rangle &= 0 \\ \langle \hat{m}_{1s}(t; \omega_{sc}, -\varphi_{sc}) \hat{m}_{dc}(t; \omega_{sc}, -\varphi_{sc}) \rangle &= 0. \end{aligned} \quad (22)$$

Also, since  $m_i(t)$  and  $m_j(t)$ ,  $i \neq j$ , are independent, we have, for example,

$$\overline{m_2(t) m_3(t)} = 0; \quad \overline{\hat{m}_2(t) \hat{m}_{1s}(t; \omega_{sc}, -\varphi_{sc})} = 0; \text{ etc.} \quad (23)$$

Thus, (13) simplifies to

$$\begin{aligned} z_0(t) = \frac{K_1^2 K_m^2}{2} \left\{ \left( \frac{4}{\pi} \right)^2 \cos^2 \varphi_c [\tilde{p}_2 D_2 - \tilde{p}_3 D_3] \sin 2\varphi_{sc} \right. \\ \left. + 2 \left( \frac{4}{\pi} \right)^2 \sqrt{\tilde{p}_2 \tilde{p}_3} n_{23}(t) + v_2(t; \varphi_c, 2\varphi_{sc}) \right\} \end{aligned} \quad (24)$$

where

$$D_i \triangleq \overline{\hat{m}_i^2(t)} = \int_{-\infty}^{\infty} S_{m_i}(\omega) |G_0(j\omega)|^2 \frac{d\omega}{2\pi}; \quad i = 2, 3 \quad (25)$$

with  $S_{m_i}(\omega)$  denoting the power spectral density of  $m_i(t)$  and  $n_{23}(t) \triangleq \hat{m}_2(t) \hat{m}_3(t)$ .

The instantaneous frequency of the VCO output is related to  $z_0(t)$  by

$$\frac{d\hat{\phi}(t)}{dt} = K_V [F(p) z_0(t)] + \omega_{sc} \quad (26)$$

where  $F(p)$  is the loop filter transfer function and  $K_V$  is the VCO gain in rad/sec/v. Thus the stochastic integro-differential equation of loop operation becomes

$$\frac{2 d\varphi(t)}{dt} = K F(p) \left\{ \left(\frac{4}{\pi}\right)^2 \cos^2 \varphi_c [\tilde{P}_2 D_2 - \tilde{P}_3 D_3] \sin 2\varphi_{sc} + \underbrace{2 \left(\frac{4}{\pi}\right)^2 \sqrt{\tilde{P}_2 \tilde{P}_3} n_{23}(t) + v_2(t; \varphi_c, 2\varphi_{sc})}_{n_e(t; \varphi_c, 2\varphi_{sc})} \right\} \quad (27)$$

where  $K \triangleq K_1^2 K_m^2 K_V$ .

#### CHARACTERIZATION OF THE EQUIVALENT ADDITIVE NOISE

We now proceed to evaluate the noise spectral density,  $N_e$ , of the equivalent delta-correlated noise process,  $n_e(t; \varphi_c, 2\varphi_{sc})$ :

$$N_e = 2 \left\{ 4 \left(\frac{4}{\pi}\right)^4 \tilde{P}_2 \tilde{P}_3 \int_{-\infty}^{\infty} R_{23}(\tau) d\tau + \int_{-\infty}^{\infty} R_{v_2}(\tau) d\tau \right\} \quad (28)$$

where

$$R_{v_2}(\tau) \triangleq \overline{v_2(t; \varphi_c, 2\varphi_{sc}) v_2(t+\tau; \varphi_c, 2\varphi_{sc})}$$

$$R_{23}(\tau) \triangleq \langle \overline{n_{23}(t) n_{23}(t+\tau)} \rangle. \quad (29)$$

Substituting (14), (15), and (16) into (29), we obtain, after considerable algebraic manipulation

$$R_{v_2}(\tau) = 4 R_{\hat{N}}^2(\tau) + 4 \left(\frac{4}{\pi}\right)^2 [\tilde{P}_2 R_{\hat{m}_2}(\tau) + \tilde{P}_3 R_{\hat{m}_3}(\tau)] R_{\hat{N}}(\tau) + 4 \left[ \tilde{P}_1 (R_{\hat{m}_{1c}}(\tau; \omega_{sc}) + R_{\hat{m}_{1s}}(\tau; \omega_{sc})) + \tilde{P}_d (R_{\hat{m}_{dc}}(\tau; \omega_{sc}) + R_{\hat{m}_{ds}}(\tau; \omega_{sc})) \right] R_{\hat{N}}(\tau)$$

$$R_{23}(\tau) = R_{\hat{m}_2}(\tau) R_{\hat{m}_3}(\tau) \quad (30)$$

where

$$\begin{aligned}
R_{\hat{m}_i}(\tau) &\triangleq \overline{\langle \hat{m}_i(t) \hat{m}_i(t+\tau) \rangle} ; \quad i = 2, 3 \\
R_{\hat{m}_{1c}}(\tau; \omega_{sc}) &\triangleq \overline{\langle \hat{m}_{1c}(t; \omega_{sc}) \hat{m}_{1c}(t+\tau; \omega_{sc}) \rangle} \\
R_{\hat{m}_{dc}}(\tau; \omega_{sc}) &\triangleq \overline{\langle \hat{m}_{dc}(t; \omega_{sc}) \hat{m}_{dc}(t+\tau; \omega_{sc}) \rangle}
\end{aligned} \tag{31}$$

and similar definitions for the autocorrelation functions  $R_{\hat{m}_{1s}}(\tau; \omega_{sc})$  and  $R_{\hat{m}_{ds}}(\tau; \omega_{sc})$ . Also,

$$R_{\hat{N}}(\tau) \triangleq \frac{N_0}{2} \int_{-\infty}^{\infty} |G_0(j\omega)|^2 e^{j\omega\tau} \frac{d\omega}{2\pi} . \tag{32}$$

Integrating (30) between  $-\infty$  and  $\infty$  and noting that

$$\begin{aligned}
\int_{-\infty}^{\infty} R_{\hat{N}}^2(\tau) d\tau &= \left(\frac{N_0}{2}\right)^2 \int_{-\infty}^{\infty} |G_0(j\omega)|^4 \frac{d\omega}{2\pi} \\
\int_{-\infty}^{\infty} R_{\hat{m}_i}(\tau) R_{\hat{N}}(\tau) d\tau &= \frac{N_0}{2} \int_{-\infty}^{\infty} S_{m_i}(\omega) |G_0(j\omega)|^4 \frac{d\omega}{2\pi} ; \quad i = 2, 3 \\
\int_{-\infty}^{\infty} R_{\hat{m}_{1c}}(\tau; \omega_{sc}) R_{\hat{N}}(\tau) d\tau &= \frac{N_0}{2} \int_{-\infty}^{\infty} S_{m_{1c}}(\omega; \omega_{sc}) |G_0(j\omega)|^4 \frac{d\omega}{2\pi} \\
\int_{-\infty}^{\infty} R_{\hat{m}_{dc}}(\tau; \omega_{sc}) R_{\hat{N}}(\tau) d\tau &= \frac{N_0}{2} \int_{-\infty}^{\infty} S_{m_{dc}}(\omega; \omega_{sc}) |G_0(j\omega)|^4 \frac{d\omega}{2\pi} \\
&\vdots \\
&\text{etc.} \\
\int_{-\infty}^{\infty} R_{\hat{m}_2}(\tau) R_{\hat{m}_3}(\tau) d\tau &= \int_{-\infty}^{\infty} S_{m_2}(\omega) S_{m_3}(\omega) |G_0(j\omega)|^4 \frac{d\omega}{2\pi} ,
\end{aligned} \tag{33}$$

with

$$\begin{aligned}
S_{m_{1c}}(\omega; \omega_{sc}) &= \text{power spectral density of } m_1(t) \cos \omega_{sc} t \\
S_{m_{dc}}(\omega; \omega_{sc}) &= \text{power spectral density of } s_d(t) \cos \omega_{sc} t \\
&\vdots \\
&\text{etc.,}
\end{aligned} \tag{34}$$

we get an expression for  $N_e$  given by

ORIGINAL PAGE IS  
OF POOR QUALITY

$$\begin{aligned}
N_e = & 4 N_0 \left\{ \frac{N_0}{2} \int_{-\infty}^{\infty} |G_0(j\omega)|^4 \frac{d\omega}{2\pi} + \left(\frac{4}{\pi}\right)^2 \left[ \tilde{P}_2 \int_{-\infty}^{\infty} S_{m_2}(\omega) |G_0(j\omega)|^4 \frac{d\omega}{2\pi} \right. \right. \\
& + \tilde{P}_3 \int_{-\infty}^{\infty} S_{m_3}(\omega) |G_0(j\omega)|^4 \frac{d\omega}{2\pi} \left. + \tilde{P}_1 \int_{-\infty}^{\infty} S_{m_1}(\omega) |G_0[j(\omega-\omega_{sc})]|^4 \frac{d\omega}{2\pi} \right. \\
& + \left. \tilde{P}_d \int_{-\infty}^{\infty} S_{m_d}(\omega) |G_0[j(\omega-\omega_{sc})]|^4 \frac{d\omega}{2\pi} \right\} \\
& + 8 \left(\frac{4}{\pi}\right)^4 \tilde{P}_2 \tilde{P}_3 \int_{-\infty}^{\infty} S_{m_2}(\omega) S_{m_3}(\omega) |G_0(j\omega)|^4 \frac{d\omega}{2\pi} .
\end{aligned} \quad (35)$$

In arriving at (35), we have used the additional relations

$$\begin{aligned}
S_{m_{1c}}(\omega; \omega_{sc}) + S_{m_{1s}}(\omega; \omega_{sc}) &= \frac{1}{2} S_{m_1}(\omega - \omega_{sc}) + \frac{1}{2} S_{m_1}(\omega + \omega_{sc}) \\
S_{m_{dc}}(\omega; \omega_{sc}) + S_{m_{ds}}(\omega; \omega_{sc}) &= \frac{1}{2} S_{m_d}(\omega - \omega_{sc}) + \frac{1}{2} S_{m_d}(\omega + \omega_{sc}) ,
\end{aligned} \quad (36)$$

where  $S_{m_1}(\omega)$  and  $S_{m_d}(\omega)$  are the power spectral densities of  $m_1(t)$  and  $s_d(t)$ , respectively. Also, we have taken note of the fact that  $S_{m_1}(\omega)$ ,  $S_{m_d}(\omega)$ , and  $|G_0(j\omega)|^4$  are even functions of  $\omega$ .

Finally, from (27), the equivalent loop signal-to-noise ratio,  $\rho'$ , is

$$\rho' = \frac{\left\{ \cos^2 \varphi_c \left(\frac{4}{\pi}\right)^2 [\tilde{P}_2 D_2 - \tilde{P}_3 D_3] \right\}^2}{N_e B_L} \triangleq \frac{\rho}{4} S_L , \quad (37)$$

where  $\rho = P/N_0 B_L$  is the loop signal-to-noise ratio of a phase-locked (CW) loop operating on the total power  $P \triangleq \tilde{P}_1 + \tilde{P}_2 + \tilde{P}_3 + \tilde{P}_d$ , and

$$S_L = \frac{4 N_0 P}{N_e} \left\{ \cos^2 \varphi_c \left(\frac{4}{\pi}\right)^2 \left[ \frac{\tilde{P}_2 D_2 - \tilde{P}_3 D_3}{P} \right] \right\}^2 \quad (38)$$

is the loop squaring loss. Defining the modulation indices  $\eta_i$ ;  $i=1,2,3$ ; and  $\eta_d$  by

$$\begin{aligned}
\eta_i &= \frac{\tilde{P}_i}{P} ; \quad i=1,2,3 \\
\eta_d &= \frac{\tilde{P}_d}{P} ,
\end{aligned}$$

ORIGINAL PAGE IS  
OF POOR QUALITY

(39)

we obtain, after much simplification,

$$S_L = \frac{\left\{ \cos^2 \varphi_c \left( \frac{4}{\pi} \right)^2 [\eta_2 D_2 - \eta_3 D_3] \right\}^2}{\widehat{\eta D K_D} + \frac{K_L}{\rho_i} + 2 \left( \frac{4}{\pi} \right)^4 \eta_2 \eta_3 \frac{P}{N_0} D_{23}} \quad (40)$$

where

$$K_L \triangleq \frac{\int_{-\infty}^{\infty} |G_0(j\omega)|^4 \frac{d\omega}{2\pi}}{\int_{-\infty}^{\infty} |G_0(j\omega)|^2 \frac{d\omega}{2\pi}}$$

$$D_{23} \triangleq \int_{-\infty}^{\infty} S_{m_2}(\omega) S_{m_3}(\omega) |G_0(j\omega)|^4 \frac{d\omega}{2\pi}$$

$$\begin{aligned} \widehat{\eta D K_D} \triangleq & \left( \frac{4}{\pi} \right)^2 \left[ \eta_2 \int_{-\infty}^{\infty} S_{m_2}(\omega) |G_0(j\omega)|^4 \frac{d\omega}{2\pi} + \eta_3 \int_{-\infty}^{\infty} S_{m_3}(\omega) |G_0(j\omega)|^4 \frac{d\omega}{2\pi} \right] \\ & + \eta_1 \int_{-\infty}^{\infty} S_{m_1}(\omega) |G_0[j(\omega - \omega_{sc})]|^4 \frac{d\omega}{2\pi} + \eta_d \int_{-\infty}^{\infty} S_{m_d}(\omega) |G_0[j(\omega - \omega_{sc})]|^4 \frac{d\omega}{2\pi} \end{aligned} \quad (41)$$

and  $\rho_i = 2P/N_0 B_i$  is the signal-to-noise ratio in the "arm filter" bandwidth\*  $B_i$  defined by

$$B_i \triangleq \frac{1}{2\pi} \int_{-\infty}^{\infty} |G_0(j\omega)|^2 d\omega. \quad (42)$$

Assuming arbitrarily that  $R_2 > R_3$ , then (40) can be rewritten as

$$S_L = \frac{\left\{ \cos^2 \varphi_c \left( \frac{4}{\pi} \right)^2 [\eta_2 D_2 - \eta_3 D_3] \right\}^2}{\widehat{\eta D K_D} + \frac{K_L B_i / R_2}{2 P_T / N_0} + 2 \left( \frac{4}{\pi} \right)^4 \eta_2 \eta_3 \left( \frac{P_T}{N_0} \right) \frac{D_{23}}{T_2}} \quad (43)$$

The tracking phase jitter performance can now be specified. In the linear region, the variance of the loop phase error  $2\varphi$  is given by

\*Note that the bandwidth defined in (42) actually characterizes the cascade of the subcarrier loop arm filter and the lowpass equivalent of the input bandpass filter.

$$\sigma_{2\varphi}^2 = \frac{1}{\rho'} = \frac{4}{\rho S_L},$$

where  $\rho'$  is given in (37). However, since the demodulation reference signals in (3) are at  $\omega_{sc}$  rather than  $2\omega_{sc}$ , then the tracking jitter on the output data streams is

$$\sigma_{\varphi}^2 = \frac{1}{4} \sigma_{2\varphi}^2 = \frac{1}{\rho S_L}. \quad (44)$$

We note that  $S_{m_d}(\omega)$  is similar to  $S_{m_1}(\omega)$  except that it is spread slightly at the high frequencies because of the multiplication of  $m_1(t)$  by  $s_2(t)$  and  $s_3(t)$ . However, since  $\omega_{sc} \ll 2\pi/T_1$ , then  $S_{m_1}(\omega)$  and  $S_{m_d}(\omega)$  are approximately the same in the vicinity of the subcarrier frequency. Thus, to a good approximation,

$$\int_{-\infty}^{\infty} S_{m_1}(\omega) \left| G_0[j(\omega - \omega_{sc})] \right|^k \frac{d\omega}{2\pi} \cong \int_{-\infty}^{\infty} S_{m_d}(\omega) \left| G_0[j(\omega - \omega_{sc})] \right|^k \frac{d\omega}{2\pi};$$

$$k = 2, 4. \quad (45)$$

Additional practical assumptions can be invoked to simplify (44) still further. Since the bandwidth  $B_i$  of  $G_0(j\omega)$  is typically selected on the order of the larger of the two data rates  $1/T_2$  and  $1/T_3$  and since  $1/T_1 \gg 1/T_2$  or  $1/T_3$ , then

$$\begin{aligned} \int_{-\infty}^{\infty} S_{m_1}(\omega) \left| G_0[j(\omega - \omega_{sc})] \right|^k \frac{d\omega}{2\pi} &\cong S_{m_1}(\omega_{sc}) \int_{-\infty}^{\infty} \left| G_0(j\omega) \right|^k \frac{d\omega}{2\pi} \\ &= \begin{cases} S_{m_1}(\omega_{sc}) B_i & ; \quad k = 2 \\ S_{m_1}(\omega_{sc}) K_L B_i & ; \quad k = 4 \end{cases} \end{aligned} \quad (46)$$

As an example, suppose  $m_1(t)$  is an NRZ modulation of rate  $R_1 = 1/T_1$ .\* Then,

$$S_{m_1}(\omega) = T_1 \left( \frac{\sin \omega T_1 / 2}{\omega T_1 / 2} \right)^2 = \frac{1}{R_1} \left( \frac{\sin \pi f_{sc} / R_1}{\pi f_c / R_1} \right)^2 \quad (47)$$

For a subcarrier frequency of 8.5 MHz, and data rate  $1/T_1 = 100$  Msps,

\* In mode 1 of the Space Shuttle Orbiter-TDRSS Ku-band return link,  $m_1(t)$  is a rate 1/2, constraint length 7, convolutional code with data rate 100 Msps.

$$\begin{aligned}
 S_{m_1}(\omega_{sc}) &= \frac{1}{100 \times 10^6} \left( \frac{\sin \pi(8.5/100)}{\pi(8.5/100)} \right) \\
 &= \frac{0.988}{100 \times 10^6} .
 \end{aligned}$$

The numerical evaluation of the subcarrier tracking jitter (44) for a fixed ratio of arm filter noise bandwidth to loop noise bandwidth ( $B_i/B_L$ ) is shown in Figures 2 through 5. Three assumptions are made:

- (a) The carrier loop is tracking perfectly; thus,  $\cos \varphi_c = 1$ .
- (b) The bandwidth of  $H(\omega)$  is much wider than that of arm filters  $G(\omega)$ .
- (c) The arm filters  $G(\omega)$  are assumed to be one-pole Butterworth (RC) filters or

$$|G(j 2\pi f)|^2 = \frac{1}{1 + (f/f_c)^2}, \quad (48)$$

where  $f_c$  is the cutoff frequency. The two-sided noise bandwidth (42) of  $G(j 2\pi f)$  is given by

$$B_i = \pi f_c. \quad (49)$$

Figures 2 and 3 illustrate the case when  $m_1(t)$  and  $m_2(t)$  are NRZ, while  $m_3(t)$  is a Manchester code. Figures 4 and 5 illustrate the case when  $m_1(t)$  is NRZ, while both  $m_2(t)$  and  $m_3(t)$  are Manchester codes. The even figures have the signal-to-noise ratio ( $PT_2/N_0$ ) as a parameter, while the odd figures have the high subcarrier data rate  $R_2$  as a parameter.

It is observed that the changes in the subcarrier tracking jitter as a function of  $B_i/R_2$  are more obvious when  $m_2(t)$  and  $m_3(t)$  are both Manchester codes than when  $m_2(t)$  is NRZ and  $m_3(t)$  is Manchester.



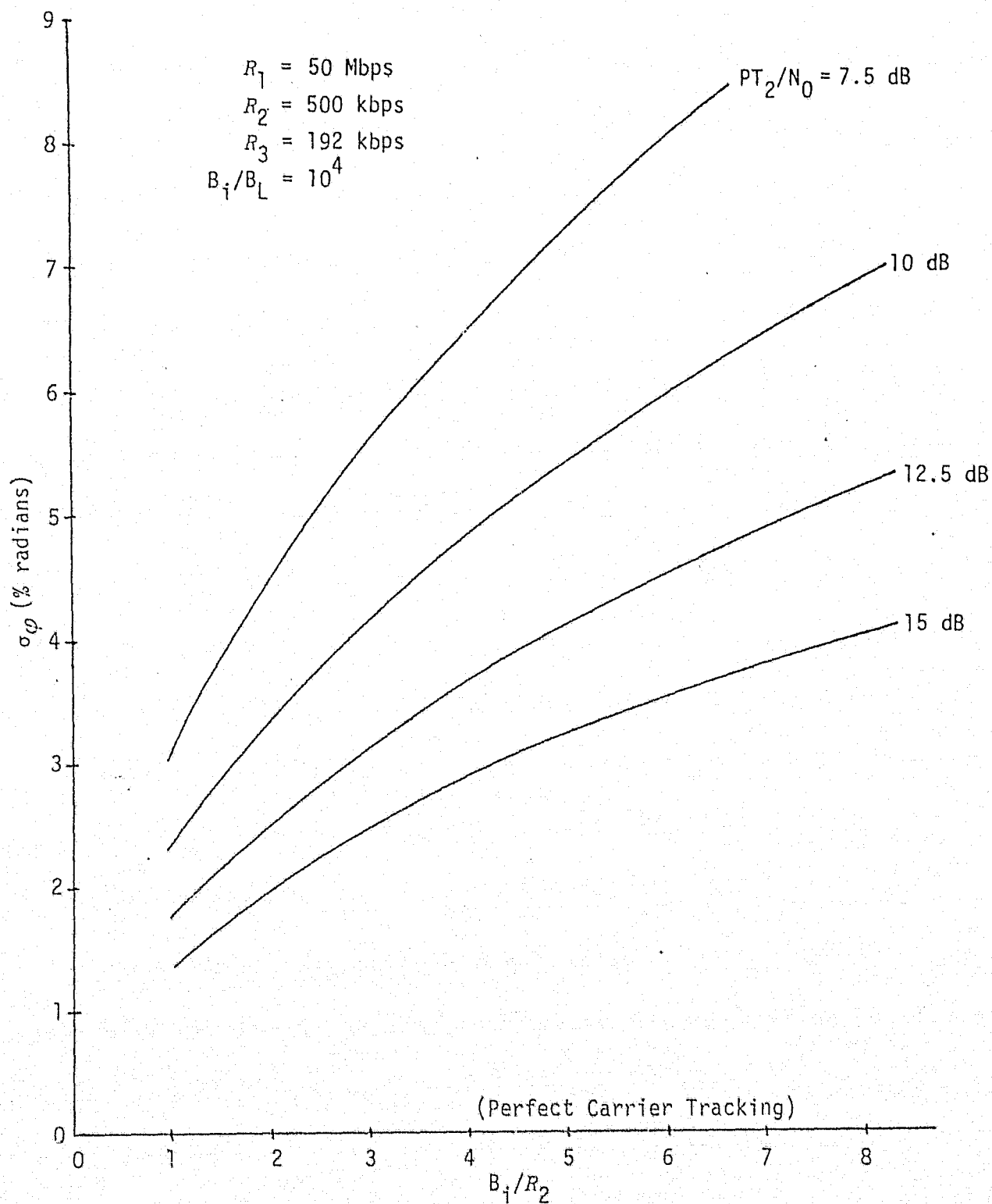


Figure 2. Subcarrier Tracking Jitter versus Ratio of Arm Filter Bandwidth to High Subcarrier Data Rate  $R_2$ ;  $PT_2/N_0$  is a parameter;  $m_1(t)$  and  $m_2(t)$  are NRZ,  $m_3(t)$  is Manchester;  $R_1 > R_2 > R_3$ .

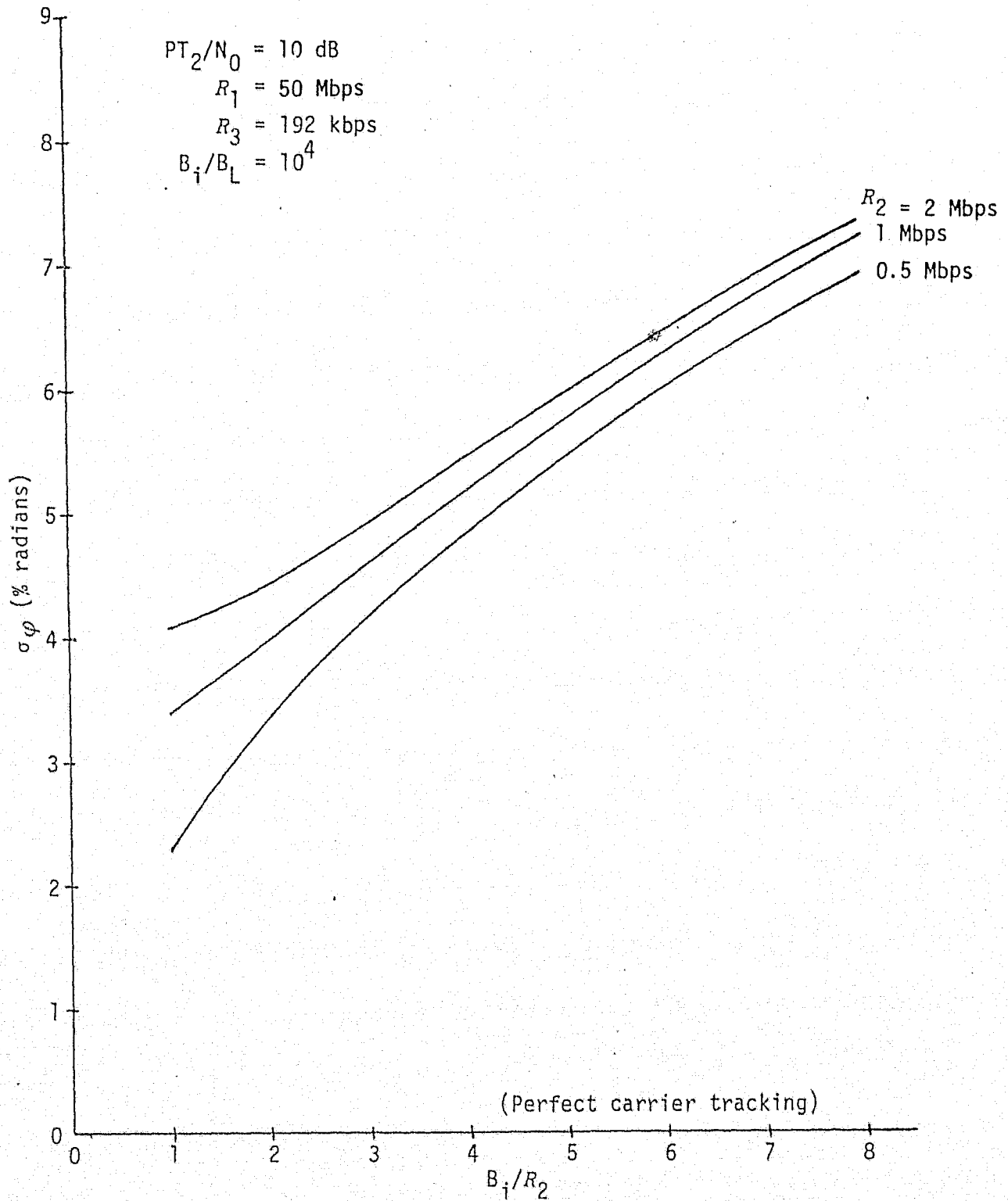


Figure 3. Subcarrier Tracking Jitter versus Ratio of Arm Filter Bandwidth to High Subcarrier Data Rate  $R_2$ ;  $R_2$  is a parameter;  $m_1(t)$  and  $m_2(t)$  are NRZ,  $m_3(t)$  is Manchester code;  $R_1 > R_2 > R_3$ .

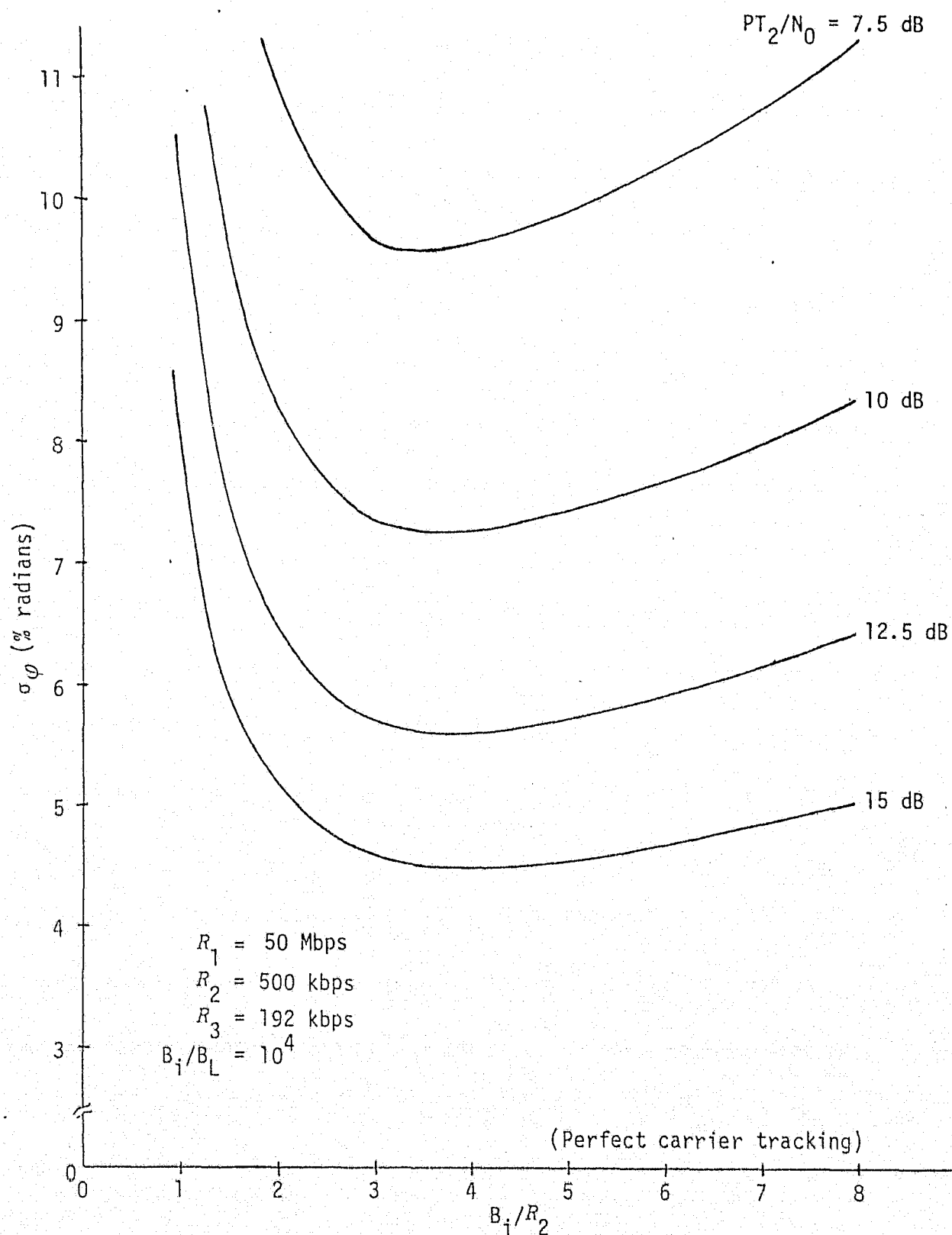


Figure 4. Subcarrier Tracking Jitter versus Ratio of Arm Filter Bandwidth to High Subcarrier Data Rate  $R_2$ ;  $PT_2/N_0$  is a parameter;  $m_1(t)$  is NRZ,  $m_2(t)$  and  $m_3(t)$  are Manchester codes,  $R_1 > R_2 > R_3$ .

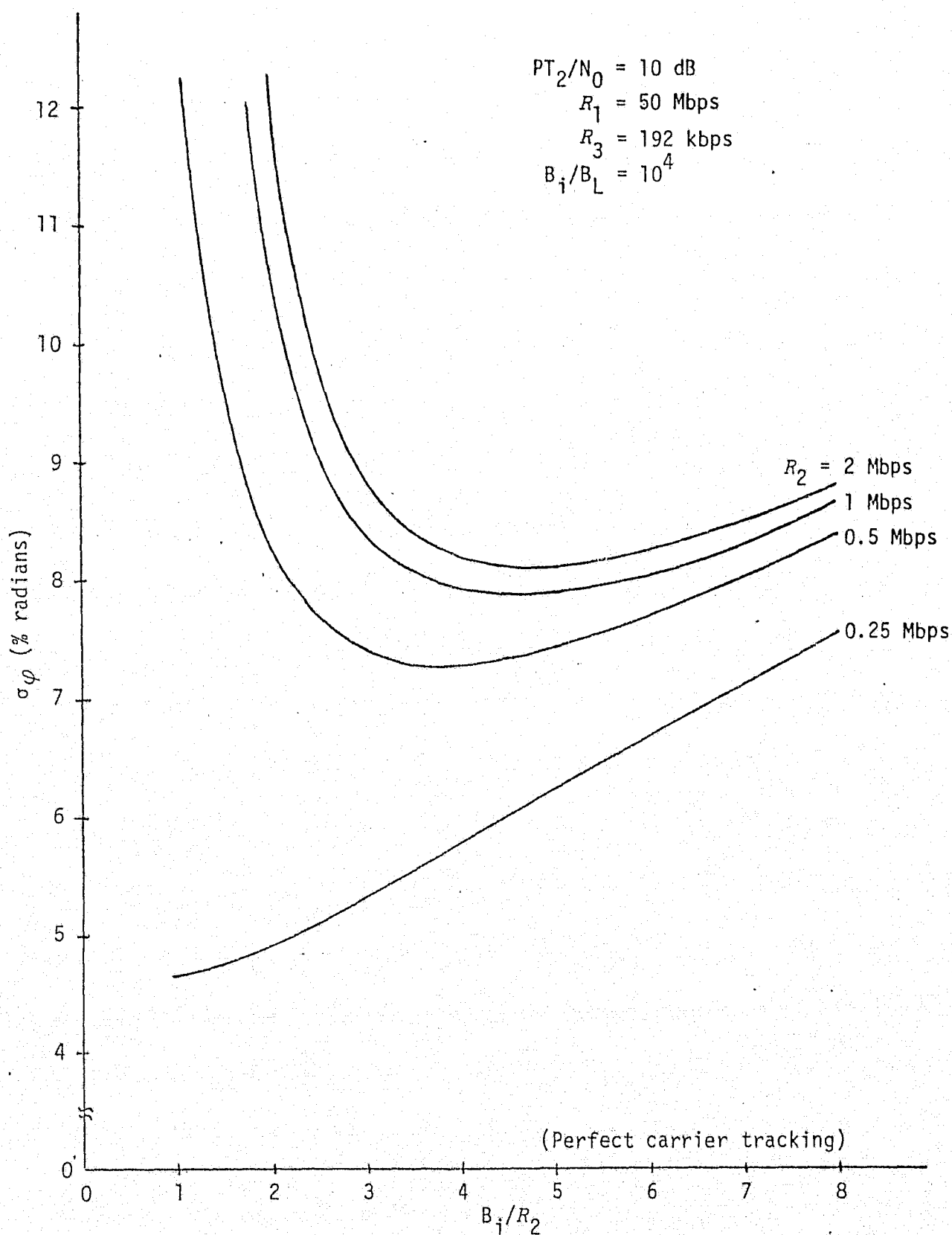


Figure 5. Subcarrier Tracking Jitter versus Ratio of Arm Filter Bandwidth to High Subcarrier Data Rate  $R_2$ ;  $R_2$  is a parameter;  $m_1(t)$  is NRZ,  $m_2(t)$  and  $m_3(t)$  are Manchester codes;  $R_1 > R_2 > R_3$ .

## REFERENCES

1. Huth, G. Integrated Source and Channel Encoded Digital Communication System Design Study, Final Report. Axiomatix Report No. R7607-3, July 31, 1976.
2. Simon, M. K., and Lindsey, W. C., "Optimum Performance of Suppressed Carrier Receivers with Costas Loop Tracking," IEEE Transactions on Communications, Vol. COM-25, February 1977, pp. 215-226.

APPENDIX I

ERROR PROBABILITY PERFORMANCE OF UNBALANCED QPSK RECEIVERS

## APPENDIX I

### ERROR PROBABILITY PERFORMANCE OF UNBALANCED QPSK RECEIVERS

by

Marvin K. Simon

#### 1.0 INTRODUCTION

Previous analyses by the author [1-5] and others [6-9] discuss the tracking performance of unbalanced QPSK receivers with particular emphasis on determining the mean-squared tracking phase jitter on the reconstructed carrier (or subcarrier) reference signal. As is true in any phase-coherent receiver, this lack of perfect coherence between the received signal and the reconstructed reference causes an additional degradation in system error probability relative to that due to the additive channel noise alone. Frequently, this increase in error probability due to noisy synchronization references is translated into an equivalent increase in signal power required to produce the same error probability as obtainable in a perfectly synchronized system. This increase in required signal power is referred to as the noisy reference loss.

Evaluation of noisy reference loss in BPSK, QPSK, and offset (staggered) QPSK systems has been extensively covered in the literature [10-15]. While the techniques used there are certainly applicable to demodulation of unbalanced QPSK, the complexity of the evaluation when the ratio of data rates in the two channels is large (this will be explained in more detail in the next section) prompts one to look for a simpler calculation procedure. Indeed, such an approach is possible when the noisy reference loss is small or equivalently the effective signal-to-noise ratio in the tracking loop bandwidth is large, i.e., the loop operates in its so-called linear region. Making such an assumption for purposes of error probability performance evaluation is quite reasonable when one realizes that this very same assumption has already been implied in the previously mentioned tracking performance studies of unbalanced QPSK. The approach taken is to expand the error probability conditioned on the loop phase error  $\phi$  in a power (Maclaurin) series in  $\phi$  and then, keeping only the first few terms of this series, average this conditional error probability over the probability density function (p.d.f.) of  $\phi$ . By doing this, we obtain the

additional error probability due to noisy synchronization references as an additive term directly proportional to the mean-squared phase jitter  $\sigma_\phi^2$  directly associated with the receiver's tracking loop. Similar arguments can be advanced to give us closed-form results for the noisy reference loss itself.

Using the above approach, this appendix presents results for the error probability and noisy reference loss performance of the unbalanced QPSK receivers corresponding to various combinations of data formats in the two channels. Specifically, for the subcarrier tracking loop associated with the two lower rate channels of the three-channel Space Shuttle Orbiter (SSO) Ku-band return link, wherein the two data channels are typically 192 kbps Manchester coded data and 2 Mbps NRZ data, numerical evaluation of this performance in these two channels is given.

## 2.0 ERROR PROBABILITY PERFORMANCE FOR SMALL NOISY REFERENCE LOSS

Common to all of the Costas-type demodulators of unbalanced QPSK previously considered [1, 2, 4, 5, 6, 8, 9] is the fact that the input signal plus noise is first demodulated with in-phase and quadrature phase detectors, the outputs of which represent the inputs to the data detectors for the two information channels. An example of this statement is illustrated in Figure 1 for the case where a conventional Costas loop is used for tracking the unbalanced QPSK signal. We shall pursue this case in detail and later indicate how the results can be extended to other Costas-type demodulators.

The input  $x(t)$  to the Costas loop of Figure 1 is the unbalanced QPSK signal plus noise, namely,

$$x(t) = \sqrt{2P_1} m_1(t) \cos \phi(t) + \sqrt{2P_2} m_2(t) \sin \phi(t) + n_i(t), \quad (1)$$

where  $\phi(t) = \omega_0 t + \theta_0$ , with  $\omega_0$  the radian carrier (or subcarrier) frequency and  $\theta_0$  the input phase (assumed time independent) to be estimated,  $m_1(t)$  and  $m_2(t)$  are independent data modulations assumed, in general, to be asynchronous, and  $n_i(t)$  is the additive channel noise which can be expressed in the form of a narrowband process about the actual frequency of the observed data, i.e.,

$$n_i(t) = \sqrt{2} \{N_c(t) \cos \phi(t) - N_s(t) \sin \phi(t)\}. \quad (2)$$



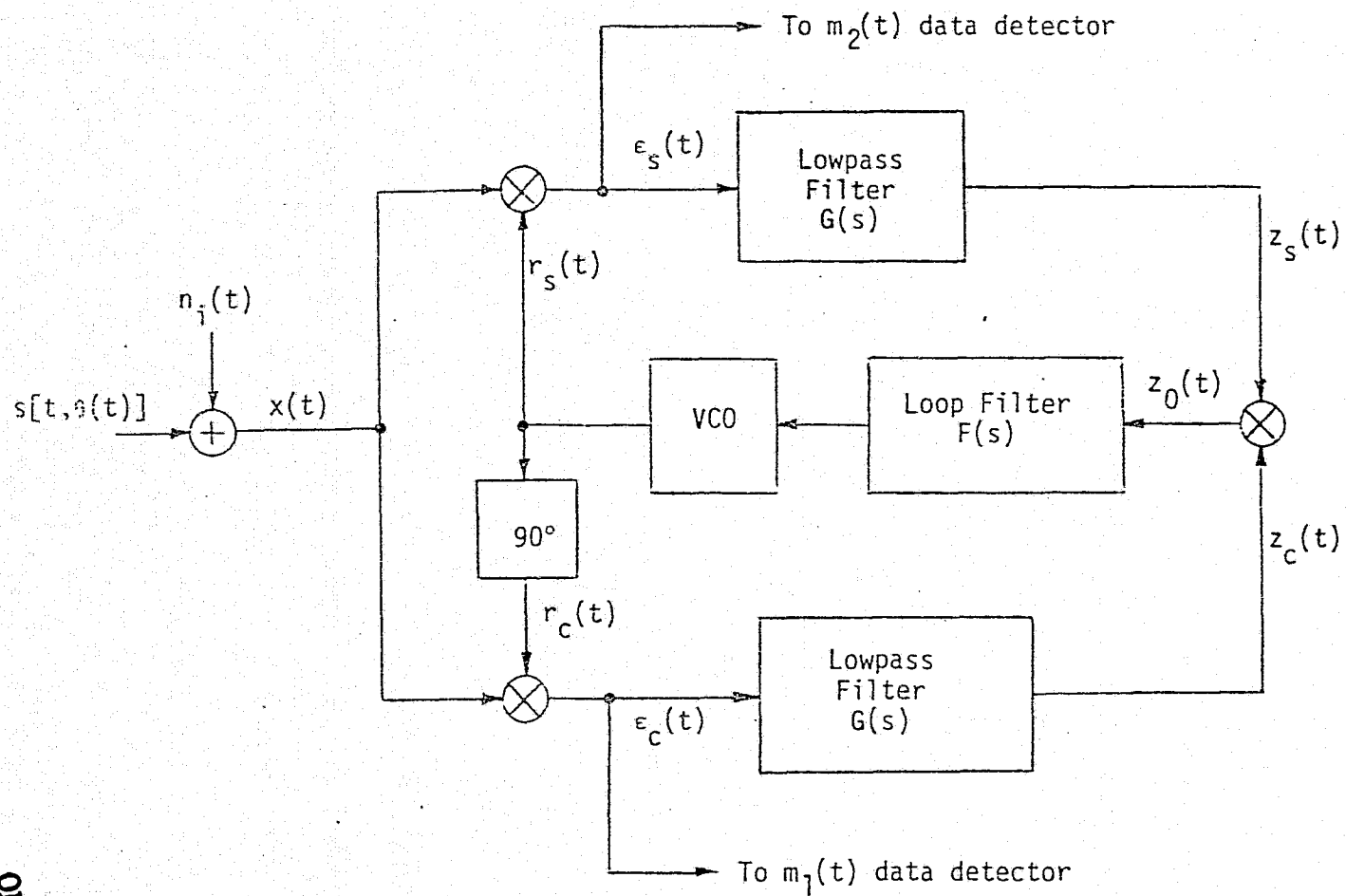


Figure 1. Costas Loop for Carrier Tracking of Unbalanced Quadriphase

In (2),  $N_c(t)$  and  $N_s(t)$  are approximately statistically independent, stationary, white Gaussian noise processes with single-sided noise spectral density  $N_0$  w/Hz, and single-sided bandwidth  $B_H < \omega_0/2\pi$ .

Assuming that the input in-phase and quadrature phase detectors are of the analog type, then when  $x(t)$  is demodulated by the quadrature reference signals

$$\begin{aligned} r_s(t) &= \sqrt{2} \sin \hat{\phi}(t) \\ r_c(t) &= \sqrt{2} \cos \hat{\phi}(t), \end{aligned} \quad (3)$$

the corresponding phase detector outputs (ignoring second harmonic terms) are\*

$$\begin{aligned} \epsilon_s(t) &\triangleq x(t) r_s(t) = \sqrt{P_2} m_2(t) \cos \varphi(t) - \sqrt{P_1} m_1(t) \sin \varphi(t) \\ &\quad - N_s(t) \cos \varphi(t) - N_c(t) \sin \varphi(t) \\ \epsilon_c(t) &\triangleq x(t) r_c(t) = \sqrt{P_2} m_2(t) \sin \varphi(t) + \sqrt{P_1} m_1(t) \cos \varphi(t) \\ &\quad - N_s(t) \sin \varphi(t) + N_c(t) \cos \varphi(t), \end{aligned} \quad (4)$$

where  $\varphi(t) \triangleq \phi(t) - \hat{\phi}(t)$  is the loop phase error. In addition to their forming a loop error signal when multiplied, these phase detector outputs also, as previously mentioned, serve as inputs to the channel data detectors which we shall assume are matched filters. The outputs of these matched filters at the end of the  $(k-1)$  signaling interval in each channel are respectively given by

$$\begin{aligned} Q_2 &= \frac{1}{T_2} \int_{(k-1)T_2 + \epsilon_2}^{kT_2 + \epsilon_2} \epsilon_s(t) p_2[t - (k-1)T_2 - \epsilon_2] dt \\ Q_1 &= \frac{1}{T_1} \int_{(k-1)T_1 + \epsilon_1}^{kT_1 + \epsilon_1} \epsilon_c(t) p_1[t - (k-1)T_1 - \epsilon_1] dt, \end{aligned} \quad (5)$$

where  $p_i(t)$ ;  $i=1,2$ , is the basic unit power symbol pulse in the  $i$ th data stream  $m_i(t)$  defined to be nonzero only on the interval  $(0, T_i)$ ,

---

\* For simplicity, we shall assume these phase detectors have unit gain.

and  $\epsilon_i$ ;  $i=1,2$ , is the arbitrary pulse epoch in these same modulations. Obviously then, the channel modulations  $m_i(t)$ ;  $i=1,2$ , are related to  $p_i(t)$  and  $\epsilon_i$  by

$$m_i(t) = \sum_{n=-\infty}^{\infty} a_{ni} p_i(t - nT_i - \epsilon_i); \quad i=1,2 \quad (6)$$

where  $\{a_{ni}\}$ ;  $i=1,2$ , are independent  $\pm 1$  sequences with the properties

$$\overline{a_{ni} a_{mi}} = \delta_{mn} = \begin{cases} 1; & m=n \\ 0; & m \neq n \end{cases}$$

$$\overline{a_{ni} a_{mj}} = 0 \quad \text{all } m,n \quad i \neq j \quad (7)$$

where the overbar denotes statistical expectation.

Substituting (4) into (5) separates the matched filter outputs into their signal and noise components, i.e.,\*

$$Q_2 = \sqrt{P_2} a_{k-1,2} \cos \phi - \sqrt{P_1} \tilde{m}_{12} \sin \phi - \tilde{N}_{s2} \cos \phi - \tilde{N}_{c2} \sin \phi$$

$$Q_1 = \sqrt{P_2} \tilde{m}_{21} \sin \phi + \sqrt{P_1} a_{k-1,1} \cos \phi - \tilde{N}_{s1} \sin \phi + \tilde{N}_{c1} \cos \phi, \quad (8)$$

where

$$\tilde{m}_{12} \triangleq \frac{1}{T_2} \int_{(k-1)T_2 + \epsilon_2}^{kT_2 + \epsilon_2} m_1(t) p_2[t - (k-1)T_2 - \epsilon_2] dt$$

$$\tilde{m}_{21} \triangleq \frac{1}{T_1} \int_{(k-1)T_1 + \epsilon_1}^{kT_1 + \epsilon_1} m_2(t) p_1[t - (k-1)T_1 - \epsilon_1] dt$$

$$\tilde{N}_{si} \triangleq \frac{1}{T_i} \int_{(k-1)T_i + \epsilon_i}^{kT_i + \epsilon_i} N_s(t) p_i[t - (k-1)T_i - \epsilon_i] dt; \quad i=1,2$$

$$\tilde{N}_{ci} \triangleq \frac{1}{T_i} \int_{(k-1)T_i + \epsilon_i}^{kT_i + \epsilon_i} N_c(t) p_i[t - (k-1)T_i - \epsilon_i] dt; \quad i=1,2. \quad (9)$$

ORIGINAL PAGE IS  
OF POOR QUALITY

\* We shall drop the dependence of  $\varphi(t)$  on  $t$  and further assume that  $\varphi(t) = \phi$  is constant over a symbol interval of either data rate.

The data estimates  $\hat{a}_{k-1,1}$  and  $\hat{a}_{k-1,2}$  of the Channel 1 and Channel 2 data bits  $a_{k-1,1}$  and  $a_{k-1,2}$  transmitted, respectively, in the  $(k-1)$  signaling interval are then given by

$$\hat{a}_{k-1,i} = \text{sgn} \{Q_i\}; \quad i=1,2 \quad (10)$$

where  $\text{sgn } x \triangleq x/|x|$  is the signum function. Note from (8) that the presence of a loop phase error due to noisy carrier synchronization references causes crosstalk, i.e., the data in one channel affects the detection of the data in the other channel. This crosstalk, which is proportional to  $\sin \phi$ , in combination with the degradation of the desired signal amplitude by  $\cos \phi$  together account for the noisy reference loss associated with the detection of an unbalanced QPSK signal.

Letting

$$\begin{aligned} \tilde{N}_2 &\triangleq -\tilde{N}_{s2} \cos \phi - \tilde{N}_{c2} \sin \phi \\ \tilde{N}_1 &\triangleq -\tilde{N}_{s1} \sin \phi + \tilde{N}_{c1} \cos \phi, \end{aligned} \quad (11)$$

then, from (9), one can immediately show that

$$\sigma_i^2 \triangleq E \{ \tilde{N}_i^2 \} = \frac{N_0}{2T_i}; \quad i=1,2. \quad (12)$$

Thus, the probability of error in each channel conditioned on a fixed phase error is given by

$$P_{E_i}(\phi) = \text{Prob} \{ \hat{a}_{k-1,i} \neq a_{k-1,i} | \phi \}; \quad i=1,2 \quad (13)$$

which, from (8), (10) and (12) becomes

$$\begin{aligned} P_{E_1}(\phi) &= \frac{1}{4} \text{erfc} \left[ \sqrt{\frac{P_1 T_1}{N_0}} \cos \phi + \sqrt{\frac{P_2 T_1}{N_0}} \tilde{m}_{21} \sin \phi \right] \\ &\quad + \frac{1}{4} \text{erfc} \left[ \sqrt{\frac{P_1 T_1}{N_0}} \cos \phi - \sqrt{\frac{P_2 T_1}{N_0}} \tilde{m}_{21} \sin \phi \right] \end{aligned} \quad (14a)$$

$$P_{E_2}(\phi) = \frac{1}{4} \operatorname{erfc} \left[ \sqrt{\frac{P_2 T_2}{N_0}} \cos \phi + \sqrt{\frac{P_1 T_2}{N_0}} \bar{m}_{12} \sin \phi \right] + \frac{1}{4} \operatorname{erfc} \left[ \sqrt{\frac{P_2 T_2}{N_0}} \cos \phi - \sqrt{\frac{P_1 T_2}{N_0}} \bar{m}_{12} \sin \phi \right], \quad (14b)$$

where the complementary error function ( $\operatorname{erfc} x$ ) is defined by

$$\operatorname{erfc} x \triangleq \frac{2}{\sqrt{\pi}} \int_x^{\infty} \exp(-y^2) dy \quad (15)$$

and the overbar denotes averaging over the data sequence and uniformly distributed random epoch dependences in  $\bar{m}_{21}$  and  $\bar{m}_{12}$ . We shall assume throughout the remainder of this report, as was done in [1,2], that the data rate  $R_2 \triangleq 1/T_2$  of  $m_2(t)$  is arbitrarily chosen to be higher than or equal to the rate  $R_1 \triangleq 1/T_1$  of  $m_1(t)$ . Then, when the ratio of these rates  $R_2/R_1 \geq 1$  is large, the statistical average over the data sequence required in  $P_{E_1}(\phi)$  of (14) involves a comparably large number of complementary error function evaluations since  $\bar{m}_{21}$  must be computed for each possible sequence of  $m_2(t)$  in the interval  $(k-1)T_1 + \epsilon_1 \leq t \leq kT_1 + \epsilon_1$ . Furthermore, for each of these contributing terms to  $P_{E_1}(\phi)$ , we must perform an average over the p.d.f.  $p(\phi)$  of the loop phase error  $\phi$  to determine the average error probability performance of Channel 1. More will be said later about this additional average over  $\phi$ .

In the meantime, to get around the computational bottleneck, we propose a scheme based upon expanding  $P_{E_i}(\phi)$  into a power series in  $\phi$  which, for small  $\sigma_\phi$ , provides credible results. In particular, we note from (14) that  $P_{E_i}(\phi)$  is of the form

$$P_{E_i}(\phi) = \frac{1}{4} \operatorname{erfc} [A_i \cos \phi + \xi_i \sin \phi] + \frac{1}{4} \operatorname{erfc} [A_i \cos \phi - \xi_i \sin \phi]; \quad i = 1, 2 \quad (16)$$

where  $A_i$  is a constant and  $\xi_i$  is a random variable in the sense that it is both data sequence and random epoch dependent. Differentiating  $P_{E_i}(\phi)$  once and twice with respect to  $\phi$  gives the results

$$\begin{aligned} \frac{d P_{E_i}(\phi)}{d \phi} = & -\frac{1}{2\sqrt{\pi}} (\xi_i \cos \phi - A_i \sin \phi) \exp [-(A_i \cos \phi + \xi_i \sin \phi)^2] \\ & + \frac{1}{2\sqrt{\pi}} (\xi_i \cos \phi + A_i \sin \phi) \exp [-(A_i \cos \phi - \xi_i \sin \phi)^2] \end{aligned} \quad (17a)$$

$$\begin{aligned} \frac{d^2 P_{E_i}(\phi)}{d \phi^2} = & \frac{1}{2\sqrt{\pi}} \left\{ (A_i \cos \phi + \xi_i \sin \phi) \exp [-(A_i \cos \phi + \xi_i \sin \phi)^2] \right. \\ & + 2(A_i \cos \phi + \xi_i \sin \phi)(\xi_i \cos \phi - A_i \sin \phi) \exp [-(A_i \cos \phi + \xi_i \sin \phi)^2] \\ & + (A_i \cos \phi - \xi_i \sin \phi) \exp [-(A_i \cos \phi - \xi_i \sin \phi)^2] \\ & \left. + 2(A_i \cos \phi - \xi_i \sin \phi)(\xi_i \cos \phi + A_i \sin \phi) \exp [-(A_i \cos \phi - \xi_i \sin \phi)^2] \right\} \end{aligned} \quad (17b)$$

which, when evaluated at  $\phi = 0$ , become

$$\begin{aligned} \left. \frac{d P_{E_i}(\phi)}{d \phi} \right|_{\phi=0} &= -\frac{1}{2\sqrt{\pi}} \overline{\xi_i} \exp(-A_i^2) + \frac{1}{2\sqrt{\pi}} \overline{\xi_i} \exp(-A_i^2) = 0 \\ \left. \frac{d^2 P_{E_i}(\phi)}{d \phi^2} \right|_{\phi=0} &= \frac{1}{\sqrt{\pi}} [A_i \exp(-A_i^2) + 2A_i \overline{\xi_i^2} \exp(-A_i^2)] \\ &= \frac{A_i \exp(-A_i^2)}{\sqrt{\pi}} [1 + 2 \overline{\xi_i^2}] \end{aligned} \quad (18)$$

Furthermore, from (16),

$$\left. P_{E_i}(\phi) \right|_{\phi=0} = \frac{1}{2} \operatorname{erfc} A_i \quad (19)$$

Thus, combining (18) and (19), we get

$$\begin{aligned}
P_{E_i}(\phi) &\cong P_{E_i}(0) + \left. \frac{d P_{E_i}(\phi)}{d \phi} \right|_{\phi=0} \phi + \frac{1}{2} \left. \frac{d^2 P_{E_i}(\phi)}{d \phi^2} \right|_{\phi=0} \phi^2 \\
&= \frac{1}{2} \operatorname{erfc} A_i + \frac{A_i \exp(-A_i^2)}{2\sqrt{\pi}} [1 + 2 \overline{\xi_i^2}] \phi^2.
\end{aligned} \quad (20)$$

Comparing (16) with (14), we can immediately identify  $A_i$  and  $\xi_i$  in terms of the receiver parameters, whereupon (20) becomes

$$\begin{aligned}
P_{E_1}(\phi) &\cong \frac{1}{2} \operatorname{erfc} \sqrt{R_1} + \frac{1}{2} \sqrt{\frac{R_1}{\pi}} \exp(-R_1) [1 + 2 R_2 \gamma_T \overline{m_{21}^2}] \phi^2 \\
P_{E_2}(\phi) &\cong \frac{1}{2} \operatorname{erfc} \sqrt{R_2} + \frac{1}{2} \sqrt{\frac{R_2}{\pi}} \exp(-R_2) \left[ 1 + 2 R_1 \left( \frac{\overline{m_{12}^2}}{\gamma_T} \right) \right] \phi^2,
\end{aligned} \quad (21)$$

with signal-to-noise ratios in each channel defined by

$$R_i \triangleq \frac{P_i T_i}{N_0}; \quad i = 1, 2 \quad (22)$$

and the ratio of data rates defined as in [1,2] by

$$\gamma_T \triangleq \frac{R_2}{R_1} = \frac{T_1}{T_2} \geq 1. \quad (23)$$

Note from (21) that, as promised, the error probability consists of a term representing the performance for perfect carrier synchronization plus a term proportional to the crosstalk,

What remains insofar as evaluating  $P_{E_i}(\phi)$  is to compute the normalized mean-squared crosstalk terms  $\overline{m_{21}^2}$  and  $\overline{m_{12}^2}$  for various combinations of data formats in Channels 1 and 2. Evaluation of  $\overline{m_{21}^2}$  and  $\overline{m_{12}^2}$  depends not only on the specific data formats in the two channels but also on the relative synchronism of the two data streams. More often than not, the two data clocks will be unsynchronized since, typically, the two data streams are generated from totally independent sources. In this situation, there is, in general, no relation between the epochs  $\epsilon_1$  and  $\epsilon_2$  of the synchronization pulses corresponding to these clocks and, furthermore, the ratio of the two data rates need not be integer. Recognizing, however, certain similarities between the definitions of

$\overline{\tilde{m}_{21}^2}$  and  $\overline{\tilde{m}_{12}^2}$ , and the computation of cross-modulation distortion  $D_{12}$  associated with the Costas loop given in [1], it is relatively straightforward to show that

$$\begin{aligned}\overline{\tilde{m}_{12}^2} &= \lim_{B_i/R_2 \rightarrow \infty} \frac{D_{12}}{T_2} \\ \overline{\tilde{m}_{21}^2} &= \lim_{B_i/R_2 \rightarrow \infty} \frac{D_{12}}{T_1} = \frac{\overline{\tilde{m}_{12}^2}}{\gamma_T},\end{aligned}\quad (24)$$

where  $D_{12}$  is given by (42), (50), (51) and (52) of [1], and  $B_i$  is also defined in that reference. These results are summarized in Table 1.

Table 1. Evaluation of  $\overline{\tilde{m}_{12}^2}$ ;  $T_1/T_2 \triangleq \gamma_T \geq 1$

		$m_2(t)$	
		Manchester	NRZ
$m_1(t)$	Manchester	$\frac{1}{6}[\gamma_T^2 - \frac{5}{\gamma_T} + 12 - 6\gamma_T];$ $R_1 \leq R_2 \leq 2R_1$ $\frac{1}{2\gamma_T}; R_2 \geq 2R_1$	$\gamma_T - \frac{1}{6}\gamma_T^2 - 1 + \frac{1}{3\gamma_T};$ $R_1 \leq R_2 \leq 2R_1$ $1 - \frac{1}{\gamma_T}; R_2 \geq 2R_1$
	NRZ	$\frac{1}{6\gamma_T}$	$1 - \frac{1}{3\gamma_T}$

Finally, averaging  $P_{E_i}(\phi)$  of (21) over the p.d.f. of  $\phi$  as determined by analysis of the Costas loop (see [1]) and assuming that the  $180^\circ$  phase ambiguity is perfectly resolved, we obtain the average error probability performance of each channel, namely,

$$P_{E_i} = \int_{-\pi/2}^{\pi/2} P_{E_i}(\phi) p(\phi) d\phi. \quad (25)$$

Substituting (21), combined with (24), into (25) gives the desired simple result

ORIGINAL PAGE IS  
OF POOR QUALITY



$$\begin{aligned}
 P_{E_1} &= \frac{1}{2} \operatorname{erfc} \sqrt{R_1} + \frac{1}{2} \sqrt{\frac{R_1}{\pi}} \exp(-R_1) [1 + 2R_2 \overline{m_{12}^2}] \sigma_\phi^2 \\
 P_{E_2} &= \frac{1}{2} \operatorname{erfc} \sqrt{R_2} + \frac{1}{2} \sqrt{\frac{R_2}{\pi}} \exp(-R_2) \left[ 1 + 2R_1 \left( \frac{\overline{m_{12}^2}}{\gamma_T} \right) \right] \sigma_\phi^2.
 \end{aligned} \quad (26)$$

Alternately, in terms of the total signal-to-noise ratio  $R_{T2}$  in the high data rate bandwidth and the transmitted modulation indices  $\eta_1$  and  $\eta_2$  defined by

$$R_{T2} = \frac{(P_1 + P_2) T_2}{N_0}; \quad \eta_i = \frac{P_i}{P_1 + P_2}; \quad i=1,2 \quad (27)$$

the results of (26) become

$$\begin{aligned}
 P_{E_1} &= \frac{1}{2} \operatorname{erfc} \sqrt{R_{T2} \gamma_T \eta_1} + \frac{1}{2} \sqrt{\frac{R_{T2} \gamma_T \eta_1}{\pi}} \exp(-R_{T2} \gamma_T \eta_1) [1 + 2R_{T2} \eta_2 \overline{m_{12}^2}] \sigma_\phi^2 \\
 P_{E_2} &= \frac{1}{2} \operatorname{erfc} \sqrt{R_{T2} \eta_2} + \frac{1}{2} \sqrt{\frac{R_{T2} \eta_2}{\pi}} \exp(-R_{T2} \eta_2) [1 + 2R_{T2} \eta_1 \overline{m_{12}^2}] \sigma_\phi^2.
 \end{aligned} \quad (28)$$

The mean squared phase error  $\sigma_\phi^2$  may be related to the receiver parameters already defined by noting that, for the Costas loop of Figure 1,\*

$$\sigma_\phi^2 = \frac{1}{\rho S_L}, \quad (29)$$

where  $\rho \triangleq (P_1 + P_2)/N_0 B_L$  is the equivalent total signal-to-noise ratio in the single-sided loop bandwidth  $B_L$  of a linear loop, and  $S_L$  is the loop "squaring loss" which reflects the fact that the Costas loop error signal is formed by a nonlinear operation, namely, multiplication of the in-phase and quadrature filtered phase detector outputs. In terms of  $R_{T2}$  defined in (27) and the ratio of loop bandwidth  $B_L$  to higher data rate  $R_2$ , the loop signal-to-noise ratio  $\rho$  can be expressed as

$$\rho = \frac{R_{T2}}{B_L/R_2}. \quad (30)$$

\* Actually, the relationship in (29) is not restricted only to the conventional Costas loop of Figure 1 but also holds for a wide variety of other types of unbalanced QPSK demodulators (see [4, 5, 8, 9]).

An expression for  $S_L$  can be obtained from Eq. (28) of [1], namely,

$$S_L = \frac{(\eta_2 D_2 - \eta_1 D_1)^2}{\eta_1 D_1 K_{D_1} + \eta_2 D_2 K_{D_2} + \frac{B_i/R_2}{2R_{T2}} K_L + 2\eta_1 \eta_2 \frac{D_{12}}{T_2}} \quad (31)$$

where the parameters  $D_1$ ,  $D_2$ ,  $K_{D_1}$ ,  $K_{D_2}$ ,  $K_L$  and  $D_{12}$  depend on the magnitude squared of the arm filter transfer function  $|G(j2\pi f)|^2$  and the power spectral densities  $S_{m_1}(f)$ ,  $S_{m_2}(f)$  of the modulations  $m_1(t)$ ,  $m_2(t)$  according to the relations

$$\begin{aligned} D_k &= \int_{-\infty}^{\infty} S_{m_k}(f) |G(j2\pi f)|^2 df; \quad k=1,2 \\ D_{12} &\triangleq \int_{-\infty}^{\infty} S_{m_1}(f) S_{m_2}(f) |G(j2\pi f)|^4 df \\ K_{D_k} &\triangleq \frac{\int_{-\infty}^{\infty} S_{m_k}(f) |G(j2\pi f)|^4 df}{\int_{-\infty}^{\infty} S_{m_k}(f) |G(j2\pi f)|^2 df}; \quad k=1,2 \\ K_L &\triangleq \frac{\int_{-\infty}^{\infty} |G(j2\pi f)|^4 df}{\int_{-\infty}^{\infty} |G(j2\pi f)|^2 df}. \end{aligned} \quad (32)$$

Specific closed-form expressions for the above parameters, when the Costas loop has single-pole (RC) arm filters and the modulations  $m_1(t)$  and  $m_2(t)$  are variously NRZ and Manchester coded data streams, can be found in [1].

### 3.0 EVALUATION OF NOISY REFERENCE LOSS IN EACH CHANNEL

Letting  $P_{E_i}^i$  denote the value of  $P_{E_i}$  when  $\sigma_\phi = 0$  (i.e., ideal PSK performance) and approximating the complementary error function of (15) by the first term of its asymptotic expansion, i.e.,

$$\operatorname{erfc} x \approx \frac{\exp(-x^2)}{\sqrt{\pi} x} \quad (33)$$

then, from (26), we have

$$\begin{aligned}\frac{P_{E1}}{P'_{E1}} &= 1 + R_1 [1 + 2 R_2 \overline{\tilde{m}_{12}^2}] \sigma_\phi^2 \\ \frac{P_{E2}}{P'_{E2}} &= 1 + R_2 \left[ 1 + 2 R_1 \left( \frac{\overline{\tilde{m}_{12}^2}}{\gamma_T} \right) \right] \sigma_\phi^2\end{aligned}\quad (34)$$

or

$$\begin{aligned}\log_{10} P_{E1} - \log_{10} P'_{E1} &= \log_{10} \left\{ 1 + R_1 [1 + 2 R_2 \overline{\tilde{m}_{12}^2}] \sigma_\phi^2 \right\} \\ \log_{10} P_{E2} - \log_{10} P'_{E2} &= \log_{10} \left\{ 1 + R_2 \left[ 1 + 2 R_1 \left( \frac{\overline{\tilde{m}_{12}^2}}{\gamma_T} \right) \right] \sigma_\phi^2 \right\}\end{aligned}\quad (35)$$

For small noisy reference losses and small error probabilities, a curve of  $\log_{10} P_{Ei}$  versus  $R_i$  in dB would be parallel to the corresponding ideal performance curve, namely,  $\log_{10} P'_{Ei}$  versus  $R_i$  in dB. Thus, letting  $r_i$  be the dB equivalent of  $R_i$ , i.e.,

$$r_i = 10 \log_{10} R_i; \quad i=1,2 \quad (36)$$

then

$$\frac{d \log_{10} P'_{Ei}}{d r_i} \cong \frac{\log_{10} P_{Ei} - \log_{10} P'_{Ei}}{r'_i - r_i}, \quad (37)$$

where

$$r'_i = 10 \log_{10} R'_i \quad (38)$$

and  $R'_i$  is the signal-to-noise ratio required to achieve an error probability  $P'_{Ei}$  in the presence of the noisy synchronization reference. Thus, the quantity  $r'_i - r_i$  represents the noisy reference loss (in dB) at the given value of error probability  $P'_{Ei}$ . To compute an expression for it, we proceed as follows. Taking  $\log_{10}$  of  $P'_{Ei}$  and differentiating with respect to  $r'_i$  gives

$$\frac{d \log_{10} P'_{Ei}}{d r_i} = - \frac{1}{10\sqrt{\pi}} \frac{\sqrt{R_i} \exp(-R_i)}{\operatorname{erfc} \sqrt{R_i}}. \quad (39)$$

Using the approximation of (33) in (39) gives

$$\frac{d \log_{10} P_{Ei}'}{d r_i} \approx 0.1 R_i \quad (40)$$

Finally, combining (35), (37), and (40) and solving for the noisy reference loss  $r_i' - r_i$  in Channel  $i$ ;  $i=1,2$  gives

$$\begin{aligned} L_1 &\triangleq r_1' - r_1 = \frac{10 \log_{10} \left\{ 1 + R_1 [1 + 2 R_2 \bar{m}_{12}^2] \sigma_\phi^2 \right\}}{R_1} \\ L_2 &\triangleq r_2' - r_2 = \frac{10 \log_{10} \left\{ 1 + R_2 \left[ 1 + 2 R_1 \left( \frac{\bar{m}_{12}^2}{\gamma_T} \right) \right] \sigma_\phi^2 \right\}}{R_2} \end{aligned} \quad (41)$$

#### 4.0 NUMERICAL RESULTS

As an example of the application of the previous results, consider the performance of the two lower rate channels of the three-channel SSO Ku-band return link wherein  $m_1(t)$  is a Manchester coded data stream at  $R_1 = 192$  kbps and  $m_2(t)$  is NRZ data with a maximum rate  $R_2 = 2$  Mbps. We further assume that the power allocation is chosen so that, for the given data rate ratio  $\gamma_T = R_2/R_1 = 10.42$ , the signal-to-noise ratios  $R_1, R_2$  in the two channels are made equal, i.e., both channels operate at the same error rate. Thus,  $R_1 = R_2$  implies  $P_1 T_1 = P_2 T_2$  and the modulation indices  $\eta_1, \eta_2$  become

$$\begin{aligned} \eta_1 &\triangleq \frac{P_1}{P_1 + P_2} = \frac{1}{1 + \gamma_T} = 0.0876 \\ \eta_2 &\triangleq \frac{P_2}{P_1 + P_2} = \frac{\gamma_T}{1 + \gamma_T} = 0.9124 \end{aligned} \quad (42)$$

Further, it is typical to design the Costas loop bandwidth on the order of  $R_2/100$  (or less) since most of the power is in the high rate channel which controls the performance of the tracking loop. Thus, assuming  $B_L/R_2 = 0.01$ ,\* Figures 2 and 3 illustrate  $L_1$  and  $L_2$  of (41) versus  $B_i/R_2$

---

\* Smaller values of  $B_L/R_2$  as would be typical in practical receiver design would yield insignificant losses in  $L_1$  and  $L_2$ .

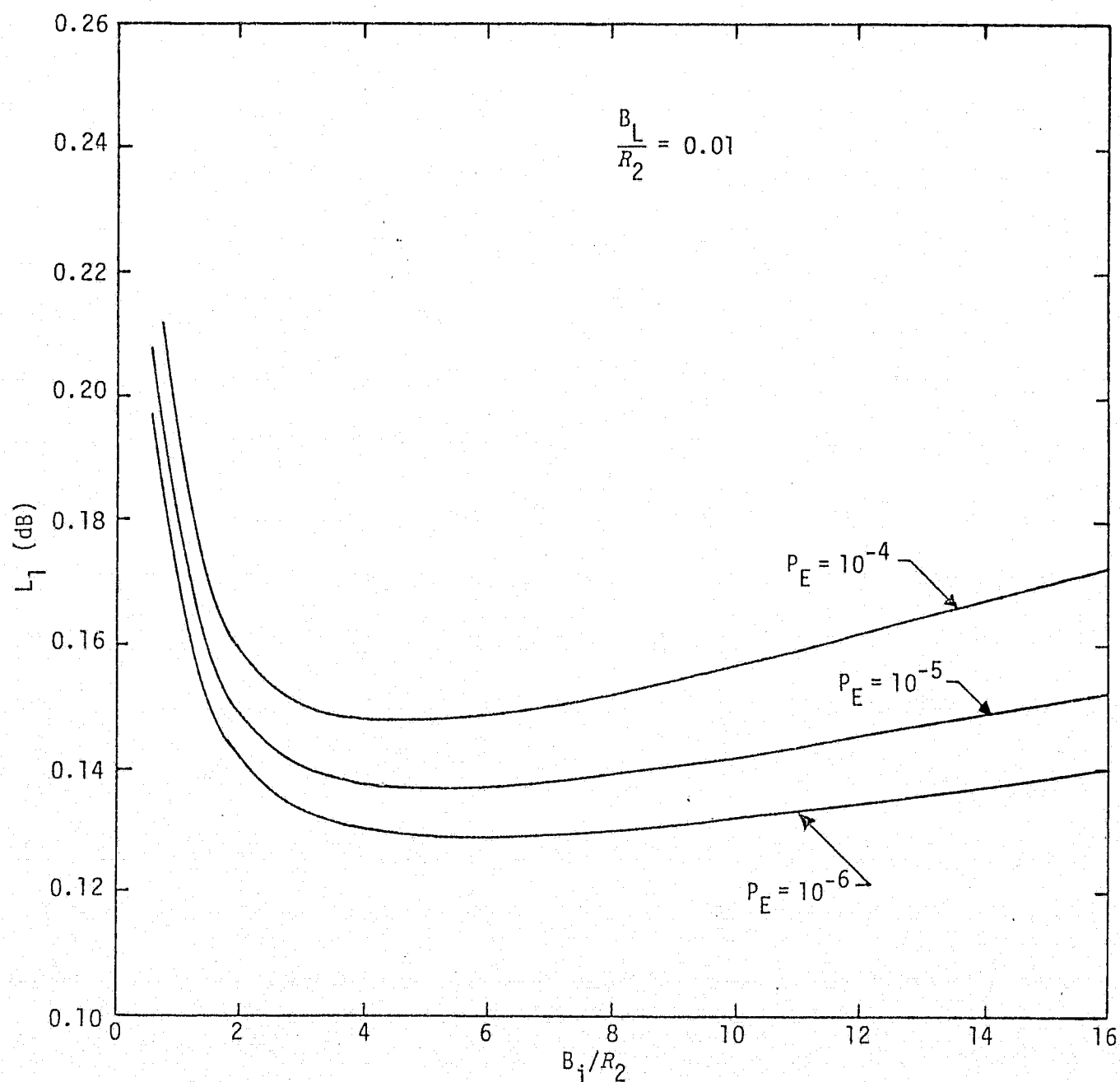


Figure 2. Channel 1 Noisy Reference Loss (in dB) vs. the Ratio of Two-Sided Costas Loop Arm Filter Bandwidth to Channel 2 Data Rate;  $m_1(t)$  is 192 kbps Manchester coded data,  $m_2(t)$  is 2 Mbps NRZ data.

ORIGINAL PAGE IS  
OF POOR QUALITY

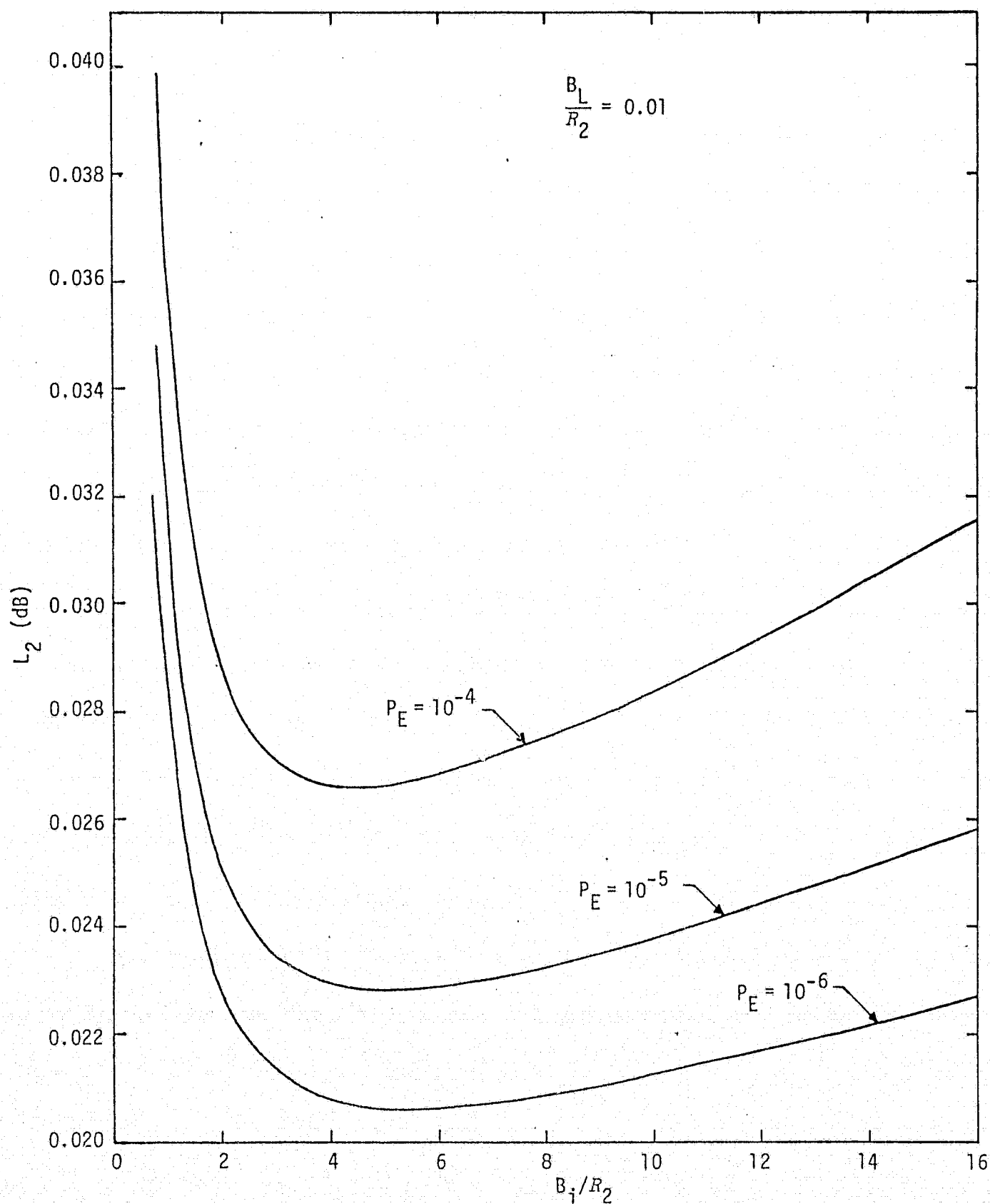


Figure 3. Channel 2 Noisy Reference Loss (in dB) vs. the Ratio of Two-Sided Costas Loop Arm Filter Bandwidth to Channel 2 Data Rate;  $m_1(t)$  is 192 kbps Manchester coded data,  $m_2(t)$  is 2 Mbps NRZ data.

for error probabilities of  $10^{-4}$ ,  $10^{-5}$ , and  $10^{-6}$ , corresponding respectively to  $R_1 = R_2 = 8.4, 9.6$ , and  $10.5$  dB. Several conclusions may be drawn from these figures. First, the noisy reference loss on Channel 2 is considerably smaller than that on Channel 1. The principal reason for this can be easily explained in terms of the result in (41), where it is observed that the effective cross-modulation loss on Channel 2,  $\tilde{m}_{12}^2$ , is divided by  $\gamma_T$  which in this case has a value equal to 10.42. Secondly, for either channel, the noisy reference loss decreases with increasing error probability. This is intuitively satisfying when one realizes that the slope of the error probability versus signal-to-noise ratio curves becomes steeper as  $P_E$  becomes smaller and thus, for a given  $\sigma_\phi$ , the parallel ideal and noisy sync error probability curves become closer together. Finally, we observe that there exists an optimum arm filter bandwidth (for fixed  $R_2$ ) in the sense of minimizing  $L_i$ ,  $i=1,2$ . Since only  $\sigma_\phi^2$  depends on this bandwidth, it is clear that this bandwidth choice is identical to that which minimizes  $\sigma_\phi^2$  or, equivalently, the loop squaring loss. Note that, if  $B_L/R_2$  is decreased, then the noisy reference loss will also decrease, since the equivalent loop signal-to-noise ratio  $\rho$  of (30) increases.

We conclude by noting that, while the results of this appendix have been directed principally toward the demodulation of unbalanced QPSK by a conventional (single-channel) Costas loop such as in Figure 1, the expressions for average error probability [see (26) and (28)] and noisy reference loss [see (41)] apply in a much broader sense. In particular, the two-channel type Costas loops discussed in [8,9] have a mean-squared phase jitter given by (29) where, however,  $S_L$  is a much more complex function of the various system parameters such as data rates and channel power ratios. Nevertheless, once  $S_L$  (and thus  $\sigma_\phi^2$ ) is determined, (26) and (41) apply directly toward evaluation of the noisy synchronization reference effects of these loops on error probability performance. Other possible applications of the results pertain to demodulation of unbalanced QPSK using a biphasic Costas loop with switching type multipliers. Once again, (26), (41) and (29) apply, provided that an expression for the squaring loss can be found (see, for example, [5,16]).

## 5.0 CONCLUSIONS

This appendix has demonstrated a simple technique for calculating the error probability performance and associated noisy reference loss of practical unbalanced QPSK receivers. The result for error probability is in the form of a leading term representing the ideal (perfect synchronization references) performance plus a term proportional to the mean-squared crosstalk. For the Ku-band return link subcarrier demodulation of 192 kbps Manchester coded data and 2 Mbps NRZ by a conventional Costas loop, it is concluded that the crosstalk degradation due to noisy subcarrier demodulation references is quite small (on the order of tenths of a dB or less, depending on the particular channel and the ratio of loop bandwidth to data rate in that channel). When the higher data rate channel is 1 Mbps Manchester coded data, then since both channels are now Manchester coded, the crosstalk loss would be even smaller yet (see Table 1). The general results obtained can also be applied to other unbalanced QPSK receivers with more complex Costas-type loop structures.



## REFERENCES

1. M. K. Simon and W. K. Alem. "Tracking Performance of Unbalanced QPSK Demodulators: Part I - Biphase Costas Loop with Passive Arm Filters," Axiomatix Report No. R7707-5, July 29, 1977. Also submitted for publication in the IEEE Transactions on Communications.
2. M. K. Simon. "Tracking Performance of Unbalanced QPSK Demodulation: Part II - Biphase Costas Loop with Active Arm Filters," Axiomatix Report No. R7707-6, July 29, 1977. Also submitted for publication in the IEEE Transactions on Communications.
3. M. K. Simon and W. K. Alem. "Subcarrier Tracking Analysis for Three-Channel Orbiter Ku-Band Return Link," Axiomatix Report No. R7707-4, July 28, 1977.
4. M. K. Simon. "Practical Design Considerations Associated with Optimum Carrier Reconstruction Techniques for Unbalanced QPSK," Axiomatix Report No. R7709-5, September 30, 1977.
5. M. K. Simon. "Power Allocation and Costas Loop Subcarrier Tracking Performance Associated with a Digital Phase Shift Implementation of the Three-Channel Orbiter Ku-Band Modulator," Axiomatix Report No. R7709-4, September 29, 1977.
6. C. L. Weber. "Candidate Receivers for Unbalanced QPSK," 1976 ITC Proceedings, Vol. XII, pp. 455-464.
7. B. K. Levitt, J. R. Lesh, and J. C. Springett. "Shuttle/TDRSS Ku-Band Telemetry Study," Final Report 900-742, Jet Propulsion Laboratory, Pasadena, California, April 5, 1976.
8. W. R. Braun and W. C. Lindsey. "Carrier Synchronization Techniques for Unbalanced QPSK Signals - Parts I & II," submitted for publication in the IEEE Transactions on Communications. Part I also presented at the 1977 International Conference on Communications, Chicago, Illinois. Part II presented at the 1977 National Telecommunications Conference, Los Angeles, California.
9. W. C. Lindsey and W. R. Braun. "TDRSS Communication Analysis and Modeling Study, Phase I Report," TR-09-7614-2, LinCom Corp., Pasadena, California, October 15, 1976.
10. W. C. Lindsey. "Phase-Shift-Keyed Signal Detection with Noisy Reference Signals," IEEE Transactions on Aerospace Electronic Systems, Vol. AES-2, July, 1966, pp. 393-401.
11. W. C. Lindsey and M. K. Simon. "The Effect of Loop Stress on the Performance of Phase-Coherent Communication Systems," IEEE Transactions on Communication Technology, Vol. COM-18, No. 5, October 1970, pp. 569-588.

C-4

12. R. J. Sherman. "Quadri-Phase Shift Keyed Signal Detection with Noisy Reference Signals," EASCON'69 Convention Record, pp. 46-52.
13. W. C. Lindsey and M. K. Simon. "Carrier Synchronization and Detection of Polyphase Signals," IEEE Transactions on Communications, Vol. COM-20, No. 3, June 1972, pp. 441-454.
14. S. A. Rhodes. "Performance of Offset-QPSK Communications with Partially-Coherent Detection," National Telecommunications Conference Record, November 1973, pp. 32A-1 - 32A-6.
15. M. K. Simon and J. G. Smith. "Offset Quadrature Communications with Decision-Feedback Carrier Synchronization," IEEE Transactions on Communications, Vol. COM-22, No. 10, October 1974, pp. 1576-1584.
16. M. K. Simon. "Tracking Performance of Costas Loops with Hard-Limited In-Phase Channel," to appear in the April 1978 issue of IEEE Transactions on Communications.

APPENDIX J

PRACTICAL DESIGN CONSIDERATIONS ASSOCIATED WITH OPTIMUM  
CARRIER RECONSTRUCTION TECHNIQUES FOR UNBALANCED QPSK

## APPENDIX J

### PRACTICAL DESIGN CONSIDERATIONS ASSOCIATED WITH OPTIMUM CARRIER RECONSTRUCTION TECHNIQUES FOR UNBALANCED QPSK

by

Marvin K. Simon

#### INTRODUCTION

In a recent paper [1], the authors address the problem of carrier synchronization of an unbalanced QPSK (UQPSK) signal format, starting with the well-known maximum a posteriori (MAP) estimation technique as motivation for deriving closed loop tracking configurations. In particular, such carrier reconstruction implementations are suggested upon examining the gradient of the likelihood function whose solution is the MAP estimator of carrier phase. While the MAP approach leads to closed loop implementations with active arm filters which are matched to the signal pulse shape (integrate-and-dump circuits for digital signals) and thus require knowledge of the data timing clock, one can, in practice, replace these filters with passive lowpass filters with, however, an attendant loss in performance. Nevertheless, it is common practice to accept this performance penalty so as to avoid the necessity of having to lock up the bit synchronizer prior to achieving carrier lock.

Before going into the specific details of the performance of these so-called "optimum" carrier reconstruction loops for unbalanced QPSK, it is perhaps worthwhile reviewing these same considerations first for simple PSK and then for balanced or conventional QPSK. In the latter case, we will come upon a new structure which, performance-wise, is theoretically identical to the well-known quadriphase Costas loop [2]. Also, as we shall see, the nature of the approximation to the true MAP solution, which allows us to arrive at this new configuration, has application in the unbalanced QPSK situation, thereby permitting us to carry the work initiated in [1] one step closer to an "optimum" solution. Indeed, the generalization proposed here of the linear in-phase channel configuration given in [1] allows carrier reconstruction from a UQPSK signal at all ratios of data rates and powers in the two channels, even in the limit as these ratios simultaneously approach unity, i.e., balanced quadriphase.

Finally, we shall discuss the practicality of the unbalanced QPSK carrier reconstruction loops found in [1], paying particular attention

to their sensitivity to variations in channel gains. It will be shown that, whereas the channel gains were "optimally" chosen in [1] from MAP estimation considerations, a different selection of these gains based upon directly optimizing the loop's tracking performance can yield as much as a 10 dB improvement in this performance. The significance of this statement is not so much the fact that the tracking performance can be enhanced by a better choice of gains, particularly since these gains are now theoretically signal-to-noise ratio dependent, but rather the high degree of sensitivity of the performance of the MAP estimation-type loop to variations in the channel gains themselves. This point will be explored numerically to provide quantitative verification of this sensitivity behavior.

## CARRIER RECONSTRUCTION LOOPS MOTIVATED BY MAP ESTIMATION THEORY

### PSK Modulation

Consider the problem of finding the MAP estimate of carrier phase from an observation made on a biphas-modulated, suppressed-carrier signal in additive Gaussian noise. In particular, the signal  $s[t, \theta(t)]$  is of the form

$$s[t, \theta(t)] = \sqrt{2S} m(t) \sin [\omega_0 t + \theta(t)], \quad (1)$$

where  $S$  is the average signal power,  $m(t)$  is a binary modulation (a  $\pm 1$  digital waveform) of rate  $R=1/T$  and pulse shape  $p(t)$ ,  $\omega_0$  is the radian carrier frequency, and  $\theta(t) \triangleq \theta_0 + \Omega_0 t$  is the received carrier phase. The total received signal  $x(t)$  is then

$$x(t) = s[t, \theta(t)] + n_i(t), \quad (2)$$

where  $n_i(t)$  is the additive channel noise which can be expressed in the form of a narrowband process about the actual frequency of the observed data, viz.,

$$n_i(t) = \sqrt{2} \{N_c(t) \cos [\omega_0 t + \theta(t)] - N_s(t) \sin [\omega_0 t + \theta(t)]\}, \quad (3)$$

where  $N_c(t)$  and  $N_s(t)$  are approximately statistically independent, stationary, white Gaussian noise processes with single-sided noise spectral density  $N_0$  w/Hz (see [2]) and single-sided bandwidth  $B_H < \omega_0/2\pi$ .

The MAP estimation problem may now be stated as follows. Based upon observation of  $x(t)$  over the interval  $0 \leq t \leq KT$  and knowledge of  $S$ ,  $m(t)$ ,  $\omega_0$ , and the precise time instants at which the modulation can change states, we wish to choose that value of  $\theta(t) = \theta$  (assumed constant over  $0 \leq t \leq KT$ ) which maximizes the a posteriori probability  $p(\theta(t)|x(t))$ . The solution to this problem, i.e., the best estimate of  $\theta$  in the MAP sense, is well known [2] to be that value that maximizes the function

$$f(\theta) = \prod_{k=1}^K \cosh \left[ \frac{2}{N_0} \int_{(k-1)T}^{kT} \sqrt{2S} x(t) \sin(\omega_0 t + \theta) p(t) dt \right] \quad (4)$$

or, equivalently,

$$\ln f(\theta) = \sum_{k=1}^K \ln \cosh \left[ \frac{2}{N_0} \int_{(k-1)T}^{kT} \sqrt{2S} x(t) \sin(\omega_0 t + \theta) p(t) dt \right]. \quad (5)$$

The physical interpretation of (5) implies an open loop estimation in the sense that, for each value of  $\theta$  in the continuum  $(-\pi, \pi)$ , we form the function  $\ln f(\theta)$  and then choose that particular value which corresponds to the maximum of this function. A discrete (in the sense of a finite number of trial values of  $\theta$ ) version of this interpretation is illustrated in Figure 1.

To go from open loop to closed loop configurations, we consider an alternate interpretation of the MAP estimate solution. Defining

$$g(\theta) \triangleq \frac{d \ln f(\theta)}{d\theta} = \sum_{k=1}^K \frac{2}{N_0} \int_{(k-1)T}^{kT} \sqrt{2S} x(t) \cos(\omega_0 t + \theta) p(t) dt \\ \times \tanh \left[ \frac{2}{N_0} \int_{(k-1)T}^{kT} \sqrt{2S} x(t) \sin(\omega_0 t + \theta) p(t) dt \right], \quad (6)$$

then the MAP estimate  $\hat{\theta}$  is also the solution to

$$g(\hat{\theta}) = 0. \quad (7)$$

For any value of  $\theta$  other than  $\hat{\theta}$ ,  $g(\hat{\theta})$  will be either positive or negative, depending on the sign of  $\theta - \hat{\theta}$ . Thus,  $g(\hat{\theta})$  is intuitively an appropriate choice for an error signal in a carrier phase tracking loop. Using this motivation, Figure 2 illustrates such a closed loop implementation which herein will be referred to as the MAP estimation loop.

ORIGINAL PAGE IS  
OF POOR QUALITY

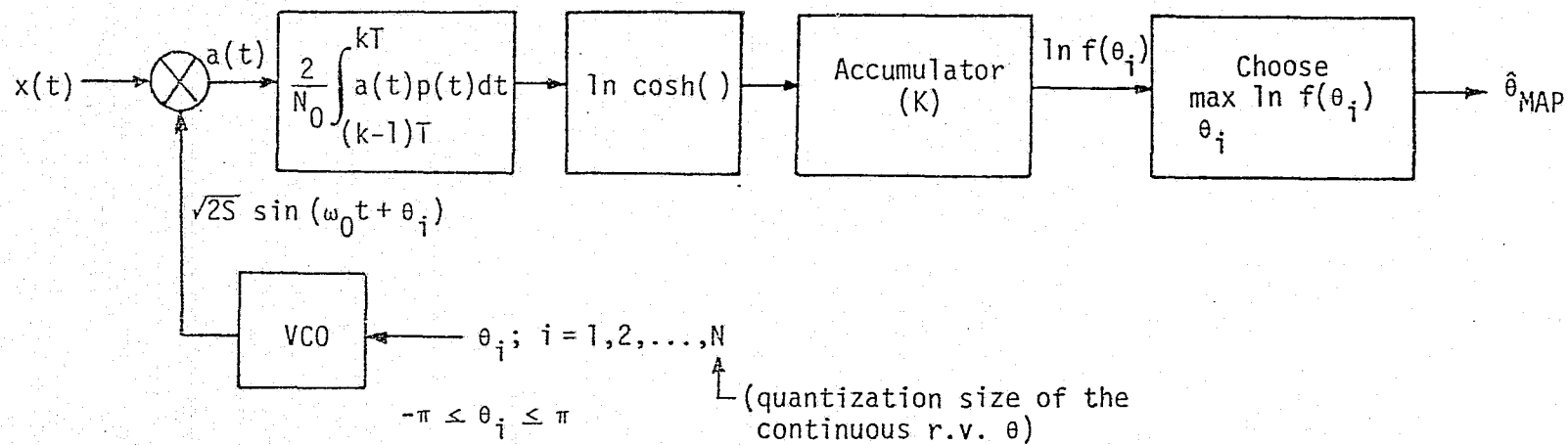


Figure 1. A Block Diagram Interpretation of the MAP Estimate of Carrier Phase Solution

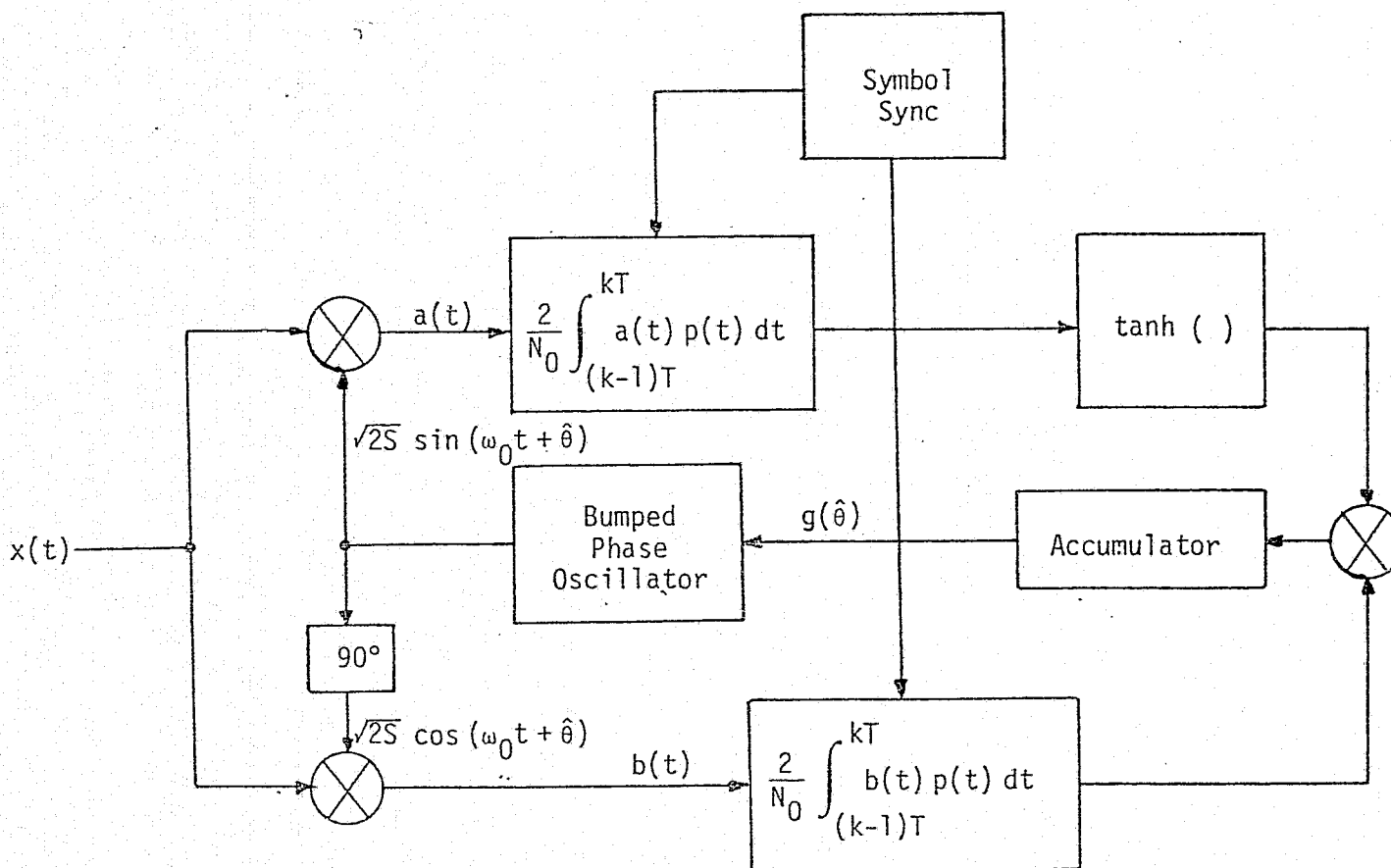


Figure 2. The MAP Estimation Loop for Carrier Phase (PSK)



The MAP estimation loop of Figure 2 is impractical, primarily because of the difficulty of implementing the hyperbolic tangent nonlinearity. To arrive at practical realizations, one must first approximate this nonlinearity with simpler, more easily implementable functions. In particular, we have that

$$\tanh x \cong \operatorname{sgn} x; \quad x \text{ large} \quad (8)$$

and\*

$$\tanh x \cong x; \quad x \text{ small.} \quad (9)$$

Since the input to the nonlinearity is a monotonic function of signal-to-noise ratio (SNR), then the approximations of (8) and (9) correspond, respectively, to conditions of high and low SNR. Using these approximations, then, in (6) leads to the practical implementations of Figures 3 and 4. In Figure 3, the arm filters are, as in the MAP estimation loop, of the integrate-and-dump type and thus require a knowledge of symbol sync. In Figure 4, these same filters have been replaced by lowpass filters and, in accordance with this change, the digital filter and NCO are replaced by an analog loop filter and VCO. The tracking performances of these familiar loops, i.e., the conventional Costas loop (Figure 4a) and the polarity-type Costas loop (Figure 4b) or, equivalently, the Costas loop with hard-limited in-phase channel, have recently been documented in the literature [3,4] wherein the bandlimiting effects of the arm filters on both the input data modulation and the noise have been accounted for. In both cases, it is shown that, by properly selecting the arm filter bandwidth, one can optimize the loop's tracking performance in the sense of minimizing its squaring loss or, equivalently, in the linear region of performance, minimize its mean-squared tracking jitter.

#### QPSK Modulation

Quadrature-phase-shift-keyed (QPSK) modulation, as is well known, offers the opportunity of achieving a given bit error rate performance with half the channel bandwidth required by PSK. Carrier reconstruction loops for

---

\* We shall see that, in the case of quadrature modulation, this approximation of the hyperbolic tangent function for small values of its argument is not sufficient.

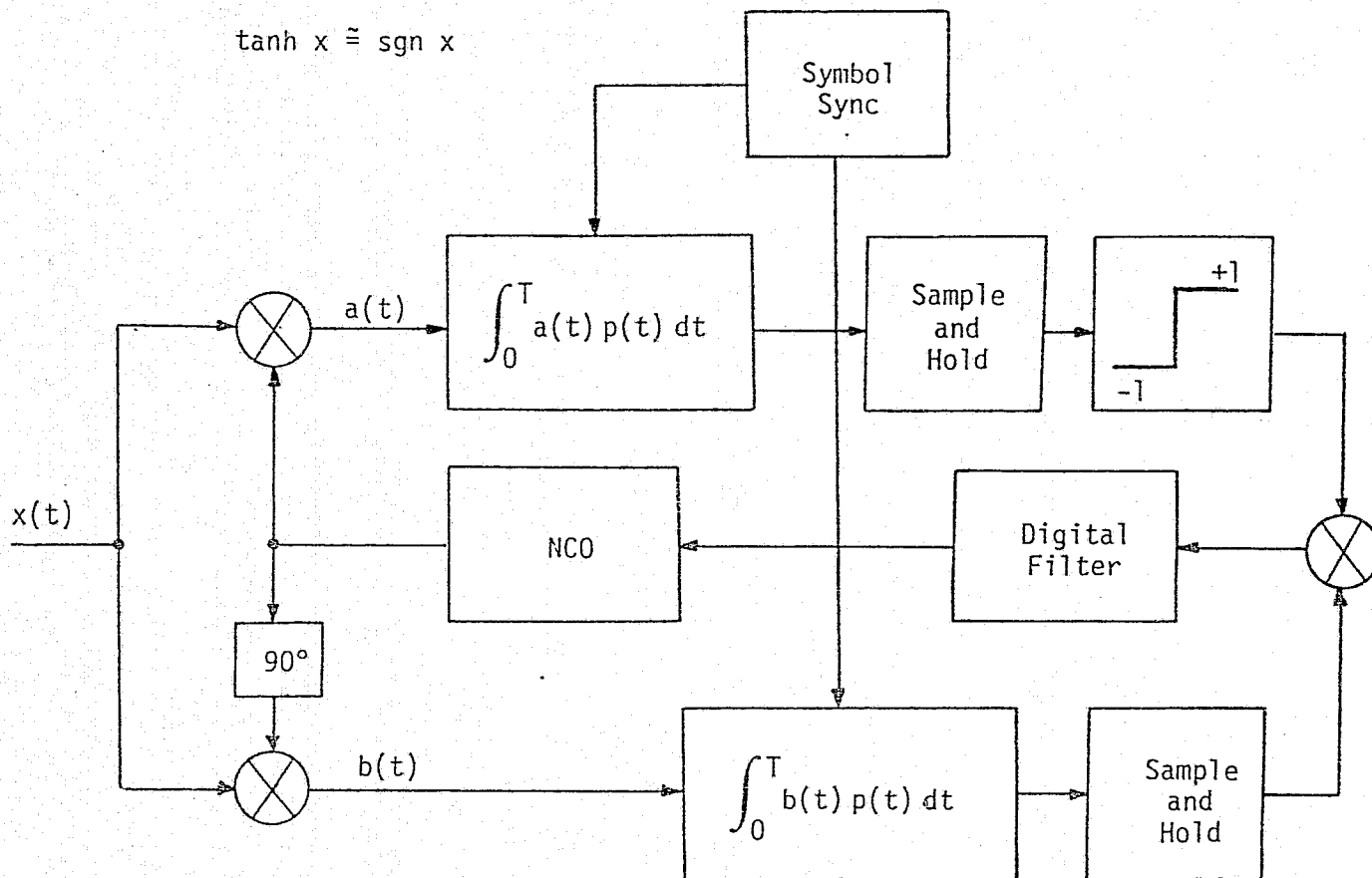


Figure 3b. Practical Realizations of the MAP Estimation Loop - Active Arm Filters  
Integrate-and-Dump Filters (Large SNR)  
(Polarity-Type I-Q Loop)

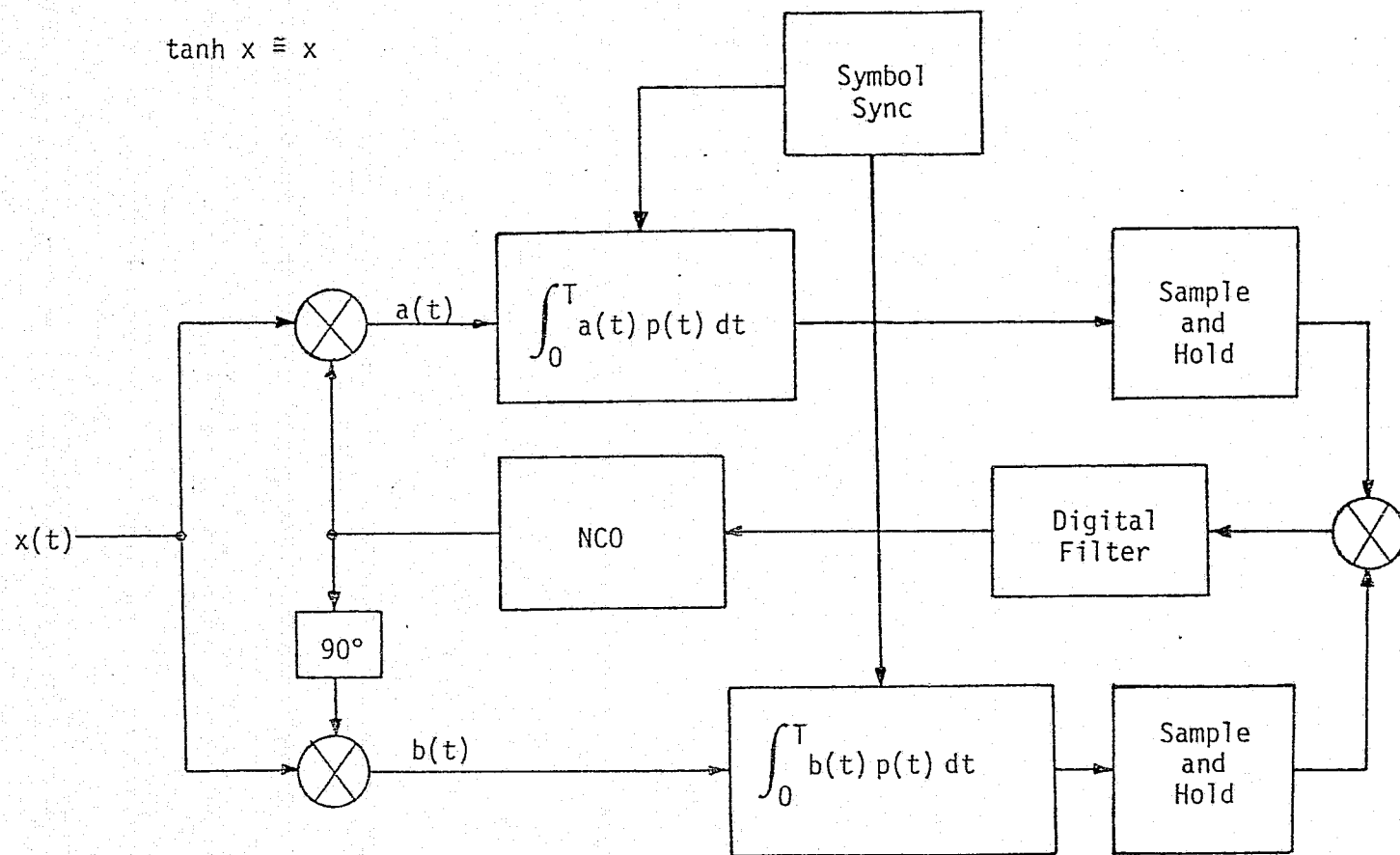
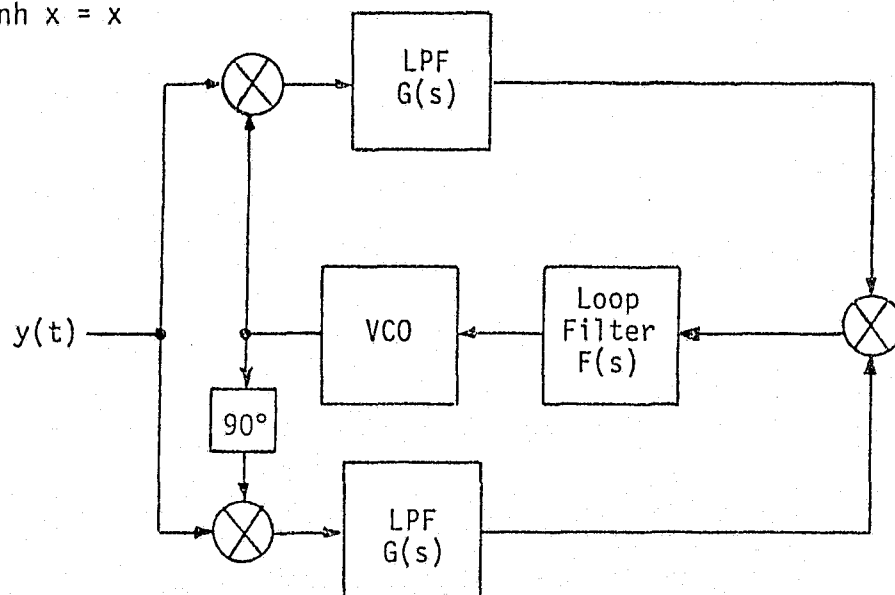


Figure 3a. Practical Realizations of the MAP Estimation Loop - Active Arm Filters  
Integrate-and-Dump Filters (Small SNR)  
(I-Q Loop)

a) Passive Arm Filters (Small SNR) - (Conventional Costas Loop)

$$\tanh x = x$$



b) Passive Arm Filters (Large SNR) - (Polarity-Type Costas Loop)

$$\tanh x = \operatorname{sgn} x$$

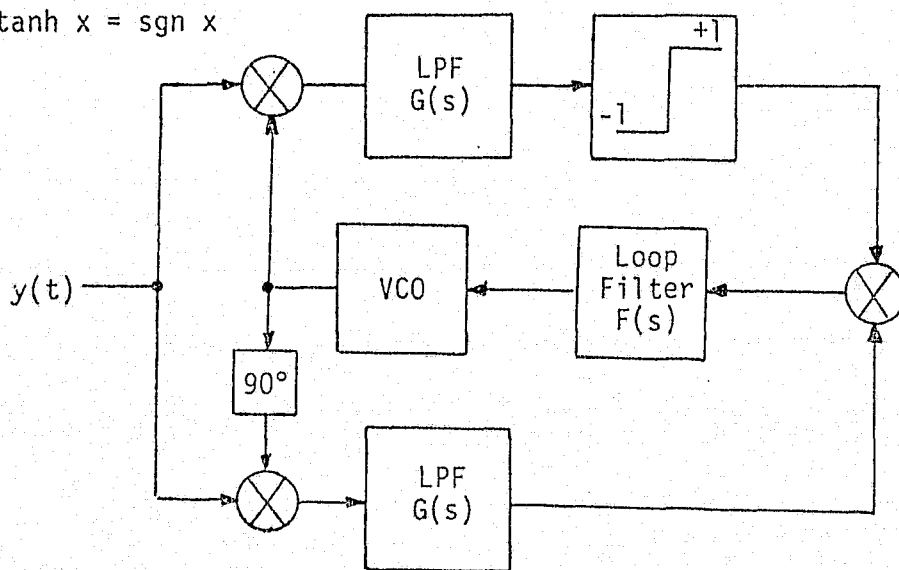


Figure 4. Practical Realizations of the MAP Estimation Loop

such a modulation are variously referred to as the fourth-power loop and the quadrphase Costas loop [2]. Assuming analog (four quadrant type) multipliers, these two loops have been shown [2] to be stochastically equivalent.

In this section, we derive the MAP estimation loop for a QPSK signal, and by suitable approximations to the nonlinearity which arises as a consequence of the MAP theory, reconfigure this loop with practical realizations which are valid for high and low signal-to-noise ratios. In particular, for the low signal-to-noise ratio case, we are led directly to a new structure which, like the fourth-power loop, will be shown to be stochastically equivalent to the quadrphase Costas loop mentioned above. This new structure, however, has decided implementation advantages over the conventional quadrphase Costas loop, particularly in applications where the receiver may be operated in either a biphasic or quadrphase mode. The significance of this statement will become clearer after we have had an opportunity to examine this new structure in finer detail.

As a generalization of (1), a quadrphase-modulated, suppressed-carrier signal takes the form

$$s[t, \theta(t)] = \sqrt{2S} m_1(t) \sin [\omega_0 t + \theta(t)] + \sqrt{2S} m_2(t) \cos [\omega_0 t + \theta(t)], \quad (10)$$

where  $S$  is the average signal power in either of the two data channels,  $m_1(t)$  and  $m_2(t)$  are the corresponding independent, binary modulations, both (for balanced quadrphase) of rate  $R=1/T$  and pulse shape  $p(t)$ , and  $\theta(t)$ , as previously defined, is again the received carrier phase. Based upon an observation of this signal in additive noise as described by (2) and (3), then by an analogous approach to that used in deriving (4), we find that the MAP estimate of carrier phase is that value that maximizes the function

$$\begin{aligned} f(\theta) = & \prod_{k=1}^K \cosh \left\{ \frac{2}{N_0} \int_{(k-1)T}^{kT} \sqrt{2S} x(t) \sin (\omega_0 t + \theta) p(t) dt \right\} \\ & \times \cosh \left\{ \frac{2}{N_0} \int_{(k-1)T}^{kT} \sqrt{2S} x(t) \cos (\omega_0 t + \theta) p(t) dt \right\} \end{aligned} \quad (11)$$

or, equivalently,

$$\ln f(\theta) = \sum_{k=1}^K \left\{ \ln \cosh \left[ \frac{2}{N_0} \int_{(k-1)T}^{kT} \sqrt{2S} x(t) \sin(\omega_0 t + \theta) p(t) dt \right] \right. \\ \left. + \ln \cosh \left[ \frac{2}{N_0} \int_{(k-1)T}^{kT} \sqrt{2S} x(t) \cos(\omega_0 t + \theta) p(t) dt \right] \right\}. \quad (12)$$

Once again, to go from an open loop MAP estimate to a closed loop tracking configuration, we introduce the function  $g(\theta) \triangleq (d \ln f(\theta))/d\theta$  and use  $g(\theta)$  as an error signal in such a closed loop. Differentiating (12) with respect to  $\theta$  gives

$$g(\theta) \triangleq \frac{d \ln f(\theta)}{d\theta} = \sum_{k=1}^K \left\{ \frac{2}{N_0} \int_{(k-1)T}^{kT} \sqrt{2S} x(t) \cos(\omega_0 t + \theta) p(t) dt \right. \\ \times \tanh \left[ \frac{2}{N_0} \int_{(k-1)T}^{kT} \sqrt{2S} x(t) \sin(\omega_0 t + \theta) p(t) dt \right] \\ - \frac{2}{N_0} \int_{(k-1)T}^{kT} \sqrt{2S} x(t) \sin(\omega_0 t + \theta) p(t) dt \\ \left. \times \tanh \left[ \frac{2}{N_0} \int_{(k-1)T}^{kT} \sqrt{2S} x(t) \cos(\omega_0 t + \theta) p(t) dt \right] \right\}. \quad (13)$$

The corresponding MAP estimation loop for QPSK is illustrated in Figure 5.

To achieve a practical realization of Figure 5 for high SNR, we again approximate the hyperbolic tangent function as in (8). The resulting loop, using passive arm filters, is illustrated in Figure 6. If one tries to use the approximation of  $\tanh x$  given in (9) to construct a low SNR implementation of the MAP estimate loop, then substituting (9) in (13), we immediately see that  $g(\theta) = 0$  for all  $\theta$ ; hence, no error signal is generated. To circumvent this apparent dilemma, we go one step further by approximating the hyperbolic tangent function by the first two terms of its power series, namely,

$$\tanh x \approx x - \frac{x^3}{3}; \quad x \text{ small}. \quad (14)$$

Substituting this approximation into (13) results in

ORIGINAL PAGE IS  
OF POOR QUALITY

ORIGINAL PAGE IS  
OF POOR QUALITY

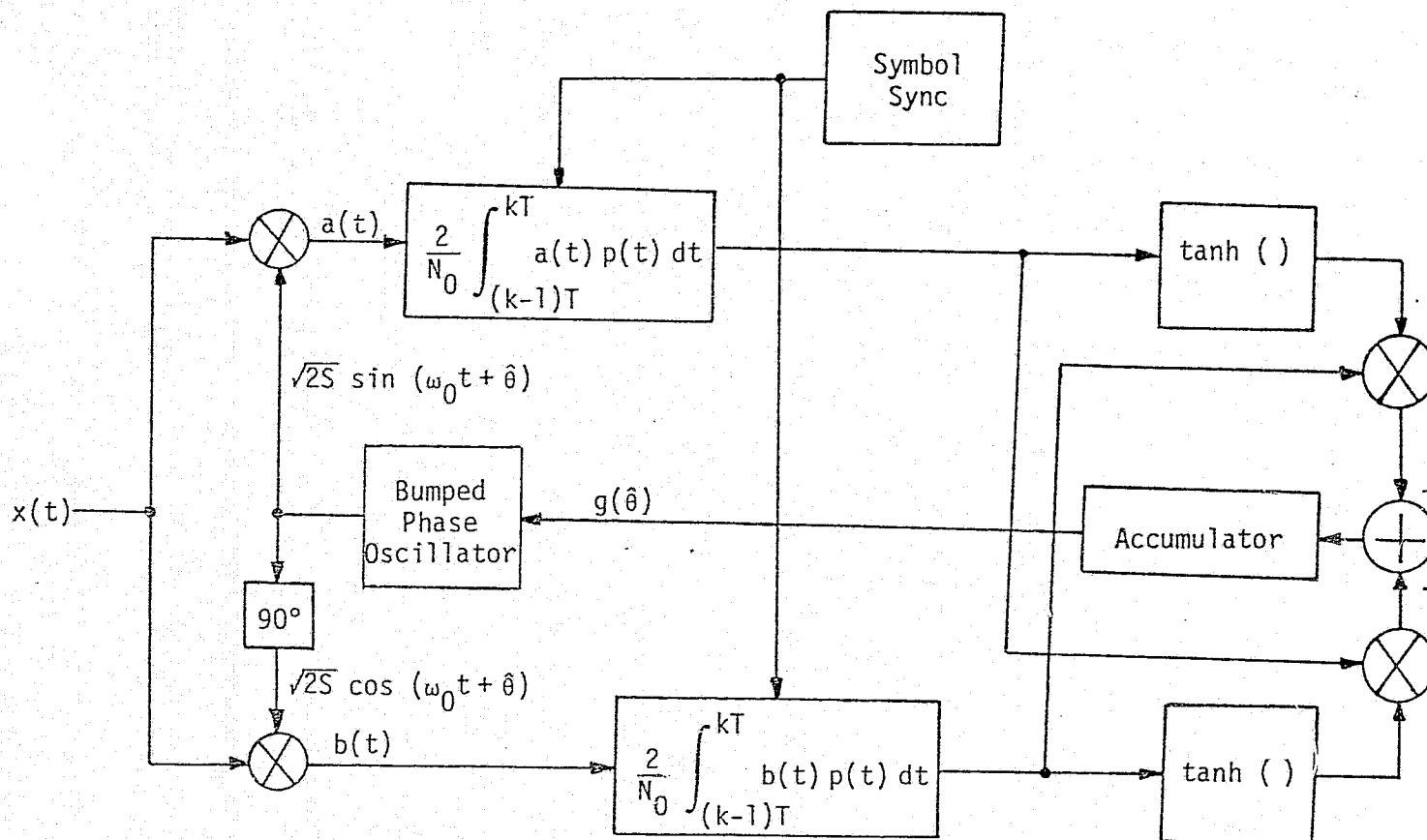


Figure 5. The MAP Estimation Loop for Carrier Phase (QPSK)

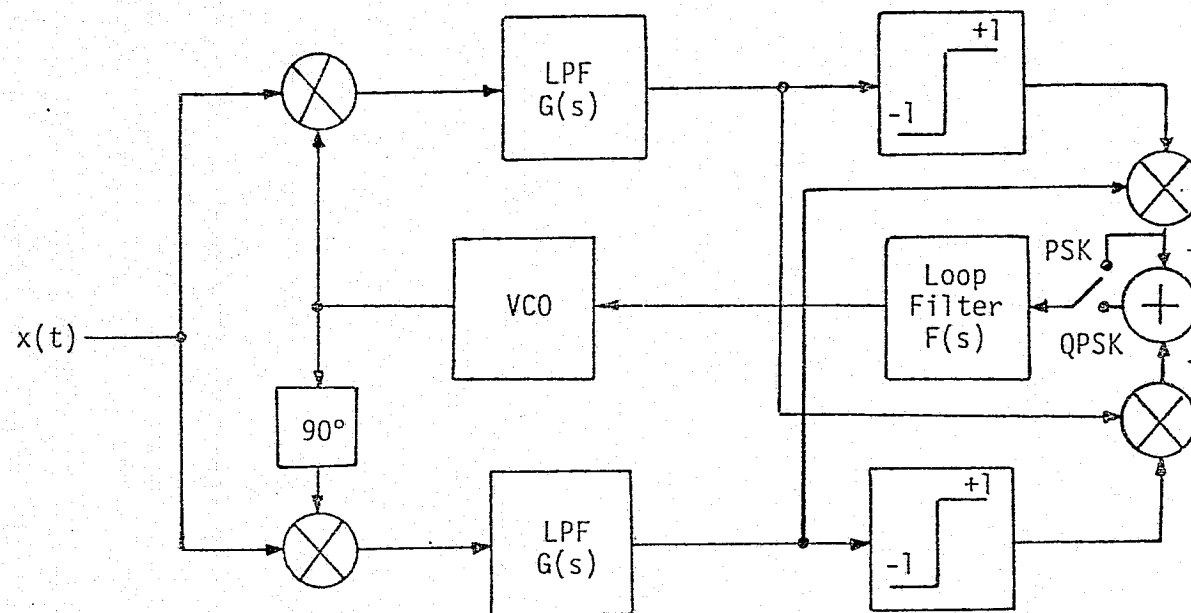


Figure 6. A Practical Realization of the MAP Estimation Loop,  
Passive Arm Filters, Large SNR  
(Polarity-Type Quadriphase Costas Loop)



$$\begin{aligned}
g(\theta) = & \sum_{k=1}^K \left\{ \frac{2}{N_0} \int_{(k-1)T}^{kT} \sqrt{2S} x(t) \sin(\omega_0 t + \theta) p(t) dt \right. \\
& \times \frac{1}{3} \left( \frac{2}{N_0} \int_{(k-1)T}^{kT} \sqrt{2S} x(t) \cos(\omega_0 t + \theta) p(t) dt \right)^3 \\
& - \frac{2}{N_0} \int_{(k-1)T}^{kT} \sqrt{2S} x(t) \cos(\omega_0 t + \theta) p(t) dt \\
& \left. \times \frac{1}{3} \left( \frac{2}{N_0} \int_{(k-1)T}^{kT} \sqrt{2S} x(t) \sin(\omega_0 t + \theta) p(t) dt \right)^3 \right\} \quad (15)
\end{aligned}$$

which is of the form

$$g(\theta) = \frac{1}{3} \sum_{k=1}^K (AB^3 - BA^3), \quad (16)$$

where A and B are immediately identified from (15). Rewriting (16) as

$$g(\theta) = \frac{1}{3} \sum_{k=1}^K [AB(B^2 - A^2)] \quad (17)$$

allows us to draw the practical realization of the MAP estimation loop for low SNR (see Figure 7).<sup>\*</sup> Several interesting observations can be made from both (17) and Figure 7. The signal product AB represents the error signal generated in a conventional biphase Costas loop. The signal difference  $B^2 - A^2$  represents the output of a lock detector associated with the same biphase Costas loop. Thus, the quadriphase error signal of (17), namely,  $AB(B^2 - A^2)$ , is the product of the error signal and lock detector output of a conventional biphase Costas loop. The accumulation required in (17) is, as before, accomplished in the analog version (Figure 7) by the loop filter  $F(s)$ .

Implementing a quadriphase carrier tracking loop in Figure 7 has several implementation advantages over the conventional quadriphase Costas loop. First, it allows for either biphase or quadriphase operation, since the biphase error signal AB is already available. This choice of operation

---

<sup>\*</sup>This particular quadriphase Costas loop configuration was originally suggested to the author by J. C. Springett of Axiomatix, apart from its motivation by MAP estimation theory.

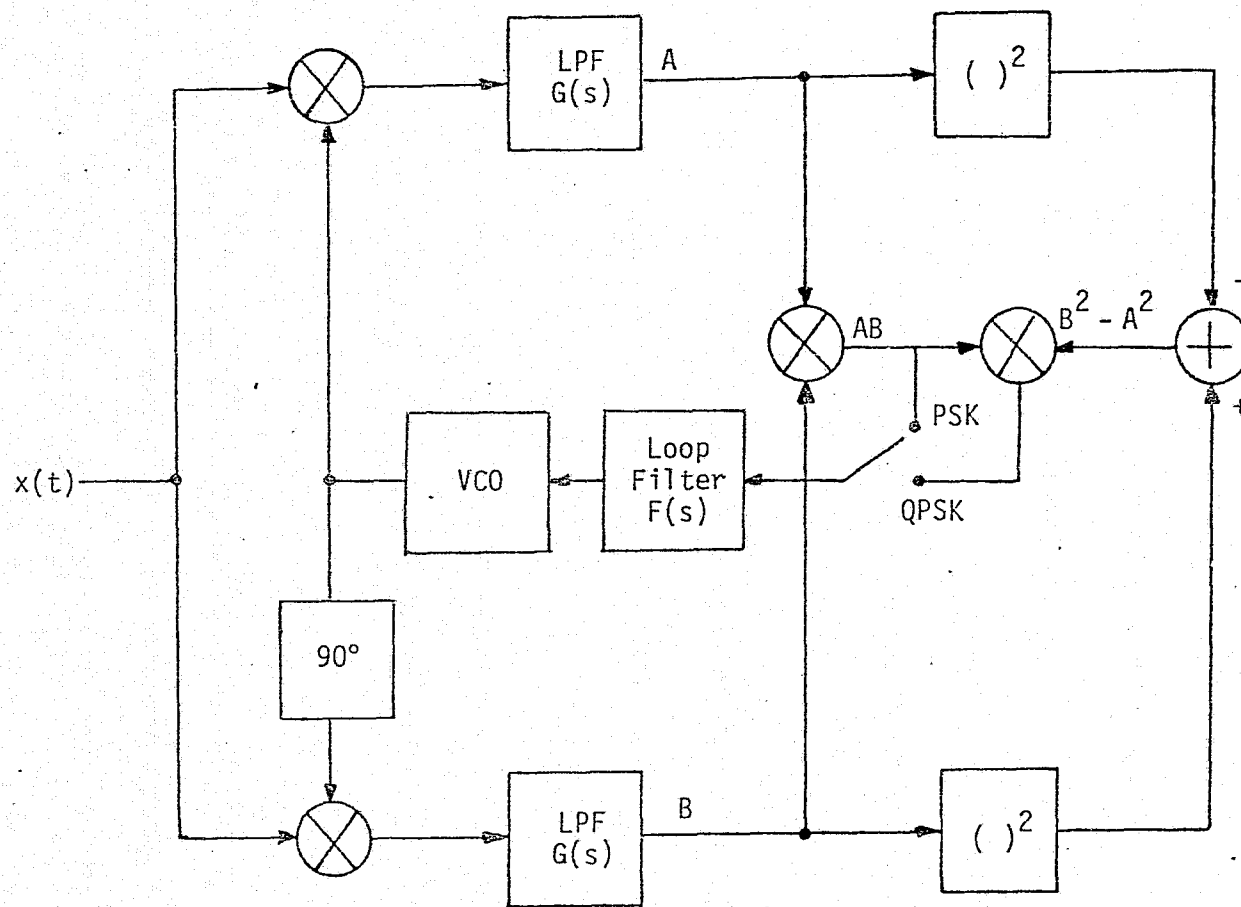


Figure 7. A Practical Realization of the MAP Estimation Loop, Passive Arm Filters, Small SNR

mode can be accomplished using a simple switch (see Figure 7). Thus, relative to the hardware required to implement a biphase Costas loop and its associated lock detector, all that is needed to generate a quadriphase error signal is one additional analog multiplier. We hasten to add that the large SNR loop of Figure 6 can also, as shown in this figure, be made to operate either as a biphase or quadriphase polarity-type Costas loop. Second, even if the loop is designed strictly for carrier tracking of balanced QPSK, the implementation of Figure 7 requires only two quadrature reference signals and two arm filters, as opposed to the four reference signals (spaced by  $\pi/4$  radians) and the four arm filters needed to build the conventional quadriphase Costas loop.

The only point that remains is: How does the performance of the loop in Figure 7 compare with that of the conventional quadriphase loop? The answer to this question is that the two loops are stochastically equivalent, i.e., it can be shown [5] that the two have identical stochastic differential equations of operation. Thus, by starting with MAP estimation theory as a mathematical basis, we have proven, via the introduction of a new configuration, that the conventional quadriphase Costas loop and its equivalent (the fourth power loop) are low SNR practical realizations of the MAP estimate loop for QPSK.

#### Unbalanced QPSK

With the results for PSK and QPSK as background, we are now in a position to better understand, interpret, and augment previously obtained results [1] for the case of interest here, namely, carrier reconstruction techniques for unbalanced QPSK (UQPSK) as motivated by MAP estimation theory. While it is true that, depending on the ratio of powers in the two channels of the UQPSK signal, a simple biphase or quadriphase Costas loop can be employed for carrier reconstruction [6,7,8], the purpose of the study in [1] was to search for "optimum" carrier reconstruction techniques in the sense that the loop would make full use of the total power in the two channels to enhance its tracking capability. Also, by applying MAP estimation theory directly to the UQPSK signal, the intuitive feeling was that some sort of hybrid configuration would arise which would present a continuous compromise between the extreme desires of tracking a highly unbalanced QPSK signal and the more common balanced QPSK signal in which

the powers and data rates in the two channels are equal.

Indeed, the results derived in [1] largely represent this dream come true. Unfortunately, however, the low SNR realizations of the MAP estimate loop for UQPSK suffer from the fact that they cannot track a balanced QPSK signal. The problem herein lies again in the way in which the hyperbolic tangent nonlinearity is approximated at low signal-to-noise ratios. We shall demonstrate shortly that, by using (14) rather than (9) at low SNR, one obtains a practical implementation which allows carrier reconstruction from a UQPSK signal at all ratios of data rates and powers in the two channels, in particular, in the limit as these ratios simultaneously approach unity, i.e., balanced QPSK. In fact, in this limiting case, the loop becomes equivalent to the quadriphase loop of Figure 7.

An unbalanced QPSK signal takes the form

$$s[t, \theta(t)] = \sqrt{2P_1} m_1(t) \cos [\omega_0 t + \theta(t)] + \sqrt{2P_2} m_2(t) \sin [\omega_0 t + \theta(t)], \quad (18)$$

where  $P_1$  and  $P_2$  are the average signal powers, respectively, in channels 1 and 2, and  $m_1(t)$  and  $m_2(t)$  are the corresponding independent binary modulations with rates  $R_1 = 1/T_1$ ,  $R_2 = 1/T_2$  and, in general, different pulse shapes  $p_1(t)$  and  $p_2(t)$ . Applying the MAP estimation theory to an observation of the signal (18) in noise, the error signal  $g(\hat{\theta})$  for the MAP estimation loop is derived in [1] as

$$\begin{aligned} g(\hat{\theta}) \triangleq \left. \frac{d \ln f(\theta)}{d\theta} \right|_{\theta=\hat{\theta}} &= \sum_{k=1}^{K_2+1} \frac{2}{N_0} \int_{\delta_{k-1}}^{\delta_k} \sqrt{2P_2} x(t) \cos (\omega_0 t + \hat{\theta}) p_2(t) dt \\ &\times \tanh \left[ \frac{2}{N_0} \int_{\delta_{k-1}}^{\delta_k} \sqrt{2P_2} x(t) \sin (\omega_0 t + \hat{\theta}) p_2(t) dt \right] \\ &- \sum_{k=1}^{K_1+1} \frac{2}{N_0} \int_{\tau_{k-1}}^{\tau_k} \sqrt{2P_1} x(t) \sin (\omega_0 t + \hat{\theta}) p_1(t) dt \\ &\times \tanh \left[ \frac{2}{N_0} \int_{\tau_{k-1}}^{\tau_k} \sqrt{2P_1} x(t) \cos (\omega_0 t + \hat{\theta}) p_1(t) dt \right] \dots \end{aligned} \quad (19)$$

ORIGINAL PAGE IS  
OF POOR QUALITY

In (19),  $\tau_k$  ( $k=1,2,\dots,K_1$ ) is the ordered set of time instants at which the modulation  $m_1(t)$  may potentially have a symbol transition in the observation interval  $(0,T)$ . Similarly,  $\delta_k$  ( $k=1,2,\dots,K_2$ ) is the ordered set of time instants at which the modulation  $m_2(t)$  may have a symbol transition in the same observation interval. Note that, since the two modulations might, in general, be generated from independent data clocks, no restriction is placed on the relative synchronization between the taus and the deltas. This same assumption could also have been made for the balanced quadriphase case with the appropriate modification of (13).

Illustrated in Figure 8 is the MAP estimation loop for UQPSK with  $g(\hat{\theta})$  of (19) as its error signal. A practical realization of this loop for high SNR, obtained by using the approximation to the hyperbolic tangent function of (8) in (19), is illustrated in Figure 9. For small SNR, using (9) as an approximation to  $\tanh x$ , the authors of [1] suggest the loop illustrated in Figure 10. Unfortunately, this loop (or its equivalent using active arm filters of the type given in Figure 8) has the disadvantage that, as the ratio of rates and powers both approach unity, i.e., balanced quadriphase, the two lowpass filters  $LPF_1$  and  $LPF_2$  would become identical (or equivalently integrate-and-dump filters of equal duration), and thus the error signal at the input to the loop filter goes to zero for all loop phase errors. If, instead of (9), one were to use (14) as an approximation to  $\tanh x$ , then making this substitution in (19) results in the loop illustrated in Figure 11, where again we have drawn the case where the arm filters are of the passive type. Note that this two-channel Costas loop configuration reduces (except for the one-third gain factor) to Figure 7 when the input signal becomes balanced QPSK, i.e.,  $LPF_1 = LPF_2$  and, thus, it is capable of tracking such a signal. Rather than go into the details of the performance of the loop in Figure 11 at this point, we shall turn to an investigation of the sensitivity to gain variations of the simpler loop in Figure 10 and use these results qualitatively as being indicative of two-channel Costas-type configurations. Actually, to make life even simpler, we shall perform our sensitivity analysis on the equivalent loop to Figure 10 where active (integrate-and-dump) arm filters of the type illustrated in Figure 8 are used in place of the passive arm filters. Making this substitution greatly simplifies the analysis, but nevertheless allows us to illustrate the conclusions we are after.

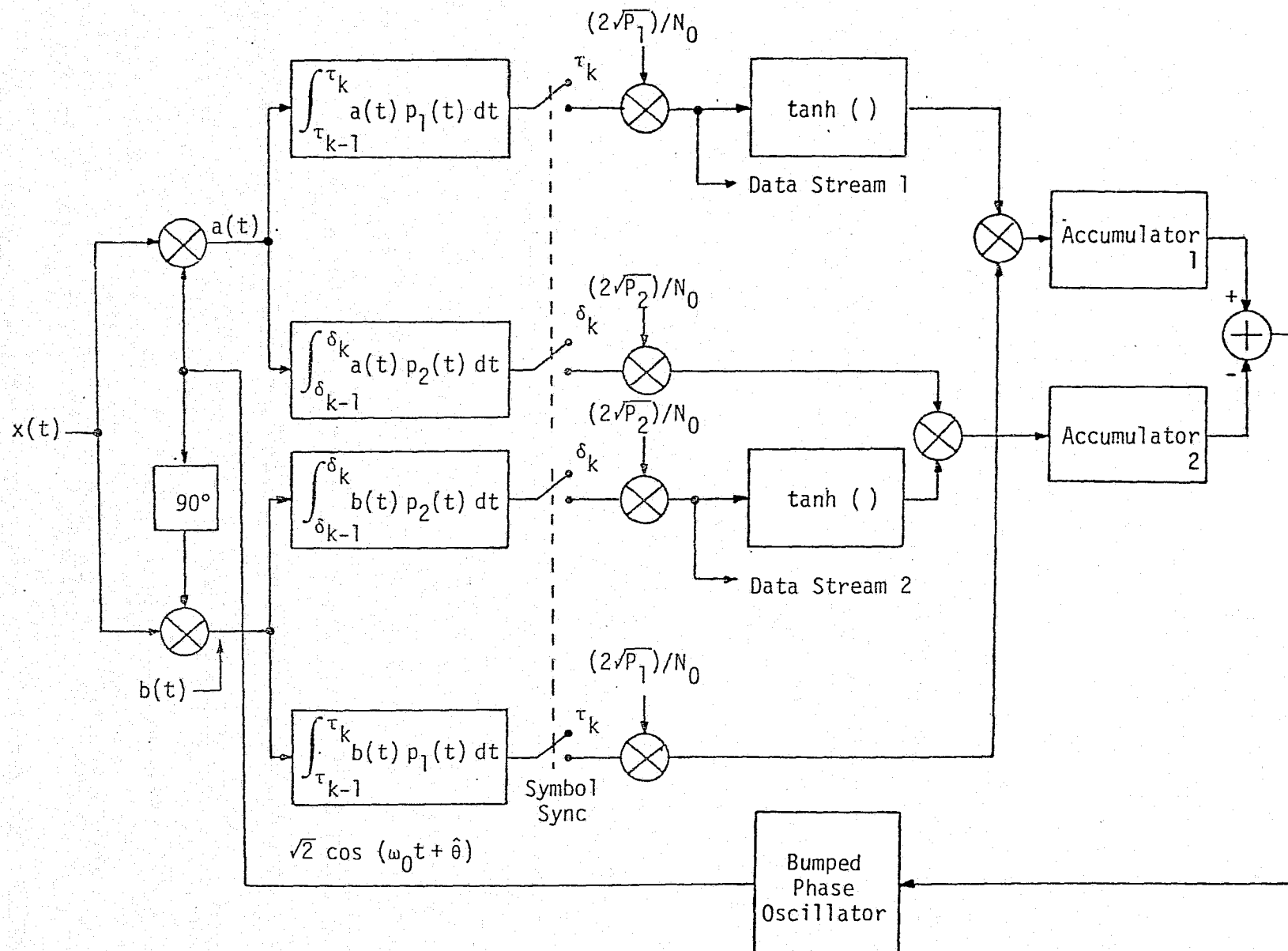


Figure 8. The MAP Estimation Loop for Carrier Phase (UQPSK)

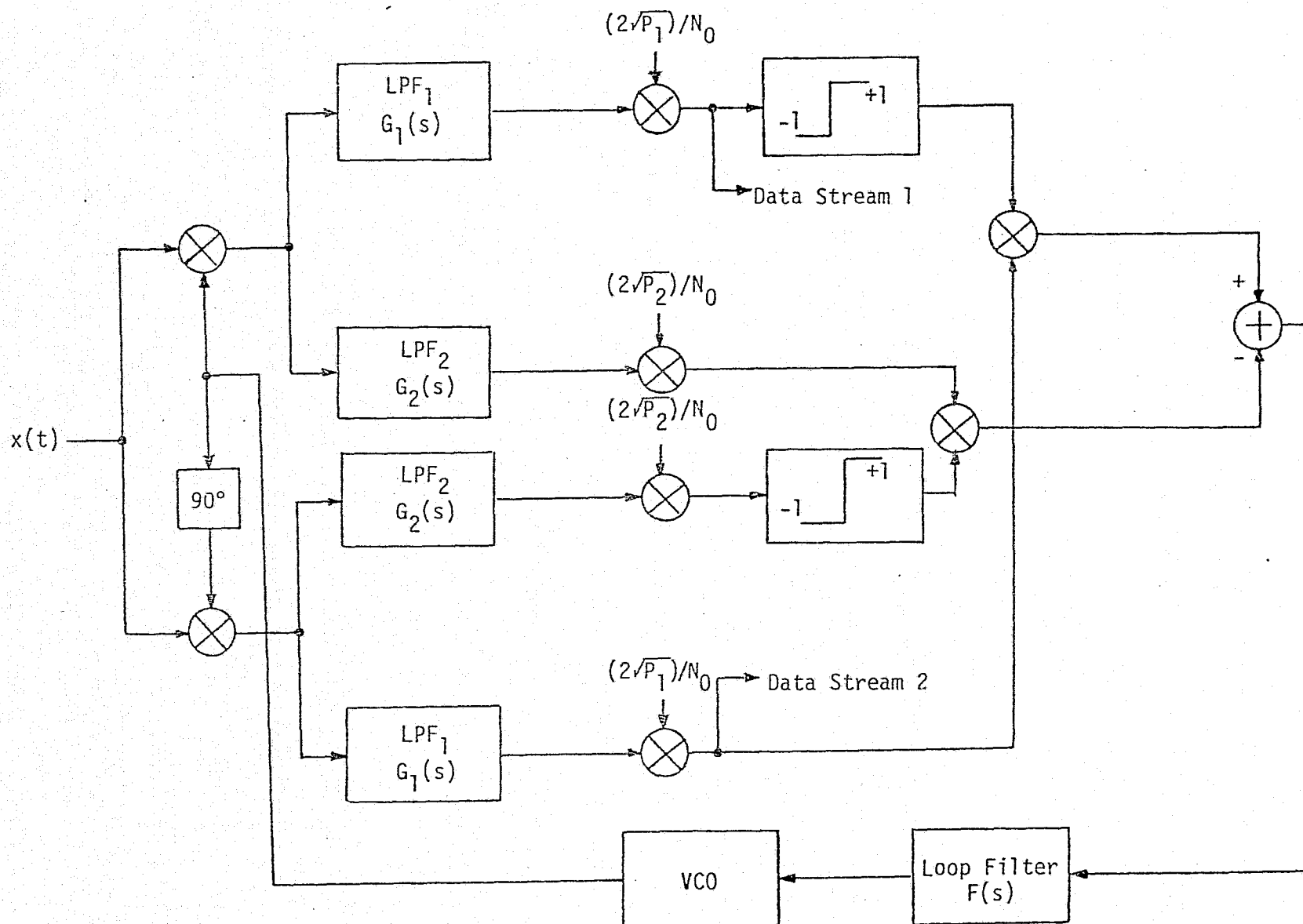


Figure 9. A Practical Realization of the MAP Estimation Loop; Passive Arm Filters, Large SNR

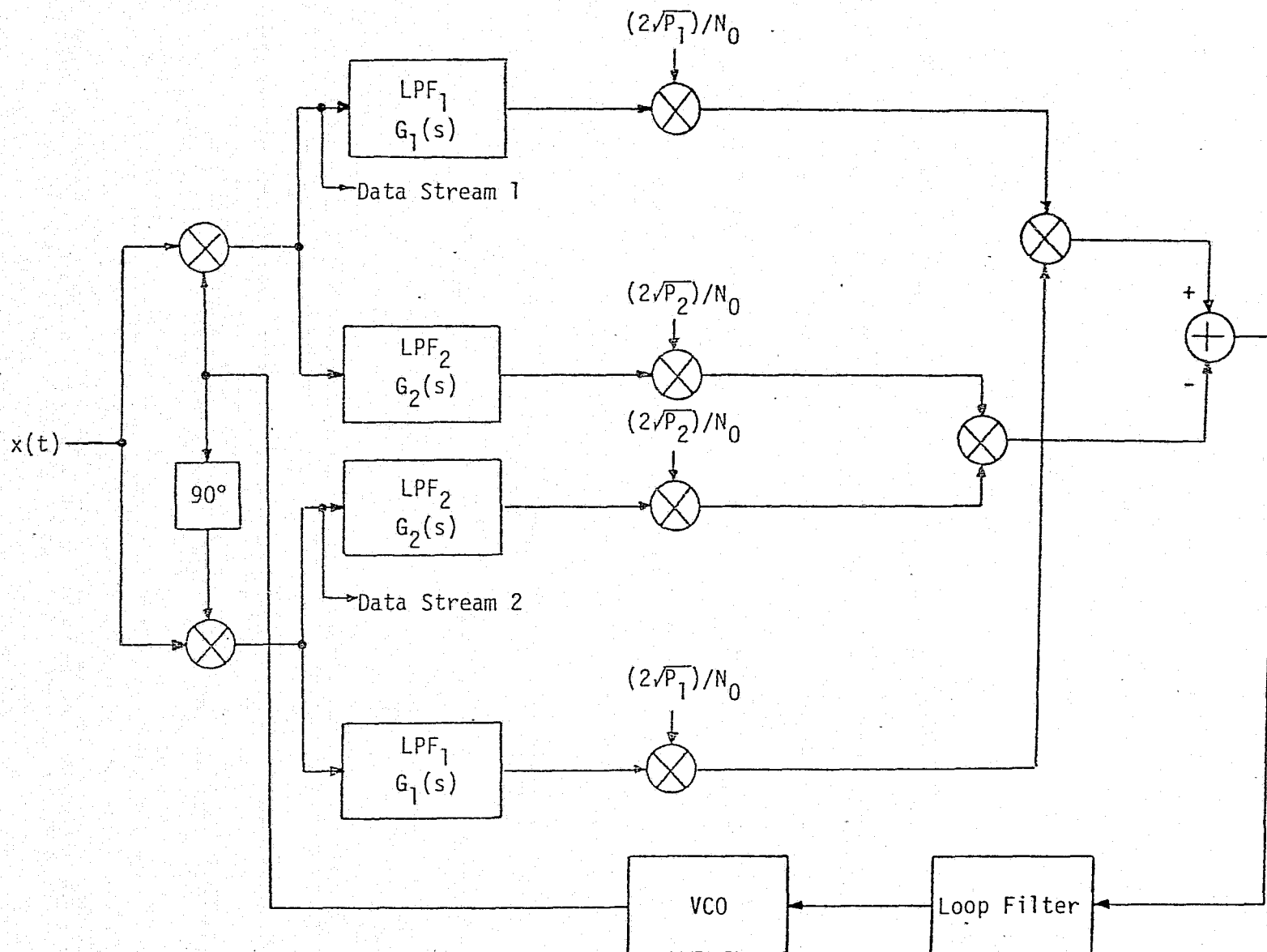


Figure 10. A Practical Realization of the MAP Estimation Loop;  
Passive Arm Filters, Small SNR;  $\tanh x \cong x$



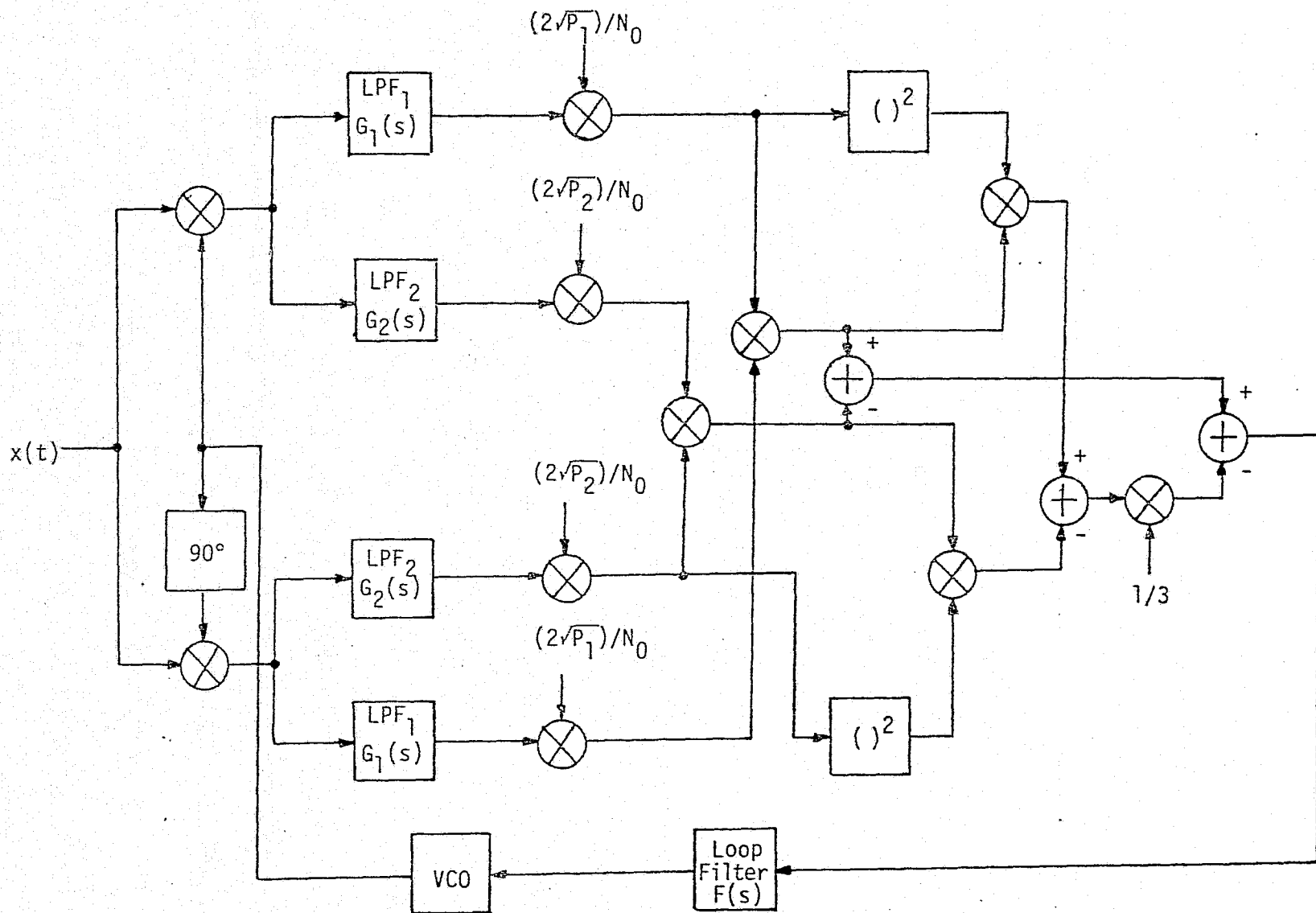


Figure 11. A Practical Realization of the MAP Estimation Loop for UQPSK; Passive Arm Filters, Small SNR;  $\tanh x = x - x^3/3$

# SENSITIVITY OF TRACKING PERFORMANCE OF TWO-CHANNEL COSTAS-TYPE LOOPS TO CHANNEL GAIN VARIATIONS

The tracking performance of the UQPSK carrier reconstruction loops illustrated in Figures 9 and 10 has been studied in great detail in [1]. Part II of this reference treats the passive arm filter case, i.e., Figures 9 and 10 as they are drawn, while Part I presents the results for the equivalent loops with active arm filters. In each case, the phase tracking jitter based on a linear loop model is calculated as a function of such system parameters as signal-to-noise ratio in each channel, the ratio of powers in the two channels, and the ratio of data rates in the two channels. Although the theoretical results were derived as a function of the ratio of the gains in the two channels, specific numerical results were presented only for the "optimum" choice for this ratio based upon MAP estimation theory.

Unfortunately, as we shall see shortly, selection of this gain ratio as motivated by MAP estimation theory does not necessarily optimize the tracking performance. In fact, the selection of this gain ratio to directly optimize the tracking performance in the sense of minimum mean-squared phase tracking jitter, can yield as much as a 10 dB improvement in this performance relative to the MAP estimation choice of gain ratio.

To illustrate this point, we shall begin by extracting pertinent results from [1] for the equivalent loop to Figure 10 with active arm filters and arbitrary channel gains  $\sqrt{K_1}$  and  $\sqrt{K_2}$ . In particular, it is shown in [1] that the variance of the loop phase error (phase tracking jitter  $\sigma_{2\phi}^2$  for a linear loop model is given by

$$\sigma_{2\phi}^2 = 4 N_0 B_L \frac{\left[ B_0 + B_1 \left( \frac{K_2}{K_1} \right) + B_2 \left( \frac{K_2}{K_1} \right)^2 \right]}{\left[ A_0 + A_1 \left( \frac{K_2}{K_1} \right) \right]^2}, \quad (20)$$

where

$$A_0 = P_1 - P_2$$

$$A_1 = P_2 n^2 - P_1 n$$

$$B_0 = P_1 + \frac{N_0}{2T_1} + P_2 + \frac{2 P_1 P_2 T_1}{N_0}$$

$$\begin{aligned}
 B_1 &= -2 \left[ n \left( p_1 + \frac{N_0}{2T_1} \right) + n^2 \left( p_2 + \frac{2p_1 p_2 T_1}{N_0} \right) \right] \\
 B_2 &= n^3 \left( p_1 + \frac{N_0}{2T_1} \right) + n^4 \left( p_2 + \frac{2p_1 p_2 T_1}{N_0} \right)
 \end{aligned} \tag{21}$$

and we have implicitly assumed that the two data clocks are synchronized with the ratio of data rates being integer, i.e.,

$$n \triangleq \frac{T_2}{T_1} > 1; \quad n \text{ integer.} \tag{22}$$

Equivalently, the loop "squaring loss" is given by

$$S_L \triangleq \frac{4N_0 B_L}{\sigma_{2\phi}^2 (p_1 + p_2)} = \frac{\left[ A_0 + A_1 \left( \frac{K_2}{K_1} \right) \right]^2}{(p_1 + p_2) \left[ B_0 + B_1 \left( \frac{K_2}{K_1} \right) + B_2 \left( \frac{K_2}{K_1} \right)^2 \right]}. \tag{23}$$

Clearly, from (20) and (23), minimizing the phase tracking jitter  $\sigma_{2\phi}^2$  is directly equivalent to maximizing  $S_L$  (minimizing the squaring loss). From the form of (23), it is a simple matter to differentiate this equation with respect to  $K_2/K_1$ , and thus find that value of channel gain ratio which maximizes  $S_L$ . After some routine algebra, the solution to the equation

$$\frac{\partial S_L}{\partial (K_2/K_1)} = 0 \tag{24}$$

is

$$\begin{aligned}
 \left( \frac{K_2}{K_1} \right)_{\text{opt}} &= \frac{2A_1 B_0 - A_0 B_1}{2A_0 B_2 - A_1 B_1} \\
 &= \frac{p_2 \left( p_1 + \frac{N_0}{2T_1} \right) + p_1 \left( p_2 + \frac{2p_1 p_2 T_1}{N_0} \right)}{n p_1 \left( p_1 + \frac{N_0}{2T_1} \right) + n^2 p_1 \left( p_2 + \frac{2p_1 p_2 T_1}{N_0} \right)}
 \end{aligned} \tag{25}$$

Alternately, defining the ratio of powers in the two channels by

$$\lambda = p_2/p_1, \tag{26}$$

we can rewrite (25) in the form

ORIGINAL PAGE IS  
OF POOR QUALITY

$$\left(\frac{K_2}{K_1}\right)_{\text{opt}} = \left(\frac{\lambda}{n}\right) \frac{\left[2 + \frac{1+\lambda}{2\zeta_1} + \frac{2\zeta_1}{1+\lambda}\right]}{\left[1 + n\lambda + \frac{1+\lambda}{2\zeta_1} + n\lambda \frac{2\zeta_1}{1+\lambda}\right]}, \quad (27)$$

where, in addition, we have defined (as in [1])  $\zeta_1$  as the total power-to-noise ratio in the high data rate bandwidth, i.e.,

$$\zeta_1 = \frac{(P_1 + P_2) T_1}{N_0}. \quad (28)$$

Note that the first factor in (27) is the "optimum" value of  $K_2/K_1$  as motivated by the MAP estimation theory, i.e.,

$$\frac{K_2}{K_1} = \frac{\lambda}{n}, \quad (29)$$

which is independent of signal-to-noise ratio. Only when the channels have equal energy, i.e.,  $\lambda = 1/n$ , are the results of (27) and (29) equal, i.e.,  $K_2/K_1 = \lambda^2$ .

Substituting (27) into (23) results in an expression for the minimum squaring loss, namely,

$$S_L = \frac{\left(1 + \frac{1+\lambda}{2\zeta_1}\right)(1 - 2\lambda + n\lambda^2) + \lambda(n-1)\left(1 + \frac{2\zeta_1}{1+\lambda}\right)}{(1+\lambda)\left(1 + \frac{1+\lambda}{2\zeta_1}\right)\left[\left(1 + \frac{1+\lambda}{2\zeta_1}\right) + n\lambda\left(1 + \frac{2\zeta_1}{1+\lambda}\right)\right]}. \quad (30)$$

On the other hand, using (29) in (23) gives the result obtained in [1], namely,

$$S_L = \frac{(1 - 2\lambda + n\lambda^2)^2}{(1+\lambda)\left[\left(1 + \frac{1+\lambda}{2\zeta_1}\right)(1 - 2\lambda + n\lambda^2) + \lambda\left(1 + \frac{2\zeta_1}{1+\lambda}\right)(1 - n\lambda)^2\right]}. \quad (31)$$

Figures 12 through 15 illustrate  $S_L$  as computed from (30) and (31) versus the power ratio  $\lambda$  with  $n$  fixed and  $\zeta_1 = -3$  dB and 10 dB. The values of  $n$  selected for these plots range from balanced ( $n=1$ ) to highly unbalanced ( $n=10$ ) data rates. Note that, for the balanced data rate case ( $n=1$ ,  $\lambda$  arbitrary), both (30) and (31) reduce to the same result, namely,

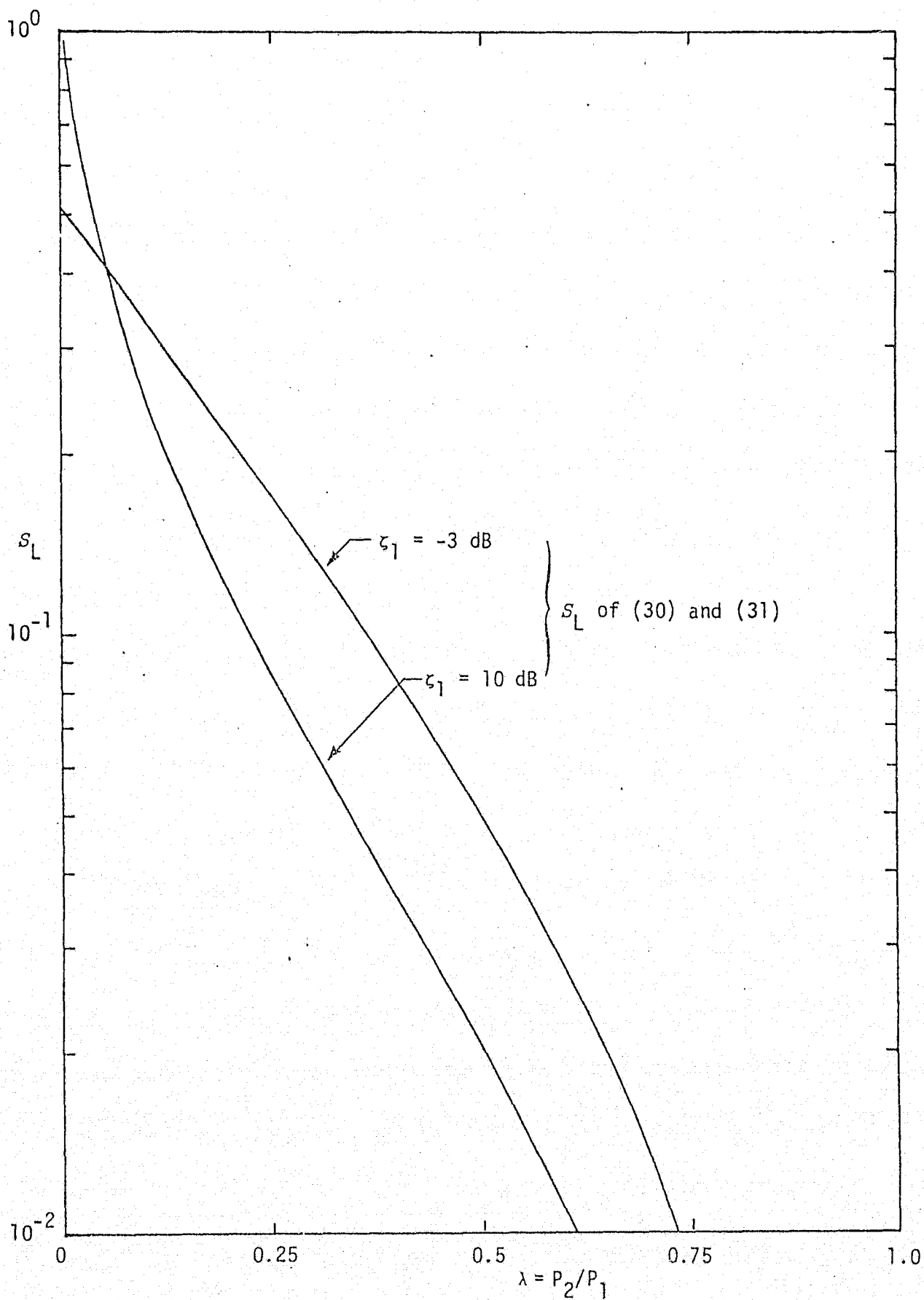


Figure 12. Squaring Loss vs. Power Ratio for Unbalanced QPSK; Two-Channel Costas Loop;  $n = T_2/T_1 = 1$

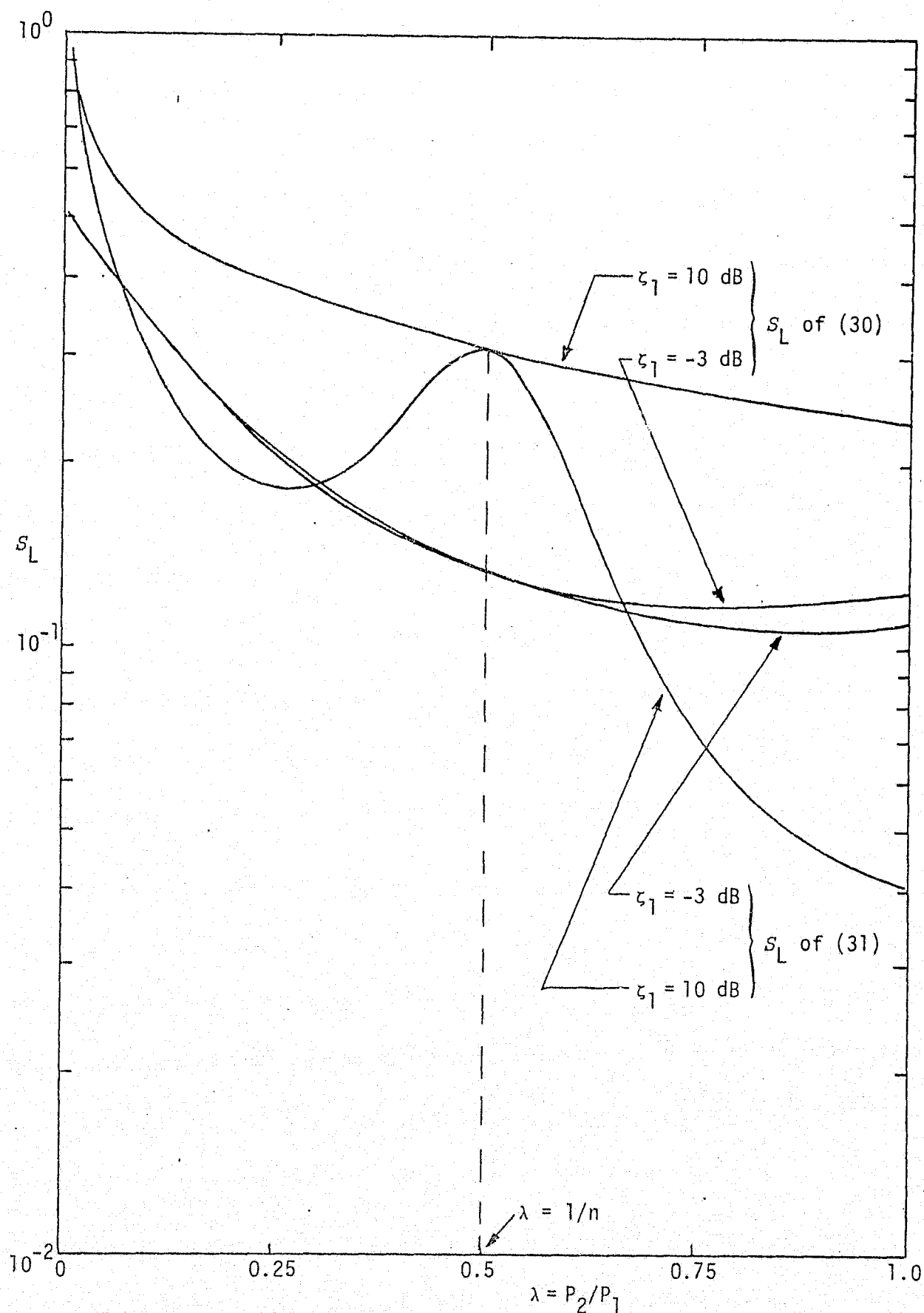


Figure 13. Squaring Loss vs. Power Ratio for Unbalanced QPSK; Two-Channel Costas Loop;  $n = T_2/T_1 = 2$

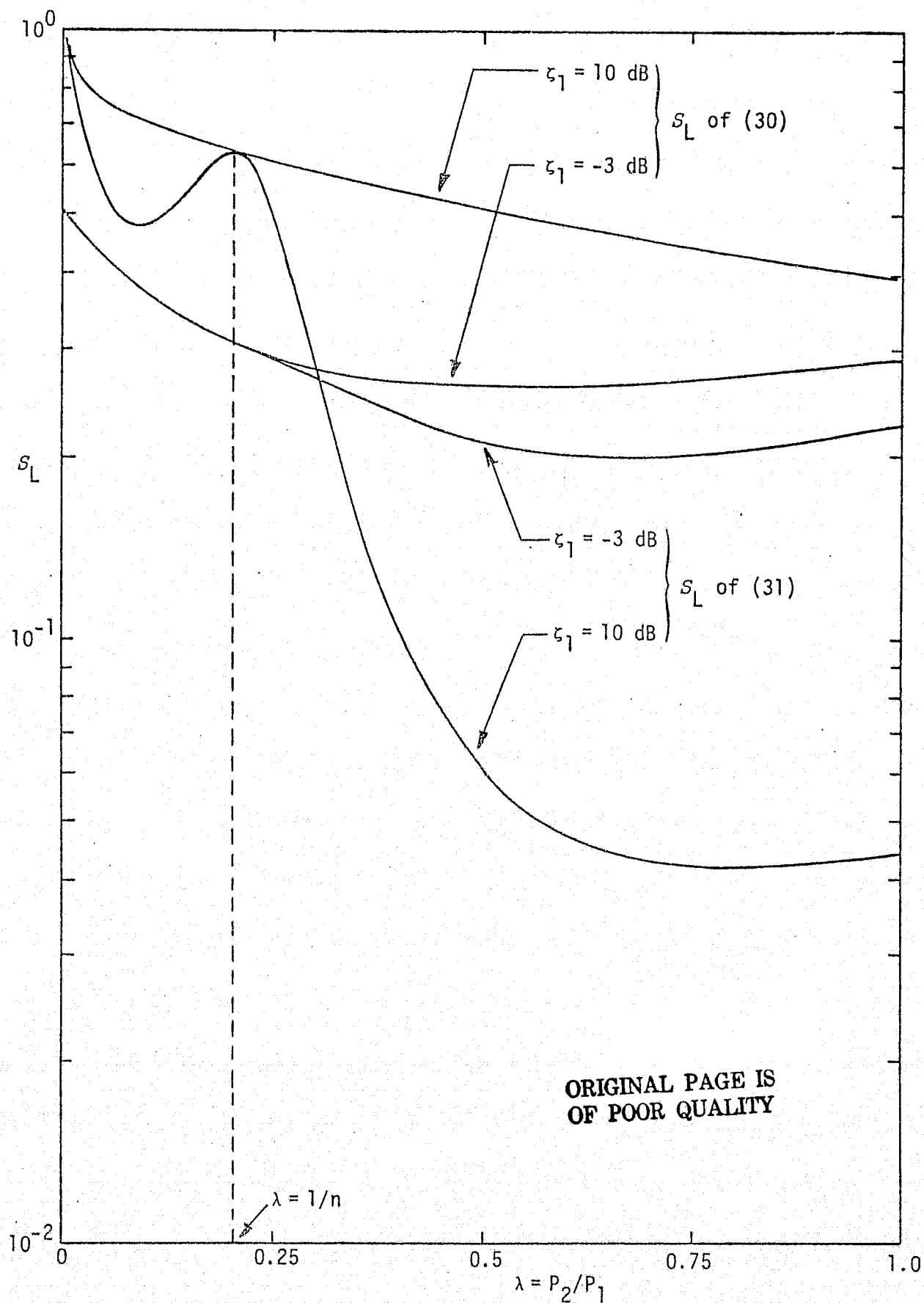


Figure 14. Squaring Loss vs. Power Ratio for Unbalanced QPSK; Two-Channel Costas Loop;  $n = T_2/T_1 = 5$

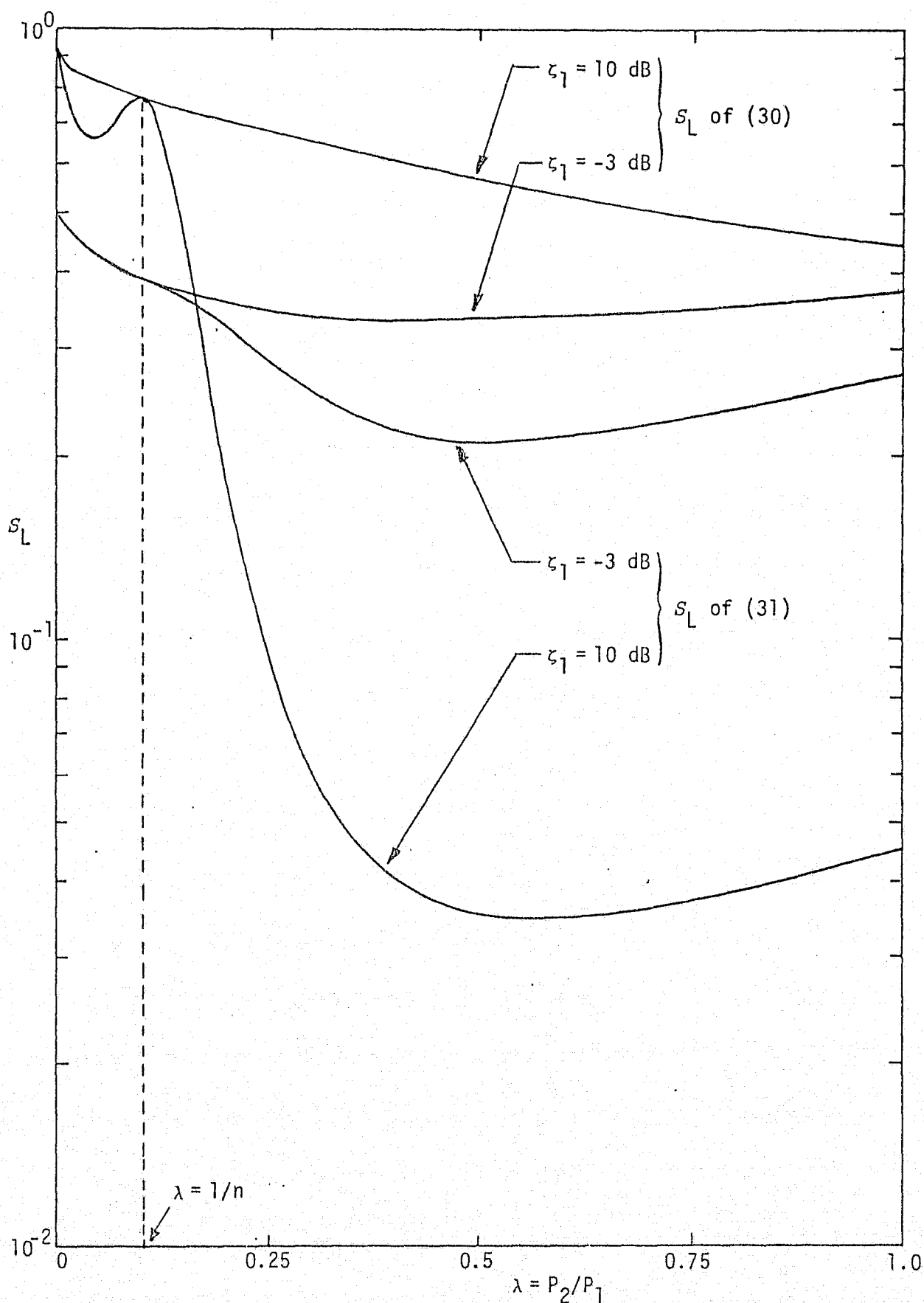


Figure 15. Squaring Loss vs. Power Ratio for Unbalanced QPSK; Two-Channel Costas Loop;  $n = T_2/T_1 = 10$



$$S_L = \frac{(1 - \lambda)^2}{(1 + \lambda) \left[ 1 + \frac{1 + \lambda}{2\zeta_1} + \lambda \left( 1 + \frac{2\zeta_1}{1 + \lambda} \right) \right]}, \quad (32)$$

despite the fact that the channel gain ratios (27) and (29) are not, in general, equal. Furthermore, the result in (32) is also identical to the squaring loss of a conventional (one-channel) Costas loop when used to track unbalanced QPSK with both unequal data rates and unequal powers [8]. In this case, the identical in-phase and quadrature integrate-and-dump arm filters are assumed to be chosen to accommodate the higher data rate modulation.

Several important conclusions can be drawn from the numerical results illustrated in Figures 12 through 15. First, since we have already observed, Figure 12 is representative of the one-channel Costas loop performance for all  $n$  and  $\lambda$ , these curves represent lower bounds on the squaring loss performance of the two-channel configuration. That is, for fixed  $\zeta_1$  and  $\lambda$ , the two-channel Costas loop will exhibit a smaller squaring loss for any data rate ratio  $n$  than the value indicated in Figure 12. This performance comparison between one- and two-channel Costas loops will be made in the next section of this report.

Second, the difference between the true optimum squaring loss [Eq. (30)] and the value given by (31), as in [1], increases with increasing  $n$ . Also, for fixed  $n$ , these differences are much more significant at higher values of total power-to-noise ratio  $\zeta_1$  in the high data rate bandwidth than at the lower values. As an example, for  $n=10$  and  $\zeta_1=10$  dB, we see from Figure 15 that, for equal powers ( $\lambda=1$ ), the squaring loss as given by (30) is 10 dB smaller than that predicted by (31). The same comparison at  $\zeta_1=-3$  dB only shows a 1.4 dB improvement.

Finally, the true optimum squaring loss [Eq. (30)] decreases with increasing  $\zeta_1$ , regardless of the values of  $n$  and  $\lambda$ , except for the case of small  $\lambda$  and  $n=1$ . Using the result of (31) for squaring loss, we observe that, for fixed  $n$ , this "optimum" squaring loss can actually increase with increasing  $\zeta_1$ , depending on the value of  $\lambda$ .

To further illustrate the sensitivity of the two-channel Costas loop squaring loss performance to the particular choice of gain ratio  $K_2/K_1$  or, more important, variations in this ratio about some nominal design value, e.g.,  $\lambda/n$ , Figures 16 through 18 illustrate  $S_L$  versus  $K_2/K_1$  for fixed values of  $n$  and  $\zeta_1$ , with  $\lambda$  as a parameter. In these

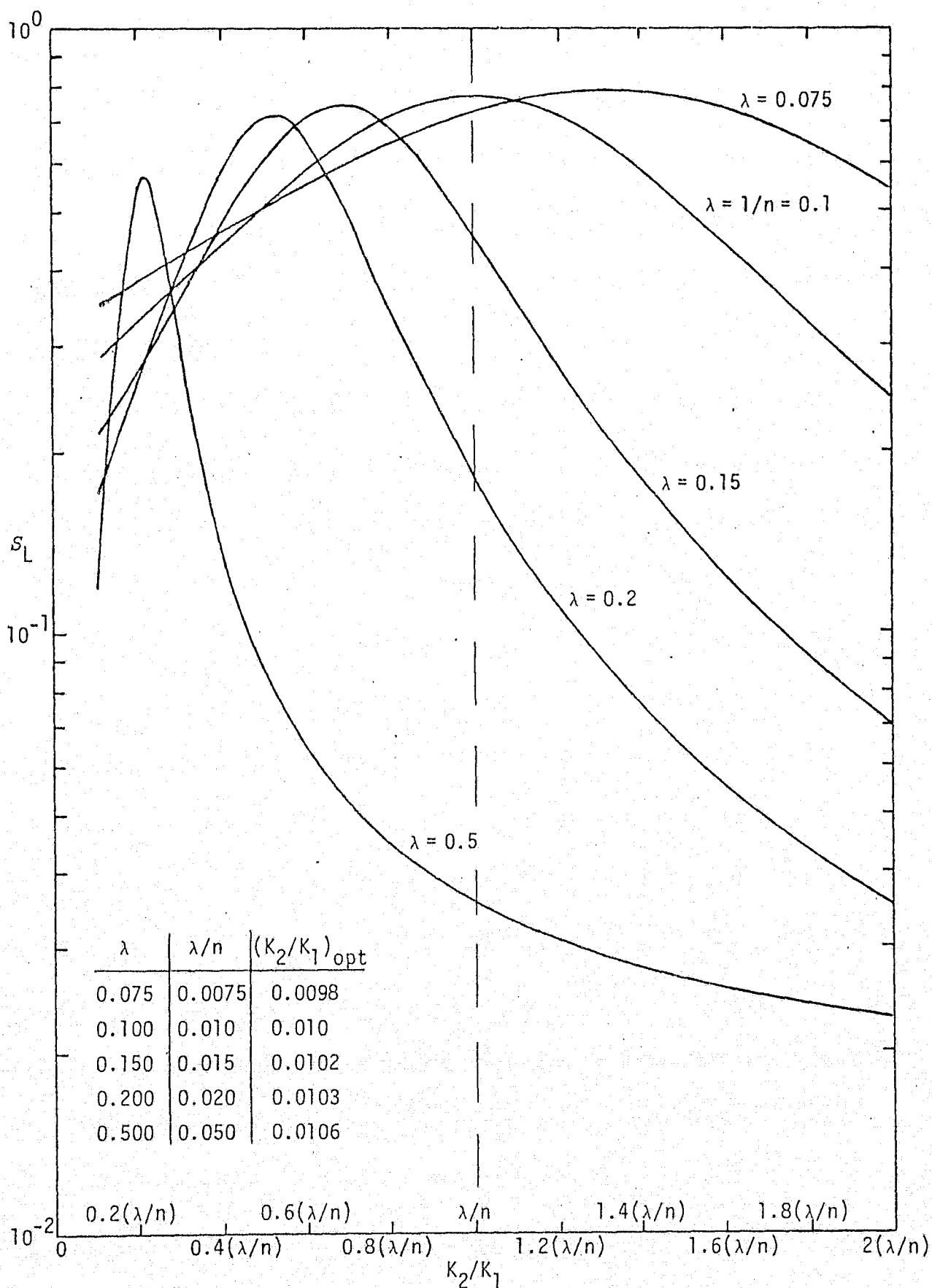


Figure 16. Squaring Loss vs. Channel Gain Ratio for Unbalanced QPSK; Two-Channel Costas Loop;  $\epsilon_1 = 10$  dB,  $n = 10$

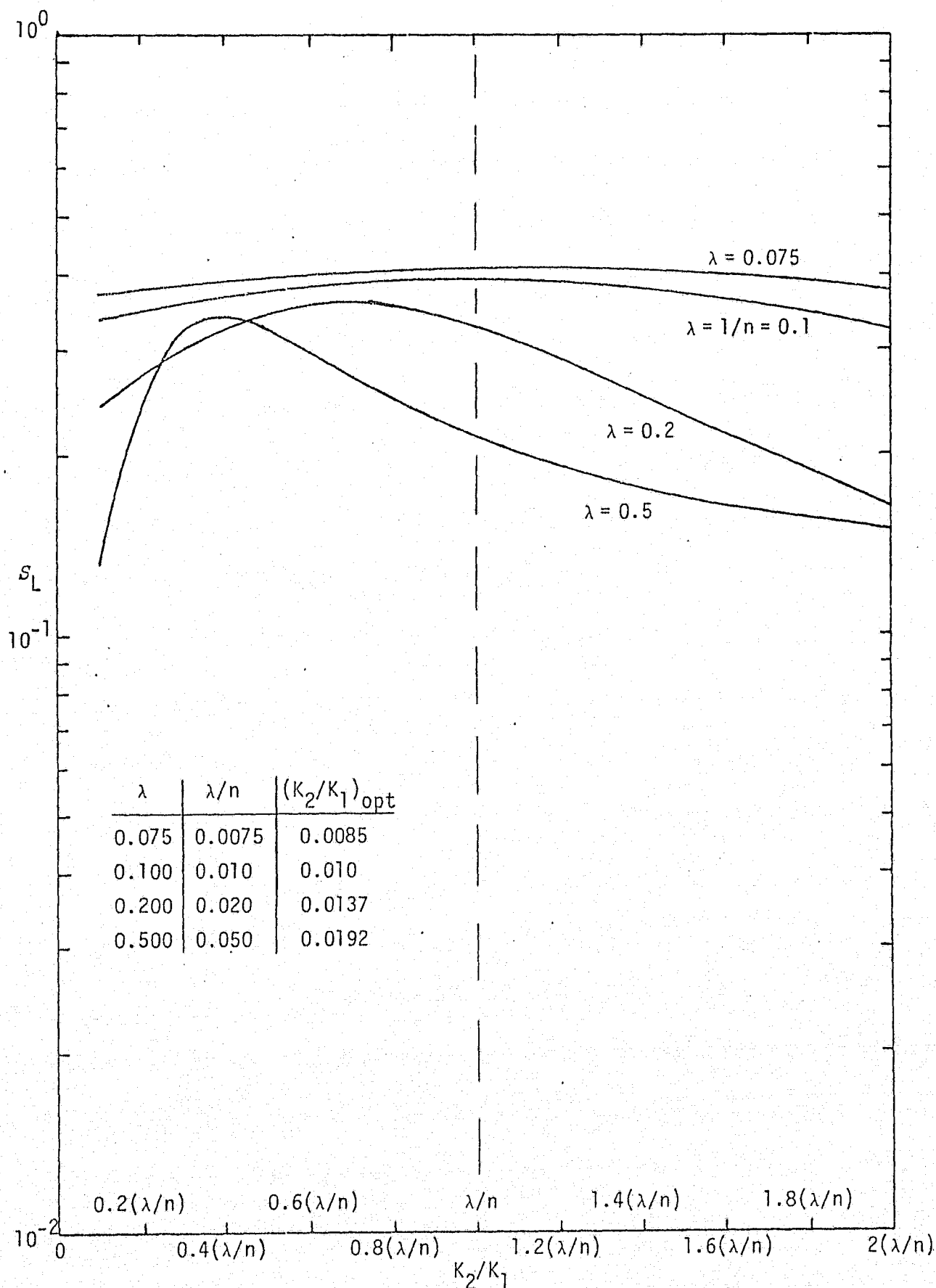


Figure 17. Squaring Loss vs. Channel Gain Ratio for Unbalanced QPSK;  
Two-Channel Costas Loop;  $\epsilon_1 = -3$  dB;  $n = 10$

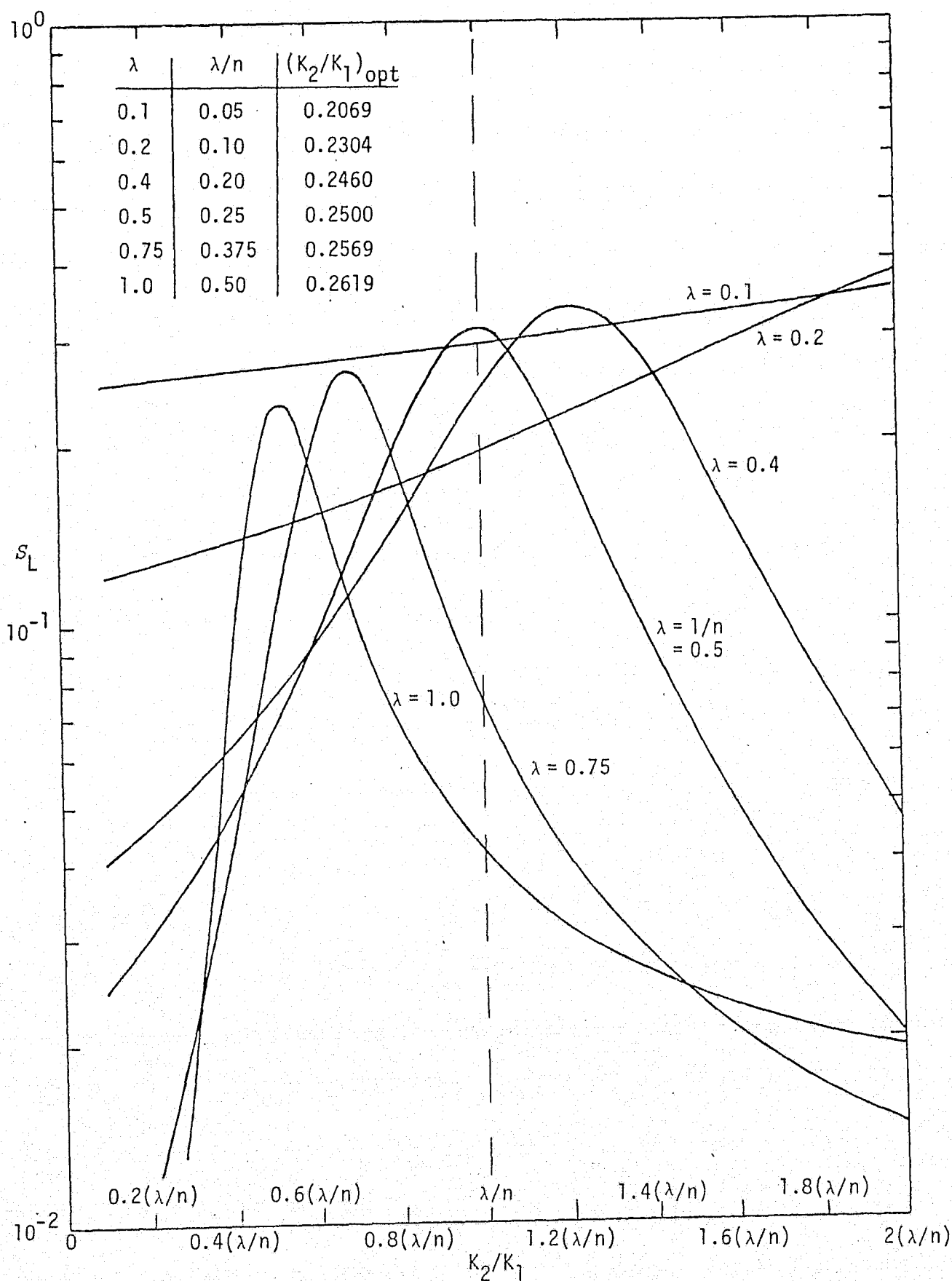


Figure 18. Squaring Loss vs. Channel Gain Ratio for Unbalanced QPSK;  
Two-Channel Costas Loop;  $\zeta_1 = 10$  dB,  $n = 2$

figures,  $K_2/K_1$  is allowed to vary from  $0.1(\lambda/n)$  to  $2(\lambda/n)$  with the optimum values corresponding to (27) clearly indicated by the peaks of the curves. The expression used for plotting these curves is a rewrite of (23) in terms of the definitions of  $n$ ,  $\lambda$ , and  $\zeta_1$ , namely,

$$S_L = \frac{\left[ A'_0 + A'_1 \left( \frac{K_2}{K_1} \right) \right]^2}{(1+\lambda) \left[ B'_0 + B'_1 \left( \frac{K_2}{K_1} \right) + B'_2 \left( \frac{K_2}{K_1} \right)^2 \right]} \quad (33)$$

where

$$\begin{aligned} A'_0 &= 1 - \lambda; & A'_1 &= n(n\lambda - 1) \\ B'_0 &= 1 + \frac{1+\lambda}{2\zeta_1} + \lambda \left( 1 + \frac{2\zeta_1}{1+\lambda} \right) \\ B'_1 &= -2n \left[ 1 + \frac{1+\lambda}{2\zeta_1} + n\lambda \left( 1 + \frac{2\zeta_1}{1+\lambda} \right) \right] \\ B'_2 &= n^3 \left[ 1 + \frac{1+\lambda}{2\zeta_1} + n\lambda \left( 1 + \frac{2\zeta_1}{1+\lambda} \right) \right] \end{aligned} \quad (34)$$

#### A COMPARISON OF THE SQUARING LOSS PERFORMANCE OF ONE- AND TWO-CHANNEL COSTAS LOOPS

We have already mentioned the fact that one-channel (conventional) Costas loops are inferior to two-channel Costas loops when tracking unbalanced QPSK. The squaring loss performance for the one-channel loop (assuming both data modulations are NRZ) was given in (32). To allow a simple comparison with the performance of two-channel loops, we shall assume in the latter case that both channels have equal energy, i.e.,  $P_2T_2 = P_1T_1$  or, equivalently,  $\lambda = 1/n$ . For this case, we have already observed that the value of  $K_2/K_1$  selected by MAP estimation theory considerations is identical to that which minimizes the squaring loss. Thus, from (30) [or (31)], we find that

$$S_L = \frac{(1-\lambda)}{(1+\lambda) \left[ 1 + \frac{1+\lambda}{2\zeta_1} \right]} \quad (35)$$

Taking the ratio of (35) to (32) then gives the improvement in tracking performance of the two-channel Costas loop over the conventional loop.

Letting  $\beta_L$  denote this ratio, we have

$$\beta_L = \frac{S_L|_{2\text{-channel}}}{S_L|_{1\text{-channel}}} = \frac{1 + \frac{1+\lambda}{2\zeta_1} + \lambda \left(1 + \frac{2\zeta_1}{1+\lambda}\right)}{\left(1 + \frac{1+\lambda}{2\zeta_1}\right)(1-\lambda)} \quad (36)$$

Figure 19 illustrates  $\beta_L$  (in dB) versus  $\lambda$  with  $\zeta_1$  (in dB) as a parameter. Clearly, for  $\lambda$  approaching unity, the improvement becomes infinite; however, we recall that, in this limiting case, neither the one-channel nor the two-channel loop is capable of tracking at all, i.e.,  $S_L$  goes to zero for both.

## CONCLUSIONS

In conclusion, we point out that the MAP estimation theory provides good intuition for implementing closed loop tracking configurations for BPSK, QPSK, and UQPSK modulations. In the latter case, however, care must be exercised in selecting the ratio of gains between the two channels of the resulting configuration. In this regard, two options are available, namely, that gain ratio which is motivated by MAP estimation theory and is independent of signal-to-noise ratio, and that ratio which minimizes the loop squaring loss and is dependent on signal-to-noise ratio. The difference in squaring loss between these two choices of gain ratios can be as much as 10 dB for certain values of data rate ratio and power ratio. When the signal energies in the channels are chosen equal, then both gain ratios also become equal and yield identical squaring loss performance. Even in this case, the two-channel Costas loop can considerably outperform the one-channel (conventional) Costas loop. However, neither the conventional nor the two-channel loop of [1] is capable of tracking balanced quadriphase. By an extension of the power series approximation used for the hyperbolic tangent nonlinearity which arises from the MAP estimation approach, we have been able to demonstrate a carrier reconstruction loop for UQPSK which should yield better performance than the above-mentioned two-channel loop as the modulation becomes more balanced; in particular, it acts like a quadriphase Costas loop in the limiting case of balanced QPSK. A detailed analysis of the tracking performance of this loop is the subject of a future report.

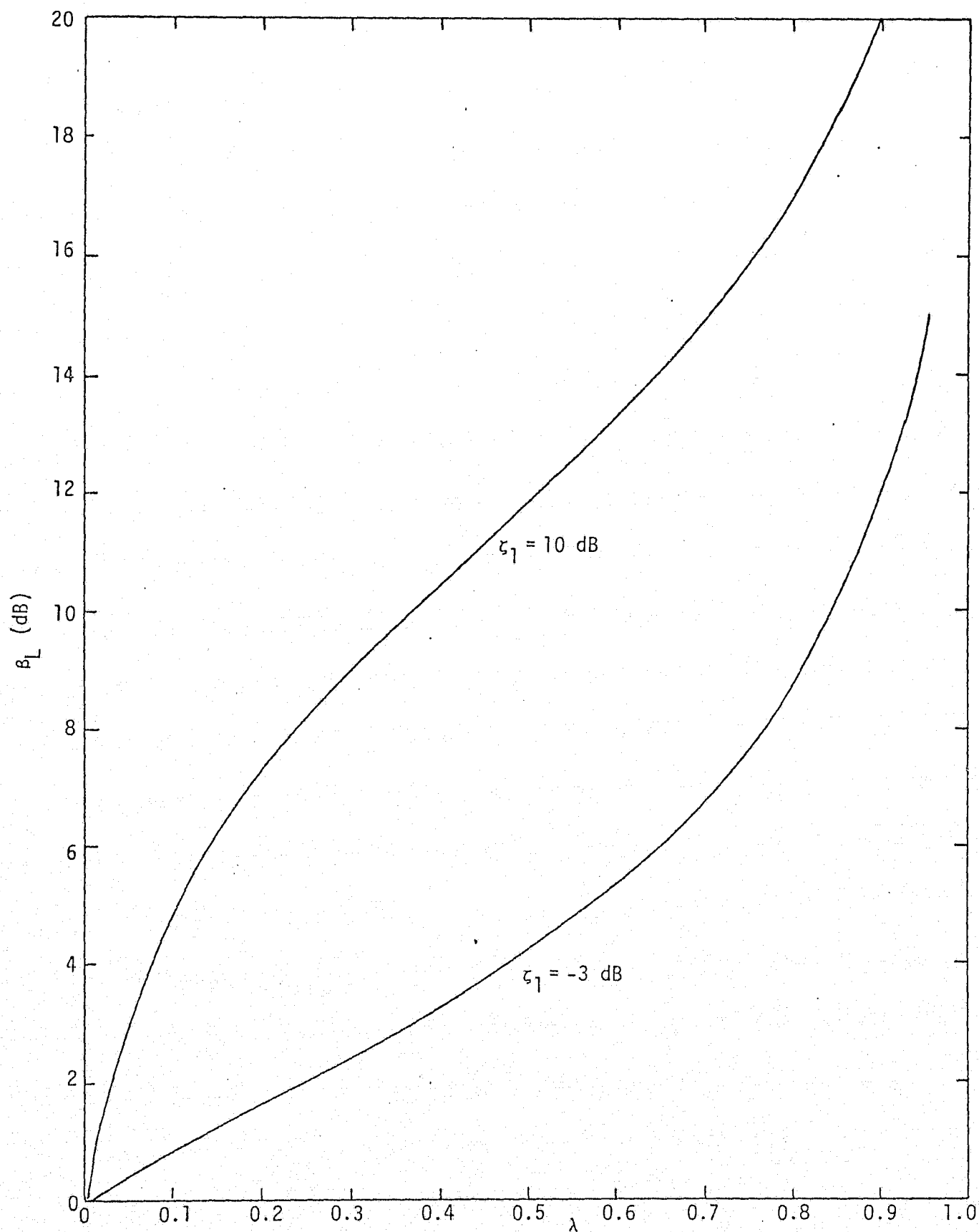


Figure 19. A Comparison of the Squaring Loss Performance of One- and Two-Channel Costas Loops;  $\lambda = 1/n$

## REFERENCES

1. W. R. Braun and W. C. Lindsey. "Carrier Synchronization Techniques for Unbalanced QPSK Signals - Parts I, II," submitted for publication in the IEEE Transactions on Communications. Part I also presented at the 1977 International Conference on Communications. Part II presented at the 1977 National Telecommunications Conference.
2. W. C. Lindsey and M. K. Simon. Telecommunication System Engineering. Englewood Cliffs, N.J.: Prentice-Hall, Inc., 1973, Chapter 2.
3. M. K. Simon and W. C. Lindsey. "Optimum Performance of Suppressed Carrier Receivers with Costas Loop Tracking," IEEE Transactions on Communications, Vol. COM-25, No. 2, February 1977, pp. 215-227.
4. M. K. Simon. "Tracking Performance of Costas Loops with Hard-Limited In-Phase Channel," to appear in the April 1978 issue of the IEEE Transactions on Communications.
5. M. K. Simon. "On the Equivalence in Performance of a Practical Realization of a MAP Estimation Loop for Balanced QPSK and a Conventional Quadriphase Costas Loop," Axiomatix Report No. R7710-6, October 31, 1977.
6. C. L. Weber. "Candidate Receivers for Unbalanced QPSK," Proceedings of the 1976 International Telemetry Conference, Vol. XII, pp. 455-464.
7. M. K. Simon and W. K. Alem. "Tracking Performance of Unbalanced QPSK Demodulators, Part I - Biphase Costas Loop with Passive Arm Filters," Axiomatix Report No. R7707-5, July 29, 1977. Also submitted for publication in the IEEE Transactions on Communications.
8. M. K. Simon. "Tracking Performance of Unbalanced QPSK Demodulators, Part II - Biphase Costas Loop with Active Arm Filters," Axiomatix Report No. R7707-6, July 29, 1977. Also submitted for publication in the IEEE Transactions on Communications.



APPENDIX K

ON THE EQUIVALENCE IN PERFORMANCE OF A PRACTICAL REALIZATION  
OF A MAP ESTIMATION LOOP FOR BALANCED QPSK AND  
A CONVENTIONAL QUADRI PHASE COSTAS LOOP

## APPENDIX K

### ON THE EQUIVALENCE IN PERFORMANCE OF A PRACTICAL REALIZATION OF A MAP ESTIMATION LOOP FOR BALANCED QPSK AND A CONVENTIONAL QUADRI-PHASE COSTAS LOOP

by

Marvin K. Simon

#### 1.0 INTRODUCTION

In Appendix J (also [1]), the author considered the similarities in structure of carrier reconstruction loops motivated by MAP estimation theory for PSK, QPSK, and unbalanced QPSK modulations. In particular, for the balanced QPSK case, it was shown that, by approximating the hyperbolic tangent nonlinearity in the MAP estimation loop by the first two terms in its power series, an interesting practical realization of this loop results which applies at low signal-to-noise ratio (see Figure 1). Indeed, the error signal in this loop is formed by multiplying the error signal and lock detector output signal of a conventional biphase Costas loop. We also note from Figure 1 that such a quadri-phase loop can be constructed using only a pair of quadrature reference signals and a pair of arm filters, as opposed to the four reference signals (separated by  $\pi/4$  radians) and four arm filters required in a conventional quadriphase Costas loop (see Figure 2). The loop of Figure 1 also has the advantage that it can easily be switched from a biphase mode to a quadriphase mode depending on the form of the input modulation. With all this in its favor, the only question remaining is: How does the performance of the loop in Figure 1 compare with that of the conventional quadriphase loop in Figure 2?

In the next section, we shall derive the stochastic differential equation of operation of the loop in Figure 1. Following that, we shall make an analogous derivation for the conventional quadriphase Costas loop. (The result of this derivation is available in [2] if the signal distortion effects of the arm filters are ignored.) Comparing the two results, we shall then reach the conclusion that the two loops are stochastically equivalent, i.e., they have identical stochastic differential equations of operation. Thus, an alternate conclusion is that the conventional quadriphase Costas loop and its previously shown equivalent [2], the fourth power loop, are low signal-to-noise ratio practical realizations of the MAP estimate loop for QPSK.

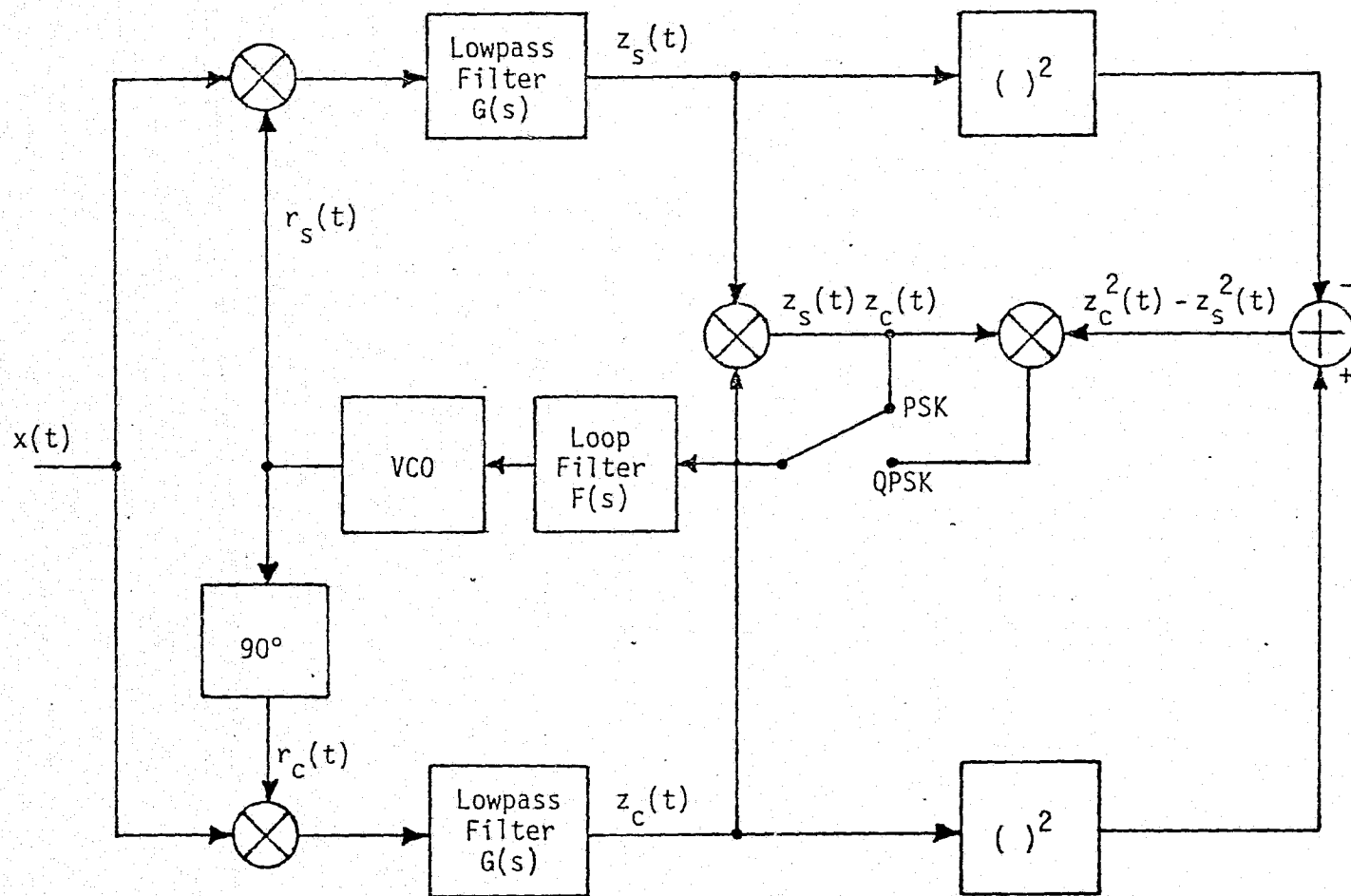


Figure 1. A Practical Realization of the MAP Estimation Loop; Passive Arm Filters, Small SNR

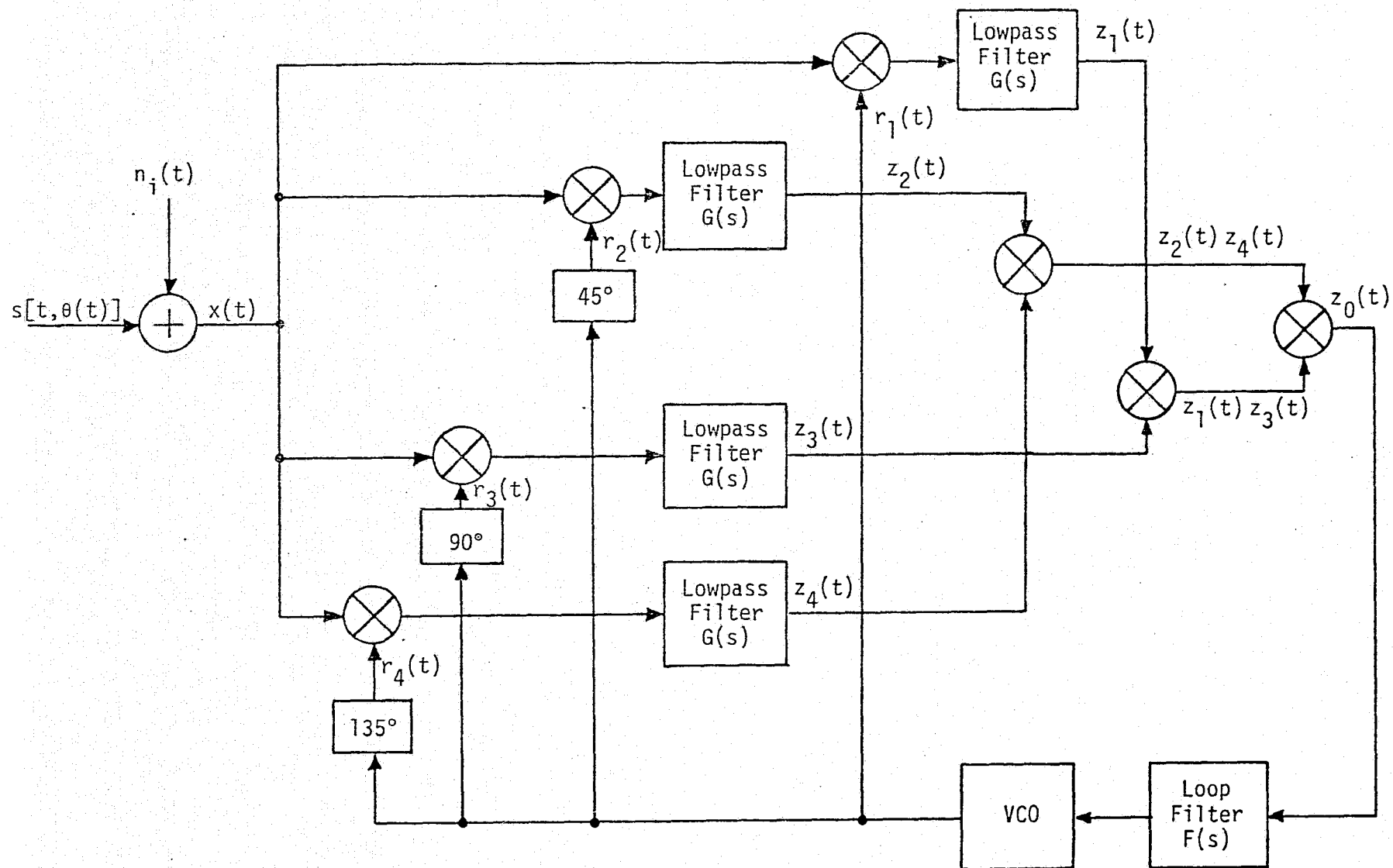


Figure 2. A Conventional Quadriphase Costas Loop

## 2.0 DERIVATION OF THE STOCHASTIC DIFFERENTIAL EQUATION OF OPERATION FOR THE CARRIER RECONSTRUCTION LOOP (Figure 1)

As mentioned in the introduction, the error signal for the quadri-phase loop of Figure 1 is formed from the product of the error signal and lock detector output signal of a biphase Costas loop, namely,  $z_1(t)$  and  $z_2(t)$ , respectively. Since the performance of a biphase Costas loop whose input is an unbalanced quadriphase modulation plus additive Gaussian noise has been previously treated [3], we shall be brief in our presentation here. Assuming then that the input to the loop of Figure 1 is the balanced QPSK modulation

$$x(t) = \sqrt{2P} m_1(t) \cos \phi(t) + \sqrt{2P} m_2(t) \sin \phi(t) + n_i(t), \quad (1)$$

then from [3], letting  $P_1 = P_2 = P$ , we have for the arm filter outputs

$$\begin{aligned} z_s(t) &\triangleq G(p) \epsilon_s(t) = K_1 K_m \left[ \sqrt{P} \hat{m}_2(t) - \hat{N}_s(t) \right] \cos \varphi(t) \\ &\quad - K_1 K_m \left[ \sqrt{P} \hat{m}_1(t) + \hat{N}_c(t) \right] \sin \varphi(t) \\ z_c(t) &\triangleq G(p) \epsilon_c(t) = K_1 K_m \left[ \sqrt{P} \hat{m}_2(t) - \hat{N}_s(t) \right] \sin \varphi(t) \\ &\quad + K_1 K_m \left[ \sqrt{P} \hat{m}_1(t) + \hat{N}_c(t) \right] \cos \varphi(t) \end{aligned} \quad (2)$$

where the "hats" denote filtering of the corresponding signals, e.g.,  $\hat{m}_1(t) \triangleq G(p) m_1(t)$ . Thus, the output of the third multiplier is the dynamic error signal

$$\begin{aligned} z_1(t) &\triangleq z_c(t) z_s(t) \\ &= \frac{K_1^2 K_m^2}{2} \left\{ P \left[ \hat{m}_2^2(t) - \hat{m}_1^2(t) \right] \sin 2\varphi(t) + 2P \hat{m}_1(t) \hat{m}_2(t) \cos 2\varphi(t) \right. \\ &\quad + \left[ \hat{N}_s^2(t) - \hat{N}_c^2(t) - 2\sqrt{P} \hat{m}_2(t) \hat{N}_s(t) - 2\sqrt{P} \hat{m}_1(t) \hat{N}_c(t) \right] \sin 2\varphi(t) \\ &\quad \left. + \left[ 2\sqrt{P} \hat{m}_2(t) \hat{N}_c(t) - 2\sqrt{P} \hat{m}_1(t) \hat{N}_s(t) - 2\hat{N}_c(t) \hat{N}_s(t) \right] \cos 2\varphi(t) \right\}. \end{aligned} \quad (3)$$

Similarly, taking the difference of the squared filter outputs gives

$$\begin{aligned}
z_2(t) &\triangleq z_c^2(t) - z_s^2(t) \\
&= K_1^2 K_m^2 \left\{ -P \left[ \hat{m}_2^2(t) - \hat{m}_1^2(t) \right] \cos 2\varphi(t) + 2P \hat{m}_1(t) \hat{m}_2(t) \sin 2\varphi(t) \right. \\
&\quad - \left[ \hat{N}_s^2(t) - \hat{N}_c^2(t) - 2\sqrt{P} \hat{m}_2(t) \hat{N}_s(t) - 2\sqrt{P} \hat{m}_1(t) \hat{N}_c(t) \right] \cos 2\varphi(t) \\
&\quad \left. + \left[ 2\sqrt{P} \hat{m}_2(t) \hat{N}_c(t) - 2\sqrt{P} \hat{m}_1(t) \hat{N}_s(t) - 2\hat{N}_c(t) \hat{N}_s(t) \right] \sin 2\varphi(t) \right\} \\
&= 2z_1(t) \Big|_{2\varphi(t) \Rightarrow 2\varphi(t) - \frac{\pi}{2}}, \tag{4}
\end{aligned}$$

where the notation " $\Rightarrow$ " means "replaced by." As before (see (9) of [3]), letting

$$\begin{aligned}
v_2[t, 2\varphi(t)] &\triangleq \left[ \hat{N}_s^2(t) - \hat{N}_c^2(t) - 2\sqrt{P} \hat{m}_2(t) \hat{N}_s(t) - 2\sqrt{P} \hat{m}_1(t) \hat{N}_c(t) \right] \sin 2\varphi(t) \\
&\quad + \left[ 2\sqrt{P} \hat{m}_2(t) \hat{N}_c(t) - 2\sqrt{P} \hat{m}_1(t) \hat{N}_s(t) - 2\hat{N}_c(t) \hat{N}_s(t) \right] \cos 2\varphi(t), \tag{5}
\end{aligned}$$

then the product of  $z_1(t)$  and  $z_2(t)$  gives the resulting quadriphase error signal

$$\begin{aligned}
z_0(t) &\triangleq z_1(t) z_2(t) \\
&= \frac{K_1^4 K_m^4}{4} \left\{ P^2 \left[ 6 \hat{m}_1^2(t) \hat{m}_2^2(t) - \hat{m}_1^4(t) - \hat{m}_2^4(t) \right] \sin 4\varphi(t) \right. \\
&\quad + 4P^2 \hat{m}_1(t) \hat{m}_2(t) \left[ \hat{m}_1^2(t) - \hat{m}_2^2(t) \right] \cos 4\varphi(t) \\
&\quad \left. + v_4[t, 4\varphi(t)] \right\}, \tag{6}
\end{aligned}$$

where

$$\begin{aligned}
v_4[t, 4\varphi(t)] &\triangleq 2u_2[t, 2\varphi(t)] v_2[t, 2\varphi(t) - \frac{\pi}{2}] \\
&\quad + 2u_2[t, 2\varphi(t) - \frac{\pi}{2}] v_2[t, 2\varphi(t)] \\
&\quad + 2v_2[t, 2\varphi(t)] v_2[t, 2\varphi(t) - \frac{\pi}{2}] \tag{7}
\end{aligned}$$

and

$$\begin{aligned}
u_2[t, 2\varphi(t)] &= P \left[ \hat{m}_2^2(t) - \hat{m}_1^2(t) \right] \sin 2\varphi(t) \\
&\quad + 2P \hat{m}_1(t) \hat{m}_2(t) \cos 2\varphi(t). \tag{8}
\end{aligned}$$

Substituting (5) and (8) into (7) and simplifying yields

$$v_4[t, 4\varphi(t)] = A_s(t) \sin 4\varphi(t) + A_c(t) \cos 4\varphi(t), \quad (9)$$

where

$$\begin{aligned} A_s(t) = & -\hat{N}_c^4(t) - \hat{N}_s^4(t) + 4\sqrt{P} [\hat{m}_2(t) \hat{N}_s^3(t) - \hat{m}_1(t) \hat{N}_c^3(t)] \\ & + 6\hat{N}_s^2(t) \hat{N}_c^2(t) - 12\sqrt{P} [\hat{m}_2(t) \hat{N}_s(t) \hat{N}_c^2(t) - \hat{m}_1(t) \hat{N}_c(t) \hat{N}_s^2(t)] \\ & + 6\hat{N}_c^2(t) - \hat{N}_s^2(t) [\hat{m}_2^2(t) - \hat{m}_1^2(t)] \\ & - 4P^{3/2} \hat{m}_2(t) \hat{N}_s(t) [3\hat{m}_1^2(t) - \hat{m}_2^2(t)] \\ & + 4P^{3/2} \hat{m}_1(t) \hat{N}_c(t) [3\hat{m}_2^2(t) - \hat{m}_1^2(t)] \\ & - 24P \hat{m}_1(t) \hat{m}_2(t) \hat{N}_s(t) \hat{N}_c(t) \\ A_c(t) = & 4\hat{N}_c(t) \hat{N}_s^3(t) - 4\hat{N}_s(t) \hat{N}_c^3(t) + 4\sqrt{P} [\hat{m}_2(t) \hat{N}_c^3(t) + \hat{m}_1(t) \hat{N}_s^3(t)] \\ & + 12P \hat{m}_1(t) \hat{m}_2(t) [\hat{N}_c^2(t) - \hat{N}_s^2(t)] + 12P \hat{N}_c(t) \hat{N}_s(t) [\hat{m}_2^2(t) - \hat{m}_1^2(t)] \\ & - 12\sqrt{P} [\hat{m}_2(t) \hat{N}_c(t) \hat{N}_s^2(t) + \hat{m}_1(t) \hat{N}_s(t) \hat{N}_c^2(t)] \\ & + 4P^{3/2} \hat{m}_2(t) \hat{N}_c(t) [3\hat{m}_1^2(t) - \hat{m}_2^2(t)] \\ & + 4P^{3/2} \hat{m}_1(t) \hat{N}_s(t) [3\hat{m}_2^2(t) - \hat{m}_1^2(t)]. \end{aligned} \quad (10)$$

The instantaneous frequency of the VCO output is related to  $z_0(t)$  by

$$\frac{d\hat{\phi}(t)}{dt} = K_V [F(p) z_0(t)] + \omega_0 \quad (11)$$

and hence the stochastic equation of loop operation becomes

$$\begin{aligned} \frac{4d\varphi(t)}{dt} = & 4\omega_0 - KF(p) \left\{ P^2 [6\hat{m}_1^2(t) \hat{m}_2^2(t) - \hat{m}_1^4(t) - \hat{m}_2^4(t)] \sin 4\varphi(t) \right. \\ & + 4P^2 \hat{m}_1(t) \hat{m}_2(t) [\hat{m}_1^2(t) - \hat{m}_2^2(t)] \cos 4\varphi(t) \\ & \left. + v_4[t, 4\varphi(t)] \right\}, \end{aligned} \quad (12)$$

where  $K \triangleq K_1^4 K_m^4 K_V$ .

### 3.0 DERIVATION OF THE STOCHASTIC DIFFERENTIAL EQUATION OF OPERATION FOR THE CONVENTIONAL QUADRI PHASE COSTAS LOOP

For the quadriphase Costas loop of Figure 2, the input  $x(t)$  is again given by (1) and the demodulation reference signals  $r_i(t)$ ;  $i=1, 2, 3, 4$ , are respectively

$$r_i(t) = \sqrt{2} K_1 \sin [\hat{\phi}(t) + (i-1) \frac{\pi}{4}]; \quad i=1, 2, 3, 4. \quad (13)$$

Multiplying  $x(t)$  by  $r_i(t)$  and ignoring second harmonic terms gives the four phase detector outputs which, after arm filtering by  $G(s)$ , become

$$\begin{aligned} z_i(t) &= K_1 K_m [\sqrt{P} \hat{m}_2(t) - \hat{N}_s(t)] \cos [\varphi(t) - (i-1) \frac{\pi}{4}] \\ &\quad - K_1 K_m [\sqrt{P} \hat{m}_1(t) + \hat{N}_c(t)] \sin [\varphi(t) - (i-1) \frac{\pi}{4}]; \quad i=1, 2, 3, 4 \\ &\triangleq K_1 K_m \left\{ a_c(t) \cos [\varphi(t) - (i-1) \frac{\pi}{4}] - a_s(t) \sin [\varphi(t) - (i-1) \frac{\pi}{4}] \right\}. \end{aligned} \quad (14)$$

Multiplying  $z_1(t)$  and  $z_3(t)$  gives

$$z_1(t) z_3(t) = K_1^2 K_m^2 \left\{ [a_c^2(t) - a_s^2(t)] \frac{\sin 2\varphi(t)}{2} + a_c(t) a_s(t) \cos 2\varphi(t) \right\}. \quad (15)$$

Similarly,

$$\begin{aligned} z_2(t) z_4(t) &= K_1^2 K_m^2 \left\{ [a_c^2(t) - a_s^2(t)] \frac{\sin [2(\varphi(t) - \frac{\pi}{4})]}{2} \right. \\ &\quad \left. + a_c(t) a_s(t) \cos [2(\varphi(t) - \frac{\pi}{4})] \right\} \\ &= K_1^2 K_m^2 \left\{ -[a_c^2(t) - a_s^2(t)] \frac{\cos 2\varphi(t)}{2} + a_c(t) a_s(t) \sin 2\varphi(t) \right\}. \end{aligned} \quad (16)$$

Thus, the quadriphase error signal  $z_0(t)$  is obtained by multiplying (15) and (16), namely,

$$\begin{aligned} z_0(t) &\triangleq \prod_{i=1}^4 z_i(t) = \frac{K_1^4 K_m^4}{2} \left\{ -[a_c^2(t) - a_s^2(t)]^2 + 4 a_c^2(t) a_s^2(t) \right\} \frac{\sin 4\varphi(t)}{4} \\ &\quad + \frac{K_1^4 K_m^4}{2} a_c(t) a_s(t) [a_c^2(t) - a_s^2(t)] \cos 4\varphi(t) \end{aligned} \quad (17a)$$



or

$$z_0(t) = \frac{-K_1^4 K_m^4}{8} \sum_{\ell=0,2,4} (-1)^{\ell/2} {}_4C_{\ell} a_c^{\ell}(t) a_s^{4-\ell}(t) \sin 4\varphi(t) + \frac{K_1^4 K_m^4}{8} \sum_{\ell=1,3} (-1)^{(\ell-1)/2} {}_4C_{\ell} a_c^{\ell}(t) a_s^{4-\ell}(t) \cos 4\varphi(t), \quad (17b)$$

where  ${}_nC_k$  is the combinatorial coefficient defined by

$${}_nC_k = \frac{n!}{k!(n-k)!}. \quad (18)$$

From the defining expressions for  $a_c(t)$  and  $a_s(t)$  in (14), we get that

$$a_c^{\ell}(t) = \sum_{m=0}^{\ell} (-1)^{\ell-m} {}_{\ell}C_m (\sqrt{P} \hat{m}_2(t))^m (\hat{N}_s(t))^{\ell-m} \\ a_s^{4-\ell}(t) = \sum_{k=0}^{4-\ell} {}_{4-\ell}C_k (\sqrt{P} \hat{m}_1(t))^k (\hat{N}_c(t))^{4-\ell-k}. \quad (19)$$

Substituting (19) in (17) gives the final results for  $z_0(t)$ , namely,

$$z_0(t) = \frac{-K_1^4 K_m^4}{8} \left\{ \sum_{\ell=0,2,4} (-1)^{\ell/2} {}_4C_{\ell} \sum_{m=0}^{\ell} \sum_{k=0}^{4-\ell} (-1)^{\ell-m} {}_{\ell}C_m {}_{4-\ell}C_k P^{(m+k)/2} \right. \\ \left. \times \hat{m}_2^m(t) \hat{m}_1^k(t) \hat{N}_s^{\ell-m}(t) \hat{N}_c^{4-\ell-k}(t) \right\} \sin 4\varphi(t) \\ + \frac{K_1^4 K_m^4}{8} \left\{ \sum_{\ell=1,3} (-1)^{(\ell-1)/2} {}_4C_{\ell} \sum_{m=0}^{\ell} \sum_{k=0}^{4-\ell} (-1)^{\ell-m} {}_{\ell}C_m {}_{4-\ell}C_k P^{(m+k)/2} \right. \\ \left. \times \hat{m}_2^m(t) \hat{m}_1^k(t) \hat{N}_s^{\ell-m}(t) \hat{N}_c^{4-\ell-k}(t) \right\} \cos 4\varphi(t). \quad (20)$$

The terms which are independent of the noise components  $\hat{N}_c(t)$  and  $\hat{N}_s(t)$  are obtained by letting  $\ell = m$  and  $k = 4 - \ell = 4 - m$ . Thus,

$$z_0(t) \Big|_{\substack{\ell=m \\ k=4-m}} = \frac{-K_1^4 K_m^4}{8} \left\{ P^2 \left[ \hat{m}_1^4(t) + \hat{m}_2^4(t) - 6 \hat{m}_1^2(t) \hat{m}_2^2(t) \right] \sin 4\varphi(t) \right. \\ \left. - 4 P^2 \hat{m}_1(t) \hat{m}_2(t) \left[ \hat{m}_1^2(t) - \hat{m}_2^2(t) \right] \cos 4\varphi(t) \right\}. \quad (21)$$

Comparing (21) with the first two terms of (6), we see that, except for a factor of two in gain, the two are identical. Furthermore, evaluating

the remaining terms in the summations in (20), we get the identical signal  $\times$  noise and noise  $\times$  noise terms as in (9) combined with (10), except again for the same factor of two in gain. (Carrying out the algebra to prove this identity is left to the reader.) Thus,

$$z_0(t) = \frac{K_1^4 K_m^4}{8} \left\{ P^2 \left[ 6 \hat{m}_1^2(t) \hat{m}_2^2(t) - \hat{m}_1^4(t) - \hat{m}_2^4(t) \right] \sin 4\varphi(t) + 4 P^2 \hat{m}_1(t) \hat{m}_2(t) \left[ \hat{m}_1^2(t) - \hat{m}_2^2(t) \right] \cos 4\varphi(t) + v_4[t, 4\varphi(t)] \right\} \quad (22)$$

and letting  $K$  now equal  $K_1^4 K_m^4 K_V/2$ , we get the identical stochastic equation of loop operation as in (12).

#### 4.0 CONCLUSIONS

We conclude by pointing out that, while we have indeed shown that the low signal-to-noise ratio realization of the MAP estimation loop for QPSK is stochastically equivalent to the conventional quadriphase Costas loop, we have not attempted to give the tracking performance of these loops nor compare it to that of a biphasic Costas loop. Determining the tracking performance of the quadriphase loop of Figure 1 (or Figure 2), taking into account the bandlimiting effects of the arm filters, is considerably more complicated than the equivalent analysis for the biphasic loop. The principle reason for this stems from the fact that the signal  $\times$  signal, signal  $\times$  noise, and noise  $\times$  noise terms now require evaluation of fourth order moments of the filtered signal and noise components. While indeed such evaluation is possible, the resulting expressions and necessary algebra to arrive at them are quite complicated, even for the simplest case of a single-pole (RC) arm filter. Nevertheless, these results, upon completion by the author, will be presented in a future report.

## REFERENCES

1. M. K. Simon. "Practical Design Considerations Associated with Optimum Carrier Reconstruction Techniques for Unbalanced QPSK," Axiomatix Report No. R7709-5, September 30, 1977.
2. W. C. Lindsey and M. K. Simon. Telecommunication Systems Engineering. Englewood Cliffs, N.J.: Prentice-Hall, Inc., 1973, Chapter 2.
3. M. K. Simon and W. K. Alem. "Tracking Performance of Unbalanced QPSK Demodulators: Part I - Biphase Costas Loop with Passive Arm Filters," Axiomatix Report No. R7707-5, July 29, 1977.

APPENDIX L

THE EFFECTS OF RESIDUAL CARRIER ON COSTAS LOOP PERFORMANCE  
AS APPLIED TO THE SHUTTLE S-BAND UPLINK

## APPENDIX L

### THE EFFECTS OF RESIDUAL CARRIER ON COSTAS LOOP PERFORMANCE AS APPLIED TO THE SHUTTLE S-BAND UPLINK

by

Marvin K. Simon

#### 1.0 INTRODUCTION

Traditionally, a Costas loop is intended for use in receivers which must reconstruct a carrier reference from an input signal whose carrier component is totally suppressed, e.g., a biphase modulated carrier. In certain applications, however, the Costas loop is called upon to accurately track a signal whose carrier component is not completely suppressed. One such application occurs on the Shuttle S-band uplink during the time when both data and a ranging subcarrier are linearly modulated on the same carrier and the data modulation index is not  $\pi/2$ . A simple block diagram which, for the sake of analysis, characterizes this situation is illustrated in Figure 1. Included in this illustration are the means by which the data and the ranging subcarrier are extracted using the in-phase demodulation reference generated by the loop.

Several key questions arise relative to the performance of the Costas loop under these unorthodox conditions:

1. Is the loop capable of successfully tracking the input independent of the value of the data modulation index?
2. Is it possible to extract the ranging subcarrier as shown if the data modulation is removed?
3. What is the additional threshold power-to-noise ratio required to operate the loop in the PM (ranging and data) mode as compared to the PSK (data only) mode?
4. What tradeoffs exist between power in the ranging channel and loop threshold performance as a function of the data and ranging modulation indices?

This appendix attempts to answer these and other questions related to the performance of Costas loops in the presence of residual carrier by establishing a theory for such performance as a function of the key system parameters. For example, we shall first demonstrate that there exists a critical data modulation index below which the loop will not operate, regardless of the value of signal-to-noise ratio.

ORIGINAL PAGE IS  
OF POOR QUALITY

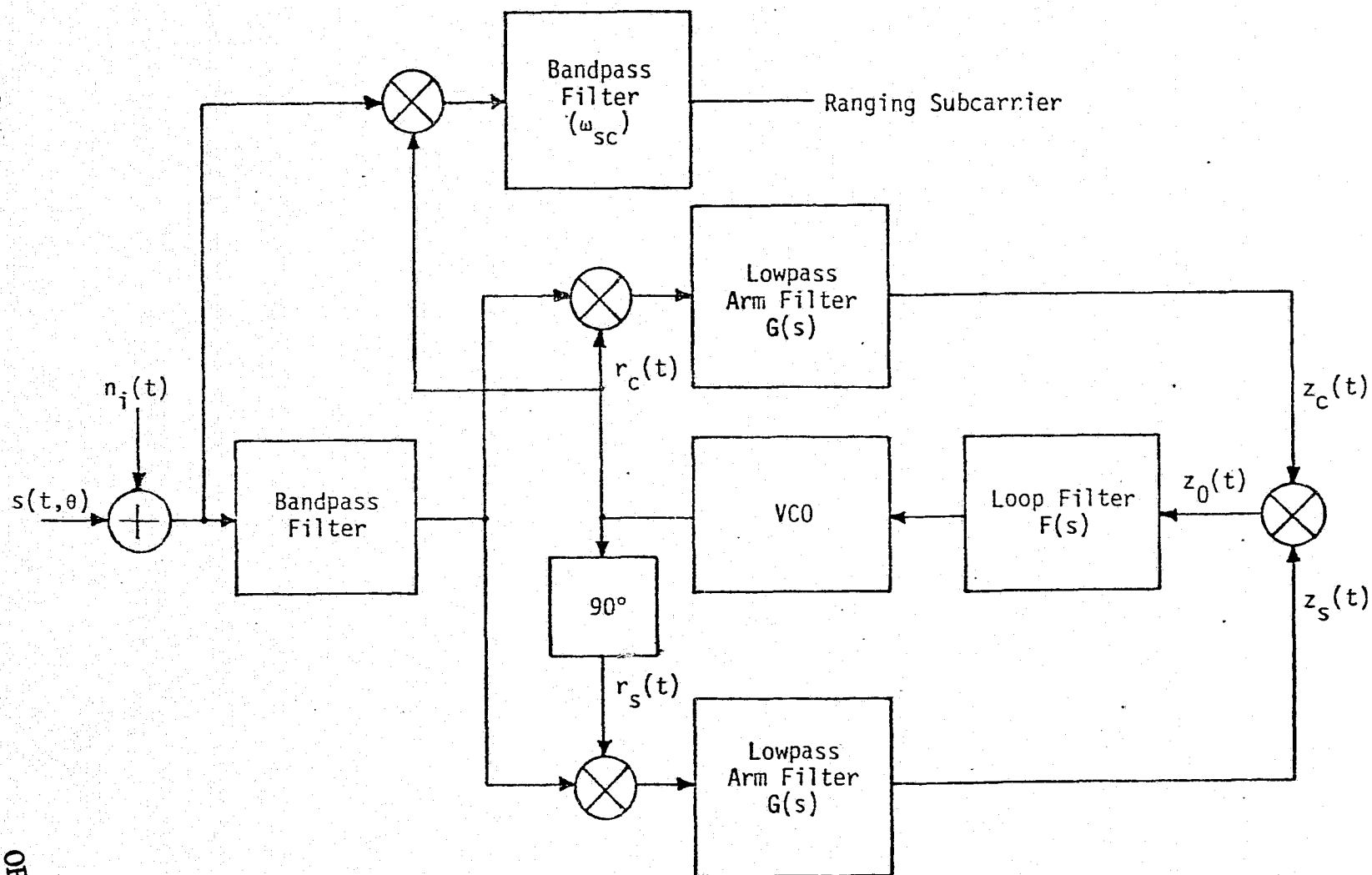


Figure 1. Costas Loop and Ranging Demodulator

## 2.0 SYSTEM MODEL

Consider the Costas demodulator illustrated in Figure 1 whose input signal is of the form

$$s(t, \theta) = \sqrt{2P} \sin [\omega_0 t + \beta_d d(t) + \beta_s \sin (\omega_{sc} t + \theta_r(t)) + \theta], \quad (1)$$

where  $P$  is the total received power,  $\omega_0$  is the carrier radian frequency and  $\theta$  the corresponding input phase to be estimated,  $\beta_d$  is the data modulation index with  $d(t)$  the data waveform, and  $\beta_s$  is the ranging subcarrier modulation index with  $\omega_{sc}$  the radian subcarrier frequency and  $\theta_r(t)$  the tone ranging modulation. Using simple trigonometry,  $s(t, \theta)$  of (1) may be decomposed into its carrier, ranging, and data components, namely,

$$\begin{aligned} s(t, \theta) = & \sqrt{2P} \sin [\omega_0 t + \beta_d d(t) + \theta] \cos [\beta_s \sin (\omega_{sc} t + \theta_r(t))] \\ & + \sqrt{2P} \cos [\omega_0 t + \beta_d d(t) + \theta] \sin [\beta_s \sin (\omega_{sc} t + \theta_r(t))] \end{aligned} \quad (2)$$

or, making use of the relations,

$$\begin{aligned} \cos [\beta \sin x] &= \sum_{n=0}^{\infty} \epsilon_n J_{2n}(\beta) \cos 2n x; \quad \epsilon_n = \begin{cases} 1; & n=0 \\ 2; & n>0 \end{cases} \\ \sin [\beta \sin x] &= 2 \sum_{n=0}^{\infty} J_{2n+1}(\beta) \sin (2n+1) x \end{aligned} \quad (3)$$

where  $J_n(x)$  is the  $n$ th order Bessel function of the first kind, then

$$\begin{aligned} s(t, \theta) = & \sqrt{2P} \cos \beta_d \sin (\omega_0 t + \theta) \left\{ \sum_{n=0}^{\infty} \epsilon_n J_{2n}(\beta_s) \cos [2n (\omega_{sc} t + \theta_r(t))] \right\} \\ & + \sqrt{2P} \sin \beta_d d(t) \cos (\omega_0 t + \theta) \left\{ \sum_{n=0}^{\infty} \epsilon_n J_{2n}(\beta_s) \cos [2n (\omega_{sc} t + \theta_r(t))] \right\} \\ & + \sqrt{2P} \cos \beta_d \cos (\omega_0 t + \theta) \left\{ 2 \sum_{n=0}^{\infty} J_{2n+1}(\beta_s) \sin [(2n+1) (\omega_{sc} t + \theta_r(t))] \right\} \\ & - \sqrt{2P} \sin \beta_d d(t) \sin (\omega_0 t + \theta) \left\{ 2 \sum_{n=0}^{\infty} J_{2n+1}(\beta_s) \sin [(2n+1) (\omega_{sc} t + \theta_r(t))] \right\} \end{aligned} \quad (4)$$

The additive channel noise  $n_i(t)$  can be expressed in the form of a narrowband process about the frequency of the observed data, namely,

$$n_i(t) = \sqrt{2} \{N_c(t) \cos(\omega_0 t + \theta) - N_s(t) \sin(\omega_0 t + \theta)\}, \quad (5)$$

where  $N_c(t)$  and  $N_s(t)$  are approximately statistically independent, stationary, white Gaussian noise processes with single-sided noise spectral density  $N_0$  w/Hz and single-sided bandwidth  $B_H < \omega_0/2\pi$ .

The input signal plus noise is bandpass filtered where the filter bandwidth is narrow enough to exclude the ranging subcarrier and its harmonics. Thus, demodulating the bandpass filtered signal plus noise by the quadrature reference signals

$$\begin{aligned} r_c(t) &= \sqrt{2} K_1 \cos(\omega_0 t + \hat{\theta}) \\ r_s(t) &= -\sqrt{2} K_1 \sin(\omega_0 t + \hat{\theta}) \end{aligned} \quad (6)$$

gives the corresponding phase detector outputs (ignoring second harmonic terms)

$$\begin{aligned} \epsilon_c(t) &= K_1 K_m \sqrt{P} \cos \beta_d \left\{ \sum_{n=0}^{\infty} \epsilon_n J_{2n}(\beta_s) \cos[2n(\omega_{sc} t + \theta_r(t))] \right\} \sin \varphi \\ &\quad + K_1 K_m \sqrt{P} \sin \beta_d d(t) \left\{ \sum_{n=0}^{\infty} \epsilon_n J_{2n}(\beta_s) \cos[2n(\omega_{sc} t + \theta_r(t))] \right\} \cos \varphi \\ &\quad + K_1 K_m [N_c(t) \cos \varphi - N_s(t) \sin \varphi] \\ \epsilon_s(t) &= -K_1 K_m \sqrt{P} \cos \beta_d \left\{ \sum_{n=0}^{\infty} \epsilon_n J_{2n}(\beta_s) \cos[2n(\omega_{sc} t + \theta_r(t))] \right\} \cos \varphi \\ &\quad + K_1 K_m \sqrt{P} \sin \beta_d d(t) \left\{ \sum_{n=0}^{\infty} \epsilon_n J_{2n}(\beta_s) \cos[2n(\omega_{sc} t + \theta_r(t))] \right\} \sin \varphi \\ &\quad + K_1 K_m [N_c(t) \sin \varphi + N_s(t) \cos \varphi], \end{aligned} \quad (7)$$

where  $K_m$  is the phase detector gain and  $\varphi \triangleq \theta - \hat{\theta}$  is the loop phase error. Assuming that  $\omega_{sc}/2\pi \gg B_i/2$ , where  $B_i$  is the two-sided arm filter bandwidth, i.e.,

$$B_i \triangleq \int_{-\infty}^{\infty} |G(j 2\pi f)|^2 df, \quad (8)$$

ORIGINAL PAGE IS  
OF POOR QUALITY



then only the  $n=0$  term in the summations of (7) pass through these filters. Thus, the arm filter outputs are simply

$$\begin{aligned}
 z_c(t) &= K_1 K_m \left[ \sqrt{P} \cos \beta_d J_0(\beta_s) - \hat{N}_s(t) \right] \sin \varphi \\
 &\quad + K_1 K_m \left[ \sqrt{P} \sin \beta_d \hat{d}(t) J_0(\beta_s) + \hat{N}_c(t) \right] \cos \varphi \\
 z_s(t) &= -K_1 K_m \left[ \sqrt{P} \cos \beta_d J_0(\beta_s) - \hat{N}_s(t) \right] \cos \varphi \\
 &\quad + K_1 K_m \left[ \sqrt{P} \sin \beta_d \hat{d}(t) J_0(\beta_s) + \hat{N}_c(t) \right] \sin \varphi
 \end{aligned} \tag{9}$$

where the "hats" denote filtering of the corresponding signals by the arm filters, e.g.,  $\hat{d}(t) \triangleq G(p) d(t)$ . Thus, the output of the third multiplier is the dynamic error signal

$$\begin{aligned}
 z_0(t) &\triangleq z_c(t) z_s(t) \\
 &= \frac{K_1^2 K_m^2}{2} \left\{ J_0^2(\beta_s) P [\hat{d}^2(t) \sin^2 \beta_d - \cos^2 \beta_d] \sin 2\varphi \right. \\
 &\quad \left. - J_0^2(\beta_s) P \sin 2\beta_d \hat{d}(t) \cos 2\varphi + v_2[t, 2\varphi] \right\},
 \end{aligned} \tag{10}$$

where

$$\begin{aligned}
 v_2(t, 2\varphi) &\triangleq \left[ \hat{N}_c^2(t) - \hat{N}_s^2(t) + 2\sqrt{P} \cos \beta_d J_0(\beta_s) \hat{N}_s(t) \right. \\
 &\quad \left. + 2\sqrt{P} \sin \beta_d \hat{d}(t) J_0(\beta_s) \hat{N}_c(t) \right] \sin 2\varphi \\
 &\quad - \left[ 2\sqrt{P} \cos \beta_d J_0(\beta_s) \hat{N}_c(t) - 2\sqrt{P} \sin \beta_d \hat{d}(t) J_0(\beta_s) \hat{N}_s(t) \right. \\
 &\quad \left. - 2\hat{N}_c(t) \hat{N}_s(t) \right] \cos 2\varphi.
 \end{aligned} \tag{11}$$

The instantaneous frequency (relative to  $\omega_0$ ) of the VCO output is related to  $z_0(t)$  by

$$\frac{d\hat{\theta}}{dt} = K_V [F(p) z_0(t)]. \tag{12}$$

Thus, the stochastic equation of operation of the loop becomes

$$\begin{aligned}
\frac{2d\varphi}{dt} = & -KF(p) \left\{ J_0^2(\beta_s) P \left[ D_m \sin^2 \beta_d - \cos^2 \beta_d \right] \sin 2\varphi \right. \\
& + J_0^2(\beta_s) P \sin^2 \beta_d \underbrace{[\hat{d}^2(t) - D_m]}_{\substack{\text{self-noise} \\ \text{of data}}} \sin 2\varphi \\
& \left. - J_0^2(\beta_s) P \sin 2\beta_d \hat{d}(t) \cos 2\varphi + v_2(t, 2\varphi) \right\}, \quad (13)
\end{aligned}$$

where

$$D_m \triangleq \langle \hat{d}^2(t) \rangle = \int_{-\infty}^{\infty} S_m(f) |G(j 2\pi f)|^2 df \quad (14)$$

represents the power in the data modulation at the arm filter output with  $S_m(f)$  denoting the power spectral density of the unfiltered data  $d(t)$ , and  $K \triangleq K_1^2 K_m^2 K_V$ .

The first term in the braces of (13) is the loop S-curve, while the remaining terms are all zero mean and thus contribute to the total noise perturbing the loop. Note that, when  $\cos^2 \beta_d = D_m \sin^2 \beta_d$ , or, equivalently,

$$\cot^2 \beta_d = D_m, \quad (15)$$

the loop S-curve vanishes and thus the loop will not lock at any loop signal-to-noise ratio. For values of  $\beta_d$  less than the critical value satisfying (15), the loop locks at  $\varphi = \pm (2n+1) \pi/2$ ,  $n=0,1,2,\dots$ . For values of  $\beta_d$  greater than this critical value, the loop locks at  $\varphi = \pm n\pi$ ,  $n=0,1,2,\dots$ .

As a specific illustration of (15), consider the case of Manchester coded data (all of the S-band uplink low and high data rate tracking modes) and single-pole Butterworth arm filters (typical of Costas loop in network transponder). Then the mean-squared filtered data power,  $D_m$ , is given by [1]

$$D_m = 1 - \frac{3 - 4 \exp(-B_i/R_s) + \exp(-2B_i/R_s)}{2B_i/R_s} \quad (16)$$

where  $R_s = 1/T$  is the data (coded or uncoded) symbol rate. For a single-pole Butterworth filter with transfer function

$$|G(j2\pi f)|^2 = \frac{1}{1 + (f/f_c)^2} \quad (17)$$

and 3 dB cutoff frequency  $f_c$ , the noise bandwidth  $B_i$  is given by

$$B_i = \pi f_c. \quad (18)$$

Using (15), (16) and (18), Table 1 tabulates the critical values of data modulation index for the various data symbol rates of interest on the S-band uplink.

Table 1

$R_s$	$f_c$	$B_i/R_s$	$D_m$	$(\beta_d)_{crit}$
32 kbps (Low Data Rate Uncoded)	134 kHz	13.155	0.886	0.8157 rad
96 kbps (Low Data Rate Coded)	134 kHz	4.385	0.6636	0.8872 rad
72 kbps (High Data Rate Uncoded)	308 kHz	13.44	0.8884	0.815 rad
216 kbps (High Data Rate Coded)	308 kHz	4.48	0.670	0.8848 rad

### 3.0 STATISTICAL CHARACTERIZATION OF THE EQUIVALENT ADDITIVE NOISE

As mentioned above, the equivalent additive noise terms in (13) all have zero mean. Furthermore, each has a continuous power spectral density component. Since the bandwidth of these processes is very wide with respect to the loop bandwidth, it is sufficient to find for each one only the power spectral density at the origin which, when multiplied by the loop bandwidth, gives the contribution to the total noise power of that component.

In previous analyses of this type [1,2], it was shown that, for cases of practical interest, the effect of the self-noise of the data modulation on loop tracking performance was negligible. Making this same assumption here, and further assuming that  $\varphi = 0$  (high loop signal-to-noise ratio), the equivalent noise of (13) reduces to

$$\begin{aligned} n_e(t) &= -J_0^2(\beta_s) P \sin 2\beta_d \hat{d}(t) + v_2(t,0) \\ &= -J_0^2(\beta_s) P \sin 2\beta_d \hat{d}(t) - 2\sqrt{P} \cos \beta_d J_0(\beta_s) \hat{N}_c(t) \\ &\quad + 2\sqrt{P} \sin \beta_d \hat{d}(t) J_0(\beta_s) \hat{N}_s(t) + 2\hat{N}_c(t) \hat{N}_s(t). \end{aligned} \quad (19)$$

The autocorrelation function  $R_e(\tau)$  of  $n_e(t)$  is easily shown to be

$$\begin{aligned} R_e(\tau) &\triangleq \langle \overline{n_e(t) n_e(t+\tau)} \rangle \\ &= J_0^4(\beta_s) P^2 \sin^2 2\beta_d R_d(\tau) + 4P \cos^2 \beta_d J_0^2(\beta_s) R_N(\tau) \\ &\quad + 4P \sin^2 \beta_d J_0^2(\beta_s) R_d(\tau) R_N(\tau) + 4R_N^2(\tau) \end{aligned} \quad (20)$$

where

$$\begin{aligned} R_d(\tau) &\triangleq \langle \overline{\hat{d}(t) \hat{d}(t+\tau)} \rangle = \int_{-\infty}^{\infty} S_d(f) |G(j2\pi f)|^2 e^{j2\pi f\tau} df \\ R_N(\tau) &\triangleq \overline{\hat{N}_c(t) \hat{N}_c(t+\tau)} = \overline{\hat{N}_s(t) \hat{N}_s(t+\tau)} \\ &= \frac{N_0}{2} \int_{-\infty}^{\infty} |G(j2\pi f)|^2 e^{j2\pi f\tau} df. \end{aligned} \quad (21)$$

The equivalent noise power spectral density at the origin is then

$$\begin{aligned} N_e &\triangleq 2 \int_{-\infty}^{\infty} R_e(\tau) d\tau \\ &= 2J_0^4(\beta_s) P^2 \sin^2 2\beta_d S_d(0) + 4N_0 P \cos^2 \beta_d J_0^2(\beta_s) \\ &\quad + 4N_0 P \sin^2 \beta_d J_0^2(\beta_s) \int_{-\infty}^{\infty} S_d(f) |G(j2\pi f)|^4 df \\ &\quad + 2N_0^2 \int_{-\infty}^{\infty} |G(j2\pi f)|^4 df. \end{aligned} \quad (22)$$

ORIGINAL PAGE IS  
OF POOR QUALITY

Letting

$$K_L = \frac{\int_{-\infty}^{\infty} |G(j 2\pi f)|^4 df}{\int_{-\infty}^{\infty} |G(j 2\pi f)|^2 df}$$

$$K_D = \frac{\int_{-\infty}^{\infty} S_d(f) |G(j 2\pi f)|^4 df}{\int_{-\infty}^{\infty} S_d(f) |G(j 2\pi f)|^2 df} \quad (23)$$

and making use of (8) and (14), we can rewrite (22) as

$$N_e = 4 N_0 P \left\{ \frac{1}{2} \left( \frac{PT}{N_0} \right) J_0^4(\beta_s) \sin^2 2\beta_d \left( \frac{S_d(0)}{T} \right) + J_0^2(\beta_s) \left[ \cos^2 \beta_d + D_m K_D \sin^2 \beta_d \right] + \frac{K_L}{\rho_i} \right\} \quad (24)$$

where, in addition, we have defined

$$\rho_i = \frac{2P}{N_0 B_i} \quad (25)$$

as the signal-to-noise ratio in the arm filter bandwidth.

#### 4.0 EFFECTIVE LOOP SIGNAL-TO-NOISE RATIO AND TRACKING PHASE JITTER

From the loop equation of operation in (13), we can see that the effective loop signal-to-noise ratio is given by

$$\rho_e = \frac{J_0^4(\beta_s) (D_m \sin^2 \beta_d - \cos^2 \beta_d)^2}{N_e B_L}, \quad (26)$$

where  $B_L$  is the single-sided loop tracking bandwidth (typically 200 Hz for the S-band network transponder). Substituting (24) into (26) and simplifying results in

$$\rho_e = \frac{\rho}{4} S_L; \quad \rho = \frac{P}{N_0 B_L} \quad (27)$$

where  $S_L$  is the loop "squaring loss" defined by

$$S_L = \frac{J_0^4(\beta_s) (D_m \sin^2 \beta_d - \cos^2 \beta_d)^2}{J_0^2(\beta_s) [\cos^2 \beta_d + D_m K_D \sin^2 \beta_d] + \frac{K_L}{\rho_i} + R_d J_0^4(\beta_s) \frac{\sin^2 2\beta_d}{2} \left( \frac{S_d(0)}{T} \right)} \quad (28)$$

and  $R_d \triangleq PT/N_0$  is the data signal-to-noise ratio. The comparable result for operation in the PSK (data only) mode can be obtained from (28) by letting  $\beta_s = 0$  and  $\beta_d = \pi/2$ , namely [1],

$$S_L = \frac{D_m^2}{D_m K_D + \frac{K_L}{\rho_i}} \quad (29)$$

Again, for Manchester coded data and single-pole Butterworth arm filters, we have that  $S_d(0) = 0$  and  $K_L = 1/2$ . Thus, (28) simplifies to

$$S_L = \frac{J_0^4(\beta_s) (D_m \sin^2 \beta_d - \cos^2 \beta_d)^2}{J_0^2(\beta_s) [\cos^2 \beta_d + D_m K_D \sin^2 \beta_d] + \frac{1}{2\rho_i}} \quad (30)$$

What remains is to characterize the tracking phase jitter performance. In the linear region (high loop signal-to-noise ratio), the mean-squared phase jitter  $\sigma_{2\varphi}^2$  of the loop phase error  $2\varphi$  is given by

$$\sigma_{2\varphi}^2 = \frac{1}{\rho_e} = \frac{4}{\rho S_L} \quad (31)$$

Since the demodulation reference for the data and ranging signals is at  $\omega_0$  rather than  $2\omega_0$ , then the jitter which degrades the power in these components has variance

$$\sigma_{\varphi}^2 = \frac{1}{4} \sigma_{2\varphi}^2 = \frac{1}{\rho S_L} \quad (32)$$

## 5.0 RANGING CHANNEL PERFORMANCE CHARACTERISTICS

### 5.1 Data Modulation On

The ranging subcarrier with its tone modulation is extracted from the input signal plus noise by demodulating this input with the

in-phase reference ( $r_c(t)$ ) generated by the loop in a wideband phase detector and then bandpass filtering the output of this detector (see Figure 1). The signal and noise components at the filter output are obtained from (4), (5) and (6), and are given by

$$\begin{aligned}
 y(t) &= K_m \left\{ \sqrt{2P} \cos \beta_d \cos (\omega_0 t + \theta) [2J_1(\beta_s) \sin (\omega_{sc} t + \theta_r(t))] \right. \\
 &\quad \left. + \sqrt{2} [\hat{N}_c(t) \cos (\omega_0 t + \theta) - \hat{N}_s(t) \sin (\omega_0 t + \theta)] \right\} \sqrt{2} K_1 \cos (\omega_0 t + \hat{\theta}) \\
 &= K_1 K_m \left\{ 2 \sqrt{P} \cos \beta_d J_1(\beta_s) \cos \varphi \sin (\omega_{sc} t + \theta_r(t)) \right. \\
 &\quad \left. + \hat{N}_c(t) \cos \varphi - \hat{N}_s(t) \sin \varphi \right\}, \quad (33)
 \end{aligned}$$

where the "hat" now denotes filtering by the ranging channel bandpass filter (bandwidth equal to  $B_r$ ). Thus, the signal power into the ranging channel is

$$P_r = 2P \cos^2 \beta_d J_1^2(\beta_s) \overline{\cos^2 \varphi} \quad (34)$$

and the corresponding noise power is

$$N_r = N_0 B_r. \quad (35)$$

From Chapter 2 of [3], we have that

$$\overline{\cos^2 \varphi} = \frac{1 + \overline{\cos 2\varphi}}{2} = \frac{1}{2} \left[ 1 + \frac{I_2(\rho S_L)}{I_0(\rho S_L)} \right]. \quad (36)$$

Furthermore, since

$$I_2(x) = I_0(x) - \frac{2}{x} I_1(x), \quad (37)$$

(36) simplifies to

$$\overline{\cos^2 \varphi} = 1 - \frac{1}{\rho S_L} \left[ \frac{I_1(\rho S_L)}{I_0(\rho S_L)} \right] \quad (38)$$

or, for large  $\rho S_L$ ,

$$\overline{\cos^2 \varphi} \approx 1 - \frac{1}{\rho S_L}. \quad (39)$$

ORIGINAL PAGE IS  
OF POOR QUALITY

Note from (34) that, as the value of  $\beta_d$  is increased beyond its critical value, the carrier becomes more suppressed and thus the Costas loop tends to track better. However, as  $\beta_d$  is increased,  $\cos \beta_d$  decreases and thus the power in the ranging channel  $P_r$  tends to decrease because of this. Since the power in the ranging channel is proportional to both  $\cos^2 \beta_d$  and the accuracy of Costas loop tracking (through the factor  $\cos^2 \varphi$ ), a tradeoff exists with regard to the selection of the data modulation index.

## 5.2 Data Modulation Off

When the data modulation is removed, i.e.,  $\beta_d = 0$ , then as previously mentioned, the loop will now lock up around  $\varphi = \pi/2$  (as opposed to  $\varphi = 0$ ). This is equivalent to saying that the in-phase and quadrature demodulation reference signals switch roles. Thus, since the ranging subcarrier component in the input signal  $s(t, \theta)$  is now demodulated by the quadrature carrier reference signal, then from (34), we have that (for large loop signal-to-noise ratio)  $P_r \approx 0$ . The conclusion to be reached then is that, in order to extract range information as in Figure 1, the data modulation cannot be turned off at the transmitter.

## 6.0 PM VERSUS PSK THRESHOLD TRACKING PERFORMANCE

Tracking threshold is typically specified as the minimum input signal level for which the mean time to loss of lock is greater than or equal to 10 seconds. This condition is uniquely specified by the loop signal-to-noise ratio or, equivalently,  $\sigma_2 \varphi$ . Thus, two modes of operation, e.g., PM and PSK, will have identical tracking thresholds if the total power-to-noise ratio  $P/N_0$  is adjusted in one relative to the other to produce the same  $\sigma_2 \varphi$  in both.

Using (29), (30) and (31), one can determine in accordance with the above equivalence the additional  $P/N_0$  required in the PM mode to produce the same tracking threshold as for PSK operation. Letting  $P'/N_0$  ( $> P/N_0$ ) denote the power-to-noise ratio required in the PM mode, then,

$$\frac{P}{4 N_0 B_L} \left[ \frac{D_m^2}{D_m K_D + \frac{N_0 B_i}{4 P}} \right] = \frac{P'}{4 N_0 B_L} \left[ \frac{J_0^4(\beta_s) (D_m \sin^2 \beta_d - \cos^2 \beta_d)^2}{J_0^2(\beta_s) [\cos^2 \beta_d + D_m K_D \sin^2 \beta_d] + \frac{N_0 B_i}{4 P'}} \right] \quad (40)$$



Solving for  $P'/N_0$  in terms of  $P/N_0$  gives the quadratic equation

$$A(P'/N_0)^2 + B(P'/N_0) + C = 0, \quad (41)$$

where

$$\begin{aligned} A &= J_0^4(\beta_s) [D_m \sin^2 \beta_d - \cos^2 \beta_d]^2 \\ B &= -J_0^2(\beta_s) [\cos^2 \beta_d + D_m K_D \sin^2 \beta_d] \left( \frac{P}{N_0} \right) \left[ \frac{D_m^2}{D_m K_D + \frac{N_0 B_i}{4P}} \right] \\ C &= -\frac{N_0 B_i}{4P} \left( \frac{P}{N_0} \right)^2 \left[ \frac{D_m^2}{D_m K_D + \frac{N_0 B_i}{4P}} \right]. \end{aligned} \quad (42)$$

The solution to (41) is well known to be

$$P'/N_0 = -\frac{B}{2A} + \sqrt{\left(\frac{B}{2A}\right)^2 - \frac{C}{A}}. \quad (43)$$

Note that, if arm filter degradations are ignored, i.e.,  $D_m = K_D \approx 1$  (corresponding to  $B_i \rightarrow \infty$ ), then

$$\frac{P'}{N_0} = \left( \frac{P}{N_0} \right) \frac{\left( \frac{4P}{N_0 B_i} \right)}{2J_0^2(\beta_s) \cos^2 2\beta_d} \left[ 1 + \sqrt{1 + 4 \cos^2 2\beta_d \left( \frac{1 + \frac{4P}{N_0 B_i}}{\left( \frac{4P}{N_0 B_i} \right)^2} \right)} \right] \quad (44)$$

which is bounded below by

$$\frac{P'}{N_0} = \frac{P/N_0}{J_0^2(\beta_s) |\cos 2\beta_d|} \quad \text{for} \quad \frac{2P}{N_0 B_i} \ll 1 \quad (45)$$

and bounded above by

$$\frac{P'}{N_0} = \frac{P/N_0}{J_0^2(\beta_s) \cos^2 2\beta_d} \quad \text{for} \quad \frac{2P}{N_0 B_i} \gg 1. \quad (46)$$

## 7.0 APPLICATION TO THE S-BAND NETWORK TRANSPONDER DESIGN

The baseline design of the S-band network transponder under development by TRW calls for  $\beta_s = 1.0$  rad and  $\beta_d = 1.1$  rad. Performance tests on the engineering model, as reported in the network transponder CDR package [4], reveal the following tracking threshold signal levels in the PSK mode (through TDRS):

Table 2

<u>Data Rate</u>	<u>Temperature</u>	<u>Signal Level</u>
Low Data Rate (32 kbps uncoded or 96 ksps coded)	70°F	-104.2 dBm
	120°F	-102.4 dBm
	-20°F	-104.2 dBm
High Data Rate (72 kbps uncoded or 216 ksps coded)	70°F	-103.7 dBm
	120°F	-101.4 dBm
	-20°F	(SSP will not hold lock -100. dBm)

The input noise power spectral density is -151 dBm/Hz. Thus, the maximum measured  $P/N_0$  is 48.6 for the low rate and 49.6 for the high rate modes. Assuming these threshold values of  $P/N_0$  for PSK operation through the TDRS, Table 3 tabulates the values of various system parameters leading up to the calculation of  $P'/N_0$  from (43). Also indicated in the table is the dB increase in power-to-noise ratio required to go from the PSK to the PM mode through the TDRS.

Table 4 illustrates the power-to-noise ratio  $P_r/N_0$  in the ranging channel [as computed from (34)] for the same parameters as in Table 3 and operation in the PM mode.

## 8.0 PERFORMANCE AS A FUNCTION OF DATA AND RANGING MODULATION INDICES

The tracking threshold of the Costas loop when operating in the PM mode can be reduced (relative to that in the PSK mode) by reducing the ranging modulation index  $\beta_s$  and/or increasing the data modulation index  $\beta_d$  (i.e., suppressing the carrier more). Unfortunately, however, both of these changes also reduce the power-to-noise ratio in the ranging channel. To see these effects quantitatively, Figure 2 illustrates

Table 3

$P/N_0 = 48.6 \text{ dB}$ ,  $\beta_s = 1.0 \text{ rad}$ ,  $\beta_d = 1.1 \text{ rad}$

Data Rate	$K_D D_m$	$P\dot{T}/N_0 \text{ (dB)}$	$\rho_i \text{ (dB)}$	$P'/N_0 \text{ (dB)}$	$\Delta P/N_0 \text{ (dB)}$
32 kbps	0.829	3.549	-4.642	54.23	5.63
96 ksps	0.5078	-1.223	-4.642	55.01	6.41
72 kbps	0.8326	0.0267	-8.257	53.83	5.23
216 ksps	0.5166	-4.745	-8.257	54.50	5.90

Table 4

$P/N_0 = 48.6 \text{ dB}$ ,  $\beta_s = 1.0 \text{ rad}$ ,  $\beta_d = 1.1 \text{ rad}$ ,  $B_L = 200 \text{ Hz}$

Data Rate	$P_r/N_0 \text{ (dB)}$
32 kbps	43.21
96 ksps	43.97
72 kbps	42.78
216 ksps	43.41

the tracking threshold power-to-noise ratio for PM operation as a function of ranging modulation index for fixed data modulation index, and Figure 3 illustrates the ranging channel power-to-noise ratio as a function of these same parameters. The value of  $P/N_0$  for PSK operation is again chosen equal to 48.6 dB and the results are given for both uncoded and coded low data rates. We observe from Figure 2 that, as  $\beta_d$  approaches  $\pi/2$  (fully suppressed carrier), the tracking threshold becomes virtually insensitive to data rate. A similar phenomenon is observed in Figure 3 for the ranging channel power-to-noise ratio. Using the information in these curves, along with the ranging channel bandwidth and the required signal-to-noise ratio in this bandwidth turned around to the ground, one can select values of  $\beta_s$  and  $\beta_d$  to meet the additional requirements on increase in tracking threshold for PM versus PSK operation.

## 9.0 CONCLUSIONS

The operation of a Costas loop in a PM mode produces performance degradation (relative to PSK operation) because of the presence of residual carrier. This appendix has numerically evaluated such degradation for parameters of interest on the Shuttle S-band uplink. The corresponding performance of the ranging channel is also given as a function of these same system parameters, thus allowing the necessary tradeoffs (choice of modulation indices) to be made between such performance and that of the Costas loop when tracking under threshold conditions.

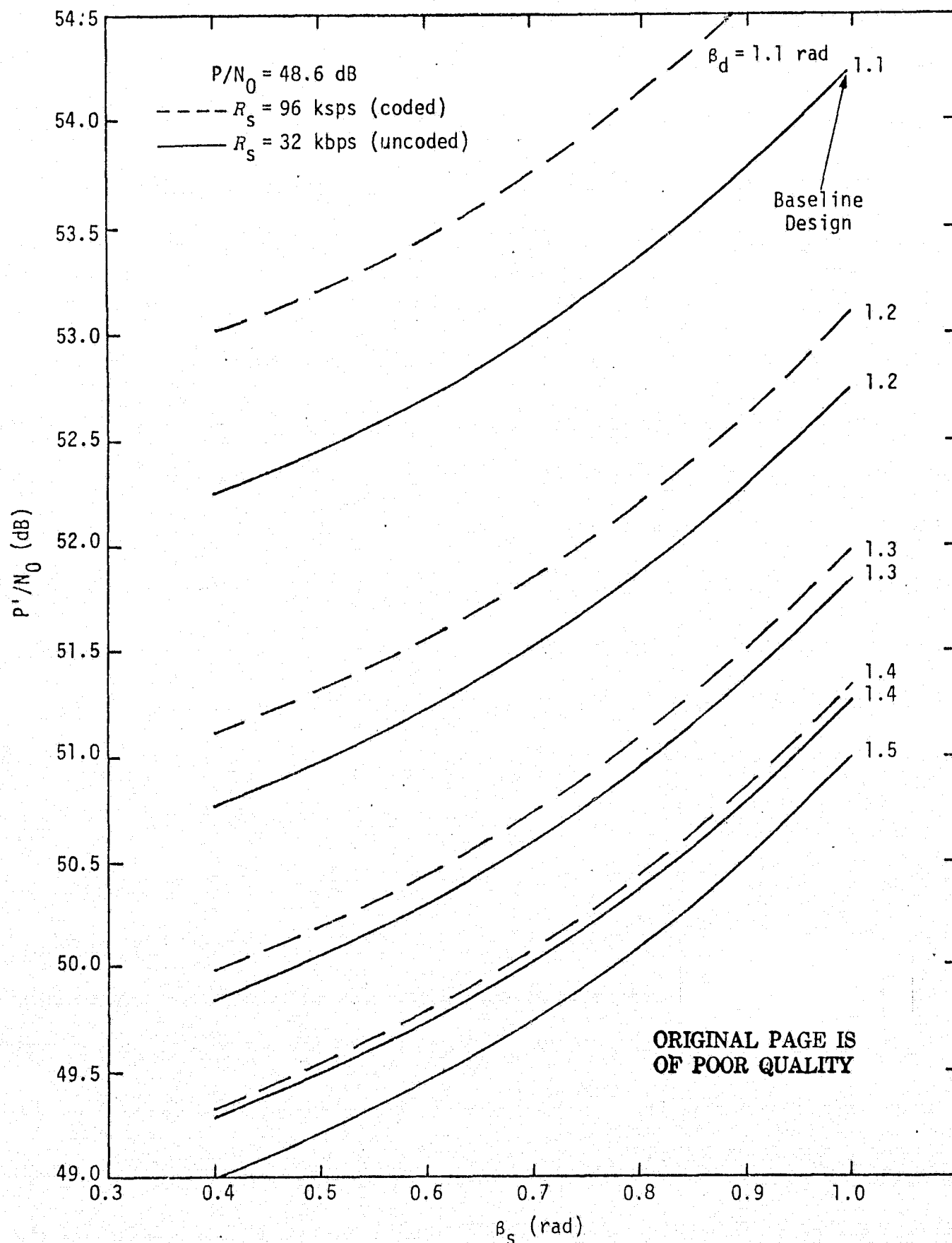


Figure 2. Tracking Threshold Power-to-Noise Ratio for PM Mode vs. Ranging Modulation Index with Data Modulation Index as a Parameter

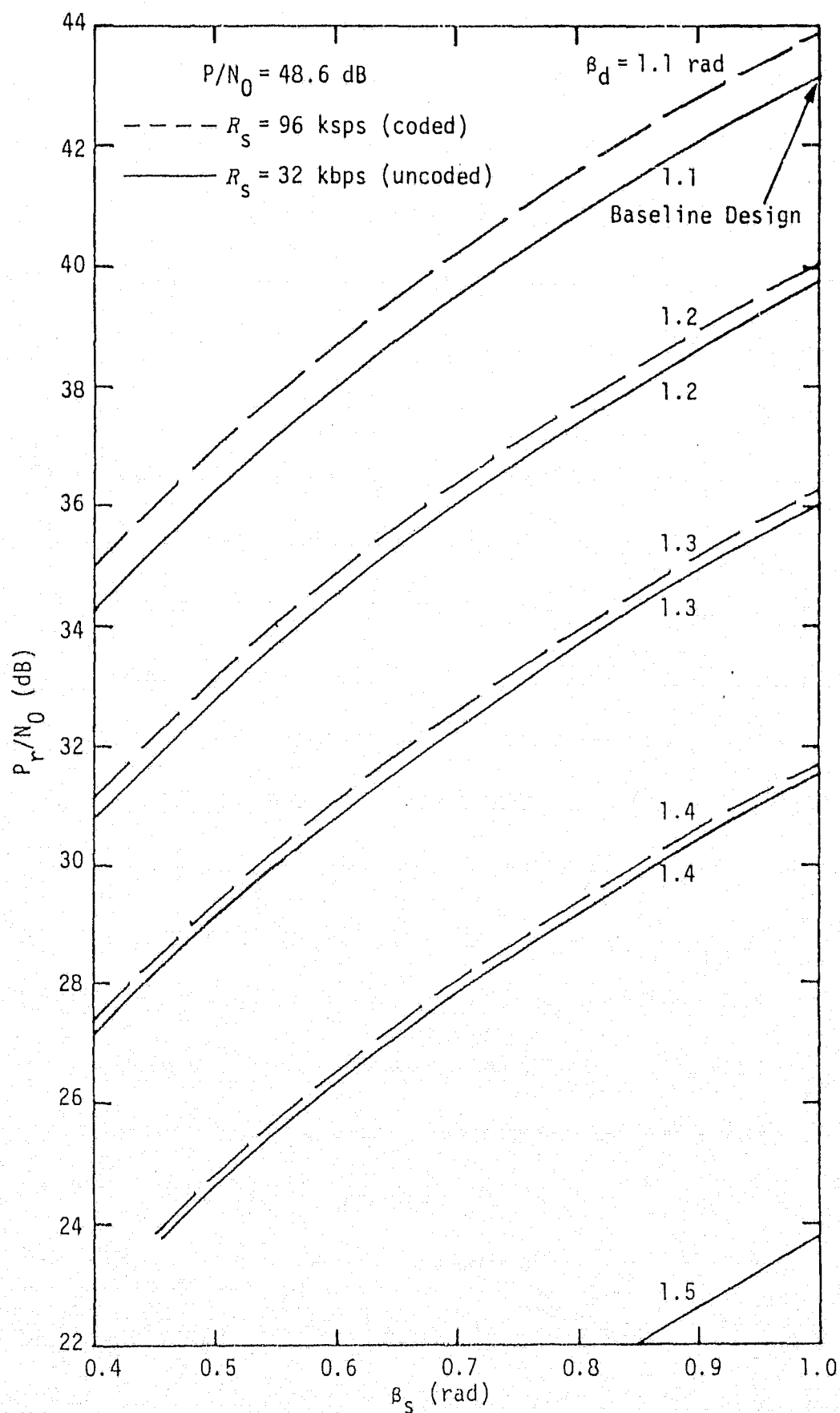


Figure 3. Ranging Channel Power-to-Noise Ratio Versus Ranging Modulation Index with Data Modulation Index as a Parameter

## REFERENCES

1. W. C. Lindsey and M. K. Simon. "Optimum Performance of Suppressed Carrier Receivers with Costas Loop Tracking," IEEE Transactions on Communications, Vol. COM-25, No. 2, February 1977, pp. 215-226.
2. M. K. Simon and W. K. Alem. "Tracking Performance of Unbalanced QPSK Demodulators: Part I - Biphase Costas Loop with Passive Arm Filters," Axiomatix Report No. R7707-5, July 29, 1977.
3. W. C. Lindsey and M. K. Simon. Telecommunication Systems Engineering. Prentice-Hall, 1973.
4. "Shuttle Communications and Tracking Equipment by TRW for Rockwell International/NASA: Monthly Review, Network Transponder CDR," November 15-18, 1977, TRW Systems Group, Redondo Beach, California.